

**Design of First-Row Metal Catalysts Featuring Bifunctional [SNS]-Pincer Ligands:  
Challenging the Conventions of Metal-Ligand Cooperative Catalysis**

By

**Matthew Elsby**

Thesis Submitted to the University of Ottawa  
in Partial Fulfillment of the Requirements for the  
Degree of Doctor of Philosophy  
Department of Chemistry and Biomolecular Sciences  
University of Ottawa

## DECLARATION OF CO-AUTHORSHIP AND PREVIOUS PUBLICATIONS

I hereby declare that this dissertation incorporates material that is a result of joint research as follows: this dissertation contains six chapters, of which five chapters have been previously published in seven peer-reviewed journals. All work contained herein was performed in consultation with my supervisor, Prof. R. Tom Baker. Nearly all experimental work was carried out by me, however, some work was performed by expert collaborators. Density functional theory (DFT) calculations presented in Chapters 3 and 4 pertaining to reaction profiles of manganese catalysts were performed by Ms. Mina Son, Mr. Changjin Oh, and Prof. Mookie Baik from KAIST, Korea, and those at the beginning of Chapter 3 were performed by myself in collaboration with Prof. Stephan Steinmann from ENS Lyon, France. DFT calculations presented in Chapter 5 were performed by Mr. Aleksa Radovic and Prof. Michael Neidig from the University of Rochester, and Dr. Adiran de Aguirre and Prof. Feliu Maseras from ICIQ, Tarragona, Spain. Mr. Scott Kim, an undergraduate student under my supervision, collected cyclic voltammetry data presented in Chapter 3. Mr. Aleksa Radovic, Dr. Jeffrey Sears, and Prof. Michael Neidig collected and interpreted Mössbauer data presented in Chapter 5. Mr. Lhoussain Khrouz and Prof. Christophe Bucher from ENS Lyon, France, collected and interpreted electrochemistry and EPR data presented in Chapter 5. Dr. Massimiliano Delferro, Dr. David Kaphan, and Dr. Jeremy Kropf from Argonne National Lab, USA, collected and interpreted X-ray absorption near-edge spectroscopy (XANES) data presented in Chapter 5.

Chapter 1 contains material published from the review article “Strategies and Mechanisms of Metal-Ligand Cooperativity in First-Row Metal Complex Catalysts.” Elsby, M. R; Baker, R. T. *Chem. Soc. Rev.* **2020**, 49, 8933-8987.

Chapter 2 contains results from the communication, “Cu(I)-SNS Complexes for Outer-Sphere Hydroboration and Hydrosilylation of Carbonyls.” Elsby, M. R; Baker, R. T. *Chem. Commun.* **2019**, 55, 13574-13577.

Chapter 3 contains results from two publications: the communication “Same Ligand, Three First Row Metals: Comparing M-amido Bifunctional Reactivity (Mn, Fe, Co).” Elsby, M. R; Kim, S. Y. H; Steinmann, S. N; Baker, R. T. *Dalton Trans.* **2021**, *50*, 14542-14546; and the full article “A Mechanistic Study of Metal-Ligand Cooperativity in Mn(II)-Catalyzed Hydroborations: Hemilabile SNS Ligand Enables Metal-Hydride Free Reaction Pathway.” Elsby, M. R; Son, M; Oh, C; Martin, J; Baik, M. H; Baker, R. T. *ACS Catal.* **2021**, *11*, 9043-9051.

Chapter 4 contains results published in two full articles: “Iron-SNS and -CNS Complexes: Selective C<sub>aryl</sub>-S Bond Cleavage and Amine-Borane Dehydrogenation Catalysis.” Elsby, M. R; Ghostine, K; Das, U. K; Gabidullin, B; Baker, R. T. *Organometallics*, **2019**, *38*, 3844-3851; and “A Cooperative Mn(I)-Thiolate Complex for Photo-Catalyzed Nitrile Dihydroboration.” Elsby, M. R; Oh, C; Son, M; Kim, S. Y. H; Baik, M. H; Baker, R. T. *J. Am. Chem. Soc.* **2021**, Under Review, ja-2021-11090c.

Chapter 5 contains results published in the full article “Metal Ligand Electron Sharing Between Iron and a Redox Non-Innocent [N<sub>2</sub>S<sub>3</sub>] Ligand Scaffold.” Elsby, M. R; Radovic, A; de Aguirre, A; Khrouz, L; Sears, J. D; Gabidullin, B; Kropf, A. J; Kaphan, D. M; Delferro, M; Bucher, C; Maseras, F; Neidig, M. L; Baker, R. T. *Inorg. Chem.* **2021**, In Revision, ic-2020-038055.

I acknowledge my supervisor as a co-author in this work as he made a significant contribution to the editing and preparation of these manuscripts. I acknowledge that other listed authors on the manuscripts contributed through raw data acquisition and interpretation of results.

I declare that this is a true copy of my thesis, including any final revisions, as approved by my thesis committee and the Graduate Studies office.

## **II. Published Contributions**

All thesis publications with contributions from Matthew R. Elsby from the period of **2017-2021** appear below and are enumerated by date.

- (8) **M. R. Elsby**, A. Radovic, A. de Aguirre, L. Khrouz, J. D. Sears, B. Gabidullin, A. J. Kropf, D. M. Kaphan, M. Delferro, C. Bucher,\* F. Maseras,\* M. L. Neidig,\* R. T. Baker\* “Metal-Ligand Electron Sharing Between Iron and a Redox Non-Innocent [N<sub>2</sub>S<sub>3</sub>] Ligand Scaffold” *Inorg. Chem.* In Revision, ic-2020-038055, **2021**.
- (7) **M. R. Elsby**, C. Oh, M. Son, S. Y. Kim, M. H. Baik,\* R. T. Baker\* “A Cooperative Mn-Thiolate Complex for Photo-Catalyzed Nitrile Dihydroboration.” *J. Am. Chem. Soc.*, Submitted, **2021**, ja-2021-11090c
- (6) **M. R. Elsby**, S. Y. Kim, S. N. Steinmann,\* R. T. Baker\* “Evaluating the Bifunctional Activity of Amido Donors for Metal-Ligand Cooperation Across a Series of First-Row Transition Metals (Mn, Fe, Co).” *Dalton Trans.*, **2021**, 50, 14542-14546.
- (5) **M. R. Elsby**, M. Son, C. Oh, J. Martin, M. H. Baik,\* R. T. Baker\* “A Mechanistic Study of Metal-Ligand Cooperativity in Mn(II)-Catalyzed Hydroborations: Hemilabile SNS Ligand Enables Metal Hydride-Free Reaction Pathway.” *ACS. Catal.*, **2021**, 11, 9043-9051.
- (4) **M. R. Elsby**,\* R. T. Baker\* “Strategies and Mechanisms of Metal-Ligand Cooperativity in First Row Transition Metal Complex Catalysts.” *Chem. Soc. Rev.*, **2020**, 49, 8933-8987.
- (3) A. Rochon, **M. R. Elsby**, R. T. Baker\* “Regioselective Formation of Fluorinated Metallacycles from Fluoroalkenes and an Electron-Rich Ni(0) Difluorocarbene.” *Can. J. Chem.*, **2020**, 99, 209-215.
- (2) **M. R. Elsby**, R. T. Baker\* “Cu(I)-SNS Complexes for Outer-Sphere Hydroboration and Hydrosilylation of Carbonyls.” *Chem. Commun.*, **2019**, 55, 13574-13577.
- (1) **M. R. Elsby**, K. Ghostine, U. K. Das, B. Gabidullin, R. T. Baker\* “Iron-SNS and -CNS Complexes: Selective C<sub>aryl</sub>-S Bond Cleavage and Amine-Borane Dehydrogenation Catalysis.” *Organometallics*, **2019**, 38(19), 3844-3851.

## ABSTRACT

A cooperative ligand is defined as one which actively participates in substrate activation to facilitate catalysis with a metal ion in a synergistic fashion. This dissertation focuses on the synthesis and catalytic activity of base-metal complexes with cooperative SNS pincer ligands to explore unconventional reaction pathways that are a consequence of diverging from traditional phosphine-based ligands.

Two new NHC–Cu(I)-[ $\kappa^2$ -SNS] complexes were synthesized to directly compare the bifunctional catalytic activity between the two SNS ligands. The Cu thiolate complex catalyzed ketone hydroboration but not hydrosilylation, while the Cu amido complex is a high-performing carbonyl reduction catalyst boranes and silanes, through a conventional outer-sphere mechanism.

The bifunctional reactivity of three  $M[S^{Me}NS^{Me}]_2$  complexes was computationally assessed by comparing the nucleophilicity of the M–N<sub>amido</sub> donor (M = Mn, Fe, Co), and the Mn analogue was identified as the most promising catalyst candidate. A combined experimental and mechanistic study of the chemoselective hydroboration of carbonyls by  $Mn[S^{Me}NS^{Me}]_2$  follows. The catalyst allows for room temperature hydroboration of carbonyls at low catalyst loadings (0.1 mol%) and reaction times (<30 min). Mechanistic studies highlight the significance of bifunctional amido bis(thioether) ligand to the success of the reaction. DFT calculations showed that thioether hemilability is crucial during catalysis for providing the active coordinating site. A non-traditional inner-sphere reaction pathway with carbonyl coordination to the metal center and amido-

promoted B–H reactivity is proposed to be operative, as opposed to the traditional metal-hydride pathway enabled by phosphine-based bifunctional ligands.

The manganese(I)-thiolate complex  $\text{Mn}(\kappa^3\text{-S}^{Me}\text{NS})(\text{CO})_3$  is an active precatalyst for the photo-catalyzed dihydroboration of nitriles. Reaction optimization studies revealed that catalysis requires the presence of UV light to enter and remain in the catalytic cycle. Stoichiometric mechanistic studies showed that HBpin borylates the imine  $\text{N}=\text{C}$  of the ligand backbone in the absence of nitrile, forming an inactive off-cycle by-product. Isotopic labeling studies with  $^{13}\text{C}$ O revealed that the catalyst resting state features a single CO ligand coordinated to the Mn center. DFT calculations showed that the bifunctional thiolate donor, coordinative flexibility of the  $\text{S}^{Me}\text{NS}$  ligand, and access to an open-shell intermediate are all crucial to accessing low-energy intermediates during catalysis.

The electronic structure of a  $\text{Fe}[\text{N}_2\text{S}_3]$  complex was investigated in detail. Cyclic voltammetry and spectroelectrochemistry studies show a reversible oxidation and reduction to stable species. The anionic redox partner of  $\text{Fe}[\text{N}_2\text{S}_3]$  was synthesized and characterized by X-ray diffraction, Mössbauer spectroscopy, and X-ray absorption techniques along with  $\text{Fe}[\text{N}_2\text{S}_3]$ . Both Mössbauer and X-ray absorption near edge structure (XANES) data indicated a ligand-based reduction and DFT studies of the Zn analogs allowed us to propose a new bonding scheme for the reduced ligand. Redox interconversions in these complexes are dominated by changes in electron population in the  $\text{N}_2\text{S}_3$  ligand, and intimate mixing with the Fe  $d_{xy}$  orbital due to a high degree of covalency.

## ACKNOWLEDGEMENTS

Prof. Baker; for your endless support and belief in me; for your infectious enthusiasm which always sustained my passion and motivation; for your mentorship and lessons – both personal and research related; for your forgetfulness when you recommended an experiment that would send me down a rabbit hole; for your encouragement in pursuing opportunities and collaborations to improve myself; and finally, for being a person I will always strive to emulate.

Manar; for always having an open-door policy despite the distance of the past four years; for all the advice and mentorship you have given me the past seven years; for your encouragement and belief in me when I doubted my potential; and for remaining the epitome of an ideal friend and colleague.

Behnaz; for your guidance in future career steps; for your valuable comments and perspective on my work; and for always keeping a fresh pot of coffee.

Scott; for your excitement to learn which reignited my own passion towards the end of my doctoral studies; for teaching me how to be a good mentor and keeping me accountable; for being the absolute ideal undergraduate mentee in all respects; for the croissants, coffee, and of course...sandwiches.

My mother, Maria; for the many visits over the years; for the donuts and copious amounts of tea which fueled me; for your loving encouragement since I left home; for your unselfish understanding as I frequently put work first; and for your unconditional presence as a pillar of support in my life.

My father, Rick; for your trust in me as I pursued a long-dreamt goal; for your skepticism always keeping me alert and accountable; for your rational and pragmatic advice; for your understanding when I was hard to reach; and for your unconditional presence as a pillar of support in my life.

The Cobalt; for all the loving pigeon coos; for the endless entertainment; for motivating me to get into cobalt chemistry; and for the weekend morning cuddles.

Alexe; for your patience as I frequently (endlessly) obsessed about my chemistry; for all the music-filled road trips, the endless adventures, and memories you have given me these past three years; for your tolerance of my stupidity, poor singing, and random cooking cravings; for all the eye rolls and telling facial expressions; and finally, simply for your presence, which has been my best source of calm amidst chaos.

Thank you to all.

## TABLE OF CONTENTS

<b>DECLARATION OF CO-AUTHORSHIP AND PREVIOUS PUBLICATIONS</b> .....	ii
<b>ABSTRACT</b> .....	v
<b>ACKNOWLEDGEMENTS</b> .....	vii
<b>LIST OF TABLES</b> .....	xiii
<b>LIST OF FIGURES</b> .....	xiv
<b>LIST OF SCHEMES</b> .....	xvii
<b>LIST OF APPENDICES</b> .....	xx
<b>LIST OF ABBREVIATIONS/SYMBOLS</b> .....	xxi
<b>Chapter 1 – Towards Sustainable Bifunctional SNS Ligands for First-Row Metal Complex Catalysts Using Metal-Ligand Cooperativity</b> .....	1
1.1 General Introduction .....	1
1.2 Homogeneous Catalysis .....	2
1.2.1 Moving from precious to base metals .....	2
1.3 Bifunctional Ligands for Metal-Ligand Cooperative Catalysis .....	5
1.3.1 Ligand acts as a Lewis base .....	7
1.3.1.1 Nitrogen based ligands .....	8
1.3.1.1.1 De(hydrogenation) catalysis .....	8
1.3.1.1.2 E–H bond activations (E = B, Si): hydroboration & hydrosilylation.....	15
1.3.1.2 Sulfur based ligands .....	20
1.3.1.3 Oxygen based ligands .....	25
1.3.1.4 Carbon based ligands .....	27
1.3.2 Ligand acts as a Lewis acid.....	29
1.3.2.1 Boron acceptors .....	30
1.3.3 Aromatization / dearomatization.....	34
1.3.4 Redox active ligands .....	40
1.3.4.1 Enhancing Lewis acidity/basicity .....	42

1.3.4.2 Redox active ligand as electron reservoir .....	43
1.4 Towards Sustainable Ligand Development .....	48
1.4.1 Motivation for [SNS] ligands.....	48
1.4.2 Previous work with nitrogen and sulfur containing pincer ligands.....	48
1.4.3 Two [SNS] ligands with different bifunctional donors .....	49
1.4.4 Reactivity of an SNS-thiolate ligand .....	50
1.4.5 Reactivity of an SNS-amido ligand .....	52
1.5 Scope of Thesis .....	54
1.6 References.....	56
<b>Chapter 2 – Comparing the SNS Thiolate and Amido Ligands: Cu(I) SNS Complexes for Outer-Sphere Hydroboration and Hydrosilylation of Carbonyls.....</b>	<b>72</b>
2.1 Introduction.....	72
2.2 Results and Discussion .....	74
2.2.1 Synthesis of copper complexes .....	74
2.2.2 Amido vs. thiolate for bifunctional reactivity .....	76
2.2.3 Mechanistic studies of Cu-catalyzed hydroboration .....	79
2.3 Conclusions.....	81
2.4 Experimental .....	82
2.4.1 Materials and methods .....	82
2.4.2 Synthesis and characterization of copper complexes.....	82
2.4.3 Catalytic and mechanistic studies .....	85
2.4.4 Key spectroscopic data .....	89
2.4.5 Single crystal X-ray diffraction data .....	90
2.5 References.....	92
<b>Chapter 3 – Comparing Amido Bifunctional Reactivity Across Base Metals and Associated Mechanistic Study of Metal-Ligand Cooperativity in Mn(II) Catalyzed Hydroborations .....</b>	<b>97</b>
3.1 Introduction.....	97
3.1.1 Significance of Mn(SNS) <sub>2</sub> catalyst .....	97
3.2 Results and Discussion .....	101

3.2.1 Synthesis of manganese complexes .....	101
3.2.2 A computational comparison of bifunctional potential across Mn, Fe, and Co .....	103
3.2.3 Exploring potential hemilability .....	107
3.2.4 Hydroboration catalysis .....	108
3.2.5 Variable time normalization analysis of kinetic data .....	110
3.2.6 Mechanistic studies of Mn(II)-catalyzed hydroboration.....	111
3.2.6.1 Experimental mechanistic studies.....	111
3.2.6.2 Computational mechanistic studies.....	115
3.3 Conclusions.....	119
3.4 Experimental.....	122
3.4.1 Materials and methods .....	122
3.4.2 Synthesis and characterization of manganese complexes.....	123
3.4.3 Catalytic, kinetic, and mechanistic studies .....	124
3.4.4 Key spectroscopic data .....	130
3.4.5 Single crystal X-ray diffraction data.....	132
3.4.6 Details of DFT calculations .....	133
3.5 References.....	137
<b>Chapter 4 – Avoiding C<sub>aryl</sub>-S Bond Cleavage in the Design of a Cooperative Mn(I)-Thiolate Complex for Photo-Catalyzed Nitrile Dihydroboration.....</b>	<b>146</b>
4.1 Introduction.....	146
4.2 Results and Discussion .....	150
4.2.1 Design of mono-ligated Fe-SNS-thiolate complexes.....	150
4.2.2 Synthesis of manganese complex .....	152
4.2.3 Catalytic nitrile dihydroboration.....	153
4.2.4 Mechanistic studies of Mn-catalyzed nitrile dihydroboration .....	156
4.2.4.1 Photoexcitation and carbonyl ligand dissociation.....	156
4.2.4.2 Catalytic cycle for nitrile dihydroboration.....	160
4.3 Conclusions.....	164
4.4 Experimental.....	166
4.4.1 Materials and Methods.....	166

4.4.2 Synthesis and characterization of iron and manganese complexes.....	167
4.4.3 Catalytic and mechanistic studies .....	169
4.4.4 Key spectroscopic data .....	175
4.4.5 Single crystal X-ray diffraction data .....	177
4.4.6 Details of DFT calculations .....	178
4.4.6.1 DFT figures.....	180
4.5 References.....	183
<b>Chapter 5 – Highly Covalent Metal-Ligand Electron Sharing in Redox Non-Innocent Iron [N<sub>2</sub>S<sub>3</sub>] Complexes.....</b>	<b>194</b>
5.1 Introduction.....	194
5.2 Results and Discussion .....	199
5.2.1 Electrochemical studies.....	199
5.2.3 Synthesis of anion partner and metrical analysis .....	203
5.2.4 Mössbauer and XANES .....	205
2.2.3 DFT investigation: ground states, orbital occupancies, and molecular orbitals .....	208
5.3 Conclusions.....	215
5.4 Experimental .....	217
5.4.1 Materials and methods .....	217
5.4.1.1 Electrochemistry and EPR .....	218
5.4.1.2 <sup>57</sup> Fe Mössbauer spectroscopy.....	219
5.4.1.4 X-ray absorption near-edge spectroscopy (XANES).....	219
5.4.2 Synthesis and characterization of iron complexes .....	220
5.4.3 Single crystal X-ray diffraction data .....	222
5.4.4 Details of DFT data.....	223
5.5 References.....	225
<b>Chapter 6 – Conclusions and Future Work .....</b>	<b>232</b>
6.1 Key Findings and Contributions to the Overall Field and Connecting the Chapters .....	232
6.2 Critical Evaluation of Research Approach and Methodology .....	238
6.3 Recent Advancements and Future Directives .....	240

6.4 References.....	246
<b>APPENDICES</b> .....	249
Appendix A – Chapter 2 .....	249
Appendix B – Chapter 3 .....	263
Appendix C – Chapter 4 .....	294
Appendix D – Chapter 5 .....	308
Appendix E – Copyright Permission .....	326
<b>VITA AUCTORIS</b> .....	327

## LIST OF TABLES

<b>Table 2.1.</b> Substrate scope of hydroboration and hydrosilylation reactions of carbonyls with catalytic <b>2.1<sub>Cu</sub></b> and <b>2.2<sub>Cu</sub></b> . <sup>a</sup> Conditions: Copper catalyst (1 mol%), room temperature, 5-15 min. All reactions gave quantitative conversion. <sup>b</sup> Yield was determined from <sup>1</sup> H NMR integration relative to internal standard mesitylene. ....	78
<b>Table 4.1</b> Optimization of reaction conditions.....	154
<b>Table 4.2.</b> Catalytic nitrile dihydroboration with <b>4.1<sub>Mn</sub></b> . ....	156
<b>Table 5.1.</b> Ground state and spin density DFT calculations (kcal/mol) on <b>5.1<sub>Fe</sub></b> , <b>5.1<sub>Fe</sub><sup>-</sup></b> , and <b>5.1<sub>Fe</sub><sup>+</sup></b> . ....	208

## LIST OF FIGURES

<b>Figure 1.1.</b> Prominent examples of homogeneous catalysts based upon precious metals.....	3
<b>Figure 1.2.</b> Unique reaction strategies enabled by the first-row metals.....	5
<b>Figure 1.3.</b> Different modes of metal-ligand cooperativity. ....	7
<b>Figure 1.5.</b> Three MLC methods for redox-active ligands in catalysis.....	41
<b>Figure 1.5.</b> Examples of reported catalytic reactions facilitated by Fe[PDI][N <sub>2</sub> ] <sub>2</sub> (1.76).....	46
<b>Figure 2.1.</b> ORTEP depiction of the solid-state molecular structures of (A) <b>2.1</b> <sub>Cu</sub> : Selected bond lengths (Å): Cu(1)-S(1) 2.4820(14), Cu(1)-N(3) 1.948(2), Cu(1)-C(16) 1.919(3); (B) <b>2.2</b> <sub>Cu</sub> : Selected bond lengths (Å): Cu(1)-S(1) 2.1802(8), Cu(1)-N(3) 2.130(2), Cu(1)-C(15). ....	75
<b>Figure 2.2.</b> Stacked plot of <sup>1</sup> H NMR spectra showing stoichiometric conversion from A) <b>2.1</b> <sub>Cu</sub> to B) Cu–H intermediate, and C) subsequent conversion to hydroboration product, reforming <b>2.1</b> <sub>Cu</sub> .....	89
<b>Figure 2.3.</b> <sup>1</sup> H NMR spectrum of reaction of <b>2.1</b> <sub>Cu</sub> with DBpin. ....	89
<b>Figure 2.4.</b> <sup>2</sup> H NMR spectrum of reaction of <b>2.1</b> <sub>Cu</sub> with DBpin. ....	90
<b>Figure 3.1.</b> A) Recently reported Mn catalysts; B) Our current report on Mn-catalyzed hydroboration of carbonyls. ....	99
<b>Figure 3.2.</b> Energy reaction profile for H <sub>2</sub> activation across M–N <sub>amido</sub> bond in <b>3.1</b> <sub>Mn</sub> (purple), <b>3.1</b> <sub>Fe</sub> (orange), and <b>3.1</b> <sub>Co</sub> (teal). ....	106
<b>Figure 3.3.</b> Substrate scope of catalytic hydroboration of carbonyls with <b>3.1</b> <sub>Mn</sub> . Reaction conditions: pinacolborane (0.16 mmol), carbonyl (0.16 mmol), benzene (0.6 g), and <b>3.1</b> <sub>Mn</sub> (0.1 mol%) at room temperature for 5-10 min. Yields were determined from <sup>1</sup> H NMR integrals relative to mesitylene internal standard after workup. ....	110
<b>Figure 3.4.</b> VTNA of the kinetics data: (A) rate dependence on [ <b>3.1</b> <sub>Mn</sub> ]; (B) rate dependence on [5-hexene-2-one]; (C) rate dependence on [HBpin]. ....	111
<b>Figure 3.5.</b> EI-MS spectrum of crude reaction mixture of <b>3.1</b> <sub>Mn</sub> and pinacolborane showing observation of L1Bpin.....	114
<b>Figure 3.6.</b> Comparison of key reaction steps and transitions states of possible mechanisms. Gibbs free energies in kcal/mol are given in parenthesis.....	116
<b>Figure 3.7.</b> Proposed energy profile for <b>3.1</b> <sub>Mn</sub> -catalyzed carbonyl hydroboration .....	119
<b>Figure 3.8</b> Classification of mechanisms for bifunctional hydroboration of carbonyls. ....	121
<b>Figure 3.9.</b> 273 K EPR spectrum of Mn( $\kappa^3$ -S <sup>Me</sup> NS <sup>Me</sup> ) <sub>2</sub> ( <b>3.1</b> <sub>Mn</sub> ) in THF. ....	130
<b>Figure 3.10.</b> 100 K EPR spectrum of Mn( $\kappa^3$ -S <sup>Me</sup> NS <sup>Me</sup> ) <sub>2</sub> ( <b>3.1</b> <sub>Mn</sub> ) as frozen THF solution.....	131

<b>Figure 3.11.</b> Stack plot of $^{11}\text{B}$ NMR spectra of A) stoichiometric reaction of <b>3.1<sub>Mn</sub></b> with HBpin; B) reaction of <b>3.1<sub>Mn</sub></b> with 2 equiv. HBpin. * unreacted HBpin.....	131
<b>Figure 3.12.</b> DFT calculated reaction profile of Mn–H formation. ....	135
<b>Figure 3.12.</b> Possible hydroboration mechanisms after Mn–H formation. ....	136
<b>Figure 4.1.</b> A) Notable high-performing manganese catalysts featuring phosphine-based pincers; B) Recent base-metal nitrile hydroboration catalysts; C) This work: Mn-catalyzed nitrile dihydroboration using a bifunctional [SNS]-thiolate ligand. ....	148
<b>Figure 4.1.</b> NTO pairs for the excitation responsible for CO dissociation. The top two contributing transitions are described. Other contributions each contribute to less than 15%. ....	160
<b>Figure 4.2.</b> DFT-calculated energy profile for the dihydroboration of benzonitrile with catalyst <b>4.1</b> . ....	163
<b>Figure 4.3.</b> Summary of the catalytic cycle for the photodissociation and two borylation steps involved in the reaction. ....	164
<b>Figure 4.4.</b> Stack plot of $^1\text{H}$ spectra showing A) complex <b>4.1<sub>Mn</sub></b> in THF- $d_8$ , and B) reaction of <b>4.1<sub>Mn</sub></b> and 1.2 equiv. HBpin – irradiated for 30 min. # is THF.....	175
<b>Figure 4.5.</b> Stacked plot of $^{13}\text{C}\{^1\text{H}\}$ spectra showing reaction of 10 mol% $^{13}\text{C}$ -labelled <b>4.1<sub>Mn</sub>*</b> with benzonitrile and 2.2 equiv. of HBpin. (A) (Blue trace) Initial $^{13}\text{C}\{^1\text{H}\}$ spectrum of reaction mixture prior to light exposure showing unreacted <b>4.1<sub>Mn</sub>*</b> . (B) (Red trace) $^{13}\text{C}\{^1\text{H}\}$ spectrum of reaction mixture after shining light for 1 h showing disappearance of <b>4.1<sub>Mn</sub>*</b> and growth of a new species at 240 ppm. (C) (Purple trace) $^{13}\text{C}\{^1\text{H}\}$ spectrum of reaction mixture after shining light for 3 h total, showing same species at 240 ppm with appearance of free $^{13}\text{CO}$ . ....	176
<b>Figure 4.6.</b> 298 K EPR isotropic spectrum of catalytic reaction mixture after irradiation for 45 min. ....	177
<b>Figure 4.8.</b> Comparison of hydride transfer transition states differentiating formation of Mn–S–B–O metallacycle <i>vs.</i> direct boryl coordination and hydride transfer. ....	181
<b>Figure 4.9.</b> Comparison of the energy profile for the reaction under THF and benzene as the solvent.....	181
<b>Figure 4.10.</b> Comparison between <i>fac</i> - and <i>mer</i> - conformations in the turnover limiting transition state. ....	182
<b>Figure 1.</b> A) Wiegardt's Fe- $\text{L}^2$ complexes with determined ground states and proposed oxidation states. B) Five theoretical redox states of the bis( <i>o</i> -iminothioquinone) ligand ( <b>L</b> ).....	197
<b>Figure 5.2.</b> Voltammetric curves recorded under argon for <b>5.1<sub>Fe</sub></b> ( $1 \cdot 10^{-3}$ M in THF + 0.1 M tetra- <i>n</i> -butylammonium hexafluorophosphate) at (solid line) a stationary vitreous carbon working electrode ( $\varnothing = 3$ mm, $E$ vs $\text{Ag}/\text{Ag}^+$ ( $10^{-2}$ M), $v = 0.1$ V/s)	

and (dotted line) a rotating carbon disk electrode ( $\varnothing = 3$ mm, $v = 0.01$ V·s <sup>-1</sup> , 550 rd/min).....	200
<b>Figure 5.3.</b> Voltammetric curves recorded under argon for <b>5.1</b> <sub>Fe</sub> ( $1 \times 10^{-3}$ M + 0.1 TBAP in THF) at a rotating carbon disk electrode ( $\varnothing = 3$ mm, $v = 0.01$ V/s, 550 rd/min) before electrolysis (black curve), after exhaustive reduction at $(E_{ap})_1 = -900$ mV (red dashed curve) and after exhaustive oxidation at $(E_{ap})_1 = +300$ mV (blue dashed curve) (Three compartment cell, Pt gauze working electrode, 12 mL of electrolyte, duration of each electrolysis ~30 min).....	200
<b>Figure 5.4.</b> Simulated (red) and experimental (black) X-band EPR spectrum of electrogenerated <b>5.1</b> <sub>Fe</sub> <sup>+</sup> recorded at 110 K (microwave power, 6 mW; modulation amplitude, 2 G). .....	201
<b>Figure 5.5.</b> UV/Vis spectra recorded during the electrolysis (1 e- per molecule) of <b>5.1</b> <sub>Fe</sub> ( $\sim 3 \cdot 10^{-4}$ mol L <sup>-1</sup> ) at <b>A</b> ) $E_{app} = -1$ V and <b>B</b> ) $E_{app} = +0.5$ V in THF (0.1 M TBAP) (working electrode : Pt, $l = 1$ mm).....	202
<b>Figure 5.6.</b> Bond distances (Å) for <b>A</b> ) Wieghardt's dimer (R = <i>t</i> -Bu), <b>B</b> ) [Fe(□-N <sub>2</sub> S <sub>2</sub> ) <sub>2</sub> ], <b>C</b> ) <b>5.1</b> <sub>Fe</sub> and <b>D</b> ) <b>5.1</b> <sub>Fe</sub> <sup>-</sup> .....	205
<b>Figure 5.7.</b> Mössbauer spectra of <b>A</b> ) solid [Fe(□-N <sub>2</sub> S <sub>2</sub> ) <sub>2</sub> ] dimer, <b>B</b> ) solid Fe-57-labeled <b>5.1</b> <sub>Fe</sub> , <b>C</b> ) frozen solution of Fe-57-labeled <b>5.1</b> <sub>Fe</sub> <sup>-</sup> and <b>D</b> ) solid <b>5.1</b> <sub>Fe</sub> <sup>-</sup> . Spectrum of <b>B</b> contains several unidentified impurities in addition to some Fe(□-N <sub>2</sub> S <sub>2</sub> ) <sub>2</sub> dimer (blue) and that of <b>C</b> contains ca. 12% of a high-spin Fe(II) impurity (green trace). .....	206
<b>Figure 5.8.</b> Fe/K edge XANES spectra of neutral ( <b>5.1</b> <sub>Fe</sub> ; purple dotted line) and anionic ( <b>5.1</b> <sub>Fe</sub> <sup>-</sup> ; blue solid line) Fe[N <sub>2</sub> S <sub>3</sub> ] complexes.....	207
<b>Figure 5. 9.</b> Calculated bond distances (Å) for <b>A</b> ) <b>5.1</b> <sub>Fe</sub> <sup>+</sup> <b>B</b> ) <b>5.1</b> <sub>Fe</sub> and <b>C</b> ) <b>5.1</b> <sub>Fe</sub> <sup>-</sup> . 211	
<b>Figure 5.10.</b> Optimized structures of Zn complexes of reduced N <sub>2</sub> S <sub>2</sub> ligands.....	212
<b>Figure 5.11.</b> Alternate depiction of reduced bis(N,S-phenylene) ligands, (L•) <sup>3-</sup> ( <b>A</b> ) and (L) <sup>4-</sup> ( <b>B</b> ). .....	213
<b>Figure 5.12.</b> Calculated β-FMO energy diagrams for all complexes and selected orbital depictions.....	214

## LIST OF SCHEMES

<b>Scheme 1.1.</b> Reaction pathway for catalytic hydrogenation of ethylene with Wilkinson's catalyst, highlighting the 2 electron redox changes enabled by oxidative addition / reductive elimination. ....	3
<b>Scheme 1.2.</b> Proposed activation of H <sub>2</sub> by [FeFe]-hydrogenase. ....	6
<b>Scheme 1.3.</b> General mechanism for N-based precatalyst activation in carbonyl hydrogenation. ....	9
<b>Scheme 1.4.</b> Proposed reaction pathway for hydrogenation of ketones catalyzed by Fe-PN <sup>H</sup> P complexes. ....	10
<b>Scheme 1.5.</b> Proposed reaction pathway for outer-sphere hydrogenation of alkenes catalyzed by Fe-PN <sup>H</sup> P complexes. ....	11
<b>Scheme 1.6.</b> Proposed reaction outer- and inner-sphere pathways for <b>1.7</b> in hydrogenation of ketones (left) and alkenes (right). ....	13
<b>Scheme 1.7.</b> Proposed intermediates in the outer-sphere reaction pathway for Mn-catalyzed hydrogenation of nitriles. ....	14
<b>Scheme 1.8.</b> Double B–H bond activation across Fe–N bond. ....	16
<b>Scheme 1.9.</b> Isolation of Mn–H intermediate from bifunctional B–H activation. .	17
<b>Scheme 1.10.</b> Proposed outer-sphere mechanism for HBpin activation by Co-amido complex <b>1.19</b> . ....	18
<b>Scheme 1.11.</b> Proposed mechanism for dihydroboration of nitriles by Co-complex. ....	20
<b>Scheme 1.12.</b> Heterolytic cleavage of H–H and B–H bonds across a Ni–S bond. .	21
<b>Scheme 1.13.</b> Proposed mechanism for Fe thiolate complex-catalyzed hydroboration of aryl epoxides. ....	23
<b>Scheme 1.14.</b> Proposed mechanism for Fe-catalyzed hydroboration of <i>N</i> -heteroarenes. ....	24
<b>Scheme 1.15.</b> Fe-alkoxide-assisted Si–H bond activation. ....	26
<b>Scheme 1.16.</b> Proposed mechanism for Ni-catalyzed hydroboration of <i>N</i> -heteroarenes. ....	27
<b>Scheme 1.19.</b> Cooperative activation of A) C–H, B) Si–H bonds, and C) CO <sub>2</sub> across a nickel-carbene. ....	29
<b>Scheme 1.20.</b> A) Reversible Ni-catalyzed activation of H <sub>2</sub> and hydrogenation of styrene (P = PPh <sub>2</sub> ); B) Formation of Ni-H <sub>2</sub> adduct (P = P <sup><i>i</i></sup> Pr <sub>2</sub> ). ....	32
<b>Scheme 1.21.</b> Reversible bifunctional activation of Si–H bonds in organosilanes by <b>1.58</b> . ....	33
<b>Scheme 1.22.</b> Activation of CO <sub>2</sub> utilizing electronically flexible phosphinine donor. ....	33
<b>Scheme 1.23.</b> General mechanism for aromatization / dearomatization MLC. ....	35

<b>Scheme 1.24.</b> Proposed mechanism for Fe-catalyzed hydrogenation of ketones via aromatization / dearomatization MLC. ....	36
<b>Scheme 1.25.</b> Proposed mechanism for dehydrogenative coupling of alcohols and amines. ....	38
<b>Scheme 1.26.</b> Syntheses of aromatized ( <b>1.72</b> ), singly dearomatized ( <b>1.74</b> ), and doubly dearomatized ( <b>1.73</b> ) structures of Mn[N <sub>2</sub> S <sub>2</sub> ] complexes. ....	39
<b>Scheme 1.27.</b> Different product selectivity in styrene oxidation catalyzed by neutral and cationic Mn complexes. ....	43
<b>Scheme 1.28.</b> Proposed mechanism of [Fe(PDI)]-catalyzed [2+2] cycloaddition of dienes. ....	45
<b>Scheme 1.29.</b> Modified Ojima mechanism for Mn-catalyzed hydrosilylation of carbonyls. ....	47
<b>Scheme 1.30.</b> Previous report of a [S <sup>t-Bu</sup> N <sup>H</sup> S] ligand. ....	49
<b>Scheme 1.31.</b> Synthesis of two SNS ligand, <b>L1<sup>H</sup></b> and <b>L2<sup>H</sup></b> . ....	50
<b>Scheme 1.32.</b> Summary of previously reported reactivity of <b>L2<sup>H</sup></b> with iron. ....	52
<b>Scheme 1.33.</b> Summary of previously reported reactivity of <b>L1<sup>H</sup></b> with iron. ....	53
<b>Scheme 2.1.</b> Synthesis of <b>2.1<sub>Cu</sub></b> and <b>2.2<sub>Cu</sub></b> . ....	75
<b>Scheme 2.2.</b> Mechanistic studies performed with <b>2.1<sub>Cu</sub></b> . ....	79
<b>Scheme 2.3.</b> Proposed mechanism for E–H bond activation and reaction with carbonyls. ....	80
<b>Scheme 3.1.</b> Synthesis and ORTEP depiction of <b>3.1<sub>Mn</sub></b> with thermal ellipsoids shown at 50%. H atoms are omitted for clarity. Selected bond lengths (Å): Mn(1)–S(1) 2.624(9), Mn(1)–S(2) 2.734(9), Mn(1)–S(3) 2.647(8), Mn(1)–S(4) 2.682(8), Mn(1)–N(1) 2.099(2), Mn(1)–N(2) 2.112(2). ....	103
<b>Scheme 3.2.</b> Synthesis and ORTEP depiction of <b>3.2<sub>Mn</sub></b> with thermal ellipsoids shown at 50%. H atoms are omitted for clarity. Selected bond lengths (Å): Mn(1)–S(1) 2.7290(5), Mn(1)–S(2) 2.7070(5), Mn(1)–N(1) 2.1227(14), Mn(1)–N(2) 2.1135(15), Mn(1)–N(3) 2.3141(15), Mn(1)–N(4) 2.660(14). ....	108
<b>Scheme 4.1.</b> Syntheses of ( <b>4.1<sub>Fe</sub></b> ) and ( <b>4.2<sub>Fe</sub></b> ). ....	151
<b>Scheme 4.2.</b> Synthesis and molecular depiction of <b>4.1<sub>Mn</sub></b> . Thermal ellipsoids are set at 50% probability and hydrogen atoms are omitted for clarity. Selected bond lengths (Å): Mn–N 2.0587(16), Mn–S(1) 2.3898(6), Mn–S(2) 2.3592(6), Mn–C(1) 1.797(2), Mn–C(2) 1.802(2), Mn–C(3) 1.805(2). ....	153
<b>Scheme 4.3.</b> Spectroscopic and isotope-labeling experiments with <b>4.1<sub>Mn</sub></b> . ....	158
<b>Scheme 4.4</b> Off-pathway intermediate with absence of nitrile. ....	161
<b>Scheme 5.1.</b> Synthesis of M(N <sub>2</sub> S <sub>2</sub> ) complexes via imine C–C bond formation ...	195
<b>Scheme 5.2.</b> A) Synthesis of previously reported dinuclear [Fe(μ-N <sub>2</sub> S <sub>2</sub> )] <sub>2</sub> complex. <sup>41</sup> B) Solid-state molecular structure of monomer Fe[N <sub>2</sub> S <sub>3</sub> ] <b>5.1<sub>Fe</sub></b> (from partially	

hydrolyzed $\text{Fe}[\text{N}_2\text{S}_3]\cdot\text{Fe}(\text{OH})_2(\text{NCMe})_4$ co-crystal) with thermal ellipsoids shown at 50%. H-atoms are omitted for clarity. ....	198
<b>Scheme 5.3.</b> Synthesis of $[\text{Na}(\text{THF})_6]^+[\text{Fe}(\text{N}_2\text{S}_3)]^-$ ( <b>5.1Fe<sup>-</sup></b> ). ....	203
<b>Scheme 6.1.</b> <i>Ortho</i> -directed C–H activation of pyridine N-oxide by a cooperative Ni–Al.....	242
<b>Scheme 6.3.</b> Proposed reaction pathway for C(2)–H silylation of pyridines by a Rh–Al complex.....	244

## LIST OF APPENDICES

### **Appendix A**

Supporting Information for Chapter 2.....245

### **Appendix B**

Supporting Information for Chapter 3.....259

### **Appendix C**

Supporting Information for Chapter 4.....290

### **Appendix D**

Supporting Information for Chapter 5.....304

### **Appendix A**

Copyright Permissions.....322

## LIST OF ABBREVIATIONS/SYMBOLS

$\alpha$	alpha position, or angle label (X-ray crystallography)
Å	Ångström
ADC	alcohol dehydrogenative coupling
AH	asymmetric hydrogenation
Al	aluminum
Anal.	Analysis
Ar	aryl
ATH	asymmetric transfer hydrogenation
aq.	aqueous workup
av	average
B	boron
Br	bromine
$\beta$	beta position, or angle label (X-ray crystallography)
br	broad (NMR spectroscopy)
$\text{cm}^{-1}$	wavenumbers
C	carbon
$^{13}\text{C}$	carbon-13
Cl	chlorine
CO	carbonyl ligand
$\text{CO}_2$	carbon dioxide

Co	cobalt
Cu	copper
CN	nitrile
C <sub>6</sub> D <sub>6</sub>	benzene-d <sub>6</sub>
CD <sub>3</sub> CN	acetonitrile-d <sub>3</sub>
δ	chemical shift
Δ	delta (difference between variables)
‡	double dagger (transition state)
D	deuterium
d	doublet (NMR spectroscopy)
dd	doublet of doublets (NMR spectroscopy)
deg (or °)	degrees
DFT	density functional theory
dmpe	1,2-bis(dimethylphosphino)ethane
e <sup>-</sup>	electron
E	element
EA	elemental analysis
EI-MS	electron impact mass spectroscopy
ESI-MS	electron spray ionization mass spectroscopy
equiv.	equivalents
<i>F</i>	structure factors (X-ray crystallography)

Fe	iron
FW	formula weight
$\gamma$	gamma, angle label (X-ray crystallography)
g	gram
GOF	goodness of fit
$\Delta G$	Gibbs free energy
$\Delta G^\ddagger$	Gibbs free energy of activation
$\eta^n$	n-hapticity
h	hour(s)
H	hydrogen or hydride ligand
H <sub>2</sub>	dihydrogen
HBpin	pinacolborane
HRMS	high-resolution mass spectroscopy
<sup>1</sup> H	proton
{ <sup>1</sup> H}	proton decoupled
Hz	Hertz
$\Delta H$	enthalpy
$\Delta H^\ddagger$	enthalpy of activation
I	iodine
Ir	Iridium
IPr	1,3-bis[2,6-diisopropylphenyl]-1,3-dihydro-2H-imidazol-2-ylidene

J	Joules
${}^nJ_{AB}$	n-bond scalar coupling constant between nuclei A and B (NMR spectroscopy)
$k$	rate constant
K	Kelvin
Kcal	kilocalorie
kJ	kilojoules
$\lambda$	wavelength
L	neutral ligand donor
$\mu$	bridging ligand or absorption coefficient (X-ray crystallography)
M	central metal atom (or molar when referring to concentration)
$M^+$	parent ion
m	multiplet
Me	methyl, $-CH_3$
mg	milligram
MHz	Megahertz
min	minutes
mL	milliliter
MLC	metal-ligand cooperation/cooperativity
Mn	manganese
mmol	millimoles

mol	moles
MW	molecular weight
N	nitrogen
Na	sodium
Ni	nickel
Np	naphthalene
NHC	N-heterocyclic carbene
NMR	nuclear magnetic resonance
No.	number
OMe	methoxy group, $-\text{CH}_3$
OTf	triflate
ORTEP	Oak Ridge Thermal Ellipsoid Plot Program
$\pi$	pi-bonding or orbital
p	pentet
P	phosphorous
Pd	palladium
Pt	platinum
Ph	phenyl group, $-\text{C}_6\text{H}_6$
<sup>i</sup> Pr	isopropyl group, $-\text{CH}(\text{CH}_3)_2$
ppm	parts per million
%	percent

$\Theta$	theta diffraction/Bragg angle (X-ray crystallography)
q	quartet (NMR spectroscopy)
R	alkyl group
Re	rhenium
Rh	rhodium
Ru	ruthenium
<i>R</i>	reliability factor (X-ray crystallography)
Reflns	reflections (X-ray crystallography)
$\sigma$	estimated standard deviation (x-ray crystallography), bonding, orbital
S	sulfur
s	singlet
Si	silicon
t	triplet (NMR spectroscopy)
T	temperature in Kelvin or degrees
THF	tetrahydrofuran
TMS	tetramethylsilane
TOF	turnover frequency
TON	turnover number
TS	transition state
<i>V</i>	unit cell volume

$W_{1/2}$	width at half height
X	halide substituent (or negative ligand donor)
Z	asymmetric units per unit cell (X-ray crystallography)
Zn	zinc

**Chapter 1 – Towards Sustainable Bifunctional SNS Ligands for First-Row Metal Complex Catalysts Using Metal-Ligand Cooperativity**

**1.1 General Introduction**

This dissertation is primarily based upon the synthesis of first-row transition metal complexes decorated with bifunctional [SNS]-pincer ligands and their catalytic applications. Here, the term bifunctional is used to describe a ligand that not only serves in an ancillary capacity (monofunctional), but also participates in chemical reactions with the metal (bifunctional). This strategy of reactivity was coined as metal-ligand cooperation by Hansjörg Grützmacher<sup>1</sup> in 2008 and has been thoroughly explored over the last decade and a half. The work in this thesis places a large emphasis on the mechanisms of catalytic reaction pathways. As such, this chapter includes a brief overall discussion on all strategies of metal-ligand cooperation. This is followed by discussion of why SNS ligands are the target ligand scaffold of this work, and finally, a summary of the following chapters.

## **1.2 Homogeneous Catalysis**

The world relies on catalysis for its crucial role in the industrial production of liquid fuels and bulk chemicals.<sup>2</sup> Today, more than 85% of commercial chemical processes involve catalysts that decrease total energy use, increase product selectivity, and contribute to process intensification, i.e., by combining multiple reaction steps into one.<sup>3</sup> The realm of catalysis comprises the varieties of heterogeneous, homogeneous, and biological (enzymatic) catalysis. While industrial scale commodity chemical manufacturing typically employs heterogeneous solid catalysts, the production of higher valued chemicals often involves use of molecular homogeneous catalysts.<sup>4</sup> These have several benefits, including: i) definite knowledge of the characterized catalyst for intentionally designed separation/purification techniques; ii) ability to rationally “tune” the molecular catalyst to improve kinetic performance, increase yield and selectivity for desired products, and iii) ability to gain a deep mechanistic understanding of the reaction to enable discovery of new reaction pathways.<sup>5</sup>

### **1.2.1 Moving from precious to base metals**

Homogeneous transition metal catalysis has long been used to facilitate difficult chemical transformations to afford valuable products.<sup>5-6</sup> Homogeneously catalyzed processes such as hydroformylation,<sup>7</sup> hydrogenation,<sup>8</sup> metathesis,<sup>9</sup> and hydrocyanation<sup>10</sup> contribute millions of tons to the overall inventory of bulk chemicals worldwide.<sup>4</sup> This platform has been dominated traditionally by the precious metals (Pd, Pt, Rh, Ru, Ir). Some of the most prominent high-performing catalysts for these purposes are shown in **Figure 1.1**, including Crabtree’s and Wilkinson’s catalysts for hydrogenation,  $[\text{Rh}(\text{COD})\text{Cl}]_2$  as a precursor for hydroformylation, and Grubb’s catalysts for olefin metathesis.

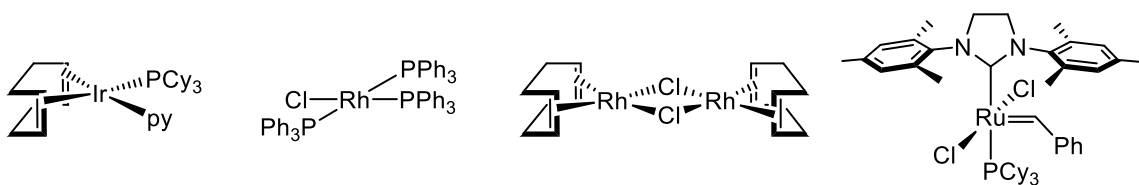
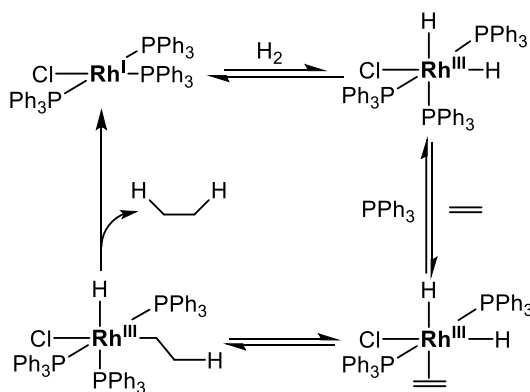


**Figure 1.1.** Prominent examples of homogeneous catalysts based upon precious metals.

The widespread use of precious metals for catalysis can be attributed to several factors. These complexes often display remarkable stability to high temperatures and pressures occasionally needed to facilitate catalysis, and additionally often demonstrate stability to air and moisture. Another intrinsic property of these metals is their predictable nature to undergo simple 2e- elementary steps in most reaction pathways,<sup>11</sup> enabling some of the most significant reaction manifolds (C–C and C–N coupling, C–H bond functionalization, olefin metathesis, H–X additions) (**Scheme 1.1**).<sup>12-14</sup> While the high performance of the precious metals is undeniable and has attributed to the rapid and significant growth of catalysis over the last 50 years, continued reliance on these metals is not sustainable.<sup>15</sup>



**Scheme 1.1.** Reaction pathway for catalytic hydrogenation of ethylene with Wilkinson's catalyst, highlighting the 2 electron redox changes enabled by oxidative addition / reductive elimination.

*Chapter 1 – Towards Sustainable Bifunctional SNS Ligands for First-Row Metal Complex Catalysts Using Metal-Ligand Cooperativity*

There has been a movement over the last 30 years for the chemistry community to expand its use of base metals in homogeneous catalysis<sup>16-25</sup> for their economy, high natural abundance,<sup>15</sup> and relative non-toxicity.<sup>26</sup> There are, however, additional challenges that are associated with their use such as sensitivity to O<sub>2</sub>, and a lesser degree of robustness. Additionally, the reactivity of second and third-row transition metal complexes is often not analogous with their first-row counterparts due to stark differences in electronic structure, orbital overlap, and bonding character. For instance, the base metals often prefer to undergo one electron transformations in lieu of the powerful 2 electron transformations of their heavier congeners. This can lead to unpredictable reactivity that makes it difficult to construct base-metal catalysts for transformations easily performed by the noble metals.

While this differing reactivity may come across as a detriment, one may argue that recreating analogous reactions with the base metals should not be the primary goal.<sup>27</sup> Instead, the community should openly embrace the unique and often unpredictable reactivity associated with the base metals. Many groups frequently utilize these metals for one electron transformations in photoredox catalysts for instance.<sup>28</sup> The last 15 years have also brought about new ligand design strategies that exploit the base-metals' penchant for 1 electron reactions by employing a ligand to work in tandem with the metal to facilitate net two electron reactions (*vide infra*).<sup>29</sup> In order to truly move towards widespread application of base metals in homogeneous catalysis, new strategies that exploit their unique qualities must be conceptualized and employed.

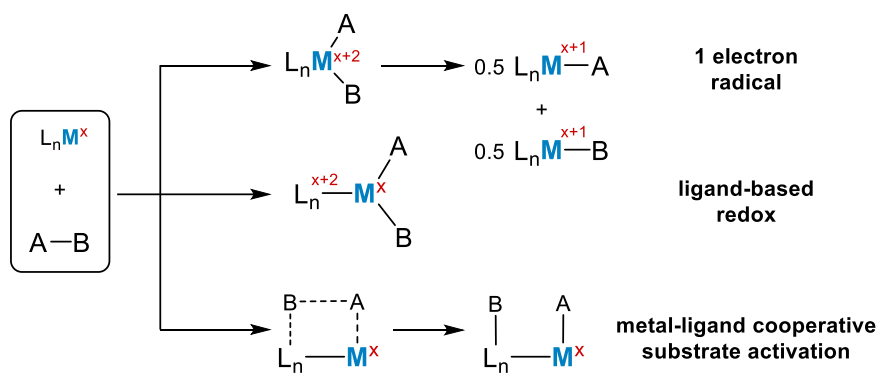
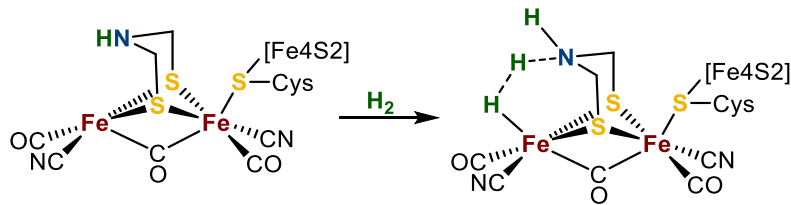


Figure 1.2. Unique reaction strategies enabled by the first-row metals.

### 1.3 Bifunctional Ligands for Metal-Ligand Cooperative Catalysis

The design of ancillary ligands to tune and optimize the electronic and structural properties of transition metal complexes is a powerful tool that has allowed chemists to improve upon existing protocols and has led to the discovery of novel reaction pathways.<sup>30-</sup>  
<sup>31</sup> “Actor ligands” can directly participate in the crucial bond breaking/forming, which has led to the rapidly developing field of metal-ligand bifunctional catalysis.<sup>1,32</sup> Metal-ligand cooperativity (MLC) has experienced a renaissance over the past 10 years as a powerful mechanistic strategy in homogeneous catalysis, particularly with the base metals.<sup>33-34</sup> With both metal and ligand working in a synergistic fashion, the overall activity and/or selectivity of a system can be dramatically altered and improved. Examining nature unearths several elegant examples of bifunctional catalysis in the form of enzymatic processes.<sup>35-36</sup> For instance, the enzyme [FeFe]-hydrogenase, consisting of a dinuclear Fe complex with bridging thiolates, effectively catalyzes the reversible formation of dihydrogen from protons and electrons [ $2H^+ + 2 e^- \rightleftharpoons H_2$ ] (**Scheme 1.2**).<sup>37</sup> Multiple theoretical and experimental studies have shown the pendant amine moiety is crucial in facilitating heterolytic  $H_2$  activation.<sup>38-40</sup>



**Scheme 1.2.** Proposed activation of H<sub>2</sub> by [FeFe]-hydrogenase.

Multiple strategies may be employed to use MLC for bond activation in a catalytic cycle (**Figure 1.3**): 1) a metal-bound or pendant X ligand may act as a Lewis base, synergistically cleaving a substrate E–H bond in cooperation with a metal center; 2) a metal-bound or pendant ligand may serve as a Lewis acid to accept electrons from a substrate donor with the metal serving as a Lewis base, to cooperatively cleave a substrate bond; 3) an aromatic chelating ligand framework may undergo dearomatization by deprotonation, thereby serving as a site for cooperative bond activation with a metal; 4) a redox non-innocent ligand may act as an electron reservoir to maintain the metal oxidation state throughout a catalytic cycle, or may directly participate in bond activation by acting as a radical source.

The context of this dissertation is most concerned with the use of base-metal catalysts which use the first mode of MLC: a Lewis base donor for cooperative bond activations. As such, this topic will be most heavily focused on *vide infra*, although a brief discussion of the other strategies will be briefly included.

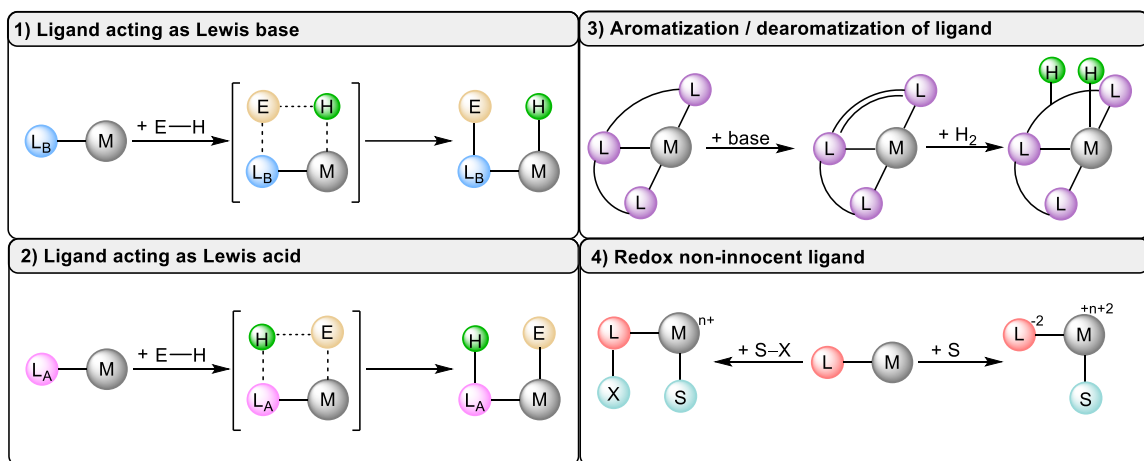


Figure 1.3. Different modes of metal-ligand cooperativity.

### 1.3.1 Ligand acts as a Lewis base

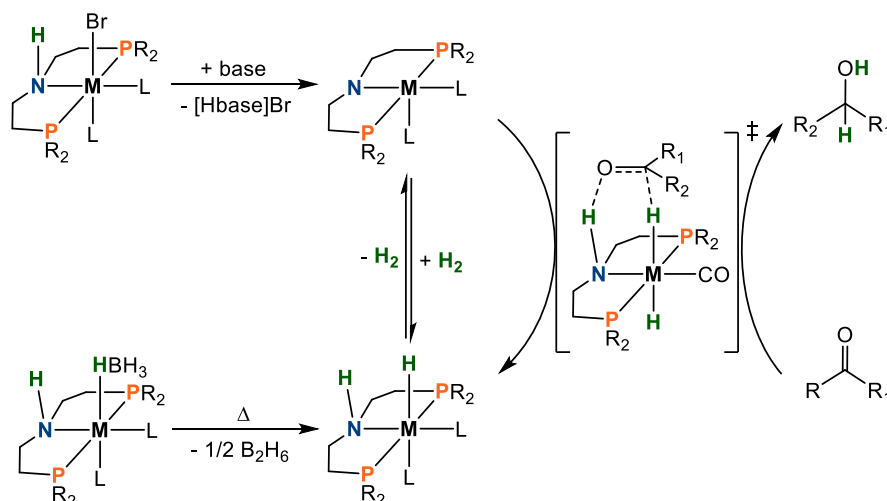
A cooperative ligand has been defined as one which actively participates in substrate activation to facilitate catalysis with a metal ion in a synergistic fashion.<sup>33</sup> The chemical structure of the ligand may either remain intact during the reaction or undergo a reversible transformation (i.e., protonation/deprotonation). The most prominent class of cooperative ligands are those which use a Lewis base in a multidentate framework. Electron-rich transition metal complexes with amido ligands are particularly well suited for this application due to high N-centered basicity, leading to the emergence of  $[P,N]$  multidentate ligands to the forefront of this field. Pioneering work by Fryzuk on heterolytic  $H_2$  splitting with Rh and Ir disilylamido bis(phosphine) complexes laid the groundwork for future development of bifunctional catalysis.<sup>41-42</sup> A decade later, Noyori's work in asymmetric hydrogenation (AH) and asymmetric transfer hydrogenation (ATH) with Ru catalysts containing diamine and bisphosphine ligands highlighted the immense potential of this catalyst design strategy.<sup>43</sup> In this case, the cooperative effect of an N-H functionality adjacent to the metal center is essential to the unprecedented reactivity, and contributes to

the metal-ligand cooperative H<sub>2</sub> activation and outer-sphere transfer to the substrate.<sup>44</sup> This section summarizes the development of bifunctional first-row transition metal catalysts using Lewis base donors, highlighting the different heteroatoms, patterns, and frequently utilized strategies for various reactions. Several reviews are available for a comprehensive discussion of collective work from a synthetic chemistry standpoint.<sup>19,23,45</sup>

### 1.3.1.1 Nitrogen based ligands

#### 1.3.1.1.1 De(hydrogenation) catalysis

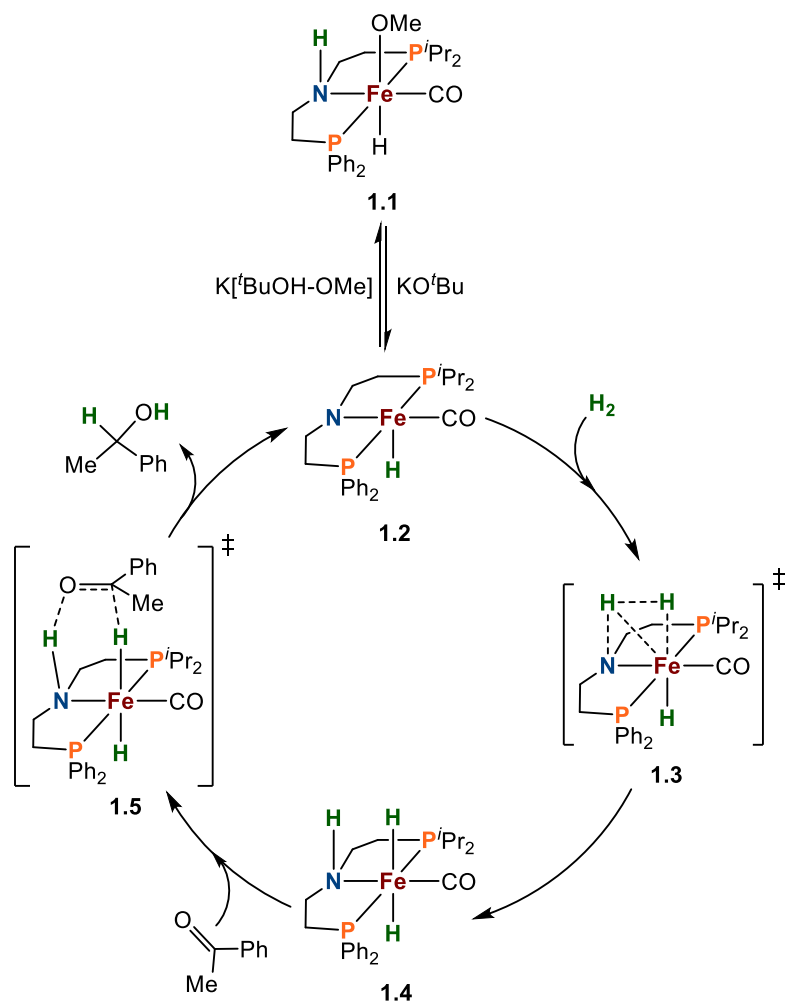
Complexes with polar metal-nitrogen bonds are the most prominent representatives within bifunctional catalysis and are continually at the forefront of MLC. Hydrogenation of unsaturated organics is perhaps the most ubiquitous use of these catalysts, and there have been innumerable reports of base metal complex-catalyzed hydrogenations of a breadth of substrates. The [P,N] multidentate scaffold is most widely used for these bifunctional catalysts. There are two common starting reaction pathways by which an N-donor may be used for bifunctional activity (**Scheme 1.3**). After the active amido/amine hydride catalyst states are generated *in situ*, the amido conjugate base facilitates heterolytic cleavage of H<sub>2</sub> across the M–N bond. Key to the success of this strategy are the strong-field phosphine ligands which stabilize the active catalyst species in low spin states [particularly with *d*<sup>6</sup> manganese(I) and iron(II)]. The substrate may then react with the H–N–M–H fragment via an outer-sphere transition state (TS) to furnish the hydrogenated product. A main control experiment often performed to discourage an outer-sphere mechanism is replacement of the N–H moiety in the catalytically active species with an N–Me group.



**Scheme 1.3.** General mechanism for N-based precatalyst activation in carbonyl hydrogenation.

The Morris group reported a series of iron complexes equipped with an unsymmetrical chiral  $[PN^H P]$  ligand for asymmetric hydrogenation of ketones and imines.<sup>46-49</sup> The Fe catalysts exhibit remarkable activity (TOF = 2000 h<sup>-1</sup>) at 50 °C (5-20 atm H<sub>2</sub>) with 0.1 mol% loading and high enantioselectivities (89%, 60%) for ketones and imines, respectively. To initiate the catalytic cycle, alkoxide complex **1.1** is converted to amido complex **1.2** by reaction with KO<sup>t</sup>Bu (alkoxide complex **1.1** reacts with H<sub>2</sub> only in the presence of excess base; **Scheme 1.4**). Reaction of **1.2** with dihydrogen forms a dihydrogen complex, followed by splitting of the coordinated hydrogen across the iron and the amido group through transition state (TS) **1.3**, to form iron-dihydride complex **1.4**. Transition state **1.3** was found to have a barrier of 18.7 kcal/mol and is a potential turnover-limiting step under certain conditions. Complex **1.4** then forms a weak adduct with acetophenone, with transfer of the metal hydride to the ketone proceeding through TS**1.5** (19.4 kcal/mol). The similar activation barrier of this step led the authors to propose this as a rate-limiting

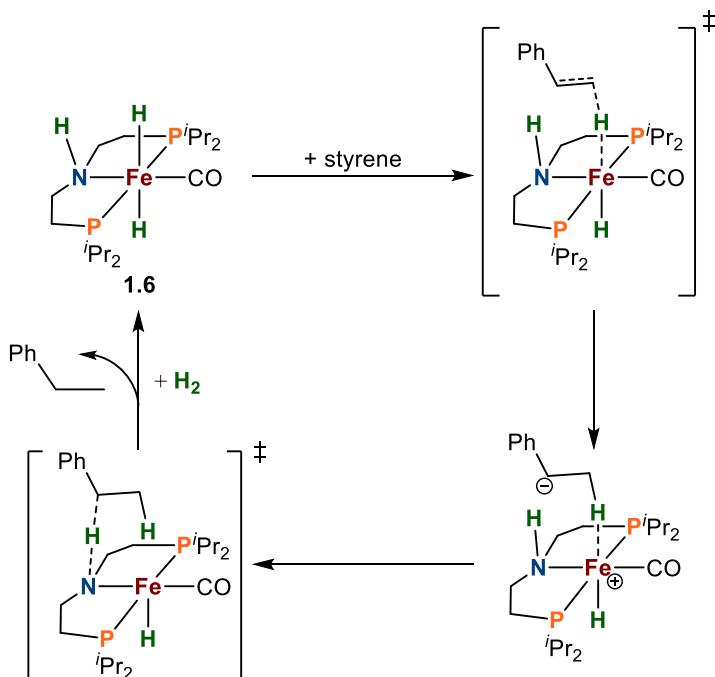
step with bulkier substrates. Final liberation of the alcohol product reforms iron amido intermediate **1.2**.



**Scheme 1.4.** Proposed reaction pathway for hydrogenation of ketones catalyzed by Fe-PN<sup>H</sup>P complexes.

Many groups have contributed substantially to the growth of this field, utilizing variants of a [PN<sup>H</sup>P] framework with iron for bifunctional catalytic hydrogenation of amides,<sup>50-51</sup> nitriles,<sup>52-53</sup> and esters.<sup>51,54-55</sup> Several of these iron precatalysts make use of borohydride precursors as ‘masked’ hydrides that release B<sub>2</sub>H<sub>6</sub> or L•BH<sub>3</sub> upon heating or treatment with weak base L (**Scheme 1.3**). Notably, Jones and co-workers expanded the

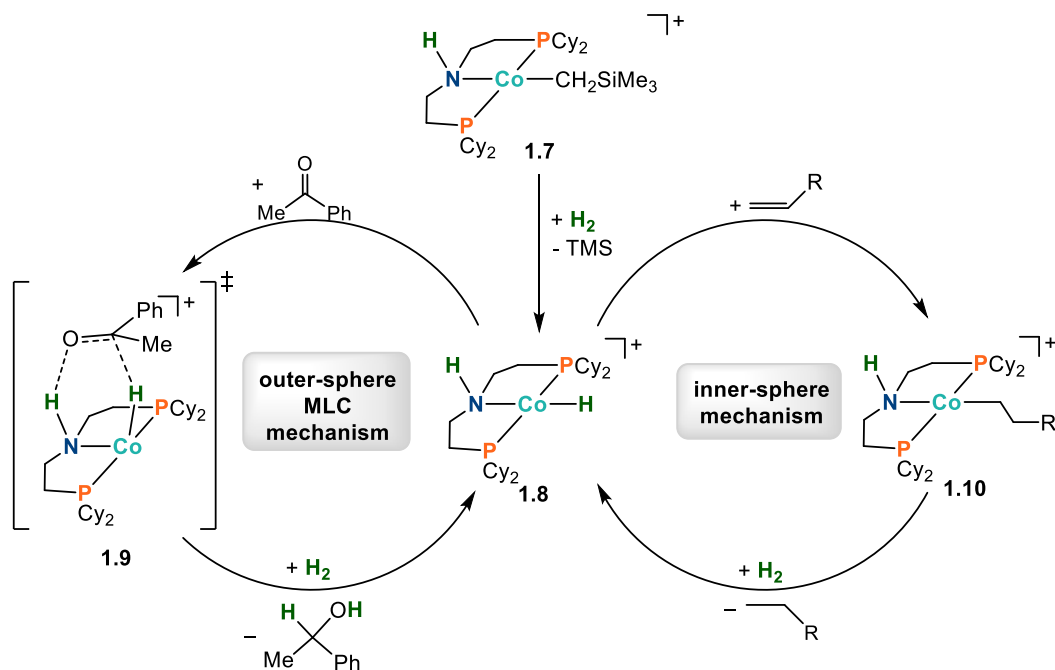
capabilities of this catalyst system beyond polar substrates, reporting the Fe-catalyzed chemoselective hydrogenation of alkenes.<sup>56</sup> Interestingly, while stoichiometric hydrogenation of styrene proceeded smoothly for *in situ* generated **1.6**, the N–Me analogue gave no conversion to product. This led the authors to propose a stepwise outer-sphere hydrogen transfer mechanism, unusual for this reaction type (**Scheme 1.5**).



**Scheme 1.5.** Proposed reaction pathway for outer-sphere hydrogenation of alkenes catalyzed by Fe-PN<sup>H</sup>P complexes.

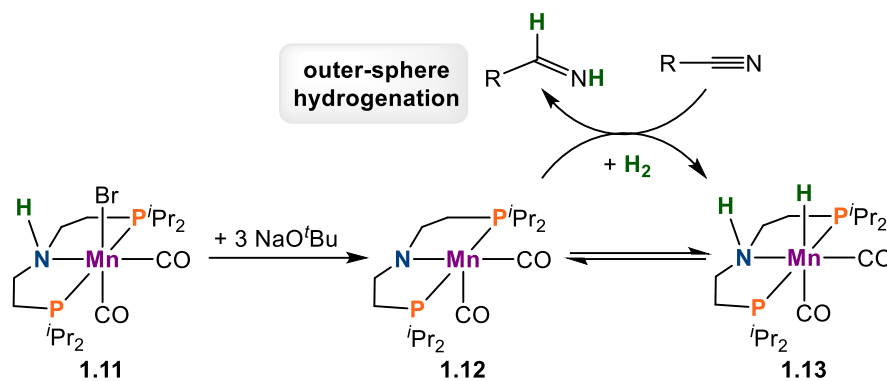
The use of base metal complexes for catalytic hydrogenation via a bifunctional mechanism is not limited to iron. In 2012, Hanson reported Co-catalyzed hydrogenation of alkenes, ketones, and imines.<sup>57</sup> Catalysis is facilitated by a Co(II)-alkyl complex (**1.7**) featuring a [PN<sup>H</sup>P] ligand, which can be generated *in situ* by reaction of Co<sup>I</sup>[PNP][CH<sub>2</sub>SiMe<sub>3</sub>] with Brookhart's acid. Initial stoichiometric and isotopic labelling studies implicated a Co–hydride species as a likely intermediate; however, no insight into

a potential bifunctional mechanism was reported. Shortly thereafter, Hanson reported **1.7** as an efficient transfer hydrogenation catalyst for carbonyls and imines.<sup>57</sup> It was found that the N–Me analogue of **1.7** performed just as efficiently as the N–H analogue, thereby ruling out an outer-sphere bifunctional mechanism. After a follow-up report on catalytic dehydrogenation of alcohols with **1.7**,<sup>58</sup> a detailed mechanistic study by the Hanson group made novel insights into the different reaction pathways enabled by **1.7**.<sup>59</sup> The N–Me of analogue of **1.7** was ineffective as a hydrogenation catalyst for ketones, suggesting the N–H is crucial for an outer-sphere bifunctional mechanism. Hydrogenolysis of **1.7** generates **1.8** with concomitant loss of tetramethylsilane, and the ketone hydrogenation pathway likely proceeds through six-membered TS (**1.9**), similar to previously reported species (**Scheme 1.6**).<sup>60</sup> Elimination of alcohol and addition of H<sub>2</sub> reforms active **1.8**. Conversely, the N–Me of analogue **1.7** was an efficient catalyst for both hydrogenation and dehydrogenation of alkenes and alcohols, respectively. Observation of alkene isomerization as well as H/D scrambling led the authors to suggest an inner sphere mechanism (**Scheme 1.6**). Insertion of the alkene into the Co–H forms Co(II)-alkyl intermediate **1.10**. Reaction of **1.10** with hydrogen releases the product and turns over the catalyst. The authors made brief mention that the P–Ph substituted analogue of **1.7** was essentially ineffective as a hydrogenation catalyst. It would be of interest to learn more about ancillary ligand effects on both the activity and chemoselectivity of this reaction.



**Scheme 1.6.** Proposed reaction outer- and inner-sphere pathways for **1.7** in hydrogenation of ketones (left) and alkenes (right).

The last four years have witnessed an explosion of interest in the development of pincer manganese complexes<sup>61</sup> and their utilization as bifunctional catalysts.<sup>62</sup> In 2016, Beller reported the first instance of Mn complex-catalyzed hydrogenation for nitriles, ketones, and aldehydes.<sup>63</sup> The Mn complex **1.11** featuring a [PN<sup>H</sup>P] ligand facilitated hydrogenation with low catalyst loadings (1-3 mol%), moderate H<sub>2</sub> pressures (10-30 bar), and varied temperatures (60-120 °C) depending on the substrate. Reaction of 3 equiv of NaO<sup>t</sup>Bu in the presence of 5 bar of H<sub>2</sub> yielded isolable Mn-hydride complex **1.13** purportedly derived from H<sub>2</sub> addition to amido complex **1.12** (**Scheme 1.7**). DFT calculations supported an equilibrium between the two species. Complex **1.13** was proposed to operate via an outer-sphere mechanism involving simultaneous transfer of Mn–H and N–H to the nitrile to provide the imine product, which undergoes subsequent reduction to the amine.



**Scheme 1.7.** Proposed intermediates in the outer-sphere reaction pathway for Mn-catalyzed hydrogenation of nitriles.

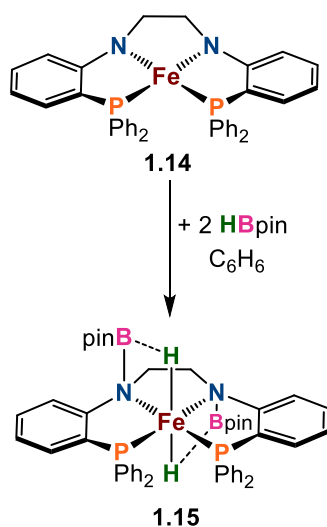
These initial reports by Beller motivated more groups to further investigate the potential of manganese in bifunctional catalysis. In 2017, Milstein and co-workers reported an example of Mn-catalyzed ester hydrogenation.<sup>64</sup> Notably, even though the alternate ligand scaffold being used was the pyridyl-based PNN<sup>H</sup> type, they observed reversible activation of H<sub>2</sub> at the Mn–N bond via MLC. Further advances in Mn-catalyzed hydrogenations were made that same year. Beller reported Mn-catalyzed hydrogenation of amides,<sup>65</sup> while Clarke<sup>66</sup> and Beller<sup>67</sup> independently reported asymmetric hydrogenation of ketones and esters. Despite the recent discovery of manganese as a powerful metal for bifunctional catalysis, it has already demonstrated significant progress.

Overall, most detailed experimental and computational studies of the mechanism of H<sub>2</sub> transfer via bifunctional MLC pathway have been performed with Ru. However, to fully integrate the use of base metals as sustainable alternatives for precious metal-catalyzed systems, more work must be done to gain a fundamental understanding of the energies and mechanisms that govern them.

### **1.3.1.1.2 E–H bond activations (E = B, Si): hydroboration & hydrosilylation**

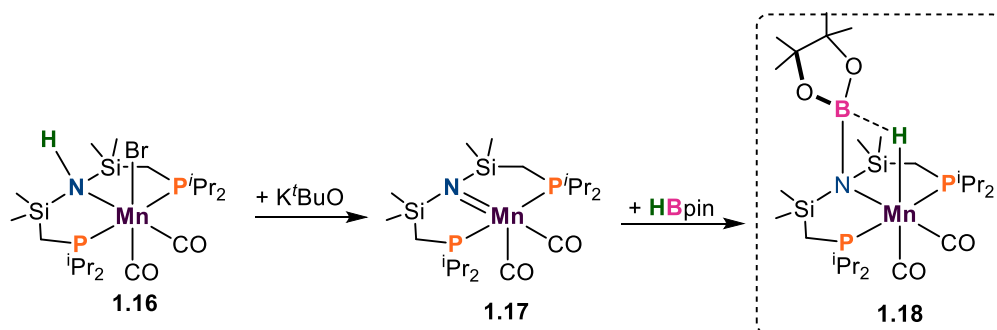
The reactivity scope of bifunctional catalysis extends beyond activation of dihydrogen.<sup>68</sup> Organosilicon and organoboron compounds are highly sought after organic synthons for palladium-catalyzed cross-coupling.<sup>14,69</sup> Base-metal complex catalyzed reactions to construct these organic building blocks, such as hydrosilylation and hydroboration, have been extensively studied and pursued.<sup>17</sup> Hydrosilanes and boranes are consistently likened to dihydrogen due to similar electronegativity values. The heterolytic cleavage of comparatively weaker Si–H and B–H bonds may be facilitated by catalysts that utilize MLC.<sup>68</sup> Although the majority of these reactions have been performed using precious metals (Ru, Ir, Rh), the past five years have seen numerous advances in the application of first-row metals for this reaction manifold.<sup>17</sup> While there are many examples of base-metal hydroborations and hydrosilylations, the majority employ redox non-innocent ligands (*Section 5*), and there are fewer examples which use Lewis base moieties. A recent review has described the cleavage of E–H bonds (E = Si, B, C) by MLC,<sup>45</sup> however, we aim to cover only those examples employing first row metals.

The conceptual pathway by which Si–H or B–H bonds may be cleaved by MLC is similar to that for H<sub>2</sub> with the electrophilic Si/B fragment ending up on the Lewis basic ligand site. In a recent example, Thomas et al. isolated and characterized the double borane addition product (**1.15**) to both Fe–N bonds in the Fe complex **1.14** featuring a tetradentate bisphosphine-bisamido PNNP ligand (**Scheme 1.8**).<sup>70</sup>



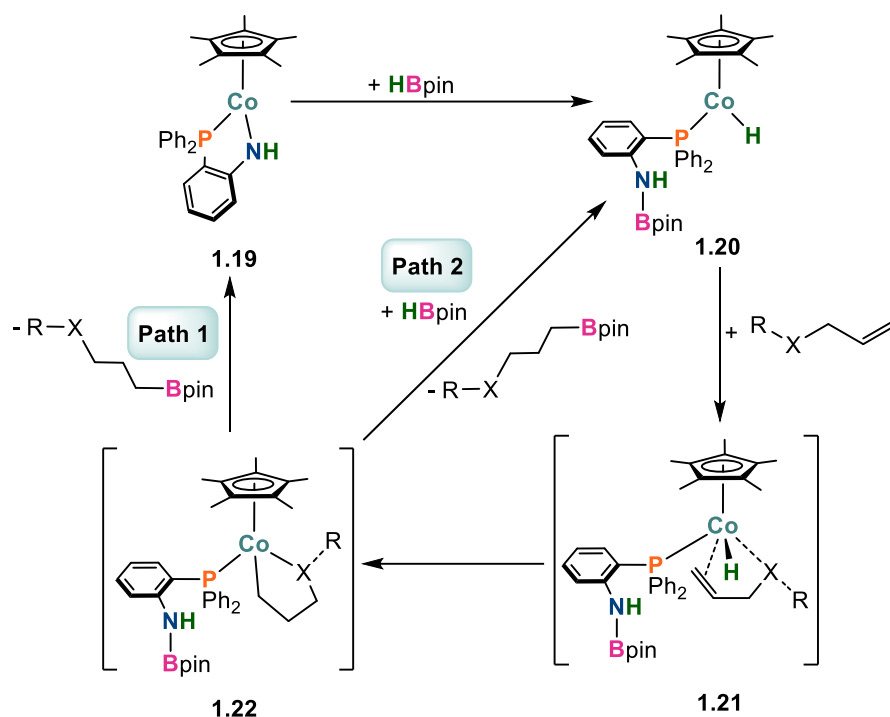
**Scheme 1.8.** Double B–H bond activation across Fe–N bond.

Leitner *et al.* isolated a key intermediate in the reaction pathway of Mn-catalyzed CO<sub>2</sub> hydroboration, shedding light on the mechanism (**Scheme 1.9**).<sup>71</sup> Complex **1.16** effectively reduces carboxylic acids and carbonates as well as CO<sub>2</sub>, operating at 80-120 °C and low catalyst loadings (0.1-0.2 mol%). Stoichiometric base is needed to generate the active catalyst **1.17**, which upon reaction with 1 equiv. of HBpin, allowed for isolation of key intermediate **1.18**. This Mn(I) complex, which was crystallographically characterized, notably features a four membered ring (Mn–H–B–N) that represents heterolytic B–H bond cleavage across the Mn–amido bond. Reaction with CO<sub>2</sub> was proposed to occur in three hydroboration cycles, proceeding through formyl boronate ester, formaldehyde, and the final methylboronate ester products. While it has been recently shown that carboxylic acids may undergo hydroboration in the absence of transition-metal catalysts,<sup>72</sup> the reduction of carbonates and carbon dioxide is not trivial. Furthermore, isolation of a 4-membered Mn–H–B–N ring intermediate in the reaction pathway provides further support for systems proposed to undergo a bifunctional mechanism.



**Scheme 1.9.** Isolation of Mn–H intermediate from bifunctional B–H activation.

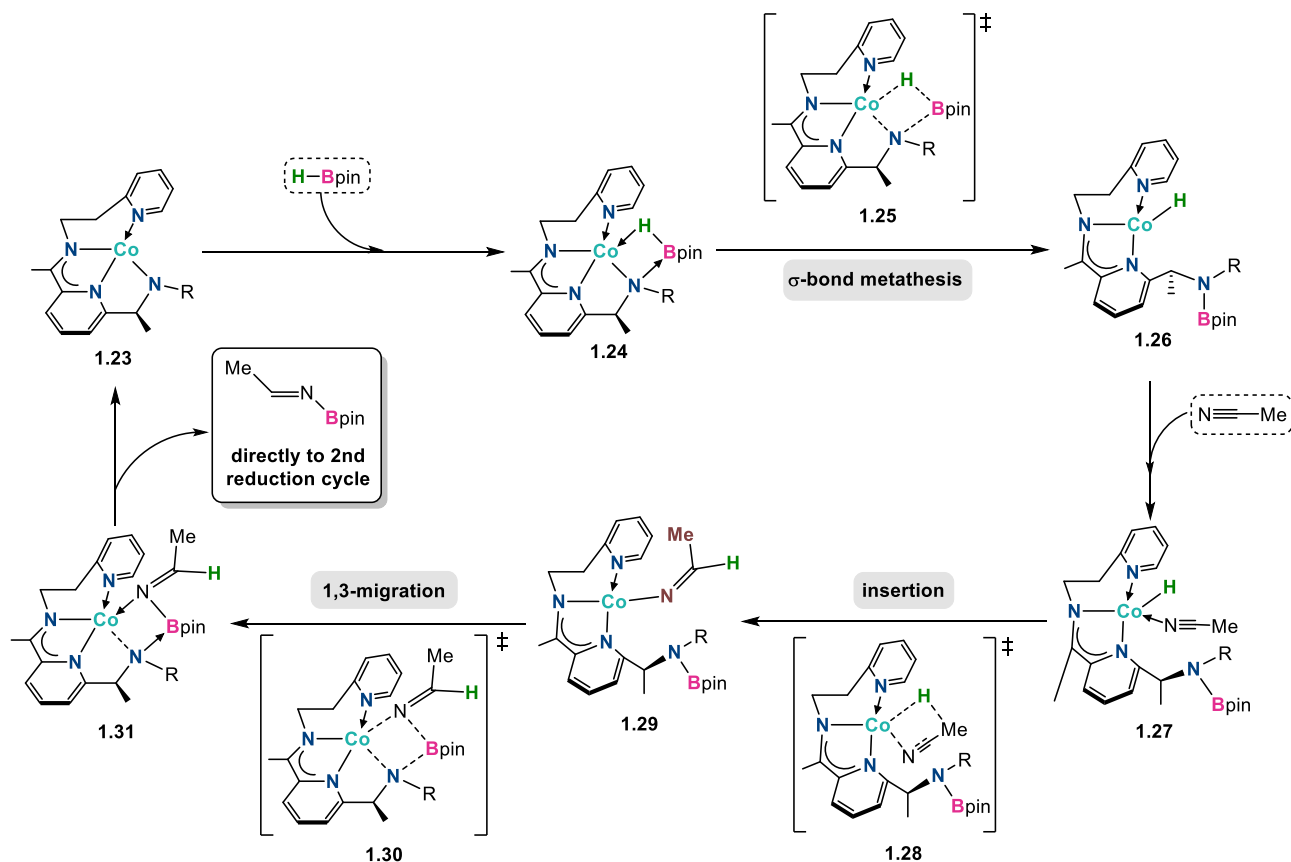
Another intermediate in base-metal hydroboration has been isolated by the Wang group in their study on Co-catalyzed hydroboration of olefins.<sup>73</sup> Whereas treatment of **1.19** with olefin yielded no product, the Co(II)–amido enables facile cleavage of the B–H bond to afford isolable intermediate **1.20** a Co(II) hydride complex in which the borenium ion is captured by the uncoordinated nitrogen atom of the ligand (**Scheme 1.10**). This species was crystallographically characterized and showed no interaction between the Co–H and borylated amine. The presence of a heteroatom (N or O) on the olefin significantly increased the reaction rate and subsequent 1,2-insertion of the olefin into the Co–H of **1.21** forms **1.22**. The authors proposed two potential pathways for hydroborated product formation from **1.22**. Path 1 involves concurrent intramolecular B–C and Co–N bond formation while Path 2 relies on a  $\sigma$ -bond metathesis step with a second equivalent of HBpin, affording product and **1.20**. Overall, this work provided the first evidence of direct addition of a B–H bond across a Co–N bond by MLC, displaying excellent activity for the hydroboration of olefins, operating at 40 °C with 2 mol% catalyst loading.



**Scheme 1.10.** Proposed outer-sphere mechanism for HBpin activation by Co-amido complex **1.19**.

Finally, the Trovitch group recently reported an excellent mechanistic study on Co-catalyzed dihydroboration of nitriles.<sup>74</sup> The reaction fully reduces nitriles to diborylated amines through two catalytic cycles, occurring at room temperature in 2 h with 1 mol% loading. Stoichiometric studies of **1.23** and nitrile showed no activity, indicative of an activation step involving addition of HBpin. Alternatively, reaction of **1.23** with 2.2 equiv of HBpin resulted in the isolation of a Co complex containing two boryl functionalities, one of which was bound to the chelated amide. While this was found to be a deactivation product, a previous report on Co-catalyzed nitrile hydroboration speculated that oxidative addition of borane to form a metal hydride was a key activation step.<sup>75</sup> In-depth DFT analysis of the reaction pathway led the authors to propose a mechanistic pathway utilizing MLC (**Scheme 1.11**). The first step involves reaction of **1.23** with HBpin to yield **1.24**

featuring a 4-membered Co–H–B–N– metallacycle analogous to Leitner’s work.<sup>71</sup> Nearly barrierless s-bond metathesis through **1.25** forms the Co–H species **1.26** that is the key intermediate for effective Bpin transfer. Binding of nitrile to Co forms **1.27**, and subsequent insertion into Co–H through TS **1.28** yields **1.29**. While this step is overall exergonic due to formation of a stable C–H bond, its associated barrier is the highest and rate-limiting for the first reduction cycle. Finally, intermediate **1.29** undergoes ligand-assisted borylation in which the pendant amine arm carrying the boryl initiates 1,3-migration through TS **1.30** to produce **1.31**. Liberation of the final borylimine product regenerates precatalyst **1.23**. From here, the authors propose that the borylimine may directly enter the second reduction cycle, as this monoborylated product was not observed throughout catalysis. This work represents an ingenious approach, utilizing a catalyst design strategy involving a ligand capable of electron storage, as well as Lewis base bifunctional behaviour enabling previously unattainable reactivity for base metals.



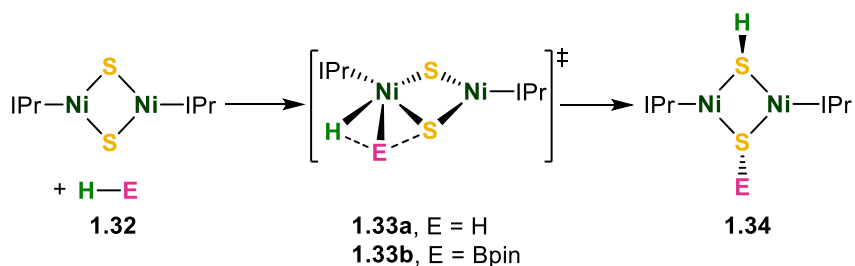
**Scheme 1.11.** Proposed mechanism for dihydroboration of nitriles by Co-complex.

### 1.3.1.2 Sulfur based ligands

It has been established that the synergistic interplay of a Lewis acidic metal and adjacent Lewis base is a powerful strategy for homogeneous catalysis. Complexes composed of polar-metal-nitrogen bonds represent the overwhelming majority of examples, representing the most applied and established catalyst types in the MLC community. Alternatively, transition metal catalysts incorporating metal-sulfur bonds as the Lewis basic reactive site remain underdeveloped. The metal-sulfur bond is a crucial feature in living systems, often playing a key role in biological processes such as dihydrogen activation by hydrogenases. Extensive work has been performed to elucidate the mechanism of these various enzymatic processes. Therefore, the inclusion of sulfur donors

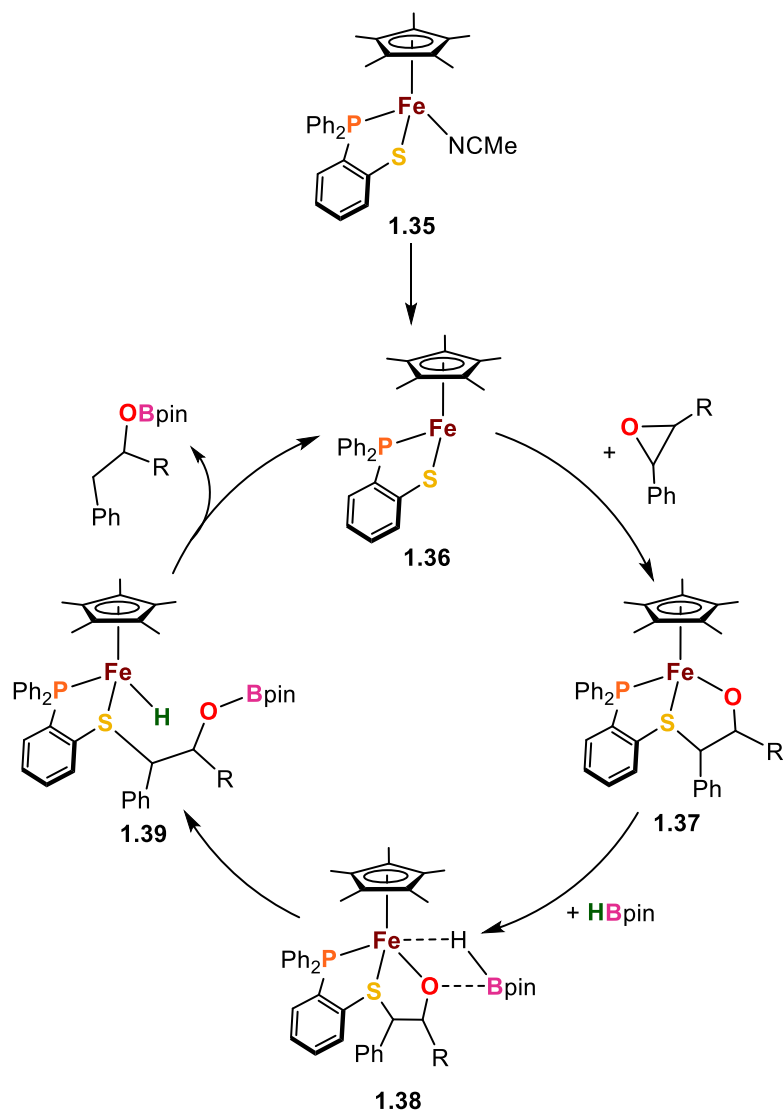
in bifunctional ligands for MLC catalysis may potentially provide insight into biological mechanisms, while helping propel homogeneous catalysis towards greener biomimetic systems.

Oestreich and co-workers have pioneered the use of bifunctional metal-thiolate complexes for MLC catalysis, particularly for the activation of Si–H bonds with ruthenium.<sup>76</sup> In 1999, one of the earliest reported instances of Si–H bond cleavage by first row MLC was reported by Bergman and Anderson with a titanocene sulfide complex.<sup>77</sup> Continuing work initiated by Hillhouse, Cundari and Jordan reported a dinuclear nickel complex with bridging sulfides for the cleavage of E–H bonds.<sup>78</sup> Reaction of **1.32** with dihydrogen afforded the bis thiolate-bridged Ni complex **1.34**. Combined kinetic and computational studies revealed that formation of **1.34** proceeds via heterolytic cleavage of H<sub>2</sub> across a cooperative Ni–S bond (**Scheme 1.12**). Subsequent *cis/trans* isomerization at Ni followed by H atom migration from Ni to S forms **1.33a**. Similar reactivity was observed with HBpin to afford **1.33b**, displaying the utility of metal-sulfur complexes for more generalized E–H activations.



**Scheme 1.12.** Heterolytic cleavage of H–H and B–H bonds across a Ni–S bond.

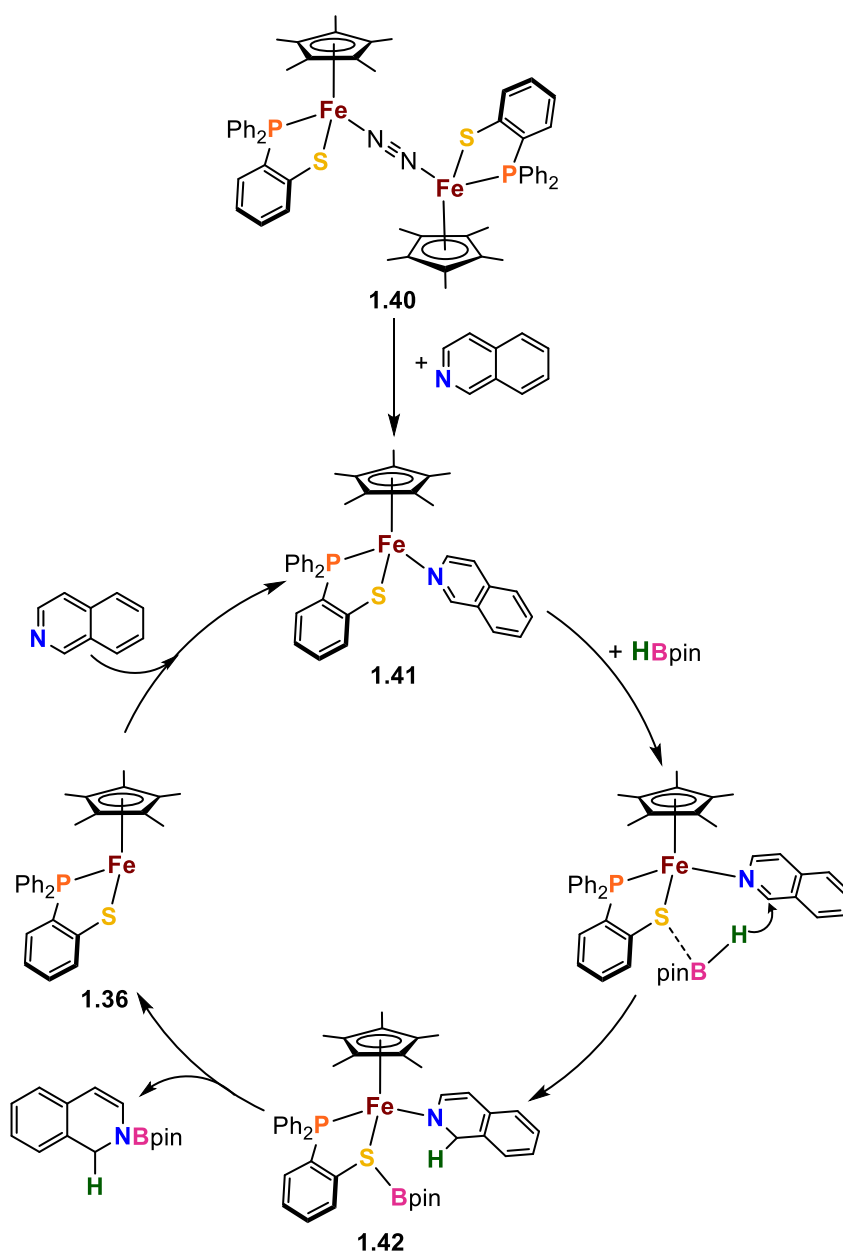
The Wang group has also extended the capabilities of base-metal thiolate complexes for MLC in catalysis. In 2017, they reported iron thiolate complex **1.35** for regioselective hydroboration of aryl epoxides (**Scheme 1.13**).<sup>79</sup> Interestingly, rather than initial B–H bond activation, direct addition of the epoxide across the Fe–S bond is the critical first step. While reaction of **1.35** with Lewis acidic boranes such as H<sub>3</sub>B•THF and 9-H-BBN afforded the corresponding iron-borane adducts featuring Fe B–H interactions, DFT studies found that addition of HBpin across the iron-thiolate bond was endergonic by 12.9 kcalmol<sup>-1</sup> (9-BBN = 9-borabicyclo[3.3.1]nonyl). Stoichiometric reaction of **1.35** with *trans*-2,3-diphenyloxirane yielded the 5-membered cyclic Fe alkoxide complex **1.37**. The authors proposed a mechanism initiated by loss of acetonitrile ligand forming **1.36**, followed by epoxide ring-opening through Fe–S cooperativity affording **1.37**. Electrophilic addition of HBpin forms **1.38** and turnover-limiting S–C bond cleavage/H transfer through **1.39** furnishes the final hydroborated product and regenerates **1.36**. This work presented a counterintuitive mechanistic pathway in which direct addition of HBpin is in fact thermodynamically unfavorable, providing potentially valuable insight for future catalytic systems.



**Scheme 1.13.** Proposed mechanism for Fe thiolate complex-catalyzed hydroboration of aryl epoxides.

The Wang group then furthered the potential of cooperative metal-thiolate reactivity, broadening the scope of hydroboration to include heteroarenes. The  $\text{N}_2$ -bridged diiron complex **1.40** efficiently provided  $N$ -borylated 1,2-reduced products with low catalyst loadings (1 mol%) and excellent regioselectivity.<sup>80</sup> Stoichiometric studies suggested a similar reaction pathway (**Scheme 1.14**) in which B-H bond cleavage is not the initial activation step, as  $\text{HBPin}$  did not react readily with **1.40**. Instead, catalysis was initiated by

displacement of N<sub>2</sub> by the *N*-heteroarene yielding mononuclear **1.41**. Subsequent turnover-limiting, thiolate-facilitated hydride transfer from HBpin to C<sub>2</sub> forming **1.42** showed a kinetic isotope effect (KIE) of 2.33. Final transfer of the Bpin group to the reduced heterocycle provides the hydroborated product and reforms 16e<sup>-</sup> active species **1.36**.



**Scheme 1.14.** Proposed mechanism for Fe-catalyzed hydroboration of *N*-heteroarenes.

Recent work over the last four years has highlighted the potential utility of thiolate donors in cooperativity with base metals. Future work should further investigate the potential scope of reactivity for thiolate systems and developing truly biomimetic base metal catalysts.

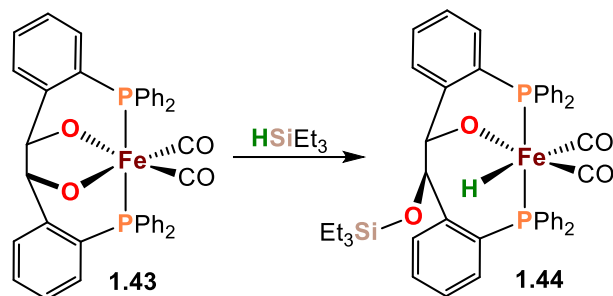
### **1.3.1.3 Oxygen based ligands**

Despite the widespread presence of oxygen in several hydrogenase enzymes, the involvement of alkoxide/alcohol weak field donors in MLC for bond activation is limited. The greater lability of alcohols over amines, and the lower Lewis basicity of coordinated alkoxides hinders utility in bond activation. There are several examples involving Ir and Ru that are beyond the scope of this review but have been discussed elsewhere.<sup>81</sup> Otherwise, there are relatively few reports involving cooperation between a base-metal and oxygen.

Pioneering work by the Adolffson group demonstrated that a base-activated mixture of iron acetate and hydroxyethyl-imidazolium salts provided efficient and selective catalysts for the hydrosilylation of a broad scope of aldehydes and ketones using polymeric poly(methylhydrosiloxane).<sup>82</sup> Although they were unable to characterize any Fe intermediates, they proposed bidentate alkoxide-NHC coordination and showed no conversion using the O-tosyl analogue.

Rauchfuss *et al.* prepared a related diphosphine-dialkoxide Fe(II) complex **1.43** and showed its cooperative Si–H bond activation to fully characterized Fe–H complex **1.44** (Scheme 1.15).<sup>83</sup> While **1.44** was not an active hydrosilylation catalyst, substitution of one

CO ligand by  $\text{PMe}_3$  or  $\text{NCMe}$  gave precursors that effected the hydrosilylation of benzaldehyde, acetophenone, and even styrene with catalyst loadings of 1 mol%.

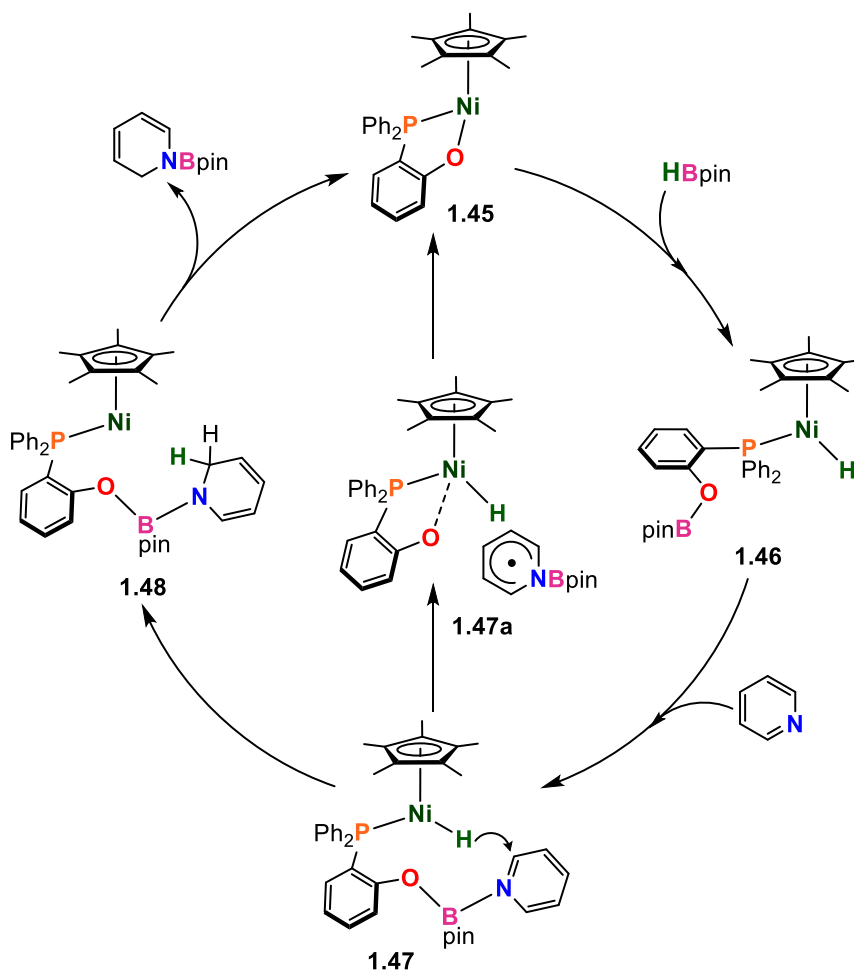


**Scheme 1.15.** Fe-alkoxide-assisted Si–H bond activation.

The Thomas group applied a similar NHC-alkoxide ligand for Markovnikov-selective Fe-catalyzed vinylarene hydroboration. Although the authors were unable to characterize Fe–H intermediates, deuterium labelling and mass spectral data provided solid evidence for MLC.<sup>84</sup>

Wang and co-workers recently applied the half-sandwich framework of their previous work to construct a Ni(II) complex bearing a phosphinophenolato ligand for the catalytic activation of pyridine and other *N*-heteroarenes.<sup>85</sup> Air-stable catalyst **1.45** enabled catalysis with 2 mol% loadings at room temperature, readily reducing a broad scope of pyridines and *N*-heterocycles under mild conditions. The necessity of the phosphinophenolato ligand was highlighted by the lack of activity of nickel-hydride complex  $\text{Cp}^*\text{Ni}(\text{H})(\text{PPh}_3)$ . Ni-alkoxide-assisted cleavage of the B–H bond initiates the catalytic cycle, affording fully characterized 18e- complex **1.46** which features an oxygen-stabilized boron moiety (**Scheme 1.16**). DFT calculations supported heteroatom coordination of the substrate to boron, and subsequent hydride transfer from Ni to the pyridine ortho carbon through **1.47** affords **1.48**. Final cleavage of the B–O bond releases the 1,2-reduced pyridine and

regenerates **1.45**. Deuterium labelling studies supported the hydride being transferred to the *ortho*-site, and this report demonstrates the crucial role played by MLC for both generating the active Ni–H and supporting in-cycle catalytic intermediates.



**Scheme 1.16.** Proposed mechanism for Ni-catalyzed hydroboration of *N*-heteroarenes.

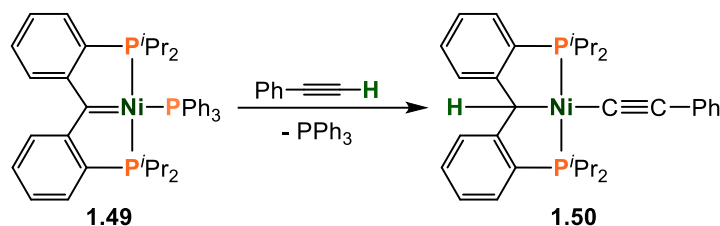
#### 1.3.1.4 Carbon based ligands

Carbenes have garnered recent interest as platforms to enable cooperative bond activation.<sup>86</sup> Cooperative addition of a substrate across a  $\text{M}=\text{C}$  bond results in formation of a transition-metal alkyl complex. Nucleophilic carbene species with late transition metals

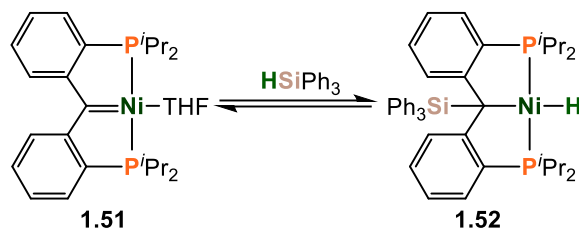
have had the most success to date; however, the only reports of this reactivity with base metals are with nickel.

The Piers group has reported several Ni-carbene complexes effective for cooperative bond activation, utilizing a rigid PC<sub>sp2</sub>P pincer ligand to stabilize the carbene. Addition of E–H substrates (H<sub>2</sub>, H<sub>2</sub>O, NH<sub>3</sub>, HC≡CPh) to **1.49** resulted in rapid cleavage across the Ni=C bond, affording species of the type **1.50** with concomitant loss of PPh<sub>3</sub> (**Scheme 1.19**).<sup>87</sup> A follow-up study expanded the reactivity of Ni-carbene **1.51** for the reversible activation of tertiary and secondary phenyl-silanes to afford **1.52**.<sup>88</sup> Kinetic and isotope labelling studies supported a concerted 4-centred addition across the Ni=C bond, similar to previously discussed E–H activations across metal–amido/thiolate bonds. A more rigid [PC<sub>sp2</sub>P] ligand was developed for CO<sub>2</sub> activation using **1.53**. Upon reaction with CO<sub>2</sub> the authors observed clean [2+2] addition of the C=O bond across the Ni=C bond yielding **1.54**. Formation of the NC<sup>t</sup>Bu derivative was clearly evidenced by NMR spectroscopy, and labelling studies demonstrated the reversibility of CO<sub>2</sub> activation in solution. The more soluble PMe<sub>2</sub>Ph derivative was characterized by single crystal X-ray diffraction. While these compounds have not yet been reported in catalytic applications, the potentially powerful reactivity of the carbene unit has been demonstrated, particularly in its ability to activate C–H bonds, the only example of a base metal in that context.

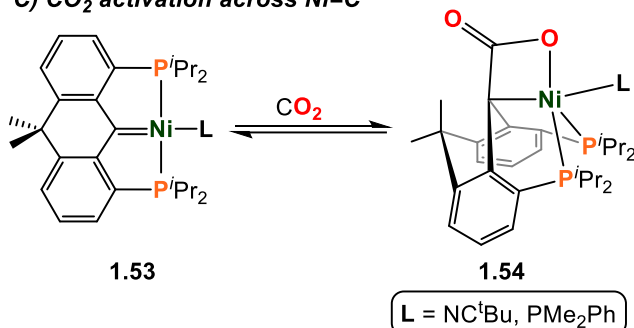
A) C-H activation across Ni=C



B) Si-H activation across Ni=C



C) CO<sub>2</sub> activation across Ni=C



**Scheme 1.19.** Cooperative activation of A) C–H, B) Si–H bonds, and C) CO<sub>2</sub> across a nickel-carbene.

### 1.3.2 Ligand acts as a Lewis acid

Despite the decades of work and remarkable achievements of metal-Lewis base cooperativity in catalysis, the use of ligands that present a Lewis acid functionality for MLC has only gained prominence over the last ten years. Due to the propensity of late 3d metals to preferentially undergo 1e<sup>-</sup> processes, the installation of a Lewis acidic moiety in the supporting ligand scaffold has emerged as another tactic for imparting nobility to these first-row metals.<sup>89</sup> The labile interaction between a transition metal center and a Lewis acid component in the ligand has been likened to an organometallic frustrated Lewis pair (FLP),

whereby an electron-rich, low valent metal center acts as a Lewis base.<sup>90</sup> While there have been instances of cooperation between 2<sup>nd</sup> and 3<sup>rd</sup> row metals and Lewis acid moieties installed in the ligand framework,<sup>91-92</sup> work with the base metals remains underdeveloped.

### 1.3.2.1 Boron acceptors

The most ubiquitous Lewis acid functionality installed into a ligand framework is the pendant borane.<sup>91</sup> The first metalloborane featuring a first-row metal was reported by Rabinovich and co-workers who described the synthesis of a cobalt(II) tris(mercaptoindazolyl)borate complex **1.55** (Figure 1.4).<sup>93</sup> This was quickly followed by reports from the Parkin group on metalloboranes with Fe (**1.56**),<sup>94</sup> and Ni (**1.57**).<sup>95</sup> They further described the ability of these complexes to facilitate E–E' bond activations (E = H, Si, C; E' = H, Cl, Br). Metalloboranes have been well established to facilitate oxidative addition of E–H bonds across the metal-borane platform, dating back to the first reported instance of H<sub>2</sub> activation by a Rh-borane complex by Owens.<sup>96</sup>

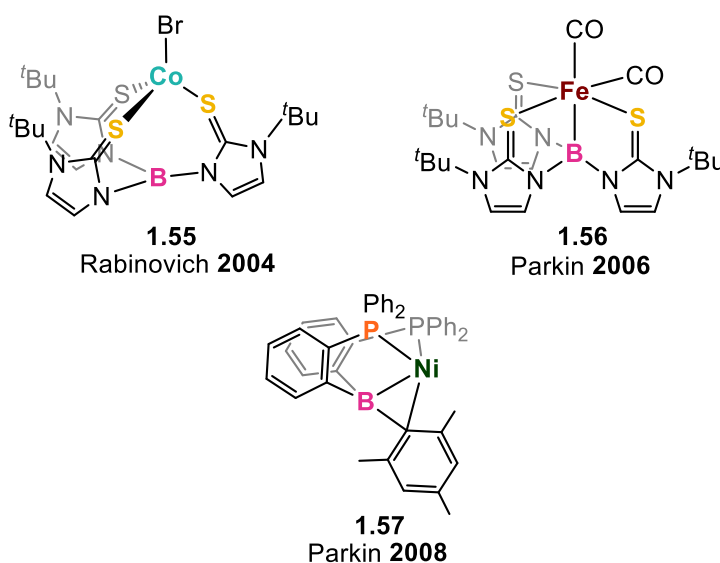
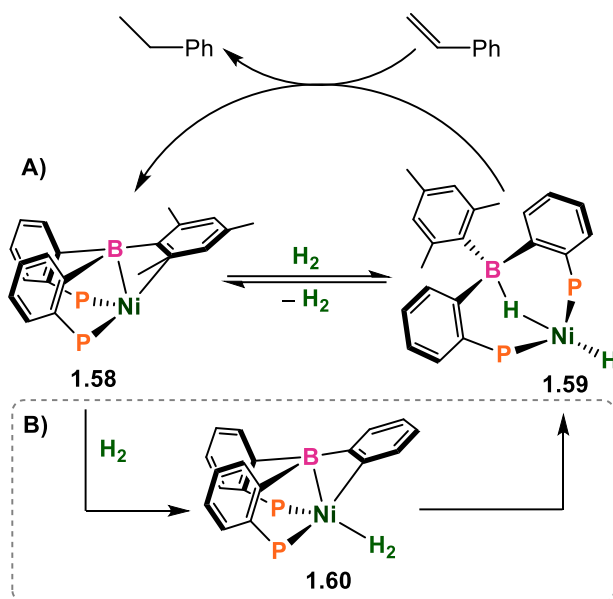


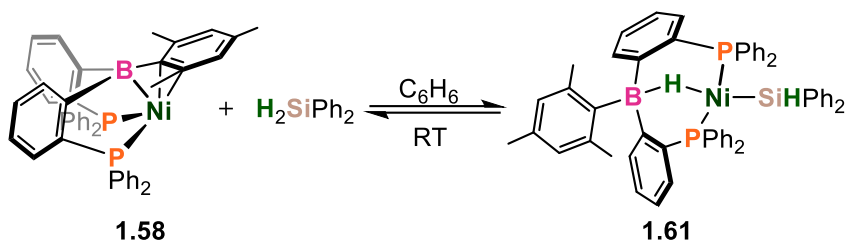
Figure 1.4. Earliest examples of metalloboranes of first-row transition metals.

Since these early reports, both the interest and knowledge in this field have grown significantly, most notably in work by the Peters group. In 2012, Harman and Peters detailed the synthesis of a bromo-nickel bis(2-diphenylphosphino-phenyl)mesitylborane complex which upon reduction by Na/Hg furnished the zerovalent complex  $[\text{Ni}(\eta^3\text{-BC-Mes}^{\text{Mes}}\text{DPB})]$  (**1.58**).<sup>97</sup> They discovered that **1.58** readily adds  $\text{H}_2$  across the Ni–B bond forming Ni(II)–hydride-borohydride complex **1.59** (Scheme 1.20). Interestingly, the  $\beta$ -phenyl derivative was inactive towards reaction with dihydrogen. Complex **3.8** was characterized by a series of multinuclear NMR experiments and was found to be in equilibrium with **1.58** in a 5:1 ratio under 1 atm of  $\text{H}_2$ . They also demonstrated that **1.58** is an active precatalyst for the hydrogenation of styrene using 1 mol% loading at room temperature. To more closely follow the formation of **1.59**,  $i\text{Pr}$  groups were installed on the phosphine donors to enhance  $\text{H}_2$  binding and impede  $\text{H}_2$  cleavage.<sup>98</sup> This allowed the authors to structurally characterize the Ni– $\text{H}_2$  adduct **1.60** as an intermediate during  $\text{H}_2$  cleavage, and the intact nature of  $\text{H}_2$  was confirmed by deuterium labelling studies.



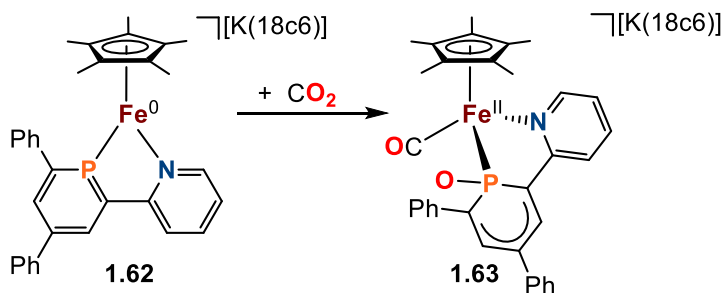
**Scheme 1.20.** A) Reversible Ni-catalyzed activation of H<sub>2</sub> and hydrogenation of styrene (P = PPh<sub>2</sub>); B) Formation of Ni-H<sub>2</sub> adduct (P = P<sup>i</sup>Pr<sub>2</sub>).

Operating with these established complexes, the Peters group expanded their work to the activation of E-H bonds with various first-row metals. Inspired by the affinity of **1.58** to facilitate H<sub>2</sub> activation at room temperature, they investigated its potential as a bifunctional hydrosilylation catalyst. Stoichiometric reaction of **1.58** with either phenyl- or diphenyl-silane resulted in immediate Si-H bond cleavage, affording nickel silyl borohydride complex **1.61** (Scheme 1.21).<sup>99</sup> Complex **1.61** exists in a solution equilibrium with **1.58** and is proposed to be an intermediate in the hydrosilylation of a variety of *para*-substituted benzaldehydes. Elegant kinetic and isotopic labelling studies led the authors to propose a mechanism whereby insertion of the aldehyde into the Ni-Si bond of **1.61** generates a nickel siloxyalkyl intermediate that furnishes the hydrosilylated product via reductive elimination, regenerating **1.58**.



**Scheme 1.21.** Reversible bifunctional activation of Si–H bonds in organosilanes by **1.58**.

In addition to B and Al Lewis acids, MLC has been reported with metal complexes of N-heterocyclic phosphonium cations (NHPs). Although not yet demonstrated for a catalytic reaction, Muller, Wolf and co-workers described C–O bond cleavage of CO<sub>2</sub> using iron phosphinine complex **1.62** (Scheme 1.22).<sup>100</sup> Addition of CO<sub>2</sub> to **1.62** results in complete cleavage of one C=O bond, with coordination of the resultant CO to the Fe centre and O-atom transfer to the P without cleavage occurring in the ligand backbone as previously observed by Milstein.<sup>101</sup> The authors attribute this unique reactivity to the electronic flexibility of the phosphinine moiety.



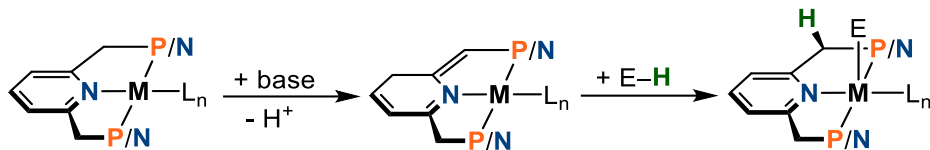
**Scheme 1.22.** Activation of CO<sub>2</sub> utilizing electronically flexible phosphinine donor.

The use of Lewis acidic moieties has tremendous potential and more groups are taking note and making use. The Lu group has installed Lewis acidic moieties directly to base metals to increase reactivity.<sup>102-104</sup> While the Lewis acid component is not directly involved in the catalysis, it plays a key role in modifying the metal reactivity, further demonstrating

the utility of this strategy. The potential of these ligand systems to expand reactivity into, for example dehydrogenative C–H activation, which has been reported with Pt, with first row metals would be a great move forward.

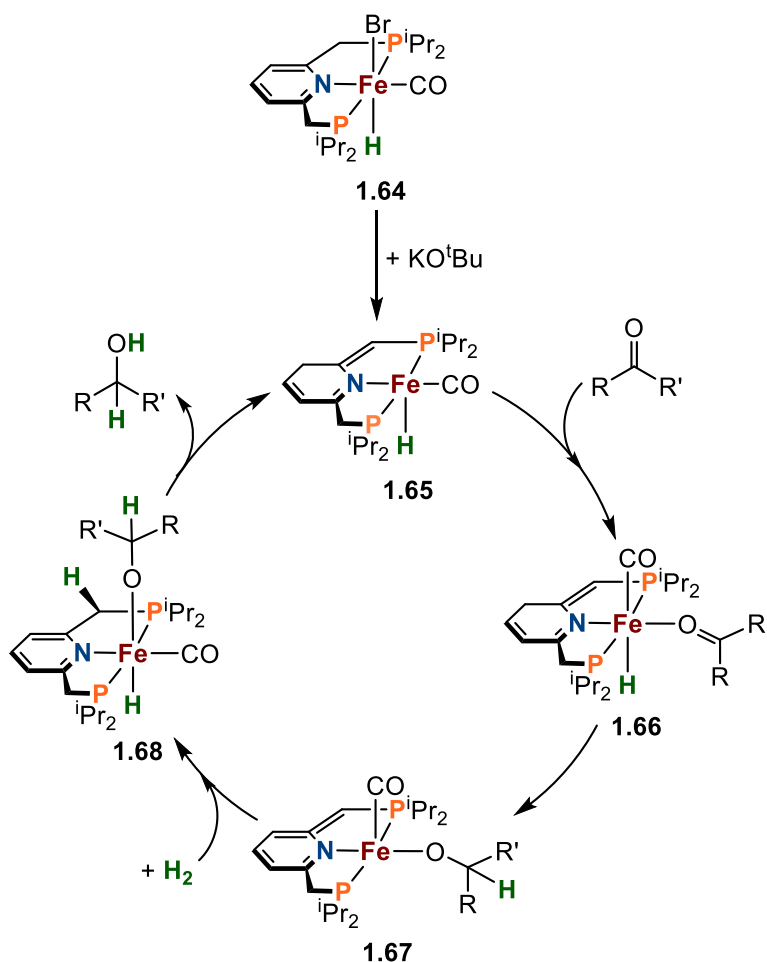
### **1.3.3 Aromatization / dearomatization**

Since the inception of pincer ligands by Shaw in 1976,<sup>105</sup> there have been countless reported variations of meridional ligand scaffolds with a variety of donors.<sup>106</sup> The strategic design of pincer ligands is often a critical element in the successful implementation of a catalytic cycle.<sup>107</sup> When partnered with late metals, formally neutral tridentate pincers have attracted attention for alternative chemistry compared to their monoanionic analogues. More specifically, Milstein has pioneered the use of substituted lutidine, picoline, and associated ligands for MLC resembling that of previously discussed Lewis bases.<sup>33</sup> Such pyridine-based pincer complexes feature methylene linkers in the *ortho* positions that are susceptible to deprotonation by strong base, thereby undergoing dearomatization of the ligand scaffold with no formal oxidation change at the metal centre. The deprotonated methylene generates amido character at N which acts as a reactive center in the first coordination sphere of the metal. Cooperative E–H heterolysis of a substrate via 1,3-addition across the metal-ligand framework then results in rearomatization of the substituted pyridine ring (**Scheme 1.23**). The elegantly cooperative nature of these lutidine-derived ligands has led to significant advancements in catalysis, particularly with 2<sup>nd</sup> and 3<sup>rd</sup> row metals. Remarkably, this potential has only been extended to first-row metals within the last decade. There have been several reviews and accounts covering the progress made in this area, but we discuss only advances made with the base-metals, of which the last five years have been particularly productive.



**Scheme 1.23.** General mechanism for aromatization / dearomatization MLC.

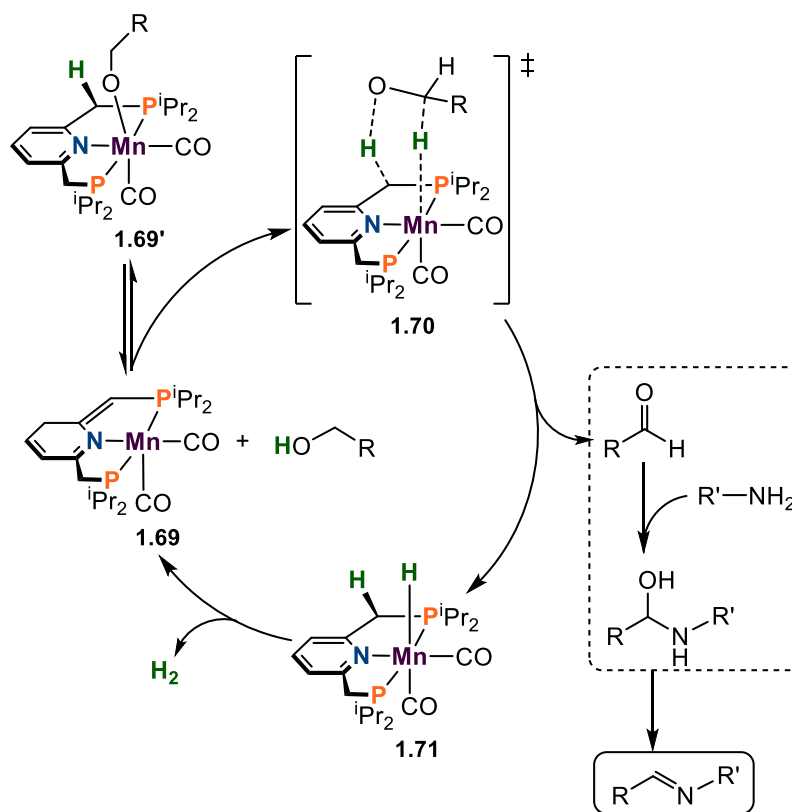
Dating back to Milstein's first observation of this phenomenon in Ru complexes,<sup>108</sup> the aromatization/dearomatization (A/D) mechanism has been utilized on numerous occasions with Ru and Ir. This was followed by early observations by van der Vlugt of A/D in Ni and Cu complexes bearing [PNP] ligands. Milstein then extended this reactivity to iron for catalytic hydrogenation of ketones with TONs up to 1880.<sup>109</sup> Complex **1.64** was found to be an efficient precatalyst for ketone hydrogenation under mild conditions with low loadings of base and catalyst (0.1 and 0.05 mol% respectively). Shortly thereafter, the iron-hydride-borohydride derivative of **1.64** was reported to display similar catalytic activity without the need for added base to initiate the catalytic cycle.<sup>110</sup> Associated stoichiometric experiments and comprehensive DFT analysis led the authors to propose a reaction pathway (**Scheme 1.24**). Deprotonation of precatalyst **1.64** forms dearomatized intermediate **1.65**, followed by ketone coordination and isomerization to **1.66**. Insertion of the ketone into Fe–H affords **1.67**, and subsequent bifunctional activation of dihydrogen forms aromatized intermediate **1.68**. Final product release by MLC regenerates dearomatized **1.65** to close the catalytic cycle.



**Scheme 1.24.** Proposed mechanism for Fe-catalyzed hydrogenation of ketones via aromatization / dearomatization MLC.

Since this initial report, the application of A/D in cooperative catalysis has markedly increased to encompass more transformations across the first-row metals. Milstein has investigated Fe-catalyzed dehydrogenation of formic acid,<sup>111</sup> and hydrogenation of aldehydes,<sup>112</sup> esters,<sup>113</sup> amides,<sup>114</sup> and  $\text{CO}_2$ .<sup>115</sup> Notably, in 2016 the same group expanded the compatibility of the pyridine-based PNP ligand framework to catalysis with manganese.<sup>116</sup> Complex **1.69** was reported as the first instance of (de)hydrogenation-type reactivity for manganese, in the dehydrogenative coupling of alcohols and amines to yield imines with liberation of  $\text{H}_2$ . In-depth mechanistic studies entailing NMR monitoring and

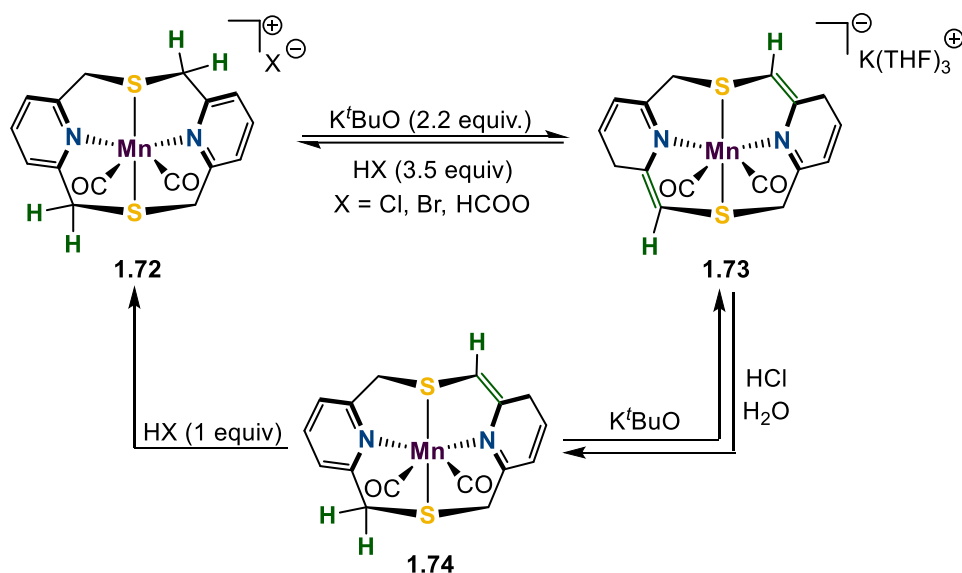
isolation of intermediates allowed the authors to propose a mechanism involving MLC (**Scheme 1.25**). Under the reaction conditions, dearomatized **1.69** was found to be in dynamic equilibrium with alkoxo complex **1.69'** with concomitant aromatization. The latter complex was independently synthesized to confirm characterization and highlights the O–H bond activation by MLC. Dehydrogenation of benzyl alcohol was thus proposed to proceed through the concerted bifunctional TS **1.70**, releasing benzaldehyde and forming new Mn–H complex **1.71**, which was isolated and characterized crystallographically. The benzaldehyde product reacts with amine to form an unstable hemiacetal which releases water to furnish the final imine product, while loss of H<sub>2</sub> from **1.71** regenerates **1.69** for another catalytic cycle. This work effectively advanced the capabilities of A/D manganese, providing a first look into relevant catalytic intermediates and resting states.



**Scheme 1.25.** Proposed mechanism for dehydrogenative coupling of alcohols and amines.

Finally, similar to ligands operating via Lewis base MLC, a potential drawback of these ligand systems is their reliance on strong  $\sigma$ -donor phosphines that offer the remarkable stability displayed (reaction temperatures often  $>100$  °C). The expense and instability of phosphine-based ligand systems makes the pivoting towards more biomimetic ligand frameworks containing sulfur highly desirable. In earlier work, Milstein showed that ruthenium complexes bearing a sulfide-based PNS ligand undergo spontaneous dimerization via C–S bond cleavage resulting in net loss of an S<sup>IBu</sup> group. Undesirable side reactions, low stability, and lack of a convenient NMR handle make the study of sulfur-supported catalysts more challenging. Recently, Khusnutdinova reported a Mn complex bearing a macrocyclic N<sub>2</sub>S<sub>2</sub> pyridinophane ligand which provided uncommon stability.<sup>117</sup>

This allowed for the opportunity to investigate and characterize the reversible formation of a doubly dearomatized, singly dearomatized, and aromatized species based on a biomimetic *N,S*-ligand via deprotonation of the methylene linkers (**Scheme 1.26**). Reaction of **1.72** with 2.2 equiv of  $\text{KO}^t\text{Bu}$  results in the doubly deprotonated species **1.73** which was characterized by X-ray crystallography and NMR. The reversibility of this transformation was demonstrated by addition of 3.5 equiv of either HBr, HCl, or formic acid to regenerate **1.72**. Attempts to access the mono deprotonated species by deprotonation of **1.72** were unsuccessful; reaction of **1.73** with 1 equiv of HCl formed the desired complex **1.74**. Complex **1.73** showed no activity for direct or transfer hydrogenation chemistry, however, likely due to the strongly bound CO ligands not allowing for an open coordination site. Replacement with potentially more labile ligands may enable entrance into a catalytic cycle, which would represent significant progress towards the replacement of phosphines in A/D MLC catalytic systems.



**Scheme 1.26.** Syntheses of aromatized (**1.72**), singly dearomatized (**1.74**), and doubly dearomatized (**1.73**) structures of  $\text{Mn}[\text{N}_2\text{S}_2]$  complexes.

### **1.3.4 Redox active ligands**

Homogeneous transition metal catalysis is traditionally based on precious metal complexes that enable predictable 2e- redox events to facilitate the crucial cleavage and formation of new bonds during catalytic turnover.<sup>118</sup> Efforts have more recently focused on developing new catalysts based on earth abundant first row transition metals not only for their economy and lower toxicity, but also for potentially new catalytic processes. First-row transition metals from manganese to copper offer an array of accessible oxidation and spin states that may facilitate novel reactions,<sup>119-122</sup> however, these metals generally prefer to undergo 1e- redox events. Redox-active ligands can enable reversible electron transfer with a transition metal and offer the opportunity to mediate odd-electron pathways.<sup>29</sup> Furthermore, cooperation between a redox-active ligand and a base metal can facilitate valuable multi-electron transformations usually carried out by noble metals.<sup>123</sup> Several reviews have effectively covered this topic from different perspectives.<sup>124-130</sup>

While chemical redox events traditionally take place at the metal, redox-active ligands possess frontier orbitals of similar or lower energies. Instead of acting as spectators, redox-active ligands can actively participate in the redox event. This results in either exclusively ligand-based redox events that leave the metal in the same oxidation state, or alternatively, both ligand and metal change oxidation state in a synergistic fashion leading to ambiguity about the electronic nature of each. These properties were identified originally in catecholate, dithiolene, and porphyrin ligands which have more recently been joined by a multitude of redox-active ligand frameworks, including bis(imino)pyridine,  $\alpha$ -bisimine, dithiolene, porphyrin, and salen. The Wieghardt group in particular has made remarkable contributions towards further understanding the intricacies of both the coordination

chemistry, and the electronic structures of redox-active ligand frameworks with the late transition metals.<sup>131-134</sup>

There are three common modes of operation whereby redox-active ligands cooperate with a metal centre: i) Enhancing the Lewis acidity/basicity of the metal center via ligand-based oxidation or reduction; ii) Acting as an ‘electron-reservoir’, allowing the metal to either store electrons on the ligand, or provide ligand electrons to the metal to modulate its oxidation state; iii) Formation of reactive ligand-based (or substrate) radicals to directly participate in bond cleavage and formation. In summation, redox non-innocent ligands can participate in a catalytic cycle by either accepting/releasing electrons or forming/breaking chemical bonds (**Figure 1.5**).

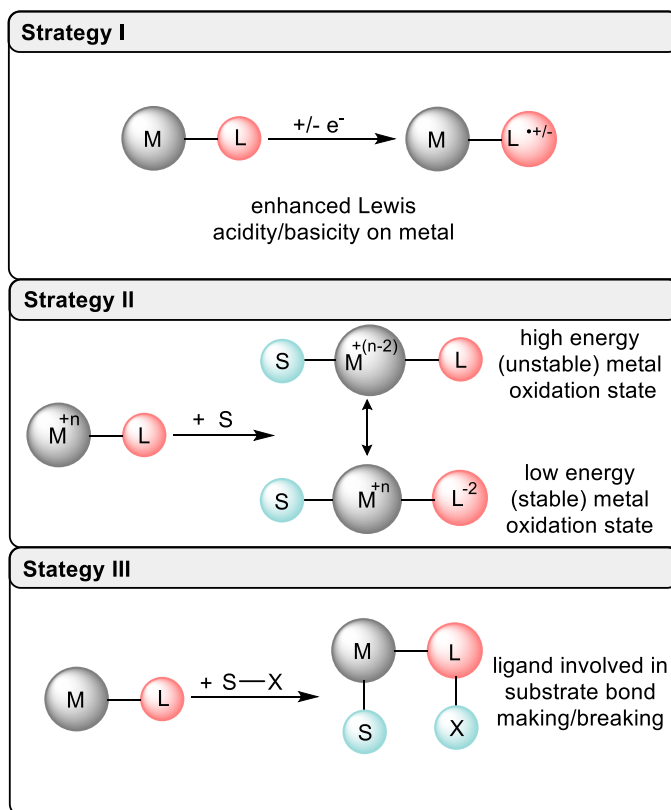
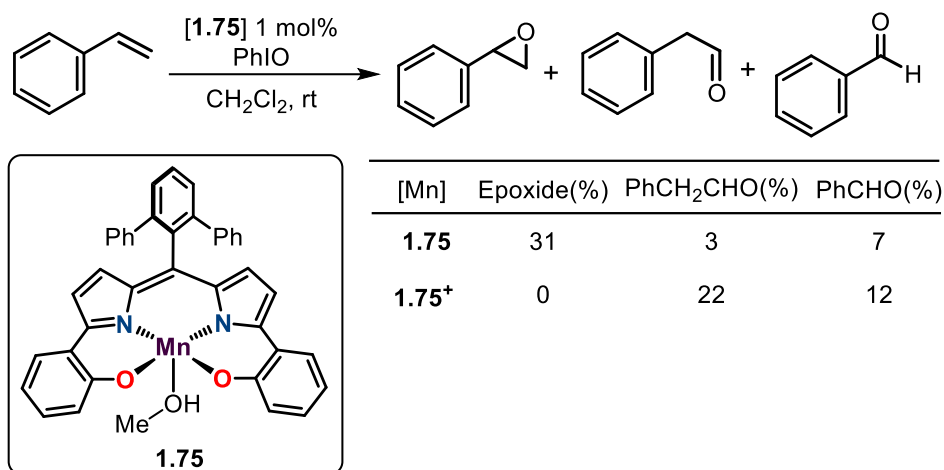


**Figure 1.5.** Three MLC methods for redox-active ligands in catalysis.

#### **1.3.4.1 Enhancing Lewis acidity/basicity**

Often the most straightforward and rudimentary approach applied when optimizing a catalytic cycle is to alter the ancillary ligand design by either steric or electronic modification.<sup>31</sup> Altering the electronic properties by installing appropriate electron-donating or electron-withdrawing substituents on the ligand, often requires laborious and multistep syntheses. A more direct approach involves oxidizing or reducing a redox non-innocent ligand, thereby directly tuning the Lewis acid character of the metal, avoiding expensive ligand modification syntheses, and not affecting the steric environment.

The literature is rich with examples of redox-active ligands enabling a change in the oxidation state of the metal, however, accounts of enhanced reactivity of the metal center are rare. Rauchfuss first reported this phenomenon in work with Ir and Ru complexes.<sup>135</sup> Even less frequent is utilizing this concept with first-row metals. The most straightforward approach is direct oxidation/reduction with an appropriate redox reagent.<sup>136</sup> Storr and co-workers reported a square pyramidal Mn(III) complex (**1.75**) bearing a bis(phenolate)dipyrrin ligand with a methanol in the axial position. Complex **1.75** showed two reversible oxidations waves at 0.00 and 0.47 V vs. Cp<sub>2</sub>Fe<sup>+0</sup> which were assigned as ligand-centered processes. Reaction with AgSbF<sub>6</sub> gave 1e<sup>-</sup> oxidized species **1.75**<sup>+</sup> which exhibits an S = 3/2 ground state due to antiferromagnetic coupling between Mn(III) and the ligand radical. While both **1.75** and **1.75**<sup>+</sup> serve as catalysts for styrene oxidation, **1.75** yields styrene oxide while the cation forms mostly phenylacetaldehyde (**Scheme 1.27**).<sup>137</sup>



**Scheme 1.27.** Different product selectivity in styrene oxidation catalyzed by neutral and cationic Mn complexes.

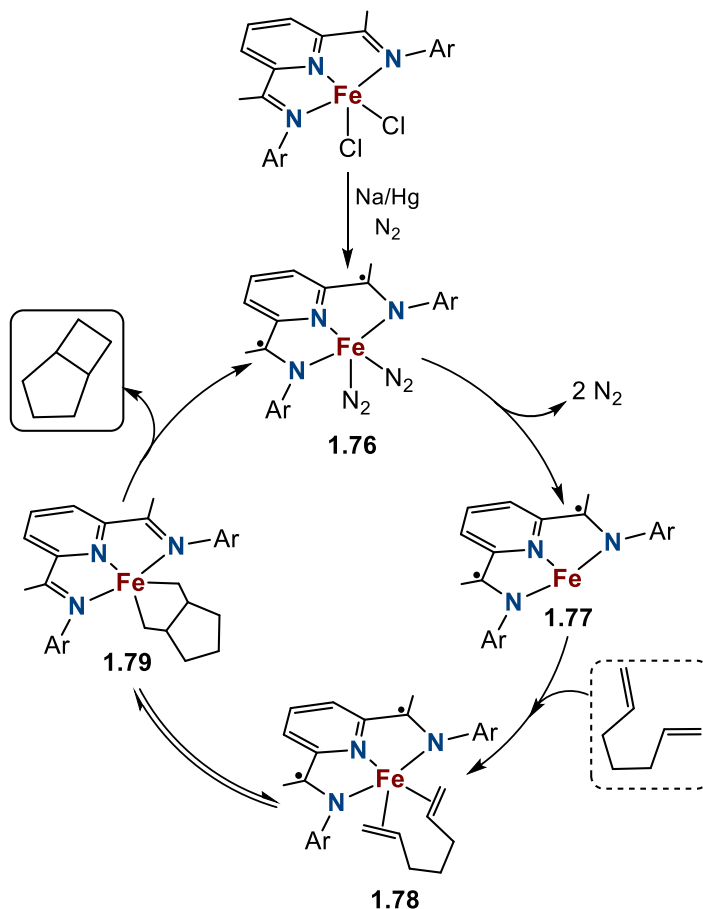
Despite the seminal results reported by Rauchfuss (*vide supra*), there have been relatively few examples of tuning metal-based reactivity via ligand-based redox events, especially with the first-row metals. Further work utilizing redox-active ligands to alter and tune the metal center may unearth new reactivity with the same structural skeleton.

### 1.3.4.2 Redox active ligand as electron reservoir

Some of the most powerful transition metal catalyzed transformations rely upon classic 2e<sup>-</sup> oxidation state changes. Many catalytic cycles that follow this *modus operandi* are initiated by oxidative addition and conclude with reductive elimination, each proceeding via 2e<sup>-</sup> steps (M<sup>n+</sup> and M<sup>n+2</sup>). Contrarily, first-row metals often prefer single-electron changes (i.e. Fe<sup>II</sup>/Fe<sup>III</sup>). The use of a redox-active ligand to temporarily store additional electrons without affecting the oxidation state of the metal may impart nobility to the first-row metals allowing them to facilitate 2e<sup>-</sup> reactions traditionally dominated by the late 2<sup>nd</sup> and 3<sup>rd</sup> row metals.<sup>123</sup>

Chirik and coworkers have made significant contributions to the advancement of this application. They spent over a decade developing iron and cobalt complexes featuring redox-active ligands based on the bis(imino)pyridine [PDI] framework.<sup>17,119</sup> The PDI ligand is a well-established redox-active framework able to undergo discrete 1e- redox events and stabilize a multitude of metal oxidation states.<sup>138</sup> In 2004, they reported an Fe(II) complex [Fe(PDI)Cl<sub>2</sub>] that upon sodium amalgam reduction under nitrogen furnished bis(dinitrogen) complex, [Fe(PDI)(N<sub>2</sub>)<sub>2</sub>] (**1.76**), an active precatalyst for hydrogenation of simple olefins.<sup>139</sup> A key design feature of this complex crucial for its reactivity is that the 2e- reduction occurs at the ligand rather than the metal, allowing the iron to stay in the Fe(II) oxidation state.<sup>132</sup> Shortly thereafter, complex **1.76** was reported to facilitate the [2+2] cycloaddition of dienes to form cyclobutene bicycles (**Scheme 1.28**).<sup>140</sup> Loss of dinitrogen forms **1.77**, leaving vacant sites available for diene coordination. An equilibrium was reported between **1.78** and oxidative addition product **1.79**, which is facilitated by the two electrons conveniently stored in the dianionic PDI ligand from the previous reduction. This allows Fe to maintain its stable (II) oxidation state as opposed to energetically less stable Fe(IV). Finally, rate determining reductive elimination furnishes the cyclized product, reforming **1.76** and dianionic PDI, allowing the metal to avoid the high energy Fe(0) oxidation upon reductive elimination. Recently, Chirik and coworkers detailed thorough mechanistic work on this system, identifying the *trans*-metallacycle species **1.79** as the catalyst resting state; this is particularly of interest because the final product is the *cis*-bicycle. Computations revealed that the TS for reductive elimination of the *cis*-isomer was lower in energy, leading to preferential formation.<sup>141</sup> Overall, the [PDI] ligand adopts its 1e- reduced form which results in a more oxidized Fe-center, and the electrons stored

in the ligand also mediate the oxidation state of the metal to avoid any thermodynamically unfavorable intermediates, making the overall reaction possible.



**Scheme 1.28.** Proposed mechanism of [Fe(PDI)]-catalyzed [2+2] cycloaddition of dienes.

Both this ligand scaffold and reaction manifold have been further utilized for a multitude of catalytic reactions with iron, including enyne cyclization,<sup>142</sup> alkene hydrogenations, olefin polymerizations,<sup>143</sup> hydrosilylation of unactivated olefins,<sup>144</sup> and C–C oxidative additions (some examples are shown in **Figure 1.5**).<sup>145</sup> More recently, the system was utilized for selective intermolecular [2+2] cycloadditions of unactivated alkenes.<sup>146-147</sup> The reactivity scope of this system has been further expanded towards the coupling of CO<sub>2</sub> and ethylene as a new potential route for carboxylate synthesis.<sup>148</sup> Analogous cobalt-[PDI]

complexes exhibit similar catalytic activity in ethylene polymerization,<sup>149-150</sup> alkene<sup>151-152</sup> and alkyne<sup>153</sup> hydroboration, dehydrogenative silylation,<sup>154</sup> stereoselective alkene hydrogenation,<sup>155-156</sup> and [2+2] cycloadditions of dienes.<sup>157</sup> The Chirik group continues to explore the subtle interplay of substrate and ligand effects in these systems to design optimized catalysts for further hydrocarbon upgrading reactions.<sup>158</sup>

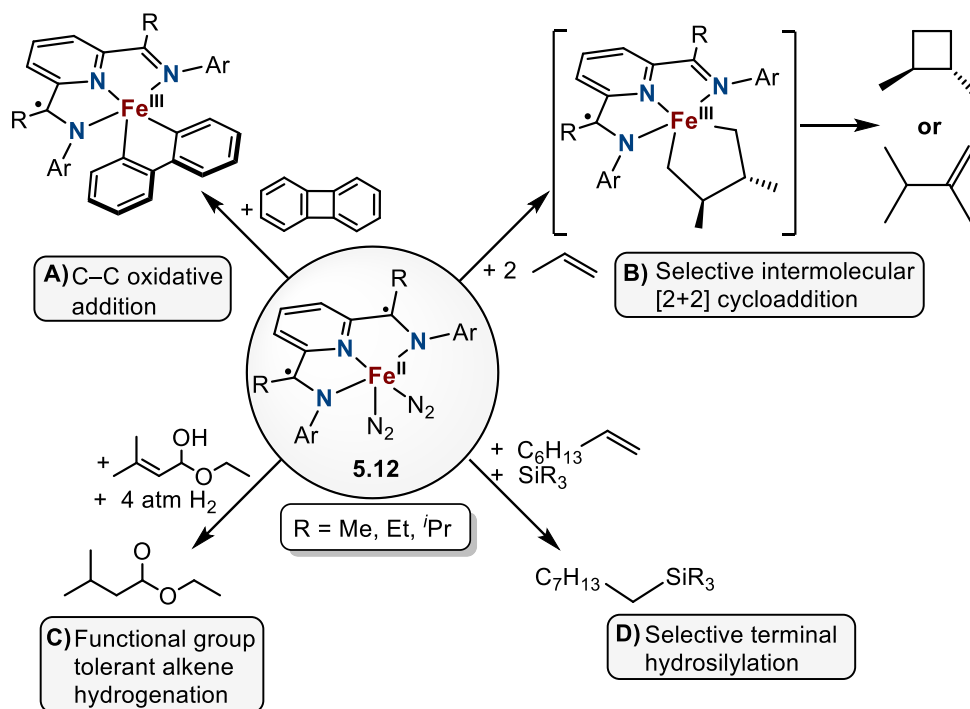
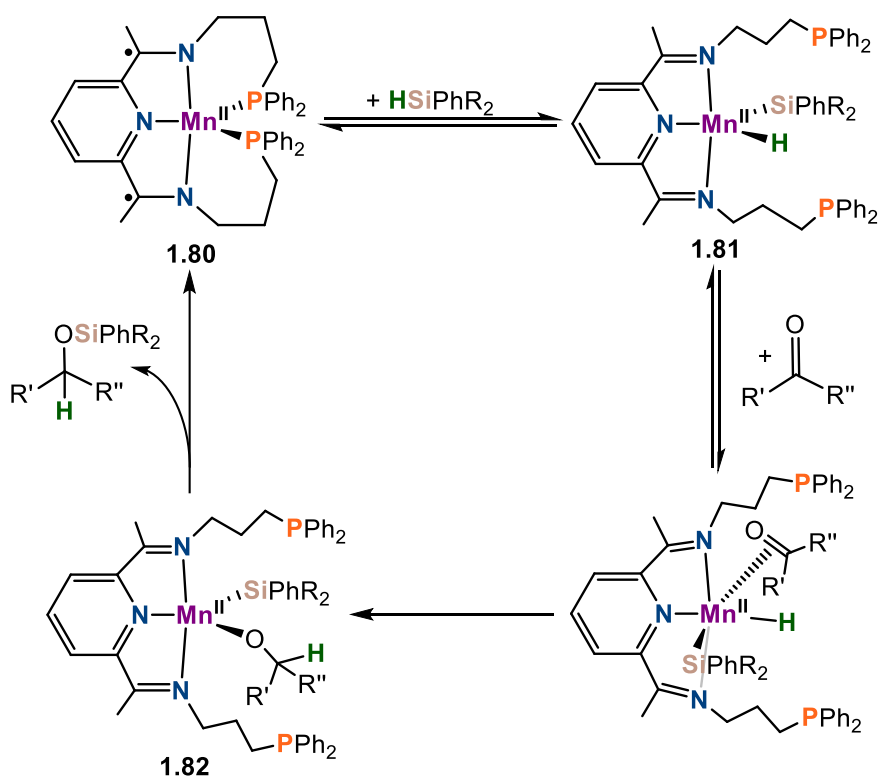


**Figure 1.5.** Examples of reported catalytic reactions facilitated by Fe[PDI][N<sub>2</sub>]<sub>2</sub> (**1.76**).

While efforts have been made towards the development of first-row transition metal catalysis with Fe, Co, and Ni historically, much less attention has been paid to Mn. The Trovitch group has contributed significantly to the application of redox-active ligands in Mn catalysis.<sup>121</sup> They developed a phosphine substituted PDI ligand framework, featuring hemilabile phosphine moieties on the imines for remarkably efficient (room temperature, < 1 mol% cat.) Mn-catalyzed hydrosilylations of ketones and aldehydes (**Scheme 1.29**).<sup>159</sup>

Sodium amalgam reduction of  $\text{Mn}[\text{Ph}_2\text{PPrPDI}][\text{Cl}]_2$  affords five-coordinate species (**1.80**). While the Mn center is formally zero-valent, detailed EPR experiments along with DFT analysis suggested a low-spin Mn(II) ( $S = 1/2$ ) ground state with a chelating dianionic ligand. In-depth kinetic and mechanistic studies led the authors to suggest a modified Ojima mechanism.<sup>160</sup> Initial dissociation of phosphine is followed by reversible Si–H oxidative addition to yield the five-coordinate silyl-hydride intermediate **1.81**. Subsequent rate-determining insertion into the M–H bond forms **1.82**, and final reductive elimination furnishes the final hydrosilylated product, reforming **1.80**. Again, the PDI framework plays a crucial role, allowing Mn to maintain its divalent oxidation state throughout the catalytic cycle.



**Scheme 1.29.** Modified Ojima mechanism for Mn-catalyzed hydrosilylation of carbonyls.

## **1.4 Towards Sustainable Ligand Development**

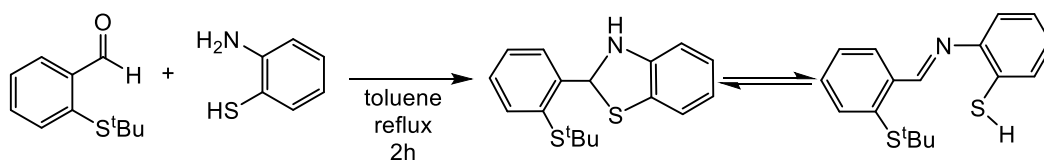
### **1.4.1 Motivation for [SNS] ligands**

As the demand for sustainability in catalysis continues to be prioritized, so does the need for each aspect of a catalyst to be critically considered. The past two decades have seen great effort being placed on the development of catalysts using abundant, cheap, and sustainable metals to achieve this long term “green” goal of sustainability. This has seen the development of novel base metal catalysts capable of facilitating a wide range of challenging catalytic transformations in an efficient manner. Often, however, these catalysts rely on phosphine-based multidentate ligands which have several drawbacks, including: i) limited large scale availability, ii) synthetically difficult to access, iii) air and moisture instability, iv) cost. These detriments may outweigh the cost benefit saving of using the abundant 3d metals for a sustainable solution. This highlights the need to develop economic, readily available, and synthetically accessible ligands. One recent strategy that has been advocated is the development of phosphine-free ligands composed of biomimetic ligand donors (C, N, O, S).

### **1.4.2 Previous work with nitrogen and sulfur containing pincer ligands**

A large variety of mixed N,S-donor pincer ligands have been reported in anionic, dianionic, and trianionic various motifs, including [SNS], [NNS], and [NSN].<sup>161-167</sup> While these ligands have been largely combined with first-row transition metals, reports of catalytic activity are rare. Of particular interest to this work is a previous report from Bouwman and coworkers, who detailed the synthesis of a simple [S<sup>*t*-Bu</sup>N<sup>H</sup>S] heterocycle.<sup>168</sup> This species was easily prepared from reaction of functionalized aldehyde with the appropriate aniline, and it was determined that the heterocycle exists in equilibrium with

the imine isomer in chloroform. Interestingly, treatment of the  $[S^{t-Bu}N^H S]$  heterocycle with nickel acetate afforded a mononuclear Ni(II) complex featuring the ring opened isomer of the  $[S^{t-Bu}N^H S]$  ligand. Alternatively, treatment of  $[S^{t-Bu}N^H S]$  heterocycle with nickel tetrafluoroborate furnished a dinuclear Ni(II) complex which featured a dianionic  $[S^-NS^-]$  ligand due to loss of the  $t$ Bu group. This influential work guided future ligand design strategies presented in this dissertation and presented trends involving ligand decomposition pathways to be strategically avoided.

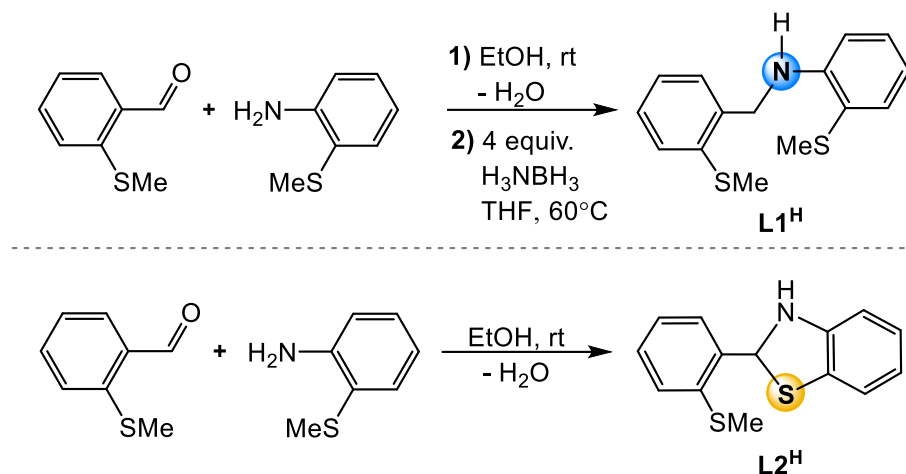


**Scheme 1.30.** Previous report of a  $[S^{t-Bu}N^H S]$  ligand.

### 1.4.3 Two [SNS] ligands with different bifunctional donors

We became interested in the study of simple [SNS] ligands to examine the effects of hard nitrogen donors vs. soft sulfur donors in the design and application of bifunctional catalysts. Commercially viable and sustainable ligands must be synthetically accessible and originate from cheap starting materials. The bis-thioether amine ligand **L1<sup>H</sup>** can be prepared in high yields from the condensation reaction of 2-(methylthio)benzaldehyde and 2-(methylthio)aniline, followed by a protonation with 4 equiv. of ammonia-borane (**Scheme 1.30**). Alternatively, the benzothiazolidine  $[S^{Me}NS]$  ligand **L2<sup>H</sup>**, featuring a thioether-imine-thiolate ligand framework, can be easily accessed by the analogous condensation reaction of 2-(methylthio)benzaldehyde and 2-aminothiophenol. A key design feature of both ligands is the hemilabile thioether donor in the 6-membered ring upon metal coordination, allowing for open coordination sites for catalysis. Over the past

6 years, these two simple ligands have displayed a remarkably diverse nature that is illustrated through their coordination chemistry in design of first-row metal complexes, and their applications as bifunctional catalysts. This section will summarize highlights of previous work to explore abundant coordination chemistry of these ligands.



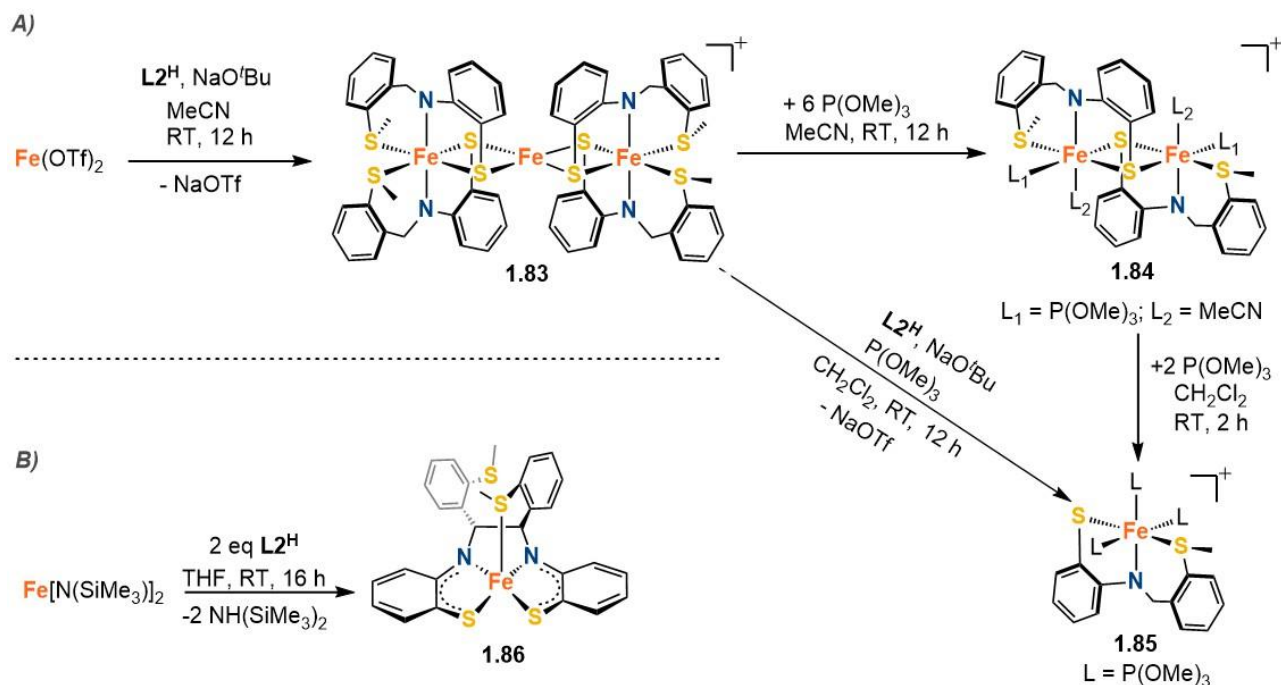
**Scheme 1.31.** Synthesis of two SNS ligand, **L1<sup>H</sup>** and **L2<sup>H</sup>**.

#### 1.4.4 Reactivity of an SNS-thiolate ligand

The most ubiquitous instance of bifunctional catalysis in nature is displayed by the active site of the metalloenzyme [Fe-Fe] hydrogenase.<sup>37</sup> As such, iron complexes containing *N,S*-donor ligands have attracted considerable interest to synthetically mimic and understand the reactivity of this natural catalyst. The Baker group initially explored the reactivity of **L2<sup>H</sup>** with several iron starting materials.<sup>169</sup> Reaction of Fe(OTf)<sub>2</sub> with 1 equiv. of both **L2<sup>H</sup>** and NaO<sup>t</sup>Bu afforded the trinuclear [Fe<sub>3</sub>(μ<sub>2</sub>-S<sup>Me</sup>NS)<sub>4</sub>](OTf)<sub>2</sub> complex (**1.83**) featuring a naked iron center bridging two pseudooctahedral Fe[κ<sup>3</sup>-S<sup>Me</sup>NS]<sub>2</sub> units in a distorted tetrahedral fashion (**Scheme 1.31**). Mossbauer, SQUID, and DFT techniques indicated that **1.83** is comprised of a central high-spin Fe<sup>II</sup> (*S* = 2), and two low-spin Fe<sup>II</sup> (*S* = 0) centers. Addition of a variety of ancillary ligands (L = PhMe<sub>2</sub>P, P(OMe)<sub>3</sub>, CNxylyl)

to **1.83** in acetonitrile all furnished the dinuclear  $[\text{Fe}(\kappa^3\text{-S}^{\text{Me}}\text{NS})(\text{L})_2(\text{L}')_2]_2$  species **1.84** featuring bridging thiolates. Addition of 2 equiv.  $\text{P}(\text{OMe})_3$  formed mononuclear **1.85**. Alternatively, **1.84** could also be accessed by reaction of **1** with excess  $\text{P}(\text{OMe})_3$  in dichloromethane. Both **1.84** and **1.85** feature low-spin diamagnetic  $\text{Fe}^{\text{II}}$  centers.

To assess potential differences in synthetic routes from alternate starting materials, two equiv. of **L2<sup>H</sup>** was reacted with the low-coordinate  $\text{Fe}(\text{II})$  starting material  $\text{Fe}[\text{N}(\text{SiMe}_3)_2]_2$ . The observed formation of **1.86** is due to coupling of the imine carbons to yield a dianionic pentanuclear  $[\text{N}_2\text{S}_3]$  redox-active ligand scaffold. Complex **1.86** was found to be an efficient precatalyst for the selective hydroboration of aldehydes with as little as 0.1 mol% catalyst loadings.<sup>170</sup> Although initial mechanistic investigations were ambiguous, a potential bifunctional activation pathway involving B–H cleavage of pinacolborane may be the reaction pathway, similar to previous work observed by the Thomas group.<sup>70</sup>

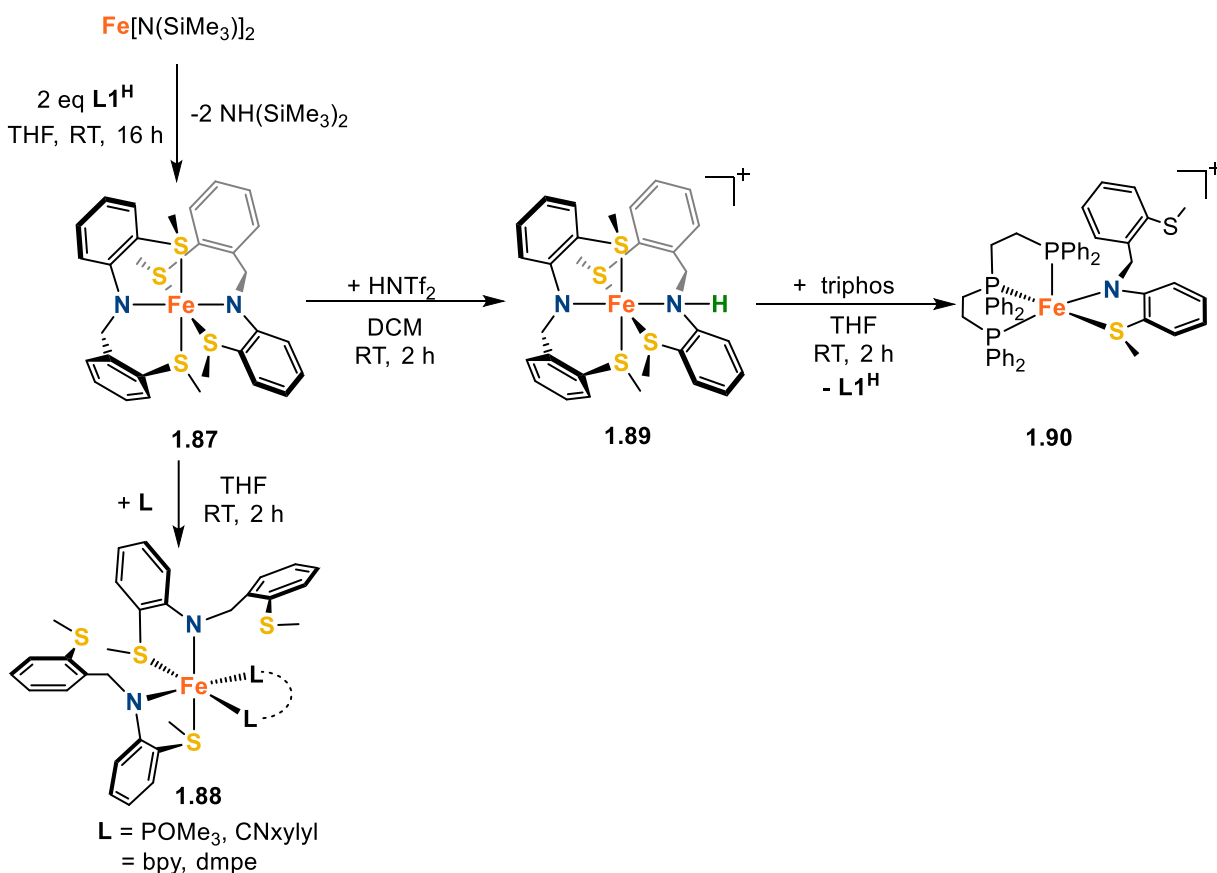


**Scheme 1.32.** Summary of previously reported reactivity of  $\text{L2}^{\text{H}}$  with iron.

#### 1.4.5 Reactivity of an SNS-amido ligand

While intentionally maintaining the biomimetic [SNS] pincer motif, the Baker group then designed an alternative ligand featuring a central bifunctional amido donor in  $\text{L1}^{\text{H}}$ , in lieu of the soft thiolate donor in  $\text{L2}^{\text{H}}$ . Beginning with the low-coordinate Fe(II) starting material  $\text{Fe}[\text{N}(\text{SiMe}_3)_2]_2$ , reaction with 2 equiv. of  $\text{L1}^{\text{H}}$  afforded the octahedral Fe(bis-amido) complex  $\text{Fe}[\kappa^3\text{-S}^{\text{Me}}\text{NS}^{\text{Me}}]_2$  (**1.87**).<sup>171</sup> Analysis of the  $^1\text{H}$  NMR displayed a paramagnetic NMR indicating that the iron center is high-spin Fe(II). This was also supported by Evans measurements giving a value of  $2.9 \mu_{\text{B}}$ . As mentioned previously, the thioether donor in the six-membered ring was intentionally designed to be hemilabile, and to investigate this potential, **1.87** was treated with several neutral ligand donors. Reaction of **1.87** with bidentate ligands dmpe or bpy resulted in ejection of both thioether donors in the six-membered ring, and subsequent coordination of the neutral bidentate donors

forming species of the type **1.88**. Similar results were obtained upon reaction with 2 equiv. of monodentate donors CNxylyl and P(OMe)<sub>3</sub>. To encourage the lability of an entire **L1** unit, **1.87** was reacted with Bronsted acid HNTf<sub>2</sub> which afforded the iron(II) amine-amido cation  $\text{Fe}[\kappa^3\text{-S}^{\text{Me}}\text{NS}^{\text{Me}}][\kappa^3\text{-S}^{\text{Me}}\text{N}^{\text{H}}\text{S}^{\text{Me}}](\text{NTf}_2)$  (**1.89**) (Tf = SO<sub>2</sub>CF<sub>3</sub>). Reaction of **1.89** with one equiv. of triphos gave 16e<sup>-</sup> complex  $[\text{Fe}(\kappa^3\text{-S}^{\text{Me}}\text{NS}^{\text{Me}})(\kappa^3\text{-triphos})](\text{NTf}_2)$  (**1.90**) (triphos = bis(2-diphenylphosphinoethyl)phenylphosphine). Complex **1.90** was demonstrated to be a selective and robust catalyst for ammonia-borane dehydrogenation.



**Scheme 1.33.** Summary of previously reported reactivity of **L1<sup>H</sup>** with iron. [L-L = bpy, dmpe]

## **1.5 Scope of Thesis**

There are five additional chapters in this dissertation which expand upon the reactivity of the two titular [SNS] ligands (**L1<sup>H</sup>** and **L2<sup>H</sup>**) with different first-row metals. Newly synthesized complexes were investigated for their potential as bifunctional catalysts. Each complex which demonstrated catalytic activity was thoroughly investigated to glean insight into the mechanisms. Chapter 2 details the synthesis of two new copper complexes of the type Cu[IPr][ $\kappa^2$ -L] featuring either **L1** or **L2**, in order to directly compare the bifunctional reactivity of the two ligands for the first time. These complexes were catalysts for the hydroboration and hydrosilylation of carbonyls, and isotopic labelling studies led to the proposal of a traditional outer-sphere reaction pathway. Chapter 3 details the synthesis of a new bifunctional Mn complex, Mn[ $\kappa^3$ -S<sup>Me</sup>NS<sup>Me</sup>], featuring **L1**. Initial DFT investigations comparing the Mn complex to previously synthesized Fe and Co complexes demonstrate Mn[ $\kappa^3$ -S<sup>Me</sup>NS<sup>Me</sup>] as the most promising bifunctional catalyst. Combined experimental and computational investigations into the mechanism of carbonyl hydroboration demonstrated a non-traditional and surprising reaction pathway for a metal-ligand cooperative catalyst. Instead of the key catalytic event involving formation of a Mn–H intermediate, it was instead found that boryl activation by the bifunctional amido allows for direct inner sphere hydride transfer to the Mn-coordinated substrate. Furthermore, the hemilability of the six-membered ring thioether donor in **L1** was found to be key to stabilizing early reaction intermediates. Chapter 4 details the extension of **L2** towards the photo-catalyzed dihydroboration of nitriles. To avoid C–S<sub>aryl</sub> bond cleavage observed in electron-rich mono-[SNS] iron complexes, the complex Mn[ $\kappa^3$ -SNS<sup>Me</sup>][CO]<sub>3</sub> was synthesized and demonstrated to be an efficient precatalyst for nitrile dihydroboration. Isotopic labelling

studies gained insight into the resting state of the catalyst which features a single coordinated CO ligand following photo-activation, and EPR studies demonstrated a critical change of the manganese spin-state which allows access to low-energy intermediates. Thorough DFT calculations which considered multiple permutations of catalyst resting states/intermediates allowed the construction of a reaction profile which further highlights how phosphine-free bifunctional ligands diverge from traditional reaction pathways. Chapter 5 details a thorough physical and computational examination of an Fe[N<sub>2</sub>S<sub>3</sub>] species previously reported by the Baker group in order to better understand its redox non-innocence. It was shown that that the Fe[N<sub>2</sub>S<sub>3</sub>] complex can undergo reversible one electron oxidation and reduction using electrochemistry, spectroelectrochemistry, and corresponding TD-DFT calculations which confirmed multiple ligand-to-metal charge transfers typical of redox-active ligands. This allowed the anionic Fe[N<sub>2</sub>S<sub>3</sub>]<sup>-</sup> to be obtained synthetically. Mössbauer and X-ray absorption near edge structure (XANES) studies of both the neutral and anionic redox partner indicated a ligand-based reduction which was not reflected in the metrical parameters of the bond distances in X-ray structures. Inspection of the frontier molecular orbitals using DFT calculations made in clear that redox interconversions are dominated by the changes in electron population in the N<sub>2</sub>S<sub>3</sub> ligand, and intimate mixing with the Fe d<sub>xy</sub> orbital due to a high degree of covalency. Finally, Chapter 6 conducts a critical examination of the contents of this thesis. Weaknesses and strengths of the work are evaluated to offer insight into the best path ahead for future work in this field.

## 1.6 References

- (1) Grützmacher, H. Cooperating Ligands in Catalysis. *Angew. Chem. Int. Ed.* **2008**, *47*, 1814-1818.
- (2) Chorkendorff, I.; Niemantsverdriet, J. W. *Concepts of Modern Catalysis and Kinetics*; John Wiley & Sons, 2017.
- (3) Cornils, B.; Herrmann, W. A. *Concepts in Homogeneous Catalysis: The Industrial View*, 2003; Vol. 216.
- (4) de Vries, J. G.; Jackson, S. D. Homogeneous and Heterogeneous Catalysis in Industry. *Catal. Sci.* **2012**, *2*, 2009-2009.
- (5) Van Leeuwen, P. W. *Homogeneous Catalysis: Understanding the Art*; Springer Science & Business Media, 2006.
- (6) Calderazzo, F.; Carmona, D.; Catellani, M.; Brintzinger, H.; Clerici, M. G.; Dwyer, C.; Fink, G.; Fraile, J.; Haynes, A.; Howard, P. *Metal-Catalysis in Industrial Organic Processes*; Royal Society of Chemistry, 2019.
- (7) Van Leeuwen, P. W.; Claver, C. *Rhodium Catalyzed Hydroformylation*; Springer Science & Business Media, 2002; Vol. 22.
- (8) Chaloner, P. A.; Esteruelas, M. A.; Joó, F.; Oro, L. A. *Homogeneous Hydrogenation*; Springer Science & Business Media, 2013; Vol. 15.
- (9) Fürstner, A. Olefin Metathesis and Beyond. *Angew. Chem. Int. Ed.* **2000**, *39*, 3012-3043.
- (10) Bini, L.; Müller, C.; Vogt, D. Mechanistic Studies on Hydrocyanation Reactions. *Chem. Cat. Chem* **2010**, *2*, 590-608.
- (11) Elschenbroich, C. *Organometallics*; John Wiley & Sons, 2016.
- (12) Hartwig, J. F. Evolution of C–H bond Functionalization from Methane to Methodology. *J. Am. Chem. Soc.* **2016**, *138*, 2-24.
- (13) Grubbs, R. H. Olefin-Metathesis Catalysts for the Preparation of Molecules and Materials (Nobel Lecture). *Angew. Chem. Int. Ed.* **2006**, *45*, 3760-3765.
- (14) Suzuki, A. Cross-Coupling Reactions of Organoboranes: An Easy Way to Construct C–C Bonds (Nobel Lecture). *Angew. Chem. Int. Ed.* **2011**, *50*, 6722-6737.
- (15) Wedepohl, K. H. The Composition of the Continental Crust. *Geochim. Cosmochim. Acta* **1995**, *59*, 1217-1232.

- (16) Loup, J.; Dhawa, U.; Pesciaoli, F.; Wencel-Delord, J.; Ackermann, L. Enantioselective C–H Activation with Earth-Abundant 3d Transition Metals. *Angew. Chem. Int. Ed.* **2019**, *58*, 12803-12818.
- (17) Obligacion, J. V.; Chirik, P. J. Earth-Abundant Transition Metal Catalysts for Alkene Hydrosilylation and Hydroboration. *Nat. Rev. Chem.* **2018**, *2*, 15.
- (18) Reed-Berendt, B. G.; Polidano, K.; Morrill, L. C. Recent Advances in Homogeneous Borrowing Hydrogen Catalysis Using Earth-Abundant First Row Transition Metals. *Org. Biomol. Chem.* **2019**, *17*, 1595-1607.
- (19) Alig, L.; Fritz, M.; Schneider, S. First-Row Transition Metal (De)Hydrogenation Catalysis Based on Functional Pincer Ligands. *Chem. Rev.* **2018**, *119*, 2681-2751.
- (20) Vogiatzis, K. D.; Polynski, M. V.; Kirkland, J. K.; Townsend, J.; Hashemi, A.; Liu, C.; Pidko, E. A. Computational Approach to Molecular Catalysis by 3d Transition Metals: Challenges and Opportunities. *Chem. Rev.* **2018**, *119*, 2453-2523.
- (21) Singh, A.; Spiccia, L. Water Oxidation Catalysts Based on Abundant 1st Row Transition Metals. *Coord. Chem. Rev.* **2013**, *257*, 2607-2622.
- (22) Wolfe, J. P.; Wagaw, S.; Marcoux, J.-F.; Buchwald, S. L. Rational Development of Practical Catalysts for Aromatic Carbon–Nitrogen Bond Formation. *Acc. Chem. Res.* **1998**, *31*, 805-818.
- (23) Filonenko, G. A.; van Putten, R.; Hensen, E. J.; Pidko, E. A. Catalytic (De)hydrogenation Promoted by Non-Precious Metals–Co, Fe and Mn: Recent Advances in an Emerging Field. *Chem. Soc. Rev.* **2018**, *47*, 1459-1483.
- (24) Tamang, S. R.; Findlater, M. Emergence and Applications of Base Metals (Fe, Co, and Ni) in Hydroboration and Hydrosilylation. *Molecules* **2019**, *24*, 3194.
- (25) Danopoulos, A. A.; Simler, T.; Braunstein, P. N-Heterocyclic Carbene Complexes of Copper, Nickel, and Cobalt. *Chem. Rev.* **2019**, *119*, 3730-3961.
- (26) Egorova, K. S.; Ananikov, V. P. Which Metals are Green for Catalysis? Comparison of the Toxicities of Ni, Cu, Fe, Pd, Pt, Rh, and Au Salts. *Angew. Chem. Int. Ed.* **2016**, *55*, 12150-12162.
- (27) Holland, P. L. Reaction: Opportunities for Sustainable Catalysts. *Chem* **2017**, *2*, 443-444.

- (28) Prier, C. K.; Rankic, D. A.; MacMillan, D. W. Visible Light Photoredox Catalysis with Transition Metal Complexes: Applications in Organic Synthesis. *Chem. Rev.* **2013**, *113*, 5322-5363.
- (29) Chirik, P. J. Preface: Forum on Redox-Active Ligands. *Inorg. Chem.* **2011**, *50*, 9737-9740.
- (30) Buchwald, S. L.; Milstein, D. *Ligand Design in Metal Chemistry: Reactivity and Catalysis*; John Wiley & Sons, 2016.
- (31) Stradiotto, M.; Lundgren, R. J. *Ligand Design in Metal Chemistry*; Wiley Online Library, 2016.
- (32) Gunanathan, C.; Milstein, D. Metal–Ligand Cooperation by Aromatization–Dearomatization: A New Paradigm in Bond Activation and “Green” Catalysis. *Acc. Chem. Res.* **2011**, *44*, 588-602.
- (33) Khusnutdinova, J. R.; Milstein, D. Metal–Ligand Cooperation. *Angew. Chem. Int. Ed.* **2015**, *54*, 12236-12273.
- (34) Fritz, M.; Schneider, S. The Renaissance of Base Metal Catalysis Enabled by Functional Ligands in *The Periodic Table II: Catalytic, Materials, Biological and Medical Applications* Mingos, D. M. P., Ed.; Springer, **2019**; Vol. 182.
- (35) Bullock, R. M.; Chen, J. G.; Gagliardi, L.; Chirik, P. J.; Farha, O. K.; Hendon, C. H.; Jones, C. W.; Keith, J. A.; Klosin, J.; Minter, S. D. Using Nature’s Blueprint to Expand Catalysis with Earth-Abundant Metals. *Science* **2020**, 369.
- (36) Fontecilla-Camps, J. C.; Volbeda, A.; Cavazza, C.; Nicolet, Y. Structure/Function Relationships of [NiFe]-and [FeFe]-Hydrogenases. *Chem. Rev.* **2007**, *107*, 4273-4303.
- (37) Kubas, G. J. Fundamentals of H<sub>2</sub> Binding and Reactivity on Transition Metals Underlying Hydrogenase Function and H<sub>2</sub> Production and Storage. *Chem. Rev.* **2007**, *107*, 4152-4205.
- (38) Nicolet, Y.; de Lacey, A. L.; Vernède, X.; Fernandez, V. M.; Hatchikian, E. C.; Fontecilla-Camps, J. C. Crystallographic and FTIR Spectroscopic Evidence of Changes in Fe Coordination Upon Reduction of the Active Site of the Fe-Only Hydrogenase from *Desulfovibrio desulfuricans*. *J. Am. Chem. Soc.* **2001**, *123*, 1596-1601.

- (39) Fan, H.-J.; Hall, M. B. A Capable Bridging Ligand for Fe-Only Hydrogenase: Density Functional Calculations of a Low-Energy Route for Heterolytic Cleavage and Formation of Dihydrogen. *J. Am. Chem. Soc.* **2001**, *123*, 3828-3829.
- (40) Barton, B. E.; Olsen, M. T.; Rauchfuss, T. B. Aza- and Oxadithiolates are Probable Proton Relays in Functional Models for the [FeFe]-Hydrogenases. *J. Am. Chem. Soc.* **2008**, *130*, 16834-16835.
- (41) Fryzuk, M. D.; MacNeil, P. A.; Rettig, S. J. Rhodium and Iridium Amides. *Organometallics* **1986**, *5*, 2469-2476.
- (42) Fryzuk, M. D.; MacNeil, P. A.; Rettig, S. J. Stereoselective Formation of Rhodium and Iridium Hydrides via Intramolecular Hydrogen Bonding. *J. Am. Chem. Soc.* **1987**, *109*, 2803-2812.
- (43) Noyori, R. Asymmetric Catalysis: Science and Opportunities (Nobel Lecture). *Angew. Chem. Int. Ed.* **2002**, *41*, 2008-2022.
- (44) Ikariya, T.; Blacker, A. J. Asymmetric Transfer Hydrogenation of Ketones with Bifunctional Transition Metal-Based Molecular Catalysts. *Acc. Chem. Res.* **2007**, *40*, 1300-1308.
- (45) Higashi, T.; Kusumoto, S.; Nozaki, K. Cleavage of Si-H, B-H, and C-H Bonds by Metal-Ligand Cooperation: Focus Review. *Chem. Rev.* **2019**, *119*, 10393-10402.
- (46) Lagaditis, P. O.; Sues, P. E.; Sonnenberg, J. F.; Wan, K. Y.; Lough, A. J.; Morris, R. H. Iron(II) Complexes Containing Unsymmetrical P-N-P' Pincer Ligands for the Catalytic Asymmetric Hydrogenation of Ketones and Imines. *J. Am. Chem. Soc.* **2014**, *136*, 1367-1380.
- (47) Smith, S. A.; Lagaditis, P. O.; Lüpke, A.; Lough, A. J.; Morris, R. H. Unsymmetrical Iron P-NH-P' Catalysts for the Asymmetric Pressure Hydrogenation of Aryl Ketones. *Chem. Eur. J.* **2017**, *23*, 7212-7216.
- (48) Zirakzadeh, A.; Kirchner, K.; Roller, A.; Stöger, B.; Widhalm, M.; Morris, R. H. Iron (II) Complexes Containing Chiral Unsymmetrical PNP' Pincer Ligands: Synthesis and Application in Asymmetric Hydrogenations. *Organometallics* **2016**, *35*, 3781-3787.
- (49) Seo, C. S.; Tannoux, T.; Smith, S. A.; Lough, A. J.; Morris, R. H. Enantioselective Hydrogenation of Activated Aryl Imines Catalyzed by an Iron (II) P-NH-P' Complex. *J. Org. Chem.* **2019**, *84*, 12040-12049.

- (50) Dong, K.; Elangovan, S.; Sang, R.; Spannenberg, A.; Jackstell, R.; Junge, K.; Li, Y.; Beller, M. Selective Catalytic Two-Step Process for Ethylene Glycol from Carbon Monoxide. *Nat. Commun.* **2016**, *7*, 1-7.
- (51) Schneck, F.; Assmann, M.; Balmer, M.; Harms, K.; Langer, R. Selective Hydrogenation of Amides to Amines and Alcohols Catalyzed by Improved Iron Pincer Complexes. *Organometallics* **2016**, *35*, 1931-1943.
- (52) Bornschein, C.; Werkmeister, S.; Wendt, B.; Jiao, H.; Alberico, E.; Baumann, W.; Junge, H.; Junge, K.; Beller, M. Mild and Selective Hydrogenation of Aromatic and Aliphatic (Di)nitriles with a Well-Defined Iron Pincer Complex. *Nat. Commun.* **2014**, *5*, 1-11.
- (53) Lange, S.; Elangovan, S.; Cordes, C.; Spannenberg, A.; Jiao, H.; Junge, H.; Bachmann, S.; Scalone, M.; Topf, C.; Junge, K. Selective Catalytic Hydrogenation of Nitriles to Primary Amines Using Iron Pincer Complexes. *Catal. Sci.* **2016**, *6*, 4768-4772.
- (54) Werkmeister, S.; Junge, K.; Wendt, B.; Alberico, E.; Jiao, H.; Baumann, W.; Junge, H.; Gallou, F.; Beller, M. Hydrogenation of Esters to Alcohols with a Well-Defined Iron Complex. *Angew. Chem. Int. Ed.* **2014**, *53*, 8722-8726.
- (55) Elangovan, S.; Wendt, B.; Topf, C.; Bachmann, S.; Scalone, M.; Spannenberg, A.; Jiao, H.; Baumann, W.; Junge, K.; Beller, M. Improved Second Generation Iron Pincer Complexes for Effective Ester Hydrogenation. *Adv. Synth. Catal.* **2016**, *358*, 820-825.
- (56) Xu, R.; Chakraborty, S.; Bellows, S. M.; Yuan, H.; Cundari, T. R.; Jones, W. D. Iron-Catalyzed Homogeneous Hydrogenation of Alkenes Under Mild Conditions by a Stepwise, Bifunctional Mechanism. *ACS Catal.* **2016**, *6*, 2127-2135.
- (57) Zhang, G.; Scott, B. L.; Hanson, S. K. Mild and Homogeneous Cobalt-Catalyzed Hydrogenation of C–C, C–O, and C–N bonds. *Angew. Chem. Int. Ed.* **2012**, *51*, 12102-12106.
- (58) Zhang, G.; Hanson, S. K. Cobalt-Catalyzed Acceptorless Alcohol Dehydrogenation: Synthesis of Imines from Alcohols and Amines. *Org. Lett.* **2013**, *15*, 650-653.
- (59) Zhang, G.; Vasudevan, K. V.; Scott, B. L.; Hanson, S. K. Understanding the Mechanisms of Cobalt-Catalyzed Hydrogenation and Dehydrogenation Reactions. *J. Am. Chem. Soc.* **2013**, *135*, 8668-8681.

- (60) Noyori, R.; Yamakawa, M.; Hashiguchi, S. Metal–Ligand Bifunctional Catalysis: A Nonclassical Mechanism for Asymmetric Hydrogen Transfer Between Alcohols and Carbonyl Compounds. *J. Org. Chem.* **2001**, *66*, 7931-7944.
- (61) Valyaev, D. A.; Lavigne, G.; Lugan, N. Manganese Organometallic Compounds in Homogeneous Catalysis: Past, Present, and Prospects. *Coord. Chem. Rev.* **2016**, *308*, 191-235.
- (62) Mukherjee, A.; Milstein, D. Homogeneous Catalysis by Cobalt and Manganese Pincer Complexes. *ACS Catal.* **2018**, *8*, 11435-11469.
- (63) Elangovan, S.; Topf, C.; Fischer, S.; Jiao, H.; Spannenberg, A.; Baumann, W.; Ludwig, R.; Junge, K.; Beller, M. Selective Catalytic Hydrogenations of Nitriles, Ketones, and Aldehydes by Well-Defined Manganese Pincer Complexes. *J. Am. Chem. Soc.* **2016**, *138*, 8809-8814.
- (64) Espinosa-Jalapa, N. A.; Nerush, A.; Shimon, L. J.; Leitus, G.; Avram, L.; Ben-David, Y.; Milstein, D. Manganese-Catalyzed Hydrogenation of Esters to Alcohols. *Chem. Eur. J.* **2017**, *23*, 5934-5938.
- (65) Papa, V.; Cabrero-Antonino, J. R.; Alberico, E.; Spanneberg, A.; Junge, K.; Junge, H.; Beller, M. Efficient and Selective Hydrogenation of Amides to Alcohols and Amines Using a Well-Defined Manganese–PNN Pincer Complex. *Chem. Sci.* **2017**, *8*, 3576-3585.
- (66) Widegren, M. B.; Harkness, G. J.; Slawin, A. M.; Cordes, D. B.; Clarke, M. L. A Highly Active Manganese Catalyst for Enantioselective Ketone and Ester Hydrogenation. *Angew. Chem. Int. Ed.* **2017**, *56*, 5825-5828.
- (67) Garbe, M.; Junge, K.; Walker, S.; Wei, Z.; Jiao, H.; Spannenberg, A.; Bachmann, S.; Scalone, M.; Beller, M. Manganese (I)-Catalyzed Enantioselective Hydrogenation of Ketones Using a Defined Chiral PNP Pincer Ligand. *Angew. Chem. Int. Ed.* **2017**, *56*, 11237-11241.
- (68) Forster, F.; Oestreich, M. Metal–Ligand Cooperative Si–H Bond Activation. *Organosilicon Chemistry: Novel Approaches and Reactions* **2019**, 115-130.
- (69) Hiyama, T. How I came across the Silicon-Based Cross-Coupling Reaction. *J. Organomet. Chem.* **2002**, *653*, 58-61.

- (70) Hatzis, G. P.; Thomas, C. M. Metal-Ligand Cooperativity Across Two Sites of a Square Planar Iron (II) Complex Ligated by a Tetradentate PNNP Ligand. *Chem. Commun.* **2020**.
- (71) Erken, C.; Kaithal, A.; Sen, S.; Weyhermüller, T.; Hölscher, M.; Werlé, C.; Leitner, W. Manganese-Catalyzed Hydroboration of Carbon Dioxide and Other Challenging Carbonyl Groups. *Nat. Commun.* **2018**, *9*, 1-9.
- (72) Xu, X.; Yan, D.; Zhu, Z.; Kang, Z.; Yao, Y.; Shen, Q.; Xue, M. Catalyst-Free Approach for Hydroboration of Carboxylic Acids Under Mild Conditions. *ACS Omega* **2019**, *4*, 6775-6783.
- (73) Pang, M.; Wu, C.; Zhuang, X.; Zhang, F.; Su, M.; Tong, Q.; Tung, C.-H.; Wang, W. Addition of a B–H Bond across an Amido–Cobalt Bond: Co<sup>II</sup>–H-Catalyzed Hydroboration of Olefins. *Organometallics* **2018**, *37*, 1462-1467.
- (74) Ghosh, C.; Kim, S.; Mena, M. R.; Kim, J.-H.; Pal, R.; Rock, C. L.; Groy, T. L.; Baik, M.-H.; Trovitch, R. J. Efficient Cobalt Catalyst for Ambient-Temperature Nitrile Dihydroboration, the Elucidation of a Chelate-Assisted Borylation Mechanism, and a New Synthetic Route to Amides. *J. Am. Chem. Soc.* **2019**, *141*, 15327-15337.
- (75) Ben-Daat, H.; Rock, C. L.; Flores, M.; Groy, T. L.; Bowman, A. C.; Trovitch, R. J. Hydroboration of Alkynes and Nitriles Using an  $\alpha$ -Diimine Cobalt Hydride Catalyst. *Chem. Commun.* **2017**, *53*, 7333-7336.
- (76) Omann, L.; Königs, C. D. F.; Klare, H. F.; Oestreich, M. Cooperative Catalysis at Metal–Sulfur Bonds. *Acc. Chem. Res.* **2017**, *50*, 1258-1269.
- (77) Sweeney, Z. K.; Polse, J. L.; Bergman, R. G.; Andersen, R. A. Dihydrogen Activation by Titanium Sulfide Complexes. *Organometallics* **1999**, *18*, 5502-5510.
- (78) Olechnowicz, F.; Hillhouse, G. L.; Cundari, T. R.; Jordan, R. F. Heterolytic H–H and H–B Bond Cleavage Reactions of {(IPr) Ni ( $\mu$ -S)}<sub>2</sub>. *Inorg. Chem.* **2017**, *56*, 9922-9930.
- (79) Song, H.; Ye, K.; Geng, P.; Han, X.; Liao, R.; Tung, C.-H.; Wang, W. Activation of Epoxides by a Cooperative Iron–Thiolate Catalyst: Intermediacy of Ferrous Alkoxides in Catalytic Hydroboration. *ACS Catal.* **2017**, *7*, 7709-7717.
- (80) Zhang, F.; Song, H.; Zhuang, X.; Tung, C.-H.; Wang, W. Iron-Catalyzed 1, 2-Selective Hydroboration of N-Heteroarenes. *J. Am. Chem. Soc.* **2017**, *139*, 17775-17778.

- (81) Drover, M. W.; Love, J. A.; Schafer, L. L. 1,3-N,O- Complexes of Late Transition Metals. Ligands with Flexible Bonding Modes and Reaction Profiles. *Chem. Soc. Rev.* **2017**, *46*, 2913-2940.
- (82) Buitrago, E.; Tinnis, F.; Adolfsson, H. Efficient and Selective Hydrosilylation of Carbonyl Compounds Catalyzed by Iron Acetate and N-Hydroxyethylimidazolium Salts. *Adv. Synth. Catal.* **2012**, *354*, 217-222.
- (83) Chu, W.-Y.; Zhou, X.; Rauchfuss, T. B. Cooperative Metal–Ligand Reactivity and Catalysis in Low-Spin Ferrous Alkoxides. *Organometallics* **2015**, *34*, 1619-1626.
- (84) MacNair, A. J.; Millet, C. R.; Nichol, G. S.; Ironmonger, A.; Thomas, S. P. Markovnikov-Selective, Activator-Free Iron-Catalyzed Vinylarene Hydroboration. *ACS Catal.* **2016**, *6*, 7217-7221.
- (85) Liu, J.; Chen, J.-Y.; Jia, M.; Ming, B.; Jia, J.; Liao, R.-Z.; Tung, C.-H.; Wang, W. Ni–O Cooperation Versus Nickel(II) Hydride in Catalytic Hydroboration of N-Heteroarenes. *ACS Catal.* **2019**, *9*, 3849-3857.
- (86) Feichtner, K.-S.; Gessner, V. H. Cooperative Bond Activation Reactions with Carbene Complexes. *Chem. Commun.* **2018**, *54*, 6540-6553.
- (87) Gutsulyak, D. V.; Piers, W. E.; Borau-Garcia, J.; Parvez, M. Activation of Water, Ammonia, and Other Small Molecules by PC<sub>carbene</sub>P Nickel Pincer Complexes. *J. Am. Chem. Soc.* **2013**, *135*, 11776-11779.
- (88) LaPierre, E. A.; Piers, W. E.; Spasyuk, D. M.; Bi, D. W. Activation of Si–H Bonds Across the Nickel Carbene Bond in Electron Rich Nickel PC<sub>carbene</sub>P Pincer Complexes. *Chem. Commun.* **2016**, *52*, 1361-1364.
- (89) Owen, G. R. Hydrogen Atom Storage Upon Z-Class Borane Ligand Functions: An Alternative Approach to Ligand Cooperation. *Chem. Soc. Rev.* **2012**, *41*, 3535-3546.
- (90) Nesbit, M. A.; Suess, D. L.; Peters, J. C. E–H Bond Activations and Hydrosilylation Catalysis with Iron and Cobalt Metalloboranes. *Organometallics* **2015**, *34*, 4741-4752.
- (91) Owen, G. R. Functional Group Migrations Between Boron and Metal Centers Within Transition Metal–Borane and–Boryl Complexes and Cleavage of H–H, E–H and E–E' Bonds. *Chem. Commun.* **2016**, *52*, 10712-10726.
- (92) Bouhadir, G.; Bourissou, D. Complexes of Ambiphilic Ligands: Reactivity and Catalytic Applications. *Chem. Soc. Rev.* **2016**, *45*, 1065-1079.

- (93) Mihalcik, D. J.; White, J. L.; Tanski, J. M.; Zakharov, L. N.; Yap, G. P.; Incarvito, C. D.; Rheingold, A. L.; Rabinovich, D. Cobalt Tris(mercaptopimidazolyl)borate Complexes: Synthetic Studies and the Structure of the First Cobaltaboratrane. *Dalton Trans.* **2004**, 1626-1634.
- (94) Figueroa, J. S.; Melnick, J. G.; Parkin, G. Reactivity of the Metal→BX<sub>3</sub> Dative σ-Bond: 1,2-Addition Reactions of the Fe→BX<sub>3</sub> Moiety of the Ferraboratrane Complex [ $\kappa^4$ -B(mimBut)<sub>3</sub>]Fe(CO)<sub>2</sub>. *Inorg. Chem.* **2006**, *45*, 7056-7058.
- (95) Pang, K.; Tanski, J. M.; Parkin, G. Reactivity of the Ni→B Dative σ-bond in the Nickel Boratrane Compounds [ $\kappa^4$ -B(mimBut)<sub>3</sub>]NiX (X= Cl, OAc, NCS, N<sub>3</sub>): Synthesis of a Series of B-Functionalized Tris(2-mercapto-1-tert-butylimidazolyl)borato Complexes, [YTmBut]NiZ. *Chem. Commun.* **2008**, 1008-1010.
- (96) Tsoureas, N.; Kuo, Y.-Y.; Haddow, M. F.; Owen, G. R. Double Addition of H<sub>2</sub> to Transition Metal–Borane Complexes: A ‘Hydride Shuttle’ Process Between Boron and Transition Metal Centers. *Chem. Commun.* **2011**, *47*, 484-486.
- (97) Harman, W. H.; Peters, J. C. Reversible H<sub>2</sub> Addition Across a Nickel–Borane Unit as a Promising Strategy for Catalysis. *J. Am. Chem. Soc.* **2012**, *134*, 5080-5082.
- (98) Harman, W. H.; Lin, T. P.; Peters, J. C. A d<sup>10</sup> Ni–(H<sub>2</sub>) Adduct as an Intermediate in H–H Oxidative Addition across a Ni–B Bond. *Angew. Chem. Int. Ed.* **2014**, *53*, 1081-1086.
- (99) MacMillan, S. N.; Harman, W. H.; Peters, J. C. Facile Si–H bond Activation and Hydrosilylation Catalysis Mediated by a Nickel–Borane complex. *Chem. Sci.* **2014**, *5*, 590-597.
- (100) Leitl, J.; Marquardt, M.; Coburger, P.; Scott, D. J.; Streitferdt, V.; Gschwind, R. M.; Müller, C.; Wolf, R. Facile C=O Bond Splitting of Carbon Dioxide Induced by Metal–Ligand Cooperativity in a Phosphinine Iron (0) Complex. *Angew. Chem. Int. Ed.* **2019**, *58*, 15407-15411.
- (101) Yang, X.; Hall, M. B. Density Functional Theory Study of the Mechanism for Ni (NHC)<sub>2</sub> Catalyzed Dehydrogenation of Ammonia–Borane for Chemical Hydrogen Storage. *J. Organomet. Chem.* **2009**, *694*, 2831-2838.
- (102) Cammarota, R. C.; Lu, C. C. Tuning Nickel with Lewis Acidic Group 13 Metalloligands for Catalytic Olefin Hydrogenation. *J. Am. Chem. Soc.* **2015**, *137*, 12486-12489.

- (103) Cammarota, R. C.; Vollmer, M. V.; Xie, J.; Ye, J.; Linehan, J. C.; Burgess, S. A.; Appel, A. M.; Gagliardi, L.; Lu, C. C. A Bimetallic Nickel–Gallium Complex Catalyzes CO<sub>2</sub> Hydrogenation via the Intermediacy of an Anionic d<sup>10</sup> Nickel Hydride. *J. Am. Chem. Soc.* **2017**, *139*, 14244-14250.
- (104) Vollmer, M. V.; Ye, J.; Linehan, J. C.; Graziano, B. J.; Preston, A.; Wiedner, E. S.; Lu, C. C. Cobalt-Group 13 Complexes Catalyze CO<sub>2</sub> Hydrogenation Using a Co<sup>(-1)</sup>/Co<sup>(I)</sup> Redox Cycle. *ACS Catal.* **2020**.
- (105) Moulton, C.; Shaw, B. *J. Chem. Soc. Dalton Trans* **1976**, *11*, 1020-1024.
- (106) Morales-Morales, D.; Jensen, C. G. *The Chemistry of Pincer Compounds*; Elsevier, 2011.
- (107) Peris, E.; Crabtree, R. H. Key Factors in Pincer Ligand Design. *Chem. Soc. Rev.* **2018**, *47*, 1959-1968.
- (108) Zhang, J.; Leitus, G.; Ben-David, Y.; Milstein, D. Facile Conversion of Alcohols into Esters and Dihydrogen Catalyzed by New Ruthenium Complexes. *J. Am. Chem. Soc.* **2005**, *127*, 10840-10841.
- (109) Langer, R.; Leitus, G.; Ben-David, Y.; Milstein, D. Efficient Hydrogenation of Ketones Catalyzed by an Iron Pincer Complex. *Angew. Chem. Int. Ed.* **2011**, *50*, 2120-2124.
- (110) Langer, R.; Iron, M. A.; Konstantinovski, L.; Diskin-Posner, Y.; Leitus, G.; Ben-David, Y.; Milstein, D. Iron Borohydride Pincer Complexes for the Efficient Hydrogenation of Ketones Under Mild, Base-Free Conditions: Synthesis and Mechanistic Insight. *Chem. Eur. J.* **2012**, *18*, 7196-7209.
- (111) Zell, T.; Butschke, B.; Ben-David, Y.; Milstein, D. Efficient Hydrogen Liberation from Formic Acid Catalyzed by a Well-Defined Iron Pincer Complex under Mild Conditions. *Chem. Eur. J.* **2013**, *19*, 8068-8072.
- (112) Zell, T.; Ben-David, Y.; Milstein, D. Highly Efficient, General Hydrogenation of Aldehydes Catalyzed by PNP Iron Pincer Complexes. *Catal. Sci.* **2015**, *5*, 822-826.
- (113) Zell, T.; Ben-David, Y.; Milstein, D. Unprecedented Iron-Catalyzed Ester Hydrogenation. Mild, Selective, and Efficient Hydrogenation of Trifluoroacetic Esters to Alcohols Catalyzed by an Iron Pincer Complex. *Angew. Chem. Int. Ed.* **2014**, *53*, 4685-4689.

- (114) Garg, J. A.; Chakraborty, S.; Ben-David, Y.; Milstein, D. Unprecedented Iron-Catalyzed Selective Hydrogenation of Activated Amides to Amines and Alcohols. *Chem. Commun.* **2016**, 52, 5285-5288.
- (115) Langer, R.; Diskin-Posner, Y.; Leitun, G.; Shimon, L. J.; Ben-David, Y.; Milstein, D. Low-Pressure Hydrogenation of Carbon Dioxide Catalyzed by an Iron Pincer Complex Exhibiting Noble Metal Activity. *Angew. Chem. Int. Ed.* **2011**, 50, 9948-9952.
- (116) Mukherjee, A.; Nerush, A.; Leitun, G.; Shimon, L. J.; Ben David, Y.; Espinosa Jalapa, N. A.; Milstein, D. Manganese-Catalyzed Environmentally Benign Dehydrogenative Coupling of Alcohols and Amines to Form Aldimines and H<sub>2</sub>: A Catalytic and Mechanistic Study. *J. Am. Chem. Soc.* **2016**, 138, 4298-4301.
- (117) Sarbajna, A.; Patil, P. H.; Dinh, M. H.; Gladkovskaya, O.; Fayzullin, R. R.; Lapointe, S.; Khaskin, E.; Khusnutdinova, J. R. Facile and Reversible Double Dearomatization of Pyridines in Non-Phosphine Mn<sup>I</sup> Complexes with N, S-Donor Pyridinophane Ligand. *Chem. Commun.* **2019**, 55, 3282-3285.
- (118) Crabtree, R. H. *The Organometallic Chemistry of the Transition Metals*; John Wiley & Sons, 2009.
- (119) Chirik, P. J. Iron- and Cobalt-Catalyzed Alkene Hydrogenation: Catalysis with Both Redox-Active and Strong Field Ligands. *Acc. Chem. Res.* **2015**, 48, 1687-1695.
- (120) Morris, R. H. Exploiting Metal-Ligand Bifunctional Reactions in the Design of Iron Asymmetric Hydrogenation Catalysts. *Acc. Chem. Res.* **2015**, 48, 1494-1502.
- (121) Trovitch, R. J. The Emergence of Manganese-Based Carbonyl Hydrosilylation Catalysts. *Acc. Chem. Res.* **2017**, 50, 2842-2852.
- (122) Dzik, W. I.; van der Vlugt, J. I.; Reek, J. N.; de Bruin, B. Ligands That Store and Release Electrons During Catalysis. *Angew. Chem. Int. Ed.* **2011**, 50, 3356-3358.
- (123) Chirik, P. J.; Wieghardt, K. Radical Ligands Confer Nobility on Base-Metal Catalysts. *Science* **2010**, 327, 794-795.
- (124) Lyaskovskyy, V.; de Bruin, B. Redox Non-Innocent Ligands: Versatile New Tools to Control Catalytic Reactions. *ACS Catal.* **2012**, 2, 270-279.
- (125) Kaim, W. The Shrinking World of Innocent Ligands: Conventional and Non-Conventional Redox-Active Ligands. *Eur. J. Inorg. Chem.* **2012**, 2012, 343-348.

- (126) Praneeth, V. K.; Ringenberg, M. R.; Ward, T. R. Redox-Active Ligands in Catalysis. *Angew. Chem. Int. Ed.* **2012**, *51*, 10228-10234.
- (127) Blanchard, S.; Derat, E.; Desage-El Murr, M.; Fensterbank, L.; Malacria, M.; Mouriès-Mansuy, V. Non-Innocent Ligands: New Opportunities in Iron Catalysis. *Eur. J. Inor. Chem.* **2012**, *2012*, 376-389.
- (128) Luca, O. R.; Crabtree, R. H. Redox-Active Ligands in Catalysis. *Chem. Soc. Rev.* **2013**, *42*, 1440-1459.
- (129) Schauer, P. A.; Low, P. J. Ligand Redox Non-Innocence in Transition-Metal  $\sigma$ -Alkynyl and Related Complexes. *Eur. J. Inor. Chem.* **2012**, *2012*, 390-411.
- (130) Broere, D. L.; Plessius, R.; van der Vlugt, J. I. New Avenues for Ligand-Mediated Processes—Expanding Metal Reactivity by the Use of Redox-Active Catechol, o-Aminophenol and o-Phenylenediamine Ligands. *Chem. Soc. Rev.* **2015**, *44*, 6886-6915.
- (131) Chaudhuri, P.; Verani, C. N.; Bill, E.; Bothe, E.; Weyhermüller, T.; Wieghardt, K. Electronic Structure of Bis(o-iminobenzosemiquinonato) Metal Complexes (Cu, Ni, Pd). The Art of Establishing Physical Oxidation States in Transition-Metal Complexes Containing Radical Ligands. *J. Am. Chem. Soc.* **2001**, *123*, 2213-2223.
- (132) Bart, S. C.; Chłopek, K.; Bill, E.; Bouwkamp, M. W.; Lobkovsky, E.; Neese, F.; Wieghardt, K.; Chirik, P. J. Electronic Structure of Bis(imino)pyridine Iron Dichloride, Monochloride, and Neutral Ligand Complexes: A Combined Structural, Spectroscopic, and Computational Study. *J. Am. Chem. Soc.* **2006**, *128*, 13901-13912.
- (133) Ray, K.; Weyhermüller, T.; Neese, F.; Wieghardt, K. Electronic Structure of Square Planar Bis(benzene-1,2-dithiolato) Metal Complexes  $[M(L)_2]^z$  ( $z = 2-, 1-, 0$ ;  $M = Ni, Pd, Pt, Cu, Au$ ): An Experimental, Density Functional, and Correlated Ab Initio Study. *Inorg. Chem.* **2005**, *44*, 5345-5360.
- (134) Römelt, C.; Weyhermüller, T.; Wieghardt, K. Structural Characteristics of Redox-Active Pyridine-1,6-diimine Complexes: Electronic Structures and Ligand Oxidation Levels. *Coord. Chem. Rev.* **2019**, *380*, 287-317.
- (135) Ringenberg, M. R.; Kokatam, S. L.; Heiden, Z. M.; Rauchfuss, T. B. Redox-Switched Oxidation of Dihydrogen Using a Non-Innocent Ligand. *J. Am. Chem. Soc.* **2008**, *130*, 788-789.

- (136) Connelly, N. G.; Geiger, W. E. Chemical Redox Agents for Organometallic Chemistry. *Chem. Rev.* **1996**, *96*, 877-910.
- (137) Lecarme, L.; Chiang, L.; Moutet, J.; Leconte, N.; Philouze, C.; Jarjayes, O.; Storr, T.; Thomas, F. The Structure of a One-Electron Oxidized Mn<sup>(III)</sup>-bis(phenolate)dipyrrin Radical Complex and Oxidation Catalysis Control via Ligand-Centered Redox Activity. *Dalton Trans.* **2016**, *45*, 16325-16334.
- (138) de Bruin, B.; Bill, E.; Bothe, E.; Weyhermüller, T.; Wieghardt, K. Molecular and Electronic Structures of Bis(pyridine-2,6-diimine) Metal Complexes [ML<sub>2</sub>](PF<sub>6</sub>)<sup>n</sup> (n= 0, 1, 2, 3; M= Mn, Fe, Co, Ni, Cu, Zn). *Inorg. Chem.* **2000**, *39*, 2936-2947.
- (139) Bart, S. C.; Lobkovsky, E.; Chirik, P. J. Preparation and Molecular and Electronic Structures of Iron(0) Dinitrogen and Silane Complexes and Their Application to Catalytic Hydrogenation and Hydrosilylation. *J. Am. Chem. Soc.* **2004**, *126*, 13794-13807.
- (140) Bouwkamp, M. W.; Bowman, A. C.; Lobkovsky, E.; Chirik, P. J. Iron-Catalyzed [2 $\pi$ +2 $\pi$ ] Cycloaddition of  $\alpha$ ,  $\omega$ -dienes: The Importance of Redox-Active Supporting Ligands. *J. Am. Chem. Soc.* **2006**, *128*, 13340-13341.
- (141) Joannou, M. V.; Hoyt, J. M.; Chirik, P. J. Investigations into the Mechanism of Inter- and Intramolecular Iron-Catalyzed [2+2] Cycloaddition of Alkenes. *J. Am. Chem. Soc.* **2020**, *142*, 5314-5330.
- (142) Sylvester, K. T.; Chirik, P. J. Iron-Catalyzed, Hydrogen-Mediated Reductive Cyclization of 1,6-enynes and Diynes: Evidence for Bis(imino)pyridine Ligand Participation. *J. Am. Chem. Soc.* **2009**, *131*, 8772-8774.
- (143) Tondreau, A. M.; Milsmann, C.; Patrick, A. D.; Hoyt, H. M.; Lobkovsky, E.; Wieghardt, K.; Chirik, P. J. Synthesis and Electronic Structure of Cationic, Neutral, and Anionic Bis(imino)pyridine Iron Alkyl Complexes: Evaluation of Redox Activity in Single-Component Ethylene Polymerization Catalysts. *J. Am. Chem. Soc.* **2010**, *132*, 15046-15059.
- (144) Tondreau, A. M.; Atienza, C. C. H.; Weller, K. J.; Nye, S. A.; Lewis, K. M.; Delis, J. G.; Chirik, P. J. Iron Catalysts for Selective Anti-Markovnikov Alkene Hydrosilylation Using Tertiary Silanes. *Science* **2012**, *335*, 567-570.
- (145) Darmon, J. M.; Stieber, S. C. E.; Sylvester, K. T.; Fernández, I.; Lobkovsky, E.; Semproni, S. P.; Bill, E.; Wieghardt, K.; DeBeer, S.; Chirik, P. J. Oxidative Addition of

Carbon–Carbon Bonds with a Redox-Active Bis(imino)pyridine Iron Complex. *J. Am. Chem. Soc.* **2012**, *134*, 17125-17137.

(146) Russell, S. K.; Lobkovsky, E.; Chirik, P. J. Iron-Catalyzed Intermolecular  $[2\pi+2\pi]$  Cycloaddition. *J. Am. Chem. Soc.* **2011**, *133*, 8858-8861.

(147) Hoyt, J. M.; Schmidt, V. A.; Tondreau, A. M.; Chirik, P. J. Iron-Catalyzed Intermolecular  $[2+2]$  Cycloadditions of Unactivated Alkenes. *Science* **2015**, *349*, 960-963.

(148) Rummelt, S. M.; Zhong, H.; Korobkov, I.; Chirik, P. J. Iron-Mediated Coupling of Carbon Dioxide and Ethylene: Macrocyclic Metallalactones Enable Access to Various Carboxylates. *J. Am. Chem. Soc.* **2018**, *140*, 11589-11593.

(149) Small, B. L. Discovery and Development of Pyridine-bis(imine) and Related Catalysts for Olefin Polymerization and Oligomerization. *Acc. Chem. Res.* **2015**, *48*, 2599-2611.

(150) Flisak, Z.; Sun, W.-H. Progression of Diiminopyridines: From Single Application to Catalytic Versatility. *ACS Catal.* **2015**, *5*, 4713-4724.

(151) Obligacion, J. V.; Chirik, P. J. Bis(imino)pyridine Cobalt-Catalyzed Alkene Isomerization–Hydroboration: A Strategy for Remote Hydrofunctionalization with Terminal Selectivity. *J. Am. Chem. Soc.* **2013**, *135*, 19107-19110.

(152) Zhang, L.; Zuo, Z.; Leng, X.; Huang, Z. A Cobalt-Catalyzed Alkene Hydroboration with Pinacolborane. *Angew. Chem. Int. Ed.* **2014**, *53*, 2696-2700.

(153) Obligacion, J. V.; Neely, J. M.; Yazdani, A. N.; Pappas, I.; Chirik, P. J. Cobalt Catalyzed Z-Selective Hydroboration of Terminal Alkynes and Elucidation of the Origin of Selectivity. *J. Am. Chem. Soc.* **2015**, *137*, 5855-5858.

(154) Atienza, C. C. H.; Diao, T.; Weller, K. J.; Nye, S. A.; Lewis, K. M.; Delis, J. G.; Boyer, J. L.; Roy, A. K.; Chirik, P. J. Bis(imino)pyridine Cobalt-Catalyzed Dehydrogenative Silylation of Alkenes: Scope, Mechanism, and Origins of Selective Allylsilane Formation. *J. Am. Chem. Soc.* **2014**, *136*, 12108-12118.

(155) Monfette, S.; Turner, Z. R.; Semproni, S. P.; Chirik, P. J. Enantiopure  $C_1$ -Symmetric Bis(imino)pyridine Cobalt Complexes for Asymmetric Alkene Hydrogenation. *J. Am. Chem. Soc.* **2012**, *134*, 4561-4564.

(156) Friedfeld, M. R.; Shevlin, M.; Margulieux, G. W.; Campeau, L.-C.; Chirik, P. J. Cobalt-Catalyzed Enantioselective Hydrogenation of Minimally Functionalized Alkenes:

Isotopic Labeling Provides Insight into the Origin of Stereoselectivity and Alkene Insertion Preferences. *J. Am. Chem. Soc.* **2016**, *138*, 3314-3324.

(157) Schmidt, V. A.; Hoyt, J. M.; Margulieux, G. W.; Chirik, P. J. Cobalt-Catalyzed  $[2\pi+2\pi]$  Cycloadditions of Alkenes: Scope, Mechanism, and Elucidation of Electronic Structure of Catalytic Intermediates. *J. Am. Chem. Soc.* **2015**, *137*, 7903-7914.

(158) Kennedy, C. R.; Zhong, H.; Joannou, M.; Chirik, P. Pyridine(diimine) Iron Diene Complexes Relevant to Catalytic  $[2+2]$ -Cycloaddition Reactions. *Adv. Synth. Catal.*

(159) Mukhopadhyay, T. K.; Flores, M.; Groy, T. L.; Trovitch, R. J. A Highly Active Manganese Precatalyst for the Hydrosilylation of Ketones and Esters. *J. Am. Chem. Soc.* **2014**, *136*, 882-885.

(160) Mukhopadhyay, T. K.; Rock, C. L.; Hong, M.; Ashley, D. C.; Groy, T. L.; Baik, M.-H.; Trovitch, R. J. Mechanistic Investigation of Bis(imino)pyridine Manganese Catalyzed Carbonyl and Carboxylate Hydrosilylation. *J. Am. Chem. Soc.* **2017**, *139*, 4901-4915.

(161) Klerman, Y.; Ben-Ari, E.; Diskin-Posner, Y.; Leitun, G.; Shimon, L. J. W.; Ben-David, Y.; Milstein, D. Pyridine-Based SNS-Iridium and Rhodium Sulfide Complexes, Including  $d^8$ - $d^8$  Metal-Metal Interactions in the Solid State. *Dalton Trans.* **2008**, *24*, 3226-3234.

(162) Singh, P.; Singh, A. K. Transfer Hydrogenation of Ketones and Catalytic Oxidation of Alcohols with Half-Sandwich Complexes of Ruthenium (II) Designed Using Benzene and Tridentate (S, N, E) Type Ligands (E = S, Se, Te). *Organometallics.* **2010**, *29*, 6433-6442.

(163) Shaffer, D. W.; Szigethy, G.; Ziller, J. W.; Heyduk, A. F. Synthesis and Characterization of a Redox-Active Bis(thiophenolato) Amide Ligand,  $[\text{SNS}]^{3-}$ , and the Homoleptic Tungsten Complexes  $\text{W}[\text{SNS}]_2$  and  $\text{W}[\text{ONO}]_2$ . *Inorg. Chem.* **2013**, *52*, 2110-2118

(164) Schnodt, J.; Manzur, J.; Garcia, A. -M.; Hartenbach, I.; Su, C. -Y.; Fiedler, J.; Kaim, W. Coordination of a Hemilabile N,N,S Donor Ligand in the Redox System  $[\text{CuL}_2]^{+/2+}$ , L = 2-Pyridyl-*N*-(2'-alkylthiophenyl)methyleneimine. *Eur. J. Inorg. Chem.* **2011**, *2011*, 1436-1441.

(165) Mikuriya, M.; Kotera, T.; Adachi, F.; Handa, M.; Koikawa, M.; Okawa, H. Syntheses and Structural Characterization of Dinuclear and Trinuclear Iron (II) Complexes of

Tridentate Thiolic Ligands with an NNS Donor Set. *Bull. Chem. Soc. Jpn.* **1995**, *68*, 574-580.

(166) Noveron, J. C.; Olmstead, M. M.; Mascharak, P. K. Effect of Carboxamido N Coordination to Iron on the Redox Potential of Low-Spin non-Heme Iron Centers with N, S Coordination: Relevance to the Iron Site of Nitrile Hydratase. *Inorg. Chem.* **1998**, *37*, 1138-1139.

(167) Xiao, J.; Deng, L. Synthesis and Reactivity Study of Iron (II) Complexes with Bulky Bis(anilido)thioether Ligation. *Organometallics.* **2012**, *31*, 428-434.

(168) Bouwman, E.; K. Henderson, R.; K. Powell, A.; Reedijk, J.; J. J. Smeets, W.; L. Spek, A.; Veldman, N.; Wocadlo, S. Anion Dependent Deprotection of a Thioether Group in Schiff Base NS<sub>2</sub> Ligands Results in New Mononuclear and Dinuclear Thiolato Nickel Complexes. *J. Chem. Soc., Dalton Trans.* **1998**, 3495.

(169) Das, U. K.; Daifuku, S. L.; Gorelsky, S. I.; Korobkov, I.; Neidig, M. L.; Le Roy, J. J.; Murugesu, M.; Baker, R. T. Mononuclear, Dinuclear, and Trinuclear Iron Complexes Featuring a New Monoanionic SNS Thiolate Ligand. *Inorg. Chem.* **2016**, *55*, 987-997.

(170) Das, U. K.; Higman, C. S.; Gabidullin, B.; Hein, J. E.; Baker, R. T. Efficient and Selective Iron-Complex-Catalyzed Hydroboration of Aldehydes. *ACS Catal.* **2018**, *8*, 1076-1081.

(171) Das, U. K.; Daifuku, S. L.; Iannuzzi, T. E.; Gorelsky, S. I.; Korobkov, I.; Gabidullin, B.; Neidig, M. L.; Baker, R. T. Iron (II) Complexes of a Hemilabile SNS Amido Ligand: Synthesis, Characterization, and Reactivity. *Inorg. Chem.* **2017**, *56*, 13766-13776.

**Chapter 2 – Comparing the SNS Thiolate and Amido Ligands: Cu(I) SNS Complexes for Outer-Sphere Hydroboration and Hydrosilylation of Carbonyls**

**2.1 Introduction**

Transition-metal complexes that include redox<sup>1-3</sup> or Lewis acid<sup>4-5</sup>/base<sup>6-7</sup> functionality in their ligands have extensive applications in homogeneous catalysis.<sup>8-9</sup> Bifunctional catalysts based on earth abundant first-row transition metals are especially sought after for their economy and low toxicity, and have been shown to facilitate difficult catalytic transformations.<sup>10-15</sup> Cooperativity between a ligand and metal center to facilitate E–H bond activation is often a crucial aspect of bifunctional carbonyl reduction mechanisms,<sup>16</sup> such as the hydrosilylation of ketones and aldehydes.<sup>17-19</sup> A key strategy of this transformation is the use of a ligand that incorporates a Lewis basic donor site to form a reactive metal-hydride intermediate after activation of an E–H bond.<sup>20</sup> Comparing the

bifunctional capacity of hard vs soft donors in these ligand frameworks may aid in the design of future ligand frameworks for catalytic applications.

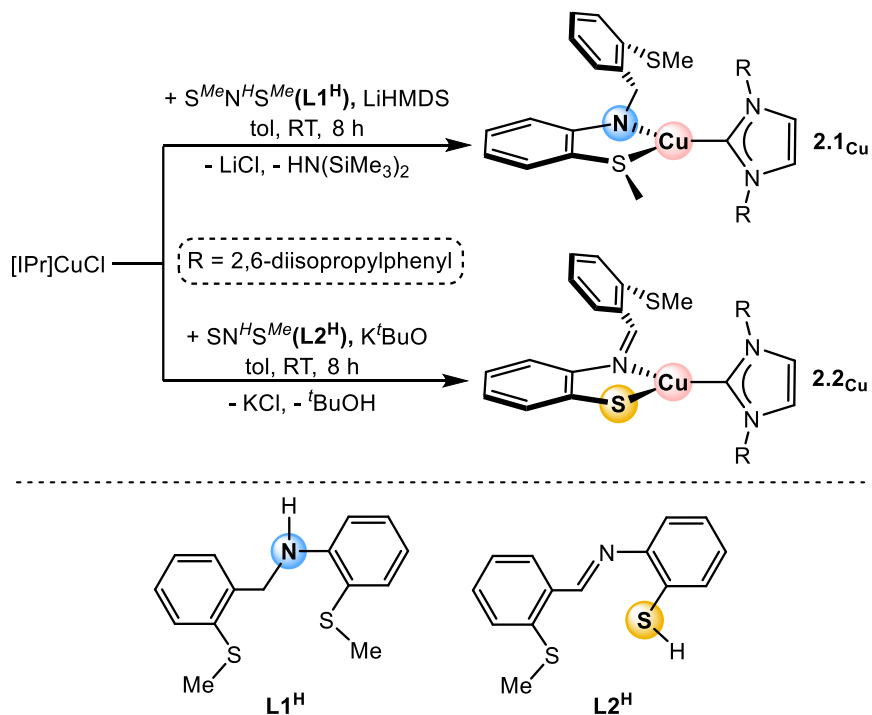
We have reported two easily prepared SNS ligands (**Scheme 2.1**) that have both demonstrated bifunctional activity in their first-row metal complexes.<sup>21-23</sup> Upon deprotonation, **L1** features a hard nitrogen donor in a thioether-amido-thioether framework, while **L2** incorporates a soft sulfur donor in a thiolate-imine-thioether framework. Previous work has shown that the coordination chemistry of **L1** and **L2** can differ greatly even under identical conditions. As part of our efforts to compare the properties and capabilities of these two ligands, we report herein the synthesis of NHC-Cu-[ $\kappa^2$ -SNS] amido and thiolate complexes as catalysts for hydroboration and hydrosilylation of ketones and aldehydes.

There are many examples of Cu[NHC] complex-catalyzed hydroboration and hydrosilylation, which have been the subject of review.<sup>24-26</sup> By combining the copper-NHC framework with **L1** and **L2**, we expected that the crowded and coordinatively saturated metal center may force an outer-sphere bifunctional mechanism.<sup>27</sup> While most Cu-catalyzed carbonyl reductions proceed via the *in-situ* formation of a copper-butoxide base to generate the active copper hydride species upon reaction with HBpin,<sup>28</sup> the use of either the thiolate or amido acting as an internal base may function in a similar capacity.<sup>29-30</sup>

## 2.2 Results and Discussion

### 2.2.1 Synthesis of copper complexes

The reaction of CuCl(IPr) with one equiv of **L1<sup>H</sup>** and LiHMDS in toluene afforded the 16 e<sup>-</sup> Cu( $\kappa^2$ -S<sup>Me</sup>NS<sup>Me</sup>)(IPr) (**2.1<sub>Cu</sub>**) complex in 92% yield (**Scheme 2.1**) (IPr = 1,3-bis[2,6-diisopropylphenyl]-1,3-dihydro-2H-imidazol-2-ylidene; HMDS = hexamethyldisilazide, N[SiMe<sub>3</sub>]<sub>2</sub>). As shown in **Figure 2.1**, the solid-state structure of **2.1<sub>Cu</sub>** features a distorted trigonal planar geometry [N(1)-Cu(1)-S(1) = 85.14(8)°; C(16)-Cu(1)-S(1) = 123.90(7)°; C(16)-Cu(1)-N(1) = 150.89(9)°], due to the long Cu–S<sub>thioether</sub> bond length [2.4820(14) Å]. The other thioether moiety is directed away from the Cu-center rather than bonding to form an 18 e<sup>-</sup> complex, presumably due to the large steric bulk. The analogous reaction of CuCl(IPr) with one equiv of **L2<sup>H</sup>** and KO<sup>t</sup>Bu gave the Cu( $\kappa^2$ -S<sup>Me</sup>NS)(IPr) (**2.2<sub>Cu</sub>**) product in 88% yield. The <sup>1</sup>H NMR spectrum showed two sets of resonances (one broad and one sharp), presumably due to E- and Z-isomers relevant to the imine C–H; slow exchange was confirmed by a 2D <sup>1</sup>H-EXSY experiment. The solid-state structure of **2.2<sub>Cu</sub>** (**Figure 2.1**) shows a less distorted trigonal planar geometry than **2.1<sub>Cu</sub>**, with a more crowded Cu-center due to the short Cu–S<sub>thiolate</sub> bond distance [2.1802(8) Å]. Furthermore, while the NHC ligand in **2.1<sub>Cu</sub>** is in the same coordination plane as the amido and thioether, in **2.2<sub>Cu</sub>**, the NHC is twisted relative to the S–Cu–N plane.



Scheme 2.1. Synthesis of **2.1<sub>Cu</sub>** and **2.2<sub>Cu</sub>**.

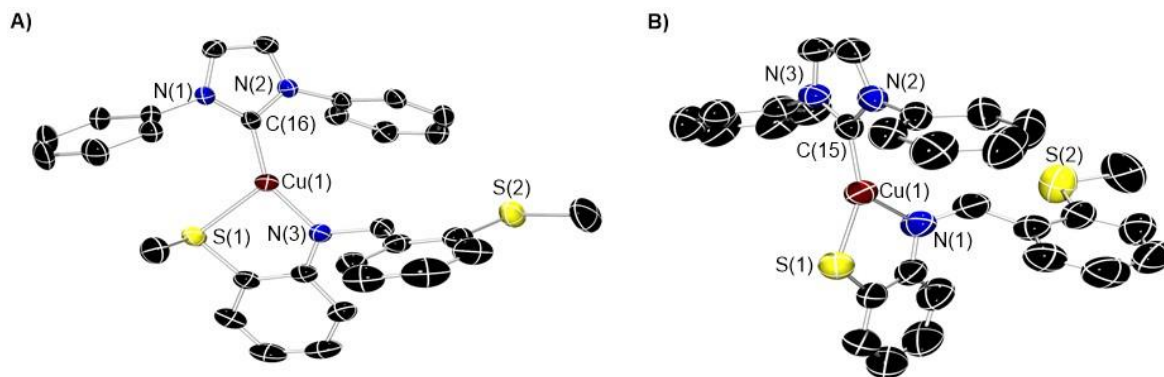


Figure 2.1. ORTEP depiction of the solid-state molecular structures of (A) **2.1<sub>Cu</sub>**: Selected bond lengths (Å): Cu(1)-S(1) 2.4820(14), Cu(1)-N(3) 1.948(2), Cu(1)-C(16) 1.919(3); (B) **2.2<sub>Cu</sub>**: Selected bond lengths (Å): Cu(1)-S(1) 2.1802(8), Cu(1)-N(3) 2.130(2), Cu(1)-C(15).

### 2.2.2 Amido vs. thiolate for bifunctional reactivity

To investigate and directly compare the bifunctional activity of the two ligand systems, a series of E–H bond activation studies were carried out (**Table 2.1**). The reaction of benzaldehyde and pinacolborane with 1 mol% **2.1**<sub>Cu</sub> gave quantitative conversion to the hydroboration product after 5 min at room temperature. The analogous reaction with acetophenone provided the same results with no decrease in activity with this less reactive substrate. Similar reactions with triethoxysilane afforded quantitative hydrosilylation products in 5 min. Lowering the catalyst loading to 0.1 mol% still gave quantitative conversion in 15 min, demonstrating the high activity and stability of **2.1**<sub>Cu</sub>. Although sterically hindered ketones commonly present problems for Cu-catalyzed hydrosilylations,<sup>31</sup> benzophenone is efficiently converted to the silyl ether product in 10 min at room temperature. Triethylsilane may also be used as the silane source, however the reaction requires gentle heating and longer reaction times to reach completion (5%, 40 °C, 30 min). In contrast, attempted reactions with 4-tert-butyl styrene were unsuccessful and resulted in catalyst decomposition. To confirm selectivity for carbonyls over alkenes, *trans*-cinnamaldehyde was treated with triethoxysilane and 1 mol% **2.1**<sub>Cu</sub>, affording the silyl ether product with no indication of the alkene hydrosilylation product. Interestingly, after 24 h we observed significant *cis-trans* equilibration in solution. In addition, aliphatic 5-hexen-2-one gave exclusive and quantitative hydrosilylation product with no indication of isomerization, providing further evidence that alkenes cannot bind to the metal center during catalysis.

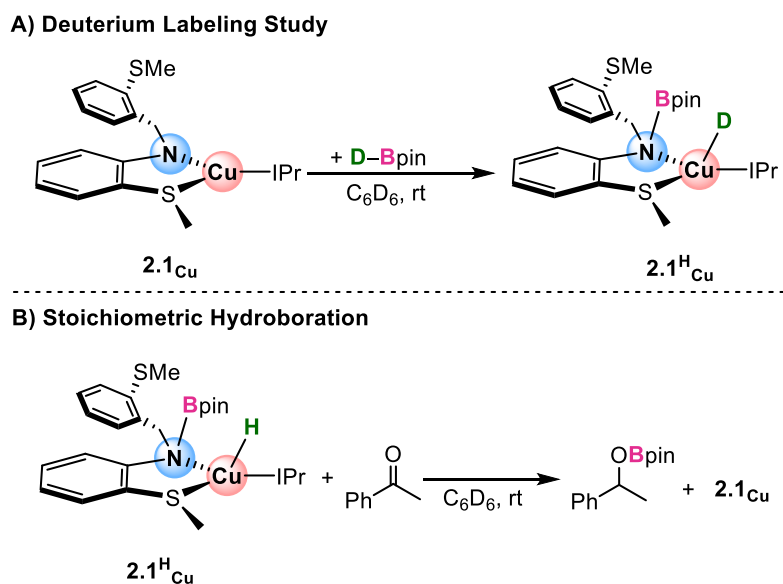
Since **2.1<sub>Cu</sub>** was found to be an efficient catalyst for both hydroboration and hydrosilylation of carbonyls, the activity of **2.2<sub>Cu</sub>** was also investigated. Reaction of benzaldehyde and pinacolborane with 1 mol% **2.2<sub>Cu</sub>** afforded the hydroboration product in near quantitative yield after 5 min. Analogous reactions with acetophenone, and even bulky benzophenone also resulted in complete conversion. However, **2.2<sub>Cu</sub>** was not an active catalyst for hydrosilylations. Attempts to facilitate the hydrosilylation of either benzaldehyde or acetophenone were unsuccessful, even with higher catalyst loadings, longer reaction times, and elevated temperatures.

<u>Catalyst</u>	<u>Substrate</u>	<u>Carbonyl</u>	<u>Product</u>	<u>Yield(%)</u>
2.1 <sub>Cu</sub>	HBpin			>99
2.1 <sub>Cu</sub>	HBpin			>99
2.1 <sub>Cu</sub>	HSi(OEt) <sub>3</sub>			>99
2.1 <sub>Cu</sub>	HSi(OEt) <sub>3</sub>			92 <sup>a</sup>
2.1 <sub>Cu</sub>	HSi(OEt) <sub>3</sub>			>99
2.1 <sub>Cu</sub>	HSi(OEt) <sub>3</sub>			>99
2.1 <sub>Cu</sub>	HSi(OEt) <sub>3</sub>			>99
<hr/>				
2.2 <sub>Cu</sub>	HBpin			>99
2.2 <sub>Cu</sub>	HBpin			>99
2.2 <sub>Cu</sub>	HBpin			>99

**Table 2.1.** Substrate scope of hydroboration and hydrosilylation reactions of carbonyls with catalytic **2.1<sub>Cu</sub>** and **2.2<sub>Cu</sub>**. <sup>a</sup>Conditions: Copper catalyst (1 mol%), room temperature, 5-15 min. All reactions gave quantitative conversion. <sup>b</sup>Yield was determined from <sup>1</sup>H NMR integration relative to internal standard mesitylene.

### 2.2.3 Mechanistic studies of Cu-catalyzed hydroboration

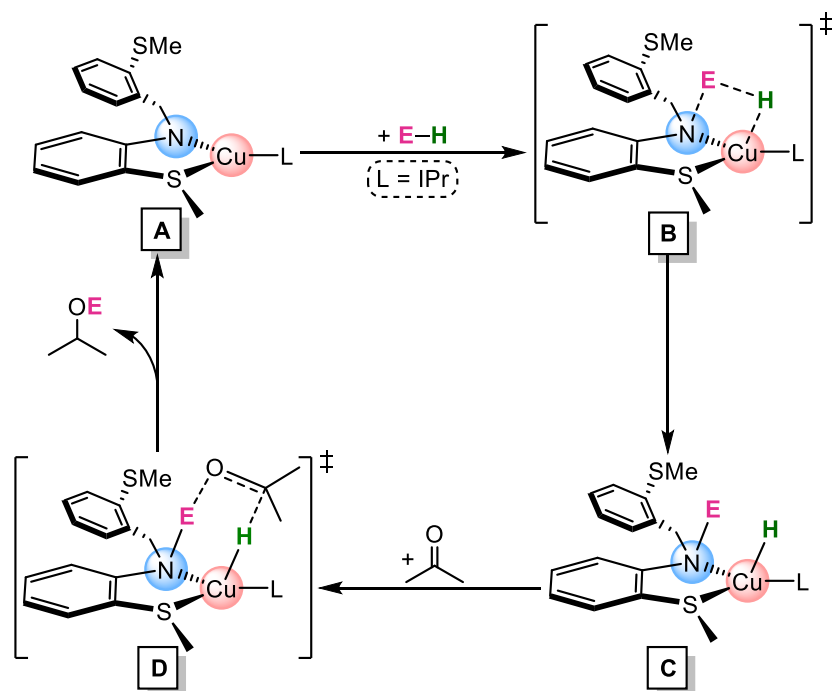
Several experiments were performed to gain insight into a plausible reaction pathway. By NMR spectroscopy, neither **2.1**<sub>Cu</sub> nor **2.2**<sub>Cu</sub> showed any reaction with stoichiometric benzaldehyde or with triethoxysilane at short reaction times; longer reaction times with the latter led to decomposition. In contrast, both complexes reacted with pinacolborane which has been shown previously to undergo B–H bond activation at metal amido<sup>32</sup> and thiolate<sup>33-34</sup> centers. Upon addition of 1 equiv of pinacolborane to a C<sub>6</sub>D<sub>6</sub> solution of **2.1**<sub>Cu</sub>, an immediate colour change from pale yellow to dark yellow was observed.<sup>a</sup> The <sup>1</sup>H NMR spectrum showed a new broad singlet at δ 2.5 assigned as a Cu–H species, as confirmed by the DBpin reaction with **2.1**<sub>Cu</sub> (Scheme 2.2). Further monitoring showed decomposition after approximately 1 h at room temperature, as evidenced by formation of a black precipitate and free **L1**.



Scheme 2.2. Mechanistic studies performed with **2.1**<sub>Cu</sub>.

<sup>a</sup> Reaction of HBpin with **2.2**<sub>Cu</sub> resulted in a complex <sup>1</sup>H NMR spectrum with multiple isomers of product due to imine rotation.

Based on the above experiments, a plausible reaction pathway for the hydroboration/hydrosilylation of carbonyls using **2.1**<sub>Cu</sub> is shown in **Scheme 2.3**. The reaction begins with E–H bond activation through the proposed transition state, B, with the amido acting as a Lewis base. This results in the formation of a Cu–H species C, which then reacts with the carbonyl substrate via outer-sphere transition state D, to furnish the final reduced carbonyl and regenerate A. The carbonyl substrate does not bind to the metal center at any step throughout the catalytic cycle, explaining the selectivity for carbonyls over alkenes and lack of isomerization of the latter. It should be noted that for **2.2**<sub>Cu</sub> catalyzed hydroboration, the thiolate donor serves as the Lewis base to promote B–H bond activation, as previously established by Wang.<sup>35</sup>



**Scheme 2.3.** Proposed mechanism for E–H bond activation and reaction with carbonyls.

## **2.3 Conclusions**

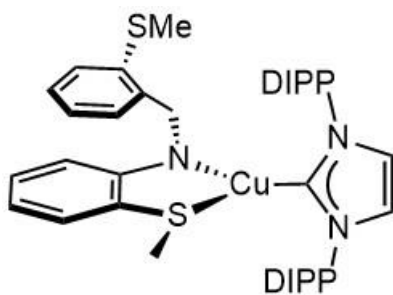
The original design of these Cu complexes was meant to crowd the Cu-center with sufficient steric bulk to force an outer-sphere bifunctional mechanism. The fact that aldehydes and ketones readily react while olefins are inactive supports the envisioned outer-sphere mechanism, as the latter requires binding to the metal center prior to activation. Complexes **2.1<sub>Cu</sub>** and **2.2<sub>Cu</sub>** also allowed a direct comparison for the bifunctional catalytic activity of the hard amido vs the soft thiolate donor in the ligands **L1** and **L2**. While thiolate complex **2.2<sub>Cu</sub>** is an efficient catalyst for hydroboration of carbonyls using pinacolborane, it was unable to affect the hydrosilylation. Amido complex **2.1<sub>Cu</sub>** was shown to be superior for carbonyl reductions using either pinacolborane or triethoxysilane, giving full conversion at room temperature in less than 15 min, even with catalyst loadings of 0.1%. Mechanistic studies support the proposed reaction pathway in which the amido/thiolate serves as a Lewis base to facilitate E–H bond activation, generating a Cu–H intermediate that reacts with carbonyl substrates via an outer-sphere mechanism. There are few instances of copper being utilized in metal-ligand bifunctional catalysis, and most examples employ dinuclear-copper complexes.<sup>36-37</sup> Furthermore, nearly all examples of Cu-NHC catalyzed hydroboration and hydrosilylation reactions require either excess substrate, elevated temperatures, longer reaction times, or the use of base to generate the active Cu–H species.<sup>24-25</sup> This work presents an extremely efficient carbonyl reduction pathway via a metal-ligand bifunctional outer-sphere mechanism that is unique for copper. Furthermore, installation of a chiral auxiliary in lieu of the uncoordinated aryl-thioether may offer an opportunity for stereospecific catalysis. Future work will further explore potential reduction catalysis with other base metals.

## 2.4 Experimental

### 2.4.1 Materials and methods

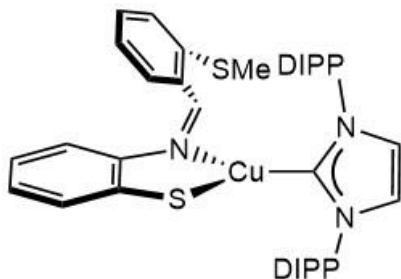
Unless otherwise stated, all reactions were carried out under an atmosphere of dry, oxygen-free dinitrogen by means of standard Schlenk or glovebox techniques. Benzene- $d_6$  was degassed by three freeze-pump-thaw cycles, and subsequently dried by running through a column of activated alumina. Toluene, hexanes, and THF were dried on columns of activated alumina using a J. C. Meyer (formerly Glass Contour) solvent purification system.  $^1\text{H}$  NMR spectra were recorded on either a Bruker Avance, Avance II, or Avance III spectrometer operating at either 300 or 500 MHz with respect to proton nuclei.  $^1\text{H}$  NMR spectra were referenced to residual protons ( $\text{C}_6\text{D}_6$ ,  $\delta$  7.15) with respect to tetramethylsilane at  $\delta$  0.00.  $^{13}\text{C}\{^1\text{H}\}$  NMR spectra were referenced relative to solvent resonance ( $\text{C}_6\text{D}_6$ ,  $\delta$  127.2). Abbreviations: s-singlet, d-doublet, tr-triplet, sept-septet, ov-overlapping, mult-multiplet, br-broad. All reagents were purchased from commercial suppliers. The compounds DBpin,<sup>38</sup>  $\text{CuCl}(\text{IPr})$ ,<sup>39</sup>  $\text{L1}^{\text{H}}$ ,<sup>22</sup> and  $\text{L2}^{\text{H}}$ <sup>23</sup> were all prepared according to literature procedures.

### 2.4.2 Synthesis and characterization of copper complexes



**Synthesis of  $[\text{Cu}(\text{S}^{\text{Me}}\text{NS}^{\text{Me}})(\text{IPr})]$  [ $2.1_{\text{Cu}}$ ].** A vial equipped with a magnetic stir bar was charged with  $\text{CuCl}(\text{IPr})$  (0.097 g, 0.199 mmol) and dissolved in 3 mL of THF. A 3 mL THF solution of  $\text{L1}^{\text{H}}$  (0.055 g, 0.199 mmol) and  $\text{LiHMDS}$  (0.033 g, 0.199 mmol) was added

dropwise to the reaction mixture while stirring, resulting in a bright yellow solution that was stirred for 18 h. The solution was evaporated in vacuo, washed with hexanes, and further dried. The residue was extracted into toluene, filtered through Celite, and concentrated in vacuo to yield a pale-yellow powder (0.133 g, 92% yield). X-ray quality crystals were grown from a concentrated solution in toluene layered with hexanes at -30 °C. **<sup>1</sup>H NMR (C<sub>6</sub>D<sub>6</sub>, 23 °C, 500 MHz):** δ 1.04 (d, 12H, CH-(CH<sub>3</sub>)<sub>2</sub>, <sup>3</sup>J<sub>HH</sub> = 7.0 Hz); 1.31 (d, 12H, CH-(CH<sub>3</sub>)<sub>2</sub>, <sup>3</sup>J<sub>HH</sub> = 7.0 Hz); 1.61 (s, 3H, S-CH<sub>3</sub>); 2.15 (s, 3H, S-CH<sub>3</sub>); 2.72 (sept, 4H, CH-(CH<sub>3</sub>)<sub>2</sub>, <sup>3</sup>J<sub>HH</sub> = 7.0 Hz); 4.39 (s, 2H, N=CH<sub>2</sub>); 6.25 (dd, 1H, Ar-H, <sup>3</sup>J<sub>HH</sub> = 8.5 Hz, <sup>4</sup>J<sub>HH</sub> = 1.0 Hz); 6.30 (ddd, 1H, Ar-H, <sup>3</sup>J<sub>HH</sub> = 8.5, 7.5 Hz, <sup>4</sup>J<sub>HH</sub> = 1.5 Hz); 6.36 (s, 2H, HC=CH); 6.82 (ddd, 1H, Ar-H, <sup>3</sup>J<sub>HH</sub> = 7.5, 7.5 Hz, <sup>4</sup>J<sub>HH</sub> = 1.5 Hz); 6.89 (ddd, 1H, Ar-H, <sup>3</sup>J<sub>HH</sub> = 8.5, 7.5 Hz, <sup>4</sup>J<sub>HH</sub> = 1.5 Hz); 7.02 (ov dd, 1H, Ar-H, <sup>4</sup>J<sub>HH</sub> = 1.5 Hz); 7.04 (m, 4H, Ph-H); 7.06 (ov ddd, 1H, Ar-H, <sup>3</sup>J<sub>HH</sub> = 7.5, 7.5 Hz, <sup>4</sup>J<sub>HH</sub> = 1.5 Hz); 7.17 (m, 2H, Ph-H); 7.29 (dd, 1H, Ar-H, <sup>3</sup>J<sub>HH</sub> = 7.5 Hz, <sup>4</sup>J<sub>HH</sub> = 1.0 Hz); 7.41 (dd, 1H, Ar-H, <sup>3</sup>J<sub>HH</sub> = 7.5 Hz, <sup>4</sup>J<sub>HH</sub> = 1.5 Hz). **<sup>13</sup>C{<sup>1</sup>H} NMR (C<sub>6</sub>D<sub>6</sub>, 23 °C, 500 MHz):** δ 14.9 (s, 1C, S-CH<sub>3</sub>); 19.8 (s, 1C, S-CH<sub>3</sub>); 23.7 (s, 4C, CH-CH<sub>3</sub>); 23.8 (s, 4C, CH-CH<sub>3</sub>); 28.5 (s, 4C, CH-CH<sub>3</sub>); 53.6 (s, 1C, N-CH<sub>2</sub>); 109.5 (s, 1C, Ar<sub>SNS</sub>-C); 111.4 (s, 1C, Ar<sub>SNS</sub>-C); 118.1 (s, 1C, Ar<sub>SNS</sub>-C); 121.7 (s, 2C, HC=CH); 123.8 (s, 1C, Ph-C); 124.1 (s, 1C, Ar<sub>SNS</sub>-C); 124.3 (s, 1C, Ar<sub>SNS</sub>-C); 125.2 (s, 1C, Ar<sub>SNS</sub>-C); 126.6 (s, 1C, Ar<sub>SNS</sub>-C); 129.6 (s, 1C, Ar<sub>SNS</sub>-C); 129.7 (s, 1C, Ph-C); 132.8 (s, 1C, Ar<sub>SNS</sub>-C); 135.9 (s, 1C, Ar<sub>SNS</sub>-C); 141.2 (s, 1C, Ar<sub>SNS</sub>-C); 145.2 (s, 1C, Ph-C); 159.2 (s, 1C, Ph-C); 186.8 (s, 1C, Cu-C). Calcd for C<sub>42</sub>H<sub>53</sub>Cu N<sub>3</sub>S<sub>2</sub>: %C 69.33; %H 7.34; %N 5.78. Found: %C 69.38; %H 7.04; %N 5.46.



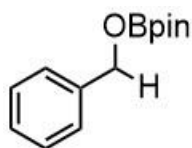
**Synthesis of Cu(S<sup>Me</sup>NS)(IPr) [2.2<sub>Cu</sub>].** In a vial charged with a magnetic stir bar, CuCl(IPr) (0.141 g, 0.289 mmol) and L2<sup>H</sup> (0.075 g, 0.289 mmol) were dissolved in 3 mL of toluene giving a dark brown solution. While stirring, potassium tert-butoxide (0.032 g, 0.289 mmol) was slowly added over one min, resulting in an immediate color change to dark red. The solution was stirred at room temperature for 6 h, filtered through Celite and concentrated in vacuo. The resulting solid was washed with hexanes and further dried, resulting in a dark red solid (0.180 g, 88% yield). X-ray quality crystals were grown from a concentrated toluene solution layered with hexanes at room temperature. **<sup>1</sup>H NMR (C<sub>6</sub>D<sub>6</sub>, 23 °C, 300 MHz):** Isomer #1: δ 1.11 (d, 12H, CH-(CH<sub>3</sub>)<sub>2</sub>, <sup>3</sup>J<sub>HH</sub> = 7.0 Hz); 1.49 (d, 12H, CH-(CH<sub>3</sub>)<sub>2</sub>, <sup>3</sup>J<sub>HH</sub> = 7.0 Hz); 2.02 (s, 3H, S-CH<sub>3</sub>); 2.86 (sept, 4H, CH-(CH<sub>3</sub>)<sub>2</sub>, <sup>3</sup>J<sub>HH</sub> = 7.0 Hz); 6.28 (ddd, 1H, Ar-H, <sup>3</sup>J<sub>HH</sub> = 8, 7 Hz, <sup>4</sup>J<sub>HH</sub> = 1.5 Hz); 6.43 (ov dd, 1H, Ar-H, <sup>3</sup>J<sub>HH</sub> = 7 Hz, <sup>4</sup>J<sub>HH</sub> = 1.5 Hz); 6.44 (s, 2H, HC=CH); 6.65 (ddd, 1H, Ar-H, <sup>3</sup>J<sub>HH</sub> = 8, 7 Hz, <sup>4</sup>J<sub>HH</sub> = 1.5 Hz); 6.70 (ddd, 1H, Ar-H, <sup>3</sup>J<sub>HH</sub> = 8, 7 Hz, <sup>4</sup>J<sub>HH</sub> = 1.5 Hz); 6.77 (dd, 1H, Ar-H, <sup>3</sup>J<sub>HH</sub> = 7 Hz, <sup>4</sup>J<sub>HH</sub> = 1.5 Hz); 6.80 (ov m, 1H, Ar-H); 6.90 (ddd, 1H, Ar-H, <sup>3</sup>J<sub>HH</sub> = 7, 7 Hz, <sup>4</sup>J<sub>HH</sub> = 1.5 Hz); 7.10 (m, 4H, Ph-H); 7.18 (m, 2H, Ph-H); 7.40 (s, 1H, N=CH); 7.81 (dd, 1H, Ar-H, <sup>3</sup>J<sub>HH</sub> = 8 Hz, <sup>4</sup>J<sub>HH</sub> = 1.5 Hz). Isomer #2: δ 1.03 (d, 12H, CH-(CH<sub>3</sub>)<sub>2</sub>, <sup>3</sup>J<sub>HH</sub> = 7.0 Hz); 1.26 (d, 12H, CH-(CH<sub>3</sub>)<sub>2</sub>, <sup>3</sup>J<sub>HH</sub> = 7.0 Hz); 1.89 (s, 3H, S-CH<sub>3</sub>); 2.73 (br sept, 4H, CH-(CH<sub>3</sub>)<sub>2</sub>, <sup>3</sup>J<sub>HH</sub> = 7.0 Hz); 6.34 (ov mult, 1H, Ar-H); 6.34 (s, 2H, HC=CH); 6.78 (ov mult, 4H, Ar-H); 6.85 (dmult, 1H, Ar-H, <sup>3</sup>J<sub>HH</sub> = 8.0 Hz); 7.05 (mult, 4H, Ph-H); 7.18 (mult, 2H, Ph-H); 7.32 (br mult, 1H, Ar-H); 8.03 (br mult, 1H, Ar-H); 8.60 (s, 1H, N=CH). **<sup>13</sup>C{<sup>1</sup>H} NMR (C<sub>6</sub>D<sub>6</sub>, 23 °C, 300 MHz):** Isomer #1: δ 15.8 (s, 1C, S-CH<sub>3</sub>); 24.0 (s, 4C, CH-CH<sub>3</sub>); 24.2 (s, 4C, CH-CH<sub>3</sub>); 28.7 (s, 4C, CH-CH<sub>3</sub>);

121.7 (s, 2C, HC=CH); 124.0, 129.8, 145.5, 154.3 (s, Ph-C); 118.9, 119.9, 125.5, 126.4, 129.0, 129.8, 135.3, 135.9, 137.7, 147.5, 151.1 (s, 1C, Ar<sub>SNS</sub>-C); 133.0 (s, 1C, N=C); 187.2 (s, 1C, Cu-C). Isomer #2:  $\delta$  13.9 (s, 1C, S-CH<sub>3</sub>); 23.7 (s, 4C, CH-CH<sub>3</sub>); 24.1 (s, 4C, CH-CH<sub>3</sub>); 28.6 (s, 4C, CH-CH<sub>3</sub>); 122.0 (s, 2C, HC=CH); 123.8, 129.9, 145.5, 155.0 (s, Ph-C); 117.8, 120.3, 125.4, 126.2, 129.1, 129.6, 135.0, 136.3, 138.2, 146.6, 152.3 (s, 1C, Ar<sub>SNS</sub>-C); 125.1 (s, 1C, N=C); 185.7 (s, 1C, Cu-C). Calcd for C<sub>41</sub>H<sub>49</sub>CuN<sub>3</sub>S<sub>2</sub>: %C 69.21; %H 6.94; %N 5.91. Found: %C 68.81; %H 7.43; %N 5.32.

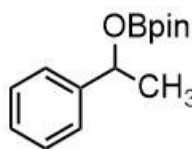
### **2.4.3 Catalytic and mechanistic studies**

**General Procedure ‘A’ for Hydroboration of Carbonyls.** A stock solution of **2.1<sub>Cu</sub>** / **2.2<sub>Cu</sub>** was prepared by dissolving the appropriate Cu-complex (10 mg) in C<sub>6</sub>D<sub>6</sub> (2 mL). A vial containing **2.1<sub>Cu</sub>** / **2.2<sub>Cu</sub>** (0.001 g, 20  $\mu$ L, 0.001 mmol, 1 mol%) in 0.6 g of C<sub>6</sub>D<sub>6</sub> was charged first with the appropriate substrate, and subsequently with pinacolborane, resulting in an immediate color change from pale-yellow to colorless. The solution was charged to an NMR tube for further analysis. Reaction times varied slightly from 2-10 min. Yield was determined by <sup>1</sup>H NMR peak integration in reference to internal standard mesitylene.

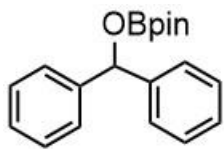
**General Procedure ‘B’ for Hydrosilylation of Carbonyls.** A stock solution of **2.1<sub>Cu</sub>** was prepared by dissolving the appropriate Cu-complex (10 mg) in C<sub>6</sub>D<sub>6</sub> (2 mL). A vial containing **2.1<sub>Cu</sub>** (0.001 g, 20  $\mu$ L, 0.001 mmol, 1 mol%) in 0.6 g of C<sub>6</sub>D<sub>6</sub> was charged first with the appropriate substrate, and subsequently with triethoxysilane, resulting in an immediate color change from pale-yellow to dark yellow. The solution was charged to an NMR tube for further analysis. Reaction times varied slightly from 2-10 min. Yield was determined by <sup>1</sup>H NMR peak integration in reference to internal standard mesitylene.



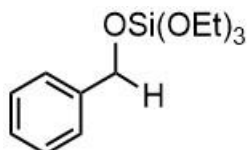
**Hydroboration of benzaldehyde.** Carried out according to *General Procedure A* using benzaldehyde (0.015 g, 14  $\mu$ L, 0.142 mmol), pinacolborane (0.018 g, 20  $\mu$ L, 0.142 mmol), and either **2.1<sub>Cu</sub>** (0.001 g, 20  $\mu$ L, 0.001 mmol, 1 mol %), or **2.2<sub>Cu</sub>** (0.001 g, 20  $\mu$ L, 0.001 mmol, 1 mol %).  $^1\text{H}$  NMR showed quantitative conversion to hydroboration product after 5 min at room temperature.  $^{11}\text{B}$  and  $^1\text{H}$  NMR shifts matched with literature values.<sup>40</sup>



**Hydroboration of acetophenone.** Conducted according to *General Procedure A* using acetophenone (0.017 g, 16  $\mu$ L, 0.142 mmol), pinacolborane (0.018 g, 20  $\mu$ L, 0.142 mmol), and **2.1<sub>Cu</sub>** (0.001 g, 20  $\mu$ L, 0.001 mmol, 1 mol %), or **2.2<sub>Cu</sub>** (0.001 g, 20  $\mu$ L, 0.001 mmol, 1 mol %).  $^1\text{H}$  NMR showed quantitative conversion to hydroboration product after 5 min at room temperature.  $^{11}\text{B}$  and  $^1\text{H}$  NMR shifts matched with literature values.<sup>40</sup>

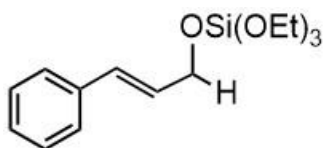


**Hydroboration of benzophenone.** Conducted according to *General Procedure A* using benzophenone (0.025 g, 0.142 mmol), pinacolborane (0.018 g, 20  $\mu$ L, 0.142 mmol), and **2.1<sub>Cu</sub>** (0.001 g, 20  $\mu$ L, 0.001 mmol, 1 mol %), or **2.2<sub>Cu</sub>** (0.001 g, 20  $\mu$ L, 0.001 mmol, 1 mol %).  $^1\text{H}$  NMR showed quantitative conversion to hydroboration product after 10 min at room temperature.  $^{11}\text{B}$  and  $^1\text{H}$  NMR shifts matched with literature values.<sup>40</sup>



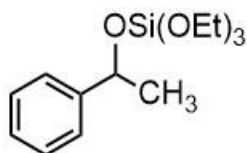
**Hydrosilylation of benzaldehyde with 2.1<sub>Cu</sub>.** Carried out according to *General Procedure B* using benzaldehyde (0.015 g, 14  $\mu$ L, 0.142 mmol), triethoxysilane (0.023 g, 26  $\mu$ L, 0.142 mmol), and **2.1<sub>Cu</sub>** (0.001 g, 20  $\mu$ L, 0.001 mmol, 1 mol %).  $^1\text{H}$  NMR showed quantitative conversion to

hydrosilylation product after 5 min at room temperature.  $^1\text{H}$  NMR shifts matched with literature values.<sup>41</sup>



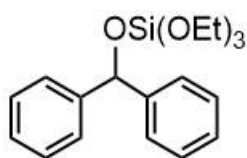
**Hydrosilylation of *trans*-cinnamaldehyde with **2.1**<sub>Cu</sub>.**

Synthesized according to *General Procedure B* using *trans*-cinnamaldehyde (0.018 g, 17  $\mu\text{L}$ , 0.142 mmol), triethoxysilane (0.023 g, 26  $\mu\text{L}$ , 0.142 mmol), and **2.1**<sub>Cu</sub> (0.001 g, 20  $\mu\text{L}$ , 0.001 mmol, 1 mol %).  $^1\text{H}$  NMR showed 92% yield in reference to internal standard mesitylene to hydrosilylation product after 5 min at room temperature.  $^1\text{H}$  NMR shifts matched with literature values.<sup>42</sup> After 24 h, we noticed significant *cis-trans* equilibration in the reaction solution.



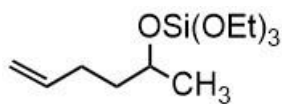
**Hydrosilylation of acetophenone with **2.1**<sub>Cu</sub>.** Conducted according

to *General Procedure B* using acetophenone (0.017 g, 16  $\mu\text{L}$ , 0.142 mmol), triethoxysilane (0.023 g, 26  $\mu\text{L}$ , 0.142 mmol), and **2.1**<sub>Cu</sub> (0.001 g, 20  $\mu\text{L}$ , 0.001 mmol, 1 mol %).  $^1\text{H}$  NMR showed quantitative conversion to hydrosilylation product after 5 min at room temperature.  $^1\text{H}$  NMR shifts matched with literature values.<sup>43</sup>



**Hydrosilylation of benzophenone with **2.1**<sub>Cu</sub>.** Carried out

according to *General Procedure B* using benzophenone (0.025 g, 0.142 mmol), triethoxysilane (0.023 g, 26  $\mu\text{L}$ , 0.142 mmol), and **2.1**<sub>Cu</sub> (0.001 g, 20  $\mu\text{L}$ , 0.001 mmol, 1 mol %).  $^1\text{H}$  NMR showed quantitative conversion to hydrosilylation product after 10 min at room temperature.  $^1\text{H}$  NMR shifts matched with literature values.<sup>44</sup>



**Hydrosilylation of 5-hexen-2-one with 2.1<sub>Cu</sub>.** Conducted according to *General Procedure B* using 5-hexen-2-one (0.013 g, 16  $\mu$ L, 0.142 mmol), triethoxysilane (0.023 g, 26  $\mu$ L, 0.142 mmol), and **2.1<sub>Cu</sub>** (0.001 g, 20  $\mu$ L, 0.001 mmol, 1 mol %). <sup>1</sup>H NMR showed quantitative conversion to hydrosilylation product after 10 min at room temperature. <sup>1</sup>H NMR shifts were similar to the known trimethylsilylether analogue.<sup>44</sup> **<sup>1</sup>H NMR (C<sub>6</sub>D<sub>6</sub>, 23 °C, 300 MHz):**  $\delta$  1.17 (tr, 9H, OCH<sub>2</sub>CH<sub>3</sub>, <sup>3</sup>J<sub>HH</sub> = 7 Hz); 1.23 (d, 3H, Si(C)(CH<sub>3</sub>), <sup>3</sup>J<sub>HH</sub> = 6 Hz); 1.48 (second order mult, 1H); 1.68 (second order mult, 1H, Si(C)(CH<sub>2</sub>)(CH<sub>2</sub>)); 2.18 (second order mult, 1H, Si(C)(CH<sub>2</sub>), <sup>3</sup>J<sub>HH</sub> = 6 Hz); 3.86 (q, 6H, OCH<sub>2</sub>CH<sub>3</sub>, <sup>3</sup>J<sub>HH</sub> = 7 Hz); 4.16 (second order mult, 1H, Si(C)(CH<sub>2</sub>), <sup>3</sup>J<sub>HH</sub> = 6 Hz); 4.97 (dmult, 1H, =CH<sub>2</sub>, <sup>3</sup>J<sub>HH</sub> = 10 Hz); 5.06 (dmult, 1H, =CH<sub>2</sub>, <sup>3</sup>J<sub>HH</sub> = 17 Hz); 5.81 (second order mult, 1H, =CH, <sup>3</sup>J<sub>HH</sub> = 17, 10 Hz).

**Attempted hydrosilylation of benzaldehyde with 2.2<sub>Cu</sub>.** Carried out according to *General Procedure B* using acetophenone (0.017 g, 16  $\mu$ L, 0.142 mmol), triethoxysilane (0.023 g, 26  $\mu$ L, 0.142 mmol), and **Cu-2** (0.001 g, 20  $\mu$ L, 0.001 mmol, 1 mol %). Crude <sup>1</sup>H NMR spectrum after 1 h showed no product formation. Decomposition was observed after 24 h. Attempts to heat above 50 °C resulted in immediate decomposition.

**Attempted hydrosilylation of acetophenone with 2.2<sub>Cu</sub>.** Conducted according to *General Procedure B* using benzaldehyde (0.015 g, 14  $\mu$ L, 0.142 mmol), triethoxysilane (0.023 g, 26  $\mu$ L, 0.142 mmol), and **Cu-2** (0.001 g, 20  $\mu$ L, 0.001 mmol, 1 mol %). Crude <sup>1</sup>H NMR after 1 h showed no product formation. Decomposition was observed after 24 h. Attempts to heat above 50 °C resulted in immediate decomposition.

### 2.4.4 Key spectroscopic data

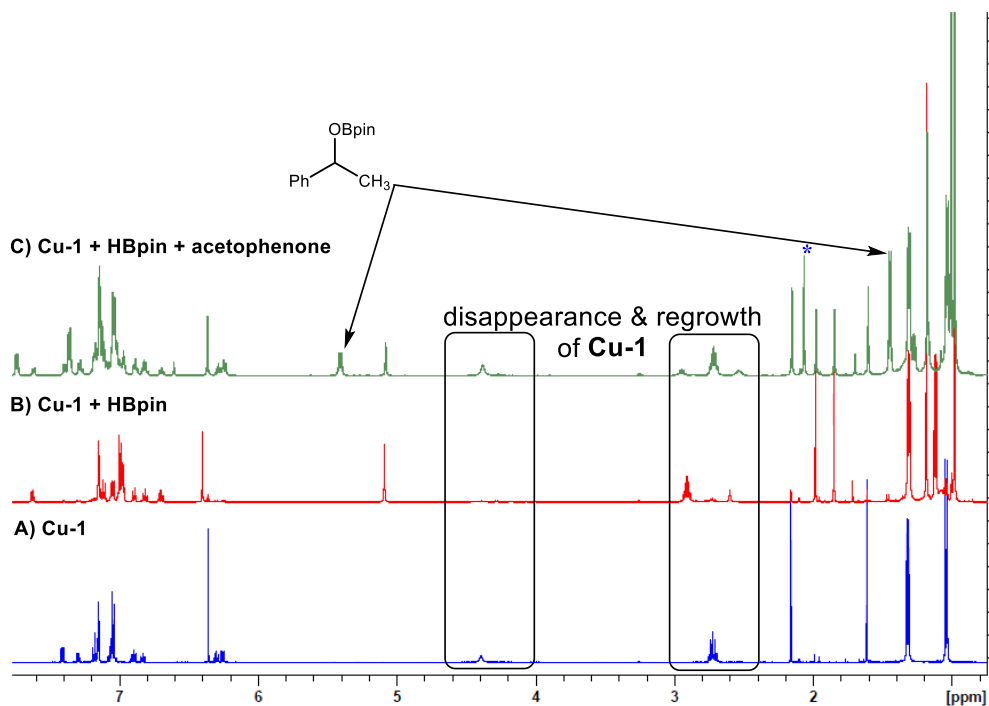


**Figure 2.2.** Stacked plot of <sup>1</sup>H NMR spectra showing stoichiometric conversion from A) **2.1**<sub>Cu</sub> to B) Cu–H intermediate, and C) subsequent conversion to hydroboration product, reforming **2.1**<sub>Cu</sub>

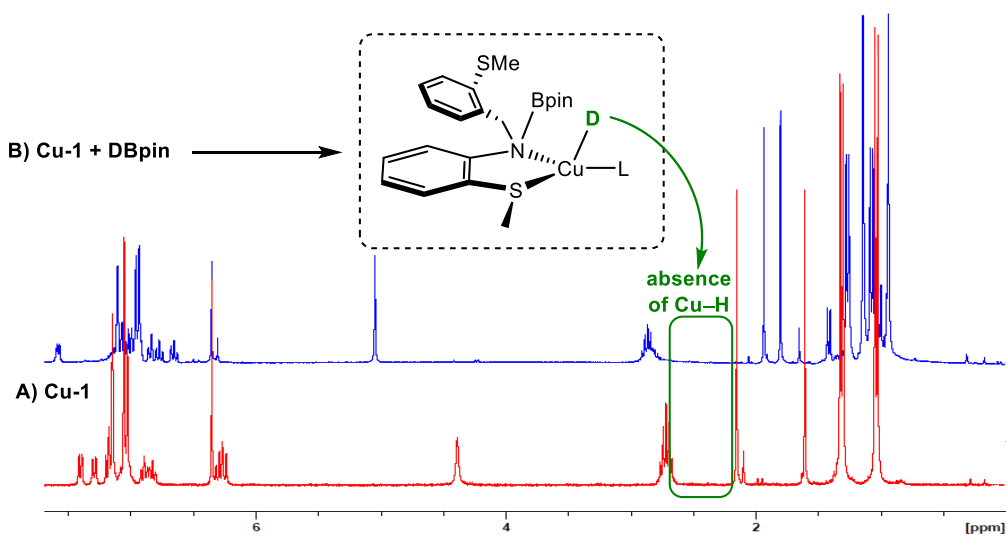


**Figure 2.3.** <sup>1</sup>H NMR spectrum of reaction of **2.1**<sub>Cu</sub> with DBpin.

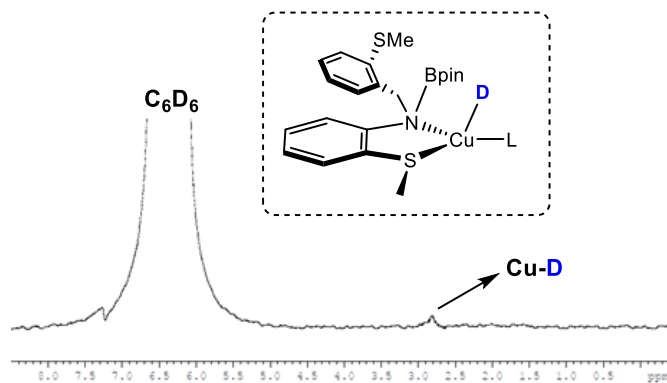


Figure 2.4.  $^2\text{H}$  NMR spectrum of reaction of **2.1**<sub>Cu</sub> with DBPin.

### 2.4.5 Single crystal X-ray diffraction data

*\*\*Key crystallographic data can be found in Appendix A. \*\**

The crystals were mounted on thin glass fibers using paraffin oil or cyanoacrylate glue. The crystals of **2.1**<sub>Cu</sub> and **2.2**<sub>Cu</sub> were cooled to  $200 \pm 2$  K during data collection. The data was collected on Bruker single-crystal diffractometer equipped with a sealed Mo tube source (wavelength  $0.71073 \text{ \AA}$ ) and APEX II CCD detector. The raw data collection and processing were performed with Bruker APEX II software package.<sup>45</sup> Semi-empirical absorption correction based on equivalent reflections were applied.<sup>46</sup> Systematic absences and unit cell parameters were consistent with monoclinic  $P2_1$  (#4) for **2.1**<sub>Cu</sub>, monoclinic  $P2_1/c$  (#14) for **2.2**<sub>Cu</sub>.

The structures were solved by intrinsic phasing and refined with full-matrix least-squares procedure based on  $F^2$ , using SHELXL.<sup>47</sup> All non-hydrogen atoms were refined anisotropically. The hydrogen atoms bonded to carbon atoms were placed in idealized positions.

**Refinement details for 2.1<sub>Cu</sub>.**

Due to the value of the Flack parameter [0.463(9)], a centrosymmetric space group was considered (P21/m), however a satisfactory structure solution was not obtained. The Flack value is therefore attributed to an inverse twin, for which the following Twin Law was applied:

TWIN -1 0 0 0 -1 0 0 0 -1

BASF 0.463

Two isopropyl carbons displayed disorder, each with 0.5 occupancy. The SADI and RIGU restraints were applied to C40, C41A, C42A, C41B, and C42B.

**Refinement details for 2.2<sub>Cu</sub>.**

The structure was refined without additional restraints/constraints. No disorder was present.

## 2.5 References

- (1) de Bruin, B.; Gualco, P.; Paul, N. D. Redox Non-innocent Ligands: Reactivity and Catalysis in *Ligand Design in Metal Chemistry: Reactivity and Catalysis*; Stradiotto, M.; Lundgren, RJ, **2016**, 176.
- (2) Lyaskovskyy, V.; de Bruin, B. Redox Non-Innocent Ligands: Versatile New Tools to Control Catalytic Reactions. *ASC. Catal.* **2012**, 2, 270-279.
- (3) Takeda, H.; Koike, K.; Inoue, H.; Ishitani, O. Development of an Efficient Photocatalytic System for CO<sub>2</sub> Reduction Using Rhenium(I) Complexes Based on Mechanistic Studies. *J. Am. Chem. Soc.* **2008**, 130, 2023-2031.
- (4) Harman, W. H.; Peters, J. C. Reversible H<sub>2</sub> Addition Across a Nickel–Borane Unit as a Promising Strategy for Catalysis. *J. Am. Chem. Soc.* **2012**, 134, 5080-5082.
- (5) Devillard, M.; Bouhadir, G.; Bourissou, D. Cooperation Between Transition Metals and Lewis Acids: A Way To Activate H<sub>2</sub> and H–E bonds. *Angew. Chem. Int. Ed.* **2015**, 54, 730-732.
- (6) Sellmann, D.; Prakash, R.; Heinemann, F. W.; Moll, M.; Klimowicz, M. Heterolytic Cleavage of H<sub>2</sub> at a Sulfur-Bridged Dinuclear Ruthenium Center. *Angew. Chem. Int. Ed.* **2004**, 43, 1877-1880.
- (7) Helm, M. L.; Stewart, M. P.; Bullock, R. M.; DuBois, M. R.; DuBois, D. L. A Synthetic Nickel Electrocatalyst with a Turnover Frequency above 100,000 s<sup>-1</sup> for H<sub>2</sub> Production. *Science* **2011**, 333, 863-866.
- (8) Khusnutdinova, J. R.; Milstein, D. Metal–Ligand Cooperation. *Angew. Chem. Int. Ed.* **2015**, 54, 12236-12273.
- (9) Ikariya, T.; Blacker, A. J. Asymmetric Transfer Hydrogenation of Ketones with Bifunctional Transition Metal-Based Molecular Catalysts. *Acc. Chem. Res.* **2007**, 40, 1300-1308.
- (10) van der Vlugt, J. I. Cooperative Catalysis with First-Row Late Transition Metals. *Eur. J. Inorg. Chem.* **2012**, 363-375.
- (11) Morris, R. H. Exploiting Metal–Ligand Bifunctional Reactions in the Design of Iron Asymmetric Hydrogenation Catalysts. *Acc. Chem. Res.* **2015**, 48, 1494-1502.

- (12) Alig, L.; Fritz, M.; Schneider, S. First-Row Transition Metal (De) Hydrogenation Catalysis Based On Functional Pincer Ligands. *Chem. Rev.* **2018**, *119*, 2681-2751.
- (13) Chirik, P. J. Iron- and Cobalt-Catalyzed Alkene Hydrogenation: Catalysis with Both Redox-Active and Strong Field Ligands. *Acc. Chem. Res.* **2015**, *48*, 1687-1695.
- (14) Zuo, W.; Lough, A. J.; Li, Y. F.; Morris, R. H. Amine (Imine) Diphosphine Iron Catalysts for Asymmetric Transfer Hydrogenation of Ketones and Imines. *Science* **2013**, *342*, 1080-1083.
- (15) Casey, C. P.; Guan, H. An Efficient and Chemoselective Iron Catalyst for the Hydrogenation of Ketones. *J. Am. Chem. Soc.* **2007**, *129*, 5816-5817.
- (16) Dub, P. A.; Gordon, J. C. Metal–Ligand Bifunctional Catalysis: The “Accepted” Mechanism, the Issue of Concertedness, and the Function of the Ligand in Catalytic Cycles Involving Hydrogen Atoms. *ASC. Catal.* **2017**, *7*, 6635-6655.
- (17) MacMillan, S. N.; Harman, W. H.; Peters, J. C. Facile Si–H Bond Activation and Hydrosilylation Catalysis Mediated by a Nickel–Borane Complex. *Chem. Sci.* **2014**, *5*, 590-597.
- (18) Nesbit, M. A.; Suess, D. L.; Peters, J. C. E–H Bond Activations and Hydrosilylation Catalysis with Iron and Cobalt Metalloboranes. *Organometallics* **2015**, *34*, 4741-4752.
- (19) Morris, R. H. Asymmetric Hydrogenation, Transfer Hydrogenation and Hydrosilylation of Ketones Catalyzed by Iron Complexes. *Chem. Soc. Rev.* **2009**, *38*, 2282-2291.
- (20) Kanai, M.; Kato, N.; Ichikawa, E.; Shibasaki, M. Power of Cooperativity: Lewis Acid–Lewis Base Bifunctional Asymmetric Catalysis. *Synlett* **2005**, *2005*, 1491-1508.
- (21) Das, U. K.; Daifuku, S. L.; Gorelsky, S. I.; Korobkov, I.; Neidig, M. L.; Le Roy, J. J.; Murugesu, M.; Baker, R. T. Mononuclear, Dinuclear, and Trinuclear Iron Complexes Featuring a New Monoanionic SNS Thiolate Ligand. *Inorg. Chem.* **2016**, *55*, 987-997.
- (22) Das, U. K.; Daifuku, S. L.; Iannuzzi, T. E.; Gorelsky, S. I.; Korobkov, I.; Gabidullin, B.; Neidig, M. L.; Baker, R. T. Iron (II) Complexes of a Hemilabile SNS Amido Ligand: Synthesis, Characterization, and Reactivity. *Inorg. Chem.* **2017**, *56*, 13766-13776.

- (23) Das, U. K.; Higman, C. S.; Gabidullin, B.; Hein, J. E.; Baker, R. T. Efficient and Selective Iron-Complex-Catalyzed Hydroboration of Aldehydes. *ASC. Catal.* **2018**, *8*, 1076-1081.
- (24) Egbert, J. D.; Cazin, C. S.; Nolan, S. P. Copper N-Heterocyclic Carbene Complexes in Catalysis. *Catal. Sci. Technol.* **2013**, *3*, 912-926.
- (25) Lazreg, F.; Nahra, F.; Cazin, C. S. Copper–NHC Complexes in Catalysis. *Coord. Chem. Rev.* **2015**, *293*, 48-79.
- (26) Tsuji, Y.; Fujihara, T. Copper-Catalyzed Transformations Using Cu–H, Cu–B, and Cu–Si as Active Catalyst Species. *Chem. Rec.* **2016**, *16*, 2294-2313.
- (27) Eisenstein, O.; Crabtree, R. H. Outer Sphere Hydrogenation Catalysis. *New J. Chem.* **2013**, *37*, 21-27.
- (28) Dong, L.; Qin, S.; Yang, H.; Su, Z.; Hu, C. Theoretical Investigation on Copper Hydrides Catalyzed Hydrosilylation Reaction of 3-methylcyclohex-2-enone: Mechanism and Ligands' Effect. *Catal. Sci. Technol.* **2012**, *2*, 564-569.
- (29) He, T.; Tsvetkov, N. P.; Andino, J. G.; Gao, X.; Fullmer, B. C.; Caulton, K. G. Mechanism of Heterolysis of H<sub>2</sub> by an Unsaturated d<sup>8</sup> Nickel Center: Via Tetravalent Nickel? *J. Am. Chem. Soc.* **2009**, *132*, 910-911.
- (30) Rakowski Dubois, M.; Dubois, D. L. Development of Molecular Electrocatalysts for CO<sub>2</sub> Reduction and H<sub>2</sub> Production/Oxidation. *Acc. Chem. Res.* **2009**, *42*, 1974-1982.
- (31) Díez-González, S.; Kaur, H.; Zinn, F. K.; Stevens, E. D.; Nolan, S. P. A Simple and Efficient Copper-Catalyzed Procedure for the Hydrosilylation of Hindered and Functionalized Ketones. *J. Org. Chem.* **2005**, *70*, 4784-4796.
- (32) Pang, M.; Wu, C.; Zhuang, X.; Zhang, F.; Su, M.; Tong, Q.; Tung, C.-H.; Wang, W. Addition of a B–H Bond Across an Amido–Cobalt Bond: Co<sup>II</sup>–H-Catalyzed Hydroboration of Olefins. *Organometallics* **2018**, *37*, 1462-1467.
- (33) Omann, L.; Königs, C. D. F.; Klare, H. F.; Oestreich, M. Cooperative Catalysis at Metal–Sulfur Bonds. *Acc. Chem. Res.* **2017**, *50*, 1258-1269.
- (34) Hesp, K. D.; McDonald, R.; Ferguson, M. J.; Stradiotto, M. New Cationic and Zwitterionic Cp\* M ( $\kappa^2$ -P, S) Complexes (M= Rh, Ir): Divergent Reactivity Pathways

Arising from Alternative Modes of Ancillary Ligand Participation in Substrate Activation. *J. Am. Chem. Soc.* **2008**, *130*, 16394-16406.

(35) Song, H.; Ye, K.; Geng, P.; Han, X.; Liao, R.; Tung, C.-H.; Wang, W. Activation of Epoxides by a Cooperative Iron–Thiolate Catalyst: Intermediacy of Ferrous Alkoxides in Catalytic Hydroboration. *ASC. Catal.* **2017**, *7*, 7709-7717.

(36) Deaton, J. C.; Switalski, S. C.; Kondakov, D. Y.; Young, R. H.; Pawlik, T. D.; Giesen, D. J.; Harkins, S. B.; Miller, A. J.; Mickenberg, S. F.; Peters, J. C. E-type Delayed Fluorescence of a Phosphine-Supported Cu<sub>2</sub>(μ-NAr<sub>2</sub>)<sub>2</sub> Diamond Core: Harvesting Singlet and Triplet Excitons in OLEDs. *J. Am. Chem. Soc.* **2010**, *132*, 9499-9508.

(37) Angamuthu, R.; Byers, P.; Lutz, M.; Spek, A. L.; Bouwman, E. Electrocatalytic CO<sub>2</sub> Conversion to Oxalate by a Copper Complex. *Science* **2010**, *327*, 313-315.

(38) Espinal-Viguri, M.; Neale, S. E.; Coles, N. T.; Macgregor, S. A.; Webster, R. L. Room Temperature Iron-Catalyzed Transfer Hydrogenation and Regioselective Deuteration of Carbon–Carbon Double Bonds. *J. Am. Chem. Soc.* **2018**, *141*, 572-582.

(39) Sakaguchi, H.; Uetake, Y.; Ohashi, M.; Niwa, T.; Ogoshi, S.; Hosoya, T. Copper-Catalyzed Regioselective Monodefluoroborylation of Polyfluoroalkenes en Route to Diverse Fluoroalkenes. *J. Am. Chem. Soc.* **2017**, *139*, 12855-12862.

(40) Arrowsmith, M.; Hadlington, T. J.; Hill, M. S.; Kociok-Köhn, G. Magnesium-Catalysed Hydroboration of Aldehydes and Ketones. *Chem. Commun.* **2012**, *48*, 4567-4569.

(41) Peterson, E.; Khalimon, A. Y.; Simionescu, R.; Kuzmina, L. G.; Howard, J. A.; Nikonov, G. I. Diversity of Catalysis by an Imido-Hydrido Complex of Molybdenum. Mechanism of Carbonyl Hydrosilylation and Silane Alcoholysis. *J. Am. Chem. Soc.* **2009**, *131*, 908-909.

(42) Vijjamarri, S.; Chidara, V. K.; Rousova, J.; Du, G. Dehydrogenative Coupling of Alcohols and Carboxylic Acids with Hydrosilanes Catalyzed by a Salen–Mn (V) Complex. *Catal. Sci. Technol.* **2016**, *6*, 3886-3892.

(43) Keess, S.; Simonneau, A.; Oestreich, M. Direct and Transfer Hydrosilylation Reactions Catalyzed by Fully or Partially Fluorinated Triarylboranes: A Systematic Study. *Organometallics* **2015**, *34*, 790-799.

*Chapter 2 – Comparing the SNS Thiolate and Amido Ligands: Cu(I)-SNS Complexes for Outer-Sphere Hydroboration and Hydrosilylation of Carbonyls*

- (44) Boone, C.; Korobkov, I.; Nikonov, G. I. Unexpected Role of Zinc Hydride in Catalytic Hydrosilylation of Ketones and Nitriles. *ASC. Catal.* **2013**, *3*, 2336-2340.
- (45) APEX 2, Bruker AXS Inc., Madison, Wisconsin, USA, 2012.
- (46) G. M. Sheldrick, SADABS, Program for Empirical Absorption Correction of Area Detector Data, University of Göttingen, Germany, 1996.
- (47) G. M. Sheldrick. SHELXL-Integrated Space-Group and Crystal-Structure Determination *Acta Cryst.* 2015, C71, 3-8.

**Chapter 3 – Comparing Amido Bifunctional Reactivity Across Base Metals and Associated Mechanistic Study of Metal-Ligand Cooperativity in Mn(II) Catalyzed Hydroborations**

**3.1 Introduction**

**3.1.1 Significance of Mn(SNS)<sub>2</sub> catalyst**

Homogeneous transition metal catalysts comprised of expensive heavy metals are proven tools for synthesizing valuable organic synthons.<sup>1-2</sup> The design of highly desirable catalysts based on first-row metals, however, is a priority for sustainable chemical synthesis.<sup>3-7</sup> One challenge in developing catalytic protocols employing base metals is their aversion to undergoing predictable 2e- redox pathways ubiquitous to the second and third row metals.<sup>8-10</sup> Metal-ligand cooperativity (MLC) has emerged as a powerful mechanistic strategy to enable multi-electron transformations across a M–L bond.<sup>11-16</sup> Such actor

ligands that are capable of MLC in conjunction with first-row metals have been demonstrated to facilitate challenging catalytic transformations.<sup>17-20</sup>

The use of manganese complexes in catalysis has flourished over the past five years.<sup>21-23</sup> While Mn catalysts for (de)hydrogenations have been thoroughly explored,<sup>24</sup> increasingly popular alternative reduction strategies<sup>25</sup> involving B–H bond activation remain comparatively underdeveloped. Pioneering reports by Zhang,<sup>26</sup> Gade,<sup>27</sup> and Thomas<sup>28</sup> demonstrated the efficiency of Mn(II) catalysts to facilitate hydroborylative reduction of alkenes and carbonyls. Trovitch has recently reported the dihydroboration of nitriles utilizing a dinuclear Mn(II) catalyst.<sup>29</sup> Alternatively, an MLC approach involving an outer-sphere reaction pathway has also been proven effective. Leitner and co-workers recently reported the Mn-catalyzed hydroboration of CO<sub>2</sub> and carboxamides in the presence of base at elevated temperatures (**Figure 3.1**).<sup>30</sup> This work notably included direct evidence of B–H bond activation across a Mn–N bond, implicating an MLC mechanism akin to established (de)hydrogenation chemistry. Furthermore, Kirchner recently detailed the hydroboration of CO<sub>2</sub> by a Mn(I)-PNP<sup>NH</sup> catalyst in the presence of Lewis acid additives. While control reactions using the N–Me substituted ligand analogue highlighted the importance of the N–H groups, further studies revealed both metal-catalyzed and metal-free processes may be involved.<sup>31</sup> Overall, MLC has rarely been implemented by Mn complexes for reductive transformations employing pinacolborane (HBpin).<sup>32</sup>

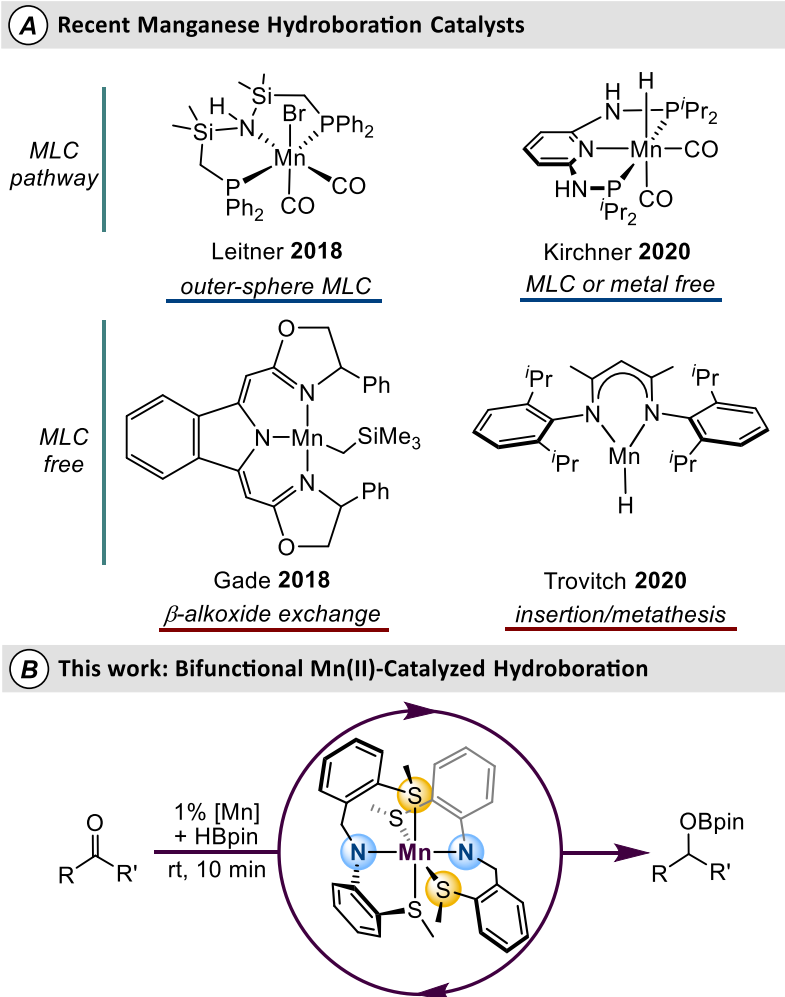


**Figure 3.1.** A) Recently reported Mn catalysts; B) Our current report on Mn-catalyzed hydroboration of carbonyls.

The overwhelming majority of manganese catalysts employ strong  $\sigma$ -donating phosphines to bolster the electrophilic Mn center. There has been recent interest in use of more biomimetic ligand manifolds employing *N,S*-donors to avoid the expense and air instability that often accompany phosphine-based ligands.<sup>33</sup> Khusnutdinova reported a Mn complex bearing a macrocyclic  $N_2S_2$  ligand capable of aromatization/dearomatization,<sup>34</sup> but it was not an active catalyst. The use of weaker field ligands may lead to alternate mechanistic pathways, and there is still much to be studied. Despite advances with Fe,<sup>35-37</sup>

sulfur-based ligands in Mn-catalyzed reductive transformations have been scarcely studied to date.

Finally, over the past decade numerous ligand sets of varying donor combinations (C, N, O, P, S)<sup>36,38-42</sup> and hapticities (classic tridentate pincer *vs.* bi/ tetradentate) have been employed to facilitate these reactions. While the boundaries of ligand design are being continually pushed to expand the catalytic scope of these reaction pathways, there has been less evaluation of how the selected base metal influences the reactivity of these bifunctional ligands. The Szymczak group reported the divergent reactivity of a series of analogous complexes across the first-row (V, Mn, Fe, Co, Zn) for hydrazine capture and N–N bond cleavage.<sup>43 44</sup> They found that while all complexes are capable of capturing hydrazine, subsequent N–N bond reduction does not occur with the Mn and Zn analogues; with Fe and Co being most active. In related work, Kirchner<sup>45</sup> and Mezzetti<sup>46</sup> both contributed to the comparison of isostructural and isoelectronic Mn(I) and Fe(II) bifunctional catalysts for (de)hydrogenations. Finally, a DFT study investigated the barrier for bifunctional H<sub>2</sub> activation with Lewis acid tris(phosphino)borane complexes across the first-row metals.<sup>47</sup> These formative works bring to the forefront the need for further systematic comparison of bifunctional complexes across the base metals. This will offer insight towards the design of catalysts capable of more challenging bond activations (C–H, C–N, N–N).<sup>14,32</sup>

We sought to use biomimetic SNS ligands to design bifunctional catalysts based on first-row metals. Within the realm of these complexes, the significance of the metal character will be explored along with the influence of weak-field thioether S donors on the mechanistic implications of MLC. The efficacy of the S<sup>Me</sup>NS<sup>Me</sup> ligand (**L1**) for catalytic hydroboration has been previously reported.<sup>41</sup> Key design features of the bifunctional **L1**

include the Lewis basic amido donor participating in MLC, and hemilability of the six-membered ring thioether donor to open a coordination site during catalysis.

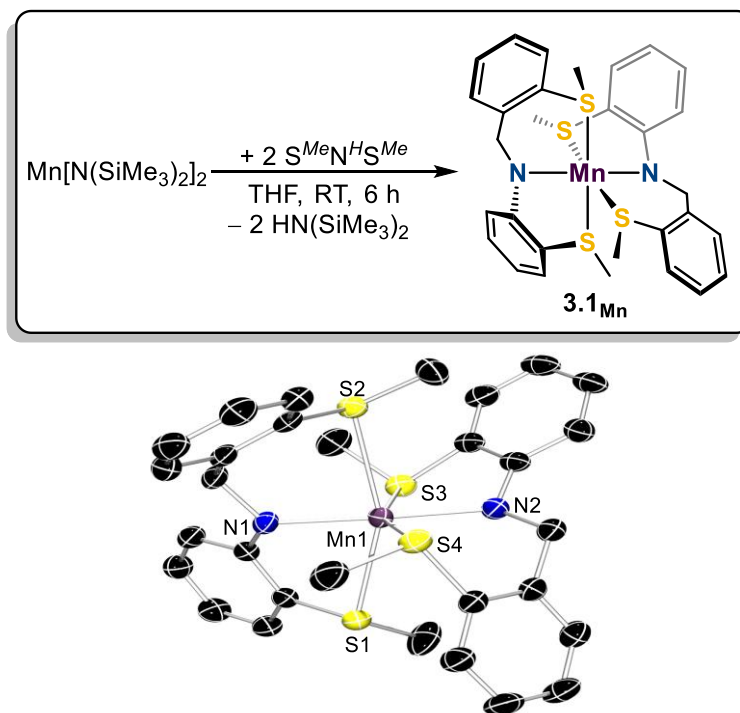
This chapter details the synthesis of a Mn(II) bis-amido complex. Including previous work by the Baker group, this gave a collection of three analogous  $M(S^{Me}NS^{Me})_2$  complexes ( $M = Mn, Fe, Co$ ) and provided a rare opportunity to directly examine identical analogues of bifunctional complexes. These three compounds were evaluated computationally for a bifunctional  $H_2$  activation reaction profile to discern reactivity patterns amongst the metals within our [SNS]-ligand platform. Preceding this work, application of the Mn(II) bis-amido complex as a chemoselective carbonyl hydroboration precatalyst was explored. Thorough experimental and computational mechanistic studies reveal that a traditional Noyori-type outer-sphere reaction pathway is unlikely. Instead, an inner-sphere route involving MLC is proposed, in which both the hemilability and bifunctional nature of **L1** are of critical importance. This proposed mechanism represents a unique product route that we attribute to the nature of our bifunctional SNS ligand framework as opposed to traditional phosphine-based bifunctional pincers.

## **3.2 Results and Discussion**

### **3.2.1 Synthesis of manganese complexes**

To prepare a Mn complex ligated with amido ligand  $[S^{Me}NS^{Me}]$  (**L1**), a THF solution of  $Mn[N(SiMe_3)_2]_2$  was treated with two equiv. of **L1<sup>H</sup>**. Stirring for 6 h afforded light-yellow complex  $Mn(\kappa^3-S^{Me}NS^{Me})_2$  (**3.1<sub>Mn</sub>**) in 90% yield (**Scheme 3.1**).  $^1H$  NMR analysis revealed a range of signals from  $\delta$  +30 to -15 (Fig. S1), and magnetic susceptibility measurements using the Evans method yielded a value of  $\mu_{obs} = 6.0$  BM. This is consistent

with a high-spin Mn(II)-d<sup>5</sup> center in an octahedral geometry featuring 5 unpaired electrons. The room temperature isotropic EPR spectrum showed a sextet at  $g = 2.01$  with Mn hyperfine coupling of 70 G (Fig. S2). Furthermore, the anisotropic 100 K EPR spectrum of **1** shows a complex array of signals ranging from  $g = 5.00$  to 1.56, several of which display Mn hyperfine coupling (Fig. S3). This is consistent with a symmetric environment about Mn(II) in a high-spin  $S = 5/2$  ground state.<sup>48</sup> Density functional theory (DFT) calculations further support the ground state assignment, confirming that the high-spin configuration is 42.4 kcal/mol lower in energy than the low-spin doublet. Recrystallization of **3.1Mn** from THF at  $-35$  °C afforded single crystals suitable for X-ray diffraction. Analysis of the solid-state structure (**Scheme 3.1**) confirms a pseudo-octahedral coordination environment about Mn featuring two meridionally bound **L** ligands. The *trans* Mn–N<sub>amido</sub> bond lengths [2.099(2), 2.112(2) Å] are similar to those in previously reported Mn(II) complexes.<sup>49</sup> The Mn–S<sup>Me</sup> bond lengths in the six-membered metallacycle rings [2.734(9), 2.682(8) Å] are longer than those of the 5-membered rings [2.624(9), 2.647(8) Å]. Interestingly, only one of the Mn–S<sup>Me</sup> bond lengths is significantly longer [2.734(9) Å], suggesting potential lability in the solution phase. DFT calculations revealed that the 5-coordinate [Mn( $\kappa^3$ -S<sup>Me</sup>NS<sup>Me</sup>)( $\kappa^2$ -S<sup>Me</sup>NS<sup>Me</sup>)] complex is only 4.0 kcal/mol higher in free energy than **3.1Mn**, suggesting that it should be accessible in the solution phase as determined previously for the Fe analogue.<sup>50</sup>



**Scheme 3.1.** Synthesis and ORTEP depiction of **3.1<sub>Mn</sub>** with thermal ellipsoids shown at 50%. H atoms are omitted for clarity. Selected bond lengths (Å): Mn(1)–S(1) 2.624(9), Mn(1)–S(2) 2.734(9), Mn(1)–S(3) 2.647(8), Mn(1)–S(4) 2.682(8), Mn(1)–N(1) 2.099(2), Mn(1)–N(2) 2.112(2).

### 3.2.2 A computational comparison of bifunctional potential across Mn, Fe, and Co

Previously in the Baker group, analogous complexes to **3.1<sub>Mn</sub>** were synthesized with both iron and cobalt (**3.1<sub>Fe</sub>** and **3.1<sub>Co</sub>**). We began our comparative investigation by first determining the potential ground state of these divalent complexes. All calculations were carried out with the M06L functional and geometry optimization and frequency calculations were performed with the def2-SVP basis set.<sup>51-52</sup> Energies of the optimized structures were re-evaluated by additional single-point calculations on each optimized geometry using the triple- $\zeta$  basis set def2-TZVP with solvation energies in THF accounted

for using the self-consistent reaction field (SCRF) approach.<sup>53</sup> It was found that complexes **3.1Mn**, **3.1Fe**, and **3.1Co** display respectively a sextet, quintet, and quartet ground state, preferentially adopting a high-spin configuration. This is attributed to the presence of the ‘hard’ amido donors and four weak-field thioether donors around the metal center. Solution state magnetic measurements using Evans’s method gave values of  $\mu_B = 6.0, 4.9,$  and  $3.8$  for **3.1Mn**, **3.1Fe**, and **3.1Co**, respectively, corroborating the ground states assigned by DFT. The metrical parameters of the DFT optimized structures match well with experimental bond lengths from single-crystal X-ray diffraction (SCXRD) experiments (**Figure 3.2A** and Tables S3-S5 in ESI†). A definite contraction of the M–N bonds is seen moving from Mn to Co, with an average decrease across both metal-amido bonds of 0.083 and 0.053 Å from Mn to Fe, and Fe to Co, respectively. Furthermore, the relative orientation of the meridional **L** ligands around the metal center also changes in the solid-state,<sup>54</sup> both **3.1Mn** and **3.1Fe** display unsymmetrical **L1** coordination, while **3.1Co** exhibits pseudo  $C_2$  symmetry.<sup>55</sup>

The optimized geometries were used to evaluate molecular orbital (MO) character and frontier molecular orbitals (FMO) (Figures S11-S13 in ESI†). The calculated HOMO-LUMO gaps for the three complexes are 2.74, 3.03, and 2.99 eV for **3.1Mn**, **3.1Fe**, and **3.1Co**, respectively. While the LUMO is highly delocalized across the ligand aromatic system for all three complexes, there is divergence in the HOMOs (**Figure 3.2B**). The HOMO of **3.1Mn** is distributed amongst both amido donors and their respective aromatic framework, as well as the Mn center. That of **3.1Fe**, is nearly exclusively based on the Fe center while the HOMO of symmetric **3.1Co** is distributed amongst the metal and both amido nitrogens.

### 3.2.2.1 Fukui indices and Hirshfeld charges

Fukui indices were calculated to assess the three bis(amido) complexes for bifunctional reactivity as a function of amido of frustrated Lewis pairs<sup>56-57</sup> (Tables B11-B13 in Appendix B). While the differences in Fukui indices are small (**Table 3.1**), there is an upward trend in the amido nucleophilicity moving from Mn to Co. In contrast, a non-monotonic trend is found for the electrophilicity, with Fe being the most electrophilic. Alternatively, Hirshfeld charges can also be used to quantify nucleophilicity/electrophilicity.<sup>58</sup> The calculated values (**Table 3.1**) offer more numerical contrast between the three complexes and are also in opposition to the trends suggested by the Fukui indices (Tables B8-B10 in Appendix B). While Fe remains the most electrophilic, the Hirshfeld charges suggest that Mn–N<sub>amido</sub> donors are the most nucleophilic, as opposed to Co–N<sub>amido</sub>.

### 3.2.2.1 Reaction profile of a bifunctional H<sub>2</sub> activation

To learn which parameter more accurately predicts reactivity trends in our system, the potential energy surface of a simple outer-sphere H–H activation across the M–N<sub>amido</sub> bond was evaluated for the three ML<sub>2</sub> complexes (**Figure 3.3**). The first step is dissociation of one of the hemilabile thioether donors of the 6-membered ring to yield a 5-coordinate species (**M2**) with a vacant coordination site for substrate activation. Previous work with **3.1Mn** and **3.1Fe** has established the validity of these proposed species,<sup>50,59</sup> and the energies for the three 5-coordinate species (**M2**) are nearly isoenergetic, ranging from 5-7 kcal/mol above their 6-coordinate precursors. Direct interaction of H<sub>2</sub> with the M–N bond of the κ<sup>3</sup>-[S<sup>Me</sup>NS<sup>Me</sup>] ligand forms **M3**, similar to previous work by Morris.<sup>60</sup> It should be noted that attempts to calculate a dihydrogen intermediate resulted in optimization towards the **M3**

species. The energies diverge here, with Fe being most exergonic at -8.2 kcal/mol, followed by Co and Mn at -4.2 and -0.5 kcal/mol, respectively. While heterolytic H–H cleavage through **M3-TS** shows the Fe pathway as the lowest energy TS, it is in fact the Mn pathway that has the lowest activation barrier at 17.2 kcal/mol, followed by Fe and Co with barriers of 21.5 and 29.9 kcal/mol, respectively. Upon arriving at the final metal-hydride species **M4**, the energies realign, with the final Mn product being lowest in energy. As tested by single-point energy evaluations based on the M06-L geometries, these reactivity trends are faithfully reproduced by a wide range of functionals (Figures B37-B42 in Appendix B).

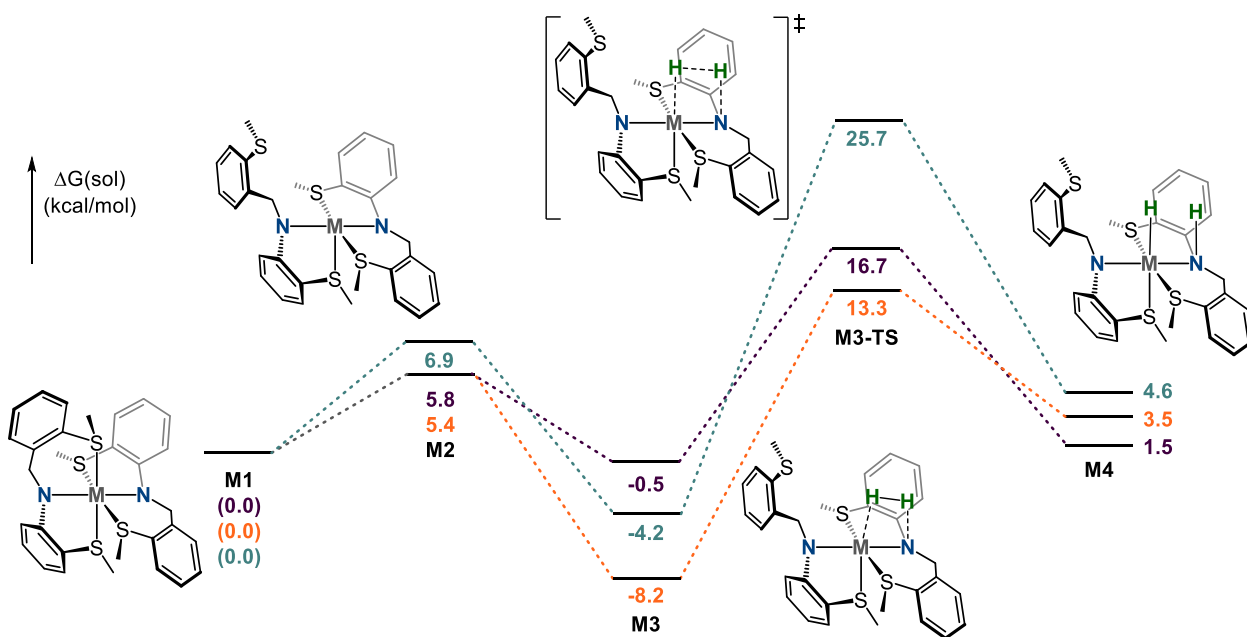


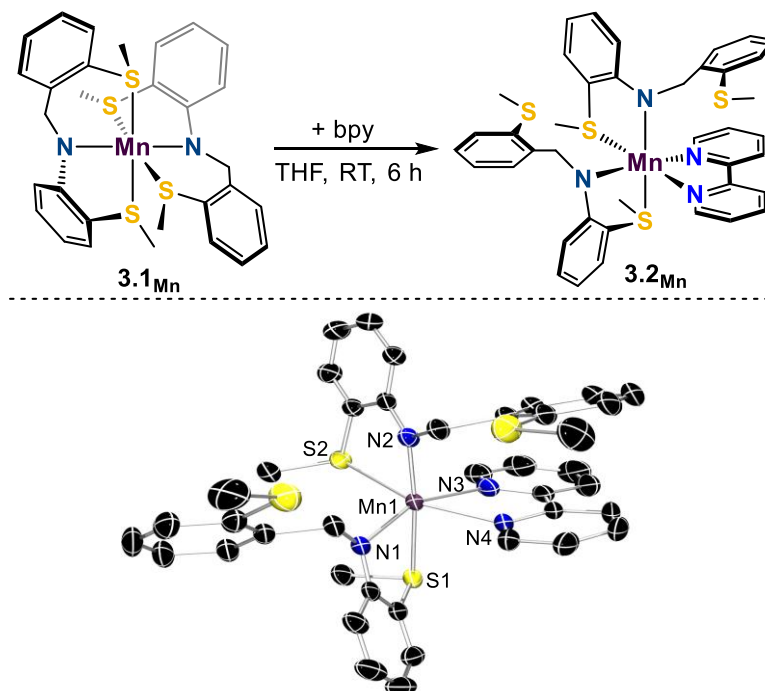
**Figure 3.2.** Energy reaction profile for H<sub>2</sub> activation across M–N<sub>amido</sub> bond in **3.1<sub>Mn</sub>** (purple), **3.1<sub>Fe</sub>** (orange), and **3.1<sub>Co</sub>** (teal).

Contextually, the Hirshfeld charges which predicted the Mn–N<sub>amido</sub> as the most nucleophilic may provide a more accurate theoretical depiction for predicting reactivity than the Fukui indices. The calculated DFT reaction profile indicates that bifunctional addition of H<sub>2</sub> to all three complexes is energetically accessible, but it is **3.1<sub>Mn</sub>**, which has

the most nucleophilic amido, that proceeds through the lowest energy barrier. This is followed by **3.1<sub>Fe</sub>** which has the second highest amido nucleophilicity, and also most electrophilic metal. While this may initially indicate that amido nucleophilicity is a more significant factor, it should be noted that Mn is nearly as electrophilic as Fe (0.230 and 0.245 respectively), while the respective amido donors exhibit a greater difference in nucleophilicity (-0.199 and -0.179). This suggests that optimizing a careful balance of these two properties – a nucleophilic Lewis base to accept a proton and an electrophilic metal to accept a hydride – is required to provide the lowest energy barrier pathway. This suggests that **3.1<sub>Mn</sub>** will be the best performing and long-lasting catalyst in related reductive transformations.

### **3.2.3 Exploring potential hemilability**

A key design feature of **L1** is that it allows both five- and six-membered ring formation upon coordination to a metal center. Further demonstration of the hemilability of the six-membered ring thioether was provided by reaction of **3.1<sub>Mn</sub>** with one equiv. of 2,2'-bipyridine (bpy) that furnished red crystals of  $[\text{Mn}(\kappa^2\text{-S}^{\text{Me}}\text{NS}^{\text{Me}})_2(\text{bpy})]$  (**3.1<sub>Mn</sub>**) in 94 % yield. The solid-state structure of **3.2<sub>Mn</sub>** (**Scheme 3.2**) includes two  $[\kappa^2\text{-S}^{\text{Me}}\text{NS}^{\text{Me}}]$  amido ligands with *cis* N donors and a  $\kappa^2$ -bipyridine in a distorted octahedral geometry about Mn. Interestingly, the Mn–S bond lengths of the five-membered ring (2.7290 and 2.7070 Å) in **2** are longer than the associated bonds in **1** (2.624 and 2.647 Å) and even that in one of the 6-membered thioether-ligated rings (2.682 Å). Furthermore, the Mn–N bond lengths of the bpy ligand are much longer (2.3141 and 2.660 Å) in comparison to similarly reported complexes.<sup>61-62</sup>



**Scheme 3.2.** Synthesis and ORTEP depiction of **3.2<sub>Mn</sub>** with thermal ellipsoids shown at 50%. H atoms are omitted for clarity. Selected bond lengths (Å): Mn(1)–S(1) 2.7290(5), Mn(1)–S(2) 2.7070(5), Mn(1)–N(1) 2.1227(14), Mn(1)–N(2) 2.1135(15), Mn(1)–N(3) 2.3141(15), Mn(1)–N(4) 2.660(14).

### 3.2.4 Hydroboration catalysis

Previous work with base-metal complexes featuring **L1** demonstrated its high affinity for E–H bond activation.<sup>41</sup> To probe the catalytic activity of Mn(II) complex **3.1<sub>Mn</sub>**, we investigated its efficacy for carbonyl hydroboration (**Figure 3.3**). Addition of benzaldehyde and HBpin to a yellow benzene-d<sup>6</sup> solution of 1 mol% **3.1<sub>Mn</sub>** resulted in an immediate decolorization, furnishing complete conversion to hydroboration product in 5 min. Lowering the catalyst loading to 0.1 mol% did not reduce activity, with full conversion being observed within 5 min, giving attributable TOF of 200 min<sup>-1</sup>. Analogous

reaction conditions with acetophenone yielded identical results. Precatalyst **3.1Mn** was found to be extremely efficient in reducing carbonyls featuring electron-donating and electron-withdrawing groups in sterically compromising positions within 5-20 min (entries i-iv and vi-x). Aliphatic substrates (entries v, xi), as well as ketones featuring bulky R groups (entry vii) also reached full conversion in less than 15 min. To probe whether binding of the alkene was taking place during catalysis, substrates featuring internal and terminal alkenes were tested (entries iv, xi). No isomerization products were observed, indicating that alkene binding followed by insertion into a Mn–H does not occur along the reaction pathway. Furthermore, a substrate possessing only an alkene moiety, 4-methoxystyrene, did not undergo hydroboration.

A competition study was performed by reaction of stoichiometric HBpin, benzaldehyde, and acetophenone with 0.1 mol% of **3.1Mn**. Total consumption of HBpin was observed after 10 min with selective formation of the aldehyde hydroboration product. Carbonyl reductions could also be performed with triethoxysilane and 1 mol% **3.1Mn**, albeit with gentle heating at 40 °C. Finally, we attempted to perform hydroboration of esters to test the capabilities of **3.1Mn** with a more complicated functionality. A solution of benzyl benzoate and 2 equiv. of HBpin in a C<sub>6</sub>D<sub>6</sub> solution of 1 mol% **3.1Mn** was heated at 60 °C for 16 h, resulting in 60% conversion to the borylation product. Monitoring the reaction for longer periods did not lead to further conversion, and attempting to run the reaction at 80 and 100 °C resulted in catalyst death.

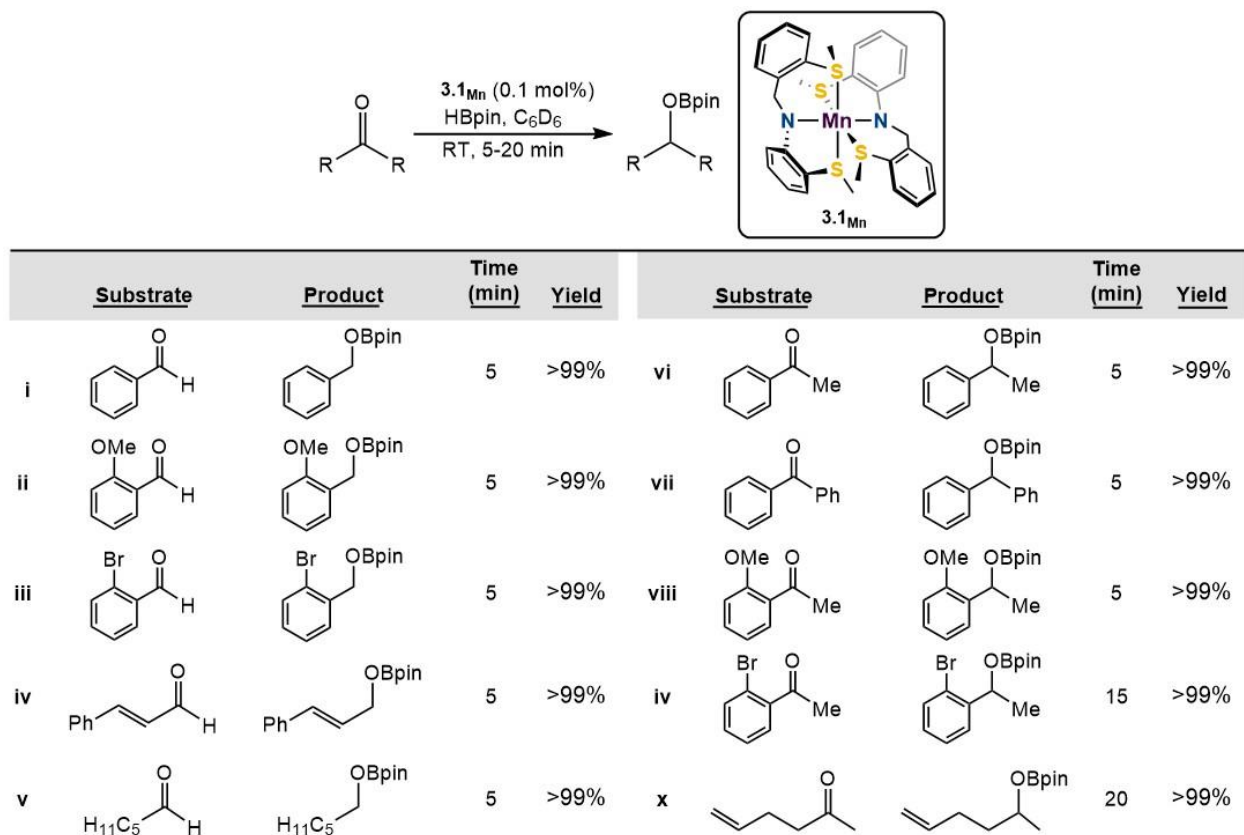


**Figure 3.3.** Substrate scope of catalytic hydroboration of carbonyls with **3.1Mn**. Reaction conditions: pinacolborane (0.16 mmol), carbonyl (0.16 mmol), benzene (0.6 g), and **3.1Mn** (0.1 mol%) at room temperature for 5-10 min. Yields were determined from  $^1\text{H}$  NMR integrals relative to mesitylene internal standard after workup.

### 3.2.5 Variable time normalization analysis of kinetic data

Previous work on a related iron-based hydroboration catalyst showed an unusual rate dependence on the concentration of HBpin.<sup>63</sup> Thus, kinetic studies to discern reactant orders in the rate law were performed by monitoring reactions using  $^{11}\text{B}$  NMR spectroscopy. The data were analyzed graphically utilizing variable time normalization analysis (VTNA).<sup>64-65</sup> Due to the rapid reactivity of this system, more slowly reacting 5-hexen-2-one was selected as the substrate for study. VTNA identified the rate law,  $\text{rate} = k[\mathbf{3.1Mn}][\text{carbonyl}][\text{HBpin}]$ , in which the rate dependence on  $[\mathbf{3.1Mn}]$ ,  $[5\text{-hexen-2-one}]$ , and

[HBpin] were all reliably first order (**Figure 3.4**). Plotting  $[C_6H_{11}OBpin]$  vs. the normalized rate components utilizing VTNA gave  $k_{obs} = 1.8 \text{ mM}^{-2}\text{s}^{-1}$ . The kinetic analysis indicates that there are no unusual steps or side reactions throughout the reaction pathway.

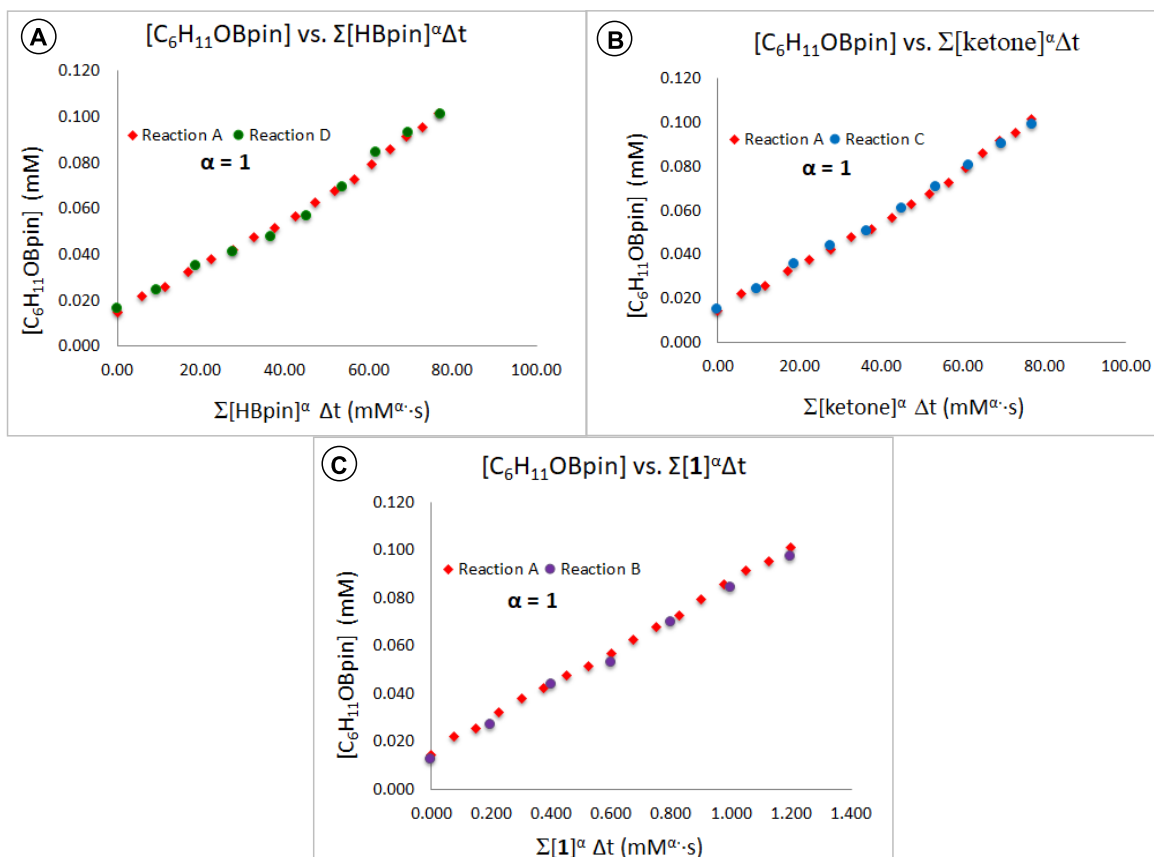


**Figure 3.4.** VTNA of the kinetics data: (A) rate dependence on  $[3.1Mn]$ ; (B) rate dependence on [5-hexene-2-one]; (C) rate dependence on [HBpin].

### 3.2.6 Mechanistic studies of Mn(II)-catalyzed hydroboration

#### 3.2.6.1 Experimental mechanistic studies

To more closely investigate the reaction pathway and obtain information about the active form of the catalyst, one equiv. of 5-hexene-2-one was added to a benzene- $d_6$  solution

of **3.1<sub>Mn</sub>**; however, no color change was observed and analysis of the <sup>1</sup>H NMR spectrum showed no reaction. Addition of one equiv of HBpin to this reaction mixture initiated hydroboration, indicating that **3.1<sub>Mn</sub>** does not react directly with either C=C, or C=O substrates, and instead requires an activation step involving reaction with HBpin. Consequently, one equiv. of HBpin was added to a benzene-*d*<sub>6</sub> solution of **3.1<sub>Mn</sub>**, resulting in an immediate color change from light-yellow to a dark brown-yellow. The <sup>11</sup>B NMR spectrum showed complete consumption of HBpin and the appearance of a new broad signal at 24.1 ppm, indicative of a B–N containing species (Fig. S28). Furthermore, the 100 K EPR spectrum of the reaction mixture showed a large broad signal at *g* = 2.09 and the loss of all Mn hyperfine coupling observed in the anisotropic spectrum of **3.1<sub>Mn</sub>** (Fig. S29). The spectroscopic data support the formation of a new species, explicitly indicating the loss of the high-symmetry environment about Mn, which likely remains high-spin Mn(II) due to observation of a small EPR signal at *g* = 5.03. Addition of 5-hexen-2-one to this reaction mixture furnished the hydroboration product, confirming this species as a reactive intermediate.<sup>b</sup> Furthermore, reaction of **1** with two equiv. of HBpin yielded the same signal in the <sup>11</sup>B NMR spectrum, along with one equiv. of unreacted HBpin, suggesting that only one **L1** is involved in the B–H activation step. Multiple attempts to scale up the stoichiometric reaction of **3.1<sub>Mn</sub>** and HBpin to isolate and characterize this paramagnetic intermediate proved unsuccessful. Finally, the reaction mixture was also investigated by UV-vis and cyclic voltammetry, neither of which revealed helpful insight.

---

<sup>b</sup> It should be noted that EPR data were not integrated, and the resulting signals may not be representative of the bulk sample.

Due to the difficulties in spectroscopically studying catalytic systems employing paramagnetic transition-metal complexes, we turned to electrospray ionization (ESI) mass spectrometry to identify potential intermediates. Exploiting a quadrupole time-of-flight (QTOF) mass spectrometer in conjunction with collision-induced dissociation (CID) allowed us to pinpoint fragments of interest observed during the full scan of reaction mixtures. Initially, running a full scan ESI run in positive mode on a solution of stoichiometric **1** and HBpin revealed a diagnostic peak. A fragment at  $m/z$  403 in the ESI run was assigned as protonated ( $\mathbf{L1}^{\text{HBpin}}\text{H}^+$ ) resulting from coordination of HBpin to the amido-*N* donor. This was supported by CID focused on the  $m/z$  403 peak which resulted in observation of several ( $\mathbf{L1}^{\text{HBpin}}\text{H}^+$ ) fragmentation products. Furthermore, an ESI run of a solution containing free  $\mathbf{L1}^{\text{H}}$  and HBpin did not give rise to the same signal, supporting that this fragment is not formed during ionization. Unfortunately, no Mn-containing fragments were observed, even when using milder ionization techniques, or with added NaBPh<sub>4</sub> to try to sequester any neutral Mn-fragments. Finally, high-resolution electron-impact mass spectrometry of a crude solid sample of the reaction mixture revealed a peak at 401.2 from the ( $\mathbf{L1}^{\text{Bpin}}\text{H}^+$ ) cation, likely a consequence of internal hydride transfer to Mn during ionization (**Figure 3.5**).

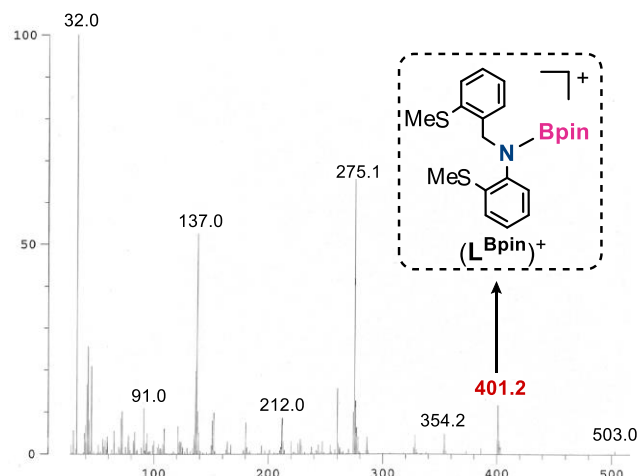


**Figure 3.5.** EI-MS spectrum of crude reaction mixture of **3.1<sub>Mn</sub>** and pinacolborane showing observation of  $L^{Bpin}$ .

The presence of  $L^{Bpin}$  implicates a possible reaction pathway whereby initial reaction of HBpin with **1** forms free  $L^{Bpin}$  and  $Mn(L)(H)$ , which may be the active state of the catalyst. To investigate the validity of this pathway, a reaction mixture of catalytic **3.1<sub>Mn</sub>** with stoichiometric HBpin and 5-hexen-2-one was prepared and instantly charged with catalytic bpy. Upon addition of bpy, no color change or change in reaction rate was observed. Additionally, monitoring by UV-vis showed no clear change of speciation, indicating that bpy likely does not bind to the metal due to lack of coordination sites. Furthermore, since complex **3.2<sub>Mn</sub>** was found to affect catalysis, the stoichiometric reaction of **3.2<sub>Mn</sub>** with HBpin was performed. This resulted in bpy dissociation from the Mn, as evidenced by precipitation of free bpy, and indicates that when **3.2<sub>Mn</sub>** is under catalytic conditions, bpy dissociates forming **3.1<sub>Mn</sub>** in solution, which immediately reacts with HBpin and enters the reaction cycle. These results suggest that  $L^{Bpin}$  remains bound to Mn and that reaction intermediates contain both **L1** and  $L^{Bpin}$  ligands coordinated to Mn.

### 3.2.3.2 Computational mechanistic studies

With the inherent difficulty of observing and characterizing the paramagnetic species, mechanistic studies via DFT calculations were performed at the B3LYP-D3/6-31G\*\*/LACVP//cc-pVTZ(-f)//LAV3P level of theory<sup>55,66-72</sup> with a self-consistent reaction field ( $\epsilon = 2.284$  for benzene) approach for solvation.<sup>53</sup> The substrate 5-hexen-2-one which bears both carbonyl and olefin moieties was employed as the model substrate. The intermediates and key transition states are summarized in **Figure 3.6**. Initially, a mechanism with a Mn–H intermediate, typically assumed to be involved in similar reaction systems, was examined.<sup>12,13,16</sup> The mechanism involving MLC previously proposed by Leitner was investigated, whereby B–H activation across the Mn–N forms a 4-membered Mn–H–B–N metallacycle that evolves to a Mn–H intermediate.<sup>13</sup> Although the formation of a Mn–H species can be achieved with a barrier of 22.7 kcal/mol, the reaction is quite endergonic with the metal hydride intermediate **A5** located at 17.1 kcal/mol.

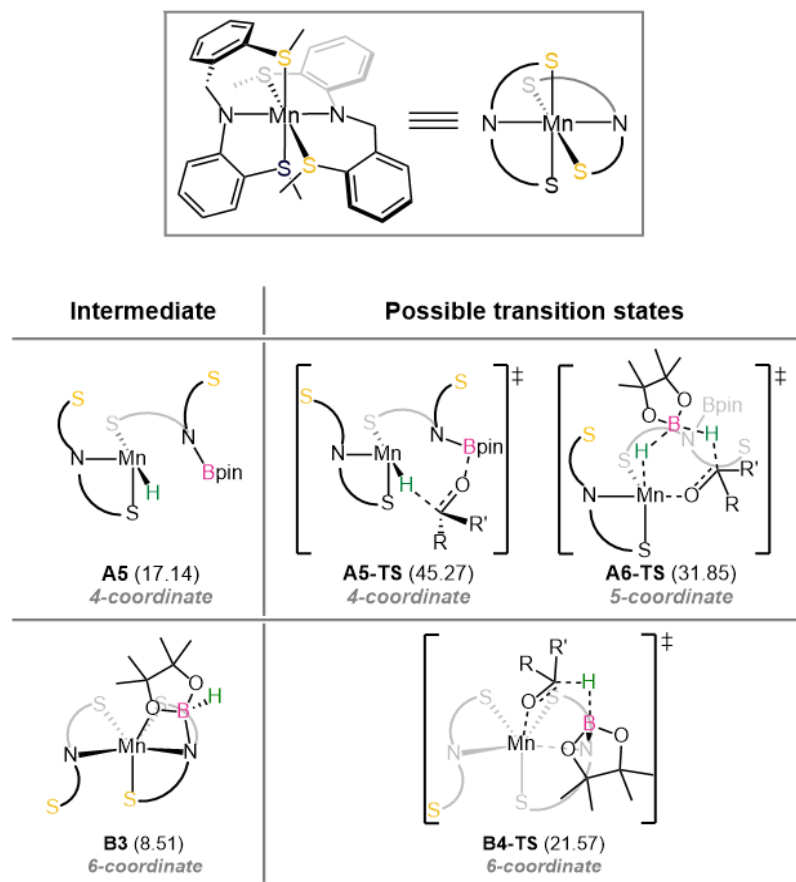


**Figure 3.6.** Comparison of key reaction steps and transition states of possible mechanisms. Gibbs free energies in kcal/mol are given in parenthesis.

Consequently, the subsequent hydroboration steps require a high activation energy. A Noyori-type transition state lacking direct coordination of the carbonyl to Mn (**A5-TS**) has an overall barrier of 45.3 kcal/mol. Alternatively, a pathway akin to previous work by Gade featuring intake of an additional HBpin and direct coordination of the carbonyl to the metal center (**A6-TS**) shows a barrier of 31.8 kcal/mol, making both mechanisms traversing the Mn–H species unlikely at room temperature. Further details of these pathways are given in the SI (Fig. S41 and S42).

The instability of the Mn–H species is expected to originate from the weak coordination environment at Mn. Activation of the B–H bond and formation of a new N–B bond changes the amido nitrogen to an amine, significantly decreasing its donor power. Intermediate **A5** with a coordination number of 4 has an overall electron count of only 13. The following transition states are also unsaturated, and additional coordination is hindered due to steric reasons. Thus, an alternative pathway which retains higher coordination numbers was found to be much more reasonable.

The proposed mechanism depicted in **Figure 3.7** begins with dissociation of the hemilabile S<sup>Me</sup> moiety from the Mn center, enabling ligand rearrangement to form a 5-coordinate Mn complex **B2** with a vacant coordination site, allowing for coordination of the Bpin oxygen in intermediate **B3**, featuring a four-membered Mn–O–B–N metallacycle. This intermediate has 6-coordinate geometry with a formal electron count of 17, and is 8.6 kcal/mol more stable than Mn–H intermediate **A5**. Intermediate **B3** also accounts for the mass spectrometric data featuring the L<sup>HBpin</sup> ligand and the observed <sup>11</sup>B NMR resonance. The carbonyl oxygen lone pair coordinates to Mn in **B4**, followed by a hydride transfer step **B4-TS** which retains the 6-coordinate geometry. This step is anticipated to be turnover-determining with an overall barrier of 21.6 kcal/mol.

Rate-determining hydride transfer also corroborates the observed selectivity of aldehyde over ketone, as the aldehyde carbon is more susceptible to hydride transfer due to the lack of an electron-donating moiety. Hydride transfer is highly exergonic with the Mn–alkoxy product at –1.0 kcal/mol. The alkoxy ligand is then transferred to the Bpin in **B5-TS** to form the hydroborated product. The product is sequentially released from the catalyst,

traversing transition state **B6-TS** with a low step barrier of 9.4 kcal/mol, and finally regenerating catalyst **3.1<sub>Mn</sub>** with an overall thermodynamic gain of 20.3 kcal/mol. These calculations highlight that the thioether is crucial to the rearrangement and stabilization of initial intermediates. Furthermore, the observed chemoselective carbonyl hydroboration in the presence of an intermolecular olefin moiety originates from the necessity of carbonyl coordination to Mn prior to hydride transfer. Due to steric congestion around the vacant coordination site, the Mn center favors  $\eta^1$  coordination of the oxygen lone pair compared to  $\eta^2$  coordination of the olefinic  $\pi$ -bond.<sup>c</sup>

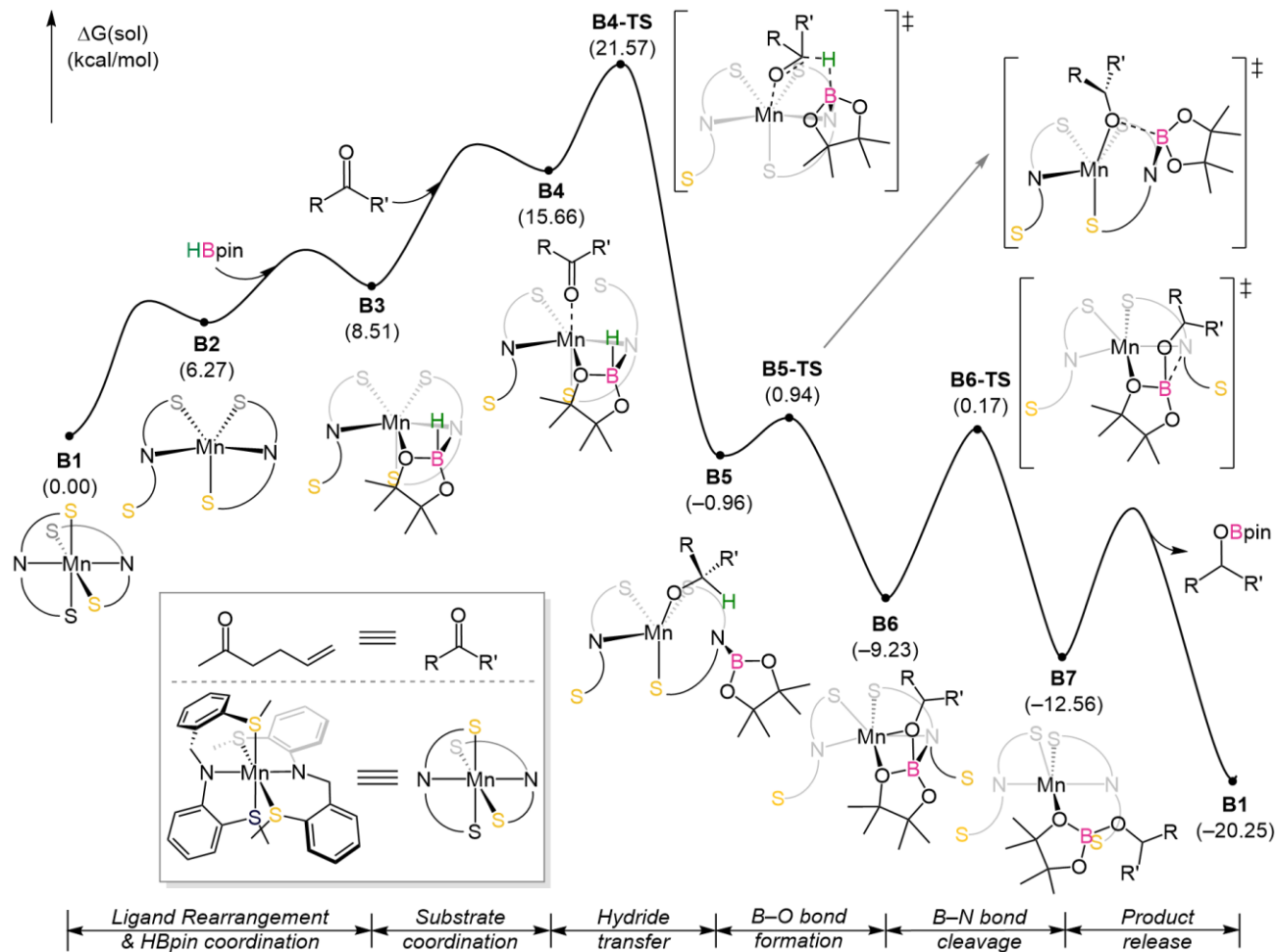
---

<sup>c</sup> It should be noted that the proposed reaction pathway proposed by DFT calculations matches with the rate law and dependencies obtained from kinetic studies using Variable Time Normalization Analysis.

Figure 3.7. Proposed energy profile for  $3.1_{Mn}$ -catalyzed carbonyl hydroboration.

### 3.3 Conclusions

Divalent  $Mn(S^{Me}NS^{Me})_2$  ( $3.1_{Mn}$ ) was prepared and characterized to study its potential for bifunctional catalysis. The Mn(II) complex was found to be an efficient and chemoselective catalyst for room-temperature carbonyl hydroboration, giving full conversion in 20 min or less with 0.1 mol% loading. Kinetic studies using VTNA revealed no unusual reaction steps, and thorough mechanistic studies were performed to investigate the reaction pathway facilitated by this paramagnetic species. Mass spectroscopy



experiments uncovered the formation of borylated amido ligand ( $L1^{HBpin}$ ), supporting that

the bifunctional nature of **L1** is crucial to the reaction. Detailed DFT calculations ruled out a traditional MLC mechanism involving a Noyori-type outer-sphere transition state (Mechanism A; **Figure 3.8**). Instead, a unique inner-sphere mechanism highlighted by cooperativity stabilizing a 4-membered Mn–O–B–N metallacycle allowing for hydride transfer to coordinated carbonyl was found to be the energetically preferred reaction route (Mechanism C; **Figure 3.8**). Hemilability of the six-membered ring  $S^{Me}$  donor was found to be integral to stabilization of early reaction intermediates, allowing the Mn center to maintain an octahedral 17 e- state.

As discussed earlier, the most common MLC mechanism for reduction of carbonyls/alkenes involves an outer-sphere 6-membered transition state, whereby there is no substrate-metal interaction (Mechanism A; **Figure 3.8**). Although a stepwise pathway must be considered,<sup>73</sup> this outer-sphere mechanism is the most frequently reported for bifunctional (de)hydrogenation of carbonyls<sup>24</sup> and has also been proposed by Leitner for bifunctional Mn-catalyzed CO<sub>2</sub> hydroboration.<sup>30</sup>

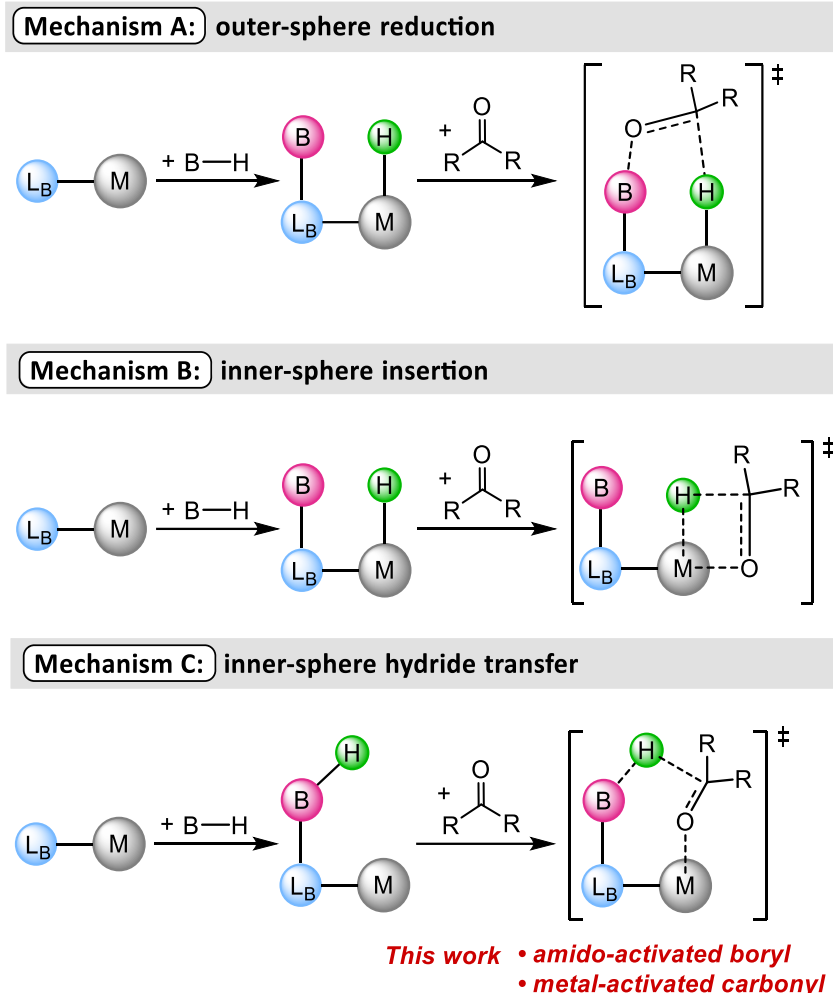


**Figure 3.8** Classification of mechanisms for bifunctional hydroboration of carbonyls.

Alternatively, the other common mechanism proceeds via an inner-sphere insertion of the unsaturated organic (C=O, C=C) into M–H (Mechanism B; **Figure 3.8**). The Wang group proposed this pathway for a Co-catalyzed alkene hydroboration reaction.<sup>74</sup> While different, both of these mechanisms rely on a M–H species generated via metal-ligand cooperative bond activation. In contrast, the divalent Mn bis(amido) catalyst described herein is proposed to operate along a metal hydride-free, inner-sphere bifunctional pathway. Instead of forming M–H that can undergo mechanisms A or B, this reaction uses the nature of the HBpin reagent to effect an alternative amido-assisted B–H bond activation

reminiscent of base-promoted transmetallation from boronic esters in the Suzuki-Miyaura reaction.<sup>75-77</sup> Thus, in our unique *trifunctional* catalyst example, one of the **L1** ligands activated the B–H bond via amido coordination to B, while the second **L1** employs its hemilabile thioether, associated with the six-membered ring, to create a vacant site for carbonyl substrate activation by coordination to the electrophilic Mn(II) center. As the number of reports of first-row metal complex-catalyzed reductive transformations grow, recent work such as that on Fe-catalyzed hydrosilylation by Tilley<sup>78</sup> highlights the need for further detailed mechanistic studies.

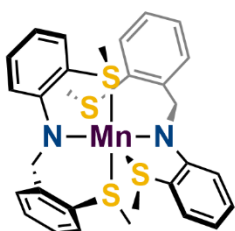
### **3.4 Experimental**

#### **3.4.1 Materials and methods**

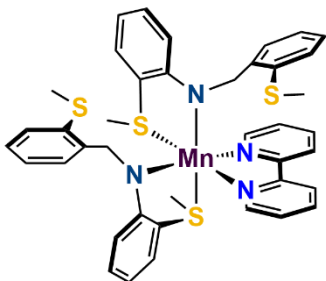
Unless otherwise stated, all reactions were carried out under an atmosphere of dry oxygen-free dinitrogen by means of standard Schlenk or glovebox techniques. Benzene-*d*<sub>6</sub> was degassed by three freeze-pump-thaw cycles, and subsequently dried by running through a column of activated alumina. Toluene, hexanes, and THF were dried on columns of activated alumina using a J. C. Meyer (formerly Glass Contour) solvent purification system and stored over activated 4 Å molecular sieves. <sup>1</sup>H and <sup>11</sup>B NMR spectra were recorded on either a Bruker Avance or AvanceII spectrometer operating at 300 MHz with respect to proton nuclei. <sup>1</sup>H NMR spectra were referenced to residual protons (C<sub>6</sub>D<sub>6</sub>, δ 7.15) with respect to tetramethylsilane at δ 0.00. EPR spectra were recorded on a Bruker Elexsys E580 X-band spectrometer equipped with nitrogen gas temperature control system. UV-vis spectra were collected on an Agilent Cary 7000 Universal Measurement spectrophotometer in dry THF using a screw-capped quartz cuvette (1.0 cm path length). Cyclic voltammetry

data were collected using a VeraSTAT 3 potentiostat and performed under a nitrogen atmosphere in a sealed one-compartment, three-electrode electrochemical cell (glassy carbon working, Pt wire auxiliary, and Ag wire reference electrodes). Tetrabutylammonium tetrafluoroborate in anhydrous THF was used as supporting electrolyte (0.1 M). All potentials are referenced to internal standard redox potential of Fc/Fc<sup>+</sup> (Fc = ferrocene). All reagents were purchased from commercial suppliers. The compounds Mn[N(SiMe<sub>3</sub>)<sub>2</sub>]<sub>2</sub><sup>79</sup> and [S<sup>Me</sup>N<sup>H</sup>S<sup>Me</sup>] (**L1<sup>H</sup>**)<sup>50</sup> were synthesized according to literature procedures.

### 3.4.2 Synthesis and characterization of manganese complexes



**Synthesis of Mn( $\kappa^3$ -S<sup>Me</sup>NS<sup>Me</sup>)<sub>2</sub> (**3.1<sub>Mn</sub>**).** Mn[N(SiMe<sub>3</sub>)<sub>2</sub>]<sub>2</sub> (0.150 g, 0.400 mmol) was dissolved in 3 mL of hexane and stirred for ca. 5 min in a vial. A solution of [S<sup>Me</sup>N<sup>H</sup>S<sup>Me</sup>] (0.218 g, 0.800 mmol, 2 equiv) in 3 mL of hexanes was added dropwise to the reaction mixture resulting in an immediate color change to dark yellow. The solution was stirred at room temperature for 6 h, affording a yellow precipitate. The reaction mixture was filtered through a glass frit and the collected precipitate was washed with hexanes (3 x 2 mL) and dried under vacuum to give 0.219 g of a light-yellow powder (90% yield). Crystals suitable for X-ray diffraction were grown from a concentrated THF solution at -35 °C. <sup>1</sup>H NMR (C<sub>6</sub>D<sub>6</sub>, 23 °C, 300 MHz; Fig. S1):  $\delta$  -1.75 (br s,  $\Delta\nu_{1/2}$  = 754 Hz); 0.01 (br s); 1.44 (br s); 1.99 (br s); 3.64 (br s,  $\Delta\nu_{1/2}$  = 132 Hz); 4.29 (br s); 5.45 (br s); 6.59 (br s); 9.98 (br s,  $\Delta\nu_{1/2}$  = 320 Hz); 25.5 (br s,  $\Delta\nu_{1/2}$  = 1235 Hz). Magnetic susceptibility (Evans method in C<sub>6</sub>D<sub>6</sub>, 25 °C):  $\mu_B$  = 6.0 BM. HRMS (ESI-QTOF, C<sub>6</sub>H<sub>5</sub>Cl): Calcd for C<sub>30</sub>H<sub>32</sub>MnN<sub>2</sub>S<sub>4</sub> m/z 604.0907 ([M<sup>+</sup>]). Found m/z 604.1166.

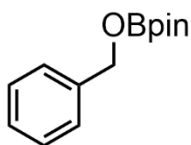


**Synthesis of Mn( $\kappa^2$ -S<sup>Me</sup>NS<sup>Me</sup>)<sub>2</sub>(bpy) (**3.2<sub>Mn</sub>**).** A solution of bpy (0.011 g, 0.073 mmol) in 0.5 mL of THF was added to a 3 mL THF solution of **1** (0.044 g, 0.073 mmol), resulting in an immediate color change from yellow to red. The solution was stirred for 6 h, filtered through Celite, and volatile materials were removed under reduced pressure. The resultant red powder was washed with hexanes (2 x 2 mL) and dried under vacuum to give 0.048 g of red powder (88% yield). Crystals suitable for X-ray diffraction were grown from a concentrated THF solution at room temperature. <sup>1</sup>H NMR (C<sub>6</sub>D<sub>6</sub>, 23 °C, 300 MHz; Fig. S4):  $\delta$  0.28 (br s); 0.87(br s); 1.19 (br s); 1.39 (br s); 1.94 (br s); 3.58 (br s); 4.28 (br s); 5.44 (br s); 6.56 (br s); 7.46 (br s); 8.70 (br s,  $\Delta\nu_{1/2} = 256$  Hz).

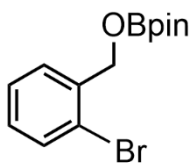
### 3.4.3 Catalytic, kinetic, and mechanistic studies

#### General Procedure ‘A’ for Hydroboration of Carbonyls.

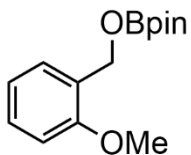
A catalyst stock solution was prepared by dissolving **3.1<sub>Mn</sub>** (10 mg) in C<sub>6</sub>D<sub>6</sub> (5 mL). A vial containing **3.1<sub>Mn</sub>** (0.1 mg, 50  $\mu$ L, 0.16  $\mu$ mol, 0.1 mol%) in 0.6 g of C<sub>6</sub>D<sub>6</sub> was charged first with the appropriate substrate (0.16 mmol), and subsequently with pinacolborane (0.020 g, 22.6  $\mu$ L, 0.16 mmol) resulting in an immediate color change from yellow to pale-yellow. Reaction times varied from 5-20 min. Full conversion of pinacolborane was determined by <sup>11</sup>B NMR. Yield was determined by <sup>1</sup>H NMR peak integration in reference to internal standard mesitylene. The reaction mixture was filtered through a short silica plug, rinsed with ethyl acetate (2 mL), and concentrated under vacuum to yield the isolated product.



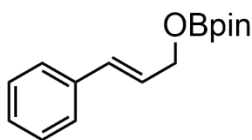
**Hydroboration of benzaldehyde.** Conducted according to *General Procedure A* using benzaldehyde (0.016 g, 16  $\mu$ L, 0.16 mmol), pinacolborane (0.020 g, 22  $\mu$ L, 0.16 mmol), and catalytic **3.1Mn**.  $^{11}\text{B}$  NMR showed quantitative conversion to hydroboration product after 5 min at room temperature.  $^1\text{H}$  NMR shifts matched with literature values.<sup>80</sup>



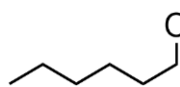
**Hydroboration of 2-bromo-benzaldehyde.** Conducted according to *General Procedure A* using 2-bromo-benzaldehyde (0.029 g, 18  $\mu$ L, 0.16 mmol), pinacolborane (0.020 g, 22  $\mu$ L, 0.16 mmol), and catalytic **3.1Mn**.  $^{11}\text{B}$  NMR showed quantitative conversion to hydroboration product after 5 min at room temperature.  $^1\text{H}$  NMR shifts matched with literature values.<sup>63</sup>



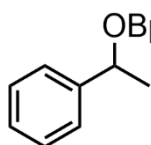
**Hydroboration of 2-methoxy-benzaldehyde.** Conducted according to *General Procedure A* using 2-methoxy-benzaldehyde (0.021 g, 19  $\mu$ L, 0.16 mmol), pinacolborane (0.020 g, 22  $\mu$ L, 0.16 mmol), and catalytic **3.1Mn**.  $^{11}\text{B}$  NMR showed quantitative conversion to hydroboration product after 5 min at room temperature.  $^1\text{H}$  NMR shifts matched with literature values.<sup>80</sup>



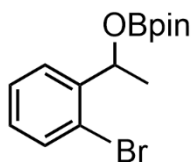
**Hydroboration of trans-cinnamaldehyde.** Conducted according to *General Procedure A* using trans-cinnamaldehyde (0.021 g, 20  $\mu$ L, 0.16 mmol), pinacolborane (0.020 g, 22  $\mu$ L, 0.16 mmol), and catalytic **3.1Mn**.  $^{11}\text{B}$  NMR showed quantitative conversion to hydroboration product after 5 min at room temperature.  $^1\text{H}$  NMR shifts matched with literature values.<sup>63</sup>



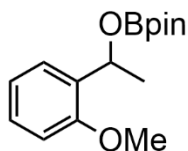
**Hydroboration of hexanal.** Conducted according to *General Procedure A* using hexanal (0.015 g, 19  $\mu$ L, 0.16 mmol), pinacolborane (0.020 g, 22  $\mu$ L, 0.16 mmol), and catalytic **3.1Mn**.  $^{11}\text{B}$  NMR showed quantitative conversion to hydroboration product after 5 min at room temperature.  $^1\text{H}$  NMR shifts matched with literature values.<sup>81</sup>



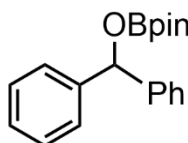
**Hydroboration of acetophenone.** Conducted according to *General Procedure A* using acetophenone (0.018 g, 18  $\mu$ L, 0.16 mmol), pinacolborane (0.020 g, 22  $\mu$ L, 0.16 mmol), and catalytic **3.1Mn**.  $^{11}\text{B}$  NMR showed quantitative conversion to hydroboration product after 5 min at room temperature.  $^1\text{H}$  NMR shifts matched with literature values.<sup>80</sup>



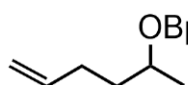
**Hydroboration of 2-bromoacetophenone.** Conducted according to *General Procedure A* using 2-bromoacetophenone (0.031 g, 0.16 mmol), pinacolborane (0.020 g, 22  $\mu$ L, 0.16 mmol), and catalytic **3.1Mn**.  $^{11}\text{B}$  NMR showed quantitative conversion to hydroboration product after 20 min at room temperature.  $^1\text{H}$  NMR shifts matched well with literature values of the hydrolyzed alcohol product.<sup>82</sup>



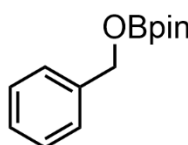
**Hydroboration of 2-methoxyacetophenone.** Conducted according to *General Procedure A* using 2-methoxyacetophenone (0.023 g, 0.16 mmol), pinacolborane (0.020 g, 22  $\mu$ L, 0.16 mmol), and catalytic **3.1Mn**.  $^{11}\text{B}$  NMR showed quantitative conversion to hydroboration product after 20 min at room temperature.  $^1\text{H}$  NMR shifts matched with literature values.<sup>83</sup>



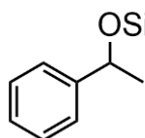
**Hydroboration of benzophenone.** Conducted according to *General Procedure A* using benzophenone (0.028 g, 0.16 mmol), pinacolborane (0.020 g, 22  $\mu$ L, 0.16 mmol), and catalytic **3.1<sub>Mn</sub>**.  $^{11}\text{B}$  NMR showed quantitative conversion to hydroboration product after 10 min at room temperature.  $^1\text{H}$  NMR shifts matched with literature values.<sup>80</sup>



**Hydroboration of 5-hexen-2-one.** Conducted according to *General Procedure A* using 5-hexen-2-one (0.015 g, 18  $\mu$ L, 0.16 mmol), pinacolborane (0.020 g, 22  $\mu$ L, 0.16 mmol), and catalytic **3.1<sub>Mn</sub>**.  $^{11}\text{B}$  NMR showed quantitative conversion to hydroboration product after 20 min at room temperature.  $^1\text{H}$  NMR shifts matched with literature values.<sup>80</sup>



**Hydroboration of benzyl benzoate.** Conducted according to *General Procedure A* using benzyl benzoate (0.015 g, 18  $\mu$ L, 0.16 mmol), pinacolborane (0.020 g, 22  $\mu$ L, 0.16 mmol), and catalytic **3.1<sub>Mn</sub>**. The reaction mixture was heated at 60°C overnight.  $^{11}\text{B}$  NMR showed a mixture of hydroboration product and unreacted pinacolborane starting material. The reaction mixture was worked up according to *General Procedure A*, and the resultant  $^1\text{H}$  NMR showed a mixture of hydroborated product and unreacted benzyl benzoate (60% yield by NMR).



**Hydrosilylation of acetophenone.** Conducted according to *General Procedure A* using acetophenone (0.018 g, 18  $\mu$ L, 0.16 mmol), triethoxysilane (0.026 g, 29  $\mu$ L, 0.16 mmol), and catalytic **3.1<sub>Mn</sub>**. The reaction mixture was heated at 60°C overnight and worked up according to *General Procedure A*.  $^1\text{H}$  NMR shifts matched with literature values (95% yield by NMR).<sup>84</sup>

*Mechanistic studies performed with 3.1Mn.*

**Stoichiometric reaction of 3.1Mn and 5-hexen-2-one.** A yellow solution of 3.1Mn (0.010 g, 0.016 mmol) in 0.6 g of C<sub>6</sub>D<sub>6</sub> was prepared. The solution was charged with 5-hexen-2-one (0.002 g, 2 μL, 0.016 mmol, 1 equiv.) and subsequently transferred to an NMR tube. No color change was observed. <sup>1</sup>H NMR showed no reaction. Monitoring for 24 h showed no further changes.

**Stoichiometric reaction of 3.1Mn and pinacolborane.** A yellow solution of 3.1Mn (0.010 g, 0.016 mmol) in 0.6 g of C<sub>6</sub>D<sub>6</sub> was prepared. The solution was charged with pinacolborane (0.002 g, mmol, 2.5 μL, 0.016 mmol, 1 equiv) resulting in an immediate color change to a dark brown-yellow solution.

→ <sup>11</sup>B NMR showed complete consumption of pinacolborane as well as a new broad resonance at 24.1 ppm (**Figure 3.9**). \*It should be noted that the <sup>11</sup>B NMR spectrum after addition of 2 equiv. of pinacolborane (0.004 g, 5 μL, 0.032 mmol) showed a mixture of the new species (24.1 ppm) as well as unreacted HBpin.

→ The 100 K EPR spectrum showed disappearance of all Mn hyperfine coupling, showing a large broad signal at g = 2.09 and a small signal at g = 5.03 (**Figure 3.10**).

→ The UV-vis spectrum and cyclic voltammograms showed only subtle changes from those of 3.1Mn (**Figures B28 and B29**).

**Stepwise stoichiometric hydroboration.** A yellow solution of 3.1Mn (0.010 g, 0.016 mmol) in 0.6 g of C<sub>6</sub>D<sub>6</sub> was prepared. The solution was charged with pinacolborane (0.002 g, mmol, 2.5 μL, 0.016 mmol, 1 equiv) resulting in an immediate color change to a dark

brown-yellow. The reaction mixture was then charged with either: A) 5-hexen-2-one (0.002 g, 2  $\mu$ L, 0.016 mmol, 1 equiv.) for EPR study; or B) hexanal (0.002 g, 2  $\mu$ L, 0.016 mmol, 1 equiv.) for UV-vis and CV study. Both scenarios result in a color change to pale-yellow.

- $^{11}\text{B}$  NMR confirmed formation of hydroboration product.
- The 100 K EPR spectrum showed a large broad signal at  $g = 2.00$  (**Figure B26**).
- The UV-vis spectrum showed no change from the spectrum of **3.1<sub>Mn</sub>** (**Figure B30**).
- The cyclic voltammogram showed a small potential shift from the scan of **3.1<sub>Mn</sub>** (**Figure B29**).

*Mechanistic studies performed with 3.2<sub>Mn</sub>.*

**Addition of catalytic bipyridine to hydroboration of 5-hexen-2-one.** Conducted according to *General Procedure A* using 5-hexen-2-one (0.015 g, 18  $\mu$ L, 0.16 mmol), pinacolborane (0.020 g, 22  $\mu$ L, 0.16 mmol), and **3.1<sub>Mn</sub>** (0.004 g, 5 mol%). After addition of HBpin affected color change and catalysis, 0.1 mL of stock solution of bipyridine (0.001 g, 5 mol%) was added to the reaction mixture. The reaction progress was monitored by  $^{11}\text{B}$  NMR. Complete conversion was noted within 20 minutes, resulting in no notable rate change.

- The UV-vis spectra of the catalytic mixture + bipyridine showed a new signal attributable to bipyridine (**Figure B30**).

**Stoichiometric reaction of 3.2<sub>Mn</sub> and pinacolborane.** An orange/yellow solution of 3.2<sub>Mn</sub> (0.010 g, 0.016 mmol) in 0.2 g of toluene was prepared. The solution was charged with pinacolborane (0.002 g, 2 μL, 0.016 mmol, 1 equiv.), resulting in an immediate color change to yellow. The solution was stored at -30 °C in the freezer for 6 h, after which a white precipitate was observed. The mother liquor was removed. The white precipitate was dried and confirmed as bipyridine by <sup>1</sup>H NMR.

→ The UV-vis spectrum of 3.2<sub>Mn</sub> and (3.2<sub>Mn</sub> + HBpin) are shown in **Figure B30**.

### 3.4.4 Key spectroscopic data

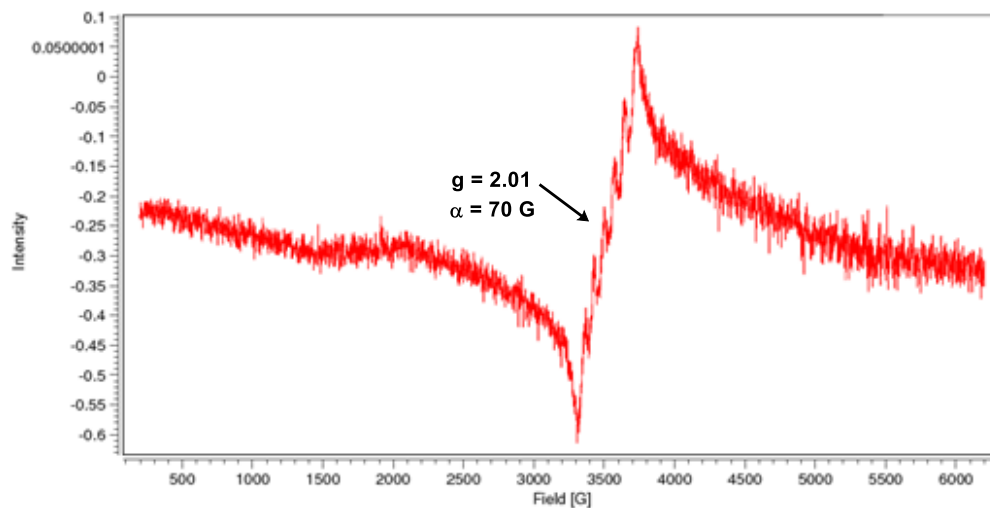


**Figure 3.9.** 273 K EPR spectrum of Mn( $\kappa^3$ -S<sup>Me</sup>NS<sup>Me</sup>)<sub>2</sub> (3.1<sub>Mn</sub>) in THF.

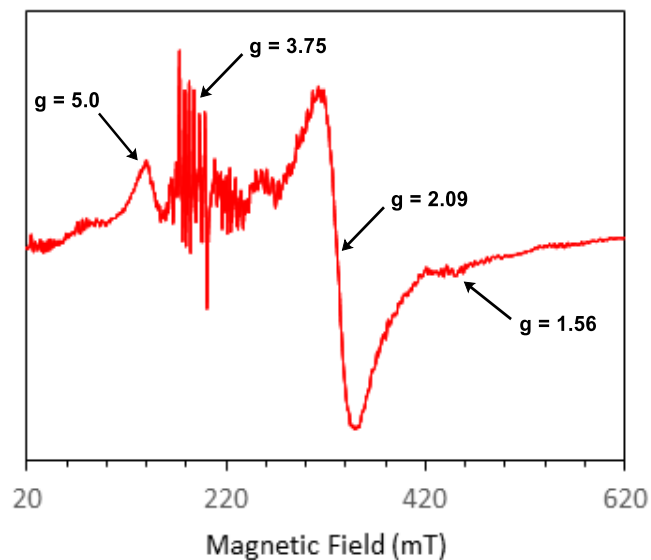


Figure 3.10. 100 K EPR spectrum of  $\text{Mn}(\kappa^3\text{-S}^{\text{Me}}\text{NS}^{\text{Me}})_2$  (**3.1<sub>Mn</sub>**) as frozen THF solution.

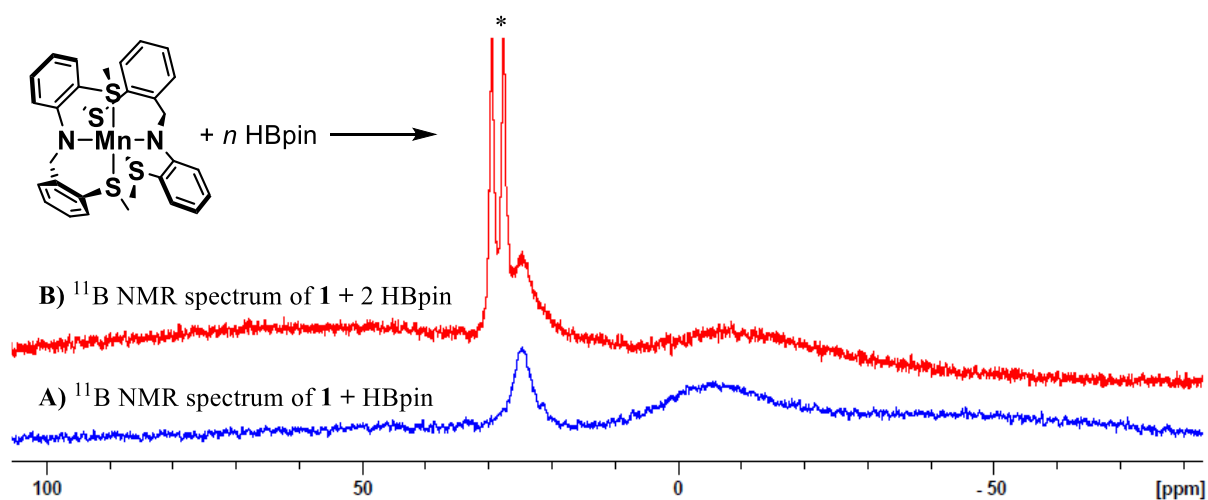


Figure 3.11. Stack plot of  $^{11}\text{B}$  NMR spectra of A) stoichiometric reaction of **3.1<sub>Mn</sub>** with HBpin; B) reaction of **3.1<sub>Mn</sub>** with 2 equiv. HBpin. \* unreacted HBpin

### 3.4.5 Single crystal X-ray diffraction data

**\*\*Key crystallographic data can be found in Appendix B.\*\***

Crystals were mounted on thin glass fibers using paraffin oil or cyanoacrylate glue. Crystals of **3.1<sub>Mn</sub>** and **3.2<sub>Mn</sub>** were cooled to  $200 \pm 2$  K during data collection. The data were collected on a Bruker single-crystal diffractometer equipped with a sealed Mo tube source (wavelength 0.71073 Å) and APEX II CCD detector. The raw data collection and processing were performed with Bruker APEX II software package.<sup>85</sup> Semi-empirical absorption correction based on equivalent reflections was applied.<sup>86</sup> Systematic absences and unit cell parameters were consistent with triclinic *P*-1 (#2) for **3.1<sub>Mn</sub>**, and monoclinic *P*<sub>21</sub>/*n* (#14) for **3.2<sub>Mn</sub>**. The structures were solved by intrinsic phasing and refined with a full-matrix least-squares procedure based on  $F^2$ , using SHELXL.<sup>87</sup> All non-hydrogen atoms were refined anisotropically. The hydrogen atoms bonded to carbon atoms were placed in idealized positions.

#### **Refinement details for Mn( $\kappa^3$ -S<sup>Me</sup>NS<sup>Me</sup>)<sub>2</sub> (3.1<sub>Mn</sub>).**

The structure was refined without additional restraints / constraints. No disorder was present.

#### **Refinement details for Mn( $\kappa^2$ -S<sup>Me</sup>NS<sup>Me</sup>)<sub>2</sub>(bpy) (3.2<sub>Mn</sub>).**

The structure was refined without additional restraints / constraints. No disorder was present.

### **3.4.6 Details of DFT calculations**

All calculations were carried out using density functional theory (DFT)<sup>88</sup> as implemented in the Jaguar 9.1 suite<sup>70</sup> of ab initio quantum chemistry programs. Geometry optimizations were performed with the B3LYP functional including Grimme's D3 dispersion correction.<sup>66-68,89-90</sup> The 6-31G\*\* basis set was used for main group atoms and Mn was represented using the Los Alamos LACVP basis set that includes relativistic effective core potentials. The energies of optimized structures were reevaluated by additional single-point calculations on each optimized geometry using Dunning's correlation consistent triple- $\zeta$  basis set cc-pVTZ(-f)<sup>71</sup> which includes a double set of polarization functions. For Mn, we used a modified version of LACVP, designated as LACV3P, in which the exponents were decontracted to match the triple- $\zeta$  quality basis of the main group elements. For boron, the 6-311G\*\* basis set was used. Solvation energies were evaluated by a self-consistent reaction field (SCRF)<sup>53,91-92</sup> approach based on accurate numerical solutions of the Poisson-Boltzmann equation. In the results reported, solvation calculations were carried out at the same level of theory as the geometry optimization, employing a dielectric constant of  $\epsilon = 2.284$  for benzene. As is the case for all continuum models, the solvation energies are subject to empirical parameterization of the atomic radii that are used to generate the solute surface. We employed the standard set of Van der Waals radii in Jaguar for H (1.150 Å), B(2.042 Å), C(1.900 Å), N(1.600 Å), O (1.600 Å), S(1.900 Å) and Mn (1.480 Å). Analytical vibrational frequencies within the harmonic approximation were computed with the 6-31G\*\*/LACVP basis set to confirm proper convergence to well-defined minima or saddle points on the potential energy surface. The intermediates were

*Chapter 3 – Comparing Amido Bifunctional Reactivity Across Base Metals and a Mechanistic Study of Metal-Ligand Cooperativity in Mn(II)-Catalyzed Hydroborations*

confirmed with no vibrational frequency, while transition states showed a single imaginary frequency.

The energy components have been computed with the following protocol. The free energy in solution-phase,  $G(\text{sol})$ , has been calculated as follows, with  $T = 298 \text{ K}$  to match the experimental room temperature conditions:

$$G(\text{sol}) = G(\text{gas}) + G_{\text{solv}}$$

$$G(\text{gas}) = H(\text{gas}) - TS(\text{gas})$$

$$H(\text{gas}) = E(\text{SCF}) + \text{ZPE}$$

$$\Delta E(\text{SCF}) = \sum E(\text{SCF}) \text{ for products} - \sum E(\text{SCF}) \text{ for reactants}$$

$$\Delta G(\text{sol}) = \sum G(\text{sol}) \text{ for products} - \sum G(\text{sol}) \text{ for reactants}$$

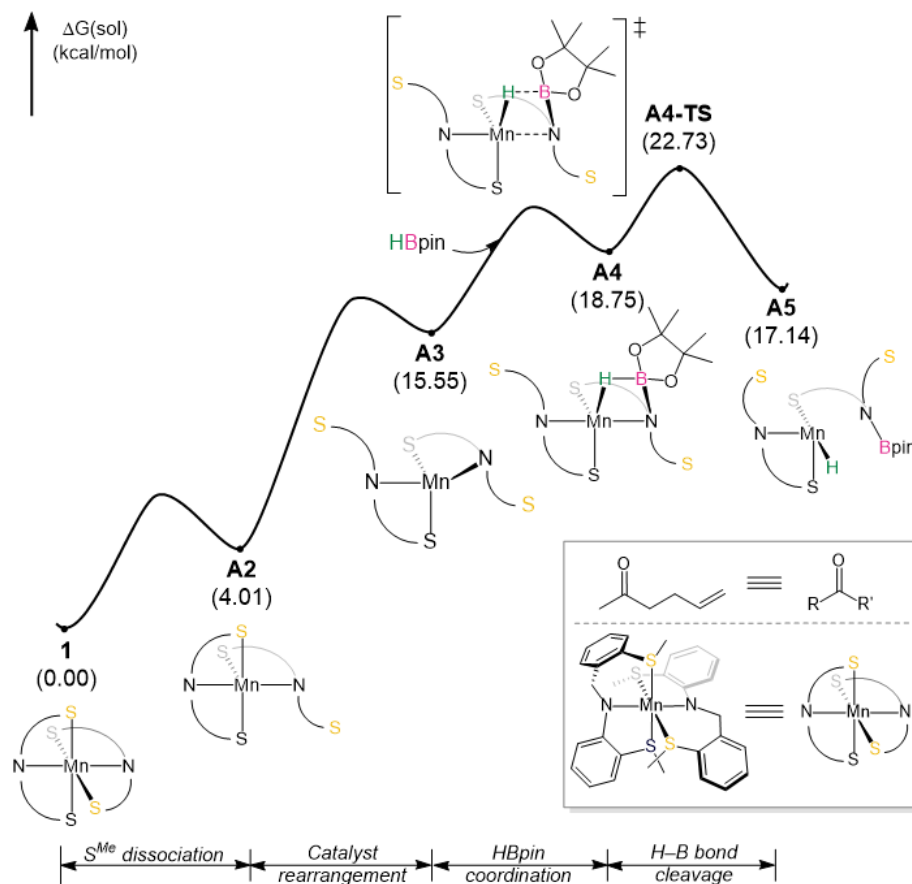
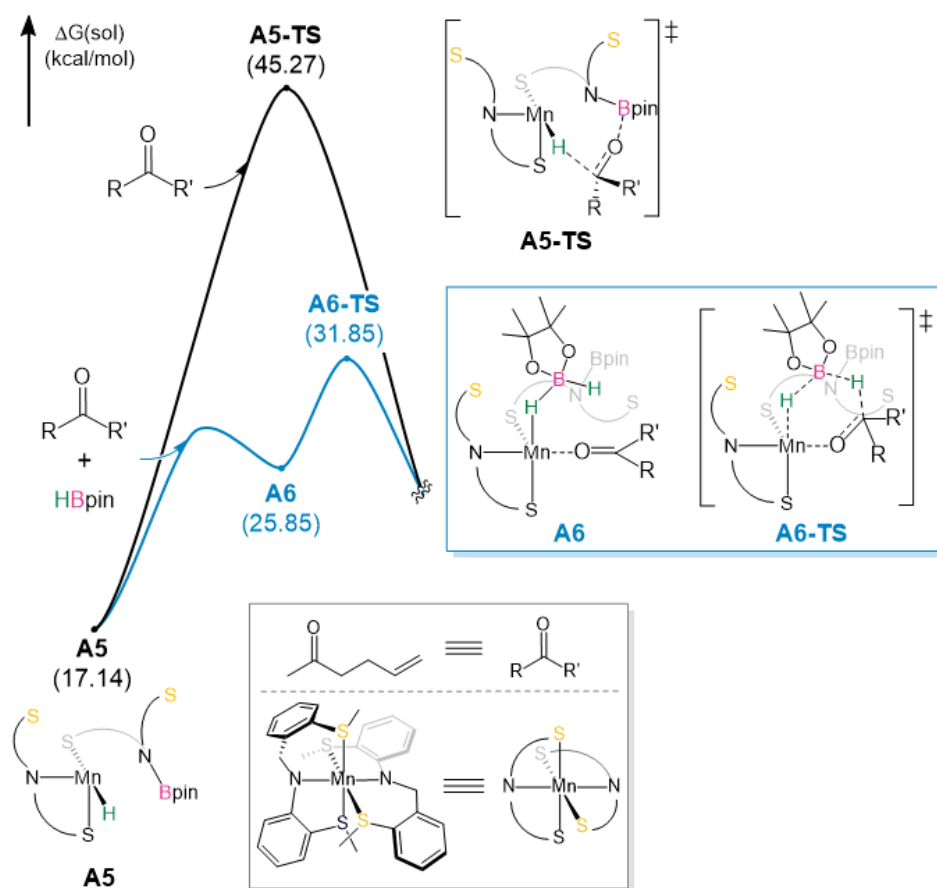


Figure 3.12. DFT calculated reaction profile of Mn-H formation.



**Figure 3.12.** Possible hydroboration mechanisms after Mn–H formation.

Two possible pathways after Mn–H formation were investigated. The pathway in black describes a direct outer-sphere hydroboration. The pathway in blue describes a process where a second equivalent of HBpin participates in the process. These pathways having an overall reaction of barrier of 45.27 (**A5-TS**) and 31.85 kcal/mol(**A6-TS**), are less likely than the inner-sphere mechanism possessing a barrier of 21.57 kcal/mol.(**B4-TS**).

### 3.5 References

- (1) Van Leeuwen, P. W. N. M. *Homogeneous Catalysis: Understanding the Art*; Springer Science & Business Media, 2006.
- (2) Chiusoli, G. P.; Maitlis, P. M. *Metal-Catalysis in Industrial Organic Processes*; Royal Society of Chemistry, 2019.
- (3) Bullock, R. M. *Catalysis Without Precious Metals*; John Wiley & Sons, 2011.
- (4) Obligacion, J. V.; Chirik, P. J. Earth-Abundant Transition Metal Catalysts for Alkene Hydrosilylation and Hydroboration. *Nat. Rev. Chem.* **2018**, *2*, 15-34.
- (5) Reed-Berendt, B. G.; Polidano, K.; Morrill, L. C. Recent Advances in Homogeneous Borrowing Hydrogen Catalysis Using Earth-Abundant First Row Transition Metals. *Org. Biomol. Chem.* **2019**, *17*, 1595-1607.
- (6) Chirik, P.; Morris, R. Getting Down to Earth: The Renaissance of Catalysis with Abundant Metals. *Acc. Chem. Res.* **2015**, *48*, 2495-2495.
- (7) Bullock, R. M.; Chen, J. G.; Gagliardi, L.; Chirik, P. J.; Farha, O. K.; Hendon, C. H.; Jones, C. W.; Keith, J. A.; Klosin, J.; Minter, S. D. Using Nature's Blueprint to Expand Catalysis with Earth-Abundant Metals. *Science* **2020**, *369*, No. abc3183.
- (8) Elschenbroich, C. *Organometallics*; John Wiley & Sons, 2016.
- (9) Crabtree, R. H. *The Organometallic Chemistry of the Transition Metals*; John Wiley & Sons, 2009.
- (10) Hartwig, J. F. *Organotransition Metal Chemistry: From Bonding to Catalysis*; University Science Books, 2010.
- (11) Khusnutdinova, J. R.; Milstein, D. Metal–ligand Cooperation. *Angew. Chem. Int. Ed.* **2015**, *54*, 12236-12273.
- (12) van der Vlugt, J. I. Cooperative Catalysis with First-Row Late Transition Metals. *Eur. J. Inorg. Chem.* **2012**, *2012*, 363-375.
- (13) Fritz, M.; Schneider, S. The Renaissance of Base Metal Catalysis Enabled by Functional Ligands, in *The Periodic Table II: Catalytic, Materials, Biological and Medical Applications*, Mingos, D. M. P., Ed. **2019**, 1-36.
- (14) Elsby, M. R.; Baker, R. T. Strategies and Mechanisms of Metal–Ligand Cooperativity in First-Row Transition Metal Complex Catalysts. *Chem. Soc. Rev.* **2020**, *49*, 8933-8987.

- (15) Morris, R. H. Exploiting Metal–Ligand Bifunctional Reactions in the Design of Iron Asymmetric Hydrogenation Catalysts. *Acc. Chem. Res.* **2015**, *48*, 1494-1502.
- (16) Bullock, R. M.; Helm, M. L. Molecular Electrocatalysts for Oxidation of Hydrogen using Earth-Abundant Metals: Shoving Protons Around with Proton Relays. *Acc. Chem. Res.* **2015**, *48*, 2017-2026.
- (17) Zuo, W.; Lough, A. J.; Li, Y. F.; Morris, R. H. Amine (Imine) Diphosphine Iron Catalysts for Asymmetric Transfer Hydrogenation of Ketones and Imines. *Science* **2013**, *342*, 1080-1083.
- (18) Tondreau, A. M.; Atienza, C. C. H.; Weller, K. J.; Nye, S. A.; Lewis, K. M.; Delis, J. G.; Chirik, P. J. Iron Catalysts for Selective Anti-Markovnikov Alkene Hydrosilylation Using Tertiary Silanes. *Science* **2012**, *335*, 567-570.
- (19) Liu, T.; DuBois, D. L.; Bullock, R. M. An Iron Complex with Pendent Amines as a Molecular Electrocatalyst for Oxidation of Hydrogen. *Nat. Chem.* **2013**, *5*, 228-233.
- (20) Helm, M. L.; Stewart, M. P.; Bullock, R. M.; DuBois, M. R.; DuBois, D. L. A Synthetic Nickel Electrocatalyst with a Turnover Frequency Above 100,000 s<sup>-1</sup> for H<sub>2</sub> Production. *Science* **2011**, *333*, 863-866.
- (21) Mukherjee, A.; Milstein, D. Homogeneous Catalysis by Cobalt and Manganese Pincer Complexes. *ACS Catal.* **2018**, *8*, 11435-11469.
- (22) Trovitch, R. J. The Emergence of Manganese-Based Carbonyl Hydrosilylation Catalysts. *Acc. Chem. Res.* **2017**, *50*, 2842-2852.
- (23) Yang, X.; Wang, C. Manganese-Catalyzed Hydrosilylation Reactions. *Chem. Asian J.* **2018**, *13*, 2307-2315.
- (24) Alig, L.; Fritz, M.; Schneider, S. First-Row Transition Metal (De)Hydrogenation Catalysis Based on Functional Pincer Ligands. *Chem. Rev.* **2018**, *119*, 2681-2751.
- (25) Tamang, S. R.; Findlater, M. Emergence and Applications of Base Metals (Fe, Co, and Ni) in Hydroboration and Hydrosilylation. *Molecules* **2019**, *24*, 3194.
- (26) Zhang, G.; Zeng, H.; Wu, J.; Yin, Z.; Zheng, S.; Fettinger, J. C. Highly Selective Hydroboration of Alkenes, Ketones and Aldehydes Catalyzed by a Well-Defined Manganese Complex. *Angew. Chem. Int. Ed.* **2016**, *55*, 14369-14372.

- (27) Vasilenko, V.; Blasius, C. K.; Wadepohl, H.; Gade, L. H. Mechanism-Based Enantiodivergence in Manganese Reduction Catalysis: A Chiral Pincer Complex for the Highly Enantioselective Hydroboration of Ketones. *Angew. Chem. Int. Ed.* **2017**, *56*, 8393-8397.
- (28) Carney, J. R.; Dillon, B. R.; Campbell, L.; Thomas, S. P. Manganese-Catalyzed Hydrofunctionalization of Alkenes. *Angew. Chem. Int. Ed.* **2018**, *57*, 10620-10624.
- (29) Nguyen, T. T.; Kim, J.-H.; Kim, S.; Oh, C.; Flores, M.; Groy, T. L.; Baik, M.-H.; Trovitch, R. J. Scope and Mechanism of Nitrile Dihydroboration Mediated by a  $\beta$ -diketiminato Manganese Hydride Catalyst. *Chem. Commun.* **2020**, *56*, 3959-3962.
- (30) Erken, C.; Kaithal, A.; Sen, S.; Weyhermüller, T.; Hölscher, M.; Werlé, C.; Leitner, W. Manganese-Catalyzed Hydroboration of Carbon Dioxide and Other Challenging Carbonyl Groups. *Nat. Commun.* **2018**, *9*, 4521–4529.
- (31) Kostera, S.; Peruzzini, M.; Kirchner, K.; Gonsalvi, L. Mild and Selective Carbon Dioxide Hydroboration to Methoxyboranes Catalyzed by Mn (I) PNP Pincer Complexes. *ChemCatChem.* **2020**, *12*, 4625-4631.
- (32) Higashi, T.; Kusumoto, S.; Nozaki, K. Cleavage of Si–H, B–H, and C–H Bonds by Metal–Ligand Cooperation: Focus Review. *Chem. Rev.* **2019**, *119*, 10393-10402.
- (33) Sarkar, K.; Das, K.; Kundu, A.; Adhikari, D.; Maji, B. Phosphine-Free Manganese Catalyst Enables Selective Transfer Hydrogenation of Nitriles to Primary and Secondary Amines Using Ammonia–Borane. *ACS Catal.* **2021**, *11*, 2786-2794.
- (34) Sarbajna, A.; Patil, P. H.; Dinh, M. H.; Gladkovskaya, O.; Fayzullin, R. R.; Lapointe, S.; Khaskin, E.; Khusnutdinova, J. R. Facile and Reversible Double Dearomatization of Pyridines in Non-Phosphine Mn(I) Complexes with N, S-Donor Pyridinophane Ligand. *Chem. Commun.* **2019**, *55*, 3282-3285.
- (35) Zhang, F.; Song, H.; Zhuang, X.; Tung, C.-H.; Wang, W. Iron-Catalyzed 1, 2-Selective Hydroboration of N-Heteroarenes. *J. Am. Chem. Soc.* **2017**, *139*, 17775-17778.
- (36) Song, H.; Ye, K.; Geng, P.; Han, X.; Liao, R.; Tung, C.-H.; Wang, W. Activation of Epoxides by a Cooperative Iron–Thiolate Catalyst: Intermediacy of Ferrous Alkoxides in Catalytic Hydroboration. *ACS Catal.* **2017**, *7*, 7709-7717.

- (37) Yu, X.; Pang, M.; Zhang, S.; Hu, X.; Tung, C.-H.; Wang, W. Terminal Thiolate-Dominated H/D Exchanges and H<sub>2</sub> Release: Diiron Thiol–Hydride. *J. Am. Chem. Soc.* **2018**, *140*, 11454-11463.
- (38) Fu, S.; Shao, Z.; Wang, Y.; Liu, Q. Manganese-Catalyzed Upgrading of Ethanol Into 1-Butanol. *J. Am. Chem. Soc.* **2017**, *139*, 11941-11948.
- (39) Dubey, A.; Nencini, L.; Fayzullin, R. R.; Nervi, C.; Khusnutdinova, J. R. Bio-inspired Mn (I) Complexes for the Hydrogenation of CO<sub>2</sub> to Formate and Formamide. *ACS Catal.* **2017**, *7*, 3864-3868.
- (40) Dubey, A.; Rahaman, S. W.; Fayzullin, R. R.; Khusnutdinova, J. R. Transfer Hydrogenation of Carbonyl Groups, Imines and N-Heterocycles Catalyzed by Simple, Bipyridine-Based MnI Complexes. *ChemCatChem.* **2019**, *11*, 3844-3852.
- (41) Elsby, M. R.; Baker, R. T. Cu (I)–SNS Complexes for Outer-Sphere Hydroboration and Hydrosilylation of Carbonyls. *Chem. Commun.* **2019**, *55*, 13574-13577.
- (42) Scharf, L. T.; Kowsari, A.; Scherpf, T.; Feichtner, K.-S.; Gessner, V. H. Cooperative Bond Activation Reactions with Nickel and Palladium Carbene Complexes with a PCarbeneS Pincer Ligand. *Organometallics* **2019**, *38*, 4093-4104.
- (43) Kiernicki, J. J.; Zeller, M.; Szymczak, N. K. Hydrazine Capture and N–N Bond Cleavage at Iron Enabled by Flexible Appended Lewis Acids. *J. Am. Chem. Soc.* **2017**, *139*, 18194-18197.
- (44) Kiernicki, J. J.; Zeller, M.; Szymczak, N. K. Examining the Generality of Metal–Ligand Cooperativity Across a Series of First-Row Transition Metals: Capture, Bond Activation, and Stabilization. *Inorg. Chem.* **2020**, *59*, 9279-9286.
- (45) Gorgas, N.; Kirchner, K. Isoelectronic Manganese and Iron Hydrogenation/Dehydrogenation Catalysts: Similarities and Divergences. *Acc. Chem. Res.* **2018**, *51*, 1558-1569.
- (46) Passera, A.; Mezzetti, A. Mn (I) and Fe (II)/PN (H) P Catalysts for the Hydrogenation of Ketones: A Comparison by Experiment and Calculation. *Adv. Synth. Catal.* **2019**, *361*, 4691-4706.

- (47) Su, P.; Li, Y.; Ke, Z. Metal Effect Meets Volcano Plots: A DFT Study on Tris (phosphino) borane-Transition Metal Complexes Catalyzed H<sub>2</sub> Activation. *Chem. Asian J.* **2021**.
- (48) Duboc, C.; Collomb, M.-N.; Neese, F. Understanding the Zero-Field Splitting of Mononuclear Manganese (II) Complexes from Combined EPR Spectroscopy and Quantum Chemistry. *Appl. Magn. Reson.* **2010**, *37*, 229-245.
- (49) Bacciu, D.; Chen, C.-H.; Surawatanawong, P.; Foxman, B. M.; Ozerov, O. V. High-Spin Manganese (II) Complexes of an Amido/Bis (Phosphine) PNP Ligand. *Inorg. Chem.* **2010**, *49*, 5328-5334.
- (50) Das, U. K.; Daifuku, S. L.; Iannuzzi, T. E.; Gorelsky, S. I.; Korobkov, I.; Gabidullin, B.; Neidig, M. L.; Baker, R. T. Iron (II) Complexes of a Hemilabile SNS Amido Ligand: Synthesis, Characterization, and Reactivity. *Inorg. Chem.* **2017**, *56*, 13766-13776.
- (51) Zhao, Y.; Truhlar, D. G. A New Local Density Functional for Main-Group Thermochemistry, Transition Metal Bonding, Thermochemical Kinetics, and Noncovalent Interactions. *J. Chem. Phys.* **2006**, *125*, 194101.
- (52) Weigend, F.; Ahlrichs, R. Balanced Basis Sets of Split Valence, Triple Zeta Valence and Quadruple Zeta Valence Quality for H to Rn: Design and Assessment of Accuracy. *Phys. Chem. Chem. Phys.* **2005**, *7*, 3297-3305.
- (53) Marten, B.; Kim, K.; Cortis, C.; Friesner, R. A.; Murphy, R. B.; Ringnalda, M. N.; Sitkoff, D.; Honig, B. New Model for Calculation of Solvation Free Energies: Correction of Self-Consistent Reaction Field Continuum Dielectric Theory for Short-Range Hydrogen-Bonding Effects. *J. Phys. Chem.* **1996**, *100*, 11775-11788.
- (54) Zhang, G.; Zeng, H.; Wu, J.; Yin, Z.; Zheng, S.; Fettinger, J. C. Highly Selective Hydroboration of Alkenes, Ketones and Aldehydes Catalyzed by a Well-Defined Manganese Complex. *Angew. Chem. Int. Ed.* **2016**, *55*, 14369-14372.
- (55) Hariharan, P. C.; Pople, J. A. The Influence of Polarization Functions on Molecular Orbital Hydrogenation Energies. *Theor. Chim. Acta.* **1973**, *28*, 213-222.
- (56) Stephan, D. W.; Erker, G. Frustrated Lewis Pair Chemistry: Development and Perspectives. *Angew. Chem. Int. Ed.* **2015**, *54*, 6400-6441.

- (57) Rokob, T. A.; Papai, I. Hydrogen Activation by Frustrated Lewis Pairs: Insights from Computational Studies in *Frustrated Lewis Pairs I* **2013**, 157-211.
- (58) Liu, S. Quantifying Reactivity for Electrophilic Aromatic Substitution Reactions with Hirshfeld Charge. *J. Phys. Chem. A* **2015**, *119*, 3107-3111.
- (59) Elsby, M. R.; Son, M.; Oh, C.; Martin, J.; Baik, M.-H.; Baker, R. T. Mechanistic Study of Metal-Ligand Cooperativity in Mn (II)-Catalyzed Hydroborations: Hemilabile SNS Ligand Enables Metal Hydride-Free Reaction Pathway. *ACS Catal.* **2021**, *11*, 9043-9051.
- (60) Seo, C. S.; Tsui, B. T.; Gradiski, M. V.; Smith, S. A.; Morris, R. H. Enantioselective Direct, Base-Free Hydrogenation of Ketones by a Manganese Amido Complex of a Homochiral, Unsymmetrical P-N-P' Ligand. *Catal. Sci. Technol.* **2021**, *11*, 3153-3163.
- (61) Bermejo, M.-J.; Ruiz, J.-I.; Solans, X.; Vinaixa, J. Dynamic Behaviour of Octahedral Complexes of Manganese (I). X-ray Crystal Structure of Fac-[Mn ( $\eta^1$ -1, 8-naphthyridine)- $\eta^2$ -1, 8-naphthyridine)(CO)<sub>3</sub>] ClO<sub>4</sub>· CH<sub>2</sub>Cl<sub>2</sub>. *J. Organomet. Chem.* **1993**, *463*, 143-150.
- (62) Dubey, A.; Rahaman, S. W.; Fayzullin, R. R.; Khusnutdinova, J. R. Transfer Hydrogenation of Carbonyl Groups, Imines and N-Heterocycles Catalyzed by Simple, Bipyridine-Based Mn<sup>I</sup> Complexes. *ChemCatChem.* **2019**, *11*, 3844-3852.
- (63) Das, U. K.; Higman, C. S.; Gabidullin, B.; Hein, J. E.; Baker, R. T. Efficient and Selective Iron-Complex-Catalyzed Hydroboration of Aldehydes. *ACS Catal.* **2018**, *8*, 1076-1081.
- (64) Nielsen, C. D.-T.; Burés, J. Visual Kinetic Analysis. *Chem. Sci.* **2019**, *10*, 348-353.
- (65) Burés, J. Variable Time Normalization Analysis: General Graphical Elucidation of Reaction Orders from Concentration Profiles. *Angew. Chem. Int. Ed.* **2016**, *55*, 16084-16087.
- (66) Becke, A. D. Density-Functional Thermochemistry. III. The Role of Exact Exchange. *J. Chem. Phys.* **1993**, *98*, 5648-5652.
- (67) Lee, C.; Yang, W.; Parr, R. G. Development of the Colle-Salvetti Correlation-Energy Formula into a Functional of the Electron Density. *Phys. Rev. B.* **1988**, *37*, 785-789.
- (68) Grimme, S.; Antony, J.; Ehrlich, S.; Krieg, H. A Consistent and Accurate Ab Initio Parametrization of Density Functional Dispersion Correction (DFT-D) for the 94 Elements H-Pu. *J. Chem. Phys.* **2010**, *132*, 154104.

- (69) Hay, P. J.; Wadt, W. R. Ab Initio Effective Core Potentials for Molecular Calculations. Potentials for the Transition Metal Atoms Sc to Hg. *J. Chem. Phys.* **1985**, *82*, 270-283.
- (70) Bochevarov, A. D.; Harder, E.; Hughes, T. F.; Greenwood, J. R.; Braden, D. A.; Philipp, D. M.; Rinaldo, D.; Halls, M. D.; Zhang, J.; Friesner, R. A. Jaguar: A High-Performance Quantum Chemistry Software Program with Strengths in Life and Materials Sciences. *Int. J. Quantum Chem.* **2013**, *113*, 2110-2142.
- (71) Dunning Jr, T. H. Gaussian Basis Sets for Use in Correlated Molecular Calculations. I. The Atoms Boron Through Neon and Hydrogen. *J. Chem. Phys.* **1989**, *90*, 1007-1023.
- (72) Woon, D. E.; Dunning Jr, T. H. Gaussian Basis Sets for Use in Correlated Molecular Calculations. III. The Atoms Aluminum Through Argon. *J. Chem. Phys.* **1993**, *98*, 1358-1371.
- (73) Dub, P. A.; Henson, N. J.; Martin, R. L.; Gordon, J. C. Unravelling the Mechanism of the Asymmetric Hydrogenation of Acetophenone by [RuX<sub>2</sub> (diphosphine)(1, 2-diamine)] Catalysts. *J. Am. Chem. Soc.* **2014**, *136*, 3505-3521.
- (74) Pang, M.; Wu, C.; Zhuang, X.; Zhang, F.; Su, M.; Tong, Q.; Tung, C.-H.; Wang, W. Addition of a B–H Bond Across an Amido–Cobalt Bond: Co<sup>II</sup>–H-Catalyzed Hydroboration of Olefins. *Organometallics* **2018**, *37*, 1462-1467.
- (75) Lennox, A. J.; Lloyd-Jones, G. C. Selection of Boron Reagents for Suzuki–Miyaura Coupling. *Chem. Soc. Rev.* **2014**, *43*, 412-443.
- (76) Lennox, A. J.; Lloyd-Jones, G. C. Transmetalation in the Suzuki–Miyaura Coupling: The Fork in the Trail. *Angew. Chem. Int. Ed.* **2013**, *52*, 7362-7370.
- (77) Braga, A. A.; Morgon, N. H.; Ujaque, G.; Maseras, F. Computational Characterization of the Role of the Base in the Suzuki–Miyaura Cross-Coupling Reaction. *J. Am. Chem. Soc.* **2005**, *127*, 9298-9307.
- (78) Smith, P. W.; Dong, Y.; Tilley, T. D. Efficient and Selective Alkene Hydrosilation Promoted by Weak, Double Si–H Activation at an Iron Center. *Chem. Sci.* **2020**, *11*, 7070-7075.
- (79) Andersen, R.; Faegri Jr, K.; Green, J. C.; Haaland, A.; Lappert, M.; Leung, W. P.; Rypdal, K. Synthesis of Bis [Bis(Trimethylsilyl)Amido] Iron (II). Structure and Bonding

*Chapter 3 – Comparing Amido Bifunctional Reactivity Across Base Metals and a Mechanistic Study of Metal-Ligand Cooperativity in Mn(II)-Catalyzed Hydroborations*

in M [N(SiMe<sub>3</sub>)<sub>2</sub>]<sub>2</sub> (M= Manganese, Iron, Cobalt): Two-Coordinate Transition-Metal Amides. *Inorg. Chem.* **1988**, *27*, 1782-1786.

(80) Arrowsmith, M.; Hadlington, T. J.; Hill, M. S.; Kociok-Köhn, G. Magnesium-Catalysed Hydroboration of Aldehydes and Ketones. *Chem. Commun.* **2012**, *48*, 4567-4569.

(81) Ma, D. H.; Jaladi, A. K.; Lee, J. H.; Kim, T. S.; Shin, W. K.; Hwang, H.; An, D. K. Catalytic Hydroboration of Aldehydes, Ketones, and Alkenes using Potassium Carbonate: A Small Key to Big Transformation. *ACS Omega* **2019**, *4*, 15893-15903.

(82) Blaquiere, N.; Diallo-Garcia, S.; Gorelsky, S. I.; Black, D. A.; Fagnou, K. Ruthenium-Catalyzed Dehydrogenation of Amine-Boranes. *J. Am. Chem. Soc.* **2008**, *130*, 14034-14035.

(83) Baishya, A.; Baruah, S.; Geetharani, K. Efficient Hydroboration of Carbonyls by an Iron (II) Amide Catalyst. *Dalton Trans.* **2018**, *47*, 9231-9236.

(84) Keess, S.; Simonneau, A.; Oestreich, M. Direct and Transfer Hydrosilylation Reactions Catalyzed by Fully or Partially Fluorinated Triarylboranes: A Systematic Study. *Organometallics* **2015**, *34*, 790-799.

(85) APEX 2, Bruker AXS Inc., Madison, Wisconsin, USA, 2012.

(86) G. M. Sheldrick, SADABS, Program for Empirical Absorption Correction of Area Detector Data, University of Göttingen, Germany, 1996.

(87) G. M. Sheldrick. SHELXL-Integrated Space-Group and Crystal-Structure Determination. *Acta Cryst.* **2015**, *C71*, 3-8.

(88) Parr, R.G.; Yang, W. *Density Functional Theory of Atoms and Molecules*. Oxford University Press: New York, 1989.

(89) Slater, J. C. *Quantum Theory of Molecules and Solids, Vol. 4: The Self-Consistent Field for Molecules and Solids*. McGraw-Hill: New York, 1974. .

(90) Vosko, S. H.; Wilk, L.; Nusair, M. Accurate Spin-Dependent Electron Liquid Correlation Energies for Local Spin Density Calculations: A Critical Analysis. *Can. J. Phys.* **1980**, *58*, 1200.

*Chapter 3 – Comparing Amido Bifunctional Reactivity Across Base Metals and a Mechanistic Study of Metal-Ligand Cooperativity in Mn(II)-Catalyzed Hydroborations*

- (91) Friedrichs, M.; Zhou, R.; Edinger, S. R.; Friesner, R. A. Poisson–Boltzmann Analytical Gradients for Molecular Modeling Calculations. *J. Phys. Chem. B* **1999**, *103*, 3057-3061.
- (92) Edinger, S. R.; Cortis, C.; Shenkin, P. S.; Friesner, R. A. Solvation Free Energies of Peptides: Comparison of Approximate Continuum Solvation Models with Accurate Solution of the Poisson–Boltzmann Equation. *J. Phys. Chem. B* **1997**, *101*, 1190-1197.

**Chapter 4 – Avoiding C<sub>aryl</sub>-S Bond Cleavage in the Design of a Cooperative Mn(I)-Thiolate Complex for Photo-Catalyzed Nitrile Dihydroboration**

**4.1 Introduction**

Homogeneous catalysts are integral to the highly selective synthesis of fine- and commodity chemicals.<sup>1-3</sup> Sustainable catalysis is a priority for a green synthetic future,<sup>4-5</sup> and the past decade has witnessed increased efforts towards the development of first-row metal catalysts to further this goal.<sup>6-8</sup> While the natural abundance<sup>9</sup> and corresponding low-cost is often touted as the main draw for mainstream use of the base-metals, less mentioned is the opportunity to exploit their propensity for diverse coordination geometries, odd-electron reaction pathways, and access to multiple spin states that could reveal new catalytic pathways.<sup>10</sup> Metal-ligand cooperativity (MLC)<sup>11-12</sup> has recently emerged as a valuable strategy that provides unique reactivity in combination with first-row metals.<sup>13-18</sup>

*Chapter 4 – Avoiding C<sub>aryl</sub>-S Bond Cleavage in the Design of a Cooperative Mn(I)-Thiolate Complex for Photo-Catalyzed Nitrile Dihydroboration*

While several MLC strategies exist,<sup>13</sup> ligands that include an additional Lewis base functionality have especially flourished for their high activity in (de)hydrogenations,<sup>19-22</sup> transfer hydrogenations,<sup>23-27</sup> and hydroelementations<sup>28-30</sup> of a wide range of organic substrates. Amongst the base metals, iron catalysts are among the most developed in terms of reaction scope, catalyst performance, and optimal conditions.<sup>31-33</sup> Alternatively, the last five years have brought a surge of growth of bifunctional manganese catalysts.<sup>34-36</sup> Since the Beller group's seminal report of Mn-catalyzed hydrogenation of carbonyls and nitriles,<sup>37</sup> this reaction manifold has proven effective for a variety of challenging (de)hydrogenative transformations.<sup>38-46</sup> The use of bifunctional manganese catalysts for alternative reductive transformations such as hydroborations, however, is not as well developed. Recent work from the Leitner group described the Mn-catalyzed hydroboration of CO<sub>2</sub>, and provided direct evidence of B-H activation across a M-N unit by isolating a key Mn-H intermediate.<sup>47</sup> Manganese catalysts have also excelled in alcohol dehydrogenative coupling transformations<sup>48-51</sup> and hydrosilylations,<sup>52-54</sup> however, these reports used different MLC strategies.

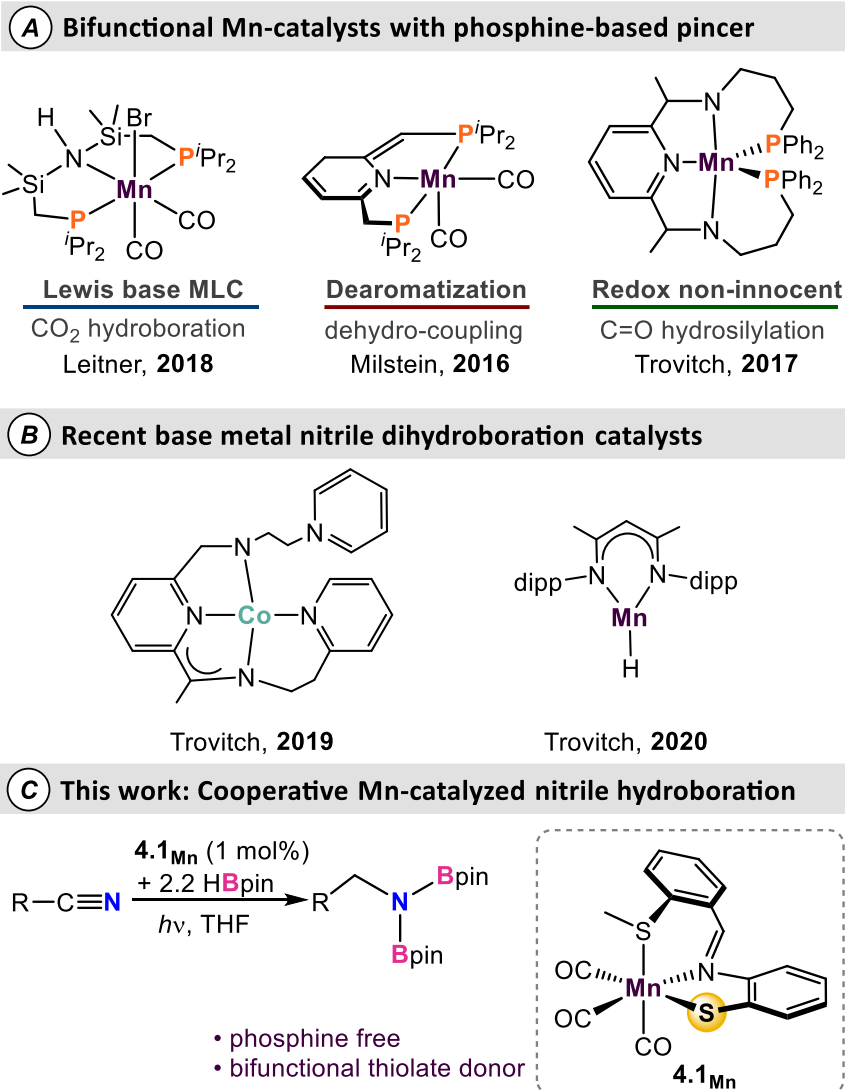


**Figure 4.1.** A) Notable high-performing manganese catalysts featuring phosphine-based pincers; B) Recent base-metal nitrile hydroboration catalysts; C) This work: Mn-catalyzed nitrile dihydroboration using a bifunctional [SNS]-thiolate ligand.

A shared motif amongst the majority of bifunctional Mn-catalysts is a phosphine-based multidentate ligand to bolster the electrophilic Mn center. This serves to both stabilize the metal complex against harsh reaction conditions, as well as promote well-behaved low-spin species (**Figure 1A**). Despite recent progress,<sup>55-57</sup> use of ligand frameworks composed of alternative biomimetic donors such as sulfur or oxygen in lieu of phosphorus is

underdeveloped. To fully realize the potential of 3d-metal catalysts as a sustainable synthetic solution, greater effort must be placed on the development of readily available and inexpensive ligands. This cannot, however, come at the sacrifice of catalyst performance, and as such, more emphasis should also be placed on studying the reaction patterns of these alternative ligand donors to allow for optimal catalyst design. Overall, the expansion of bifunctional Lewis base donors beyond nitrogen is lacking,<sup>58-59</sup> and recent work has aimed to use alternatives (thiolates, carbenes, alkoxides).<sup>60-62</sup> While the use of bifunctional thiolate donors for MLC is well known with Ru<sup>63</sup> and Ir,<sup>64</sup> their well-defined use with first-row metal catalysts is limited to a few examples with Fe and Ni.<sup>65-69</sup>

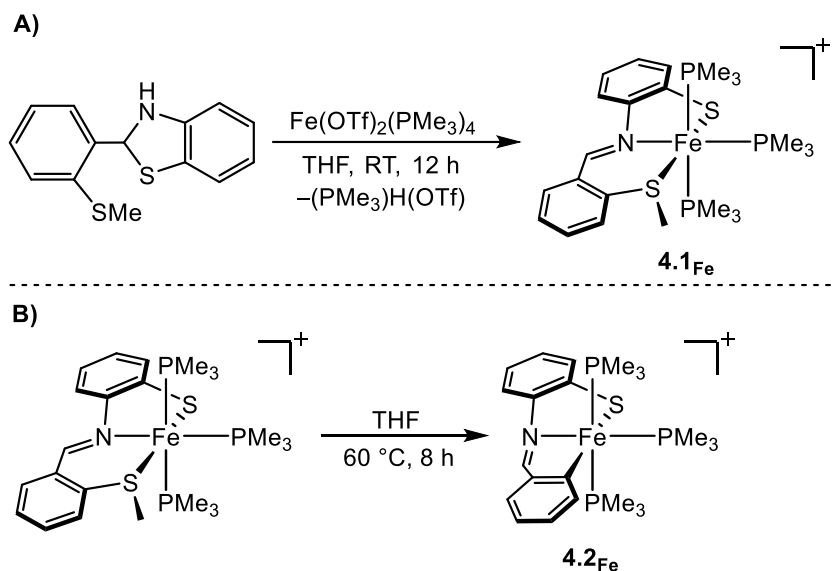
We sought to design base-metal catalysts that leverage metal-ligand cooperation with simple and economical biomimetic SNS ligands. Two bifunctional [SNS] pincer ligands have been previously detailed, differentiated by either an amido or a thiolate Lewis base donor.<sup>70-71</sup> Work presented in Chapter 3 with a Mn(S<sup>Me</sup>NS<sup>Me</sup>)<sub>2</sub> complex featuring bifunctional amido donors highlighted a new carbonyl hydroboration pathway enabled by the SNS motif that does not proceed through the traditional metal-hydride intermediate.<sup>72</sup> Bifunctional catalysis by our SNS ligands has previously been limited to carbonyl substrates, and attempts to reduce alkenes or esters have been limited by thermal instability. The reduction of more difficult substrates, such as nitriles, would be an ideal advancement of our class of complexes, however, alternate reaction pathways must be considered to overcome the intrinsic limitations of phosphine-free SNS-pincers. The dihydroboration of nitriles is an effective strategy to access synthetically valuable *N,N*-diborylamine precursors.<sup>73</sup> The Fout<sup>74</sup> and Trovitch<sup>75</sup> groups have both reported cobalt catalysts for this transformation which operate via the intermediacy of a cobalt-hydride. Trovitch and co-

workers have also reported a novel bifunctional Co-catalyst featuring a pentadentate ligand for the ambient temperature dihydroboration of nitriles with 1% loadings.<sup>29</sup> There is only one report of a Mn-catalyst for this reaction,<sup>76</sup> which also made use of a metal-hydride insertion pathway. This chapter details a Mn(I)-SNS catalyst which undergoes spin-state changes and makes use of a flexible ligand framework and a bifunctional thiolate donor for the dihydroboration of nitriles. Detailed experimental and computational mechanistic studies further illuminate the mechanistic ramifications of straying from traditional phosphine ligands.

## 4.2 Results and Discussion

### 4.2.1 Design of mono-ligated Fe-SNS-thiolate complexes

Previous work by the Baker group showed that Fe(S<sup>Me</sup>NS)[P(OMe)<sub>3</sub>]<sub>3</sub>(OTf) could be obtained in moderate yield from the trinuclear precursor using chlorinated solvents.<sup>70</sup> Unfortunately, attempts to prepare electron-rich analogues via this route gave mixtures of mono- and dinuclear products. To specifically target mononuclear complexes for catalysis, 1 equiv. of **L2<sup>H</sup>** was added to *in situ* generated [Fe(PMe<sub>3</sub>)<sub>4</sub>(OTf)]<sub>2</sub> to give the diamagnetic, cationic iron complex Fe[κ<sup>3</sup>-SNS<sup>Me</sup>](PMe<sub>3</sub>)<sub>3</sub> (**4.1<sub>Fe</sub>**) (**Scheme 4.1**). The lability of the PMe<sub>3</sub> donors in **4.1<sub>Fe</sub>** was demonstrated by <sup>31</sup>P NMR spectroscopy and ligand substitution reactions with P(OMe)<sub>3</sub>, CN<sub>x</sub>yl<sub>y</sub>l, and dmpe (dmpe = 1,2-bis(dimethylphosphino)ethane). Most interestingly however, was the observation of C–S<sub>aryl</sub> bond cleavage upon thermolysis of **4.1<sub>Fe</sub>** to furnish trivalent Fe[κ<sup>3</sup>-CNS](PMe<sub>3</sub>)<sub>3</sub> (**4.2<sub>Fe</sub>**), featuring a new aryl–imine–thiolate pincer ligand framework.



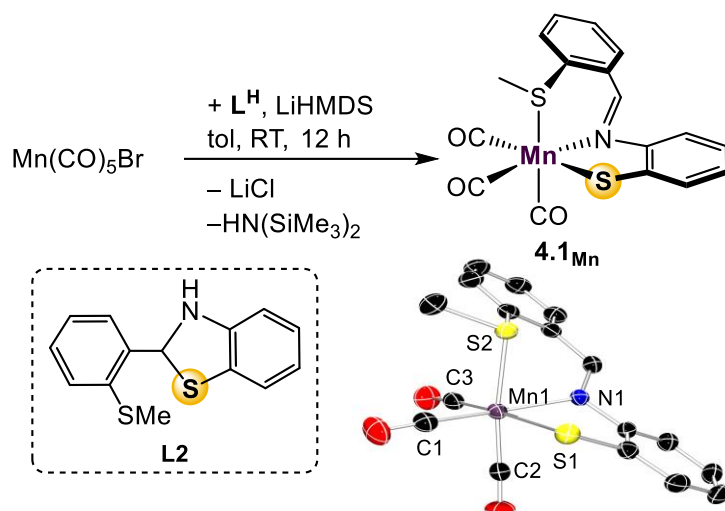
**Scheme 4.1.** Syntheses of ( $4.1_{Fe}$ ) and ( $4.2_{Fe}$ ).

Although Ni-mediated thioether C–S bond cleavage in a similar  $S^{t-Bu}NS$  ligand was observed previously by Bouwman and co-workers, the broken bond in their case was between the S and its  $^tBu$  substituent to yield a second Ni-thiolate linkage presumably by release of 2-methylpropene.<sup>77</sup> Thus, Fe-mediated cleavage of the  $C_{aryl}-S$  bond in **L2** was unexpected. While examples of C–S bond oxidative addition have been reported previously,<sup>78-80</sup> the reluctance of iron to access the tetravalent oxidation state leads presumably to formation of the  $\bullet SMe$  radical.<sup>47</sup> The electron-rich Fe(II) center likely transfers an electron to the C–S anti-bonding orbital, inducing C–S bond homolysis and Fe–C bond formation. However, rather than simply dimerizing to form dimethyl disulphide, evidence was obtained for formation of trimethylphosphine sulfide  $S=PMe_3$  (Figure C23 in Appendix C). This suggests that dissociation of  $PMe_3$  in solution is likely a key feature of the  $C_{aryl}-S$  bond cleavage and coincides with the modest 65 % yield. Carrying out the reaction with excess  $PMe_3$ , however, did not improve the yield of  $4.2_{Fe}$ . Attempts to use radical traps such as anthracene, TEMPO [(2,2,6,6-tetramethylpiperidinyl-

1-yl)oxyl], or DMPO (5,5-dimethyl-1-pyrroline-N-oxide) to trap the •SMe radical also proved unsuccessful and we were unable to ascertain the fate of the methyl group. Attempts to perform C-S<sub>aryl</sub> bond cleavage in equally electron-rich complex Fe[κ<sup>3</sup>-SNS<sup>Me</sup>](PMe<sub>3</sub>)(dmpe) did not result in the analogous Fe-CNS products. This suggests that both labile and strongly electron-donating ancillary ligands are necessary for the cleavage of the C-S<sub>aryl</sub> bond and decomposition of the original ligand framework.

#### 4.2.2 Synthesis of manganese complex

To avoid the deleterious C-S<sub>aryl</sub> bond cleavage observed in Fe complexes during the design of a mono-ligated Mn-[SNS] complex, we prepared the tricarbonyl complex. The reaction of Mn(CO)<sub>5</sub>Br with one equiv. of **L2<sup>H</sup>** and LiHMDS in toluene afforded the Mn[κ<sup>3</sup>-SNS<sup>Me</sup>][CO]<sub>3</sub> complex **4.1<sub>Mn</sub>** in 91% yield (**Scheme 4.2**). The thioether protons in the <sup>1</sup>H NMR spectrum show as a broadened singlet, suggesting hemilability of the thioether in solution. Observation of free CO in the <sup>13</sup>C{<sup>1</sup>H} NMR spectrum indicates lability of the ancillary carbonyl ligands as well, and UV-Vis absorptions at 240 and 290 nm indicate that CO ligands may be labilized upon UV irradiation, potentially offering multiple opportunities to enter a catalytic cycle. Single crystal X-ray diffraction analysis revealed the expected octahedral geometry about Mn; however, the [SNS<sup>Me</sup>] ligand is arranged in a *facial* manner. This is the first instance of this [SNS] ligand adopting this coordination pattern, suggesting potential for **L2** to demonstrate coordinative fluxionality between *fac*- and *mer*- isomers that could also play a role in a catalytic cycle.



**Scheme 4.2.** Synthesis and molecular depiction of **4.1<sub>Mn</sub>**. Thermal ellipsoids are set at 50% probability and hydrogen atoms are omitted for clarity. Selected bond lengths (Å): Mn–N 2.0587(16), Mn–S(1) 2.3898(6), Mn–S(2) 2.3592(6), Mn–C(1) 1.797(2), Mn–C(2) 1.802(2), Mn–C(3) 1.805(2).

### 4.2.3 Catalytic nitrile dihydroboration

To initially examine the bifunctional activity of the thiolate donor in **4.1<sub>Mn</sub>**, its affinity to perform a traditional bifunctional B–H activation was tested. The stoichiometric reaction of **4.1<sub>Mn</sub>** and HBpin in  $CD_3CN$  resulted in no color change, and  $^1H$  NMR analysis revealed no reaction. Heating the reaction mixture to 80 °C led to decomposition, as evidenced by observation of free **L2** in solution. Alternatively, upon irradiation with UV-light, a color change was observed from dark burgundy to light yellow. The crude  $^{11}B$  NMR spectrum displayed a very broad signal at 24 ppm, diagnostic of a B–N species, and further analysis of the  $^1H$  NMR spectrum revealed signals indicative of the dihydroboration of the acetonitrile- $d_3$  solvent.

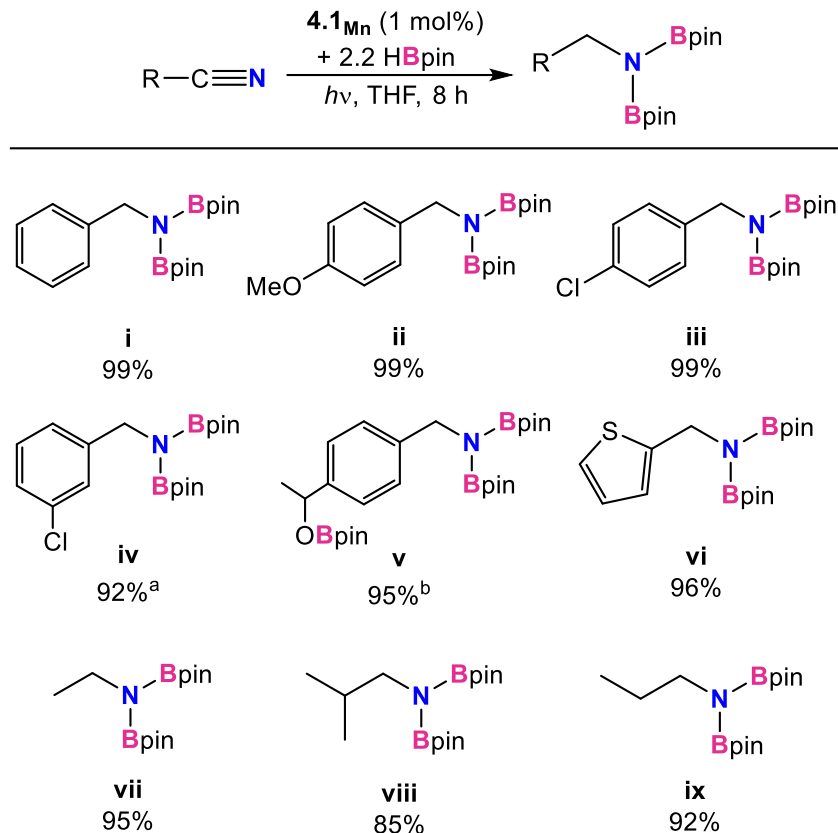
To investigate the potential of this system for nitrile dihydroboration, the reaction conditions were optimized with benzonitrile as the model substrate, and 2.2 equiv. of HBpin to ensure complete reduction (**Table 4.1**). Attempts to thermally facilitate the dihydroboration of benzonitrile were unsuccessful (*Entry 1*); only upon UV-irradiation of the reaction mixture was product formation observed. While **4.1Mn** is most soluble in acetonitrile, performing the dihydroboration of benzonitrile in this solvent expectedly results in the reduction of both benzo- and acetonitrile (*Entry 2*). Reaction in either benzene- $d_6$  or toluene- $d_8$  did not yield satisfactory conversion (*Entries 3, 4*). Reaction in THF afforded complete conversion to the dihydroboration product in reasonable time frames with as little as 1 mol% **4.1Mn** (*Entries 4, 5*). Further control reactions were performed to ensure that the presence of **4.1Mn** was crucial to a successful reaction (see section 4.4.3). Evaluating the optimized reaction conditions makes it clear that the rate is influenced by the presence of polar, coordinative solvents, suggesting a solvent-stabilized intermediate may be involved in the reaction pathway.

**Table 4.1** Optimization of reaction conditions.

Entry	mol % <b>1</b>	Temp. (°C)	$h\nu$	Solvent	Time (h)	% Conv.
1	5	80	✗	MeCN	18	0
2	5	25	✓	MeCN	18	60
3	5	25	✓	$C_6D_6$	18	54
4	5	25	✓	tol.	18	62
5	1	25	✓	THF	2	>99
6	1	25	✓	THF	6	>99

Under the optimized conditions, additional substrates for the nitrile dihydroboration reaction were investigated (**Table 4.2**). Greater than 90% yields were observed for most substrates, and isolated products were obtained from hexane recrystallization. Substitution of the benzonitrile did not significantly hinder catalysis with either electron-donating or -withdrawing groups (*ii*, *iii*) as well as heterocycles (*vi*). A functional group in more sterically compromising positions hindered catalysis, with 3-chlorobenzene requiring a 2.5% catalyst loading to reach 90% yields (*iv*). For *p*-acetyl-benzonitrile, addition of 3.3 equiv. of HBpin afforded the trihydroborated product (*v*), efficiently reducing both the carbonyl and nitrile functionalities. Using 1 equiv. of HBpin with the same substrate afforded the ketone hydroboration product exclusively in 5 min without the need for irradiation. While it was not unexpected for **4.1Mn** to be an active catalyst for carbonyl hydroboration, this reaction occurs thermally at room temperature, indicating it likely follows an alternative pathway from nitrile reduction. Finally, aliphatic nitriles were also studied (*vii-ix*), and it was found that acetonitrile, propionitrile, and isobutylnitrile were all successfully converted, albeit in slightly poorer yields than aromatic substrates. Aromatic substrates containing alkenes were also examined, however, high catalyst loadings and incomplete conversions (30–60%) deterred further investigation (see section 4.4.3).

**Table 4.2.** Catalytic nitrile dihydroboration with **4.1Mn**.



Reaction conditions: nitrile (0.16 mmol), HBpin (0.34 mmol), **4.1Mn** (1 mol%), THF (0.6 g) at room temperature with irradiation from UV-lamp for 2-8 h. <sup>a</sup> Conducted with 2.5 % loading of **4.1Mn**. <sup>b</sup> Conducted with 3.3 equiv of HBpin. Yields were determined from <sup>1</sup>H NMR integrals with respect to internal standard mesitylene after workup.

## 4.2.4 Mechanistic studies of Mn-catalyzed nitrile dihydroboration

### 4.2.4.1 Photoexcitation and carbonyl ligand dissociation

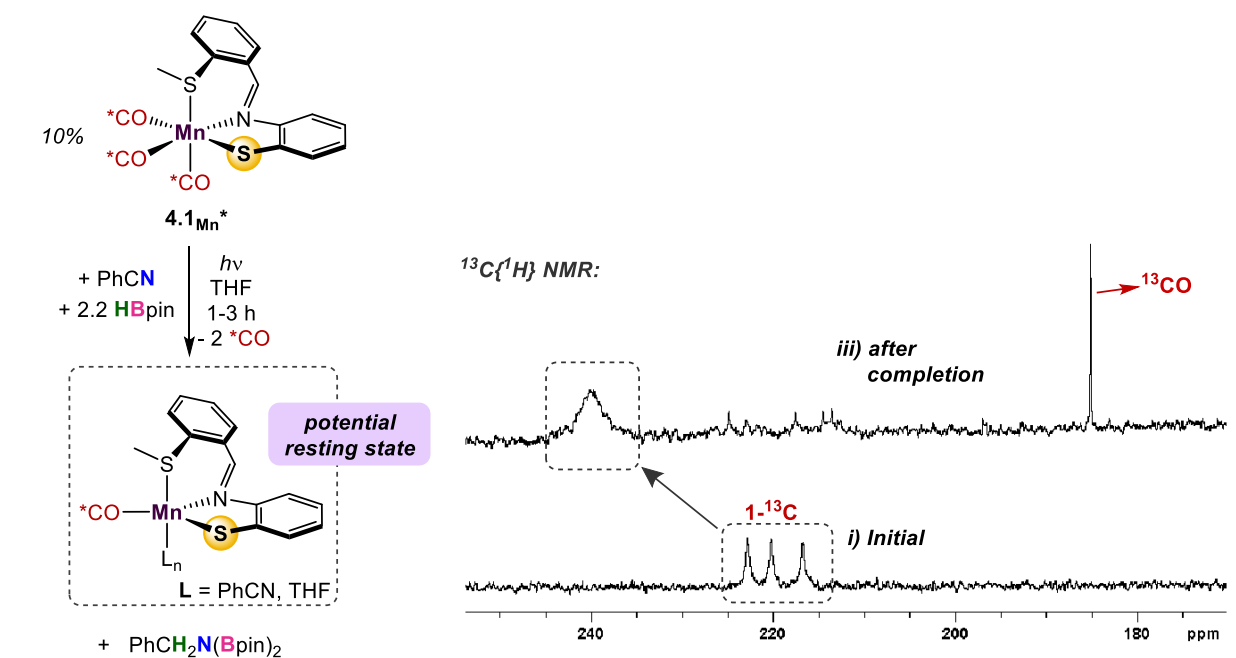
The metal-pincer complex decorated with CO ligands is a widely used catalyst platform,<sup>81-83</sup> however, many of these complexes use phosphine-based pincers and rely on elevated temperatures to kinetically access respective reaction pathways. Despite the rich history of catalysis using photoinduced CO dissociation,<sup>84-88</sup> use of UV irradiation in systems which use an MLC platform is seldom seen. This may give a potentially

advantageous way to access alternative reaction pathways involving open-shell intermediates. To further evaluate the capacity of UV-light in this system and understand the role of the bifunctional thiolate donor, a series of mechanistic experiments were performed. Initially, two parallel reaction mixtures of catalytic **4.1Mn** with benzonitrile and 2.2 equiv of HBpin were irradiated until the color change and product formation was observed. This was done to discern whether catalysis is photo-catalyzed, or photo-initiated. Subsequently, one of the samples was continually irradiated for a further 4 h, while the other was kept in the dark. Comparison of the two mixtures showed that the irradiated reaction went to completion, while catalysis in the “dark” mixture was halted, implying that the persistent presence of light is needed to complete the catalytic cycle.

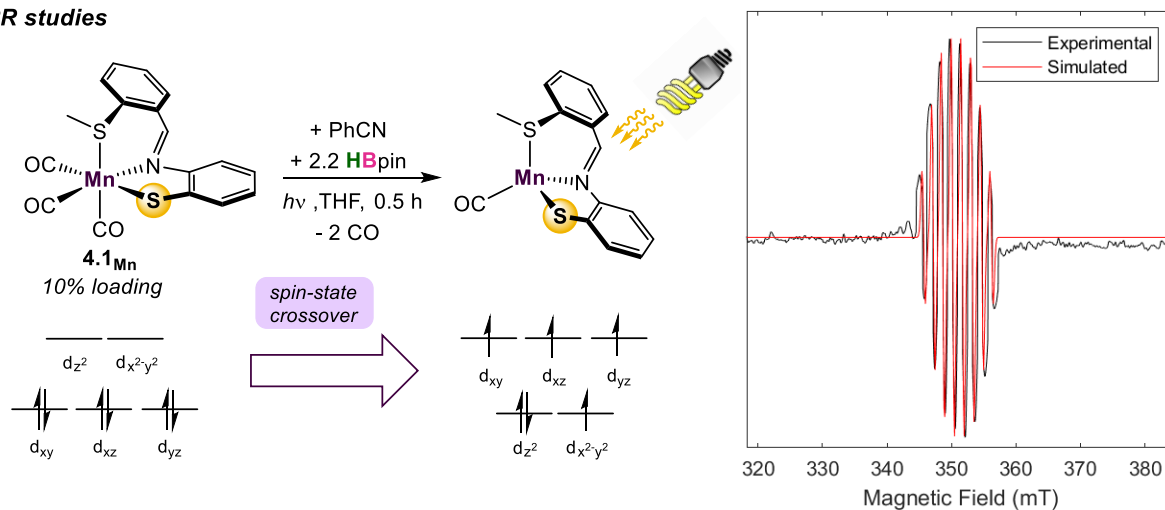
As catalysis is initiated upon UV-irradiation, it is likely that dissociation of labile CO ligand(s) is the initial step, providing a vacant coordination site for substrate/solvent coordination. To gain insight into the number of CO ligands coordinated in the resting state of the catalyst,  $^{13}\text{C}$ -labeling studies were performed. The reaction of 2.2 equiv. of HBpin and 1 equiv. benzonitrile with a 10% loading of  $^{13}\text{C}$ -labelled **4.1Mn**<sup>\*</sup> was monitored periodically by  $^{13}\text{C}\{^1\text{H}\}$  NMR (**Scheme 4.3A**). The initial spectrum of **4.1Mn**<sup>\*</sup> shows three distinct peaks in the M–CO region at 216, 220, and 222 ppm. Irradiation of the reaction mixture for 45 min initiated the expected color change and onset of catalysis. Observation of the crude  $^{13}\text{C}$  NMR spectrum showed the disappearance of the three initial Mn– $^{13}\text{CO}$  signals and the emergence of a new broadened and potentially paramagnetic signal at 240 ppm. This single peak is indicative of either a single bound  $^{13}\text{CO}$ , or a highly symmetric intermediate with multiple coordinated  $^{13}\text{CO}$ 's. Since the asymmetric nature of **L** likely precludes a high-symmetry environment, a resting state containing a single coordinated

CO ligand is most likely. The signal at 240 ppm persisted throughout the reaction and remained upon completion. Furthermore, observation of a new signal at 184 ppm during catalysis was indicative of free  $^{13}CO$  in solution.

A)  $^{13}C$ -labelling studies



B) EPR studies



Scheme 4.3. Spectroscopic and isotope-labeling experiments with  $4.1_{Mn}$

Time-dependent density functional theory (TD-DFT) was employed to probe the photoexcitation. Geometry optimization and TD-DFT were carried out at the B3LYP-D3/6-31G\*\*, LACVP level of theory. In accordance with  $^{13}\text{C}$ -labeling studies, a transition to a metal-CO antibonding orbital was observed around 5.06 eV, supporting the dissociation of two CO ligands. Natural transition orbitals (NTOs) corresponding to the major transition from metal- and ligand-based orbitals to an orbital comprising an out-of-phase combination between metal and two COs are depicted in **Figure 4.1**. With the dissociation of two strong-field carbonyl ligands, the  $d^6$  Mn center may gain access to a high-spin configuration with a single bound CO, as suggested by the  $^{13}\text{C}$  NMR. DFT investigation into intermediates containing a single carbonyl ligand consistently showed that a high-spin quartet ground state is energetically favored over the low-spin singlet state. EPR studies were performed to experimentally probe this result. Initially, an isotropic EPR spectrum of a solution of HBpin, benzonitrile, and catalytic **4.1Mn** gave no signal. Upon irradiation of light for 45 min, however, the isotropic EPR spectrum yielded a multiplet which, after spectral simulation, is attributed to hyperfine coupling between  $^{55}\text{Mn}$  and  $^{14}\text{N}$  (**Scheme 4.3B**). This emergence of a paramagnetic signal supports the initial DFT results which indicate that upon photoactivation, the Mn center preferentially adopts a high-spin state for further reaction.

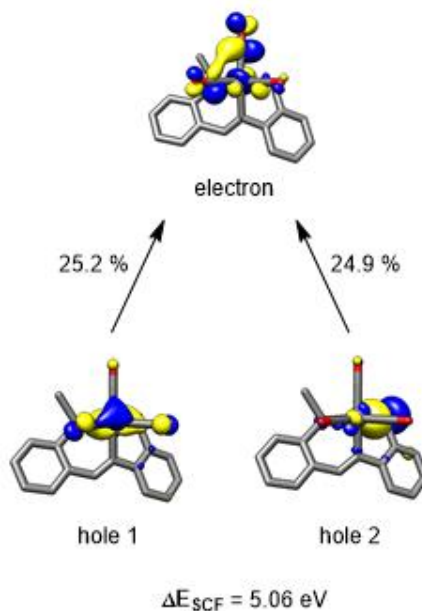
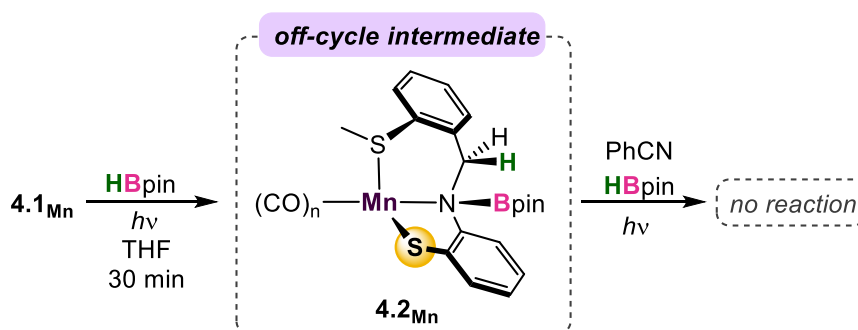


**Figure 4.1.** NTO pairs for the excitation responsible for CO dissociation. The top two contributing transitions are described. Other contributions each contribute to less than 15%.

#### 4.2.4.2 Catalytic cycle for nitrile dihydroboration

To probe the initial steps associated with the dihydroboration, a stoichiometric solution of **4.1<sub>Mn</sub>** and HBpin in THF- $d_8$  was irradiated with UV-light in the absence of nitrile, giving a color change from dark yellow to red.<sup>89</sup> The resultant  $^1H$  NMR spectrum showed the disappearance of original peaks associated with **4.1<sub>Mn</sub>** and emergence of a new species (Figure 4.4 in section 4.4.4). Specifically, disappearance of the imine  $C-H$  resonance at  $\delta$  8.81 paired with the growth of a new singlet at  $\delta$  4.85 was diagnostic for borylation of the  $C-N$  imine unit forming **4.2<sub>Mn</sub>** (Scheme 4.4). While a small resonance was observed in the hydride region ( $\delta$  -8.59), it was not of sufficient intensity to be considered as a viable reaction intermediate similar to previous work by Leitner.<sup>15</sup> Given the literature precedence for imine hydroboration<sup>90-92</sup> in addition to a previous report of activity of a ligand backbone for  $H_2$  activation,<sup>93</sup> the observed hydroboration of the imine backbone in the  $S^{Me}NS$  ligand

is not unexpected. It is of note, however, that this intermediate is preferentially formed over a Mn–H resulting from traditional bifunctional B–H activation by 41.2 kcal/mol (**Figure 4.7**). This is likely due to the absence of phosphine donors which make the Mn more amenable to stabilizing a hydride. To further investigate the species **4.2<sub>Mn</sub>** as a catalytic intermediate, 1 equiv. of benzonitrile and an additional equiv. of HBpin were added to the reaction mixture, however, no product conversion was observed upon heating or irradiation. The lack of reactivity of **4.2<sub>Mn</sub>** suggests it is either an off-cycle thermodynamic sink, or an unproductive species that does not form under catalytic conditions. Indeed, density functional theory (DFT) results showed this intermediate is largely exergonic by –17.1 kcal/mol, corresponding to the thermodynamic sink. This suggests that the initial presence of both HBpin and nitrile are required in solution to enter the productive catalytic cycle.



**Scheme 4.4** Off-pathway intermediate with absence of nitrile

With the challenges presented with monitoring the reaction in real-time, DFT calculations on the overall mechanism were carried out at the B3LYP-D3/cc-pVTZ(-f)/LACV3P//B3LYP-D3/6-31G\*\*/LACVP level of theory<sup>94-101</sup> with a self-consistent reaction field ( $\epsilon = 7.6$  for THF) approach for solvation.<sup>102</sup> Initial photoactivation and carbonyl dissociation forms **2** which undergoes a spin-state change to adopt the high-spin

conformer which is 26.8 kcal/mol more stable than the low-spin (**Figure 4.2**). Coordination of solvent THF to form the resting state **3** is followed by nitrile coordination to the metal center, leading to a stable intermediate **4**. Experimental results eliminated the possibility of the traditional formation of a Mn–H, and instead HBpin coordinates to the bifunctional thiolate sulfur which allows for direct hydride transfer to the coordinated nitrile through **4-TS** to form **5**. An alternate pathway featuring direct coordination of HBpin in lieu of solvent to form a Mn–S–B–O metallacycle was also considered, similar to previous work (**Figure 4.8**). This pathway has a barrier of 37.2 kcal/mol and reflects the penalty of forming a sterically hindered 4-membered metallacycle, indicating that a solvent molecule should be incorporated. This first hydride transfer through **4-TS** represents the turnover limiting step with a 31.1 kcal/mol barrier. Substitution of THF with a barely coordinating solvent, benzene, gives a greater hydride transfer barrier of 34.0 kcal/mol which coincides well with the observed reaction conversions in **Table 4.1** (**Figure 4.9**). Closer inspection of the hydride transfer in **4-TS** shows a transient amido species is generated, with the CO ligand *trans* to the anionic amide moiety to electronically stabilize the transition state as in structure **5**. For the *trans* influence to successfully stabilize the intermediate, the SNS ligand must be arranged in a *mer*-configuration. Indeed, comparison between *mer*- and *fac*-conformations shows the former is favored by 7.61 kcal/mol, indicating that the coordinative flexibility of the SNS ligand is crucial for rearrangement to the lowest energy conformer (**Figure 4.10**). The resulting intermediate **5** then undergoes sequential Bpin transfer to generate a monoboryl imine in **6** and complete the first reduction cycle. Traversing a similar pathway operating by sequential hydride and Bpin transfer, the second

reduction cycle furnishes intermediate **8**. Finally, product diborylamine is released, as depicted in the proposed full mechanism for both reduction cycles (**Figure 4.3**).

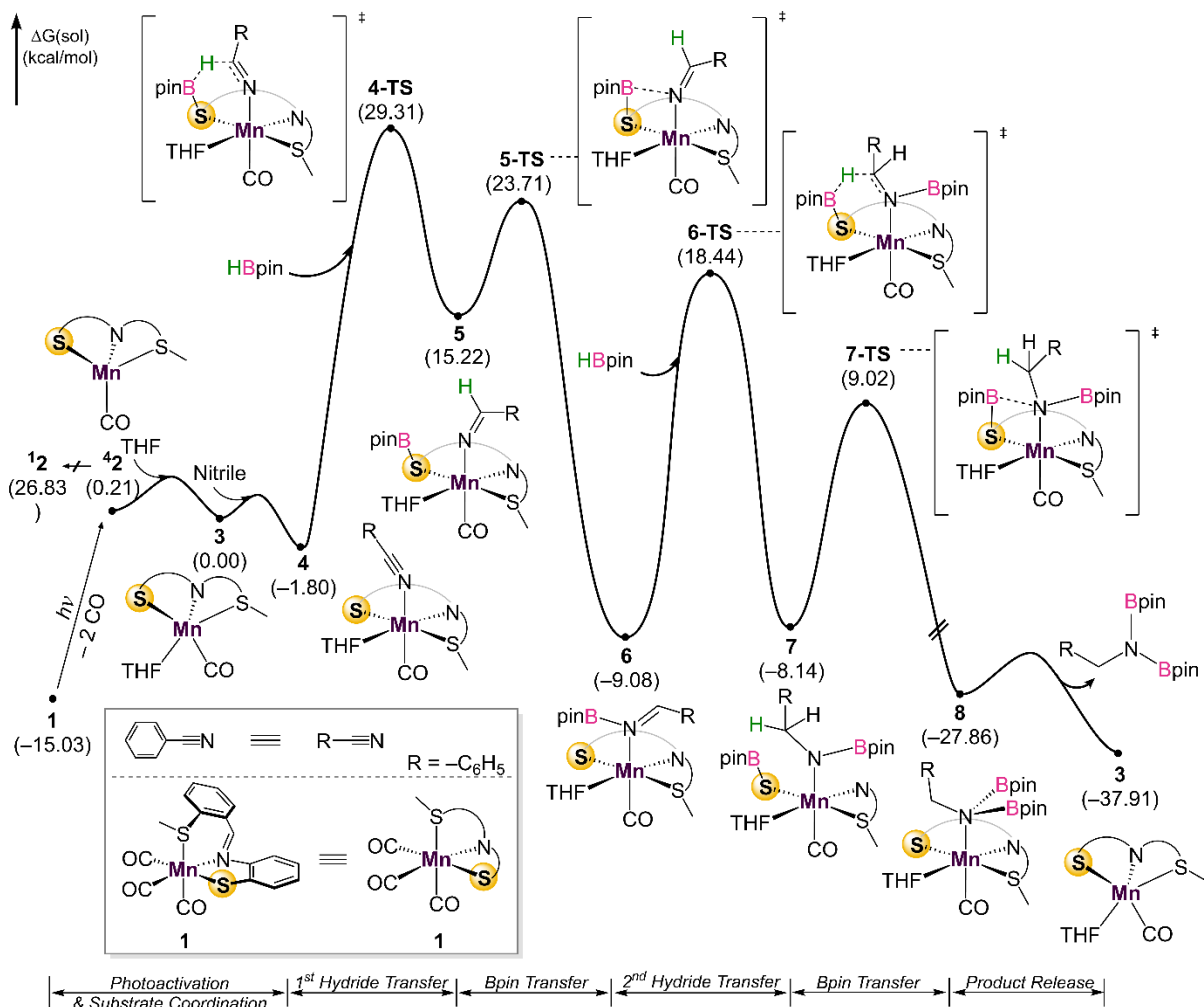


**Figure 4.2.** DFT-calculated energy profile for the dihydroboration of benzonitrile with catalyst **4.1<sub>Mn</sub>**.

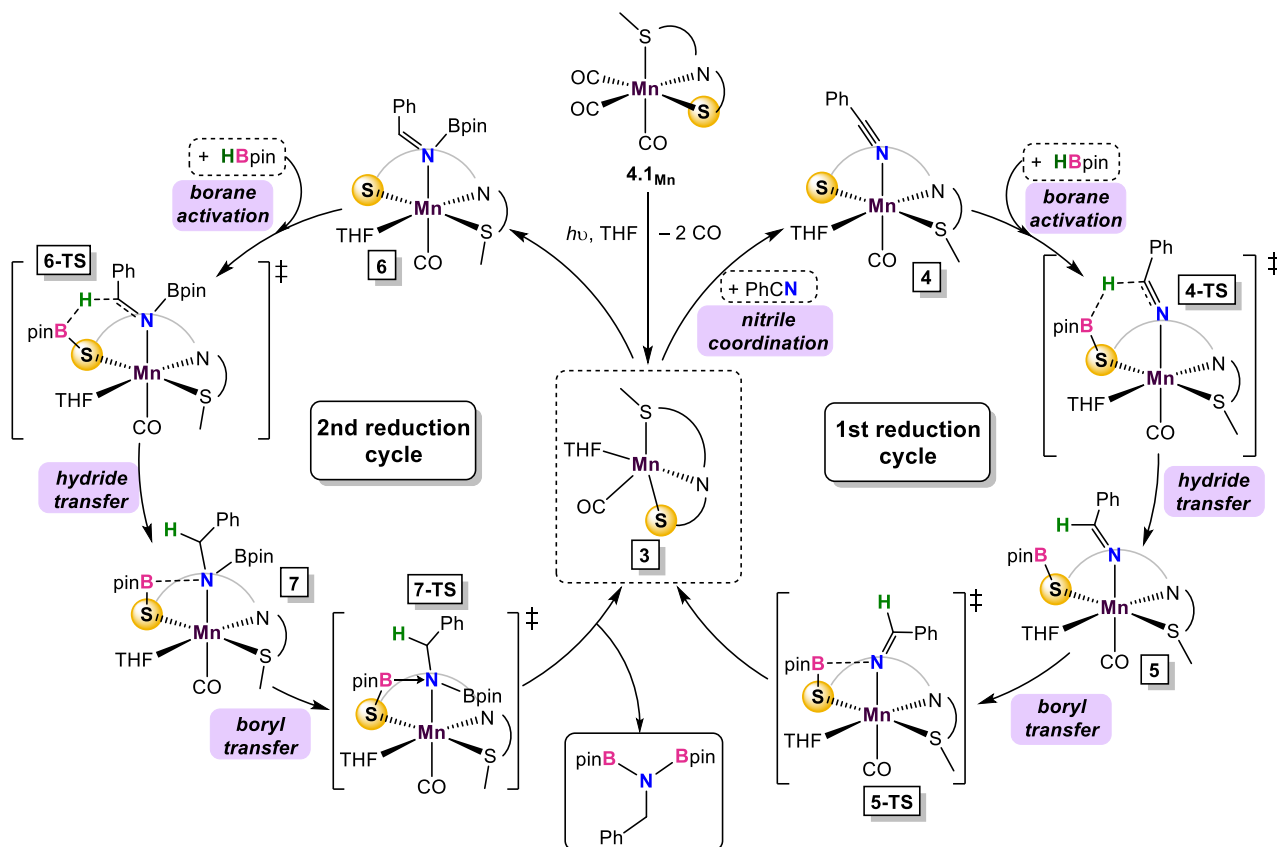


**Figure 4.3.** Summary of the catalytic cycle for the photodissociation and two borylation steps involved in the reaction.

### 4.3 Conclusions

Catalytic nitrile dihydroboration has been reported in systems using Mo,<sup>103</sup> Th,<sup>104</sup> Zn,<sup>105</sup> Mg,<sup>106</sup> and Ru<sup>91,107</sup> catalysts with catalyst loadings between 1 and 10% and temperatures between 22 and 80 °C. Previous reports of this reaction with base metals are limited to examples with Ni,<sup>108</sup> and work by the Fout and Trovitch groups using Co<sup>74,75</sup>, and Mn.<sup>76</sup> In this work a Mn(I) complex featuring a SNS-thiolate ligand was prepared to study the potential bifunctional activity of less studied thiolate donors. The Mn( $\kappa^3$ -SNS<sup>Me</sup>)(CO)<sub>3</sub> complex (**4.1<sub>Mn</sub>**) was demonstrated to be effective for photo-catalytic nitrile dihydroboration at room temperature with 1 mol% loading. <sup>13</sup>C-labeling studies revealed a catalyst resting state featuring one coordinated CO ligand which corresponds with TD-DFT

calculations.<sup>d</sup> EPR studies combined with DFT calculations indicate that the Mn-center undergoes a spin state change to preferentially adopt the high-spin configuration during catalysis. This feature is a benefit of first-row metals,<sup>10</sup> whereby embracing the electronic flexibility of the metal allows for access to lower energy intermediates. Corroborated by the experimental mechanistic studies and calculations, the catalytically active species incorporating a single CO ligand is formed under UV light, and upon traversing two reduction cycles, diborylamine is released as the product (**Figure 4.3**). The bifunctional  $S^{Me}NS$  ligand is crucial to the success of the reaction in two aspects: *i*) the bifunctional thiolate donor for participation in MLC when activating and transferring the Bpin (**5** and **5-TS** in **Figure 4.3**), and *ii*) the coordinative flexibility of the  $SNS^{Me}$  ligand enables facile rearrangement between *fac*- and *mer*-isomers which is integral to stabilization of the turnover limiting hydride transfer step (**4-TS** in **Figure 4.3**). Presence of a coordinative solvent THF in lieu of non-coordinating solvent was determined to be crucial for access to the sterically-relaxed transition state mitigating the need to form a sterically disfavored metallacycle intermediate. In the context of catalytic transformations which use metal-ligand cooperation, the predominantly suggested reaction pathway features a metal-hydride intermediate to allow for either outer-sphere hydride transfer or inner-sphere insertion.<sup>13,15</sup> This traditional reaction pathway is highly disfavored, instead preferring direct inner-sphere hydride transfer to the substrate upon Bpin activation by the bifunctional thiolate donor. Whereas previous work operating under a similar mechanism featured a bifunctional amido,<sup>72</sup> this work uses a thiolate donor. This shows that the reaction pathway

---

<sup>d</sup> It should be noted that the species observed according to <sup>13</sup>C labelling studies and EPR may not be the true resting state, however, DFT calculations on multiple permutations of intermediates showed species **3** to be the lowest in energy.

does not discriminate on the chosen bifunctional donor; it is instead likely a consequence of the weaker donors on the SNS<sup>Me</sup> ligand. Therefore, the SNS ligand not only participates in MLC with manganese, but it also enables the traversal of a non-traditional MLC pathway.

The use of synthetically simple and economical ligands comprised of biomimetic donors is vital to meet the growing demand for more sustainable catalyst options. The combination of a base metal and a thiolate donor in MLC catalysis remains rare,<sup>65-67</sup> and as more phosphine-free ligand variants emerge,<sup>109-111</sup> it will be critical to understand their associated reactivity patterns.

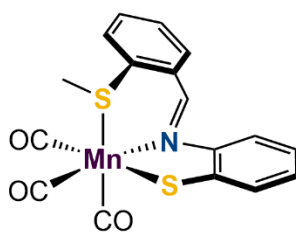
## **4.4 Experimental**

### **4.4.1 Materials and Methods**

Unless otherwise stated, all reactions were carried out under an atmosphere of dry oxygen free dinitrogen by means of standard Schlenk or glovebox techniques. Benzene-d<sub>6</sub> and acetonitrile-d<sub>3</sub> were degassed by three freeze-pump-thaw cycles, and subsequently dried by running through a column of activated alumina. THF-d<sub>8</sub> was run through a small plug of activated alumina before use. Toluene, hexanes, diethyl ether, acetonitrile, and THF were dried on columns of activated alumina using a J. C. Meyer (formerly Glass Contour) solvent purification system and stored over activated 4 Å molecular sieves. <sup>1</sup>H, <sup>13</sup>C{<sup>1</sup>H} , and <sup>11</sup>B NMR spectra were recorded on either a Bruker AvanceII or AvanceIII Spectrometer operating at 300 or 400, and 500 MHz respectively, with respect to proton nuclei. <sup>1</sup>H NMR spectra were referenced to residual protons (C<sub>6</sub>D<sub>6</sub>, δ 7.15), (CD<sub>3</sub>CN, δ 1.96), or (C<sub>4</sub>D<sub>8</sub>O, δ

3.58) with respect to tetramethylsilane at  $\delta$  0.00.  $^{13}C\{^1H\}$  NMR spectra were referenced to relative solvent resonances ( $C_6D_6$ ,  $\delta$  128.26) or ( $CD_3CN$ ,  $\delta$  118.26). EPR spectra were recorded on a Bruker Elexsys E580 X-band spectrometer and were modelled using EasySpin (v 5.25), a package developed by Stoll and Schweiger based on Matlab. Optimized values were searched for the following parameters: the isotropic g value ( $g_{iso}$ ) the zero field splitting parameters (D and E), the hyperfine coupling constants ( $a_{Mn}$  and  $a_N$ ), and the isotropic peak-to-peak line width ( $\Delta B$ ). FT-IR data were collected on a Thermo Scientific Nicolet 6700 spectrometer. All reagents were purchased from commercial suppliers. The  $[SN^H S^{Me}]$  ligand (**L2<sup>H</sup>**) was synthesized according to a literature procedure.<sup>70</sup>

#### 4.4.2 Synthesis and characterization of iron and manganese complexes



**Synthesis of  $[Mn(\kappa^3-SNS^{Me})(CO)_3]$  (**4.1<sub>Mn</sub>**).** A vial equipped with a magnetic stir bar was charged with  $Mn(CO)_5Br$  (0.200 g, 0.730 mmol) and 5 mL toluene. A solution of  $S^{Me}NS^H$  (0.188 g, 0.730 mmol) and lithium(bis(trimethylsilyl)amide) (0.122 g, 0.730 mmol) in 2 mL toluene was added dropwise to the suspension, giving an immediate color change from yellow-orange to reddish-brown. The solution was stirred for 16 h, filtered through celite, and concentrated under vacuum. The residue was washed with  $Et_2O$  (3 x 2 mL), hexane (3 x 2 mL), and dried under vacuum to yield 0.253 g of a red-brown powder (92% yield). Crystals suitable for single crystal x-ray diffraction were obtained from a concentrated acetonitrile solution at  $-30$  °C.  $^1H$  NMR ( $CD_3CN$ , 22 °C, 300.33 MHz):  $\delta$  2.47 (br s, 3H, S- $CH_3$ ); 6.94 (ddd, 1H, Ar- $H$ ,  $^4J_{HH} = 1.46$  Hz,  $^3J_{HH} = 7.29$  Hz,  $^3J_{HH} = 8.64$  Hz); 7.05 (ddd, 1H, Ar- $H$ ,  $^4J_{HH} = 1.36$  Hz,  $^3J_{HH} = 7.23$  Hz,  $^3J_{HH} = 7.74$  Hz); 7.42 (dd, 1H,

Chapter 4 – Avoiding  $C_{aryl}-S$  Bond Cleavage in the Design of a Cooperative Mn(I)-Thiolate Complex for Photo-Catalyzed Nitrile Dihydroboration

Ar-H,  $^4J_{HH} = 1.41$  Hz,  $^3J_{HH} = 7.74$  Hz); 7.49 (dd, 1H, Ar-H,  $^4J_{HH} = 1.41$  Hz,  $^3J_{HH} = 7.94$  Hz); 7.64 (multiplet, 2H, Ar-H); 7.81 (multiplet, 2H, Ar-H); 8.72 (s, 1H, imine-H).  $^{13}C\{^1H\}$  NMR ( $CD_3CN$ , 22 °C, 75.52 MHz):  $\delta$  19.5 (s, S-CH<sub>3</sub>); 110.5 (s, Ar-C); 120.6 (s, Ar-C); 122.4 (s, Ar-C); 126.1 (s, Ar-C); 127.6 (s, Ar-C); 129.1 (s, Ar-C); 131.6 (s, Ar-C); 133.5 (s, Ar-C); 134.9 (s, Ar-C); 151.5 (s, Ar-C); 15.0 (s, Ar-C); 164.3 (s, N=CH); 216.6 (s, Mn-CO); 220.1 (s, Mn-CO); 222.7 (s, Mn-CO). IR (ATM,  $cm^{-1}$ ): 1898, 1922, 2009 (CO). HRMS (ESI-QTOF,  $C_6H_5Cl$ ): calcd for  $C_{17}H_{12}MnNO_3S_2$  m/z 397.9717 ( $[M^+]$ ). Found m/z 397.9736.

**Synthesis of  $[Fe(S^{Me}NS)(PMe_3)_3](OTf)$  (**4.1<sub>Fe</sub>**).** A 250 mL Schlenk flask was charged with 1.00 g of  $Fe(OTf)_2$  (2.8 mmol), 0.73 g of  $[S^{Me}N^H S]$  (**L2**) (2.8 mmol, 1 equiv.) and 60 mL of THF, giving an off-white suspension that was vigorously stirred for 30 min. A dropping funnel was charged with a solution of 2.3 mL  $PMe_3$  (1.7 g, 22.6 mmol, 4 equiv.) in 10 mL of THF and connected to the Schlenk flask. The THF solution of  $PMe_3$  was then added drop-wise to the off-white suspension and the reaction mixture slowly turned dark purple. After stirring overnight at room temperature the solution was filtered through Celite, concentrated and cooled at  $-35^\circ C$  overnight to yield dark purple crystals of **1**. The crystals were recovered by filtration, washed with cold diethyl ether (*ca.*  $3 \times 5$  mL) and THF ( $3 \times 5$  mL) and dried *in vacuo*. Yield after crystallization: 2.5 g, 64% based on  $Fe(OTf)_2$ .  $^1H$  NMR [300 MHz,  $-40^\circ C$ ,  $(CD_3)_2CO$ ]:  $\delta$  1.24 (pseudo tr, 18H, P-CH<sub>3</sub>, 4 Hz), 1.63 (d, 9H, P-CH<sub>3</sub>,  $^2J_{HP} = 10$  Hz), 2.82 (s, 3H, S-CH<sub>3</sub>), 6.97 (br m, 1H, Ar-H), 7.07 (br m, 1H, Ar-H), 7.44 (br m, 1H, Ar-H), 7.71 (ov br m, 2H, Ar-H), 7.90 (br m, 1H, Ar-H), 8.00 (br m, 1H, Ar-H), 8.08 (br m, 1H, Ar-H), 9.61 (br s, 1H, N=C-H).  $^{31}P\{^1H\}$  NMR (121 MHz,

( $CD_3$ ) $_2CO$  at  $-20^\circ C$ ):  $-0.35$  (d, 2P,  $^2J_{PP} = 50$  Hz); 11.1 ppm (tr, 1P). Anal. Calc. for  $C_{24}H_{39}F_3FeNO_3P_3S_3$ : C, 41.68; H, 5.68; N, 2.03; S, 13.91. Found: C, 41.62; H, 5.82; N, 2.03; S, 14.11.

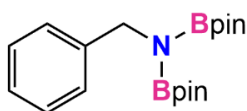
**Synthesis of  $[Fe(CNS)(PMe_3)_3](OTf)$  ( $4.2_{Fe}$ ).** A 50 mL ampoule was charged with 61 mg of complex  $4.1_{Fe}$  (0.09 mmol) and 10 mL of THF yielding a dark purple solution. After heating at  $60^\circ C$  for 8 h the color changed from dark purple to green. THF was then removed under vacuum and the resulting solution was extracted with  $CH_2Cl_2$  (15 ml), filtered and evaporated under vacuum. Finally, the resulting green residue was redissolved in THF (*ca.* 2 mL) and cooled to  $-35^\circ C$  to yield green crystals of  $4.2_{Fe}$  that were recovered by filtration, washed with cold diethyl ether ( $3 \times 2$  mL) and dried *in vacuo*. Yield after crystallization: 44 mg, 65%. Anal. Calc. for  $C_{23}H_{36}F_3FeNO_3P_3S_2$ : C, 42.87; H, 5.63; N, 2.17; S, 9.95. Found: C, 42.88; H, 5.86; N, 2.07; S, 10.53.

#### 4.4.3 Catalytic and mechanistic studies

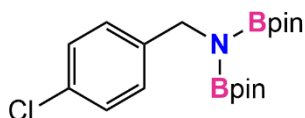
##### General Procedure ‘A’ for Dihydroboration of Nitriles.

A catalyst stock solution was first prepared by dissolving  $4.1_{Mn}$  (10 mg) in  $C_6D_6$  (1 mL). A vial containing  $4.1_{Mn}$  (0.001 g, 100  $\mu L$ , 0.003 mmol, 1 mol%) in 0.6 g of THF was charged first with nitrile substrate (0.32 mmol), and subsequently with 2.2 equiv. pinacolborane (0.090 g, 102  $\mu L$ , 0.70 mmol) to give a dark yellow-brown solution. The solution was charged to an NMR tube, removed from the glovebox, and exposed to a white-light lamp for the appropriate time period. Yield was determined by  $^1H$  NMR in reference to internal standard mesitylene. In the glovebox, volatile materials were removed under

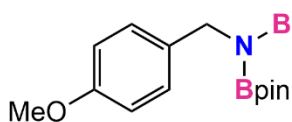
reduced pressure. Hexane was added to extract the product, the solution was filtered through celite, and placed in the freezer at  $-35\text{ }^{\circ}\text{C}$  overnight to afford white crystals.



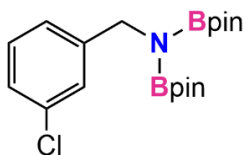
**Dihydroboration of benzonitrile.** Conducted according to *General Procedure A* using benzonitrile (0.032 g, 32  $\mu\text{L}$ , 0.32 mmol), pinacolborane (0.090 g, 102  $\mu\text{L}$ , 0.70 mmol), and catalytic **4.1Mn**. The solution was placed under white light lamp with a cooling fan for 4 h (99% NMR yield).  $^1\text{H}$  NMR shifts matched with literature values.<sup>2</sup>



**Dihydroboration of 4-chlorobenzonitrile.** Conducted according to *General Procedure A* using 4-chlorobenzonitrile (0.044 g, 0.32 mmol), pinacolborane (0.090 g, 102  $\mu\text{L}$ , 0.70 mmol), and catalytic **4.1Mn**. The solution was placed under white light lamp with a cooling fan for 4h (99% NMR yield).  $^1\text{H}$  NMR shifts matched with literature values.<sup>2</sup>

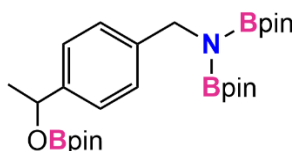


**Dihydroboration of 4-methoxybenzonitrile.** Conducted according to *General Procedure A* using 4-methoxybenzonitrile (0.042 g, 0.32 mmol), pinacolborane (0.090 g, 102  $\mu\text{L}$ , 0.70 mmol), and catalytic **4.1Mn**. The solution was placed under white light lamp with a cooling fan for 4 h (99% NMR yield).  $^1\text{H}$  NMR shifts matched with literature values.<sup>2</sup>



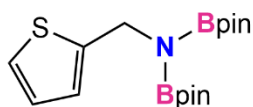
**Dihydroboration of 3-chlorobenzonitrile.** Conducted according to *General Procedure A* using 3-chlorobenzonitrile (0.044 g, 0.32

mmol), pinacolborane (0.090 g, 102  $\mu$ L, 0.70 mmol), and catalytic **4.1Mn**. The solution was placed under white light lamp with a cooling fan for 6 h (92% NMR yield).  $^1H$  NMR shifts matched with literature values.<sup>2</sup>



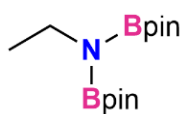
**Trihydroboration of 4-acetylbenzoinitrile.** Conducted according to *General Procedure A* using 3-chlorobenzonitrile (0.044 g, 0.32 mmol), pinacolborane (0.135 g, 153  $\mu$ L, 1.06

mmol, 3.3 equiv), and catalytic **4.1Mn**. The solution was placed under white light lamp with a cooling fan for 5 h (95% NMR yield).  $^1H$  NMR shifts matched with literature values.<sup>2</sup>



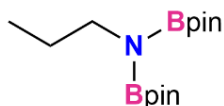
**Dihydroboration of 2-cyanyl-thiophene.** Conducted according to *General Procedure A* using 2-cyanyl-thiophene (0.035 g, 0.32

mmol), pinacolborane (0.090 g, 102  $\mu$ L, 0.70 mmol), and catalytic **4.1Mn**. The solution was placed under white light lamp with a cooling fan for 5 h (96% NMR yield).  $^1H$  NMR shifts matched with literature values.<sup>2</sup>



**Dihydroboration of acetonitrile.** Conducted according to *General Procedure A* using acetonitrile (0.013 g, 17  $\mu$ L, 0.32 mmol), pinacolborane

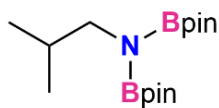
(0.090 g, 102  $\mu$ L, 0.70 mmol), and catalytic **4.1Mn**. The solution was placed under white light lamp with a cooling fan for 8h (95% NMR yield).  $^1H$  NMR shifts matched with literature values.<sup>2</sup>



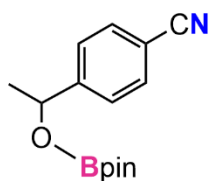
**Dihydroboration of propionitrile.** Conducted according to *General Procedure A* using propionitrile (0.017 g, 22  $\mu$ L, 0.32 mmol),

pinacolborane (0.090 g, 102  $\mu$ L, 0.70 mmol), and catalytic **4.1Mn**. The solution was placed

under white light lamp with a cooling fan for 8 h (92% NMR yield).  $^1H$  NMR shifts matched with literature values.<sup>2</sup>



**Dihydroboration of isobutylnitrile.** Conducted according to *General Procedure A* using isobutylnitrile (0.022 g, 29  $\mu$ L, 0.32 mmol), pinacolborane (0.090 g, 102  $\mu$ L, 0.70 mmol), and catalytic **4.1Mn**. The solution was placed under white light lamp with a cooling fan for 8 h (85% NMR yield).  $^1H$  NMR shifts matched with literature values.<sup>2</sup>



**Hydroboration of 4-acetyl benzonitrile.** Conducted according to a modified *General Procedure A* using 4-acetyl benzonitrile (0.022 g, 29  $\mu$ L, 0.32 mmol), pinacolborane (0.090 g, 102  $\mu$ L, 0.70 mmol), and catalytic **4.1Mn**. The solution was placed under white light lamp with a cooling fan for 10 min (99% NMR yield).  $^1H$  NMR shifts matched with literature values.<sup>3</sup>

---

## **IV. Mechanistic Studies**

### *Stoichiometric Studies*

**Stoichiometric reaction of 4.1Mn and HBpin.** A dark yellow-brown solution of **4.1Mn** (0.01 g, 0.025 mmol) and HBpin (0.003 g, 3.5  $\mu$ L, 0.025 mmol) in 0.5 mL of THF- $d_8$  was prepared and charged to an NMR tube. The solution was irradiated for 30 minutes which initiated a color change to a dark red-orange. Analysis of the resultant crude  $^1H$  NMR showed new speciation – specifically, the disappearance of the characteristic imine C–H at  $\delta$  8.81, accompanied by the growth of a new singlet at  $\delta$  4.85 indicative of a C–H<sub>2</sub> group. See **Figure 4.4**.

**Attempted stoichiometric dihydroboration.** A dark yellow-brown solution of **4.1<sub>Mn</sub>** (0.01 g, 0.025 mmol) and HBpin (0.003 g, 3.  $\mu$ L, 0.025 mmol) in 0.5 mL of THF was prepared and charged to an NMR tube. The solution was irradiated for 30 minutes which initiated a color change to a dark red-orange, and analysis of the  $^1\text{H}$  NMR confirmed borylation of the imine. Benzonitrile (0.003 g, 3  $\mu$ L, 0.025 mmol) and an additional equivalent of HBpin (0.003 g, 3.5  $\mu$ L, 0.025 mmol) were then added to the reaction mixture, which was subsequently irradiated for an additional 4 h. No color change was seen and formation of nitrile dihydroboration product was not observed.

**Stoichiometric reaction of 4.1<sub>Mn</sub> and benzonitrile.** A dark yellow-brown solution of **4.1<sub>Mn</sub>** (0.01 g, 0.025 mmol) and benzonitrile (0.003 g, 3  $\mu$ L, 0.025 mmol) in 0.5 mL of acetonitrile- $d_3$  was prepared and charged to an NMR tube. The reaction mixture was irradiated for 2 h and no color change was observed and no change in the  $^1\text{H}$  NMR was observed.

### $^{13}\text{C}$ -labelling Studies

**General Preparation of  $^{13}\text{C}$ -labelled  $[\text{Mn}(\kappa^3\text{-SNS}^{Me})(\text{CO})_3]$  (**4.1<sub>Mn</sub>\***).** A solution of **4.1<sub>Mn</sub>** (0.020 g, 0.05 mmol) in 0.6 mL THF was charged to an NMR tube equipped with a rubber septum. The NMR tube was charged with ca. 2 mL of  $^{13}\text{CO}$ , and exposed to a white-light lamp for 30 min.  $^{13}\text{C}\{^1\text{H}\}$  NMR confirmed successful transfer of the  $^{13}\text{CO}$  labels to the Mn complex as indicated by observed signals at 216, 220, and 222 ppm.

**Dihydroboration of benzonitrile catalyzed by 4.1<sub>Mn</sub>\***. A sample of **4.1<sub>Mn</sub>\*** was prepared (0.01 g, 0.025 mmol, 10 mol%) in 0.6 mL THF. Benzonitrile (0.015 g, 12  $\mu$ L, 0.143 mmol)

and HBpin (0.041 g, 46  $\mu$ L, 0.32 mmol, 2.2 equiv) were added to the solution. The NMR tube was exposed to white-light and monitored by  $^{13}\text{C}\{^1\text{H}\}$  NMR every hour until reaction completion. The resulting  $^{13}\text{C}\{^1\text{H}\}$  NMR spectra are shown in **Figure 4.5**.

### EPR Studies

**Observation of paramagnetic intermediate.** A catalytic reaction mixture of benzonitrile, HBpin, and 10% **4.1Mn** was prepared according to *General Procedure A*. An initial EPR spectrum of the mixture afforded no signal. The reaction mixture in the EPR tube was irradiated for 45 minutes and an EPR spectrum was recorded with continuous irradiation in the probe. The resulting EPR spectrum is shown in **Figure 4.6**. The spectrum was modelled with the Easyspin tool in MATLAB as a fit for coupling to  $^{55}\text{Mn}$  and  $^{14}\text{N}$ .

#### 4.4.4 Key spectroscopic data

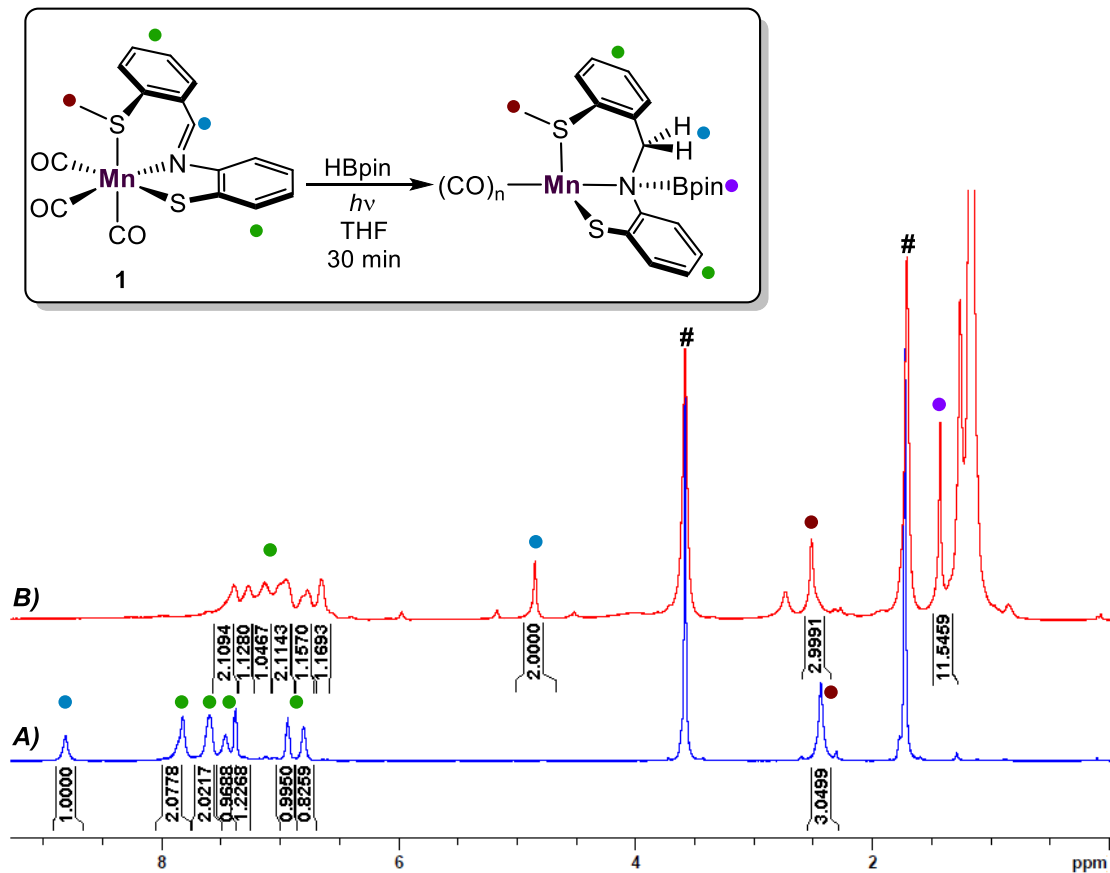


**Figure 4.4.** Stack plot of  $^1H$  spectra showing A) complex **4.1**<sub>Mn</sub> in THF- $d_8$ , and B) reaction of **4.1**<sub>Mn</sub> and 1.2 equiv. HBpin – irradiated for 30 min. # is THF.

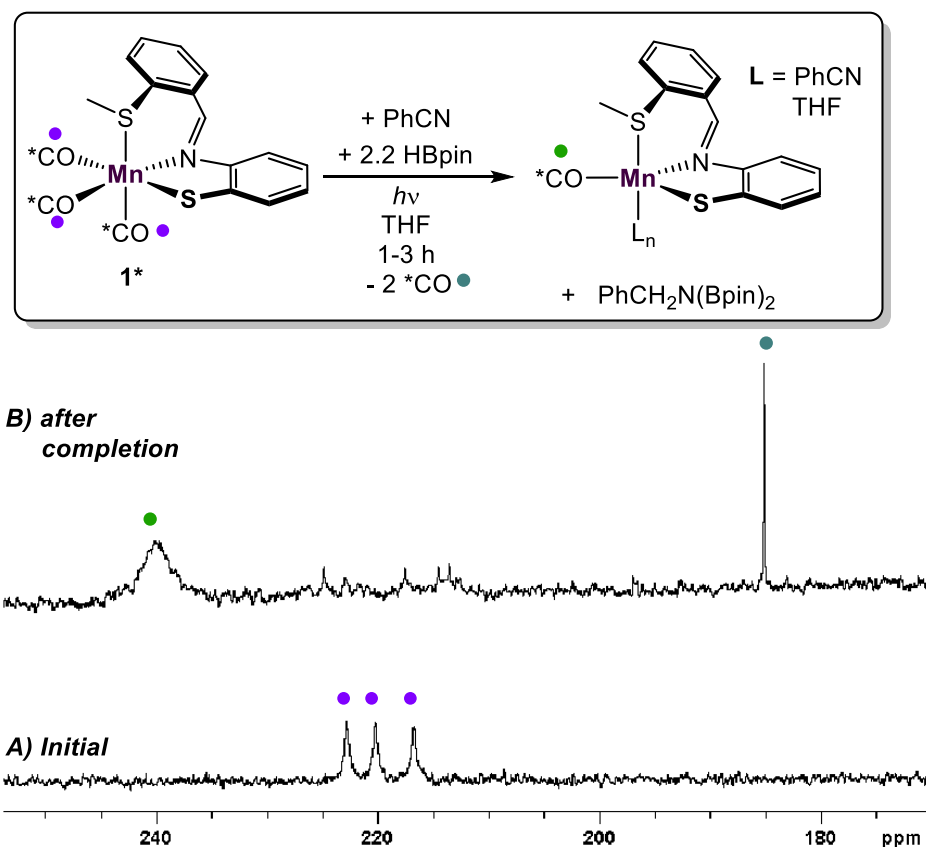


**Figure 4.5.** Stacked plot of  $^{13}\text{C}\{^1\text{H}\}$  spectra showing reaction of 10 mol%  $^{13}\text{C}$ -labelled  $4.1_{\text{Mn}}^*$  with benzonitrile and 2.2 equiv. of HBpin. **(A)** (Blue trace) Initial  $^{13}\text{C}\{^1\text{H}\}$  spectrum of reaction mixture prior to light exposure showing unreacted  $4.1_{\text{Mn}}^*$ . **(B)** (Red trace)  $^{13}\text{C}\{^1\text{H}\}$  spectrum of reaction mixture after shining light for 1 h showing disappearance of  $4.1_{\text{Mn}}^*$  and growth of a new species at 240 ppm. **(C)** (Purple trace)  $^{13}\text{C}\{^1\text{H}\}$  spectrum of reaction mixture after shining light for 3 h total, showing same species at 240 ppm with appearance of free  $^{13}\text{CO}$ .

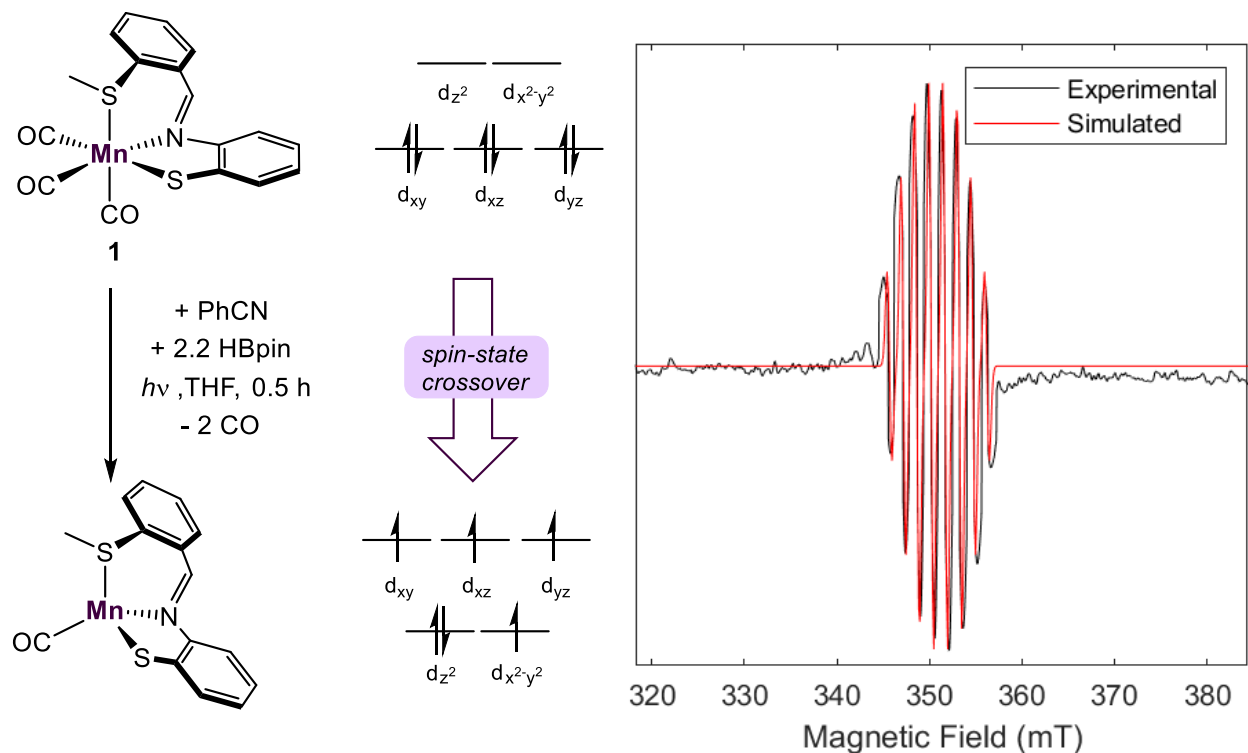


Figure 4.6. 298 K EPR isotropic spectrum of catalytic reaction mixture after irradiation for 45 min.

#### 4.4.5 Single crystal X-ray diffraction data

**\*\*Key crystallographic data can be found in Appendix C.\*\***

The crystals were mounted on thin glass fibers using paraffin oil or cyanoacrylate glue. The crystals of **4.1<sub>Mn</sub>** were cooled to  $200 \pm 2$  K during data collection. The data were collected on a Bruker single-crystal diffractometer equipped with a sealed Mo tube source (wavelength 0.71073 Å) and APEX II CCD detector. The raw data collection and processing were performed with Bruker APEX II software package.<sup>112</sup> Semi-empirical absorption correction based on equivalent reflections were applied.<sup>113</sup> Systematic absences and unit cell parameters were consistent with monoclinic  $P2_1/n$  (#14) for **4.1<sub>Mn</sub>**. The structures were solved by intrinsic phasing and refined with a full-matrix least-squares

procedure based on  $F^2$ , using SHELXL.<sup>114</sup> All non-hydrogen atoms were refined anisotropically. The hydrogen atoms bonded to carbon atoms were placed in idealized positions.

#### **Refinement details for Mn( $\kappa^3$ -S<sup>Me</sup>NS)(CO)<sub>3</sub> (4.1<sub>Mn</sub>).**

The structure was refined without additional restraints / constraints. No disorder was present

#### **4.4.6 Details of DFT calculations**

All calculations were carried out using DFT<sup>115</sup> as implemented in the Jaguar 9.1 suite<sup>99</sup> of ab initio quantum chemistry programs. Geometry optimizations were performed with the B3LYP functional including Grimme's D3 dispersion correction.<sup>94-96,116-118</sup> The 6-31G\*\* basis set was used for main group atoms and Mn was represented using the Los Alamos LACVP basis set that includes relativistic effective core potentials. The energies of optimized structures were reevaluated by additional single-point calculations on each optimized geometry using Dunning's correlation consistent triple- $\zeta$  basis set cc-pVTZ(-f)<sup>100</sup> which includes a double set of polarization functions. For Mn, we used a modified version of LACVP, designated as LACV3P, in which the exponents were decontracted to match the effective core potential with the triple- $\zeta$  quality. For boron, the 6-311G\*\* basis set was used. Solvation energies were evaluated by a self-consistent reaction field (SCRF)<sup>102,119-120</sup> approach based on accurate numerical solutions of the Poisson-Boltzmann equation. In the results reported, solvation calculations were carried out at the same level of theory as the geometry optimization, employing a dielectric constant of  $\epsilon = 2.284$  for

benzene. As is the case for all continuum models, the solvation energies are subject to empirical parameterization of the atomic radii that are used to generate the solute surface. We employed the standard set of Van der Waals radii in Jaguar for H (1.150 Å), B(2.042 Å), C(1.900 Å), N(1.600 Å), O (1.600 Å), S(1.900 Å) and Mn (1.480 Å). Analytical vibrational frequencies within the harmonic approximation were computed with the 6-31G\*\*/LACVP basis set to confirm proper convergence to well-defined minima or saddle points on the potential energy surface. The intermediates were confirmed with no vibrational frequency, while transition states showed a single imaginary frequency.

The energy components have been computed with the following protocol. The free energy in solution-phase,  $G(\text{sol})$ , has been calculated as follows, with  $T = 298 \text{ K}$  to match the experimental room temperature conditions:

$$G(\text{sol}) = G(\text{gas}) + G_{\text{solv}}$$

$$G(\text{gas}) = H(\text{gas}) - TS(\text{gas})$$

$$H(\text{gas}) = E(\text{SCF}) + \text{ZPE}$$

$$\Delta E(\text{SCF}) = \sum E(\text{SCF}) \text{ for products} - \sum E(\text{SCF}) \text{ for reactants}$$

$$\Delta G(\text{sol}) = \sum G(\text{sol}) \text{ for products} - \sum G(\text{sol}) \text{ for reactants}$$

Time dependent-density functional theory(TD-DFT) calculations were used to model dissociation of carbonyls upon UV light irradiation. Calculations were carried out with the Q-Chem 5.0 software. Using geometry obtained from the above method, TD-DFT

calculations were carried out with the B3LYP-D3 functional and 6-31G\*\*/LACVP basis set.

#### 4.4.6.1 DFT figures

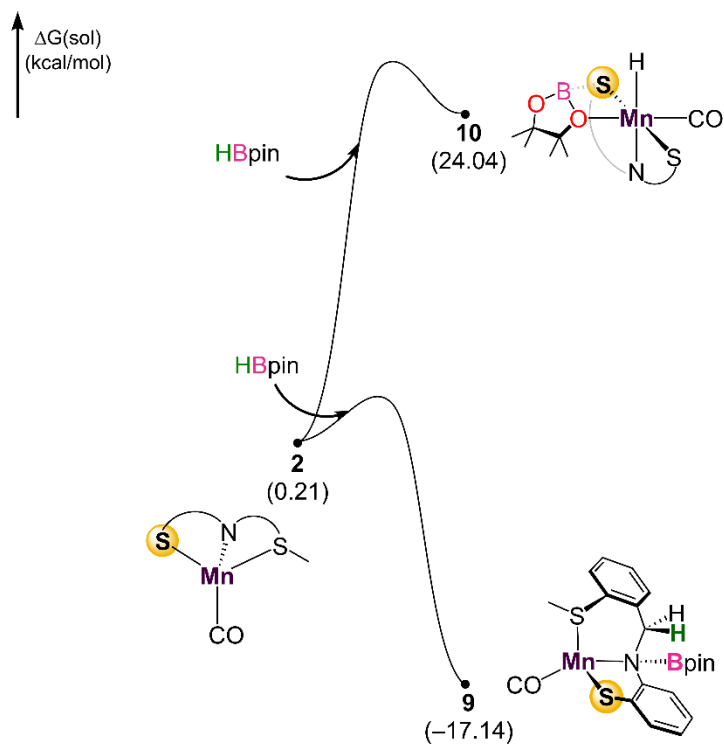


**Figure 4.7.** Comparison between B–H activation forming Mn–H vs. insertion into imine.

Chapter 4 – Avoiding  $C_{aryl}-S$  Bond Cleavage in the Design of a Cooperative Mn(I)-Thiolate Complex for Photo-Catalyzed Nitrile Dihydroboration

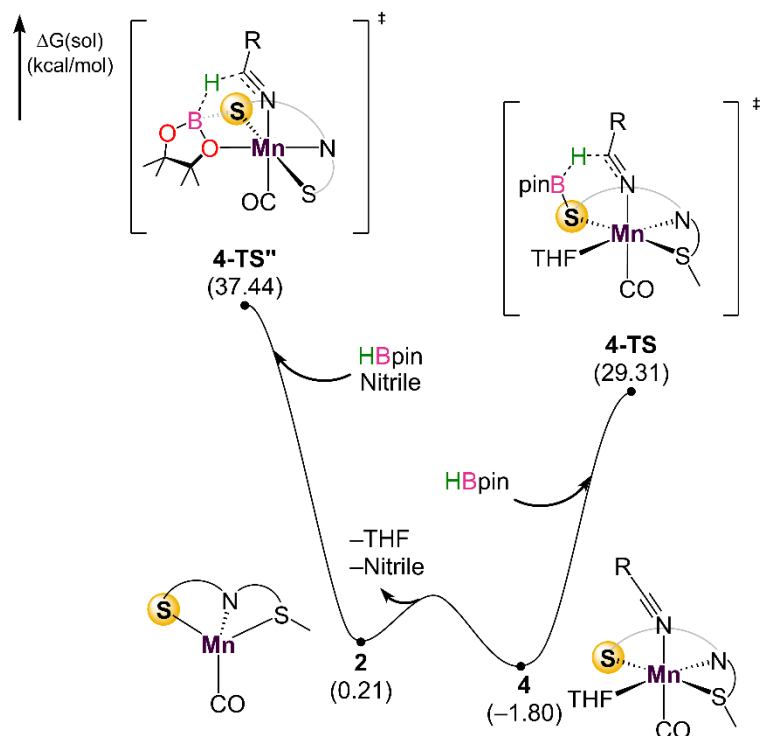


**Figure 4.8.** Comparison of hydride transfer transition states differentiating formation of Mn-S-B-O metallacycle vs. direct boryl coordination and hydride transfer.

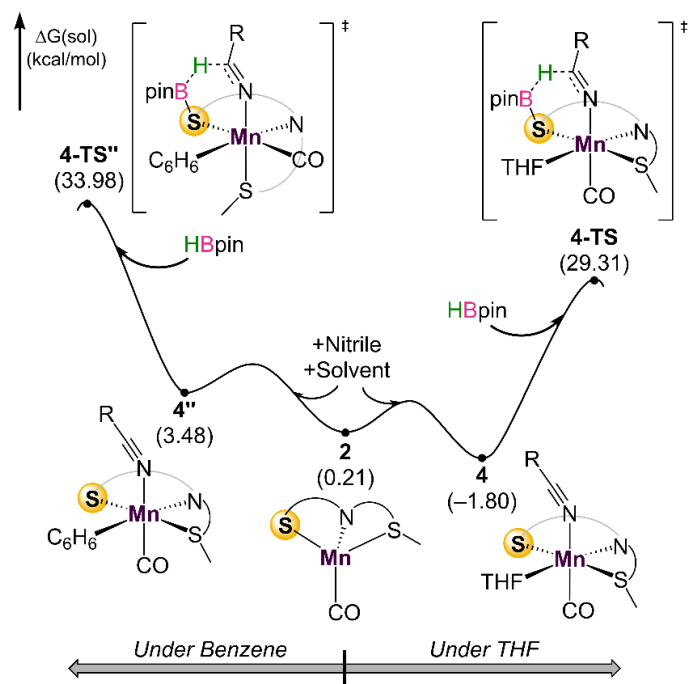


**Figure 4.9.** Comparison of the energy profile for the reaction under THF and benzene as the solvent.

Chapter 4 – Avoiding  $C_{aryl}-S$  Bond Cleavage in the Design of a Cooperative Mn(I)-Thiolate Complex for Photo-Catalyzed Nitrile Dihydroboration

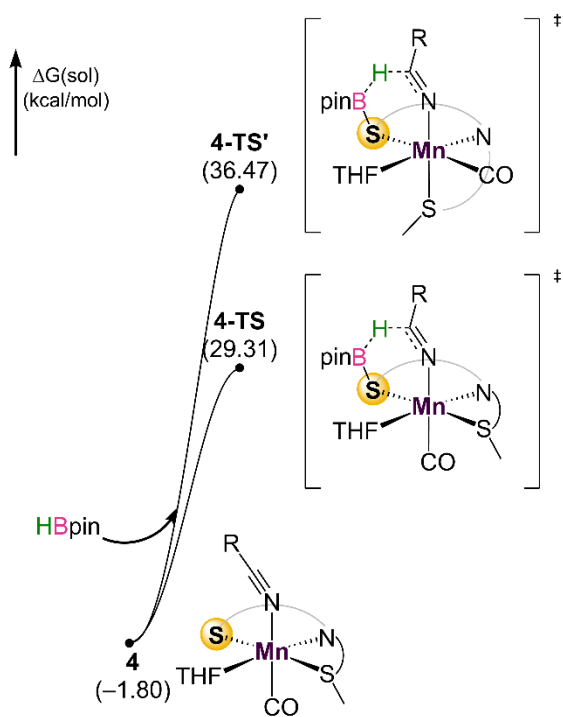


**Figure 4.10.** Comparison between *fac*- and *mer*- conformations in the turnover limiting transition state.

#### 4.5 References

- (1) Van Leeuwen, P. W. M. N. *Homogeneous Catalysis: Understanding the Art*; Springer Science & Business Media, 2006.
- (2) Chiusoli, G. P.; Maitlis, P. M. *Metal-Catalysis in Industrial Organic Processes*; Royal Society of Chemistry, 2019.
- (3) Cornils, B.; Herrmann, W. A.; Beller, M.; Paciello, R. *Applied Homogeneous Catalysis With Organometallic Compounds: A Comprehensive Handbook in Four Volumes*; John Wiley & Sons, 2017; Vol. 4.
- (4) Anastas, P. T.; Crabtree, R. H. *Green Catalysis: Homogeneous Catalysis*; John Wiley & Sons, 2014.
- (5) Ludwig, J. R.; Schindler, C. S. Catalyst: Sustainable Catalysis. *Chem* **2017**, *2*, 313-316.
- (6) Bullock, R. M. *Catalysis Without Precious Metals*; John Wiley & Sons, 2011.
- (7) Chirik, P.; Morris, R. Getting Down to Earth: The Renaissance of Catalysis with Abundant Metals. *Acc. Chem. Res.* **2015**, *48*, 2495-2495.
- (8) Bullock, R. M.; Chen, J. G.; Gagliardi, L.; Chirik, P. J.; Farha, O. K.; Hendon, C. H.; Jones, C. W.; Keith, J. A.; Klosin, J.; Minter, S. D. Using Nature's Blueprint to Expand Catalysis with Earth-Abundant Metals. *Science* **2020**, *369*, No. abc3183.
- (9) Wedepohl, K. H. The Composition of the Continental Crust. *Geochim. Cosmochim. Acta.* **1995**, *59*, 1217-1232.
- (10) Holland, P. L. Reaction: Opportunities for Sustainable Catalysts. *Chem* **2017**, *2*, 443-444.
- (11) Higashi, T.; Kusumoto, S.; Nozaki, K. Cleavage of Si-H, B-H, and C-H Bonds by Metal-Ligand Cooperation: Focus Review. *Chem. Rev.* **2019**, *119*, 10393-10402.
- (12) Khusnutdinova, J. R.; Milstein, D. Metal-Ligand Cooperation. *Angew. Chem. Int. Ed.* **2015**, *54*, 12236-12273.
- (13) Elsby, M. R.; Baker, R. T. Strategies and Mechanisms of Metal-Ligand Cooperativity in First-Row Transition Metal Complex Catalysts. *Chem. Soc. Rev.* **2020**, *49*, 8933-8987.
- (14) Fritz, M.; Schneider, S. The Renaissance of Base Metal Catalysis Enabled by Functional Ligands, in *The Periodic Table II: Catalytic, Materials, Biological and Medical Applications*, Mingos, D. M. P., Ed. **2019**, 1-36.

- (15) Alig, L.; Fritz, M.; Schneider, S. First-Row Transition Metal (De)Hydrogenation Catalysis Based on Functional Pincer Ligands. *Chem. Rev.* **2018**, *119*, 2681-2751.
- (16) van der Vlugt, J. I. Cooperative Catalysis with First-Row Late Transition Metals. *Eur. J. Inorg. Chem.* **2012**, *2012*, 363-375.
- (17) Morris, R. H. Exploiting Metal–Ligand Bifunctional Reactions in the Design of Iron Asymmetric Hydrogenation Catalysts. *Acc. Chem. Res.* **2015**, *48*, 1494-1502.
- (18) Bullock, R. M.; Helm, M. L. Molecular Electrocatalysts for Oxidation of Hydrogen using Earth-Abundant Metals: Shoving Protons Around with Proton Relays. *Acc. Chem. Res.* **2015**, *48*, 2017-2026.
- (19) Chakraborty, S.; Lagaditis, P. O.; Förster, M.; Bielinski, E. A.; Hazari, N.; Holthausen, M. C.; Jones, W. D.; Schneider, S. Well-Defined Iron Catalysts for the Acceptorless Reversible Dehydrogenation-Hydrogenation of Alcohols and Ketones. *ACS. Catal.* **2014**, *4*, 3994-4003.
- (20) Rezayee, N. M.; Samblanet, D. C.; Sanford, M. S. Iron-Catalyzed Hydrogenation of Amides to Alcohols and Amines. *ACS. Catal.* **2016**, *6*, 6377-6383.
- (21) Werkmeister, S.; Junge, K.; Wendt, B.; Alberico, E.; Jiao, H.; Baumann, W.; Junge, H.; Gallou, F.; Beller, M. Hydrogenation of Esters to Alcohols With a Well-Defined Iron Complex. *Angew. Chem. Int. Ed.* **2014**, *53*, 8722-8726.
- (22) Xu, R.; Chakraborty, S.; Yuan, H.; Jones, W. D. Acceptorless, Reversible Dehydrogenation and Hydrogenation of N-Heterocycles With a Cobalt Pincer Catalyst. *ACS Catal.* **2015**, *5*, 6350-6354.
- (23) Mikhailine, A.; Lough, A. J.; Morris, R. H. Efficient Asymmetric Transfer Hydrogenation of Ketones Catalyzed by an Iron Complex Containing a P–N–N–P Tetradentate Ligand Formed by Template Synthesis. *J. Am. Chem. Soc.* **2009**, *131*, 1394-1395.
- (24) Mikhailine, A. A.; Maishan, M. I.; Lough, A. J.; Morris, R. H. The Mechanism of Efficient Asymmetric Transfer Hydrogenation of Acetophenone Using an Iron (II) Complex Containing an (S,S)- $Ph_2PCH_2CH=NCHPhCHPhN=CHCH_2PPh_2$  Ligand: Partial Ligand Reduction Is the Key. *J. Am. Chem. Soc.* **2012**, *134*, 12266-12280.

- (25) De Luca, L.; Passera, A.; Mezzetti, A. Asymmetric Transfer Hydrogenation With a Bifunctional Iron (II) Hydride: Experiment Meets Computation. *J. Am. Chem. Soc.* **2019**, *141*, 2545-2556.
- (26) Bigler, R.; Huber, R.; Stöckli, M.; Mezzetti, A. Iron(II)/(NH)<sub>2</sub>P<sub>2</sub> macrocycles: Modular, Highly Enantioselective Transfer Hydrogenation Catalysts. *ACS. Catal.* **2016**, *6*, 6455-6464.
- (27) Pang, M.; Chen, J.-Y.; Zhang, S.; Liao, R.-Z.; Tung, C.-H.; Wang, W. Controlled Partial Transfer Hydrogenation of Quinolines by Cobalt-Amido Cooperative Catalysis. *Nat. Commun.* **2020**, *11*, 1-9.
- (28) Pang, M.; Wu, C.; Zhuang, X.; Zhang, F.; Su, M.; Tong, Q.; Tung, C.-H.; Wang, W. Addition of a B–H Bond Across an Amido–Cobalt Bond: Co<sup>II</sup>–H-Catalyzed Hydroboration of Olefins. *Organometallics* **2018**, *37*, 1462-1467.
- (29) Ghosh, C.; Kim, S.; Mena, M. R.; Kim, J.-H.; Pal, R.; Rock, C. L.; Groy, T. L.; Baik, M.-H.; Trovitch, R. J. Efficient Cobalt Catalyst for Ambient-Temperature Nitrile Dihydroboration, The Elucidation of a Chelate-Assisted Borylation Mechanism, and a New Synthetic Route to Amides. *J. Am. Chem. Soc.* **2019**, *141*, 15327-15337.
- (30) Elsbey, M. R.; Baker, R. T. Cu (I)–SNS Complexes for Outer-Sphere Hydroboration and Hydrosilylation of Carbonyls. *Chem. Commun.* **2019**, *55*, 13574-13577.
- (31) Zuo, W.; Lough, A. J.; Li, Y. F.; Morris, R. H. Amine (Imine) Diphosphine Iron Catalysts for Asymmetric Transfer Hydrogenation of Ketones and Imines. *Science* **2013**, *342*, 1080-1083.
- (32) Helm, M. L.; Stewart, M. P.; Bullock, R. M.; DuBois, M. R.; DuBois, D. L. A Synthetic Nickel Electrocatalyst with a Turnover Frequency Above 100,000 s<sup>-1</sup> for H<sub>2</sub> Production. *Science* **2011**, *333*, 863-866.
- (33) Zell, T.; Langer, R. Iron-Catalyzed Homogeneous Hydrogenation Reactions in *Homogeneous Hydrogenation with Non-Precious Catalysts* Teichert, J. F., Ed.; Wiley-VCH, **2020**, 15-38.
- (34) Trovitch, R. J. The Emergence of Manganese-Based Carbonyl Hydrosilylation Catalysts. *Acc. Chem. Res.* **2017**, *50*, 2842-2852.

- (35) Mukherjee, A.; Milstein, D. Homogeneous Catalysis by Cobalt and Manganese Pincer Complexes. *ACS Catal.* **2018**, *8*, 11435-11469.
- (36) Kallmeier, F.; Kempe, R. Manganese Complexes for (De)Hydrogenation Catalysis: A Comparison to Cobalt and Iron Catalysts. *Angew. Chem. Int. Ed.* **2018**, *57*, 46-60.
- (37) Elangovan, S.; Topf, C.; Fischer, S.; Jiao, H.; Spannenberg, A.; Baumann, W.; Ludwig, R.; Junge, K.; Beller, M. Selective Catalytic Hydrogenations of Nitriles, Ketones, and Aldehydes by Well-Defined Manganese Pincer Complexes. *J. Am. Chem. Soc.* **2016**, *138*, 8809-8814.
- (38) Elangovan, S.; Garbe, M.; Jiao, H.; Spannenberg, A.; Junge, K.; Beller, M. Hydrogenation of Esters to Alcohols Catalyzed by Defined Manganese Pincer Complexes. *Angew. Chem. Int. Ed.* **2016**, *55*, 15364-15368.
- (39) Garbe, M.; Junge, K.; Walker, S.; Wei, Z.; Jiao, H.; Spannenberg, A.; Bachmann, S.; Scalone, M.; Beller, M. Manganese(I)-Catalyzed Enantioselective Hydrogenation of Ketones Using a Defined Chiral PNP Pincer Ligand. *Angew. Chem. Int. Ed.* **2017**, *56*, 11237-11241.
- (40) Espinosa-Jalapa, N. A.; Nerush, A.; Shimon, L. J.; Leitus, G.; Avram, L.; Ben-David, Y.; Milstein, D. Manganese-Catalyzed Hydrogenation of Esters to Alcohols. *Chem. Eur. J.* **2017**, *23*, 5934-5938.
- (41) Kallmeier, F.; Irrgang, T.; Dietel, T.; Kempe, R. Highly Active and Selective Manganese C=O Bond Hydrogenation Catalysts: The Importance of the Multidentate Ligand, the Ancillary Ligands, and the Oxidation State. *Angew. Chem. Int. Ed.* **2016**, *55*, 11806-11809.
- (42) Freitag, F.; Irrgang, T.; Kempe, R. Mechanistic Studies of Hydride Transfer to Imines From a Highly Active and Chemoselective Manganate Catalyst. *J. Am. Chem. Soc.* **2019**, *141*, 11677-11685.
- (43) Demmans, K. Z.; Olson, M. E.; Morris, R. H. Asymmetric Transfer Hydrogenation of Ketones with Well-Defined Manganese (I) PNN and PNNP Complexes. *Organometallics* **2018**, *37*, 4608-4618.
- (44) Kulkarni, N. V.; Brennessel, W. W.; Jones, W. D. Catalytic Upgrading of Ethanol to N-Butanol via Manganese-Mediated Guerbet Reaction. *ACS Catal.* **2018**, *8*, 997-1002.

- (45) Fu, S.; Shao, Z.; Wang, Y.; Liu, Q. Manganese-Catalyzed Upgrading of Ethanol Into 1-Butanol. *J. Am. Chem. Soc.* **2017**, *139*, 11941-11948.
- (46) Kumar, A.; Janes, T.; Espinosa-Jalapa, N. A.; Milstein, D. Manganese Catalyzed Hydrogenation of Organic Carbonates to Methanol and Alcohols. *Angew. Chem. Int. Ed.* **2018**, *57*, 12076-12080.
- (47) Erken, C.; Kaithal, A.; Sen, S.; Weyhermüller, T.; Hölscher, M.; Werlé, C.; Leitner, W. Manganese-Catalyzed Hydroboration of Carbon Dioxide and Other Challenging Carbonyl Groups. *Nat. Commun.* **2018**, *9*, 1-9.
- (48) Das, U. K.; Kumar, A.; Ben-David, Y.; Iron, M. A.; Milstein, D. Manganese Catalyzed Hydrogenation of Carbamates and Urea Derivatives. *J. Am. Chem. Soc.* **2019**, *141*, 12962-12966.
- (49) Das, U. K.; Ben-David, Y.; Leitner, G.; Diskin-Posner, Y.; Milstein, D. Dehydrogenative Cross-Coupling of Primary Alcohols to Form Cross-Esters Catalyzed by a Manganese Pincer Complex. *ACS Catal.* **2018**, *9*, 479-484.
- (50) Masdemont, J.; Luque-Urrutia, J. A.; Gimferrer, M.; Milstein, D.; Poater, A. Mechanism of Coupling of Alcohols and Amines to Generate Aldimines and  $H_2$  by a Pincer Manganese Catalyst. *ACS Catal.* **2019**, *9*, 1662-1669.
- (51) Zou, Y.-Q.; Chakraborty, S.; Nerush, A.; Oren, D.; Diskin-Posner, Y.; Ben-David, Y.; Milstein, D. Highly Selective, Efficient Deoxygenative Hydrogenation of Amides Catalyzed by a Manganese Pincer Complex via Metal-Ligand Cooperation. *ACS Catal.* **2018**, *8*, 8014-8019.
- (52) Mukhopadhyay, T. K.; Flores, M.; Groy, T. L.; Trovitch, R. J. A Highly Active Manganese Precatalyst for the Hydrosilylation of Ketones and Esters. *J. Am. Chem. Soc.* **2014**, *136*, 882-885.
- (53) Mukhopadhyay, T. K.; Rock, C. L.; Hong, M.; Ashley, D. C.; Groy, T. L.; Baik, M.-H.; Trovitch, R. J. Mechanistic Investigation of Bis (Imino) Pyridine Manganese Catalyzed Carbonyl and Carboxylate Hydrosilylation. *J. Am. Chem. Soc.* **2017**, *139*, 4901-4915.
- (54) Mukhopadhyay, T. K.; Flores, M.; Groy, T. L.; Trovitch, R. J. A  $\beta$ -Diketimate Manganese Catalyst for Alkene Hydrosilylation: Substrate Scope, Silicone Preparation, and Mechanistic Insight. *Chem. Sci.* **2018**, *9*, 7673-7680.

- (55) van Putten, R.; Benschop, J.; de Munck, V. J.; Weber, M.; Müller, C.; Filonenko, G. A.; Pidko, E. A. Efficient and Practical Transfer Hydrogenation of Ketones Catalyzed by a Simple Bidentate Mn–NHC Complex. *ChemCatChem* **2019**, *11*, 5232.
- (56) Sarbajna, A.; Patil, P. H.; Dinh, M. H.; Gladkovskaya, O.; Fayzullin, R. R.; Lapointe, S.; Khaskin, E.; Khusnutdinova, J. R. Facile and Reversible Double Dearomatization of Pyridines in Non-Phosphine Mn(I) Complexes with N, S-Donor Pyridinophane Ligand. *Chem. Commun.* **2019**, *55*, 3282-3285.
- (57) Sarkar, K.; Das, K.; Kundu, A.; Adhikari, D.; Maji, B. Phosphine-Free Manganese Catalyst Enables Selective Transfer Hydrogenation of Nitriles to Primary and Secondary Amines Using Ammonia–Borane. *ACS. Catal.* **2021**, *11*, 2786-2794.
- (58) Dubey, A.; Rahaman, S. W.; Fayzullin, R. R.; Khusnutdinova, J. R. Transfer Hydrogenation of Carbonyl Groups, Imines and N-Heterocycles Catalyzed by Simple, Bipyridine-Based Mn<sup>I</sup> Complexes. *ChemCatChem* **2019**, *11*, 3844-3852.
- (59) Liu, J.; Chen, J.-Y.; Jia, M.; Ming, B.; Jia, J.; Liao, R.-Z.; Tung, C.-H.; Wang, W. Ni–O Cooperation Versus Nickel (II) Hydride in Catalytic Hydroboration of N-Heteroarenes. *ACS. Catal.* **2019**, *9*, 3849-3857.
- (60) Liu, J.; Chen, J.-Y.; Jia, M.; Ming, B.; Jia, J.; Liao, R.-Z.; Tung, C.-H.; Wang, W. Ni–O Cooperation Versus Nickel(II) Hydride in Catalytic Hydroboration of N-Heteroarenes. *ACS. Catal.* **2019**, *9*, 3849-3857.
- (61) Dubey, A.; Nencini, L.; Fayzullin, R. R.; Nervi, C.; Khusnutdinova, J. R. Bio-Inspired Mn (I) Complexes for the Hydrogenation of CO<sub>2</sub> to Formate and Formamide. *ACS. Catal.* **2017**, *7*, 3864-3868.
- (62) Feichtner, K.-S.; Gessner, V. H. Cooperative Bond Activation Reactions With Carbene Complexes. *Chem. Commun.* **2018**, *54*, 6540-6553.
- (63) Omann, L.; Königs, C. D. F.; Klare, H. F.; Oestreich, M. Cooperative Catalysis at Metal–Sulfur Bonds. *Acc. Chem. Res.* **2017**, *50*, 1258-1269.
- (64) Hesp, K. D.; McDonald, R.; Ferguson, M. J.; Stradiotto, M. New Cationic and Zwitterionic Cp\* M ( $\kappa^2$ -P, S) Complexes (M= Rh, Ir): Divergent Reactivity Pathways Arising From Alternative Modes of Ancillary Ligand Participation in Substrate Activation. *J. Am. Chem. Soc.* **2008**, *130*, 16394-16406.

- (65) Song, H.; Ye, K.; Geng, P.; Han, X.; Liao, R.; Tung, C.-H.; Wang, W. Activation of Epoxides by a Cooperative Iron–Thiolate Catalyst: Intermediacy of Ferrous Alkoxides in Catalytic Hydroboration. *ACS. Catal.* **2017**, *7*, 7709-7717.
- (66) Zhang, F.; Song, H.; Zhuang, X.; Tung, C.-H.; Wang, W. Iron-Catalyzed 1, 2-Selective Hydroboration of N-Heteroarenes. *J. Am. Chem. Soc.* **2017**, *139*, 17775-17778.
- (67) Yu, X.; Pang, M.; Zhang, S.; Hu, X.; Tung, C.-H.; Wang, W. Terminal Thiolate-Dominated H/D Exchanges and H<sub>2</sub> Release: Diiron Thiol–Hydride. *J. Am. Chem. Soc.* **2018**, *140*, 11454-11463.
- (68) Liu, T.; Meng, W.; Ma, Q.-Q.; Zhang, J.; Li, H.; Li, S.; Zhao, Q.; Chen, X. Hydroboration of CO<sub>2</sub> Catalyzed by Bis (Phosphinite) Pincer Ligated Nickel Thiolate Complexes. *Dalton Trans.* **2017**, *46*, 4504-4509.
- (69) Ma, N.; Tu, C.; Xu, Q.; Guo, W.; Zhang, J.; Zhang, G. Computational Study on the Mechanism of Hydroboration of CO<sub>2</sub> Catalysed by POCOP Pincer Nickel Thiolate Complexes: Concerted Catalysis and Hydride Transfer by a Shuttle. *Dalton Trans.* **2021**, *50*, 2903-2914.
- (70) Das, U. K.; Daifuku, S. L.; Gorelsky, S. I.; Korobkov, I.; Neidig, M. L.; Le Roy, J. J.; Murugesu, M.; Baker, R. T. Mononuclear, Dinuclear, and Trinuclear Iron Complexes Featuring a New Monoanionic SNS Thiolate Ligand. *Inorg. Chem.* **2016**, *55*, 987-997.
- (71) Das, U. K.; Daifuku, S. L.; Iannuzzi, T. E.; Gorelsky, S. I.; Korobkov, I.; Gabidullin, B.; Neidig, M. L.; Baker, R. T. Iron (II) Complexes of a Hemilabile SNS Amido Ligand: Synthesis, Characterization, and Reactivity. *Inorg. Chem.* **2017**, *56*, 13766-13776.
- (72) Elsby, M. R.; Son, M.; Oh, C.; Martin, J.; Baik, M.-H.; Baker, R. T. Mechanistic Study of Metal–Ligand Cooperativity in Mn (II)-Catalyzed Hydroborations: Hemilabile SNS Ligand Enables Metal Hydride-Free Reaction Pathway. *ACS. Catal.* **2021**, *11*, 9043-9051.
- (73) Hayrapetyan, D.; Khalimon, A. Y. Catalytic Nitrile Hydroboration: A Route to N, N-Diborylamines and Uses Thereof. *Chem. Asian J.* **2020**, *15*, 2575-2587.
- (74) Ibrahim, A. D.; Entsminger, S. W.; Fout, A. R. Insights Into a Chemoselective Cobalt Catalyst for the Hydroboration of Alkenes and Nitriles. *ACS. Catal.* **2017**, *7*, 3730-3734.

- (75) Ben-Daat, H.; Rock, C. L.; Flores, M.; Groy, T. L.; Bowman, A. C.; Trovitch, R. J. Hydroboration of Alkynes and Nitriles Using an  $\alpha$ -Diimine Cobalt Hydride Catalyst. *Chem. Commun.* **2017**, 53, 7333-7336.
- (76) Nguyen, T. T.; Kim, J.-H.; Kim, S.; Oh, C.; Flores, M.; Groy, T. L.; Baik, M.-H.; Trovitch, R. J. Scope and Mechanism of Nitrile Dihydroboration Mediated by a  $\beta$ -Diketiminato Manganese Hydride Catalyst. *Chem. Commun.* **2020**, 56, 3959-3962.
- (77) Bouwman, E.; Henderson, R. K.; Powell, A. K.; Reedijk, J.; Smeets, W. J.; Spek, A. L.; Veldman, N.; Wocadlo, S. Anion Dependent Deprotection of a Thioether Group in Schiff Base NS<sub>2</sub> Ligands Results in New Mononuclear and Dinuclear Thiolato Nickel Complexes. *J. Chem. Soc., Dalton Trans.* **1998**, 3495-3500.
- (78) Desnoyer, A. N.; Love, J. A. Recent Advances in Well-defined, Late Transition Metal Complexes That Make and/or break C-N, C-O and C-S bonds. *Chem. Soc. Rev.* **2017**, 46, 197-238.
- (79) Zhang, J.; Liu, T.; Ma, Q.-Q.; Li, S.; Chen, X. A reaction of [2, 6-(tBu<sub>2</sub>PO) 2C<sub>6</sub>H<sub>3</sub>] NiSCH<sub>2</sub>Ph with BH<sub>3</sub>·THF: borane mediated C-S bond cleavage. *Dalton Trans.* **2018**, 47, 6018-6024.
- (80) Kumar, S.; Guyon, F.; Knorr, M.; Labat, S. p.; Miqueu, K.; Golz, C.; Strohmann, C. Experimental and Theoretical Studies on the Mechanism of the C-S Bond Activation of Pd(II) Thiolate/Thioether Complexes. *Organometallics* **2017**, 36, 1303-1321.
- (81) Peris, E.; Crabtree, R. H. Key Factors in Pincer Ligand Design. *Chem. Soc. Rev.* **2018**, 47, 1959-1968.
- (82) O'Reilly, M. E.; Veige, A. S. Trianionic Pincer and Pincer-Type Metal Complexes and Catalysts. *Chem. Soc. Rev.* **2014**, 43, 6325-6369.
- (83) Vogt, M.; Langer, R. The Pincer Platform Beyond Classical Coordination Patterns. *Eur. J. Inorg. Chem.* **2020**, 2020, 3885-3898.
- (84) Wrighton, M. Photochemistry of Metal Carbonyls. *Chem. Rev.* **1974**, 74, 401-430.
- (85) Wrighton, M.; Hammond, G. S.; Gray, H. B. Group VI Metal Carbonyl Photoassisted Isomerization of Olefins. *J. Organomet. Chem.* **1974**, 70, 283-301.
- (86) Schroeder, M. A.; Wrighton, M. S. Pentacarbonyliron (0) Photocatalyzed Hydrogenation and Isomerization of Olefins. *J. Am. Chem. Soc.* **1976**, 98, 551-558.

- (87) Wrighton, M. S.; Ginley, D.; Schroeder, M.; Morse, D. Generation of Catalysts by Photolysis of Transition Metal Complexes. *Pure Appl. Chem.* **1975**, *41*, 671-697.
- (88) Bogdan, P. L.; Sullivan, P. J.; Donovan Jr, T. A.; Atwood, J. D. Photocatalysis of Hydrogenation and Isomerization of Alkenes by *cis*-HMn(CO)<sub>4</sub>PPh<sub>3</sub>. *J. Organomet. Chem.* **1984**, *269*, c51-c54.
- (89) The possibility of initial nitrile coordination was also investigated. Irradiating a solution of **1** in acetonitrile-*d*<sub>3</sub> afforded no color change and the <sup>1</sup>H NMR spectrum showed no indication of a new species. Additionally, addition of stoichiometric benzonitrile to a THF solution of **1** gave no reactivity and resulted in decomposition upon continual irradiation or heat.
- (90) Chong, C. C.; Kinjo, R. Catalytic Hydroboration of Carbonyl Derivatives, Imines, and Carbon Dioxide. *ACS. Catal.* **2015**, *5*, 3238-3259.
- (91) Kaithal, A.; Chatterjee, B.; Gunanathan, C. Ruthenium-Catalyzed Selective Hydroboration of Nitriles and Imines. *J. Org. Chem.* **2016**, *81*, 11153-11161.
- (92) Wang, X.; Xu, X. Hydroboration of Nitriles and Imines by Highly Active Zinc Dihydride Catalysts. *RSC Adv.* **2021**, *11*, 1128-1133.
- (93) Friedrich, A.; Drees, M.; Käss, M.; Herdtweck, E.; Schneider, S. Ruthenium Complexes With Cooperative PNP-pincer Amine, Amido, Imine, and Enamido Ligands: Facile Ligand Backbone Functionalization Processes. *Inorg. Chem.* **2010**, *49*, 5482-5494.
- (94) Becke, A. D. Density-Functional Thermochemistry. III. The Role of Exact Exchange. *J. Chem. Phys.* **1993**, *98*, 5648-5652.
- (95) Lee, C.; Yang, W.; Parr, R. G. Development of the Colle-Salvetti Correlation-Energy Formula into a Functional of the Electron Density. *Phys. Rev. B.* **1988**, *37*, 785-789.
- (96) Grimme, S.; Antony, J.; Ehrlich, S.; Krieg, H. A Consistent and Accurate Ab Initio Parametrization of Density Functional Dispersion Correction (DFT-D) for the 94 Elements H-Pu. *J. Chem. Phys.* **2010**, *132*, 154104.
- (97) Hariharan, P. C.; Pople, J. A. The Influence of Polarization Functions on Molecular Orbital Hydrogenation Energies. *Theor. Chim. Acta.* **1973**, *28*, 213-222.
- (98) Hay, P. J.; Wadt, W. R. Ab Initio Effective Core Potentials for Molecular Calculations. Potentials for the Transition Metal Atoms Sc to Hg. *J. Chem. Phys.* **1985**, *82*, 270-283.

- (99) Bochevarov, A. D.; Harder, E.; Hughes, T. F.; Greenwood, J. R.; Braden, D. A.; Philipp, D. M.; Rinaldo, D.; Halls, M. D.; Zhang, J.; Friesner, R. A. Jaguar: A High-Performance Quantum Chemistry Software Program with Strengths in Life and Materials Sciences. *Int. J. Quantum Chem.* **2013**, *113*, 2110-2142.
- (100) Dunning Jr, T. H. Gaussian Basis Sets for Use in Correlated Molecular Calculations. I. The Atoms Boron Through Neon and Hydrogen. *J. Chem. Phys.* **1989**, *90*, 1007-1023.
- (101) Woon, D. E.; Dunning Jr, T. H. Gaussian Basis Sets for Use in Correlated Molecular Calculations. III. The Atoms Aluminum Through Argon. *J. Chem. Phys.* **1993**, *98*, 1358-1371.
- (102) Marten, B.; Kim, K.; Cortis, C.; Friesner, R. A.; Murphy, R. B.; Ringnalda, M. N.; Sitkoff, D.; Honig, B. New Model for Calculation of Solvation Free Energies: Correction of Self-Consistent Reaction Field Continuum Dielectric Theory for Short-Range Hydrogen-Bonding Effects. *J. Phys. Chem.* **1996**, *100*, 11775-11788.
- (103) Khalimon, A. Y.; Farha, P.; Kuzmina, L. G.; Nikonov, G. I. Catalytic Hydroboration by an Imido-Hydrido Complex of Mo (IV). *Chem. Commun.* **2012**, *48*, 455-457.
- (104) Saha, S.; Eisen, M. S. Catalytic Recycling of a Th-H Bond via Single or Double Hydroboration of Inactivated Imines or Nitriles. *ACS. Catal.* **2019**, *9*, 5947-5956.
- (105) Das, S.; Bhattacharjee, J.; Panda, T. K. An Imidazolin-2-Iminato Ligand Organozinc Complex as a Catalyst for Hydroboration of Organic Nitriles. *New J. Chem.* **2019**, *43*, 16812-16818.
- (106) Weetman, C.; Anker, M. D.; Arrowsmith, M.; Hill, M. S.; Kociok-Köhn, G.; Liptrot, D. J.; Mahon, M. F. Magnesium-Catalysed Nitrile Hydroboration. *Chem. Sci.* **2016**, *7*, 628-641.
- (107) Geri, J. B.; Szymczak, N. K. A Proton-Switchable Bifunctional Ruthenium Complex that Catalyzes Nitrile Hydroboration. *J. Am. Chem. Soc.* **2015**, *137*, 12808-12814.
- (108) Nakamura, G.; Nakajima, Y.; Matsumoto, K.; Srinivas, V.; Shimada, S. Nitrile Hydroboration Reactions Catalysed by Simple Nickel Salts, Bis (Acetylacetonato) Nickel (II) and its Derivatives. *Catal. Sci. Technol.* **2017**, *7*, 3196-3199.

- (109) Jana, A.; Das, K.; Kundu, A.; Thorve, P. R.; Adhikari, D.; Maji, B. A Phosphine-Free Manganese Catalyst Enables Stereoselective Synthesis of (1+ n)-Membered Cycloalkanes from Methyl Ketones and 1, n-Diols. *ACS. Catal.* **2020**, *10*, 2615-2626.
- (110) Léval, A.; Agapova, A.; Steinlechner, C.; Alberico, E.; Junge, H.; Beller, M. Hydrogen Production from Formic Acid Catalyzed by a Phosphine Free Manganese Complex: Investigation and Mechanistic Insights. *Green Chem.* **2020**, *22*, 913-920.
- (111) Coufourier, S.; Gaignard Gaillard, Q.; Lohier, J.-F.; Poater, A.; Gaillard, S.; Renaud, J.-L. Hydrogenation of CO<sub>2</sub>, Hydrogenocarbonate, and Carbonate to Formate in Water Using Phosphine Free Bifunctional Iron Complexes. *ACS. Catal.* **2020**, *10*, 2108-2116.
- (112) APEX 2, Bruker AXS Inc., Madison, Wisconsin, USA, 2012.
- (113) G. M. Sheldrick, SADABS, Program for Empirical Absorption Correction of Area Detector Data, University of Göttingen, Germany, 1996.
- (114) G. M. Sheldrick. SHELXL-Integrated Space-Group and Crystal-Structure Determination *Acta Cryst.* 2015, C71, 3-8.
- (115) Parr, R.G.; Yang, W. Density Functional Theory of Atoms and Molecules. Oxford University Press: New York, 1989.
- (116) Slater, J. C. Quantum Theory of Molecules and Solids, Vol. 4: The Self-Consistent Field for Molecules and Solids. McGraw-Hill: New York, 1974. .
- (117) Vosko, S. H.; Wilk, L.; Nusair, M. Accurate Spin-Dependent Electron Liquid Correlation Energies for Local Spin Density Calculations: A Critical Analysis. *Can. J. Phys.* **1980**, *58*, 1200. .
- (118) Becke, A. D. Density-Functional Exchange-Energy Approximation with Correct Asymptotic Behavior. *Phys. Rev. A* **1988**, *38*, 3098. .
- (119) Friedrichs, M.; Zhou, R.; Edinger, S. R.; Friesner, R. A. Poisson–Boltzmann Analytical Gradients for Molecular Modeling Calculations. *J. Phys. Chem. B* **1999**, *103*, 3057-3061.
- (120) Edinger, S. R.; Cortis, C.; Shenkin, P. S.; Friesner, R. A. Solvation Free Energies of Peptides: Comparison of Approximate Continuum Solvation Models with Accurate Solution of the Poisson–Boltzmann Equation. *J. Phys. Chem. B* **1997**, *101*, 1190-1197.

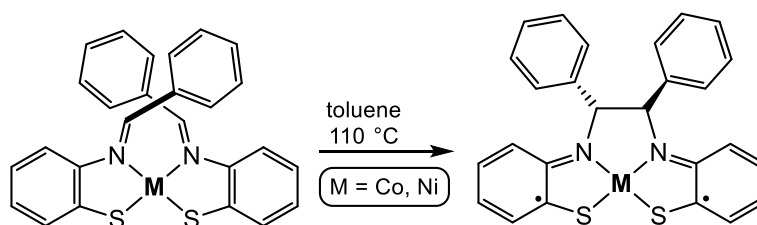
**Chapter 5 – Highly Covalent Metal-Ligand Electron Sharing in Redox Non-Innocent Iron [N<sub>2</sub>S<sub>3</sub>] Complexes**

**5.1 Introduction**

Homogeneous transition metal catalysis is traditionally based on noble metal complexes that enable predictable two-electron redox events to facilitate the crucial breakage and subsequent reformation of bonds during catalytic turnover.<sup>1-2</sup> The design of highly desired first row metal catalysts that display analogous reactivity is a challenge, due to their access to facile one-electron redox changes.<sup>2-4</sup> Consequently, installation of redox non-innocent ligands has been found to confer ‘nobility’ to base metals by providing a variety of reaction strategies to make use of both 1e- (ligand- and substrate-based radical) and 2e- (ligand serves as electron sink) transformations.<sup>5-6</sup> This strategy has led to discovery of novel reaction manifolds,<sup>7-9</sup> rivalling or surpassing analogous reactions catalyzed by precious metal complexes.<sup>10-14</sup> Continued efforts to unravel the many complexities of redox-active ligands are thus needed to further push the capabilities of these base-metal systems.<sup>15</sup>

Following early work on dithiolene, catecholate and porphyrinoid ligands by Gray,<sup>16</sup> Pierpont,<sup>17</sup> Balch<sup>18</sup> and others,<sup>19</sup> an expansive scope of redox-active ligands and associated catalytic applications have been reported over the past fifteen years.<sup>12-13</sup> One challenge presented by these ligands is the assessment of metal formal oxidation state and spin density on the ligand, as ambiguity can often exist in these complex systems.<sup>20-21</sup> The Wieghardt group and their computational chemistry collaborators have contributed significantly to further understanding the interplay of electron-sharing between base metals and redox non-innocent ligands, and outlined some effective approaches to studying such systems.<sup>22-26</sup> Specifically, *N,S*-coordination to first row metals has garnered much interest due to its resemblance to several metalloenzymes, particularly the nitrogenases.<sup>27-29</sup>

The coordination chemistry of *o*-amino-benzenethiolate ligands is very diverse as the ligand can exist in different oxidation levels and degrees of protonation.<sup>30</sup> One particularly interesting sub-class of these redox-active ligands are the tetradentate bis(amido) dithiolate  $N_2S_2$  ligands derived from imine-thiolate ligands by imine C-C bond formation (**Scheme 5.1**).<sup>31-32</sup> In their detailed experimental and computational investigation of  $[Co(N_2S_2)]^{0/1-}$  Wieghardt and coworkers concluded that “the bonding arrangement cannot be simply described using integer oxidation levels for the metal and ligands because the energy of the cobalt 3d orbitals is comparable to the ligand p-orbitals.”<sup>33</sup>



**Scheme 5.1.** Synthesis of  $M(N_2S_2)$  complexes via imine C-C bond formation

In a later study, the same group investigated the dimeric iron complex (**i**) bearing *o*-amido-thiophenolate units connected with a saturated ethanediyl bridge and featuring two bridging thiolates (**Figure 5.1A**).<sup>34</sup> Analysis of the C–C (benzene), C–N, and C–S bond lengths led to assignment of the ligand as an unsymmetrical trianionic  $\pi$  radical (**Figure 5.1B**), rendering each iron center as ferric Fe(III). Combined Mössbauer, EPR, and DFT studies supported an  $S = 0$  ground state. Reaction of **i** with iodine furnished mononuclear **ii**, again proposed to be ferric Fe(III) ( $S = 1/2$ ) due to the presence of two  $\pi$  radical anionic halves. In contrast, five-coordinate mononuclear **iii**, featuring an apical phosphine was proposed to be ferrous Fe(II) ( $S = 0$ ) with two  $\pi$  radicals. While great progress has been made in identifying the bonding modes and electron-sharing of these *N-S*-coordinated complexes, those that have been thoroughly studied are comprised mainly of tetradentate square planar ligand frameworks.<sup>30,33,35-40</sup>

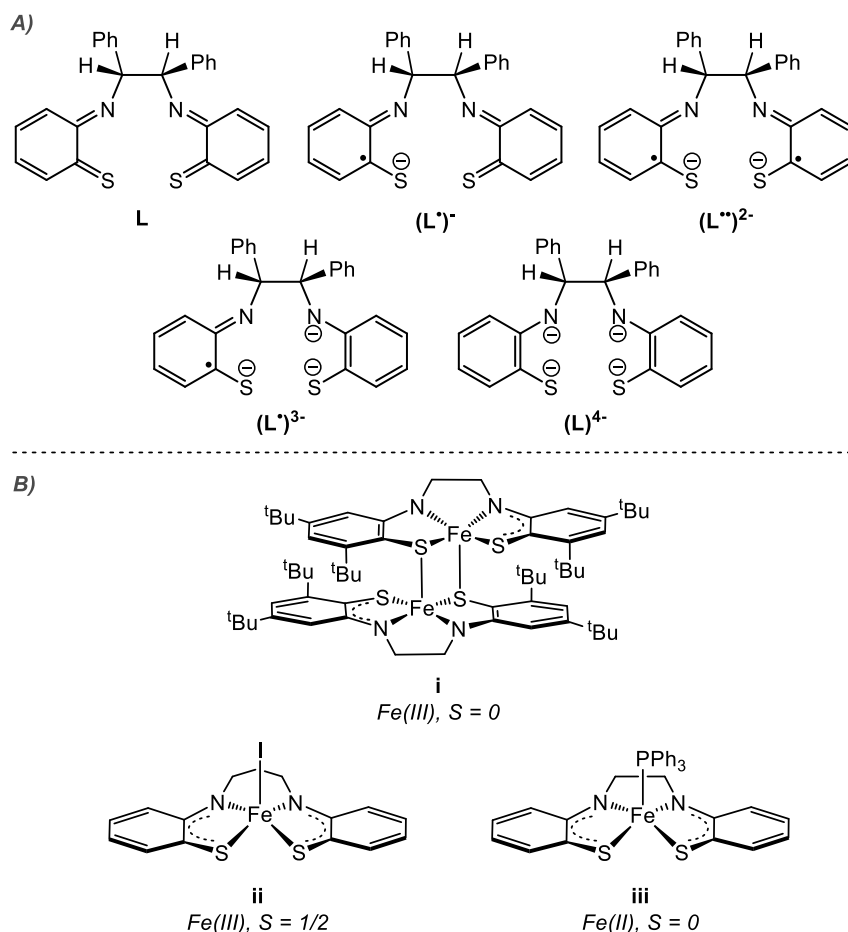
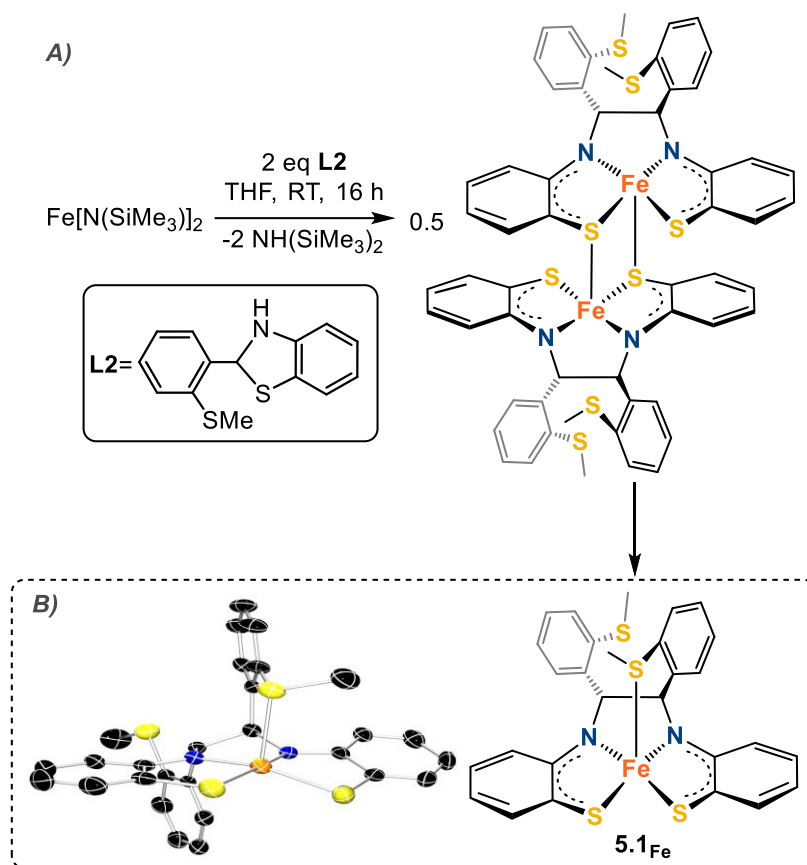


**Figure 1.** A) Wieghardt's Fe- $L^2$  complexes with determined ground states and proposed oxidation states. B) Five theoretical redox states of the bis(*o*-imino-thioquinone) ligand (**L**).

We recently reported a square-pyramidal Fe complex (**1**) featuring a pentadentate  $[N_2S_3]$  ligand which resembles the Wieghardt complexes. Treatment of low-coordinate  $Fe[N(SiMe_3)_2]_2$  with two equiv. of the easily prepared benzothiazolidine proligand (**L2<sup>H</sup>**) results in coupling of the two imine carbons to form the redox non-innocent  $[N_2S_3]$  ligand (**Scheme 5.2**).<sup>41</sup> Although **1** tends to crystallize in the diamagnetic dimeric form (similar to **i** in Fig. 1), we showed by <sup>1</sup>H NMR spectroscopy that solutions consist exclusively of paramagnetic ( $S = 1$ ) monomers featuring a pentacoordinate  $[N_2S_3]$  ligand with a bound apical thioether moiety. We have now obtained structural confirmation of this monomer

(Scheme 2B) from a co-crystal with  $Fe(OH)_2(NCMe)_4$ , obtained by recrystallization of the crude reaction mixture from a concentrated acetonitrile solution at  $-35\text{ }^\circ\text{C}$ . Herein we report a detailed investigation of the unique electron-sharing between metal and ligand in three redox states of this  $Fe[N_2S_3]$  complex, demonstrating that intuitive models are not always sufficient to describe redox non-innocent systems employing base metals for which a high degree of covalency can exist.<sup>30</sup>



**Scheme 5.2.** A) Synthesis of previously reported dinuclear  $[Fe(\mu-N_2S_2)]_2$  complex.<sup>41</sup> B) Solid-state molecular structure of monomer  $Fe[N_2S_3]$  **5.1<sub>Fe</sub>** (from partially hydrolyzed

Fe $[N_2S_3]$ •Fe(OH) $_2$ (NCMe) $_4$  co-crystal) with thermal ellipsoids shown at 50%. H-atoms are omitted for clarity.

## 5.2 Results and Discussion

### 5.2.1 Electrochemical studies

As the redox non-innocence of *o*-amido-benzenethiolate-type ligands is well established, complex **5.1<sub>Fe</sub>** was first subjected to detailed electrochemical analyses. The voltammogram (**Figure 5.2**) recorded at 100 mV/s exhibits two Nernstian, diffusion-controlled waves in the accessible potential range: a one-electron reduction observed at  $E_{1/2} = -0.60$  V ( $\Delta E_p = 63$  mV) and a one-electron oxidation wave at  $E_{1/2} = 0.05$  V ( $\Delta E_p = 63$  mV). The reversibility of these two signals, observed at all investigated scan rates (50 mV/s to 1 V/s), is consistent with the absence of chemical steps coupled to the electron transfer. This implies that the chemical coordination environment around the metal remains the same in the neutral (**5.1<sub>Fe</sub>**), oxidized (**5.1<sub>Fe</sub><sup>+</sup>**), and reduced (**5.1<sub>Fe</sub><sup>-</sup>**) species. Further insight into the stability of the electrogenerated species **5.1<sub>Fe</sub><sup>+</sup>** and **5.1<sub>Fe</sub><sup>-</sup>** was obtained from electrolysis experiments. The voltammetric curves recorded at a rotating disk electrode before and after exhaustive electrolysis of **1** at  $(E_{ap})_1 = -0.9$  V or  $(E_{ap})_2 = +0.3$  V (**Figure 5.3**) reveal the stability of both **5.1<sub>Fe</sub><sup>+</sup>** (red curve) and **5.1<sub>Fe</sub><sup>-</sup>** (blue curve) on a time scale of about 30 min.

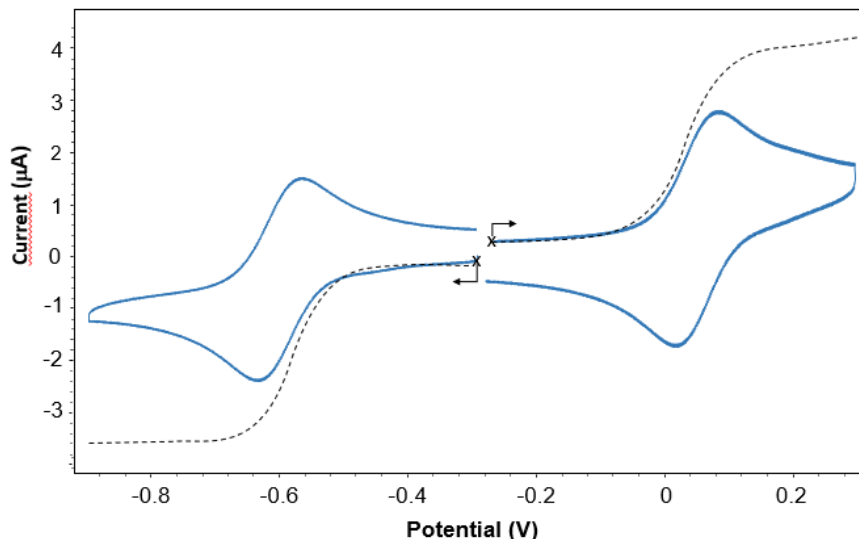


**Figure 5.2.** Voltammetric curves recorded under argon for  $5.1_{Fe}$  ( $1 \cdot 10^{-3}$  M in THF + 0.1 M tetra-*n*-butylammonium hexafluorophosphate) at (solid line) a stationary vitreous carbon working electrode ( $\varnothing = 3$  mm,  $E$  vs Ag/Ag $^+$  ( $10^{-2}$  M),  $v = 0.1$  V/s) and (dotted line) a rotating carbon disk electrode ( $\varnothing = 3$  mm,  $v = 0.01$  V $\cdot$ s $^{-1}$ , 550 rd/min).

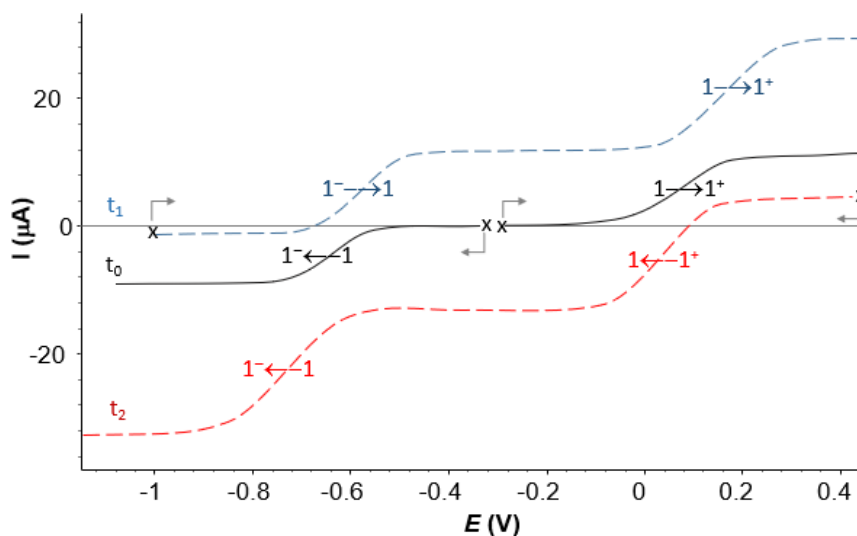


**Figure 5.3.** Voltammetric curves recorded under argon for  $5.1_{Fe}$  ( $1 \times 10^{-3}$  M + 0.1 TBAP in THF) at a rotating carbon disk electrode ( $\varnothing = 3$  mm,  $v = 0.01$  V/s, 550 rd/min) before electrolysis (black curve), after exhaustive reduction at  $(E_{ap})_1 = -900$  mV (red dashed curve) and after exhaustive oxidation at  $(E_{ap})_1 = +300$  mV (blue dashed curve) (Three compartment cell, Pt gauze working electrode, 12 mL of electrolyte, duration of each electrolysis  $\sim 30$  min).

EPR spectroscopic data were collected on electrogenerated redox partners of **1** to investigate whether the iron center or the ligand is involved in the oxidation/reduction waves observed in **Figure 5.3** (Full spectra of  $5.1_{Fe}$ ,  $5.1_{Fe^-}$  and  $5.1_{Fe^+}$  are provided in the ESI). Complexes  $5.1_{Fe}$  and  $5.1_{Fe^-}$  are EPR silent, although the latter showed a weak signal at approximately  $g = 5.0$  suggesting traces of a high-spin Fe(I) or Fe(III) impurity.<sup>42</sup> Conversely, the X-band EPR spectrum of  $5.1_{Fe^+}$  exhibits three intense signals at  $g = 2.191$ , 2.075, and 2.021, consistent with an ( $S = 1/2$ ) Fe complex featuring a rhombic distortion in the equatorial plane (**Figure 5.4**).<sup>43</sup> These data can be compared to Wieghardt's complex **ii** (**Figure 5.1**) with  $g$  values of 2.285, 2.119, and 2.037.<sup>34</sup> The observed EPR signal for Wieghardt's complex was assigned to an intermediate-spin Fe(III) center antiferromagnetically coupled to the two ligand radicals.

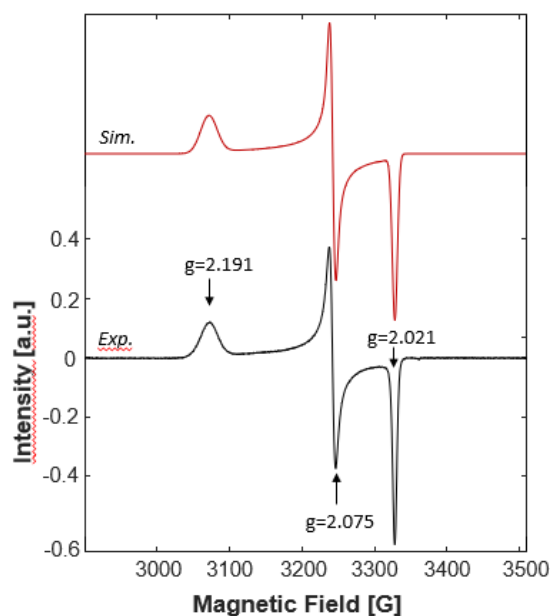


**Figure 5.4.** Simulated (red) and experimental (black) X-band EPR spectrum of electrogenerated  $5.1_{Fe^+}$  recorded at 110 K (microwave power, 6 mW; modulation amplitude, 2 G).

The oxidized and reduced species were further characterized by spectroelectrochemistry, collecting time-resolved UV-vis spectra during the electrochemical reduction or oxidation of **5.1**<sub>Fe</sub>. The accumulation of **5.1**<sub>Fe</sub><sup>-</sup> at the electrode led to the progressive hypochromic shift of the signal centered at 571 nm and to the disappearance of the broad signal centered above 600 nm at the expense of a narrow one developing at  $\lambda_{\text{max}} = 476$  nm (**Figure 5.5**). Observation of a clean isosbestic point at 485 nm also confirms that no secondary reactions occur over the considered time range. The electrochemical oxidation of **5.1**<sub>Fe</sub> was conversely found to result in a significant blue shift of both signals attributed to **5.1**<sub>Fe</sub> accompanied by a marked intensity increase of the higher energy signal (**Figure 5.5**). Here again, the progressive conversion of **5.1**<sub>Fe</sub> to **5.1**<sub>Fe</sub><sup>+</sup> proceeds with a clean isosbestic point at 660 nm.

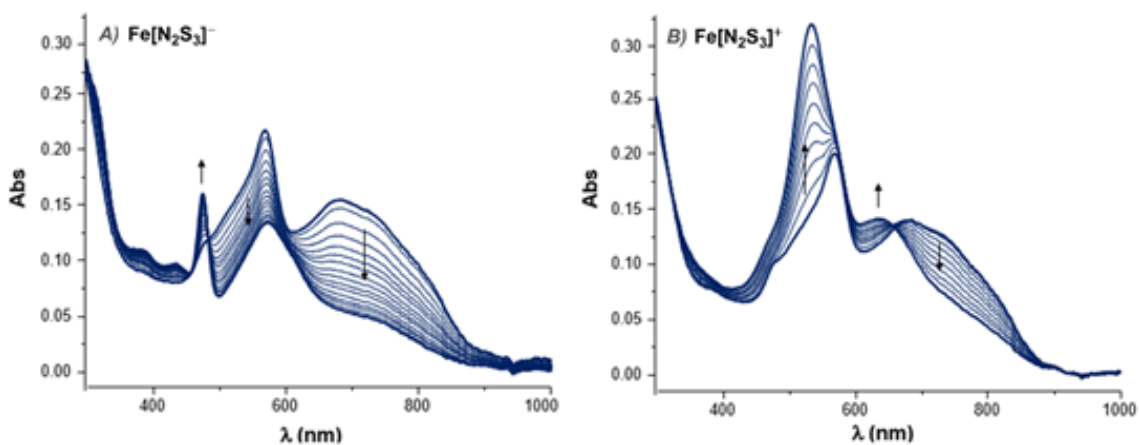


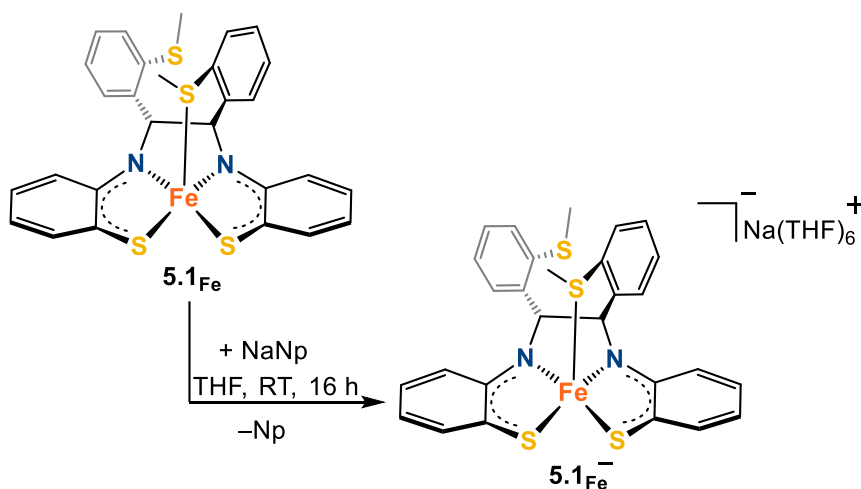
**Figure 5.5.** UV/Vis spectra recorded during the electrolysis (1 e<sup>-</sup> per molecule) of **5.1**<sub>Fe</sub> ( $\sim 3 \cdot 10^{-4}$  mol L<sup>-1</sup>) at **A)**  $E_{\text{app}} = -1$  V and **B)**  $E_{\text{app}} = +0.5$  V in THF (0.1 M TBAP) (working electrode : Pt,  $l = 1$  mm).

Lastly, time-dependent DFT calculations were performed to further verify the formation of **5.1**<sub>Fe</sub><sup>-</sup> and **5.1**<sub>Fe</sub><sup>+</sup> in the spectroelectrochemistry experiments (See Appendix D). From these calculations, good correlation between the experimentally obtained and calculated

UV-vis spectra of all three species was observed, further supporting the *in-situ* formation of  $5.1_{Fe^-}$  and  $5.1_{Fe^+}$  electrochemically. Of note, the major absorption features across this series of complexes are dominated by an array of ligand to metal charge transfer (LMCT) transitions.

### 5.2.3 Synthesis of anion partner and metrical analysis

Since electrochemical studies suggested stability of both  $5.1_{Fe^+}$  and  $5.1_{Fe^-}$ , we attempted to isolate pure samples of each for further studies. Reaction of  $5.1_{Fe}$  with sodium naphthalenide in THF afforded  $5.1_{Fe^-}$  as a dark blue-purple powder in 92 % yield (**Scheme 5.3**). X-ray quality crystals were grown from a concentrated solution of THF layered with hexanes at  $-30\text{ }^\circ\text{C}$ . The anionic species  $5.1_{Fe^-}$  crystallizes as a monomer and the structural motif of the  $N_2S_3$  ligand remains intact upon reduction consistent with spectroelectrochemical studies.



**Scheme 5.3.** Synthesis of  $[Na(THF)_6]^+[Fe(N_2S_3)]^-$  ( $5.1_{Fe^-}$ ).

Alternatively, synthesis of the oxidized species proved problematic. Numerous attempts to synthesize **5.1**Fe<sup>+</sup> with a variety of oxidants all resulted in either decomposition or impure samples due to multiple product formation (cf. monomer vs. dimer), incomplete oxidation, or unanticipated reactivity due to non-innocent oxidizing reagents. Although bulk electrolysis allowed us to obtain the EPR spectrum of **5.1**Fe<sup>+</sup>, use of this method to isolate the oxidized species for structural studies was not pursued due to solubility complications.

In keeping with their three different ground states, the molecular structures of monomeric **5.1**Fe and **5.1**Fe<sup>-</sup> differ significantly from its dimeric, thiolate bridged form (**Figure 5.6**). For the latter, we also compare the structure to Weighardt's dimer<sup>34</sup> to show that the asymmetry in C-S bond distances (1.756(3) vs. 1.710(3) Å) is actually due to the increase in coordination number at the bridging thiolate. In fact, the similarity of the Fe-N and Fe-S bond distances in all three structures is remarkable with the only major difference being the axial Fe-S distances (average Fe-S<sup>Me</sup> = 2.544(2) Å for **5.1**Fe and **5.1**Fe<sup>-</sup> vs. Fe-S<sup>thiolate</sup> = 2.3532(7) Å for the dimer). However, the most striking difference between the structures of **5.1**Fe and **5.1**Fe<sup>-</sup> vs all three five-coordinate structures in **Fig. 5.1A** is the lack of bond alternation in the N,S-substituted aryl ring. This will be returned to later.

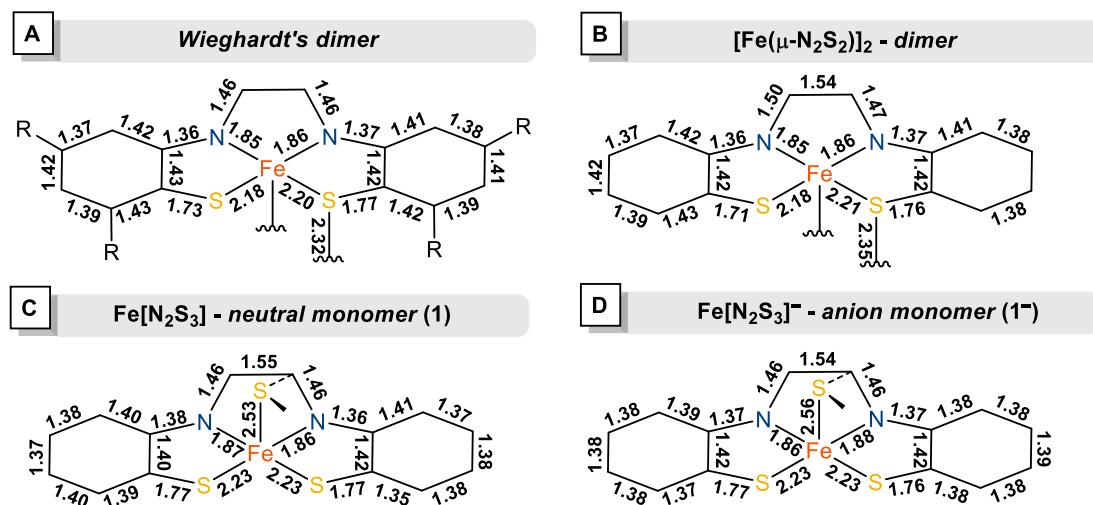


**Figure 5.6.** Bond distances (Å) for A) Wieghardt's dimer (R = *t*-Bu), B)  $[Fe(\mu-N_2S_2)]_2$ , C) **5.1<sub>Fe</sub>** and D) **5.1<sub>Fe</sub><sup>-</sup>**.

### 5.2.4 Mössbauer and XANES

With both neutral **5.1<sub>Fe</sub>** and reduced **5.1<sub>Fe</sub><sup>-</sup>** in hand, we performed Mössbauer spectroscopy to interrogate the oxidation state at the iron center. The solid-state 80 K spectrum of solid  $[Fe(\mu-N_2S_2)]_2$  dimer features an isomer shift of  $\delta = 0.15$  mm/s and  $\Delta E_Q = 2.83$  mm/s (**Figure 5.7A**). The observed isomer shift falls within the range expected for a low-spin Fe(II) complex. However, the quadrupole splitting is fairly large for such a complex and isomer shifts in this range are often ambiguous in terms of oxidation state as additional iron species [i.e. low-spin Fe(III)] can also have isomer shifts in this region.<sup>44</sup> In order to obtain the Mössbauer spectrum of monomeric **5.1<sub>Fe</sub>** we prepared an <sup>57</sup>Fe-labeled sample. Although the resulting precipitated amorphous solid contained a minor amount of  $[Fe(\mu-N_2S_2)]_2$  dimer and several unidentified impurities (**Figure 5.7B**), conversion of the former to monomeric **5.1<sub>Fe</sub>** was confirmed in the frozen solution spectrum (**Figure 5.7C**). The observed isomer shift ( $\delta = 0.94$  mm/s) and  $\Delta E_Q$  (3.02 mm/s) of **5.1<sub>Fe</sub>** are characteristic

for high spin Fe(II), which in combination with the Evans measurement showing monomer  $5.1_{Fe}$  is  $S = 1$ , suggests antiferromagnetic coupling to two ligand radicals. Importantly, the solid-state 80 K spectrum of  $5.1_{Fe^-}$  shows an observed isomer shift at  $\delta = 0.28$  with  $\Delta E_Q = 1.55$  mm/s, (**Figure 5.7D**, blue trace) which is similar to that of the diamagnetic  $[Fe(\mu-N_2S_2)]_2$  dimer, suggesting that  $5.1_{Fe^-}$  may also be Fe(II). It should also be noted that the impurity in **Figure 5.7D** is likely unreacted  $5.1_{Fe}$  due to incomplete conversion.

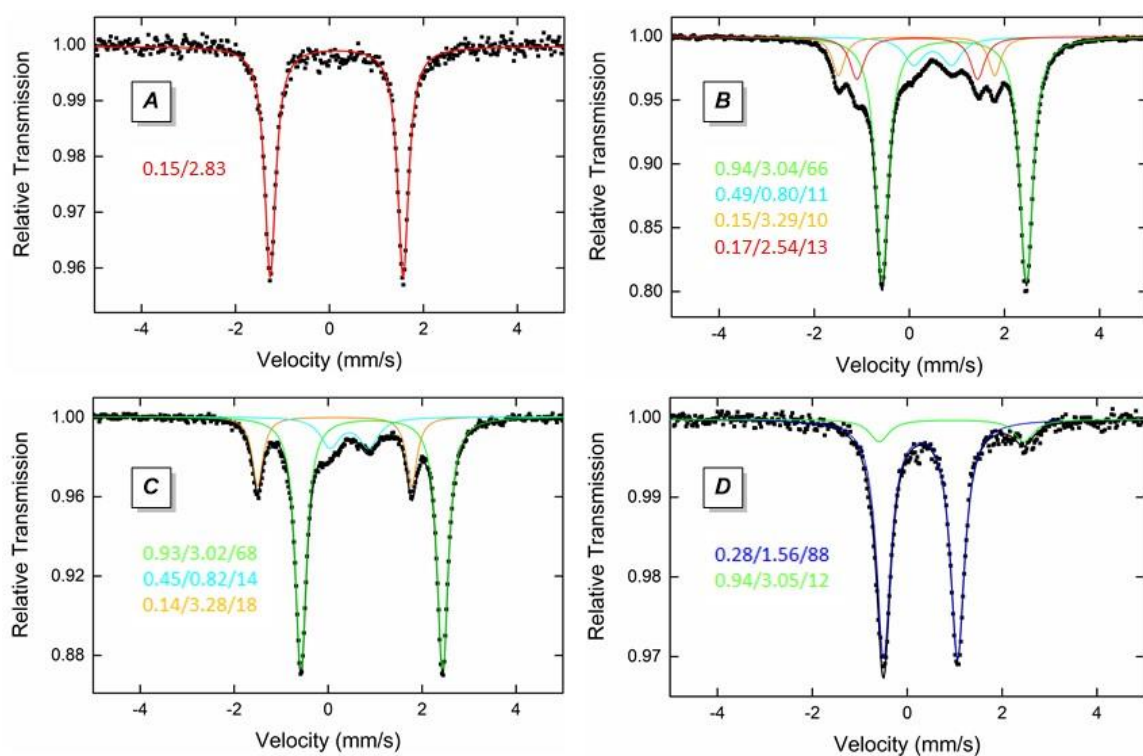


**Figure 5.7.** Mössbauer spectra of **A**) solid  $[Fe(\mu-N_2S_2)]_2$  dimer, **B**) solid Fe-57-labeled  $5.1_{Fe}$ , **C**) frozen solution of Fe-57-labeled  $5.1_{Fe^-}$  and **D**) solid  $5.1_{Fe^-}$ . Spectrum of **B** contains several unidentified impurities in addition to some  $[Fe(\mu-N_2S_2)]_2$  dimer (blue) and that of **C** contains ca. 12% of a high-spin Fe(II) impurity (green trace).

While the Mössbauer data suggest a ligand-based reduction between  $5.1_{Fe}$  and  $5.1_{Fe^-}$ , they did not provide a convincing comparison given that the parameters for  $5.1_{Fe^-}$  more

closely resemble those of the  $[Fe(\mu-N_2S_2)]_2$  dimer. Given this latter similarity, XANES experiments were performed to compare the  $[Fe(\mu-N_2S_2)]_2$  dimer and  $5.1Fe^-$ . The Fe K edge XANES of the two complexes are shown in **Figure 5.8**. While the spectra are indeed quite different, it can be concluded that both species are in fact Fe(II). The pre-edge peak centroid energies were calculated using the method described by Wilke et al.<sup>45-46</sup> The centroid energies of the two reference compounds are the same as the cited reference within measurement uncertainty. Given the relatively large gap of 1.03 eV between periclase and yoderite, the reported compounds with the maximum and minimum centroid energies for Fe(II) and Fe(III), respectively,<sup>45</sup> this suggests that both the  $[Fe(\mu-N_2S_2)]_2$  dimer and  $5.1Fe^-$  are in the Fe(II) oxidation state.

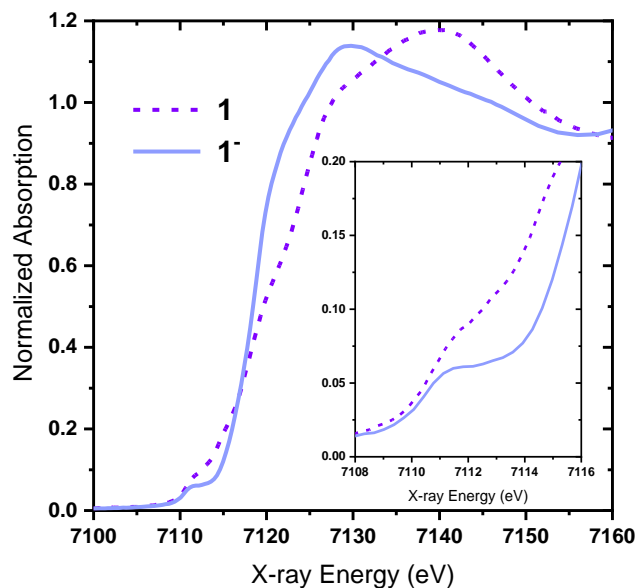
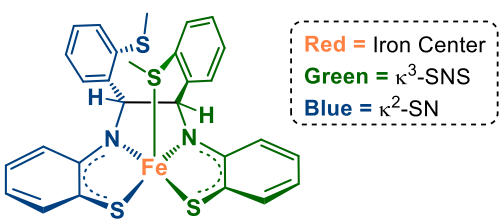


**Figure 5.8.** Fe/K edge XANES spectra of neutral ( $5.1Fe$ ; purple dotted line) and anionic ( $5.1Fe^-$ ; blue solid line)  $Fe[N_2S_3]$  complexes.

### 2.2.3 DFT investigation: ground states, orbital occupancies, and molecular orbitals

Both the Mössbauer and XANES experimental data indicate the reduction of  $5.1_{Fe}$  to  $5.1_{Fe}^-$  is ligand-centered; however, the respective metrical bond lengths in the two species do not reflect this. Due to the uncertainty concerning the electronic environment around the Fe-centers and the supporting ligand manifold, DFT calculations with the B3LYP-D3 functional were carried out to gain more insight into the redox partners. Several different spin states were considered for each complex (see Appendix D). The geometries were optimized in solvent, and the resulting Mulliken spin distributions for each species are summarized in **Table 5.1**. The spin distribution of the system was analyzed by dividing the complex into three fragments: the metal center, the right-hand side of the ligand  $\kappa^3$ -SNS featuring the apically bound thioether, and the left-hand side of the ligand  $\kappa^2$ -SN.



	Spin State	Spin Density		
		Fe	$\kappa^3$ -SNS	$\kappa^2$ -SN
$Fe[N_2S_3]$	Triplet	2.54	0.16	-0.70
$Fe[N_2S_3]^-$	Quartet	2.71	0.13	0.16
$Fe[N_2S_3]^+$	Doublet	2.54	-0.74	-0.79

**Table 5.1.** Ground state and spin density DFT calculations (kcal/mol) on  $5.1_{Fe}$ ,  $5.1_{Fe}^-$ , and  $5.1_{Fe}^+$ .

In contrast to the diamagnetic  $[Fe(\mu-N_2S_2)]_2$  dimer, neutral monomer  $5.1_{Fe}$  was found to have a triplet ground state (**Table 5.1**). This result agrees with experimental

measurements indicating a solution state effective magnetic moment of 2.7  $\mu_B$ .<sup>41</sup> Comparison of the bond lengths of the optimized structure of **5.1<sub>Fe</sub>** ( $S = 1$ ) and the experimental solid-state structure are in good agreement, which supports the triplet ground state assignment. Analysis of the spin distribution shows more than two open shells, with two alpha electrons localized on the Fe center. Another alpha electron is delocalized between the Fe center and  $\kappa^3$ -SNS, while the beta electron is localized mostly on the  $\kappa^2$ -SN fragment of the ligand. In addition, a closer comparison of the calculated and experimental bond lengths, reveals inconsistencies regarding the bond length alteration in the aryl rings of the calculated structure (**Figure 5.9**), which is not present to the same degree in the XRD structure (**Figure 5.6**). These data are consistent with an intermediate spin Fe(III) antiferromagnetically coupled to a ligand radical, similar to what Wieghardt suggested. This, however, contrasts with experimental Evans measurements, Mössbauer, and XANES data which suggested high spin Fe(II) antiferromagnetically coupled to two ligand radicals.

For the redox partners **5.1<sub>Fe</sub><sup>-</sup>** and **5.1<sub>Fe</sub><sup>+</sup>**, the ground states were found to be a quartet and doublet, respectively. Again, a strong correlation between bond distances of the optimized and solid-state experimental structures of **5.1<sub>Fe</sub><sup>-</sup>** was observed. Examining the spin distribution of **5.1<sub>Fe</sub><sup>-</sup>** shows little beta spin density, with three alpha electrons localized mostly on the Fe center. A comparison of spin density distribution shows that reduction from **5.1<sub>Fe</sub>** to **5.1<sub>Fe</sub><sup>-</sup>** is mostly ligand-based, supporting experimental results. The spin density on both Fe (2.54 to 2.71) and  $\kappa^3$ -SNS (0.16 to 0.13) does not change significantly, while  $\kappa^2$ -SN changes from -0.70 to 0.16. This can be interpreted as the transferred electron being placed on the  $\kappa^2$ -SN fragment of the ligand. Alternatively, the spin distribution of

**5.1**Fe<sup>+</sup> shows approximately three alpha electrons on the metal center, and approximately one beta electron on each side of the ligand. Again, the redox event is mostly ligand-based, with one beta electron on the κ<sup>3</sup>-SNS ligand fragment being released while the spin density on the Fe center remains unaltered.

An important observation can be made when examining the calculated metrical details (**Figure 5.9**) for **5.1**Fe<sup>+</sup> which show a clear bond alternation in the N,S-substituted aryl ring as observed for the diamagnetic dimer and Wieghardt's other two 5-coordinate complexes in **Figure 5.1**. This trend is also observed in the calculated bond lengths of **5.1**Fe and **5.1**Fe<sup>-</sup>, although it is significant to note that the difference in the degree of bond alteration decreases from **5.1**Fe<sup>+</sup> to **5.1**Fe to **5.1**Fe<sup>-</sup>. As previously mentioned, the bond alteration shown in the calculated parameters of **5.1**Fe are not well-reflected by the experimental bond lengths (**Figure 5.6**). This is also true of **5.1**Fe<sup>-</sup> whose experimental bond lengths show virtually no alteration in the N,S-substituted aryl rings.

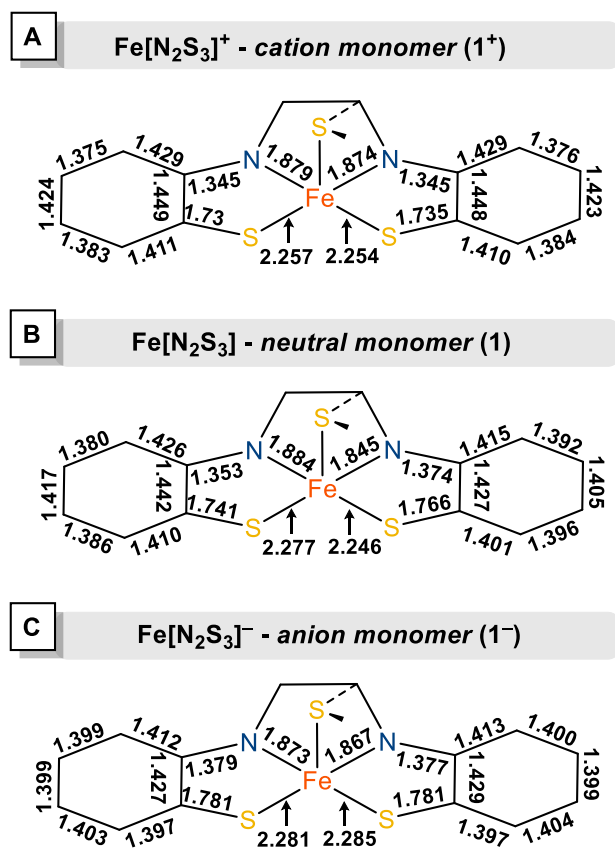


**Figure 5. 9.** Calculated bond distances (Å) for A)  $5.1_{Fe^+}$  B)  $5.1_{Fe}$  and C)  $5.1_{Fe^-}$ .

Considering the structural similarity of complexes  $5.1_{Fe}$  and  $5.1_{Fe^-}$  which contrast with the calculated metrics, it appears that the structures depicted in **Figure 5.1B** need to be revised. To get a better picture of the electronic structure of the reduced  $N_2S_2$  ligand, we investigated three redox states of the Zn complex to reduce the redox role of the metal (**Figure 5.10**). It is apparent that reduction of the ligand beyond  $L^{2-}$  decreases and then eliminates any bond alternation in the N,S-substituted aryl ring.<sup>47</sup> In contrast to previous calculations on Zn complexes with bidentate *o*-amido-thiolate phenylene ligand that also showed no aryl ring bond distance alternation in the ligand dianion,<sup>34</sup> in our tetradentate complexes both aryl C–C bonds associated with the N-bound carbon are longer than the

others in all three redox states. As a result, an alternate depiction of these reduced bis(N,S-phenylene) ligands involves a charge localization on five of the aryl ring carbons (**Figure 5.11**). Moreover, while the Mulliken spin population is balanced on both sides of the ligand in neutral  $Zn(N_2S_2)$ , the values are 0.38 and 0.64 for each side of the ligand in  $[Zn(N_2S_2)]^-$ , thus demonstrating significant delocalization of the unpaired spin across the ligand framework. A similar effect has been noted in a broken-symmetry calculation of nickel dithiolene complexes.<sup>48</sup>

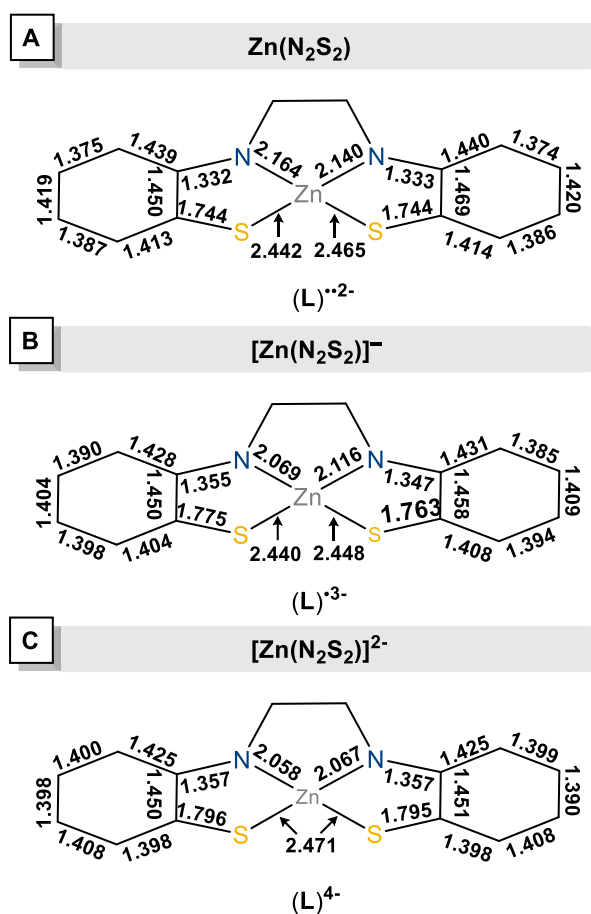


**Figure 5.10.** Optimized structures of Zn complexes of reduced  $N_2S_2$  ligands.

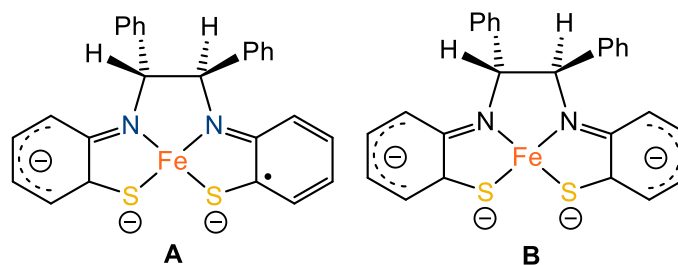


**Figure 5.11.** Alternate depiction of reduced bis(N,S-phenylene) ligands,  $(L\bullet)^{3-}$  (A) and  $(L)^{4-}$  (B).

Finally, the optimized geometries were further used to evaluate molecular orbital character and energies of frontier molecular orbitals (FMOs), with an emphasis on occupied and unoccupied FMOs of the  $\beta$  manifold. The  $\beta$  FMO diagram for  $5.1Fe^-$ ,  $5.1Fe$  and  $5.1Fe^+$  is shown in **Figure 5.12**, along with selected FMO depictions of  $5.1Fe^-$ . The FMOs of  $5.1Fe^-$  have significant d character for the three lowest unoccupied molecular orbitals (LUMO)  $\beta 143$  (61.69 %),  $\beta 144$  (68.01 %),  $\beta 145$  (72.81 %) which are identified as  $d_{xz}$ ,  $d_{yz}$ ,  $d_z^2$ , respectively, as well as for the occupied  $\beta 137$  orbital (60.95 %) identified as  $d_x^2-y^2$ . By comparison, the  $d_{xy}$  orbital ( $\beta 158$ ) has only 21.03 % d character, where strong covalency is a consequence of the strong  $\sigma$  antibonding interaction of  $d_{xy}$  orbital with p orbitals of nitrogen and sulfur atoms on the equatorial parts of ligands. Note that this significant delocalization of  $d_{xy}$  across multiple MOs is also present in the  $\alpha$ -manifold, demonstrating the inherent challenge in assigning oxidation states in such complexes. The HOMO can be identified as an antibonding orbital in equatorial parts of the ligand. Beyond that, this orbital contains a non-negligible amount of d character, a consequence of the high degree of covalency in these complexes. The rest of the orbitals between the HOMO and  $d_x^2-y^2$  are ligand-based orbitals containing significant interligand  $\pi$  bonding and antibonding interactions, as well as low lying unoccupied orbitals between  $d_z^2$  and  $d_{xy}$  orbitals.

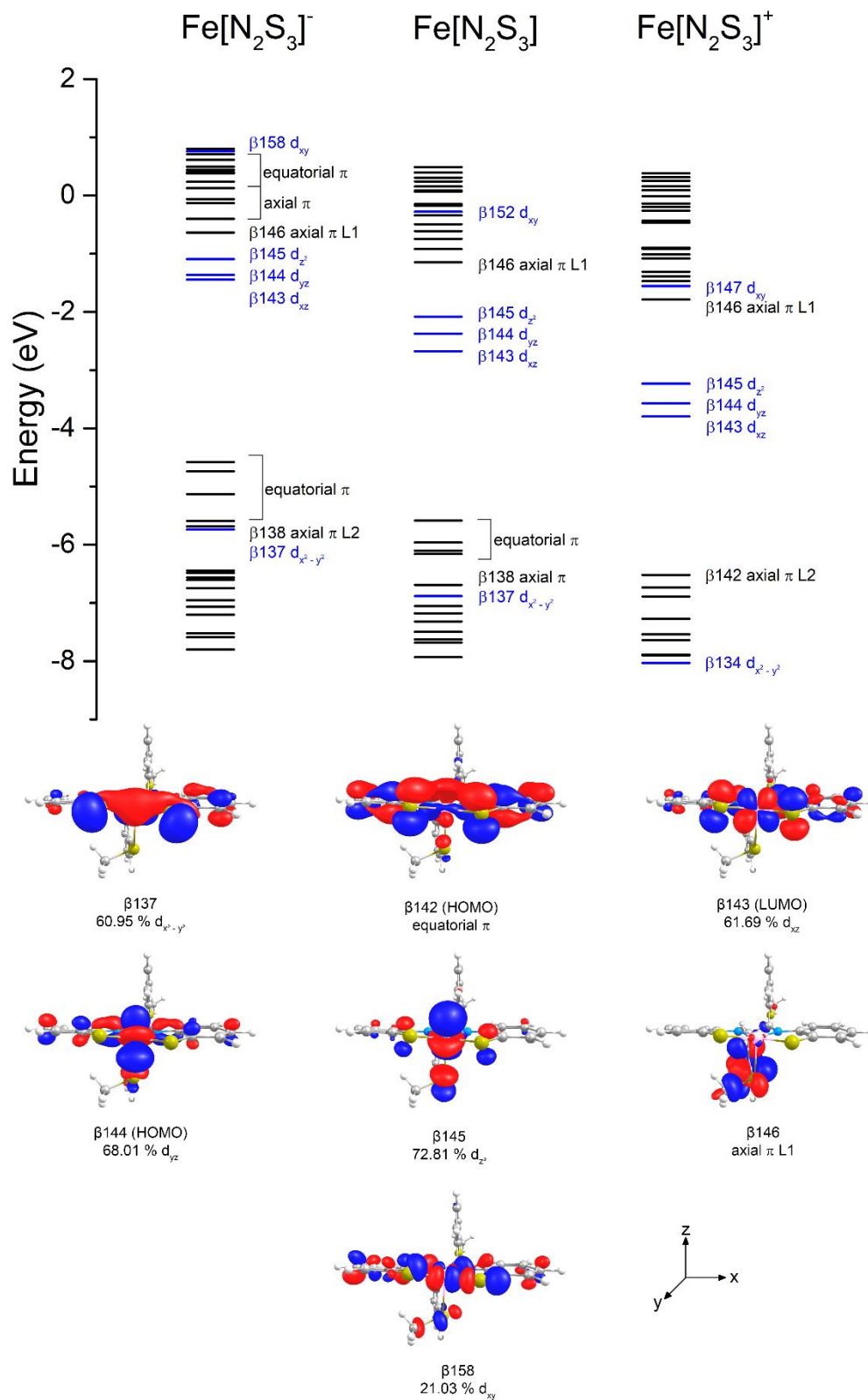


Figure 5.12. Calculated  $\beta$ -FMO energy diagrams for all complexes and selected orbital depictions.

For **5.1<sub>Fe</sub>** and **5.1<sub>Fe</sub><sup>+</sup>**, analysis of FMOs shows that the relative ordering of the Fe d orbitals stays the same. Comparing the FMOs of all three complexes, the energies of the d orbitals are lowered going from **5.1<sub>Fe</sub><sup>-</sup>** to **5.1<sub>Fe</sub><sup>+</sup>**, as are the energies of the ligand-based orbitals. It can be noted that the energy of d orbitals is more influenced by the redox events, which is manifested through the lowering of number of ligand-based orbitals between  $d_z^2$  and  $d_{xy}$  orbitals. Similar to the  $\beta$  manifold, in the  $\alpha$  manifold the HOMO orbitals are ligand-based.

Further comparison of the  $\alpha$  orbitals for **5.1<sub>Fe</sub>** and **5.1<sub>Fe</sub><sup>-</sup>** revealed that the LUMO in **5.1<sub>Fe</sub>** is an antibonding orbital mostly localized on the equatorial plane of the  $\kappa^2$ -SN ligand fragment, while after reduction the HOMO in **5.1<sub>Fe</sub><sup>-</sup>** is also antibonding but more delocalized and almost equally split between the equatorial parts of the  $\kappa^3$ -SNS and  $\kappa^2$ -SN ligand fragments. This can be correlated with the observed changes in calculated bond distances for equatorial bonds. However, these orbitals have negligible contributions from the axial parts of ligand and cannot be directly correlated with observed changes (experimental and calculated) in the axial Fe–S bond distance.

### 5.3 Conclusions

Three redox states of the square pyramidal  $Fe(N_2S_3)$  complex (**5.1<sub>Fe</sub>**) were subjected to rigorous spectroscopic and theoretical investigation to gain insight into their detailed electronic configuration. Ambiguity concerning metal-ligand electron sharing often exists in such base-metal redox non-innocent systems, and a combination of techniques revealed how the bonding subtleties in these complexes can be difficult to discern. In comparison to the Wieghardt system,<sup>34</sup> our X-ray diffraction and Mössbauer results do not support an

Fe(III) oxidation state for the diamagnetic thiolate-bridged dimer.<sup>e</sup> The bond distance alternation in the N,S-substituted aryl ring also observed for the phosphine<sup>34</sup> and phosphite<sup>41</sup> Fe complexes are consistent with an Fe(II) oxidation state and a dianionic tetradentate [N<sub>2</sub>S<sub>2</sub>]<sup>-2</sup> ligand. The open-shell singlet nature of this ligand is in accord with previous assessments of reduced diradical character in X,Y-phenylene ligands with ‘soft’ S- vs. ‘hard’ N- and O-donors.<sup>47</sup>

Although we were unable to isolate and structurally characterize a salt of [Fe(N<sub>2</sub>S<sub>3</sub>)]<sup>+</sup> (**5.1Fe<sup>+</sup>**), the similarity of its EPR spectrum to that of Wieghardt’s FeI(N<sub>2</sub>S<sub>2</sub>) complex<sup>34</sup> is consistent with an Fe(III) oxidation state and a dianionic pentadentate [N<sub>2</sub>S<sub>3</sub>]<sup>-2</sup> ligand. As stepwise 1e- reductions to afford **5.1Fe** and **5.1Fe<sup>-</sup>** have been shown by DFT to be primarily ligand-based, it is tempting to assign an Fe(III)(L<sup>•3-</sup>) and Fe(III)(L<sup>4-</sup>) electronic configuration to these complexes. This would be consistent with the observed lack of aryl ring bond distance alternation. Calculated changes in the Fe–N and Fe–S bond orders upon reduction, however, are **not** reflected in these metrical parameters<sup>24</sup> confirming the high degree of covalency suggested by the FMO analysis. Furthermore, while the orbital analysis confirms electron removal from different ‘halves’ of the ligand going from **5.1Fe<sup>-</sup>** to **5.1Fe**, the metrical details of **5.1Fe** reveal no asymmetry in the Fe–S and Fe–N bond distances nor in the other ligand bond distances. and highlights that the simplistic models we often use are not always the most accurate description. Finally, we note that the neutral Ni- (*S* = 0) and Co- (*S* = ½) N<sub>2</sub>S<sub>2</sub> complexes both show aryl bond alteration,<sup>31,33</sup> consistent with divalent oxidation states whereas this is not the case for the [Co(N<sub>2</sub>S<sub>2</sub>)]<sup>-</sup> anion (*S* = 1)

---

<sup>e</sup> It should be noted here that future work should instead qualify and compare experimental Mossbauer and XANES results with calculated results, as systems with large degrees of covalency may not give experimental values which match well with control systems used for comparison.

that Weighardt originally called out for its high degree of metal-ligand covalency.<sup>33</sup> Oftentimes, the complexities and apparent contradictions of a system should not be overlooked, and instead must be thoroughly investigated to gain a truer understanding, enabling deliberate and purposeful future reactivity studies.

## 5.4 Experimental

### 5.4.1 Materials and methods

Unless otherwise stated, all reactions were carried out under an atmosphere of dry, oxygen-free dinitrogen by means of standard Schlenk or glovebox techniques. Benzene- $d_6$  was degassed by three freeze-pump-thaw cycles, and subsequently dried by running through a column of activated alumina. Hexanes and THF were dried on columns of activated alumina using a J. C. Meyer (formerly Glass Contour) solvent purification system and stored over activated 4 Å molecular sieves.  $^1H$  NMR spectra were recorded on either a Bruker Avance or AvanceII spectrometer operating at 300 MHz with respect to proton nuclei.  $^1H$  NMR spectra were referenced to residual solvent protons ( $C_6D_6$ ,  $\delta$  7.15) with respect to tetramethylsilane at  $\delta$  0.00. SSNMR experiments were conducted using a Bruker Avance III NMR spectrometer ( $B_0 = 4.7T$ ,  $\nu L(^{13}C) = 50.3$  MHz,  $\nu L\{^1H\} = 200.1$  MHz) equipped with a triple resonance 7 mm MAS probe. Samples were ground into fine powder and packed in 7 mm o.d. zirconia rotors.  $^{13}C$  chemical shifts were externally referenced to the carbonyl signal of  $\alpha$ -glycine (176.5 ppm). The MAS frequency was 4.5 kHz. A standard  $^1H \rightarrow ^{13}C$  CPMAS experiment was used. The  $^1H \pi/2$  pulse length was 3.78  $\mu s$ . The CP contact time was 2 ms with a 50% ramped

pulse on <sup>1</sup>H. High-power <sup>1</sup>H decoupling was used during acquisition (66.7 kHz field). A recycle delay of 2 s was used and the total transients were 5600. High-resolution mass spectra were recorded on a Micromass Global QTOF mass spectrometer (CsI cluster used as calibrant) with electrospray ionization (ESI-MS) in positive mode with samples prepared to ca. 0.01 mg/mL. All reagents were purchased from commercial suppliers. The benzothiazolidine ligand<sup>49</sup> and **5.1Fe**<sup>41</sup> were synthesized according to literature procedures. Fe[N(SiMe<sub>3</sub>)<sub>2</sub>]<sub>2</sub> was synthesized according to a modified literature procedure.<sup>50</sup>

#### 5.4.1.1 Electrochemistry and EPR

*Cyclic voltammetry* (CV) data were obtained using an ESP-300 Biologic potentiostat equipped with a 1 A/48 V booster and an analog linear scan generator. All experiments were conducted under an argon atmosphere (glove box) in a standard one-compartment, three-electrode electrochemical cell. Tetra-*n*-butylammonium perchlorate (TBAP) or Tetra-*n*-butylammonium hexafluorophosphate (TBAPF<sub>6</sub>) in anhydrous THF was used as supporting electrolyte (0.1 M). An automatic ohmic drop compensation procedure was systematically implemented prior to recording CV data. All the electrodes were purchased from ALS Co. Ltd. Vitreous carbon (Ø = 3 mm) working electrodes were polished with 1 mm diamond paste before each recording. A Ag|AgNO<sub>3</sub> (10<sup>-2</sup> M + TBAP 10<sup>-1</sup> M in CH<sub>3</sub>CN) electrode was used as a reference. Spectroelectrochemical measurements were carried out with a Biologic ESP-300 potentiostat coupled to an MCS 500 UV-NIR Zeiss spectrophotometer using “thin layer” (0.5 mm or 1 mm) SEC cells purchased from ALS Co. Ltd. Voltamperometry experiments involving rotating disk electrodes (RDE) were carried out with a Radiometer instrument at a rotation rate of 550 rd·min<sup>-1</sup> using a glassy

carbon RDE tip ( $\varnothing = 3$  mm). A standard sweep rate of 0.01 V/s was used in RDE experiments.

*EPR Spectroscopy* was performed at 110 K, using a Bruker Elexsys E500 spectrometer operating at X-band (9.4 GHz) and standard cavity (4102 ST), with 100 KHz modulation frequency. The instrument settings were as follows: microwave power 6 mW; modulation amplitude 2 G; simulation of experimental spectra was performed using Easyspin (Matlab toolbox).

#### **5.4.1.2 <sup>57</sup>Fe Mössbauer spectroscopy**

Solid state samples were prepared in an inert atmosphere glovebox equipped with a liquid nitrogen fill port to enable sample freezing to 77 K within the glovebox. Each sample was loaded into a Delrin Mössbauer sample cup for measurements and loaded under liquid nitrogen. Zero-field <sup>57</sup>Fe Mossbauer measurements were performed using a See Co. MS4 Mössbauer spectrometer integrated with a Janis SVT-400T He/N<sub>2</sub> cryostat for measurements at 80 K. Isomer shifts were determined relative to A=Fe at 298 K. All Mössbauer spectra were fit using the program WMoss (SeeCo).

#### **5.4.1.4 X-ray absorption near-edge spectroscopy (XANES)**

X-ray absorption spectroscopy measurements were conducted on the Materials Research Collaborative Access Team (MRCAT) beam line 10-BM-B at the Advanced Photon Source, Argonne National Laboratory. Measurements were made in transmission mode using gas ionization detectors. The beam line is outfitted with a water-cooled double-crystal Si(111) monochromator with vertical aperture set to provide the highest energy resolution: about 1.00 eV at the Fe K edge.<sup>51</sup> The monochromator crystal pair was detuned

to 50% of the peak intensity to remove harmonics. Samples were prepared by diluting in a 50/50 mixture of boron nitride and PVP, then pressing the mixture into 7 mm diameter pellets. Iron K edge spectra were calibrated to Fe metal foil (EXAFS Materials) with the zero crossing of the 2<sup>nd</sup> derivative set at 7110.75±0.05 eV. Wilke et al<sup>45</sup> calibrated the Fe metal foil to 7111.08 eV; the cited values have been adjusted by -0.33 eV herein to reflect this difference.

XAFS data were processed using the Demeter suite<sup>52</sup> and pre-edge peaks were fit using Larch.<sup>53</sup> A Gaussian peak and a line were fit to the pre-edge, with the pre-edge peak range removed (limits varied) to simulate the background slope. In some cases, a third Gaussian peak was fit to the region above to pre-edge peaks and considered as part of the background when the initial fits showed a remaining peak in the data. After fitting the background, two pseudo-Voigt peaks with 50% Lorentzian character and with matching peak widths were fit along with the background peak and line parameters. The centroid energy only considers the non-background components. We have measured 16 iron reference compounds, some better than others. Our data set and the Wilke data set have the two spectra selected in common: Fe<sub>2</sub>O<sub>3</sub> and FeSO<sub>4</sub>·7H<sub>2</sub>O. They are shown along with the data in **Figure D4** over the approximate pre-edge fitting range. Other spectra in common are FeO and Fe<sub>3</sub>O<sub>4</sub>. **Figure D5** shows the background subtracted XANES with the peaks and fit. **Table D1** shows the fit results for these four samples.

#### 5.4.2 Synthesis and characterization of iron complexes

**Synthesis of Fe[N(SiMe<sub>3</sub>)<sub>2</sub>]<sub>2</sub>.** This complex was prepared by a modification of the literature procedure.<sup>50</sup> In the glovebox, Fe(Br)<sub>2</sub>(THF)<sub>2</sub> (2.5 g, 7.0 mmol) was charged to a

100 mL round bottom Schlenk flask equipped with stir bar. To the flask was added 20 mL of THF. A solution of Li(HMDS) (2.34 g, 14.0 mmol, 2 equiv) in 10 mL of THF was charged to a dropping funnel, and attached to the Schlenk flask. Under a dynamic  $N_2$  atmosphere using standard Schlenk techniques, the reaction mixture was allowed to stir at 0 °C for 15 min. Slow addition of Li(HMDS) was performed over the course of 30 min. The solution was allowed to warm slowly to room temperature and stirred overnight (~18 h). The solution was then evaporated in vacuo to leave behind a light brown and green mixture of oily solids. In a glovebox, the oily solid mixture was redissolved in hexanes giving a pale brown solution with a suspension of solids. The suspension was filtered through a frit (no Celite) and the filtrate was placed into a 100 mL one-neck round-bottom Schlenk flask. The filtrate was evaporated in vacuo to yield a pale brown-green solid. The green solid was distilled at 130 °C yielding a dark green oil (2.2 g, 70% yield) which solidifies upon storage at -35 °C.

**Isolation of  $Fe(N_2S_3) \cdot Fe(OH)_2(NCMe)_4$  crystals.** Complex **5.1<sub>Fe</sub>** was prepared according to the literature procedure,<sup>41</sup> albeit using acetonitrile in lieu of THF. The resulting purple powder was washed with hexanes (3 x 2 mL), and dried under vacuum. The title crystals, resulting from partial hydrolysis of **5.1<sub>Fe</sub>**, were obtained from a concentrated acetonitrile solution at -30 °C.

**Synthesis of  $[Na]^+ [Fe(N_2S_3)]^-$  (**5.1<sub>Fe</sub><sup>-</sup>**).** A vial was charged with sodium (0.012 g, 0.524 mmol) and naphthalene (0.067 g, 0.524 mmol) and 10 mL of THF and stirred until the sodium had fully dissolved. The resulting dark green solution was added dropwise to a solution of **5.1<sub>Fe</sub>** (0.300 g, 0.524 mmol) in 5 mL of THF. The reaction mixture was stirred for 18 h at room temperature and filtered through Celite. The filtrate was dried under

vacuum, and the resulting solid was washed with hexanes (3 x 3 mL). Finally, the reaction mixture was dried under vacuum, yielding 0.257 g (86 % yield) of a dark purple-blue solid. Crystals suitable for X-ray diffraction were grown from a concentrated solution of THF/hexanes at  $-30\text{ }^\circ\text{C}$ .  $^1\text{H NMR}$  ( $\text{C}_6\text{D}_6$ ,  $23\text{ }^\circ\text{C}$ , 500 MHz):  $\delta$  0.18 (br s); 1.08 (br s); 1.32 (br s); 3.35 (br s); 6.10 (br s,  $\Delta\nu_{1/2} = 466\text{ Hz}$ ); 7.60 (br s); 13.16 (br s); 14.71 (br s); 20.69 (br s). HRMS (ESI-QTOF,  $\text{CH}_3\text{CN}$ ): Calcd for  $\text{C}_{28}\text{H}_{24}\text{FeN}_2\text{S}_4\text{Na}$   $m/z$  595.0067. Found  $m/z$  595.0078.

### 5.4.3 Single crystal X-ray diffraction data

*\*\*Key crystallographic data can be found in Appendix D.\*\**

The crystals were mounted on thin glass fibers using paraffin oil or cyanoacrylate glue. The crystals were cooled to  $200 \pm 2\text{ K}$  during data collection. The data were collected on Bruker single-crystal diffractometer equipped with a sealed Mo tube source (wavelength  $0.71073\text{ \AA}$ ) and APEX II CCD detector. The raw data collection and processing were performed with Bruker APEX II software package.<sup>54</sup> Semi-empirical absorption correction based on equivalent reflections were applied.<sup>55</sup> Systematic absences and unit cell parameters were consistent with triclinic  $P-1$  (#2) for **5.1 $\text{Fe}$**  and **5.1 $\text{Fe}^-$** , and monoclinic  $P2_1/n$  (#14) for **1**. The structures were solved by direct methods and refined with a full-matrix least-squares procedure based on  $F^2$ , using SHELXL.<sup>56</sup> All non-hydrogen atoms were refined anisotropically. The hydrogen atoms bonded to carbon atoms were placed in idealized positions.

**Refinement details for  $[\text{Fe}(\text{N}_2\text{S}_3)][\text{Fe}(\text{OH})_2(\text{NCMe})_4]$  (**5.1 $\text{Fe}$** ) (monomer).**

The complex is located on an inversion center with half of it in the asymmetric unit and the Fe(2) atom's occupancy constrained to 0.5.

The H(38A) atom of the hydroxyl group and the H(39A), H(39B) atoms of the water molecule were refined with O-H and H...H distance restraints (DFIX in SHELXL) and isotropic displacement parameters constrained at 1.5U<sub>eq</sub> of the corresponding O atom.

The crystal was twinned and the refinement was performed using an HKLF5 file with two components (contributions refined to 0.65:0.35).

**Refinement details for [Na(THF)<sub>6</sub>]<sup>+</sup>[Fe(N<sub>2</sub>S<sub>3</sub>)]<sup>-</sup> (5.1Fe<sup>-</sup>).**

Most of the tetrahydrofuran (THF) molecules were disordered over two positions (See **Table D10** for occupancy ratios). They were refined with restraints applied to the 1,2- and 1,3-distances (SADI and SAME in SHELXL) and to the atomic displacement parameters (RIGU and SIMU in SHELXL).

**5.4.4 Details of DFT data**

All the calculations were carried out using Gaussian09 (Rev.D01)<sup>57</sup> at the B3LYP-D3 level of theory.<sup>58-61</sup> Grimme empirical dispersion was added with the GD3 keyword on all the calculations.<sup>62</sup> All structures were optimized in solution (benzene, ε= 2.2706), using the SMD model.<sup>63</sup> We used the 6-31+G(d)<sup>64-66</sup> basis set for light atoms (C, H, N, S) and LANL2DZ<sup>67</sup> and its corresponding pseudopotential for Fe atoms. All the stationary points were assigned to minima (zero imaginary frequencies) by frequency analyses. All reported energies in the manuscript are potential energies in solution. The Yamaguchi spin

correction formula was applied in all the calculations to account for spin contamination.<sup>68</sup>

A data set collection of computational results is available in the ioChem-BD repository.<sup>69</sup>

The molecular orbitals and spectra were calculated at the same level of theory, with the same basis set, in solution (THF,  $\epsilon = 7.4257$ ) using PCM model.<sup>70</sup> The FMOs were visualized and rendered from the Gaussian calculations using ChemCraft graphical software. The AOMix program was used to analyze MO compositions.<sup>71</sup> TD-DFT was used to calculate the electronic transition energies for the 30 lowest energy states.

## 5.5 References

- (1) Crabtree, R. H. *The Organometallic Chemistry of the Transition Metals*; John Wiley & Sons, 2009.
- (2) Van Leeuwen, P. W. M. *Homogeneous Catalysis: Understanding the Art*, Springer Science & Business Media, 2006.
- (3) Gebbink, R. J. K.; Moret, M.-E. *Non-Noble Metal Catalysis: Molecular Approaches and Reactions*, Wiley-VCH, 2019.
- (4) Hartwig, J. F. *Organotransition Metal Chemistry: From Bonding to Catalysis*, University Science Books, 2010.
- (5) Chirik, P. J.; Wieghardt, K. Radical Ligands Confer Nobility on Base-Metal Catalysts. *Science* **2010**, *327*, 794-795.
- (6) Chirik, P. J. Preface: Forum on Redox-active Ligands. *Inorg. Chem.* **2011**, *50*, 9737-9740.
- (7) Tondreau, A. M.; Atienza, C. C. H.; Weller, K. J.; Nye, S. A.; Lewis, K. M.; Delis, J. G.; Chirik, P. J. Iron Catalysts for Selective anti-Markovnikov Alkene Hydrosilylation Using Tertiary Silanes. *Science* **2012**, *335*, 567-570.
- (9) Zuo, W.; Lough, A. J.; Li, Y. F.; Morris, R. H. Amine (Imine) Diphosphine Iron Catalysts for Asymmetric Transfer Hydrogenation of Ketones and Imines *Science* **2013**, *342*, 1080-1083.
- (10) Small, B. L.; Brookhart, M. Iron-Based Catalysts with Exceptionally High Activities and Selectivities for Oligomerization of Ethylene to Linear  $\alpha$ -olefins. *J. Am. Chem. Soc.* **1998**, *120*, 7143-7144.
- (11) Lyaskovskyy, V.; de Bruin, B. Redox Non-Innocent Ligands: Versatile New Tools to Control Catalytic Reactions. *ACS. Catal.* **2012**, *2*, 270-279.
- (12) van Leest, N. P.; Epping, R. F.; van Vliet, K. M.; Lankelma, M.; van den Heuvel, E. J.; Heijtbrink, N.; Broersen, R.; de Bruin, B. Single-Electron Elementary Steps in Homogeneous Organometallic Catalysis. *Adv. Organomet. Chem.* **2018**, *70*, 71-180.

- (13) Luca, O. R.; Crabtree, R. H. Redox-Active Ligands in Catalysis. *Chem. Soc. Rev.* **2013**, *42*, 1440-1459.
- (14) Broere, D. L.; Plessius, R.; van der Vlugt, J. I. New Avenues for Ligand-Mediated Processes—Expanding Metal Reactivity by the use of Redox-active Catechol, o-Aminophenol and o-Phenylenediamine Ligands. *Chem. Soc. Rev.*, **2015**, *44*, 6886-6915.
- (15) Praneeth, V. K.; Ringenberg, M. R.; Ward, T. R. Redox Active Ligands in Catalysis. *Angew. Chem. Int. Ed.* **2012**, *51*, 10228-10234.
- (15) Elsby, M. R.; Baker, R. T. Strategies and Mechanisms of Metal–Ligand Cooperativity in First-Row Transition Metal Complex Catalysts. *Chem. Soc. Rev.* **2020**, *49*, 8933-8987.
- (16) Baker-Hawkes, M.; Billig, E.; Gray, H. B. Characterization and Electronic Structures of Metal Complexes Containing Benzene-1, 2-dithiolate and Related Ligands. *J. Am. Chem. Soc.* **1966**, *88*, 4870-4875.
- (17) Pierpont, C. G.; Buchanan, R. M. Transition Metal Complexes of o-Benzoquinone, o-Semiquinone, and Catecholate Ligands *Coord. Chem. Rev.* **1981**, *38*, 45-87.
- (18) Balch, A. L. Coordination Chemistry with Meso-hydroxylated Porphyrins (oxophlorins), Intermediates in Heme Degradation. *Coord. Chem. Rev.* **2000**, *200*, 349-377.
- (19) De Bruin, B.; Hetterscheid, D. G.; Koekkoek, A. J.; Grützmacher, H. The Organometallic Chemistry of Rh-, Ir-, Pd- and Pt-based Radicals: Higher Valent Species. *Prog. Inorg. Chem.* **2007**, *55*, 247-354.
- (20) Kaim, W. Manifestations of Non-Innocent Ligand Behavior. *Inorg. Chem.* **2011**, *50*, 9752-9765.
- (21) Butschke, B.; Fillman, K. L.; Bendikov, T.; Shimon, L. J.; Diskin-Posner, Y.; Leitun, G.; Gorelsky, S. I.; Neidig, M. L.; Milstein, D. How Innocent are Potentially Redox Non-Innocent Ligands? Electronic Structure and Metal Oxidation States in Iron-PNN Complexes as a Representative Case Study. *Inorg. Chem.* **2015**, *54*, 4909-4926.
- (22) Chaudhuri, P.; Verani, C. N.; Bill, E.; Bothe, E.; Weyhermüller, T.; Wieghardt, K. Electronic Structure of Bis (o-iminobenzosemiquinonato) Metal Complexes (Cu, Ni, Pd). The Art of Establishing Physical Oxidation States in Transition-Metal Complexes Containing Radical Ligands. *J. Am. Chem. Soc.* **2001**, *123*, 2213-2223.

- (23) Bart, S. C.; Chłopek, K.; Bill, E.; Bouwkamp, M. W.; Lobkovsky, E.; Neese, F.; Wieghardt, K.; Chirik, P. J. Electronic Structure of Bis (imino) Pyridine Iron Dichloride, Monochloride, and Neutral Ligand Complexes: A Combined Structural, Spectroscopic, and Computational Study. *J. Am. Chem. Soc.* **2006**, *128*, 13901-13912.
- (24) Ruta R. Kapre, R. R.; Bothe, E.; Weyhermüller, T.; DeBeer George, S.; Muresan, N.; Wieghardt, K. Electronic Structures of Tris(dioxolene)chromium and Tris(dithiolene)chromium Complexes of the Electron-Transfer Series [Cr(dioxolene)<sub>3</sub>]<sup>z</sup> and [Cr(dithiolene)<sub>3</sub>]<sup>z</sup> (z = 0, 1-, 2-, 3-). A Combined Experimental and Density Functional Theoretical Study. *Inorg. Chem.* **2007**, *46* (19), 7827-7839.
- (25) Ray, K.; Petrenko, T.; Wieghardt, K.; Neese, F. Joint Spectroscopic and Theoretical Investigations of Transition Metal Complexes Involving Non-Innocent Ligands. *Dalton Trans.* **2007**, 1552–1566.
- (26) Sproules, S.; Weyhermüller, T.; Goddard, R.; Wieghardt, K. The Rhenium Tris(dithiolene) Electron Transfer Series: Calibrating Covalency. *Inorg. Chem.* **2011**, *50* (24), 12623-12631.
- (27) Howard, J. B.; Rees, D. C. Structural Basis of Biological Nitrogen Fixation. *Chem. Rev.* **1996**, *96*, 2965-2982.
- (28) Eady, R. R. Structure–Function Relationships of Alternative Nitrogenases *Chem. Rev.* **1996**, *96*, 3013-3030.
- (29) Appel, A. M.; Bercaw, J. E.; Bocarsly, A. B.; Dobbek, H.; DuBois, D. L.; Dupuis, M.; Ferry, J. G.; Fujita, E.; Hille, R.; Kenis, P. J. Frontiers, Opportunities, and Challenges in Biochemical and Chemical Catalysis of CO<sub>2</sub> Fixation. *Chem. Rev.* **2013**, *113*, 6621-6658.
- (30) Sproules, S.; Wieghardt, K. o-Dithiolene and o-Aminothiolate Chemistry of Iron: Synthesis, Structure and Reactivity. *Coord. Chem. Rev.* **2010**, *254*, 1358-1382.
- (31) Kawamoto, T.; Kuma, H.; Kushi, Y. Valence Isomerization. Synthesis and Characterization of Cobalt and Nickel Complexes *Bull. Chem. Soc. Jpn.* **1997**, *70*, 1599.
- (32) D'yachenko, O. A.; Atovmyan, L. O.; Aldoshin, S. M.; Kogan, V. A.; Kochin, S. G.; Osipov, O. A. Study of X-ray Crystal Structure of Bis(benzylidene-2'-mercaptoanilinato)nickel. *Bull. Acad. Chem. Sci. USSR* **1975**, *24* (9), 219.

- (33) Sproules, S.; Kapre, R. R.; Roy, N.; Weyhermüller, T.; Wieghardt, K. The Molecular and Electronic Structures of Monomeric Cobalt Complexes Containing Redox Noninnocent o-aminobenzenethiolate Ligands. *Inorg. Chim. Acta* **2010**, *363*, 2702–2714.
- (34) Presow, S. R.; Ghosh, M.; Bill, E.; Weyhermüller, T.; Wieghardt, K. Molecular and Electronic Structures of New Iron Complexes Containing N,S-coordinated o-Iminothione-benzosemiquinonate ( $1^-$ )  $\pi$  Radical Ligands: An Experimental and Density Functional Theoretical Study. *Inorg. Chim. Acta* **2011**, *374*, 226-239.
- (35) Eisenberg, R.; Gray, H. B. Noninnocence in Metal Complexes: A Dithiolene Dawn. *Inorg. Chem.* **2011**, *50*, 9741-9751.
- (36) Chaudhuri, P.; Hess, M.; Flörke, U.; Wieghardt, K. From Structural Models of Galactose Oxidase to Homogeneous Catalysis: Efficient Aerobic Oxidation of Alcohols. *Angew. Chem. Int. Ed.* **1998**, *37*, 2217-2220.
- (37) Goswami, M.; Lyaskovskyy, V.; Domingos, S. R.; Buma, W. J.; Woutersen, S.; Troeppner, O.; Ivanović-Burmazović, I.; Lu, H.; Cui, X.; Zhang, X. P. Characterization of Porphyrin-Co (III)-‘Nitrene Radical’ Species Relevant in Catalytic Nitrene Transfer Reactions. *J. Am. Chem. Soc.* **2015**, *137*, 5468-5479.
- (38) Jazdzewski, B. A.; Tolman, W. B. Understanding the Copper–Phenoxy Radical Array in Galactose Oxidase: Contributions from Synthetic Modeling Studies. *Coord. Chem. Rev.* **2000**, *200*, 633-685.
- (39) Lyons, C. T.; Stack, T. D. P. Recent Advances in Phenoxy Radical Complexes of Salen-type Ligands as Mixed-Valent Galactose Oxidase Models. *Coord. Chem. Rev.* **2013**, *257*, 528-540.
- (40) Clarke, R. M.; Herasymchuk, K.; Storr, T. Electronic Structure Elucidation in Oxidized Metal–salen Complexes. *Coord. Chem. Rev.* **2017**, *352*, 67-82.
- (41) Das, U. K.; Higman, C. S.; Gabidullin, B.; Hein, J. E.; Baker, R. T. Efficient and Selective Iron-Complex-catalyzed Hydroboration of Aldehydes. *ACS. Catal.* **2018**, *8*, 1076-1081.
- (42) Stoian, S. A.; Yu, Y.; Smith, J. M.; Holland, P. L.; Bominaar, E. L.; Münck, E. Mössbauer, Electron Paramagnetic Resonance, and Crystallographic Characterization of a

High-spin Fe (I) Diketimate Complex with Orbital Degeneracy. *Inorg. Chem.* **2005**, *44*, 4915-4922.

(43) Wilding, M. J.; Iovan, D. A.; Betley, T. A. High-spin Iron Imido Complexes Competent for C–H Bond Amination. *J. Am. Chem. Soc.* **2017**, *139*, 12043-12049.

(44) Gütllich, P.; Bill, E.; Trautwein, A. X. *Mössbauer Spectroscopy and Transition Metal Chemistry: Fundamentals and Applications*; Springer Science & Business Media, 2010.

(45) Wilke, M.; Farges, F.; Petit, P.-E.; Brown Jr, G. E.; Martin, F. Oxidation State and Coordination of Fe in Minerals: An Fe K-XANES Spectroscopic Study. *Amer. Mineral.* **2001**, *86*, 714-730.

(46) Wilke, M.; Partzsch, G. M.; Bernhardt, R.; Lattard, D. Determination of the Iron Oxidation State in Basaltic Glasses using XANES at the K-edge. *Chem. Geol.* **2004**, *213*, 71-87.

(47) This bond distance alternation has been quantified ( $\Delta$ ) and promoted as a useful descriptor of ligand non-innocence: a) Starikov, A. G.; Minkin, V. I.; Minyaev, R. M.; Koval, V. V. A Quantum Chemical Study of Bis-(iminoquinonephenolate) Zn(II) Complexes. *J. Phys. Chem. A* **2010**, *114*, 7780–7785. b) Mukherjee, R. Assigning Ligand Redox Levels in Complexes of 2-Aminophenolates: Structural Signatures. *Inorg. Chem.* **2020**, *59*, 12961-12977.

(48) Bachler, V.; Olbrich, G.; Neese, F.; Wieghardt, K. Theoretical Evidence for the Singlet Diradical Character of Square Planar Nickel Complexes Containing Two o-semiquinonato Type Ligands. *Inorg. Chem.* **2002**, *41*, 4179-4193.

(49) Das, U. K.; Daifuku, S. L.; Gorlesky, S. I.; Korobkov, I.; Neidig, M. L.; Le Roy, J. L.; Muregesu, M.; Baker, R. T. Mononuclear, Dinuclear, and Trinuclear Iron Complexes Featuring a New Monoanionic SNS Thiolate Ligand. *Inorg. Chem.* **2016**, *55*, 987–997.

(50) Olmstead, M. M.; Power, P. P.; Shoner, S. C. Three-Coordinate Iron Complexes: X-ray Structural Characterization of the Iron Amide-Bridged Dimers  $[Fe(NR_2)_2]_2$  (R=SiMe<sub>3</sub>, C<sub>6</sub>H<sub>5</sub>) and the Adduct  $Fe[N(SiMe_3)_2]_2(THF)$  and Determination of the Association Energy of the Monomer  $Fe[N(SiMe_3)_2]_2$  in Solution. *Inorg. Chem.* **1991**, *30*, 2547-2551.

(51) “The New MRCAT (Sector 10) Bending Magnet Beamline at the Advanced Photon Source”, A.J. Kropf, J. Katsoudas, S. Chattopadhyay, T. Shibata, E.A. Lang, V.N.

Zyryanov, B. Ravel, K. McIvor, K.M. Kemner, K.G. Scheckel, S.R. Bare, J. Terry, S.D. Kelly, B.A. Bunker, C.U. Segre, CP1234, SRI 2009, The 10th International Conference on Synchrotron Radiation Instrumentation, Melbourne, Australia, Sept. 27 – Oct. 2, 2009, R. Garrett, I. Gentle, K. Nugent, S. Wilkins, eds. (American Institute of Physics, NY, 23 June 2010) 299-302. doi:10.1063/1.3463194.

(52) Ravel, B.; Newville, M. ATHENA, ARTEMIS, HEPHAESTUS. Data Analysis For X-ray Absorption Spectroscopy Using IFEFFIT, *J. Synchrotron Rad.* **2005**, *12*, 537–541.

(54) APEX 2, Bruker AXS Inc., Madison, Wisconsin, USA, 2012.

(55) G. M. Sheldricks, SADABS, Program for Empirical Absorption Correction of Area Detector Data, University of Gottingen, Germany, 1996.

(56) G. M. Sheldrick. SHELXLT-Integrated Space-Group and Crystal-Structure Determination. *Acta Cryst.*, **2015**, *C71*, 3-8.

(57) Frisch, M. J.; Trucks, G. W.; Schlegel, H. B.; Scuseria, G. E.; Robb, M. A.; Cheeseman, J. R.; Scalmani, G.; Barone, V.; Mennucci, B.; Petersson, G. A.; Nakatsuji, H.; Caricato, M.; Li, X.; Hratchian, H. P.; Izmaylov, A. F.; Bloino, J.; Zheng, G.; Sonnenberg, J. L.; Hada, M.; Ehara, M.; Toyota, K.; Fukuda, R.; Hasegawa, J.; Ishida, M.; Nakajima, T.; Honda, Y.; Kitao, O.; Nakai, H.; Vreven, T.; Montgomery, J. A., Jr.; Peralta, J. E.; Ogliaro, F.; Bearpark, M.; Heyd, J. J.; Brothers, E.; Kudin, K. N.; Staroverov, V. N.; Kobayashi, R.; Normand, J.; Raghavachari, K.; Rendell, A.; Burant, J. C.; Iyengar, S. S.; Tomasi, J.; Cossi, M.; Rega, N.; Millam, J. M.; Klene, M.; Knox, J. E.; Cross, J. B.; Bakken, V.; Adamo, C.; Jaramillo, J.; Gomperts, R.; Stratmann, R. E.; Yazyev, O.; Austin, A. J.; Cammi, R.; Pomelli, C.; Ochterski, J. W.; Martin, R. L.; Morokuma, K.; Zakrzewski, V. G.; Voth, G. A.; Salvador, P.; Dannenberg, J. J.; Dapprich, S.; Daniels, A. D.; Farkas, Ö.; Foresman, J. B.; Ortiz, J. V.; Cioslowski, J.; Fox, D. J. *Gaussian 09, revision D.01*; Gaussian, Inc., Wallingford, CT, **2013**.

(58) Becke, A. D. A New Mixing of Hartree-Fock and Local Density Functional Theories. *J. Chem. Phys.* **1993**, *98*, 1372-1377. (59) Becke, A. D. Density-Functional Thermochemistry. III. The Role of Exact Exchange. *J. Chem. Phys.* **1993**, *98*, 5648-5652.

(60) Lee, C.; Yang, W.; Parr, R. G. Development of the Colle-Salvetti Correlation-Energy Formula Into a Functional of the Electron Density. *Phys. Rev. B.* **1988**, *37*, 785-789. (61)

Stephens, P. J.; Devlin, F. J.; Chabalowski, C. F.; Frisch, M. J. Ab-Initio Calculation of Vibration Absorption and Circular Dichroism Spectra Using Density Functional Force Fields. *J. Phys. Chem.* **1994**, *98*, 11623-11627.

(62) Grimme, S.; Antony, J.; Ehrlich, S.; Krieg, H. A Consistent and Accurate *Ab Initio* Parametrization of Density Functional Dispersion Correction (DFT-D) for the 94 Elements H-Pu. *J. Chem. Phys.* **2010**, *132*, 154104.

(63) Marenich, A. V.; Cramer, C. J.; Truhlar, D. G. Generalized Born Solvation Model SM12. *J. Phys. Chem. B.* **2009**, *113*, 6378-6396.

(64) Hehre, W. J.; Ditchfield, R.; Pople, J. A. Self-Consistent Molecular Orbital Methods. XII. Further Extensions of Gaussian-Type Basis Sets for use in Molecular Orbital Studies of Organic Molecules. *J. Chem. Phys.* **1972**, *56*, 2257.

(65) Hariharan, P. C.; Pople, J. A. People. The Influence of Polarization Functions on Molecular Orbital Hydrogenation Energies. *Theor. Chim. Acta*, **1973**, *28*, 213-222.

(66) Francl, M. M.; Pietro, W. J.; Hehre, W. J.; Binkley, J. S.; Gordon, M. S.; DeFrees, D. J.; Pople, J. A. Self-Consistent- Molecular Orbital Methods. XXIII. A Polarization-Type Basis Set for Second-Row Elements. *J. Chem. Phys.* **1982**, *77*, 3654.

(67) Hay, P. J.; Wadt, W. R. *Ab Initio* Effective Core Potentials for Molecular Calculations. Potentials for the Transition Metal Atoms Sc to Hg. *J. Chem. Phys.* **1985**, *82*, 270

(68) Yamaguchi, K.; Jensen, F.; Dorigo, A.; Houk, K. N. A Spin Correction Procedure for Unrestricted Hartree-Fock and Moller-Plesset Wavefunctions for Singlet Diradicals and Polyradicals. *Chem. Phys. Lett.* **1988**, *149*, 537.

(69) Álvarez-Moreno, M.; de Graaf, C.; Lopez, N.; Maseras, F.; Poblet, J. M.; Bo, C. J. Managing the Computational Chemistry Big Data Problem: The ioChem-BD Platform. *Chem. Inf. Model.* **2015**, *55*, 95.

(70) Tomasi, J.; Mennucci, B.; Cammi, R., Quantum Mechanical Continuum Solvation Models. *Chem. Rev.* **2005**, *105* (8), 2999-3093.

(71) Gorelsky, S. I. AO Mix: Program for Molecular Orbital Analysis, version 6.8.5; 2014; <http://www.sgchem.net/>.

## **Chapter 6 – Conclusions and Future Work**

### **6.1 Key Findings and Contributions to the Overall Field and Connecting the Chapters**

Metal-ligand cooperation is a reaction strategy that has garnered increasing interest in the last decade for its efficacy in improving catalytic activity of first-row metals complexes.<sup>1</sup> In Chapter 1, the different reaction strategies of MLC are summarized, with key examples highlighted. More importantly, a large emphasis was placed on mechanistic discussion for the various reaction pathways of these base metal MLC catalysts. Additionally, this chapter effectively demonstrated the large reliance placed on phosphine-

based pincer ligands within MLC. Overall, two needs were identified to effect further advances: i) More intensive and thoughtful mechanistic investigations in MLC and ii) Further investigation into phosphine-free ligands. More interesting within the context of this dissertation was our demonstration that the use of phosphine-free [SNS] pincer ligands leads to a divergence from the traditionally proposed reaction pathways for MLC.

The Baker group has previously detailed the synthesis and reactivity of two bifunctional [SNS] pincer ligands.<sup>2-4</sup> These ligands are differentiated by their bifunctional Lewis base donor: **L1** features an amido donor, and **L2** features a thiolate donor. To this point, previous attempts in the group to directly compare these ligands were unsuccessful due to varied coordination chemistry even upon analogous reaction conditions.<sup>5</sup> In Chapter 2, a direct comparison of the bifunctional reactivity of these two ligands was successfully performed using an IPr-Cu-[SNS] framework. Reactivity investigations showed that while both ligands were effective for carbonyl hydroboration catalysis, the amido **L1** ligand demonstrated more diverse reaction capabilities. In particular, the **L1** amido ligand was effective for catalytic carbonyl hydrosilylation, whereas **L2** thiolate ligand was ineffective. Mechanistic investigations using isotope labelling studies were suggestive of a traditional outer-sphere reaction pathway operating through the intermediacy of a Cu-H.<sup>6</sup>

Carbonyl hydroboration/hydrosilylation catalysis is not a particularly challenging transformation, and there are many literature examples.<sup>7-9</sup> Additionally, the proposed reaction pathways align with conventionally proposed mechanisms for similar catalyst systems.<sup>10</sup> The largest value of this work comes in the direct comparison of amido vs. thiolate bifunctional donors. The overwhelming majority of Lewis base bifunctional

ligands make use of nitrogen donors, with very few using thiolates. Our comparison of these contrastingly studied donors indicated that upon initial investigation, the amido donor is more suitable for diverse reactivity.<sup>6</sup> Considering the structures of the two complexes, the lability of the six-membered ring in the amido complex could give rise to a two-coordinate NHC-Cu-amido species that could provide more room (vs the Cu-thiolate) to activate bulkier silanes. Therefore, future work here should use a more diverse range of borane and silane substrates to more closely investigate the trends observed in this system, as the observed reactivity may be more due to sterics and/or electronics of the chosen silane, as opposed to purely the Lewis basicity of the amido vs. the thiolate.

With early investigations indicating that the **L1** amido ligand made a more reactive bifunctional reaction system, this ligand was chosen as a focus for subsequent investigations. In Chapter 3, a Mn(bis-amido) complex was synthesized using similar reaction strategies previously used to obtain Fe and Co complexes of the same type.<sup>3,11</sup> With three structurally analogous complexes in hand differentiated only by the metal, we assessed the influence of the base-metal on bifunctional reactivity. Computationally calculated Fukui indices and Hirshfeld charges were obtained to discern potential trends, and subsequently compared to a model bifunctional H<sub>2</sub> activation pathway for the three Mn, Fe, and Co complexes. This work showed that a balance of metal electrophilicity and ligand nucleophilicity provides the lowest energy reaction pathway, as demonstrated by the Mn(bis-amido) complex. This work is one of few examples<sup>12,13</sup> to critically compare analogous metal complexes to discern the influential reactivity factors within an MLC pathway.

As the Mn(bis-amido) complex was indicated to be the most reactive catalyst candidate, Chapter 3 continues with its investigation as a carbonyl hydroboration catalyst. While there are examples of Mn hydroboration catalysts in literature,<sup>14,15</sup> most examples which utilize a paramagnetic divalent Mn-system are lacking in detailed mechanistic investigation.<sup>16</sup> Within this work a thorough combined experimental and computational mechanistic study was performed to elucidate the reaction pathway. Several critical findings were determined, including: i) the significance of the hemilabile thioether donor for the stabilization of early reaction intermediates and success of the reaction, ii) the different roles played by the two **L1** ligands (thioether hemilability vs. B–H activation), and iii) the proposed metal-hydride free reaction pathway. Formation of a metal hydride intermediate is often presumed in the context of Mn catalysis involving E-H bond activation. In this work, it was demonstrated by both experimental and computational findings that a metal-hydride is a highly disfavored intermediate. Instead, activation of the boryl by the amido led to an inner-sphere hydride transfer to the Mn-bound organic substrate. At the conclusion of this chapter, we postulate that this non-traditional reaction pathway is a product of the inherent nature of the [SNS] ligand donors, and a consequence of divergence from strong sigma-donating phosphines which would traditionally bolster the electrophilic Mn center.

Chapter 4 begins by detailing the Baker group's initial attempts to access a mono-ligated SNS complex with a base metal. Early work with Fe SNS-thiolate and -amido complexes with electron-rich ancillary phosphine ligands demonstrated the propensity of the SNS ligand to undergo C–S<sub>aryl</sub> bond cleavage to form a new dianionic CNS ligand.<sup>16</sup> To access a less electron-rich analog, Mn(CO)<sub>5</sub>Br was chosen as a starting material to

synthesize the  $\text{Mn}^{\text{I}}(\text{SNS})(\text{CO})_3$  amido and thiolate complexes. The latter complex demonstrated efficient catalytic activity for nitrile hydroboration under photolytic conditions. Combined experimental and computational mechanistic studies demonstrated several elements crucial to successful reaction: i) the bifunctional nature of the thiolate donor for boryl activation and hydride transfer; ii) the flexible nature of the SNS-thiolate ligand to enable rearrangement between *facial* and *meridional* isomers to stabilize intermediates and iii) the ability of the Mn to undergo a spin state change to adopt a lower energy high-spin configuration. Once again, the lack of phosphine donors in the catalyst system results in a non-traditional hydride-free reaction pathway attributed to the SNS ligand. In future work, a comparison should be made with the analogous Mn complex with **L1**, especially with regard to alkene hydroboration and/or hydrosilylation.

The work in Chapter 4 represents an ideal advancement of our class of complexes and demonstrates several unique design features of our ligand set. This work was the first demonstration of catalysis beyond carbonyl hydroboration with our bifunctional ligands. Nitrile dihydroboration has garnered more attention recently as a synthetic route to access diborylamines,<sup>17</sup> and this work is the second example of using Mn to catalyze this reaction.<sup>18</sup> In addition, this was the first reported combination of use of a bifunctional thiolate donor with Mn for MLC catalysis. Finally, the realization that the spin-state change of the Mn is integral to entering the catalytic cycle is an especially gratifying finding of this work. Recent literature often places excess emphasis on recreating precious metal catalysis with the base metals, and the work in Chapter 4 is an excellent example of exploiting the oftentimes problematic electronic flexibility of the base metals for a positive reaction. In future work, it would be beneficial to access an IR spectrometer that permits

continuous UV irradiation of the solution sample in order to track both the catalyst (C – O and C=N bands) and potential reactive intermediates (C=N bands) during catalysis.

Finally, Chapter 5 includes a thorough physical and theoretical examination of a previously made complex in the Baker group<sup>7</sup> to understand the nature of the new pentadentate, redox non-innocent [N<sub>2</sub>S<sub>3</sub>] ligand. The exploitation of redox non-innocent ligands for catalysis is considered to fall within the MLC strategy, and *N,S*-coordinated ligands have been well established to display redox active properties. As such, electrochemical investigations on the titular Fe[N<sub>2</sub>S<sub>3</sub>] complex showed facile reversible reduction and oxidation. After isolation of the anionic redox partner Fe[N<sub>2</sub>S<sub>3</sub>]<sup>-</sup>, a variety of techniques were used to gain insight into the nature of the electron transfer events. Contradicting experimental data (Mossbauer and XANES vs. SCRXD) made it unclear whether the redox events were based upon the ligand or at the metal center. Detailed DFT calculations demonstrated that the redox interconversions are dominated by changes in the electron population of the N<sub>2</sub>S<sub>3</sub> ligand, and intimate mixing with the Fe d<sub>xy</sub> orbital due to a high degree of metal-ligand covalency. This work, while not the first of its kind, highlights how we should not overlook the complexities and apparent contradictions in our systems. To gain a truer understanding of the myriad ways in which redox non-innocent systems can work, systems which do not follow our traditionally relied upon simplistic models should be intensively studied.

Overall, the catalytic reactions studied in this dissertation are not the most notable contributions. While the catalysts presented for carbonyl hydroboration and hydrosilylation are highly active in terms of TON and TOF, there exist many catalysts capable of

performing these reactions. Additionally, while the Mn-catalyzed dihydroboration of nitriles is among the most active for base-metal catalysts, other systems out-perform in terms of substrate scope and TOF. Instead, the most notable contributions resulting from this dissertation come from the study of the underlying mechanisms of these catalyst systems. A main goal of this work was to design bifunctional catalysts with [SNS]-pincer ligands in an effort to move away from the use of non-sustainable phosphine ligands. Within the realm of the project we uncovered that, much like one cannot expect 1<sup>st</sup> row metals to demonstrate the same reactivity as the noble metals, neither can one expect sulfur-based ligands to operate the same as phosphorous-based ligands. A new reaction pathway was identified and posited to be a direct result of not using phosphine ligands, and should provide foundational understanding for future work in exploring and expanding the reactivity of biomimetic bifunctional ligands.

## **6.2 Critical Evaluation of Research Approach and Methodology**

The work entailed in this dissertation was both enriching and challenging. Due to the inherent nature of the work, several challenges were frequently encountered which made careful mechanistic study and evaluation difficult. The two challenges most frequently encountered in the course of this dissertation were: i) the lack of a useful NMR handle beyond <sup>1</sup>H, and; ii) the frequent formation of paramagnetic complexes. Ironically, these two challenges can be directly correlated to the use of SNS pincer ligands. Traditional phosphine-based pincer ligands include the highly useful <sup>31</sup>P NMR handle and encourage well behaved low-spin diamagnetic complexes. Alternatively, the weak field SNS ligand was shown to frequently allow access to high-spin paramagnetic species and cannot always be effectively monitored using NMR.

With these two challenging hurdles commonly appearing during the course of my research these past 4 years, creative experiments needed to be performed and interpreted to gain the desired mechanistic insight. In much of the mechanistic work presented in this dissertation, stoichiometric mechanistic studies were relied upon to gain insight into the behaviour of the metal complex with catalytic reaction components. This required thoughtful experimental design, and critical analysis of the results to correctly interpolate mechanistic information. Oftentimes these types of reactions were heavily relied upon due to lack of access to more specialized equipment. For instance, as noted above, work in Chapter 4 involving a  $\text{Mn}(\text{SNS})(\text{CO})_3$  complex would have greatly benefitted from careful investigation using IR spectroscopy, as distinctive IR signals could report on the nitrile substrate, reduction intermediates, as well as both SNS and CO ligands of the catalyst. Analysis of this reaction under catalytic conditions in tandem with the presented  $^{13}\text{C}$ -labelling studies would have greatly supported the conclusions in the chapter; however, inability to satisfactorily run these IR experiments under air/moisture free conditions prohibited this type of analysis. Additionally, Chapter 3 involved a paramagnetic Mn(II) catalyst species which was not particularly amenable to divulging mechanistic information using NMR. Again, IR spectroscopy of the stoichiometric reactions may have enabled the observation of a B–H stretch on a 4-coordinate boron which would have presented strong experimental evidence of the DFT-postulated intermediate. Furthermore, more in-depth EPR experiments also would have been beneficial. Since we lacked the ability to run low temperature EPR, I was able to travel to Brock University to obtain some low temperature EPR there which was crucial to initial characterization of reaction intermediates; however,

the ability to run more specialized EPR experiments, such as ENDOR, may have allowed further characterization.

Herein lies both a strength and a weakness of this dissertation. Many critical results and insights in this dissertation were enabled through work of fantastic collaborators, whose contributions cannot go unmentioned. I often lacked the resources to effectively delve deeper into the mechanistic intricacies of my catalyst systems; however, instead of becoming appeased and accepting those limitations, we pursued collaborations wherever possible to gain the greatest possible understanding. In Chapter 3, critical evidence through DFT calculations were performed by collaborators Mina Son, Changjin Oh, and Professor Mookie Baik. Their calculations, in tandem with experimental results, provided the strongest evidence possible for the proposed reaction pathway. This is also true of work in Chapter 4, where their initial calculations guided my experimental work. Early on they indicated that the Mn complex likely adopts a high-spin configuration, which motivated me to record the EPR spectrum under continuous irradiation, thus providing beautiful experimental support of their findings. These two chapters elegantly demonstrate the power of fruitful collaborations – as without their key contributions, much of the insights proposed in this dissertation would remain mysteries or weakly-supported hypotheses.

### **6.3 Recent Advancements and Future Directives**

The use of first-row transition metals in homogeneous catalysis has flourished over the last decade.<sup>19,20</sup> The remarkable growth of this field can be partly attributed to the emergence of strategically designed, functionally active ligand platforms that utilize MLC to expand the reactivity of base-metals beyond that observed with “innocent” spectator

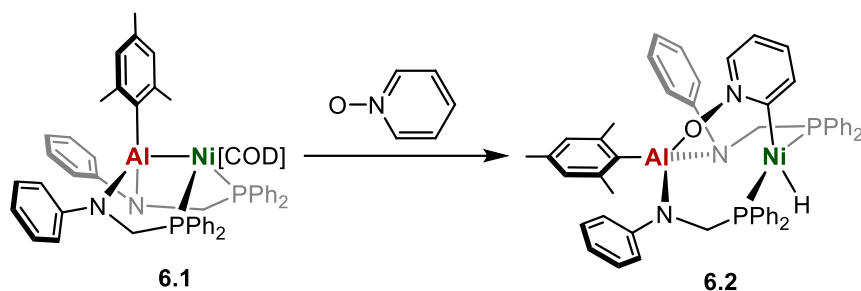
ligands. The modes of metal-ligand cooperativity are diverse, and the chosen method greatly depends on the desired reactivity.

As demonstrated in Chapter 1, the most mature mode of MLC is the utilization of Lewis bases for cooperative bond activation across an M–E unit. Within this archetype, catalytic (de)hydrogenation chemistry, specifically with iron, is by far the most well developed and studied. Although creation of isoelectronic manganese and cobalt catalysts has progressed at an astounding rate over the last 5 years, there remains much need for advancement in enantioselective catalysis with these metals. The use of N donors as the bifunctional ligand moiety encompasses the overwhelming majority of cooperative catalysis, and more progress towards utilization of alternate ligand donors may enable new catalytic pathways.

The most ideal advancement of MLC catalysis would be to expand towards the activation of more difficult and synthetically useful bond archetypes, for instance, C–H bond activation. The inherent stability of C–H bonds, however, makes their activation and subsequent functionalization a difficult task and the use of MLC in this context is in its infancy. There are several reports of C–H activation via an MLC approach utilizing either carbene or Lewis acidic borane donors, however, there are no instances of well-defined catalytic functionalization.

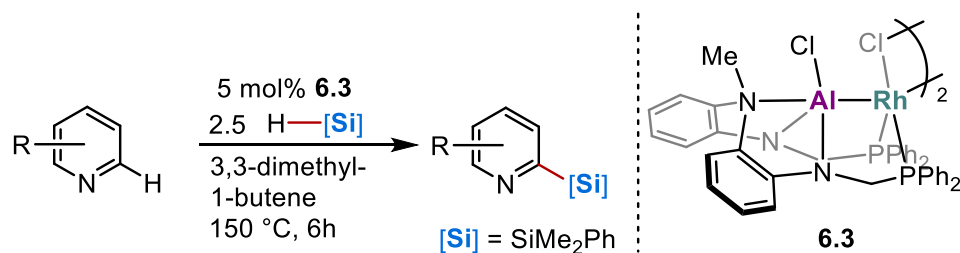
Due to the more historical success of borane donors for C–H activation activity using MLC, groups have begun to explore alternate Lewis acidic bifunctional donors. The Lu group have significantly contributed to the development of bimetallic complexes to facilitate challenging bond activations. In 2021, they reported a Ni<sup>0</sup>–Al<sup>III</sup> complex (**6.1**) which exhibited cooperative activity for the ortho-directed C–H oxidative addition of

pyridine N-oxide.<sup>21</sup> The formation of the C–H activated product (**6.2**) is enabled by a strong O → Al interaction with the pyridine N-oxide ligand, and this directed C–H bond activation likely involves the pre-coordination of the oxide donor to the oxophilic Al center.



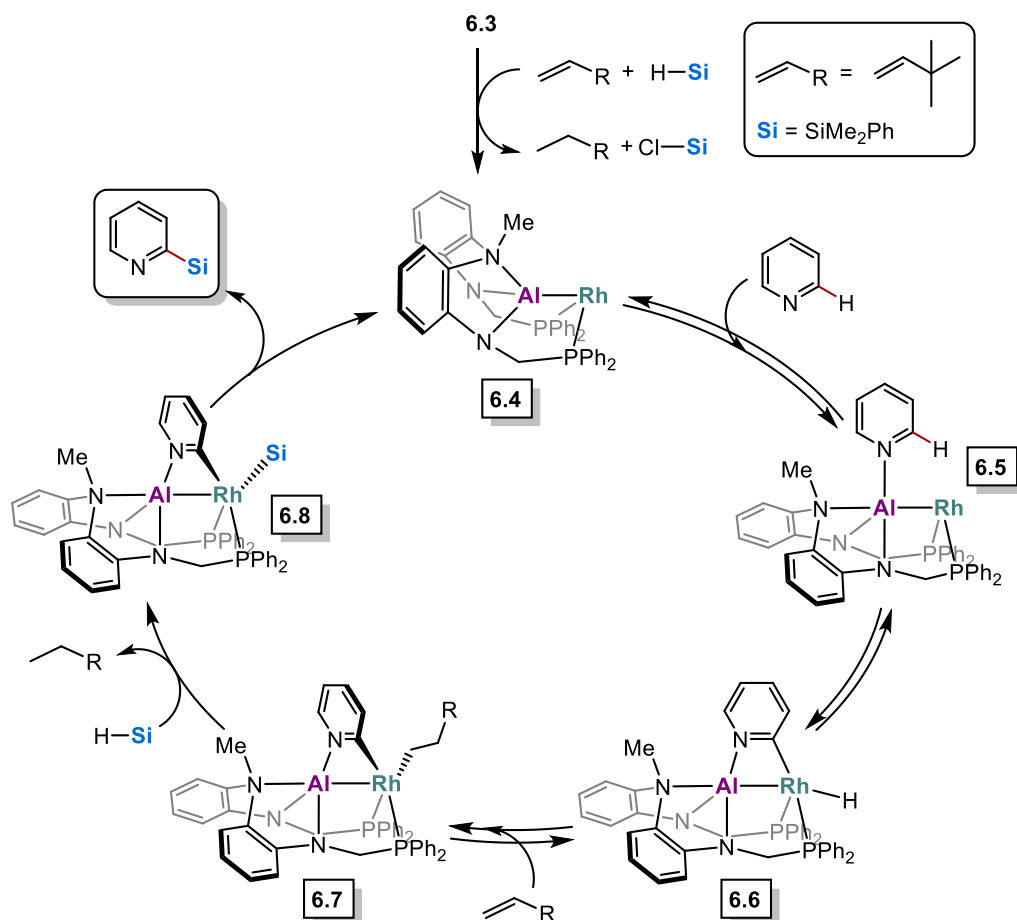
**Scheme 6.1.** *Ortho*-directed C–H activation of pyridine N-oxide by a cooperative Ni–Al.

Finally, with this recent landmark by the Lu group, another recent contribution by the Nakao group shows the potential of an Al bifunctional donor for C–H functionalization catalysis.<sup>22</sup> They report a bimetallic Rh–Al complex **6.3** for the catalytic C – H silylation of pyridines at the C2 site (**Scheme 6.2**) to afford 2-silylpyridine products exclusively. The reaction requires 2.5 equiv. of silane reagent and hydrogen acceptor 3,3-dimethyl-1-butene which is typical for most reported C–H silylations.<sup>23</sup>



**Scheme 6.2.** *Ortho*-selective silylation of pyridines by a Rh–Al complex.

The selectivity for the C2 site is attributed to the catalyst design, and after several experimental mechanistic studies the authors proposed the following reaction pathway (**Scheme 6.3**). Initial reduction of **6.3** with dimethylphenylsilane and 3,3-dimethyl-1-butene affords the proposed active state of the catalyst **6.4**. This is followed by coordination of the pyridine substrate to the Al center to give **6.5**, which the authors support by isolation of a DMAP-coordinated complex. The Rh center then performs the selective C(2)–H activation of the pyridine to afford the Rhodium hydride intermediate **6.6**. Subsequent alkene coordination and insertion into the Rh–H generates intermediate **6.7**. An additional equiv. of silane then produces intermediate **6.8**, which affords the 2-silylpyridine product after final reductive elimination.



**Scheme 6.3.** Proposed reaction pathway for C(2)-H silylation of pyridines by a Rh-Al complex.

Overall, the harnessing of metal-ligand cooperativity has led to the development of exciting and novel catalysis, and continues to impact the chemistry community, continually inspiring growth. To ensure the pace of progress continues, more judicious mechanistic studies must be performed to stimulate the growth of ligand design ingenuity and promote breakthrough catalytic applications. Additionally, the pursuit of catalytic C-H functionalization using an MLC approach is extremely early in its development. While the

previous two examples are reliant upon the interaction of the N-pyridine donor to enable the *ortho*-selective activation of the C–H bond, they provide an exciting glimpse of the potential of these systems for further development towards other heterocyclic C–H functionalizations which would be greatly desired by multiple industries.

## 6.4 References

- (1) Elsby, M. R.; Baker, R. T. Strategies and Mechanisms of Metal-Ligand Cooperativity in First-Row Transition Metal Complex Catalysts. *Chem. Soc. Rev.* **2020**, *49*, 8933-8987.
- (2) Das, U. K.; Daifuku, S. L.; Gorelsky, S. I.; Korobkov, I.; Neidig, M. L.; LeRoy, J. L.; Murugesu, M.; Baker, R. T. Mononuclear, Dinuclear and Trinuclear Iron Complexes Featuring a new Monoanionic SNS Thiolate Ligand. *Inorg. Chem.* **2016**, *55*, 987-997.
- (3) Das, U. K.; Daifuku, S. L.; Ianuzzi, T. E.; Gorelsky, S. I.; Korobkov, I.; Gabidullin, B. M.; Neidig, M. L.; Baker, R. T. Fe(II) Complexes of a Hemilabile SNS Amido Ligand; Synthesis, Characterization and Reactivity. *Inorg. Chem.* **2017**, *56*, 13766–13776.
- (4) Albkuri, Y. M.; Ovens, J. S.; Martin, J.; Baker, R. T. Nickel(II)-SNS Thiolate Complexes: Reactivity and Solution Dynamics. *Inorg. Chem.* **2021**, *60*, 10934-10942.
- (5) Das, U. K. Iron Chemistry of Hemilabile SNS Ligands: Synthesis, Reactivity, and Catalytic Applications. University of Ottawa PhD thesis, 2018.
- (6) Elsby, M. R.; Baker, R. T. Cu(I)-SNS Complexes for Outer-sphere Hydroboration and Hydrosilylation of Carbonyls. *Chem. Commun.* **2019**, *55*, 13574-13577.
- (7) Das, U. K.; Higman, C. S.; Korobkov, I.; Gabidullin, B. M.; Hein, J. E.; Baker, R. T. Efficient and Selective Iron Complex-Catalyzed Hydroboration of Aldehydes. *ACS Catal.* **2018**, *8*, 1076-1081.
- (8) Obligacion, J. V.; Chirik, P. J. Earth-Abundant Transition Metal Catalysts for Alkene Hydrosilylation and Hydroboration. *Nat. Rev. Chem.* **2018**, *2*, 15.
- (9) Tamang, S. R.; Findlater, M. Emergence and Applications of Base Metals (Fe, Co, and Ni) in Hydroboration and Hydrosilylation. *Molecules* **2019**, *24*, 3194.
- (10) Alig, L.; Fritz, M.; Schneider, S. First-Row Transition Metal (de)Hydrogenation Catalysis Based on Functional Pincer Ligands. *Chem. Rev.* **2018**, *119*, 2681-2751.
- (11) Fitchett, B. Oxidation State Roulette: Synthesis and Reactivity of Cobalt Complexes Containing SNS Ligands. University of Ottawa MSc thesis, 2018.
- (12) Kiernicki, J. J.; Zeller, M.; Szymczak, N. K. Examining the Generality of Metal-Ligand Cooperativity Across a Series of First-Row Transition Metals: Capture, Bond Activation, and Stabilization. *Inorg. Chem.* **2020**, *59*, 9279-9286.

- (13) Su, P.; Li, Y.; Ke, Z. Metal Effect Meets Volcano Plots: A DFT Study on Tris(phosphino)borane-Transition Metal Complexes Catalyzed H<sub>2</sub> Activation. *Chem. Asian J.* **2021**, *16*, 3427-3436.
- (14) Carney, J. R.; Dillon, B. R.; Campbell, L.; Thomas, S. P. Manganese-Catalyzed Hydrofunctionalization of Alkenes. *Angew. Chem., Int. Ed.* **2018**, *57*, 10620–10624.
- (15) Zhang, G.; Zeng, H.; Wu, J.; Yin, Z.; Zheng, S.; Fettinger, J. C. Highly Selective Hydroboration of Alkenes, Ketones and Aldehydes Catalyzed by a Well-Defined Manganese Complex. *Angew. Chem., Int. Ed.* **2016**, *55*, 14369–14372.
- (16) Elsby, M. R.; Ghostine, K.; Das, U. K.; Korobkov, I.; Gabidullin, B. M.; Baker, R. T. Fe-SNS and -CNS Complexes: C<sub>aryl</sub>-S Bond Cleavage and Amine-Borane Dehydrogenation Catalysis. *Organometallics* **2019**, *38*, 3844-3851.
- (17) Ghosh, C.; Kim, S.; Mena, M. R.; Kim, J.-H.; Pal, R.; Rock, C. L.; Groy, T. L.; Baik, M.-H.; Trovitch, R. J. Efficient Cobalt Catalyst for Ambient-Temperature Nitrile Dihydroboration, the Elucidation of a Chelate-Assisted Borylation Mechanism, and a New Synthetic Route to Amides. *J. Am. Chem. Soc.* **2019**, *141*, 15327-15337
- (18) Nguyen, T. T.; Kim, J.-H.; Kim, S.; Oh, C.; Flores, M.; Groy, T. L.; Baik, M.-H.; Trovitch, R. J. Scope and Mechanism of Nitrile Dihydroboration Mediated by a β-Diketiminato Manganese Hydride Catalyst. *Chem. Commun.* **2020**, *56*, 3959-3962.
- (19) Chirik, P.; Morris, R. Getting Down to Earth: The Renaissance of Catalysis with Abundant Metals. *Acc. Chem. Res.* **2015**, *48*, 2495-2495.
- (20) Bullock, R. M.; Chen, J. G.; Gagliardi, L.; Chirik, P. J.; Farha, O. K.; Hendon, C. H.; Jones, C. W.; Keith, J. A.; Klosin, J.; Minter, S. D.; Morris, R. H.; Radosevich, A. T.; Rauchfuss, T. B.; Strotman, N. A.; Vojvodic, A.; Ward, T. R.; Yang, J. Y.; Surendranath, Y. Using Nature's Blueprint to Expand Catalysis with Earth-Abundant Metals. *Science* **2020**, *369*, No. eabc3183.
- (21) Graziano, B. J.; Vollmer, M. V.; Lu, C. C. Cooperative Bond Activation and Facile Intramolecular Aryl Transfer of Nickel-Aluminum Pincer-type Complexes. *Angew. Chem. Int. Ed.* **2021**, *60*, 15087-15094.
- (22) Hara, N.; Uemura, N.; Nakao, Y. C<sub>2</sub>-Selective Silylation of Pyridines by a Rhodium-Aluminum Complex. *Chem. Commun.* **2021**, *57*, 5957-5960.

(23) Cheng, C; Hartwig, J. F. Catalytic Silylation of Unactivated C–H bonds. *Chem Rev.* **2015**, *115*, 8946-8975.

APPENDICES

Appendix A – Chapter 2

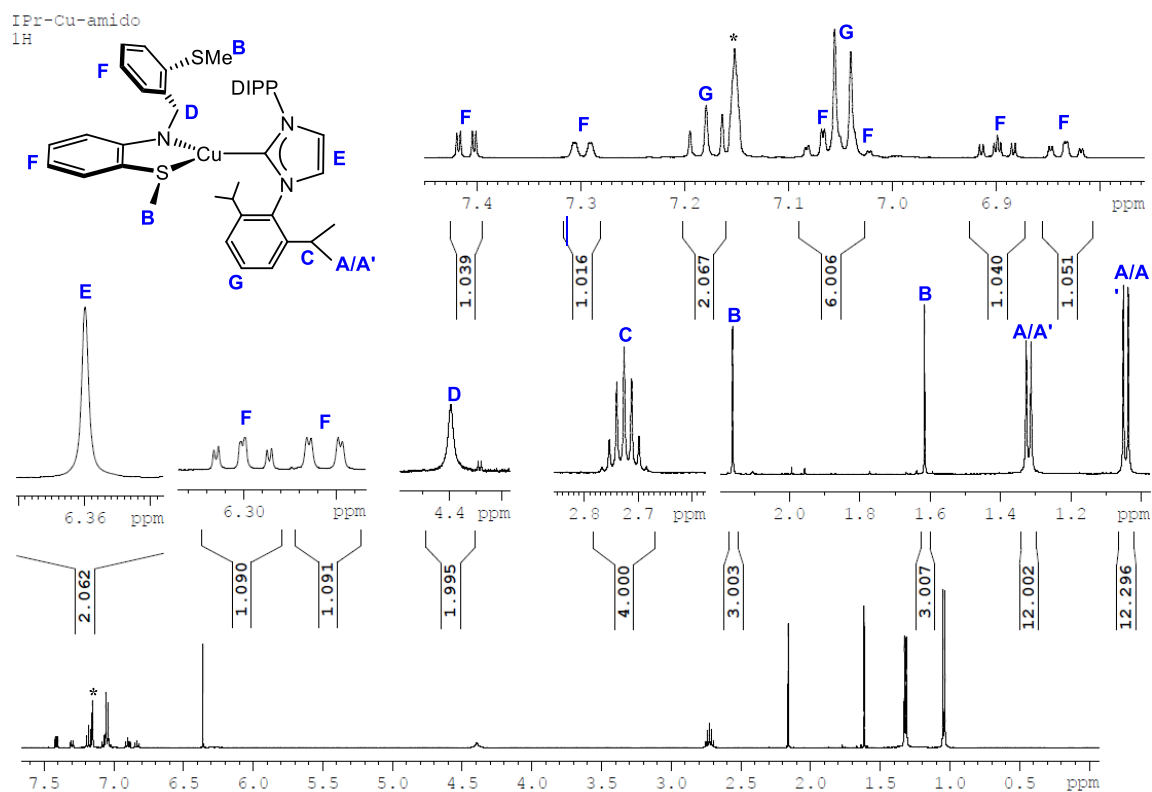
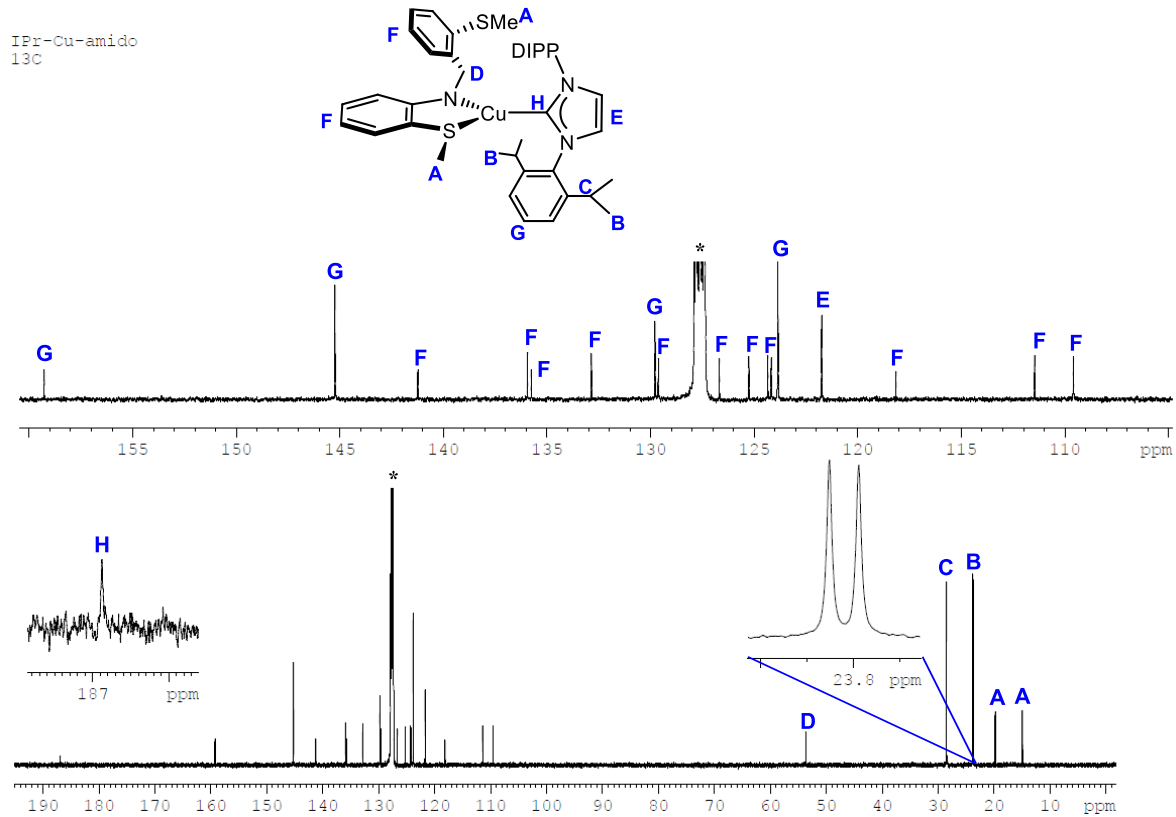
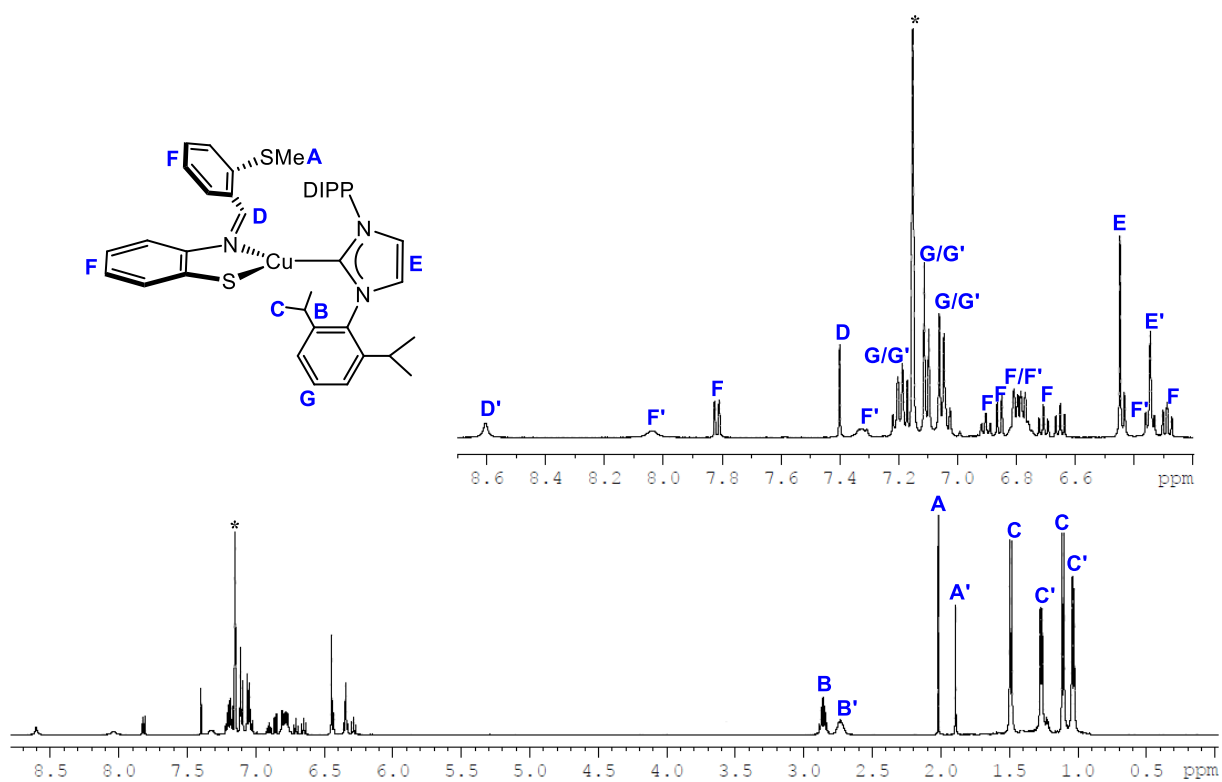


Figure A1. <sup>1</sup>H NMR spectrum of Cu(S<sup>Me</sup>NS<sup>Me</sup>)(IPr) (2.1<sub>Cu</sub>). \* indicates C<sub>6</sub>D<sub>6</sub>.



**Figure A2.**  $^{13}\text{C}\{^1\text{H}\}$  NMR spectrum of  $\text{Cu}(\text{S}^{\text{Me}}\text{N}^{\text{S}^{\text{Me}}})(\text{IPr})$  ( $\mathbf{2.1}_{\text{Cu}}$ ). \* indicates  $\text{C}_6\text{D}_6$ .



**Figure A3.**  $^1\text{H}$  NMR spectrum of  $\text{Cu}(\text{S}^{\text{Me}}\text{NS})(\text{IPr})$  ( $2.2_{\text{Cu}}$ ). \* indicates  $\text{C}_6\text{D}_6$ .

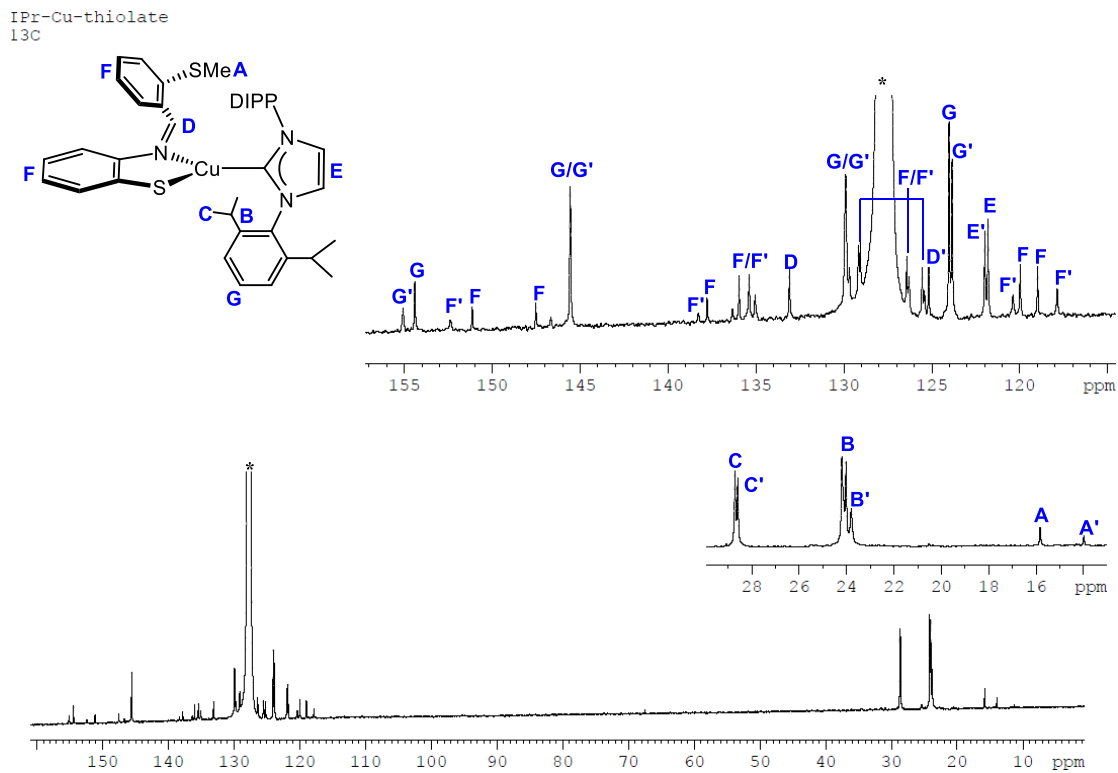


**Figure A4.**  $^{13}\text{C}\{^1\text{H}\}$  NMR spectrum of  $\text{Cu}(\text{S}^{\text{Me}}\text{NS})(\text{IPr})$  (2.2 $\text{Cu}$ ). \* indicates  $\text{C}_6\text{D}_6$ .

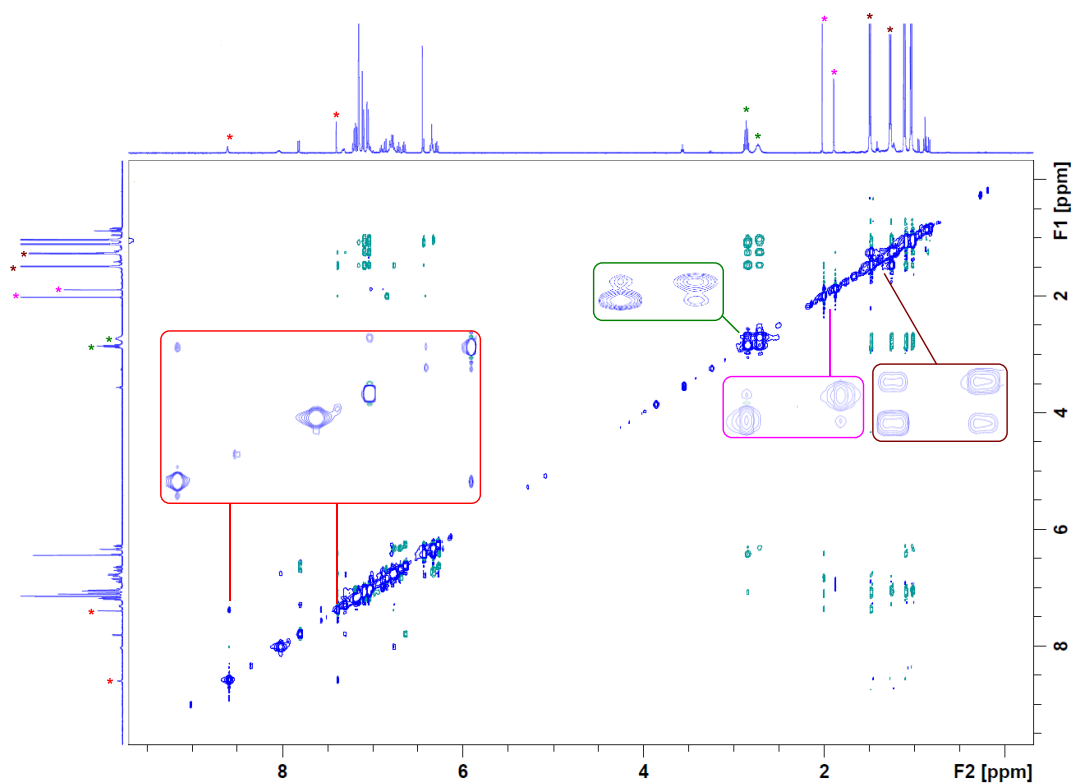


**Figure A5.** 2D  $^1\text{H}$  EXSY NMR spectrum of  $\text{Cu}(\text{S}^{\text{MeNS}})(\text{IPr})$  (**2.2Cu**).

benzaldehyde hydroboration product  
 $^1\text{H}$  NMR

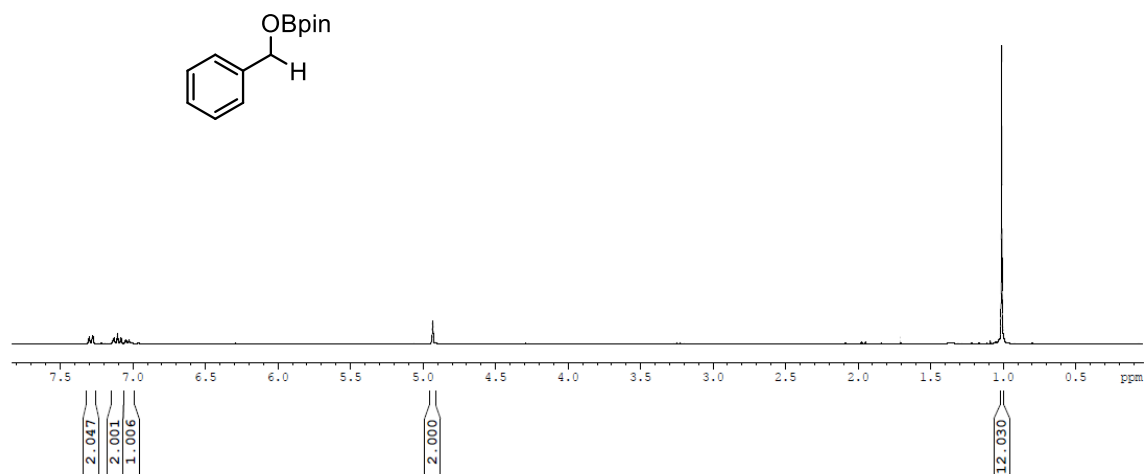


**Figure A6.**  $^1\text{H}$  NMR spectrum of benzaldehyde hydroboration product. \* indicates  $\text{C}_6\text{D}_6$ .

Appendices – Appendix A

acetophenone hydroboration product  
1H NMR

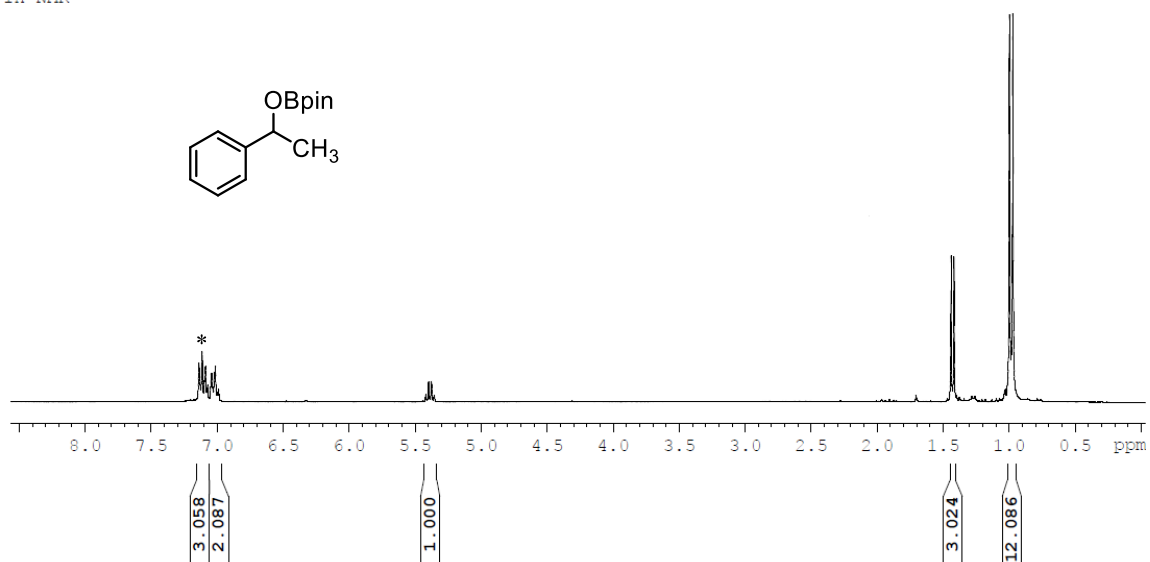


Figure A7. <sup>1</sup>H NMR spectrum of acetophenone hydroboration product \* indicates C<sub>6</sub>D<sub>6</sub>.

benzophenone hydroboration  
1H

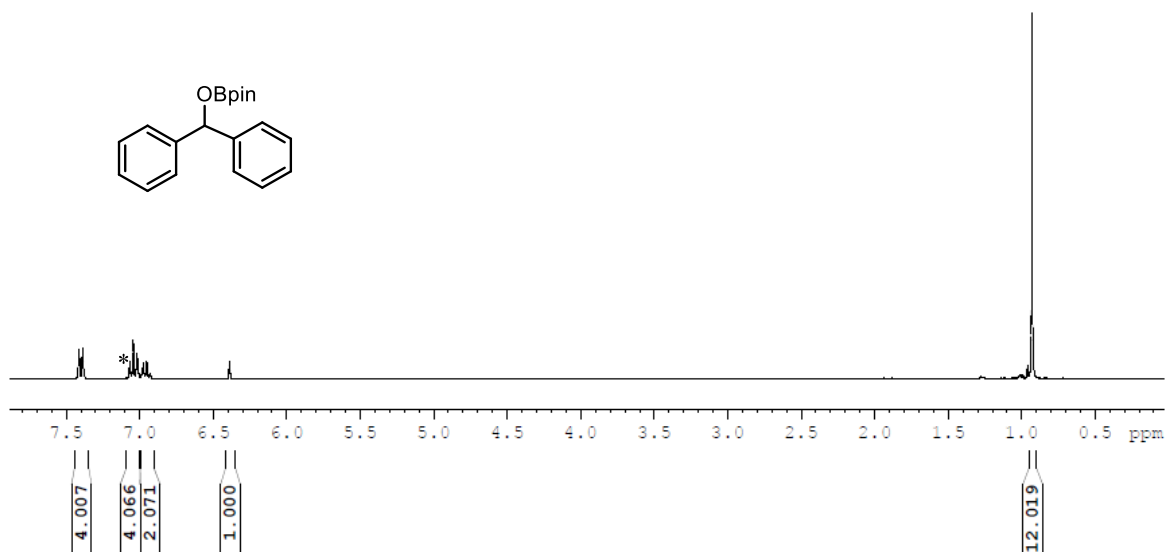
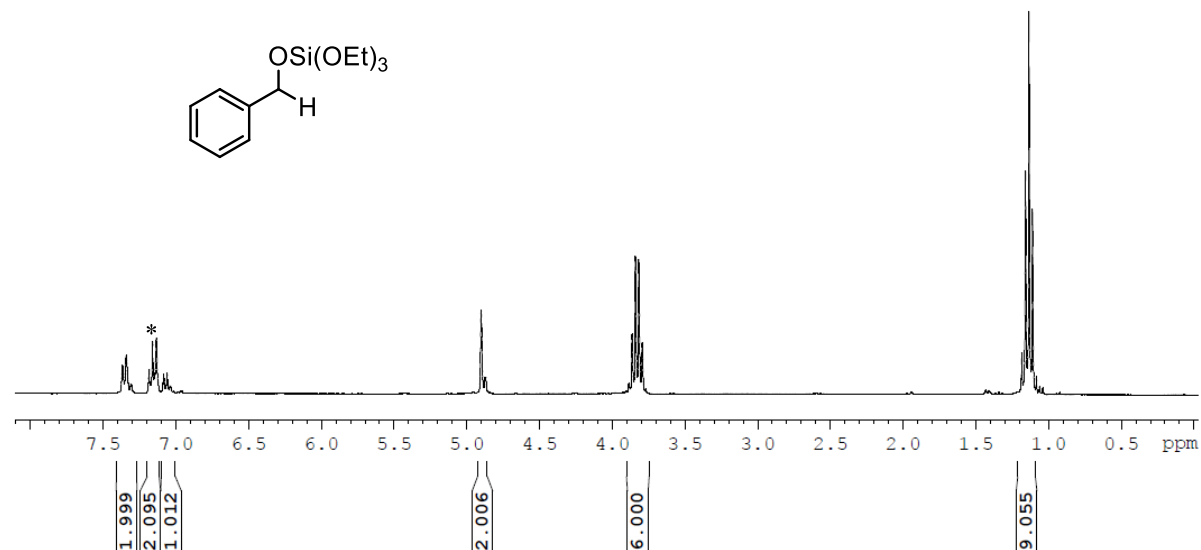
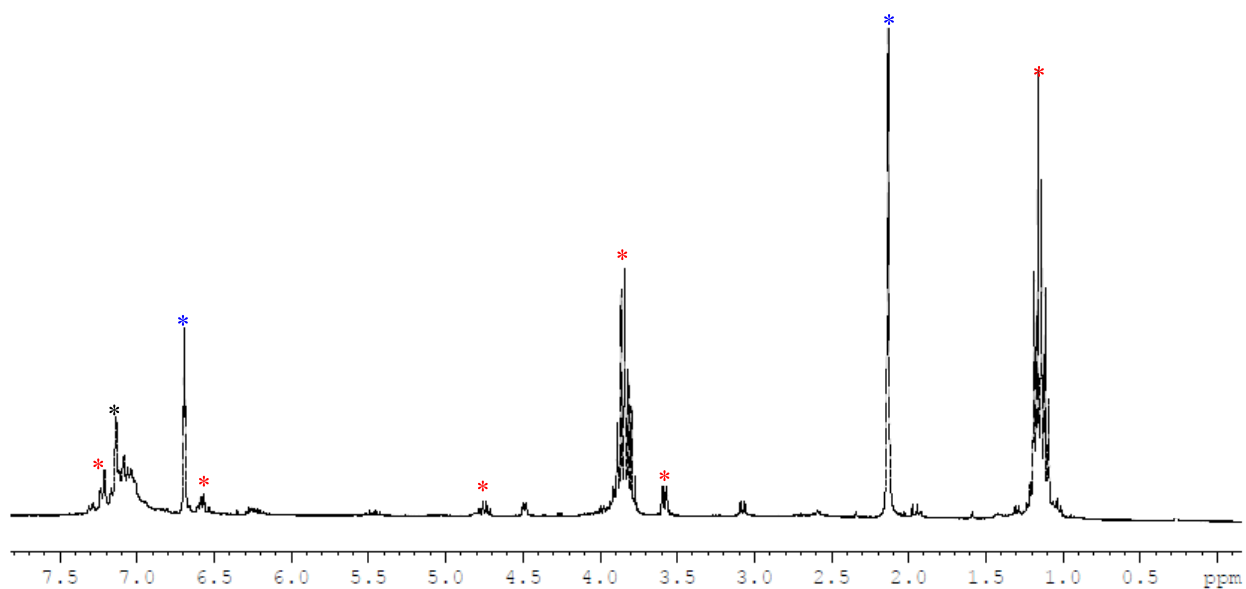


Figure A8. <sup>1</sup>H NMR spectrum of benzophenone hydroboration product \* indicates C<sub>6</sub>D<sub>6</sub>.

benzaldehyde hydrosilylation product  
<sup>1</sup>H NMR



**Figure A9.** <sup>1</sup>H NMR spectrum of benzaldehyde hydrosilylation product \* indicates C<sub>6</sub>D<sub>6</sub>.



**Figure A10.** <sup>1</sup>H NMR spectrum of *trans*-cinnamaldehyde hydrosilylation reaction mixture after 24 h. \* indicates C<sub>6</sub>D<sub>6</sub>. \* indicates *cis*-product. \* indicates internal standard mesitylene.

Appendices – Appendix A

acetophenone hydrosilylation product  
1H NMR

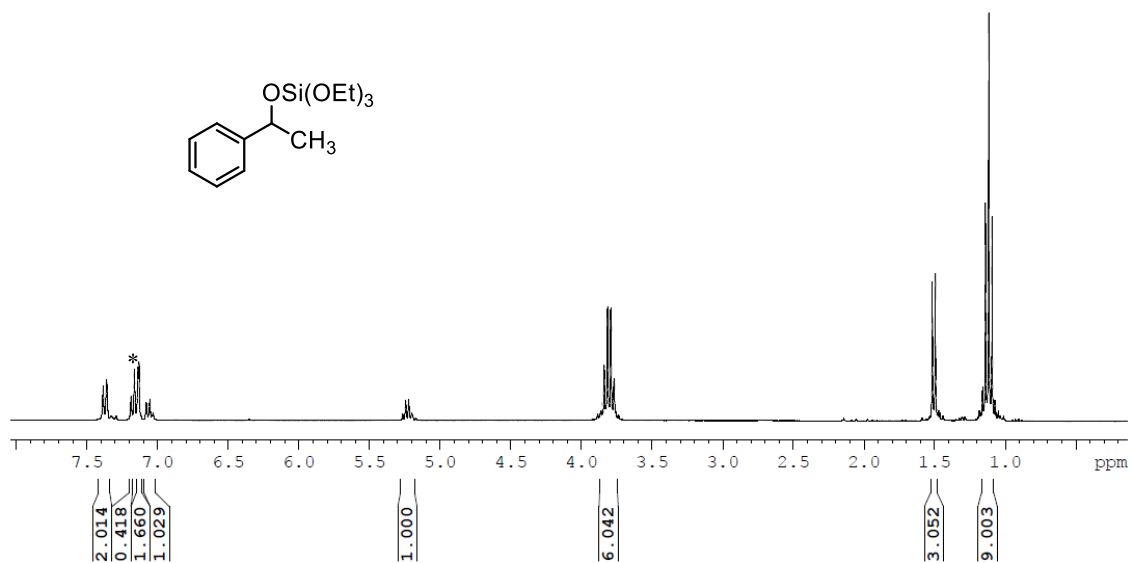


Figure A11. <sup>1</sup>H NMR spectrum of acetophenone hydrosilylation product. \* indicates C<sub>6</sub>D<sub>6</sub>.

benzophenone hydrosilylation  
1H

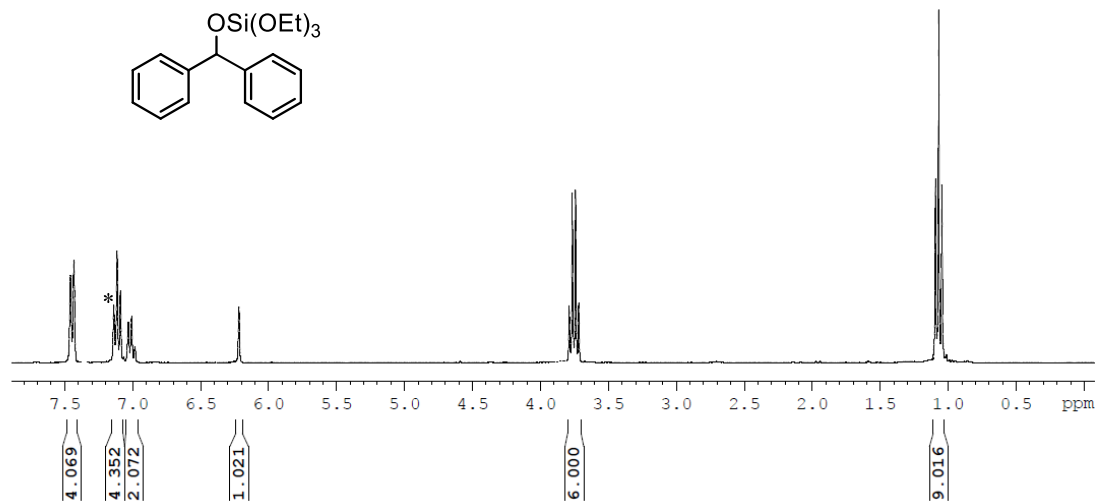


Figure A12. <sup>1</sup>H NMR spectrum of benzophenone hydrosilylation product. \* indicates C<sub>6</sub>D<sub>6</sub>.

5-hexen-2-one hydrosilylation  
<sup>1</sup>H

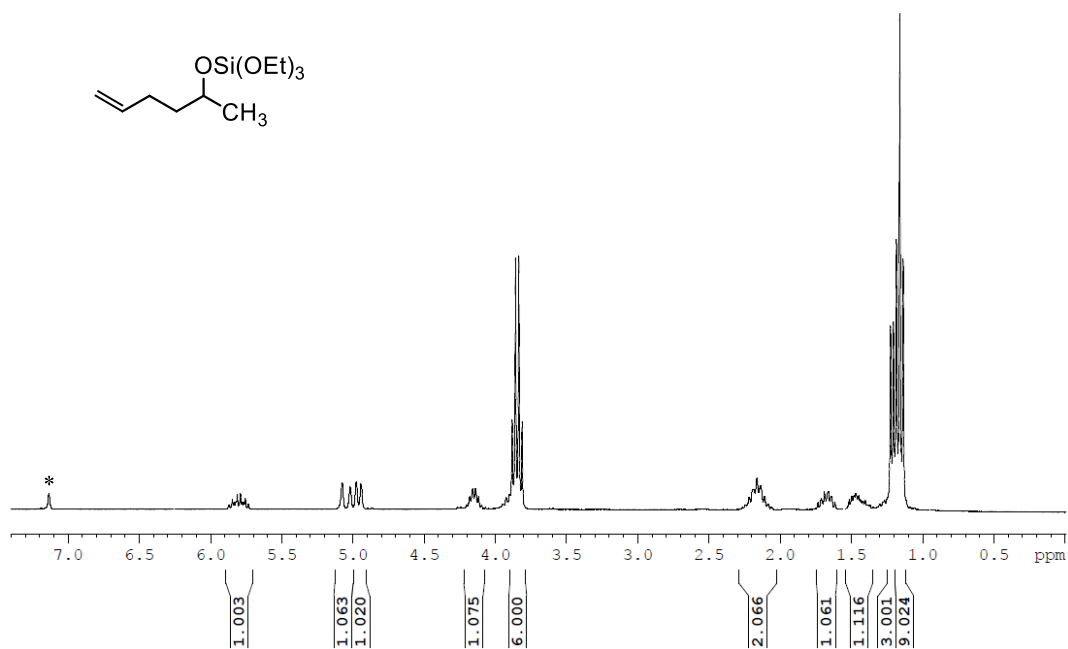


Figure A13. <sup>1</sup>H NMR spectrum of 5-hexen-2-one hydrosilylation product. \* indicates C<sub>6</sub>D<sub>6</sub>.

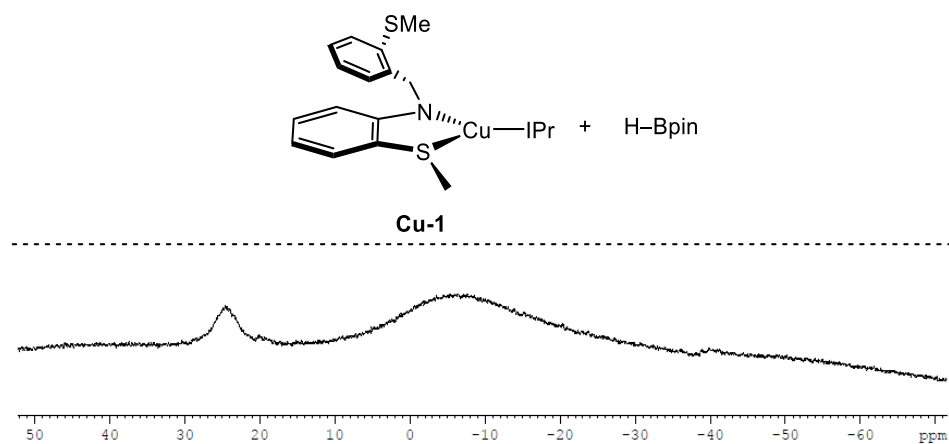


Figure A14. <sup>11</sup>B NMR spectra showing stoichiometric reaction of **2.1<sub>Cu</sub>** with pinacolborane.

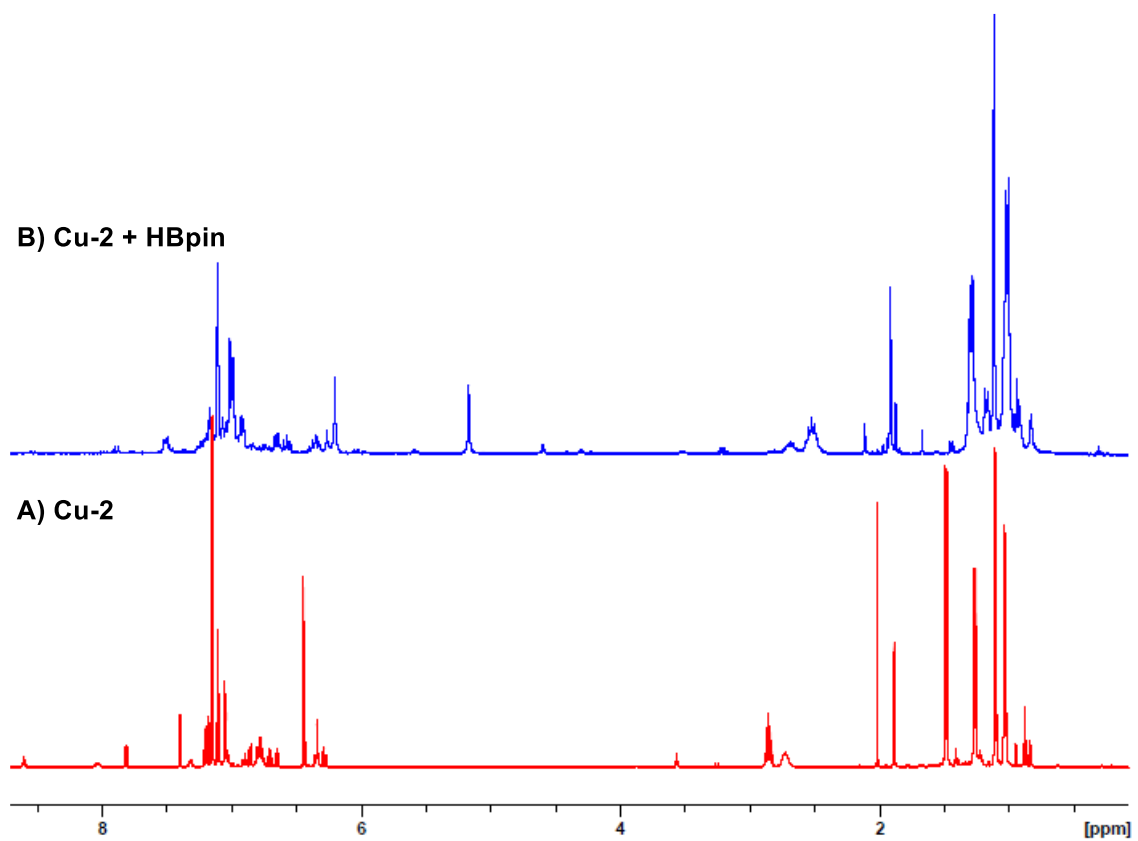


Figure A15. Stacked plot of  $^1\text{H}$  NMR spectra showing stoichiometric reaction of  $2.2_{\text{Cu}}$  with pinacolborane.

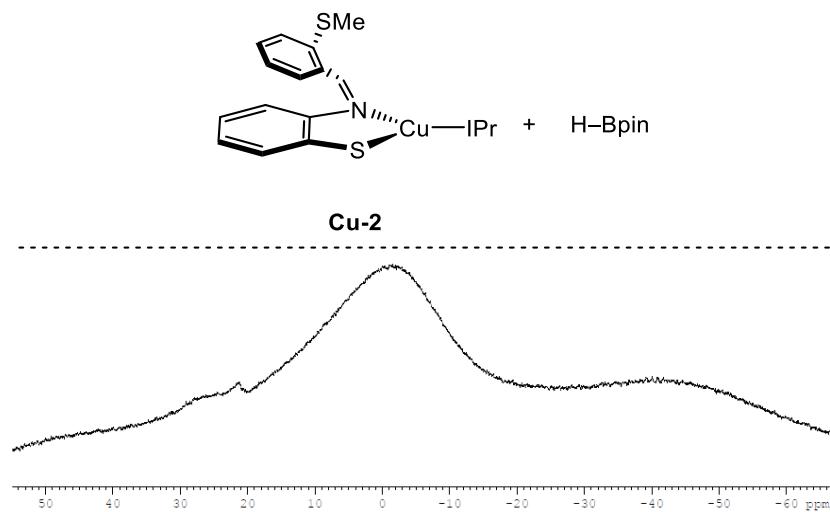


Figure A16.  $^{11}\text{B}$  NMR spectra showing stoichiometric reaction of  $2.2_{\text{Cu}}$  with pinacolborane.

**Table A1.** Crystal data and structure refinement for IPr-Cu-amido (**2.1Cu**).

Identification code	IPr-Cu-amido
Empirical formula	C <sub>42</sub> H <sub>52</sub> CuN <sub>3</sub> S <sub>2</sub>
Formula weight	726.52
Temperature/K	200.05
Crystal system	monoclinic
Space group	P2 <sub>1</sub>
a/Å	12.471(8)
b/Å	13.794(9)
c/Å	13.094(8)
α/°	90
β/°	116.562(16)
γ/°	90
Volume/Å <sup>3</sup>	2015(2)
Z	2
ρ <sub>calc</sub> /cm <sup>3</sup>	1.198
μ/mm <sup>-1</sup>	0.677
F(000)	772.0
Crystal size/mm <sup>3</sup>	0.1 × 0.05 × 0.05
Radiation	MoKα (λ = 0.71073)
2Θ range for data collection/°	3.478 to 56.164
Index ranges	-15 ≤ h ≤ 16, -17 ≤ k ≤ 18, -17 ≤ l ≤ 17
Reflections collected	26692
Independent reflections	9542 [R <sub>int</sub> = 0.0276, R <sub>sigma</sub> = 0.0312]
Data/restraints/parameters	9542/40/465
Goodness-of-fit on F <sup>2</sup>	1.050
Final R indexes [I ≥ 2σ (I)]	R <sub>1</sub> = 0.0299, wR <sub>2</sub> = 0.0706
Final R indexes [all data]	R <sub>1</sub> = 0.0345, wR <sub>2</sub> = 0.0731
Largest diff. peak/hole / e Å <sup>-3</sup>	0.45/-0.17
Flack parameter	0.463(9)

**Table A2.** Bond Lengths for IPr-Cu-amido (2.1<sub>cu</sub>).

Atom	Atom	Length/Å	Atom	Atom	Length/Å
Cu1	S1	2.4820(14)	C8	C9	1.554(4)
Cu1	N1	1.948(2)	C3	C4	1.396(5)
Cu1	C16	1.919(3)	C9	C10	1.397(4)
S1	C2	1.803(3)	C9	C14	1.421(4)
S1	C1	1.832(4)	C18	C17	1.351(3)
S2	C14	1.787(3)	C7	C6	1.452(4)
S2	C15	1.826(4)	C33	C34	1.397(4)
N3	C19	1.456(3)	C25	C27	1.551(4)
N3	C16	1.382(3)	C25	C26	1.544(5)
N3	C18	1.406(3)	C24	C23	1.403(4)
N2	C31	1.465(3)	C24	C28	1.552(4)
N2	C16	1.377(3)	C10	C11	1.410(5)
N2	C17	1.404(3)	C37	C39	1.548(5)
N1	C8	1.467(3)	C37	C38	1.531(5)
N1	C7	1.369(3)	C21	C22	1.395(4)
C20	C19	1.423(4)	C40	C42B	1.564(8)
C20	C25	1.543(4)	C40	C41B	1.512(8)
C20	C21	1.401(4)	C40	C41A	1.587(10)
C31	C36	1.415(3)	C40	C42A	1.514(10)
C31	C32	1.415(3)	C14	C13	1.423(5)
C19	C24	1.420(3)	C23	C22	1.396(5)
C36	C35	1.413(4)	C28	C30	1.539(4)
C36	C40	1.546(4)	C28	C29	1.546(5)
C32	C33	1.413(4)	C11	C12	1.387(6)
C32	C37	1.533(4)	C4	C5	1.389(5)
C35	C34	1.397(4)	C6	C5	1.396(4)
C2	C3	1.406(4)	C13	C12	1.394(6)
C2	C7	1.437(4)			

**Table A3.** Crystal data and structure refinement for IPr-Cu-thiolate (**2.2<sub>Cu</sub>**).

Identification code	IPr-Cu-thiolate
Empirical formula	C <sub>41</sub> H <sub>48</sub> CuN <sub>3</sub> S <sub>2</sub>
Formula weight	710.48
Temperature/K	298.15
Crystal system	monoclinic
Space group	P2 <sub>1</sub> /n
a/Å	12.955(3)
b/Å	15.654(3)
c/Å	19.260(4)
α/°	90
β/°	95.175(13)
γ/°	90
Volume/Å <sup>3</sup>	3889.8(15)
Z	4
ρ <sub>calc</sub> /cm <sup>3</sup>	1.213
μ/mm <sup>-1</sup>	0.700
F(000)	1504.0
Crystal size/mm <sup>3</sup>	0.382 × 0.18 × 0.179
Radiation	MoKα (λ = 0.71073)
2θ range for data collection/°	3.358 to 53.298
Index ranges	-13 ≤ h ≤ 16, -19 ≤ k ≤ 19, -24 ≤ l ≤ 24
Reflections collected	36950
Independent reflections	8089 [R <sub>int</sub> = 0.0405, R <sub>sigma</sub> = 0.0333]
Data/restraints/parameters	8089/0/433
Goodness-of-fit on F <sup>2</sup>	1.011
Final R indexes [I ≥ 2σ (I)]	R <sub>1</sub> = 0.0429, wR <sub>2</sub> = 0.1005
Final R indexes [all data]	R <sub>1</sub> = 0.0757, wR <sub>2</sub> = 0.1161
Largest diff. peak/hole / e Å <sup>-3</sup>	0.52/-0.26

**Table A4.** Bond Lengths for IPr-Cu-thiolate (2.2<sub>Cu</sub>).

<b>Atom</b>	<b>Atom</b>	<b>Length/Å</b>	<b>Atom</b>	<b>Atom</b>	<b>Length/Å</b>
Cu1	S1	2.1802(8)	C39	C40	1.528(4)
Cu1	N1	2.130(2)	C39	C41	1.513(5)
Cu1	C15	1.889(2)	C31	C36	1.508(4)
S1	C1	1.743(3)	C31	C32	1.385(4)
S2	C13	1.751(3)	C23	C27	1.503(5)
S2	C14	1.752(4)	C23	C22	1.391(4)
N2	C18	1.446(3)	C24	C25	1.522(4)
N2	C15	1.367(3)	C24	C26	1.517(5)
N2	C17	1.371(3)	C7	C8	1.470(4)
N3	C30	1.446(3)	C8	C13	1.383(4)
N3	C15	1.350(3)	C8	C9	1.375(4)
N3	C16	1.382(3)	C13	C12	1.376(4)
N1	C6	1.416(3)	C36	C38	1.501(4)
N1	C7	1.275(3)	C36	C37	1.501(4)
C18	C19	1.385(4)	C27	C28	1.529(4)
C18	C23	1.383(3)	C27	C29	1.523(5)
C30	C35	1.399(4)	C5	C4	1.368(5)
C30	C31	1.381(4)	C12	C11	1.361(5)
C17	C16	1.326(4)	C20	C21	1.369(5)
C19	C24	1.496(4)	C2	C3	1.372(6)
C19	C20	1.394(4)	C9	C10	1.362(5)
C1	C6	1.380(4)	C34	C33	1.361(5)
C1	C2	1.384(4)	C32	C33	1.358(5)
C35	C39	1.501(4)	C10	C11	1.357(5)
C35	C34	1.394(4)	C22	C21	1.348(5)
C6	C5	1.395(4)	C4	C3	1.358(7)

Appendix B – Chapter 3

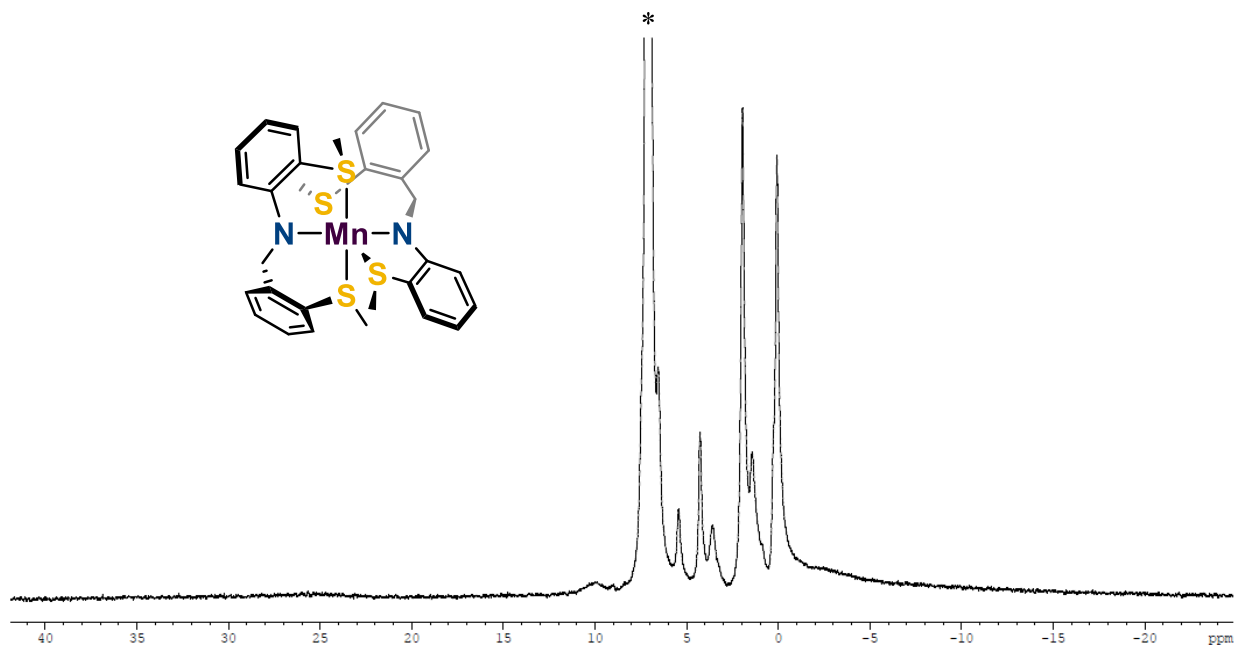


Figure B1.  $^1\text{H}$  NMR spectrum of  $\text{Mn}(\kappa^3\text{-S}^{\text{Me}}\text{NS}^{\text{Me}})_2$  (**3.1Mn**). \* is  $\text{C}_6\text{D}_6$ .

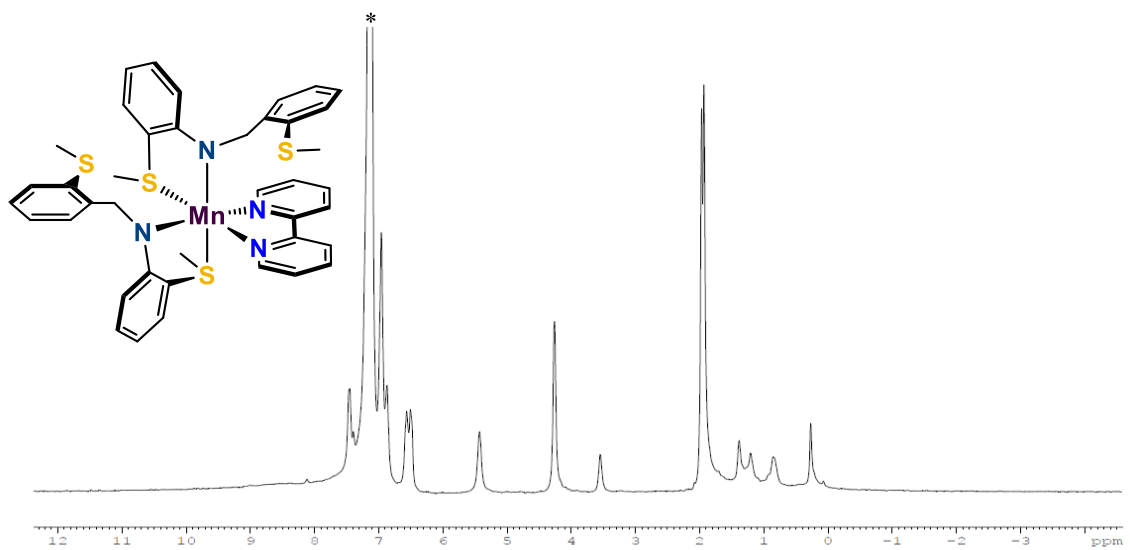
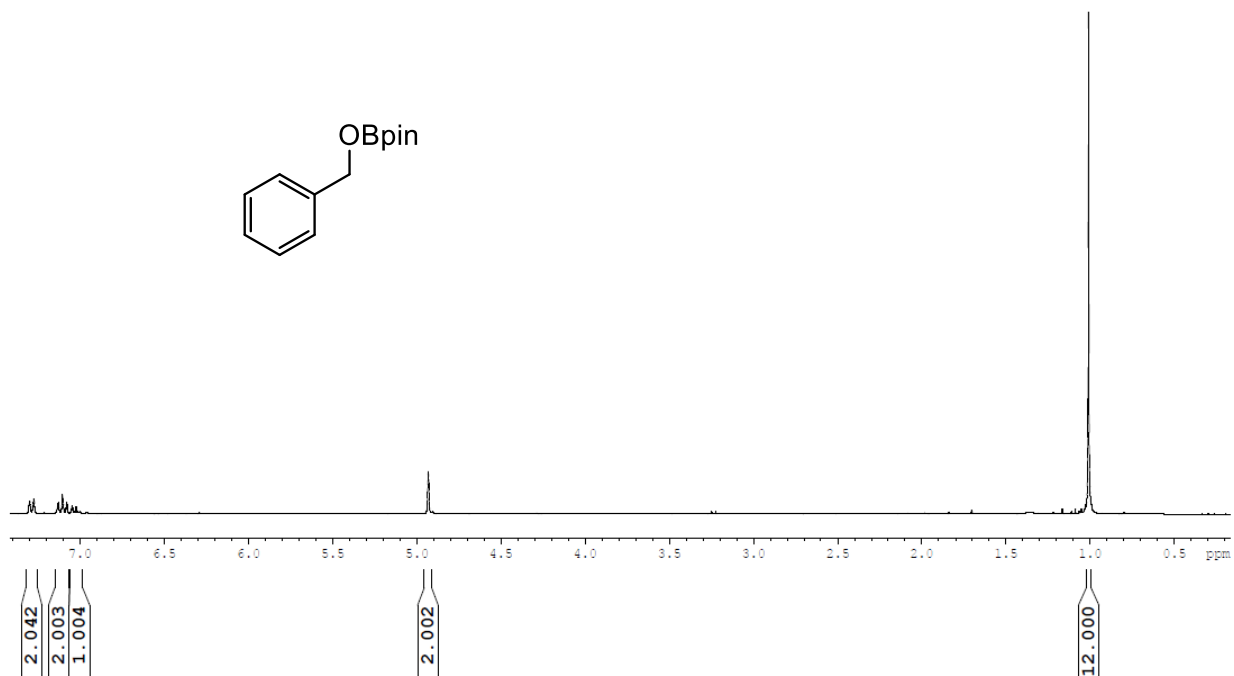
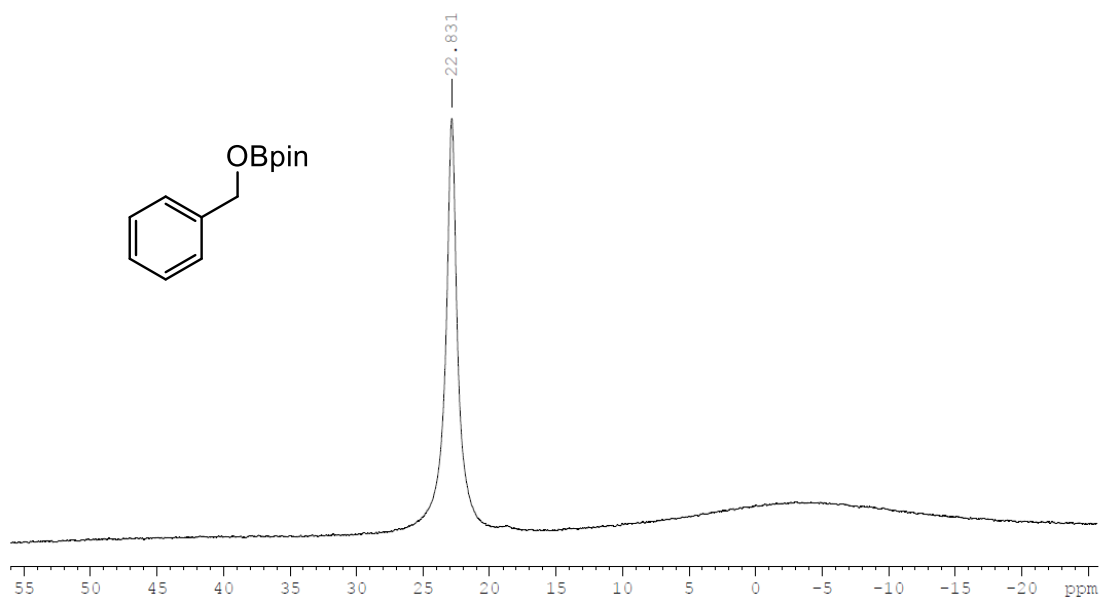


Figure B2.  $^1\text{H}$  NMR spectrum of  $\text{Mn}(\kappa^2\text{-S}^{\text{Me}}\text{NS}^{\text{Me}})_2(\text{bpy})$  (**3.2Mn**). \* is  $\text{C}_6\text{D}_6$ .



**Figure B3.** <sup>1</sup>H NMR spectrum of benzaldehyde hydroboration product.



**Figure B4.** <sup>11</sup>B NMR spectrum of benzaldehyde hydroboration product.

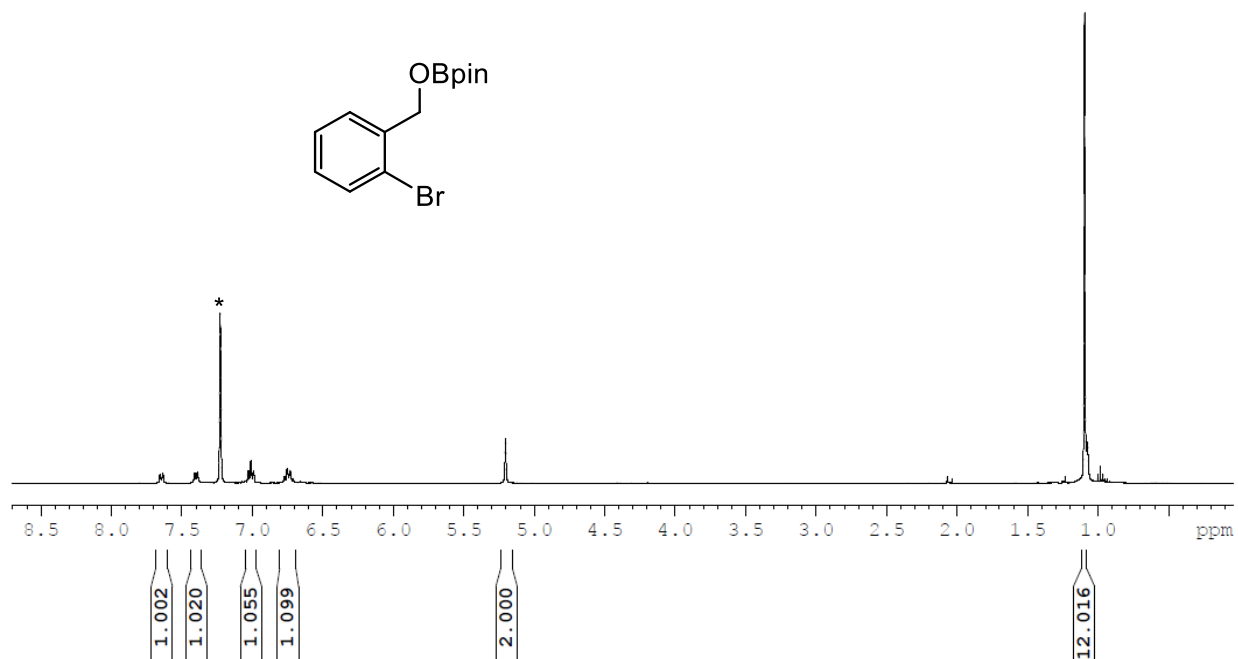


**Figure B5.** <sup>1</sup>H NMR spectrum of 2-bromo-benzaldehyde hydroboration product. \* is C<sub>6</sub>D<sub>6</sub>.

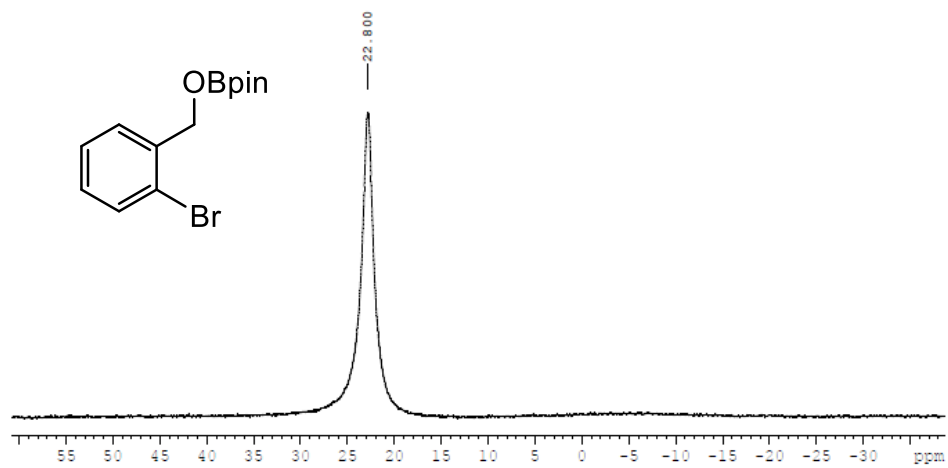


**Figure B6.** <sup>11</sup>B NMR spectrum of 2-bromo-benzaldehyde hydroboration product.

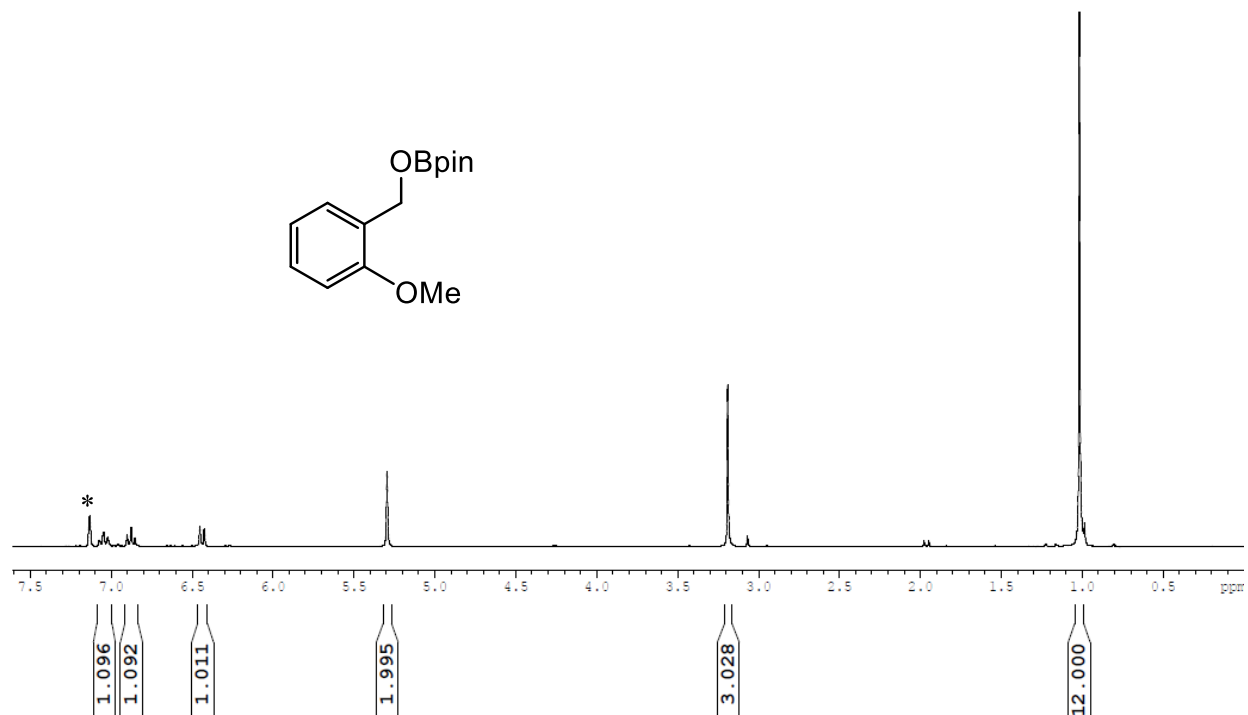


**Figure B7.** <sup>1</sup>H NMR spectrum of 2-methoxy-benzaldehyde hydroboration product. \* is C<sub>6</sub>D<sub>6</sub>.

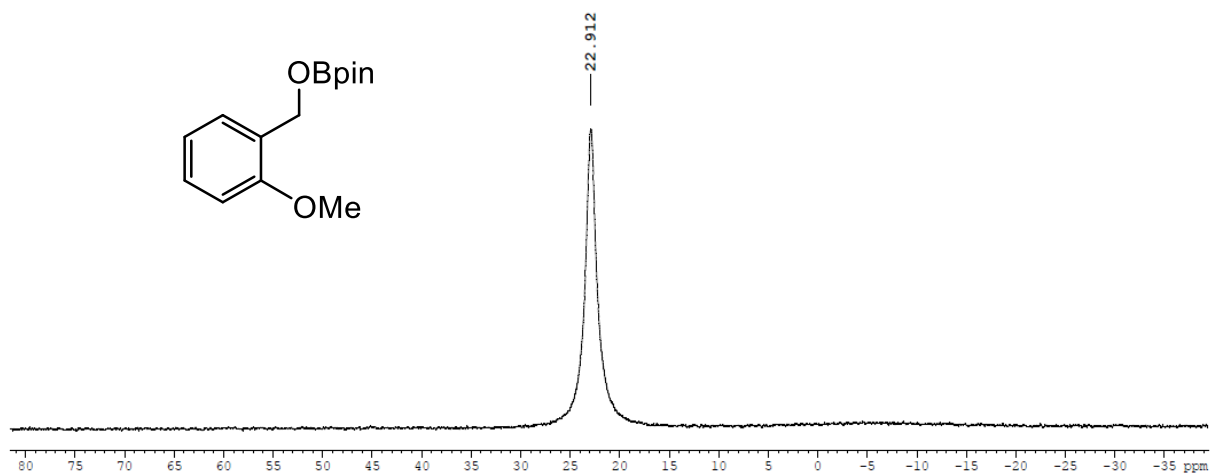


**Figure B8.** <sup>11</sup>B NMR spectrum of 2-methoxy-benzaldehyde hydroboration product.



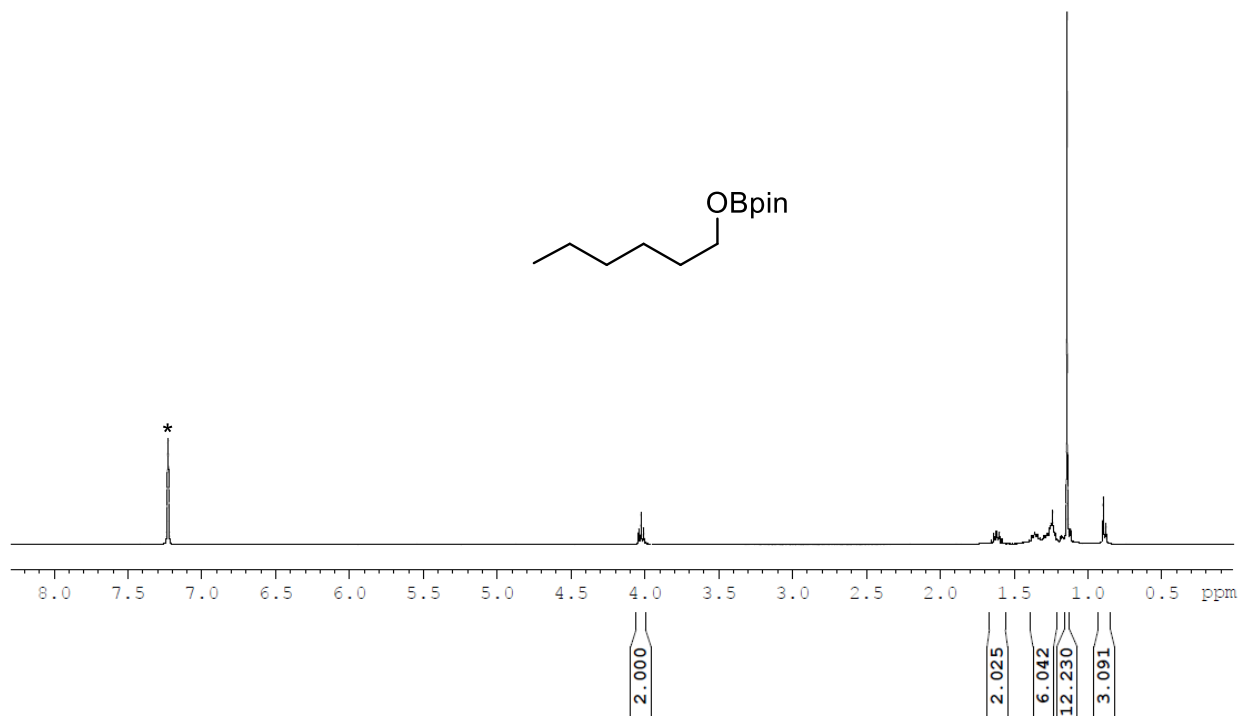


**Figure B11.**  $^1\text{H}$  NMR spectrum of hexanal hydroboration product. \* is  $\text{C}_6\text{D}_6$ .

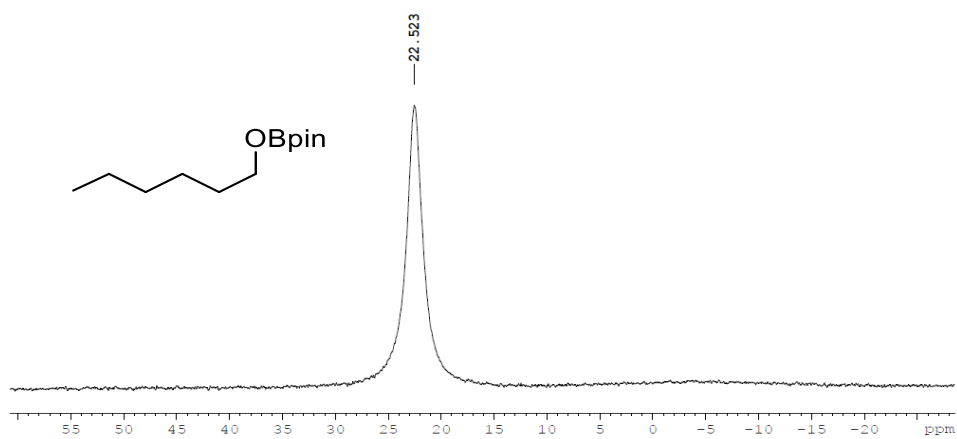


**Figure B12.**  $^{11}\text{B}$  NMR spectrum of hexanal hydroboration product

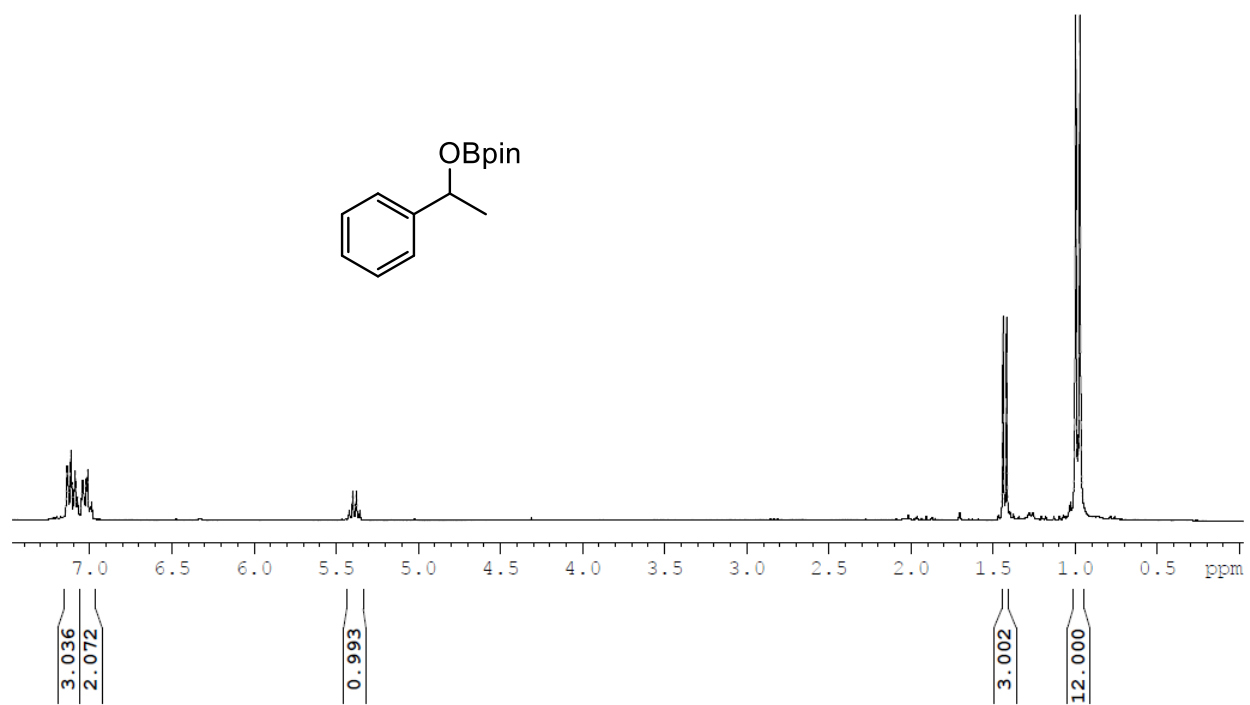


**Figure B13.** <sup>1</sup>H NMR spectrum of acetophenone hydroboration product.

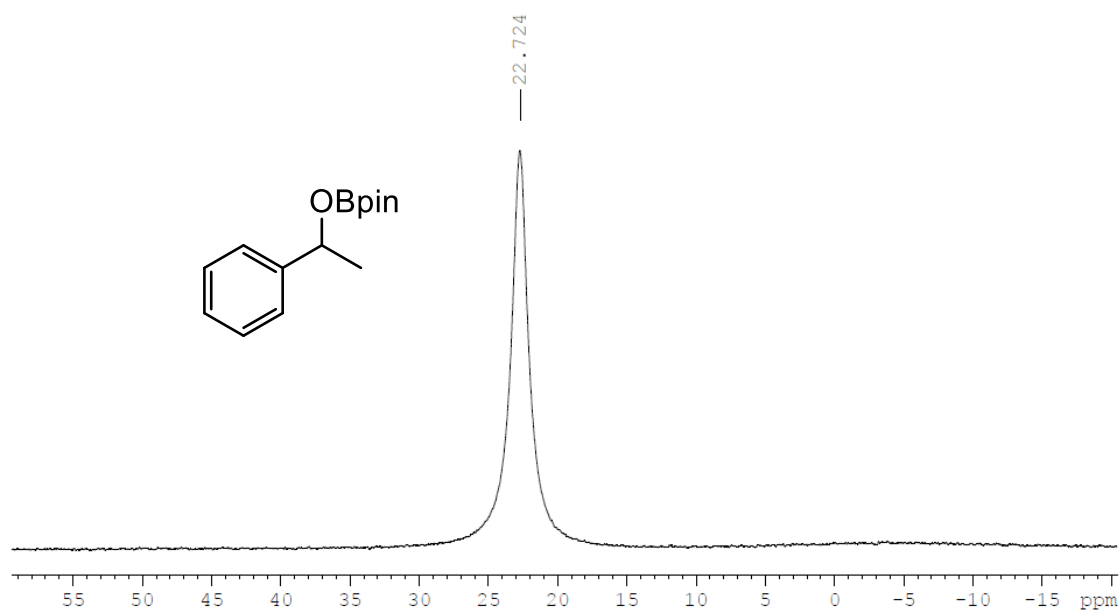


**Figure B14.** <sup>11</sup>B NMR spectrum of acetophenone hydroboration product.

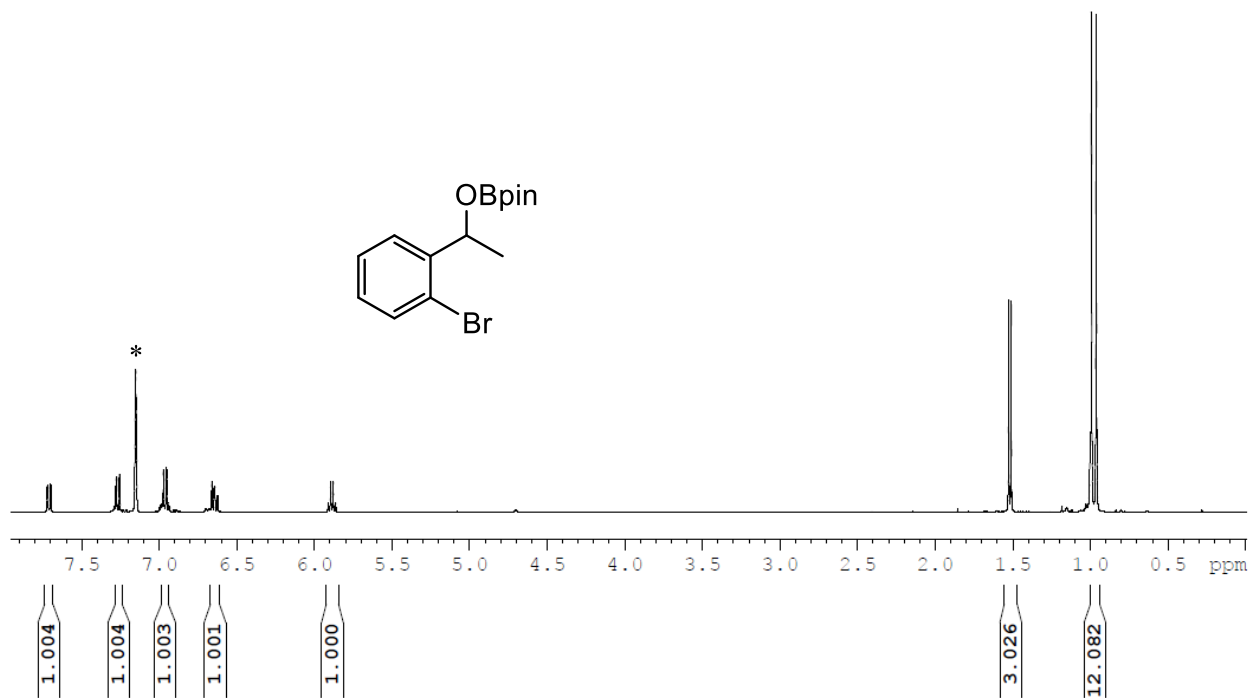


Figure B15. <sup>1</sup>H NMR spectrum of 2-bromoacetophenone hydroboration product. \* is C<sub>6</sub>D<sub>6</sub>.

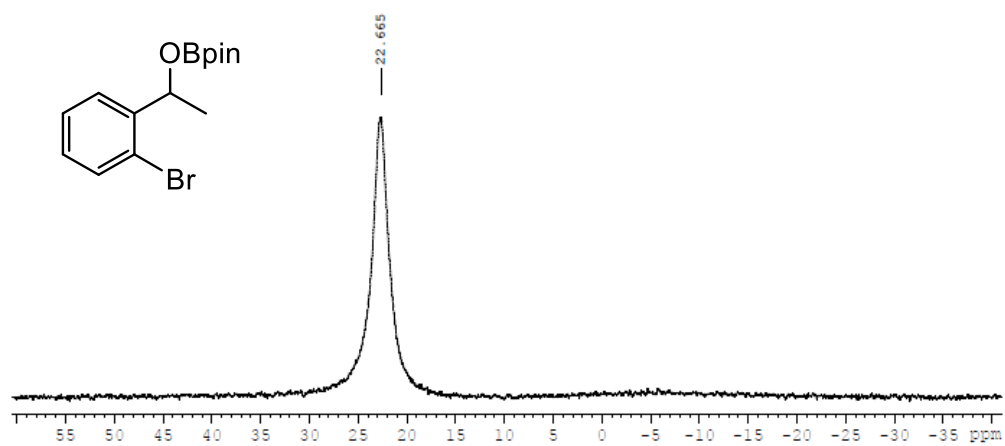
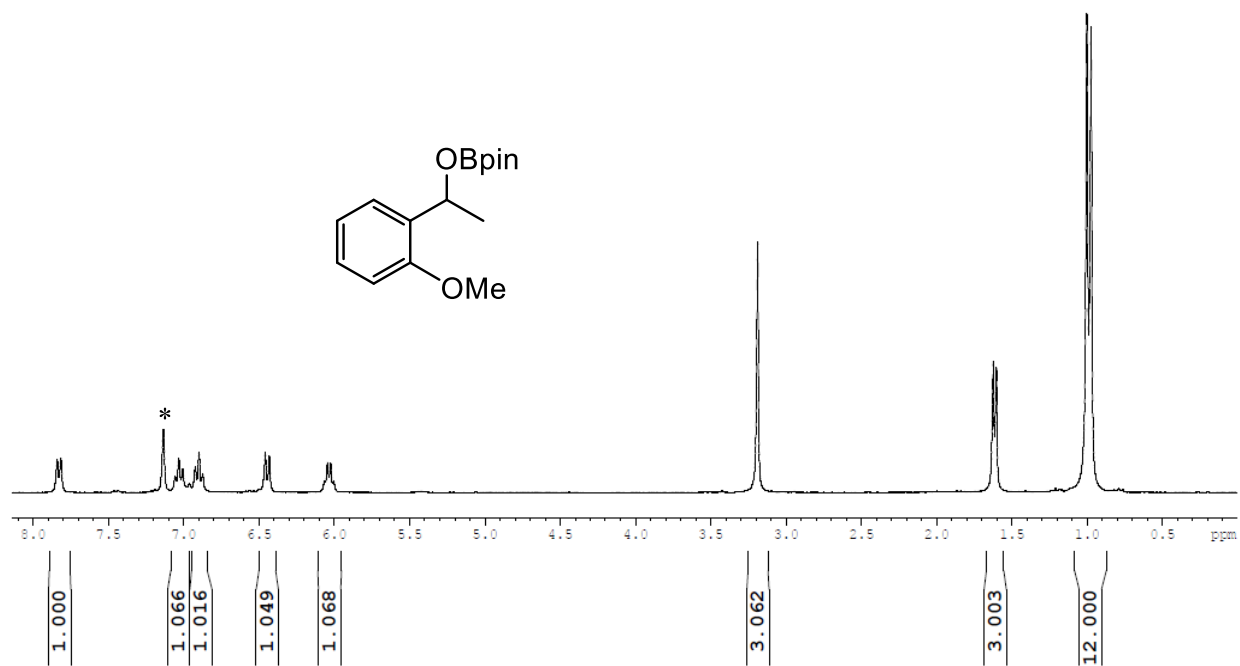
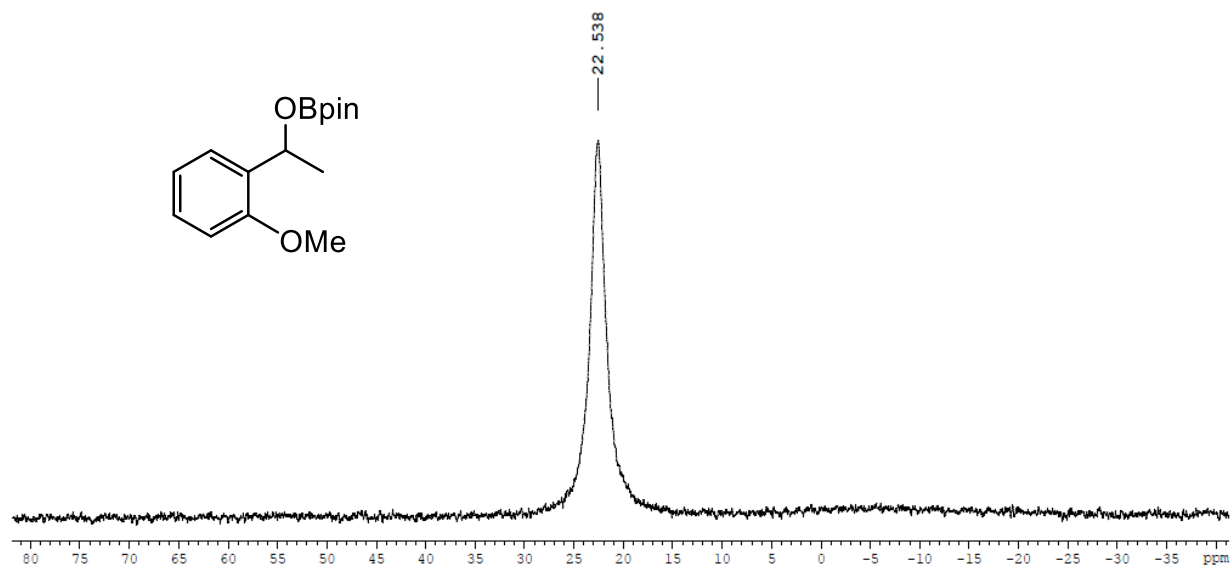


Figure B16. <sup>11</sup>B NMR spectrum of 2-bromoacetophenone hydroboration product.



**Figure B17.** <sup>1</sup>H NMR spectrum of 2-methoxyacetophenone hydroboration product. \* is C<sub>6</sub>D<sub>6</sub>.



**Figure B18.** <sup>11</sup>B NMR spectrum of 2-methoxyacetophenone hydroboration product.

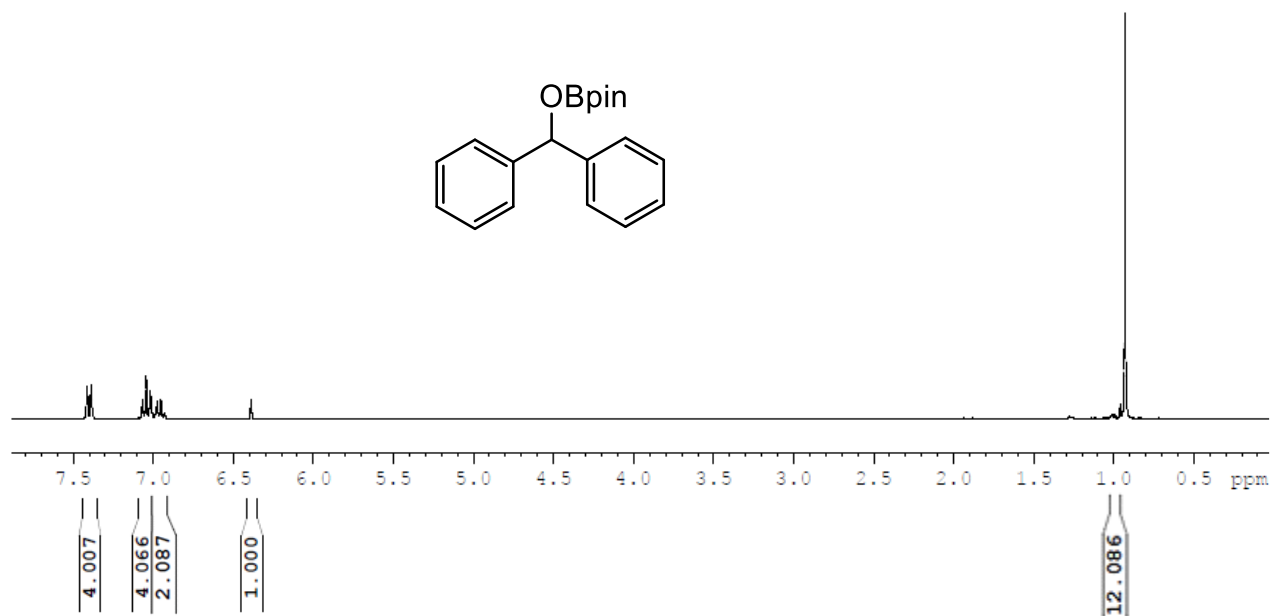


Figure B19. <sup>1</sup>H NMR spectrum of benzophenone hydroboration product.

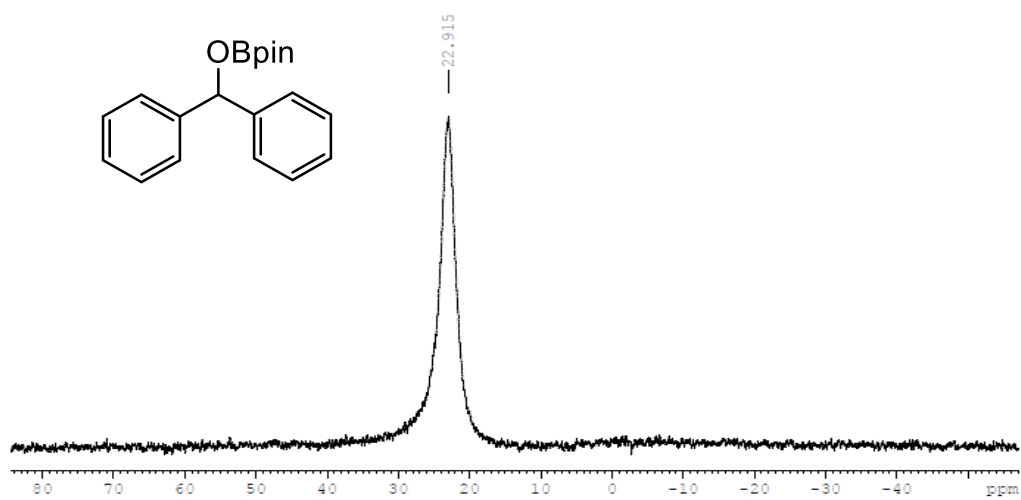
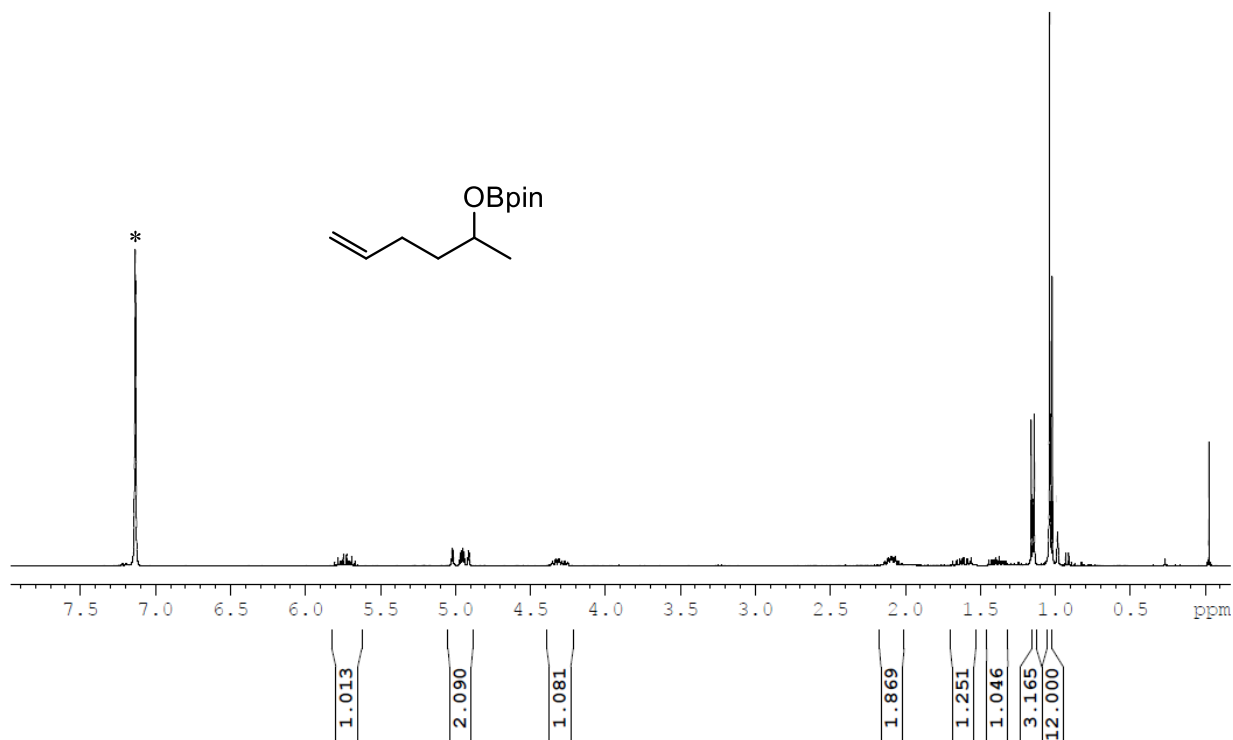
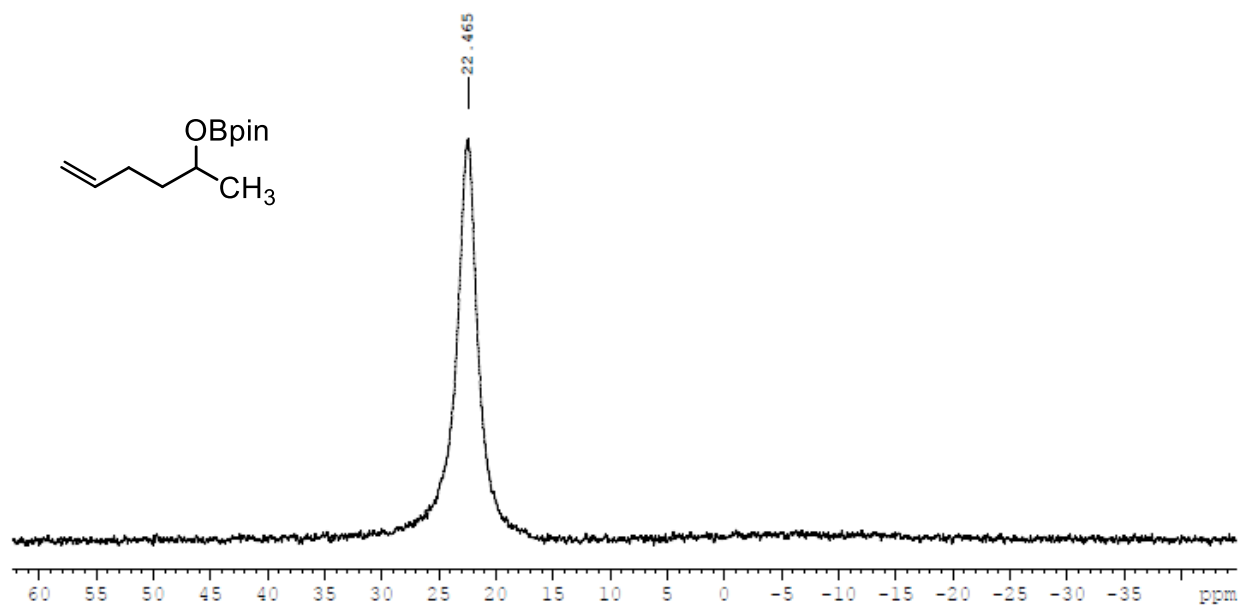


Figure B20. <sup>11</sup>B NMR spectrum of benzophenone hydroboration product.



**Figure B21.**  $^1\text{H}$  NMR spectrum of 5-hexen-2-one hydroboration product. \* is  $\text{C}_6\text{D}_6$ .



**Figure B22.**  $^{11}\text{B}$  NMR spectrum of 5-hexen-2-one hydroboration product.

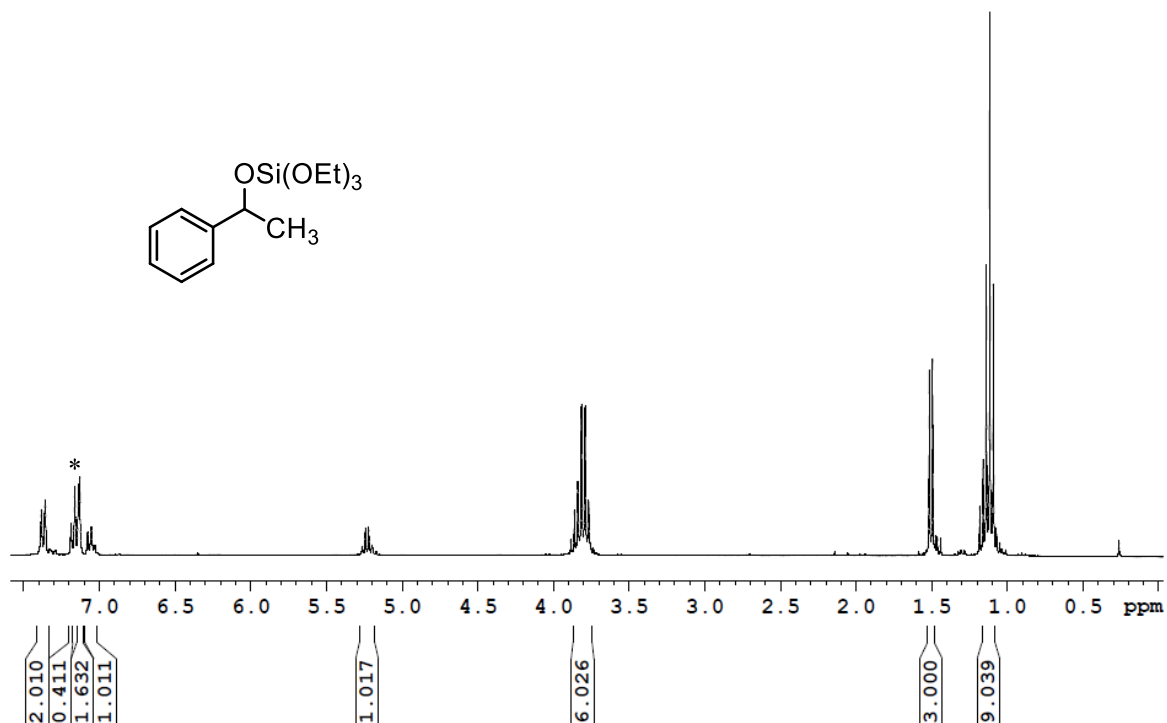


**Figure B23.** <sup>1</sup>H NMR spectrum of acetophenone hydrosilylation product. \* is C<sub>6</sub>D<sub>6</sub>

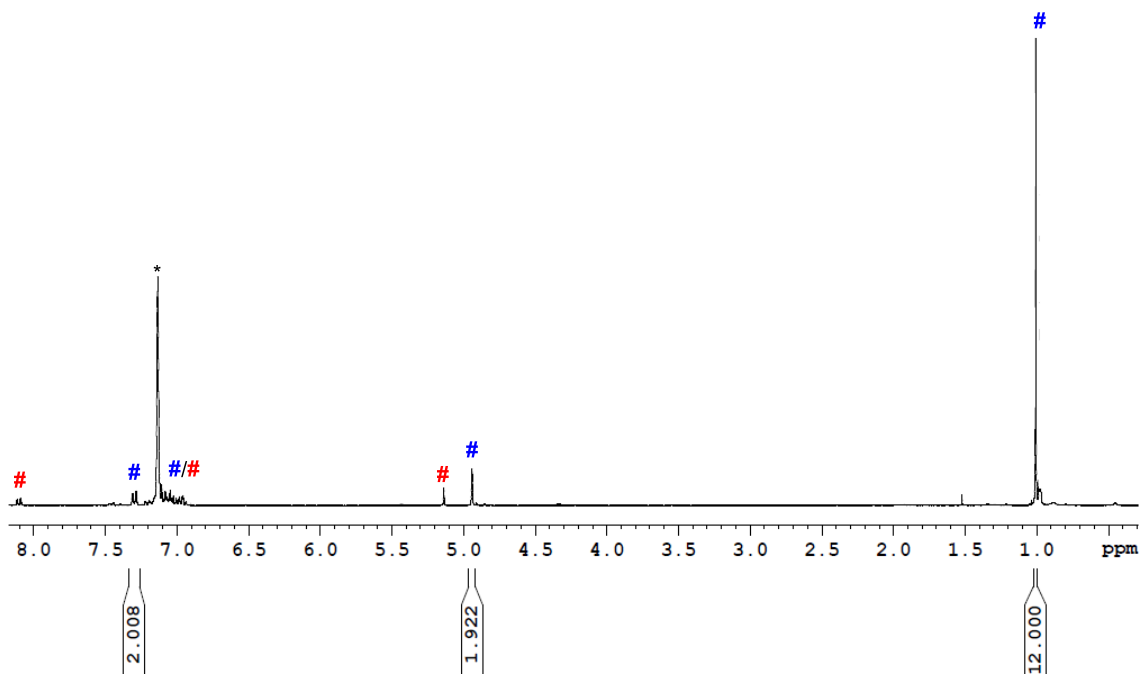


**Figure B24.** <sup>1</sup>H NMR spectrum crude reaction mixture of benzyl benzoate hydroboration. \* is C<sub>6</sub>D<sub>6</sub>. # is hydroboration product. # is unreacted benzyl benzoate.

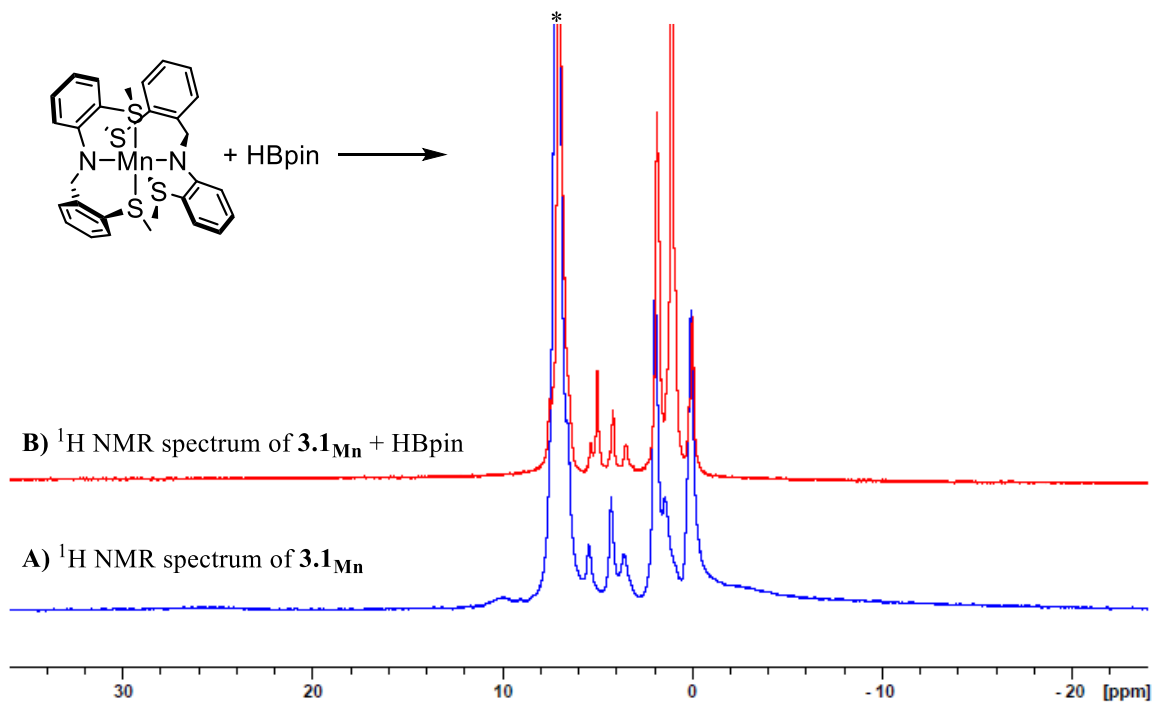


**Figure B25.** Stack plot of <sup>1</sup>H NMR spectra showing stoichiometric reaction of **3.1<sub>Mn</sub>** with HBpin. \* is C<sub>6</sub>D<sub>6</sub>

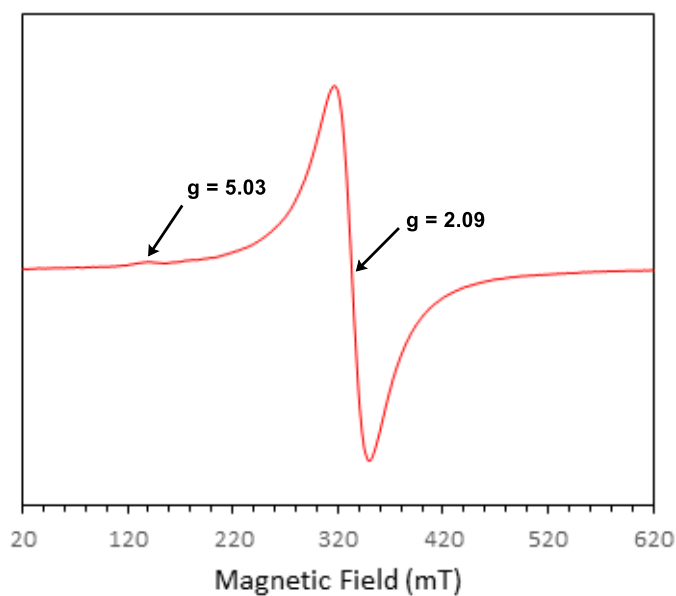


**Figure B26.** 100 K EPR spectrum of stoichiometric reaction of **3.1<sub>Mn</sub>** with HBpin as frozen THF solution.

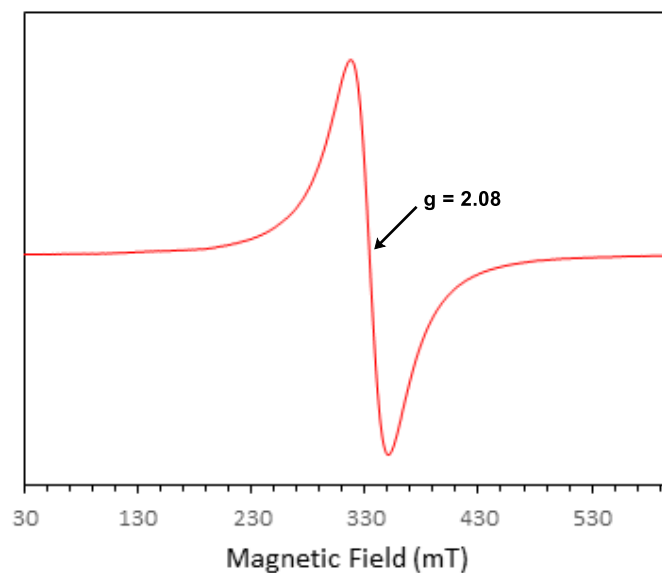


**Figure B27.** 100 K EPR spectrum of catalytic reaction mixture of **3.1<sub>Mn</sub>**, HBpin, and 5-hexen-2-one as frozen THF solution.

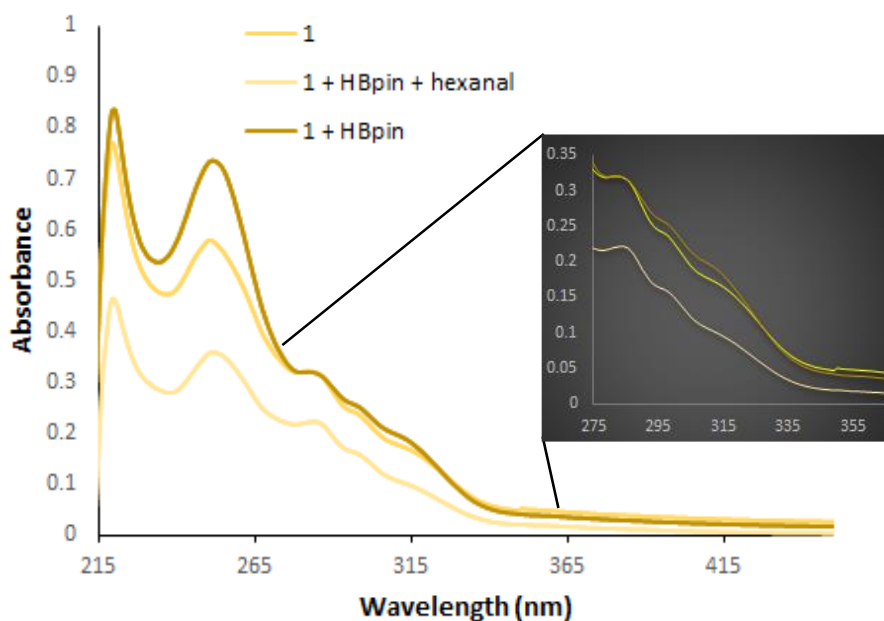


**Figure B28.** Stacked UV-vis spectra of **3.1<sub>Mn</sub>**, stoichiometric solution of **3.1<sub>Mn</sub>** and HBpin, and stoichiometric solution of **3.1<sub>Mn</sub>**, HBpin, and hexanal all in THF solution.

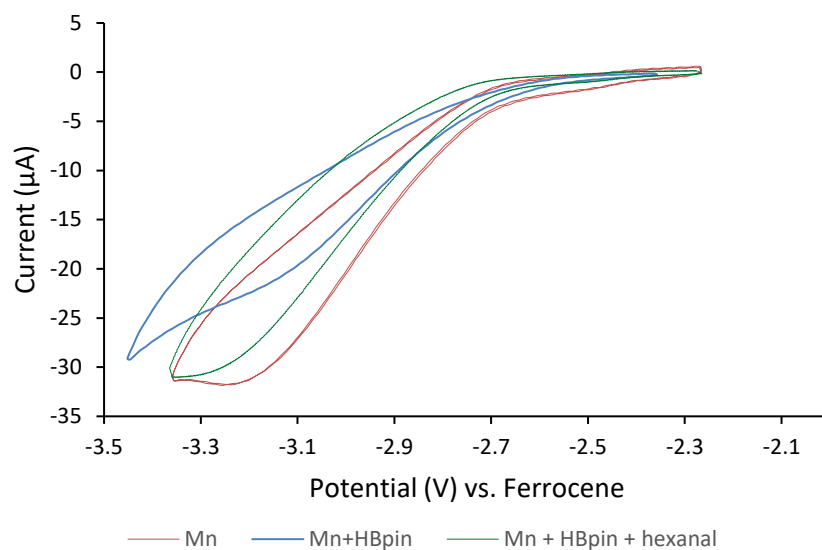


**Figure B29.** Stacked cyclic voltammograms of **3.1**<sub>Mn</sub>, stoichiometric solution of **3.1**<sub>Mn</sub> and HBpin, and stoichiometric solution of **3.1**<sub>Mn</sub>, HBpin, and hexanal. Voltammograms were collected at a scan rate of 100 mV s<sup>-1</sup> in THF.

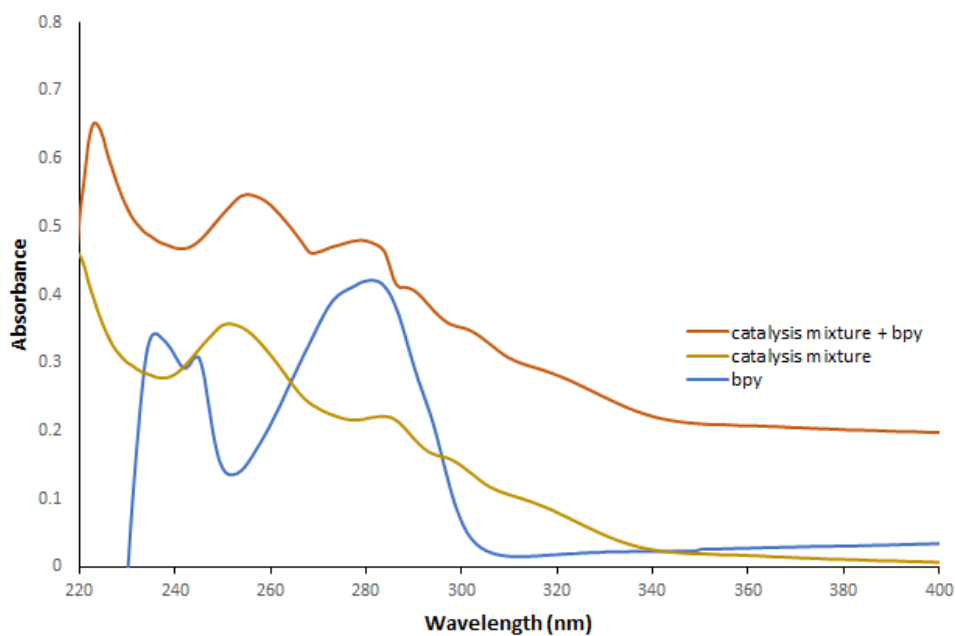


**Figure B30.** Stacked UV-vis spectra of catalytic solution of **3.1**<sub>Mn</sub>, with HBpin and hexanal (yellow), catalytic solution of **3.1**<sub>Mn</sub> and bipyridine, with HBpin and hexanal (orange), and bipyridine (blue) ; all in THF solution.

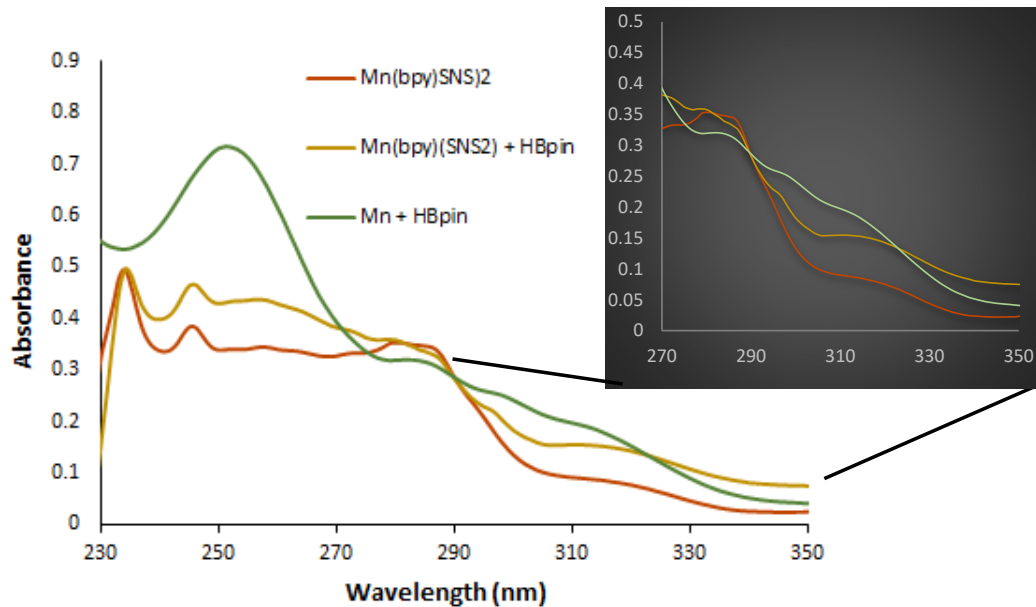


**Figure B31.** Stacked UV-vis spectra of  $3.2_{Mn}$  (orange), stoichiometric solution of  $3.2_{Mn}$  and HBpin (yellow), and stoichiometric solution of  $3.1_{Mn}$  and HBpin (green); all in THF solution.

**Table B1.** Comparison of energies for ground state determination for  $3.1_{Mn}$ ,  $3.1_{Fe}$ , and  $3.1_{Co}$ .

		Mn1	Fe1	Co1
energy (kcal/mol) of spin state, <i>l</i>	1/2	5.8		
	5/2	0		
	1		13.2	
	3		0	
	1/2			3.6
	3/2			0

**Table B2.** Comparison of key bond lengths (Å) of **3.1<sub>Mn</sub>** to DFT optimized structures for ground state determination.

Complex	Spin	Bond	Length (Å)	
			DFT	Xray
Mn(S <sup>Me</sup> NS <sup>Me</sup> ) <sub>2</sub>	6	Mn1-N1	2.118	2.099
		Mn1-N2	2.105	2.112
		Mn1-S1	2.655	2.624
		Mn1-S2	2.755	2.734
		Mn1-S3	2.657	2.647
		Mn1-S4	2.772	2.682
	2	Mn1-N1	2.055	2.099
		Mn1-N2	2.004	2.112
		Mn1-S1	2.305	2.624
		Mn1-S2	2.430	2.734
		Mn1-S3	2.375	2.647
		Mn1-S4	2.334	2.682

**Table B3.** Comparison of key bond lengths (Å) of **3.1<sub>Fe</sub>** to DFT optimized structures for ground state determination.

Complex	Spin	Bond	Length (Å)	
			DFT	Xray
Fe(S <sup>Me</sup> NS <sup>Me</sup> ) <sub>2</sub>	5	Fe1-N1	2.011	2.015
		Fe1-N2	1.965	2.031
		Fe1-S1	2.582	2.5389
		Fe1-S2	2.793	2.7156
		Fe1-S3	2.534	2.5431
		Fe1-S4	2.782	2.7014
	3	Fe1-N1	2.050	2.015
		Fe1-N2	2.035	2.031
		Fe1-S1	2.534	2.5389
		Fe1-S2	2.782	2.7156
		Fe1-S3	2.582	2.5431
		Fe1-S4	2.793	2.7014

**Table B4.** Comparison of key bond lengths (Å) of **3.1Co** to DFT optimized structures for ground state determination.

Complex	Spin	Bond	Length (Å)	
			DFT	Xray
Co(S <sup>Me</sup> NS <sup>Me</sup> ) <sub>2</sub>	2	Co1-N1	1.954	1.967
		Co1-N2	1.954	1.974
		Co1-S1	2.421	2.4723
		Co1-S2	2.598	2.6481
		Co1-S3	2.42	2.478
		Co1-S4	2.598	2.7027
	4	Co1-N1	1.989	1.967
		Co1-N2	1.989	1.974
		Co1-S1	2.516	2.4723
		Co1-S2	2.747	2.6481
		Co1-S3	2.516	2.478
		Co1-S4	2.747	2.7027

**Table B5.** Energies (eV) of alpha and beta frontier orbitals in neutral, cationic, and anionic analogues of **3.1Mn**.

Mn1							
Multiplicity = 6							
Neutral	Alpha	HOMO	-0.20577	-0.1829	-0.16034	-0.151	-0.14721
		LUMO	-0.04733	-0.04694	-0.04126	-0.03942	-0.03871
	Beta	HOMO	-0.21349	-0.2105	-0.20457	-0.16441	-0.15348
		LUMO	-0.05868	-0.05299	-0.04973	-0.04504	-0.04198
Multiplicity = 5 or 7							
+1 complex	Alpha	HOMO	-0.23464	-0.2159	-0.1991	-0.18552	
		LUMO	-0.1828	-0.06851	-0.06627	-0.06532	-0.06317
	Beta	HOMO	-0.24433	-0.23521	-0.23222	-0.21048	-0.20156
		LUMO	-0.10616	-0.1016	-0.10021	-0.08481	-0.07225
Multiplicity = 5							
-1 complex	Alpha	HOMO	-0.16849	-0.13606	-0.1259	-0.12108	-0.09983
		LUMO	-0.01715	-0.0162	-0.01257	-0.01123	-0.00981
	Beta	HOMO	-0.02954				
		LUMO	-0.02304	-0.01951	-0.01726	-0.01424	-0.01071

**Table B6.** Energies (eV) of alpha and beta frontier orbitals in neutral, cationic, and anionic analogues of **3.1<sub>Fe</sub>**.

		<b>Fe1</b>					
		<b>Multiplicity = 5</b>					
<b>Neutral</b>	<b>Alpha</b>	<b>HOMO</b>	-0.20411	-0.18387	-0.16242	-0.16111	-0.15603
		<b>LUMO</b>	-0.04478	-0.04332	-0.04167	-0.03922	-0.03609
	<b>Beta</b>	<b>HOMO</b>	-0.12639				
		<b>LUMO</b>	-0.08413	-0.07934	-0.0497	-0.04466	-0.0424
		<b>Multiplicity = 6</b>					
<b>+1 complex</b>	<b>Alpha</b>	<b>HOMO</b>	-0.24194	-0.22649	-0.21467	-0.20253	-0.20035
		<b>LUMO</b>	-0.07327	-0.07	-0.06733	-0.06468	-0.06039
	<b>Beta</b>	<b>HOMO</b>	-0.24727	-0.23642	-0.2322	-0.2137	-0.19057
		<b>LUMO</b>	-0.19375	-0.16315	-0.15288	-0.14785	-0.10282
		<b>Multiplicity = 4</b>					
<b>-1 complex</b>	<b>Alpha</b>	<b>HOMO</b>	-0.13304	-0.12323	-0.11729	-0.10753	-0.08604
		<b>LUMO</b>	-0.01949	-0.01906	-0.01395	-0.01277	-0.00916
	<b>Beta</b>	<b>HOMO</b>	-0.0465	-0.034			
		<b>LUMO</b>	-0.02121	-0.02016	-0.01575	-0.01402	-0.00898

**Table B7.** Energies (eV) of alpha and beta frontier orbitals in neutral, cationic, and anionic analogues of **3.1<sub>Co</sub>**.

		<b>Co1</b>					
		<b>Multiplicity = 4</b>					
<b>Neutral</b>	<b>Alpha</b>	<b>HOMO</b>	-0.20666	-0.18269	-0.16685	-0.15915	-0.15476
		<b>LUMO</b>	-0.04469	-0.04463	-0.04252	-0.03872	-0.03819
	<b>Beta</b>	<b>HOMO</b>	-0.16016	-0.14566			
		<b>LUMO</b>	-0.10652	-0.06207	-0.04811	-0.04291	-0.04238
		<b>Multiplicity = 5</b>					
<b>+1 complex</b>	<b>Alpha</b>	<b>HOMO</b>	-0.2357	-0.21627	-0.21582	-0.20831	-0.20221
		<b>LUMO</b>	-0.07619	-0.07607	-0.06564	-0.06168	-0.06098
	<b>Beta</b>	<b>HOMO</b>	-0.19821				
		<b>LUMO</b>	-0.18471	-0.15567	-0.10996	-0.09717	-0.07202
		<b>Multiplicity = 3</b>					
<b>-1 complex</b>	<b>Alpha</b>	<b>HOMO</b>	-0.12333	-0.11385	-0.11202	-0.09075	-0.07146
		<b>LUMO</b>	-0.02063	-0.01919	-0.01723	-0.01545	-0.01128
	<b>Beta</b>	<b>HOMO</b>	-0.07167	-0.06168	-0.04787		
		<b>LUMO</b>	-0.02075	-0.01986	-0.01775	-0.01623	-0.01056

**Table B8.** Calculated atomic Hirshfeld charges for **3.1<sub>Mn</sub>**, **3.1<sub>Mn</sub><sup>+</sup>**, and **3.1<sub>Mn</sub><sup>-</sup>**.

Atom	Hirshfeld Charges		
	Mn1	Mn1(+)	Mn1(-)
Mn	0.2304	0.282353	0.120311
N	-0.195624	-0.157384	-0.193764
N	-0.199251	-0.132784	-0.19668
S(5)	-0.047066	-0.014378	-0.069367
S(6)	-0.026408	-0.017341	-0.04849
S(5)	-0.053318	-0.012756	-0.096702
S(6)	-0.015684	0.004407	-0.057904
C5(5)-N	0.042347	0.058726	0.040025
C6(5)-S	-0.033822	-0.005598	-0.036593
C12(5)	-0.009868	0.026604	-0.025512
C13(5)	-0.050239	0.029858	-0.071582
C14(5)	-0.023589	0.021344	-0.042151
C15(5)	-0.054436	0.001312	-0.067864
C20-N	0.045082	0.085794	0.028215
C21(6)-C	0.006259	0.006364	-0.002463
C22(6)-S	-0.004044	-0.002646	-0.017405
C28(6)	0.008192	0.020207	-0.019809
C29(6)	0.008767	0.027211	-0.018427
C30(6)	0.002	0.018429	-0.042207
C31(6)	0.006646	0.018905	-0.021004
C38(5)-N	0.050092	0.057669	0.044496
C39(5)-S	-0.033544	-0.019681	-0.040251
C45(5)	0.003664	0.032761	-0.026216
C46(5)	-0.0456	0.011001	-0.074601
C47(5)	-0.009035	0.024292	-0.045908
C48(5)	-0.043501	-0.000424	-0.068489
C1-N	0.041668	0.077249	0.016027
C53(6)-C	0.009821	0.009922	-0.00178
C54(6)-S	-0.002184	-0.002129	-0.026624
C60(6)	0.015743	0.026218	-0.033274
C61(6)	0.016014	0.030501	-0.021144
C62(6)	0.007234	0.022884	-0.056127
C63(6)	0.01438	0.02501	-0.034633

**Table B9.** Calculated atomic Hirshfeld charges for **3.1<sub>Fe</sub>**, **3.1<sub>Fe</sub><sup>+</sup>**, and **3.1<sub>Fe</sub><sup>-</sup>**.

Atom	Hirshfeld Charges		
	Fe1	Fe1(+)	Fe1(-)
Mn	0.245654	0.37401	0.082033
N	-0.184164	-0.147897	-0.18633
N	-0.179387	-0.149218	-0.179683
S(5)	-0.040155	0.012199	-0.082524
S(6)	-0.038665	-0.01593	-0.062657
S(5)	-0.052738	-0.009079	-0.090355
S(6)	-0.030729	-0.011465	-0.044517
C5(5)-N	0.046925	0.052562	0.039333
C6(5)-S	-0.033425	-0.021428	-0.04025
C12(5)	-0.039995	-0.00457	-0.065815
C13(5)	-0.013049	0.020441	-0.042371
C14(5)	-0.042474	0.006768	-0.080468
C15(5)	-0.001104	0.026281	-0.025761
C20-N	0.041001	0.080022	0.008984
C21(6)-C	0.002029	0.003059	-0.001791
C22(6)-S	-0.006521	-0.008816	-0.009228
C28(6)	0.007832	0.025039	-0.019509
C29(6)	-0.002972	0.021933	-0.036068
C30(6)	0.008449	0.028671	-0.017075
C31(6)	0.005684	0.019149	-0.015732
C38(5)-N	0.053053	0.080799	0.025333
C39(5)-S	0.005331	0.006541	0.001377
C45(5)	-0.003796	-0.004046	-0.008113
C46(5)	0.008811	0.023019	-0.007529
C47(5)	0.009949	0.029013	-0.014782
C48(5)	0.000996	0.021963	-0.068489
C1-N	0.006261	0.02022	0.016027
C53(6)-C	0.051341	0.055457	-0.00178
C54(6)-S	-0.035837	-0.027575	-0.026624
C60(6)	0.001715	0.02827	-0.033274
C61(6)	-0.04462	0.002419	-0.021144
C62(6)	-0.008823	0.023479	-0.056127
C63(6)	-0.046452	-0.014751	-0.034633

**Table B10.** Calculated atomic Hirshfeld charges for **3.1Co**, **3.1Co<sup>+</sup>**, and **3.1Co<sup>-</sup>**.

Atom	Hirshfeld Charges		
	Co1	Co1(+)	Co1(-)
Mn	0.15347	0.19826	-0.014792
N	-0.157323	-0.098661	-0.166624
N	-0.15734	-0.098654	-0.166625
S(5)	-0.042628	-0.008568	-0.087835
S(6)	-0.029807	-0.01725	-0.041966
S(5)	-0.042603	-0.008531	-0.087838
S(6)	-0.029817	-0.017262	-0.041965
C5(5)-N	0.053481	0.09302	0.023844
C6(5)-S	0.005229	0.005734	0.005165
C12(5)	-0.004052	-0.002945	-0.004972
C13(5)	0.003091	0.016797	-0.011881
C14(5)	-0.003202	0.016247	-0.025013
C15(5)	0.005593	0.025011	-0.014894
C20-N	0.003421	0.015798	-0.010088
C21(6)-C	0.052399	0.061969	0.040049
C22(6)-S	-0.032568	-0.012749	-0.044242
C28(6)	-0.032568	0.003579	-0.070379
C29(6)	-0.042628	0.032124	-0.043058
C30(6)	-0.038155	0.027541	-0.090012
C31(6)	0.005	0.039814	-0.026087
C38(5)-N	0.053469	0.093016	0.023842
C39(5)-S	0.005226	0.005732	0.004164
C45(5)	-0.004053	-0.002945	-0.004971
C46(5)	0.003414	0.015792	-0.010092
C47(5)	0.005588	0.02501	-0.014892
C48(5)	-0.003209	0.016241	-0.025014
C1-N	0.003086	0.016793	-0.01183
C53(6)-C	0.052395	0.061969	0.040054
C54(6)-S	-0.032576	-0.01275	-0.044239
C60(6)	0.004997	0.039821	-0.026088
C61(6)	-0.038168	0.027548	-0.090006
C62(6)	-0.005396	0.032128	-0.043057
C63(6)	-0.040286	0.003581	-0.070384

**Table B11.** Calculated Fukui indices for main atoms in **3.1<sub>Mn</sub>**.

Atom	Fukui(+)	Fukui(-)
Mn	0.051953	0.110089
N	0.03824	-0.00186
N	0.066467	-0.00257
S(5)	0.032688	0.022301
S(6)	0.009067	0.022082
S(5)	0.040562	0.043384
S(6)	0.020091	0.04222

**Table B12.** Calculated Fukui indices for main atoms in **3.1<sub>Fe</sub>**.

Atom	Fukui(+)	Fukui(-)
Fe	0.128356	0.163621
N	0.036267	0.002166
N	0.030169	0.000296
S(5)	0.052354	0.042369
S(6)	0.022735	0.023992
S(5)	0.043659	0.037617
S(6)	0.019264	0.013788

**Table B13.** Calculated Fukui indices for main atoms in **3.1<sub>Co</sub>**.

Atom	Fukui(+)	Fukui(-)
Co	0.04479	0.168262
N	0.058662	0.009301
N	0.058686	0.009285
S(5)	0.03406	0.045207
S(6)	0.012557	0.012159
S(5)	0.034072	0.045235
S(6)	0.012555	0.012148

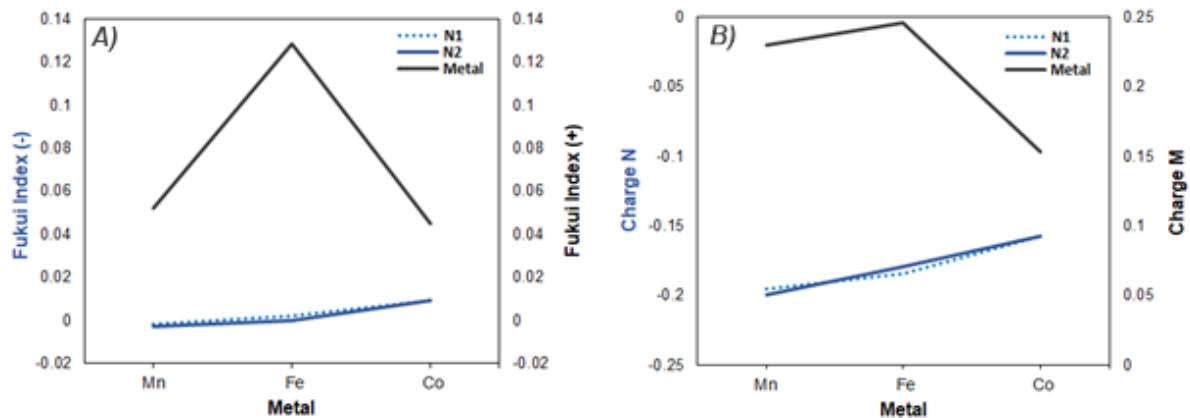


**Figure B32.** A) Chart of calculated Fukui (-/+ indices for both amido donors and metal of **3.1<sub>Mn</sub>**, **3.1<sub>Fe</sub>**, and **3.1<sub>Co</sub>**; B) Calculated Hirshfeld charges for both amido donors and metals

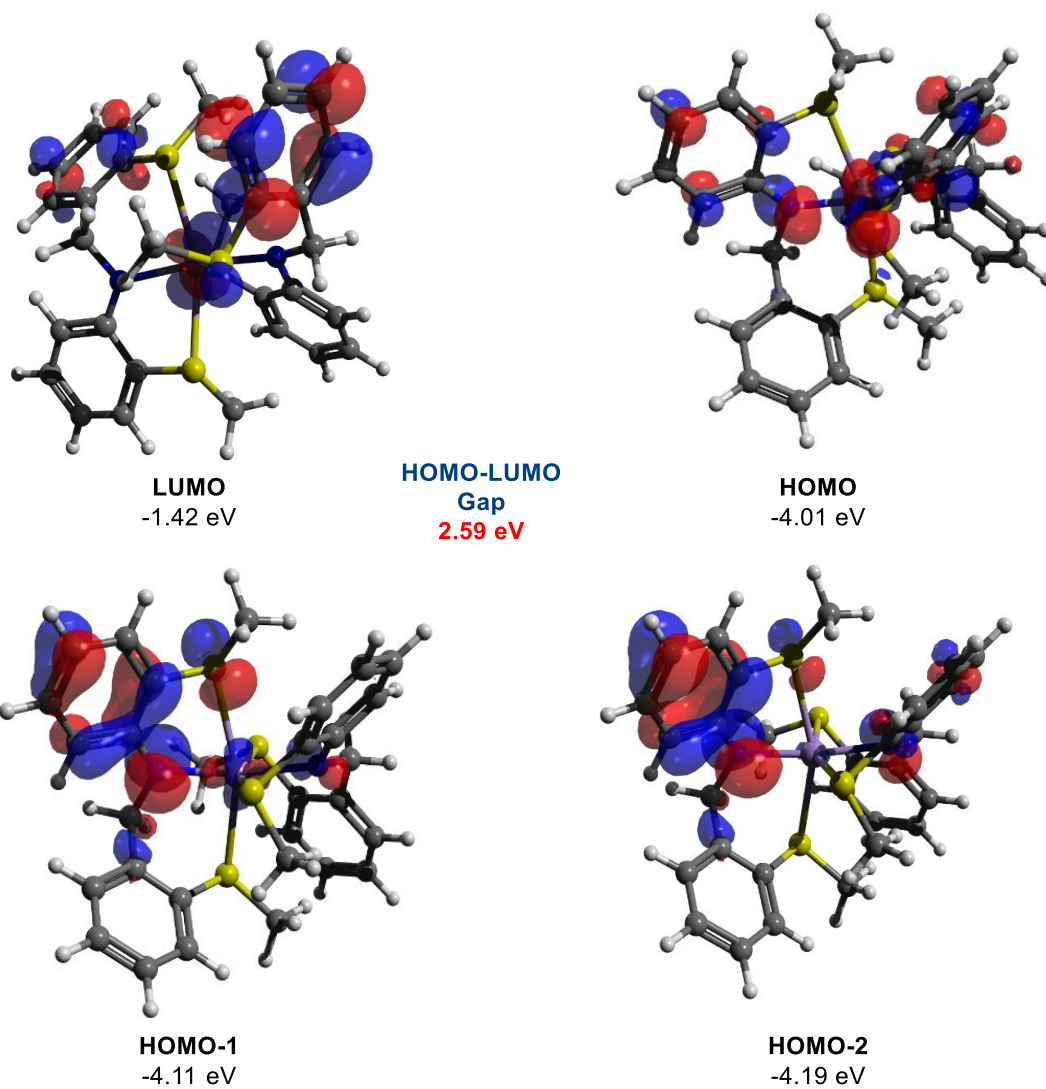
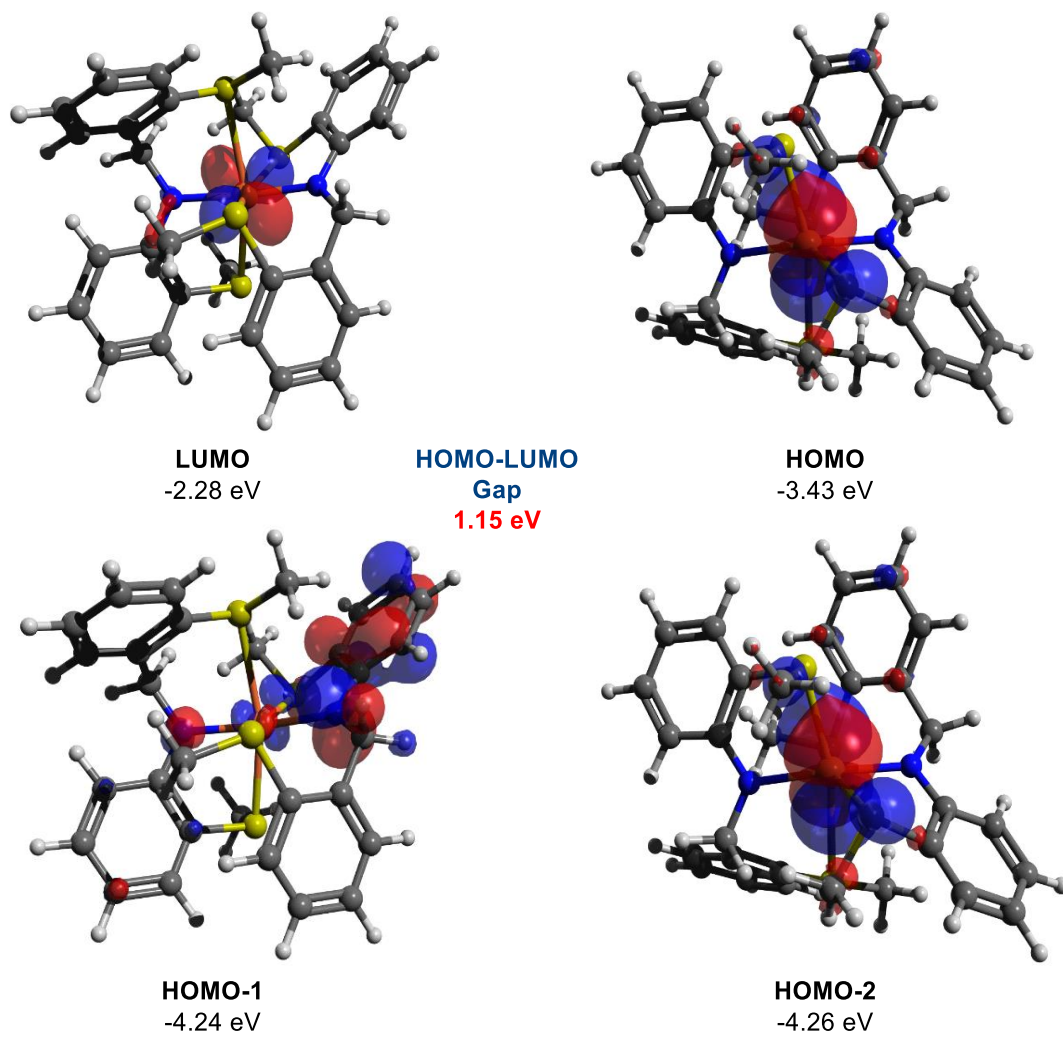


Figure B33. Frontier orbitals and energies of 3.1Mn.



**Figure B34.** Frontier orbitals and energies of **3.1<sub>Fe</sub>**.

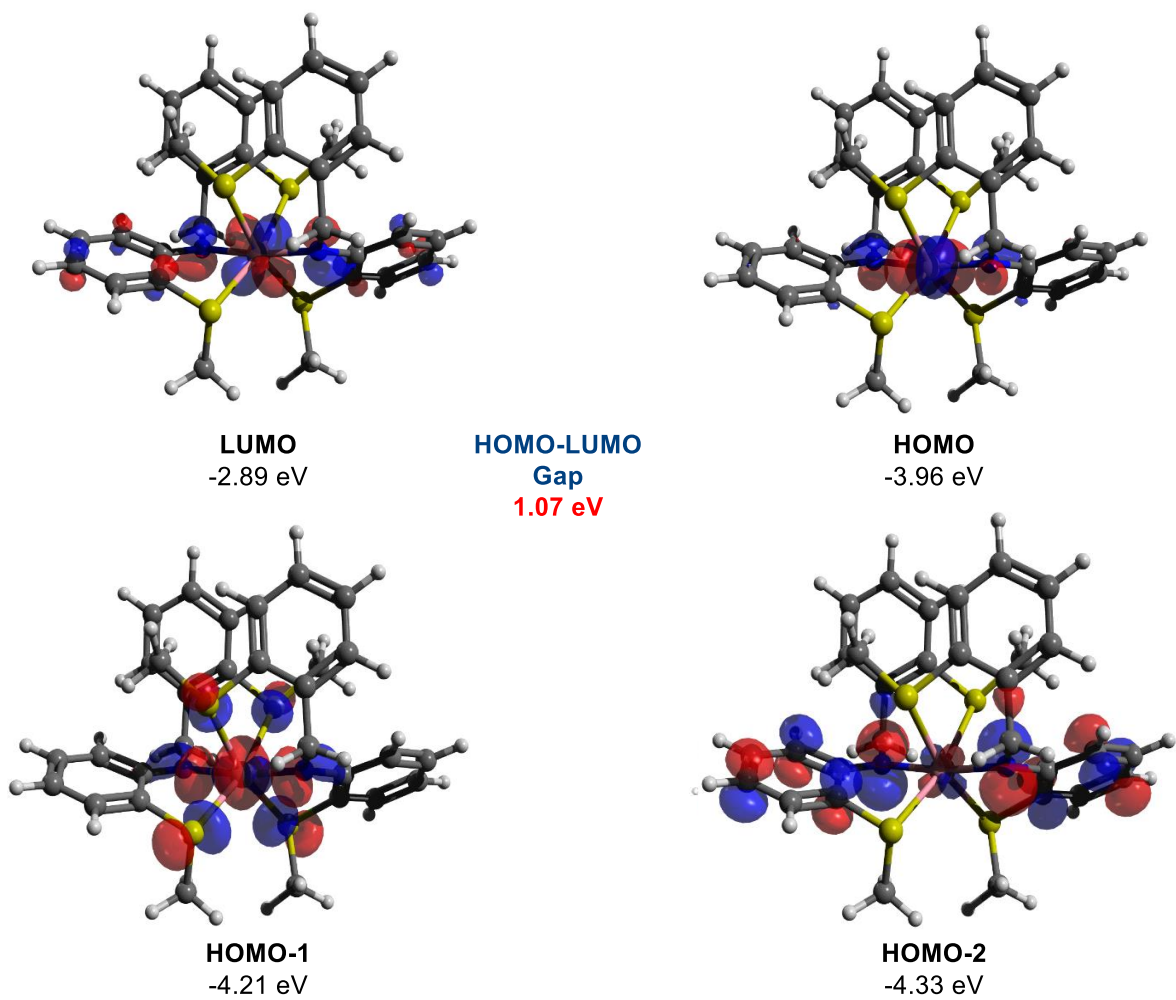


Figure B35. Frontier orbitals and energies of **3.1c**.

**Bond Lengths (Angstroms)**

	$H_1-H_2$	$N-H_1$	$M-H_2$	$H_1-H_2$	$N-H_1$	$M-H_2$	$H_1-H_2$	$N-H_1$	$M-H_2$
<b>[Mn]</b>	0.760	2.621	3.883	1.063	1.293	1.902	1.837	1.026	1.723
<b>[Fe]</b>	0.760	2.589	3.758	1.109	1.232	1.909	1.704	1.032	1.715
<b>[Co]</b>	0.761	2.728	3.653	0.871	1.582	1.861	1.687	1.032	1.645

**Figure B36.** Key bond lengths in calculated complexes **M3**, **M3-TS**, and **M4** for the Mn, Fe, and Co analogues.

**Table B14.** Energies (in Hartree) for all DFT compounds, intermediates, and transition states:  $E_{DZ}$  and thermal corrections were calculated at the M06-L/def2-SVP level of theory;  $E_{TZ}$  energy calculations were performed on the M06-L/def2-SVP at the M06-L/def2-TZVP level of theory with incorporation of solvation energy using the self-consistent reaction field (SCRf) for tetrahydrofuran.

Compound	$E_{TZ}$	$E_{DZ}$	$E_{zpe}$	Thermal Corrections (T = 298.15 K, p = 1atm)	
				H	G
<b>H<sub>2</sub></b>	-1.167912861	-1.16791286	0.009919	0.013224	-0.001571
<b>Mn1</b> (S=1/2)	-4016.076284	-4016.067541	0.549369	0.58664	0.482914
<b>Mn1</b> (S=5/2)	-4016.128128	-4014.110838	0.546559	0.58501	0.474914
<b>Mn2</b>	-4016.119331	-4014.099311	0.547363	0.586029	0.474497
<b>Mn3</b>	-4017.289724	-4015.263558	0.557822	0.599921	0.480409
<b>Mn3-TS</b>	-4017.258643	-4015.238565	0.55871	0.598427	0.484071
<b>Mn4</b>	-4017.278808	-4015.253371	0.563279	0.6043463	0.488097
<b>Fe1</b> (S=1)	-4128.804241	-4126.762886	0.547164	0.584844	0.480351
<b>Fe1</b> (S=2)	-4128.828097	-4126.791944	0.546588	0.584821	0.477596
<b>Fe2</b>	-4128.822619	-4126.784552	0.546078	0.584724	0.474418
<b>Fe3</b>	-4129.99799	-4127.953776	0.559685	0.600485	0.487135
<b>Fe3-TS</b>	-4129.961631	-4127.920483	0.560068	0.598964	0.489185
<b>Fe4</b>	-4129.973566	-4127.092979	0.564984	0.604338	0.492823
<b>Co1</b> (S=1/2)	-4247.876133	-4245.817702	0.547716	0.58536	0.480634
<b>Co1</b> (S=3/2)	-4247.883557	-4245.827935	0.547338	0.585275	0.478872

Appendices – Appendix B

<b>Co2</b>	-4247.875558	-4245.818415	0.546294	0.584742	0.475801
<b>Co3</b>	-4249.04683	-4246.984529	0.559947	0.60047	0.488643
<b>Co3-TS</b>	-4248.999398	-4246.939243	0.561543	0.600484	0.488457
<b>Co4</b>	-4249.028728	-4246.965735	0.565274	0.604576	0.492775

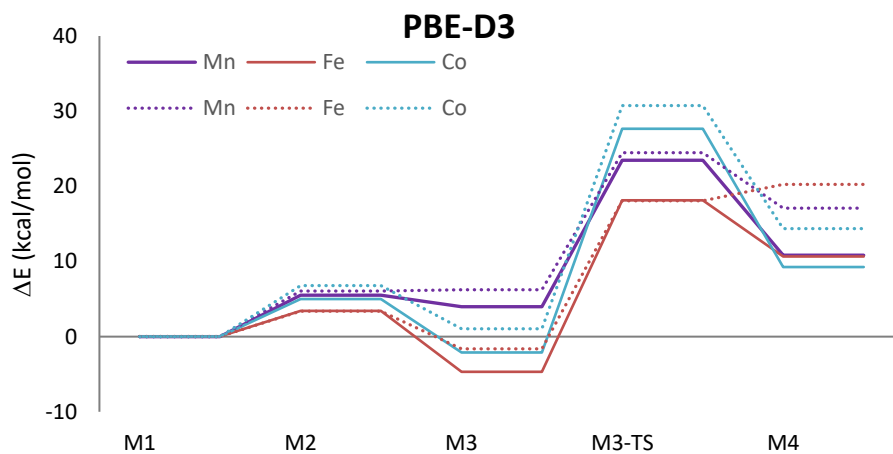


Figure B37. Reaction profiles comparing M06L functional (solid line) vs. PBE-D3 (dotted line).

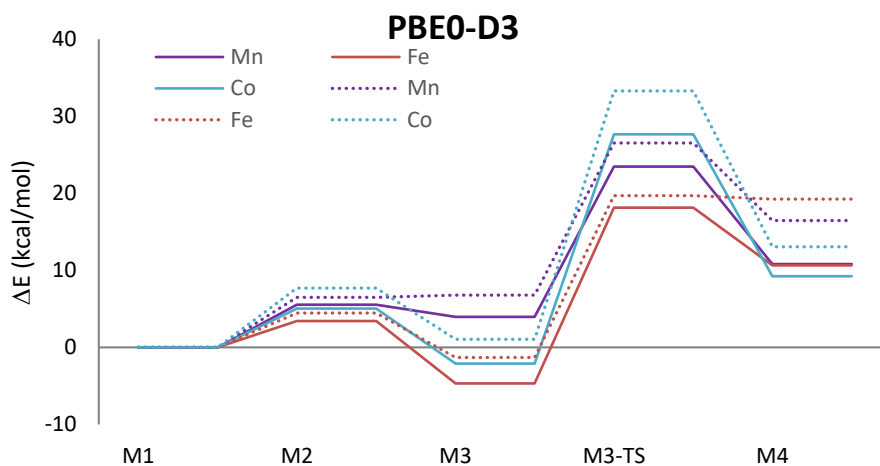


Figure B38. Reaction profiles comparing M06L functional (solid line) vs. PBE0-D3 (dotted line).

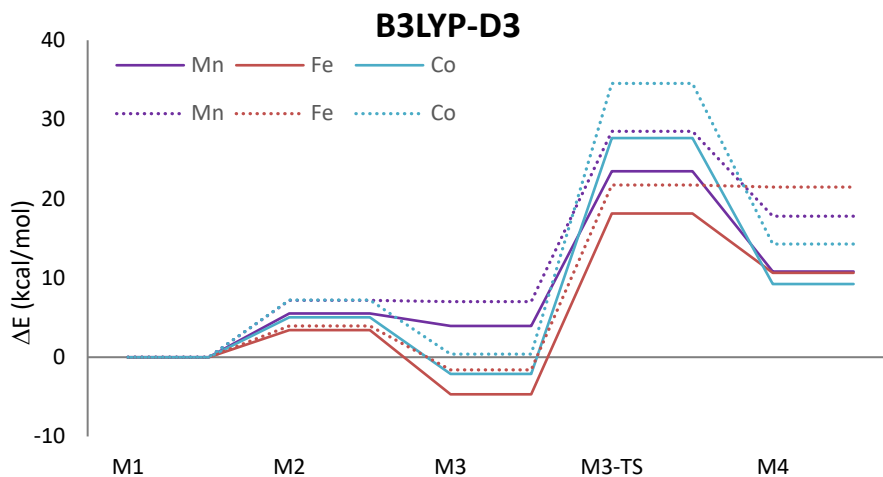


Figure B39. Reaction profiles comparing M06L functional (solid line) vs. B3LYP-D3 (dotted line).

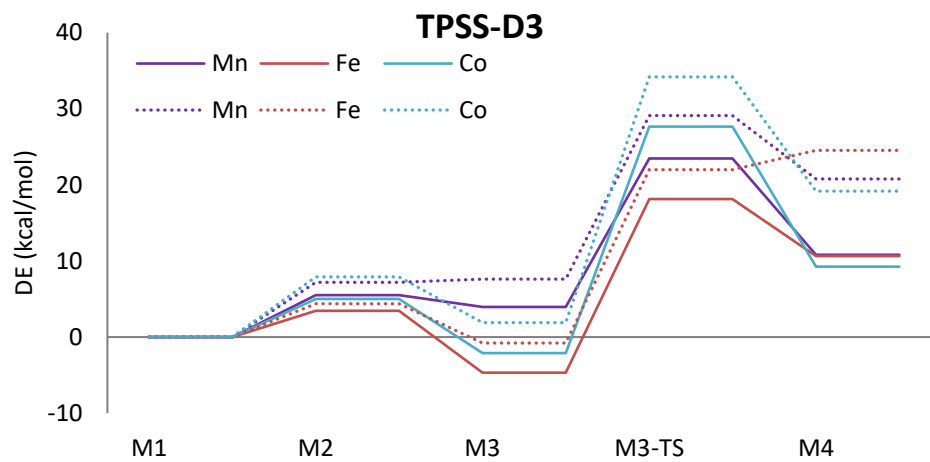
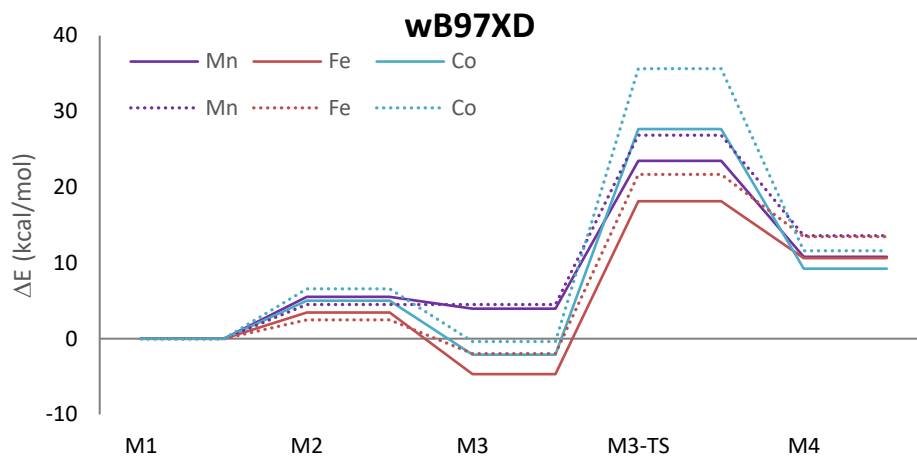
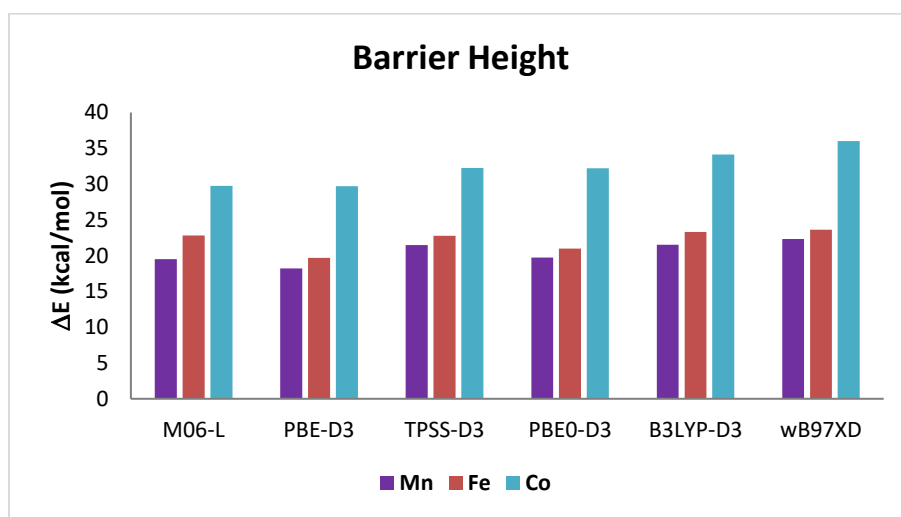


Figure B40. Reaction profiles comparing M06L functional (solid line) vs. TPSS-D3 (dotted line).



**Figure B41.** Reaction profiles comparing M06L functional (solid line) vs. wb97XD (dotted line).



**Figure B42.** Overall reaction barriers benchmarking different functionals.

Appendix C – Chapter 4

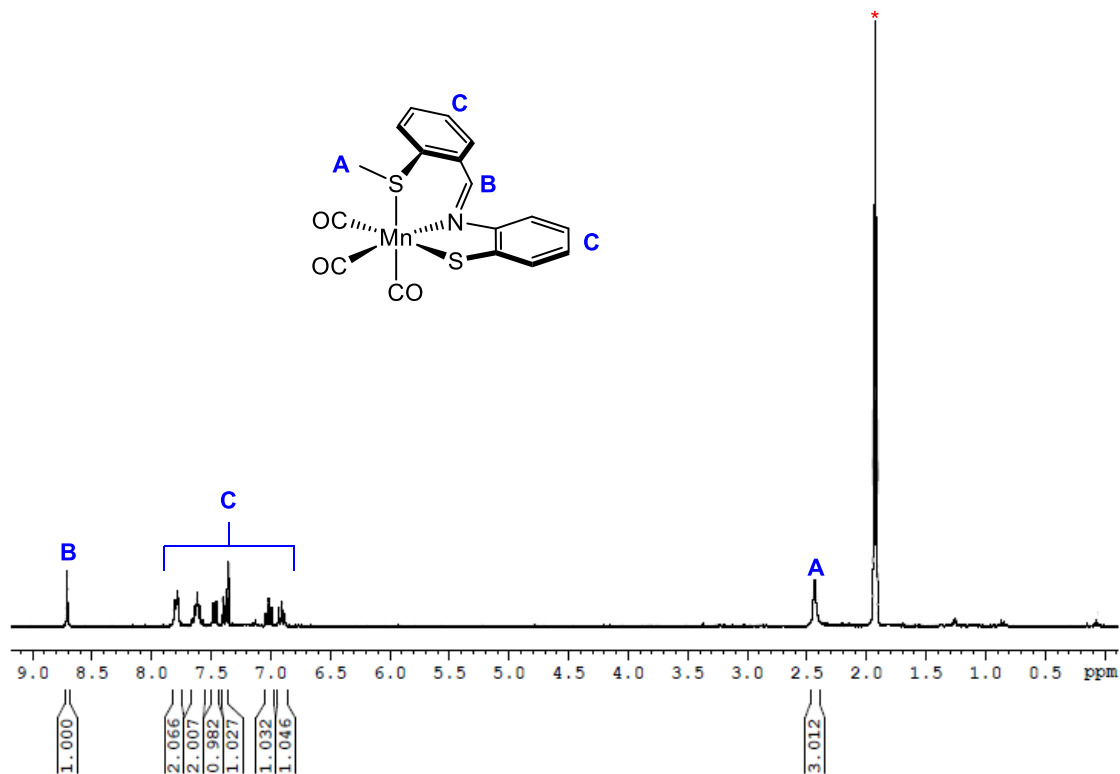


Figure C1.  $^1\text{H}$  spectrum of  $[\text{Mn}(\kappa^3\text{-SNS}^{\text{Me}})(\text{CO})_3]$  (**4.1<sub>Mn</sub>**). \* is acetonitrile- $d^3$ .

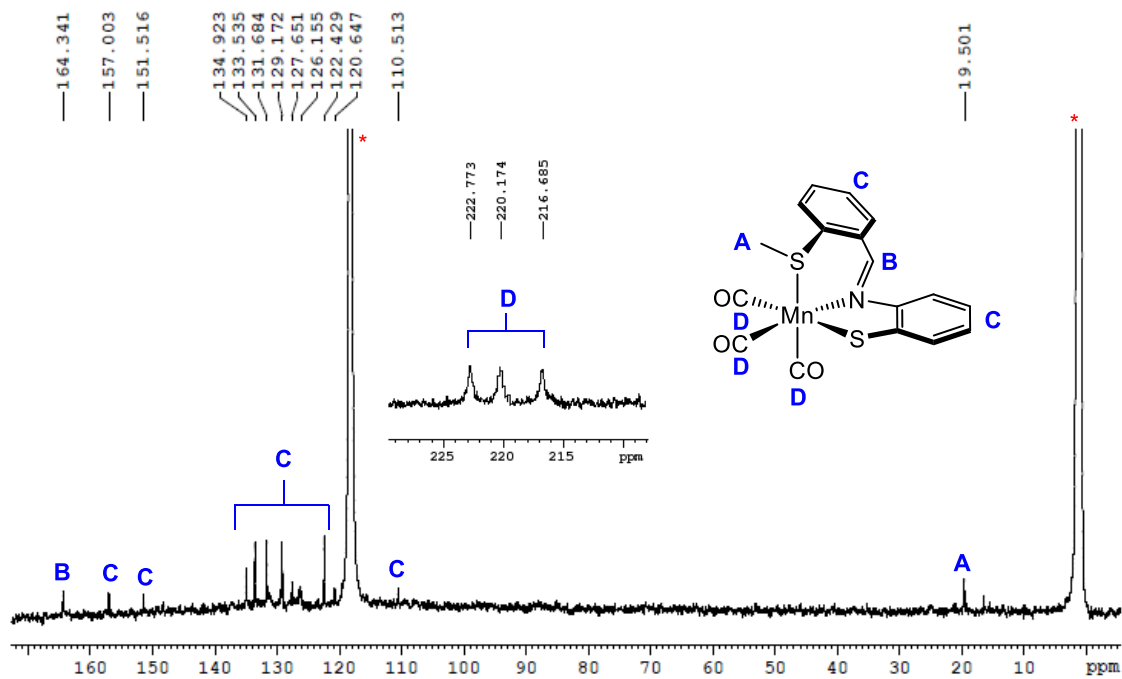


Figure C2.  $^{13}\text{C}\{^1\text{H}\}$  spectrum of  $[\text{Mn}(\kappa^3\text{-SNS}^{\text{Me}})(\text{CO})_3]$  (**4.1<sub>Mn</sub>**). \* is acetonitrile- $d^3$ .

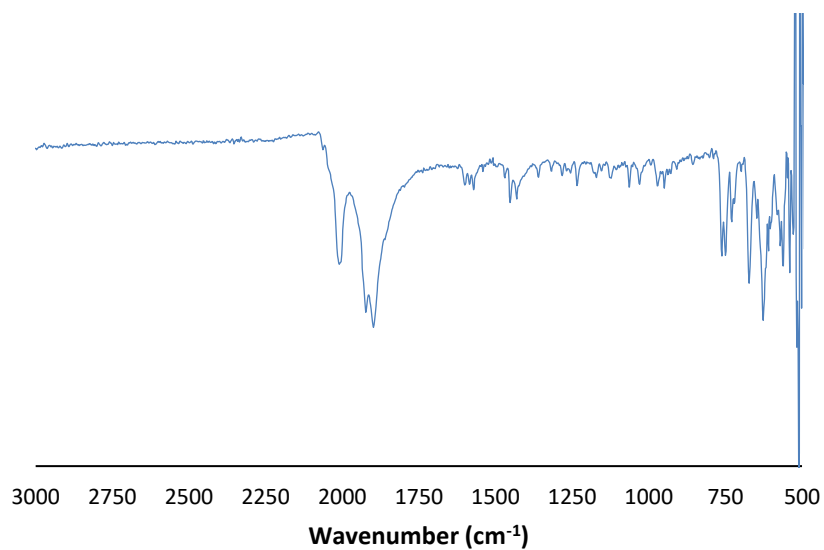


Figure C3. FT-IR (solid) spectrum of 4.1Mn.

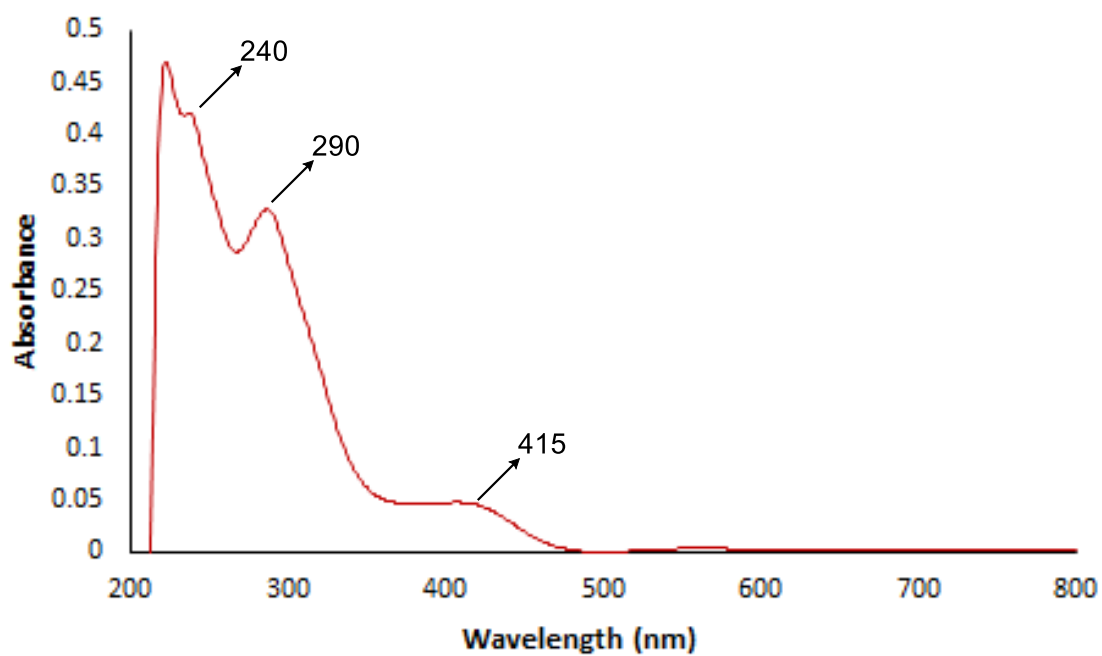


Figure C4. UV-vis spectrum of 4.1Mn.

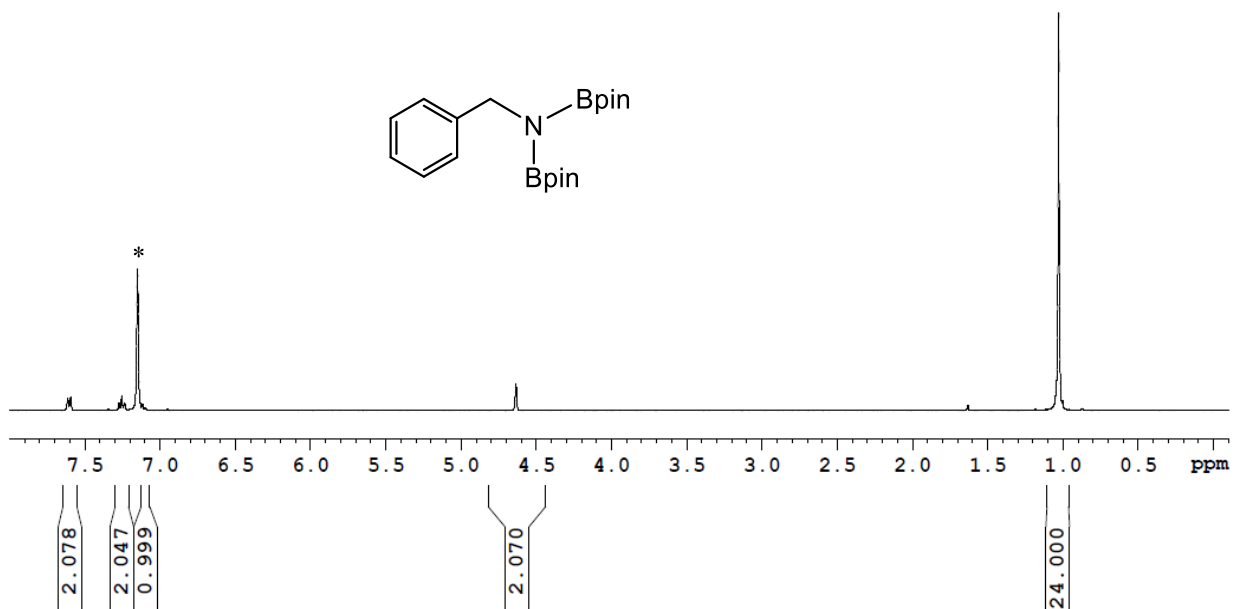


Figure C4. <sup>1</sup>H spectrum of benzonitrile dihydroboration product. \* is benzene-*d*<sup>6</sup>.

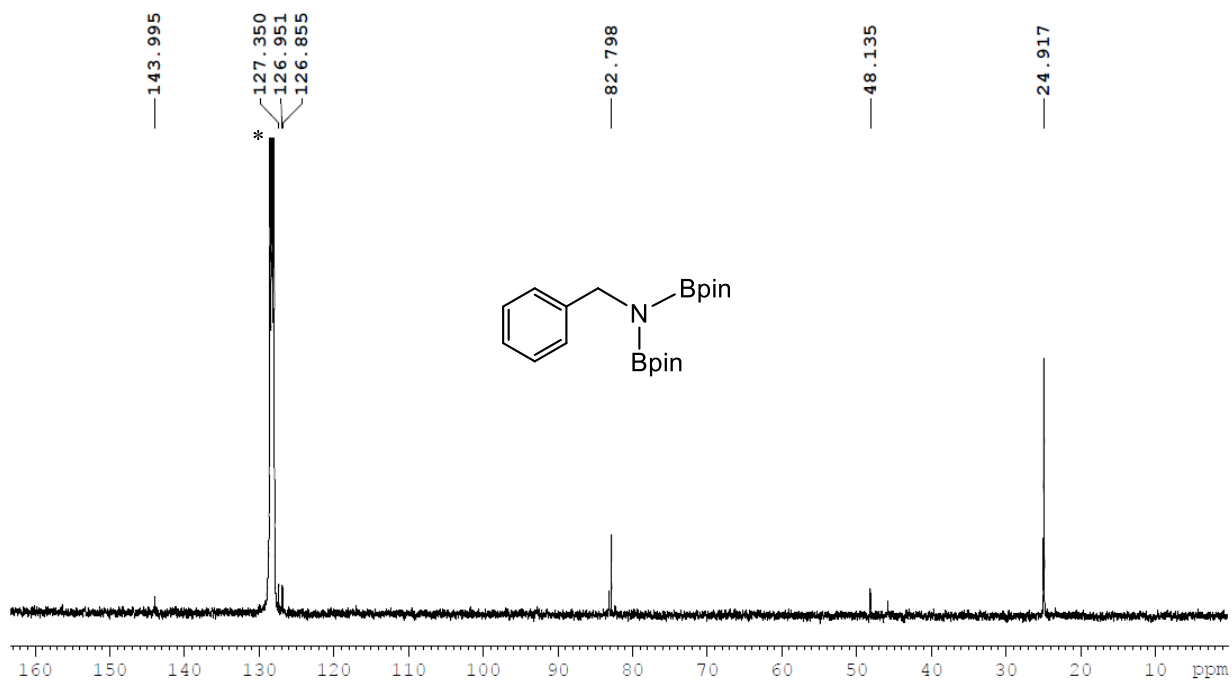


Figure C5. <sup>13</sup>C{<sup>1</sup>H} spectrum of benzonitrile dihydroboration product. \* is benzene-*d*<sup>6</sup>.

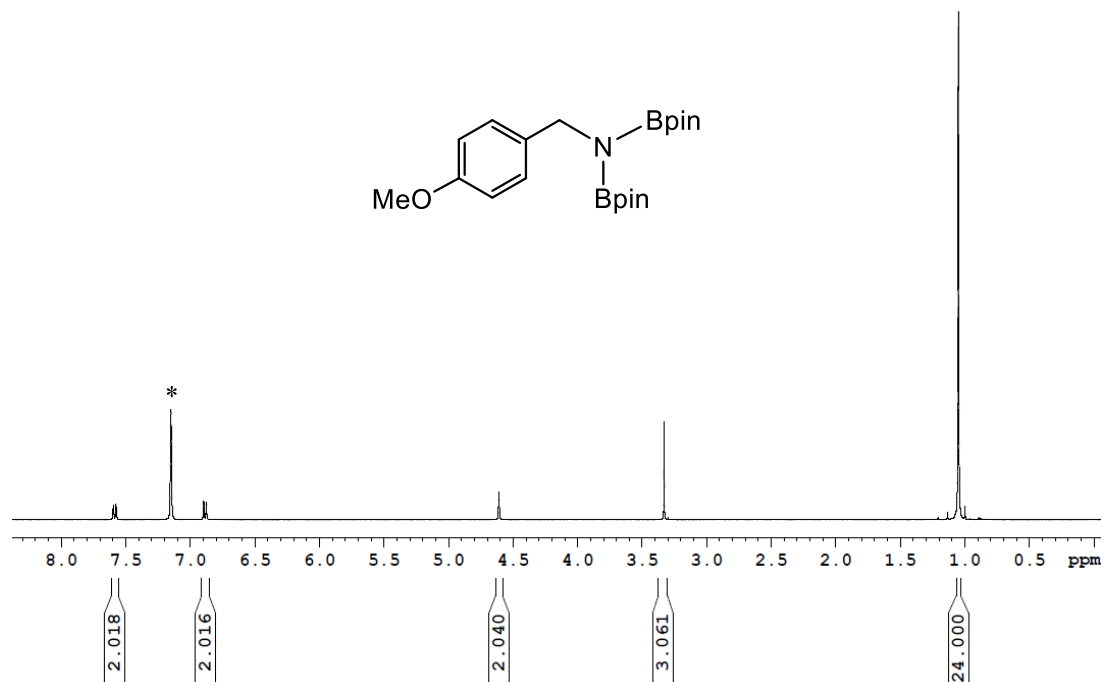


Figure C6. <sup>1</sup>H spectrum of 4-methoxy benzonitrile dihydroboration product. \* is benzene-*d*<sup>6</sup>.

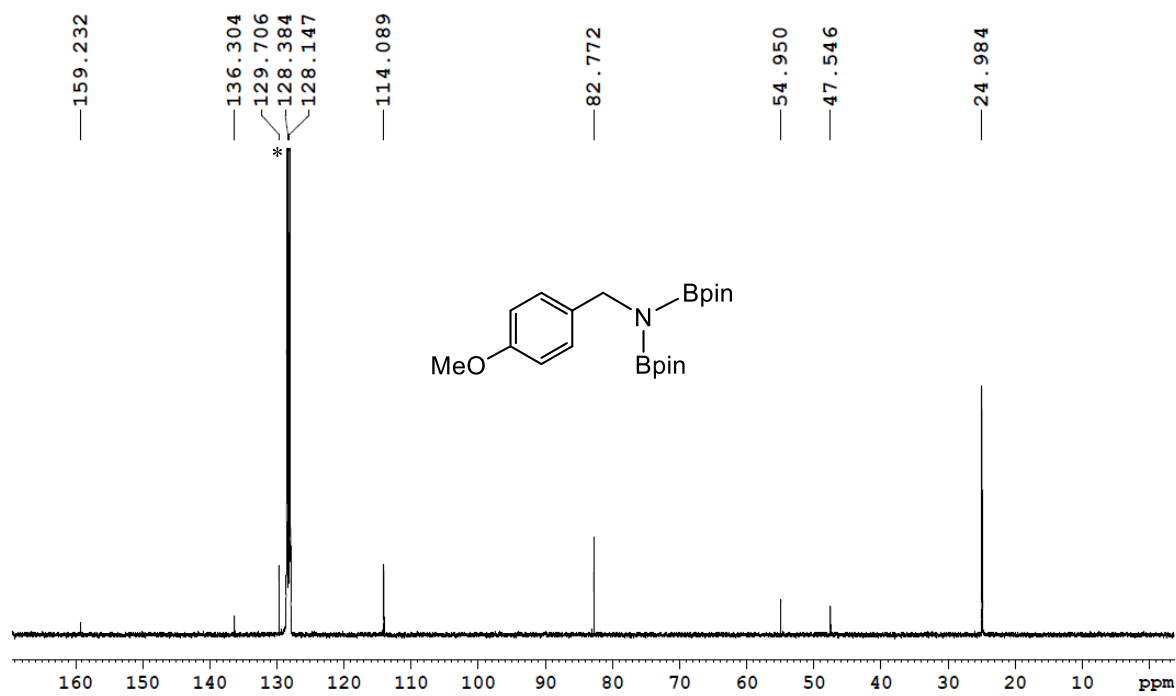


Figure C7. <sup>13</sup>C{<sup>1</sup>H} spectrum of 4-methoxy benzonitrile dihydroboration product. \* is benzene-*d*<sup>6</sup>.

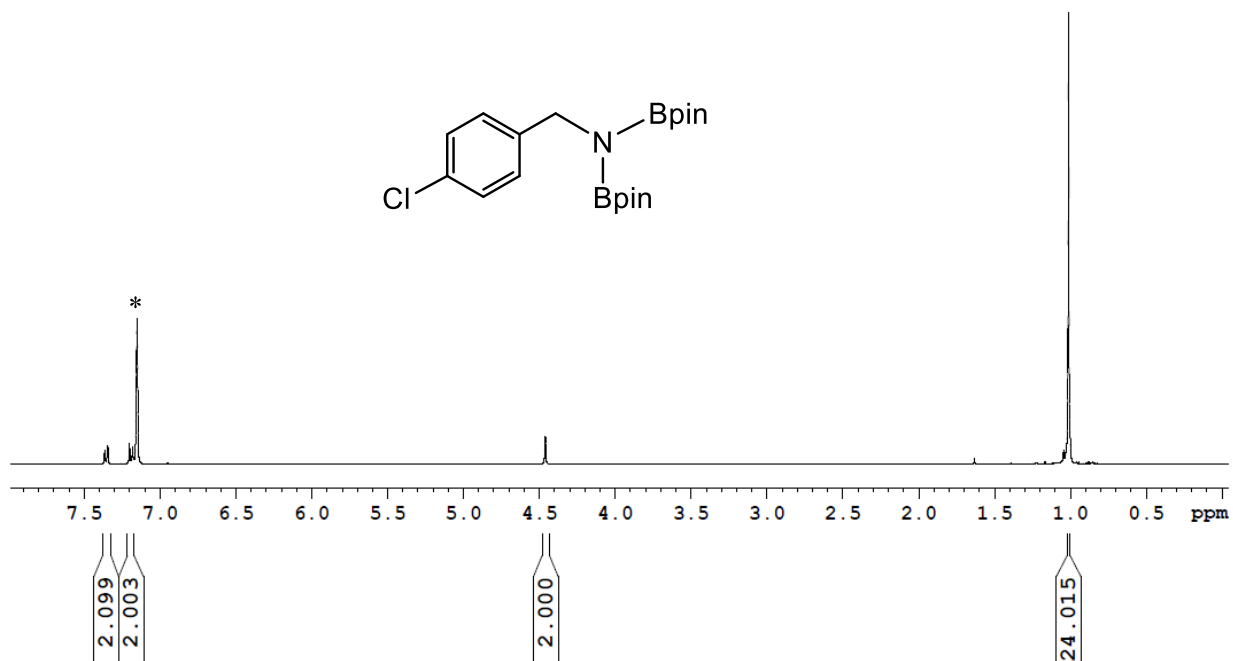


Figure C8. <sup>1</sup>H spectrum of 4-chloro benzonitrile dihydroboration product. \* is benzene-*d*<sup>6</sup>.

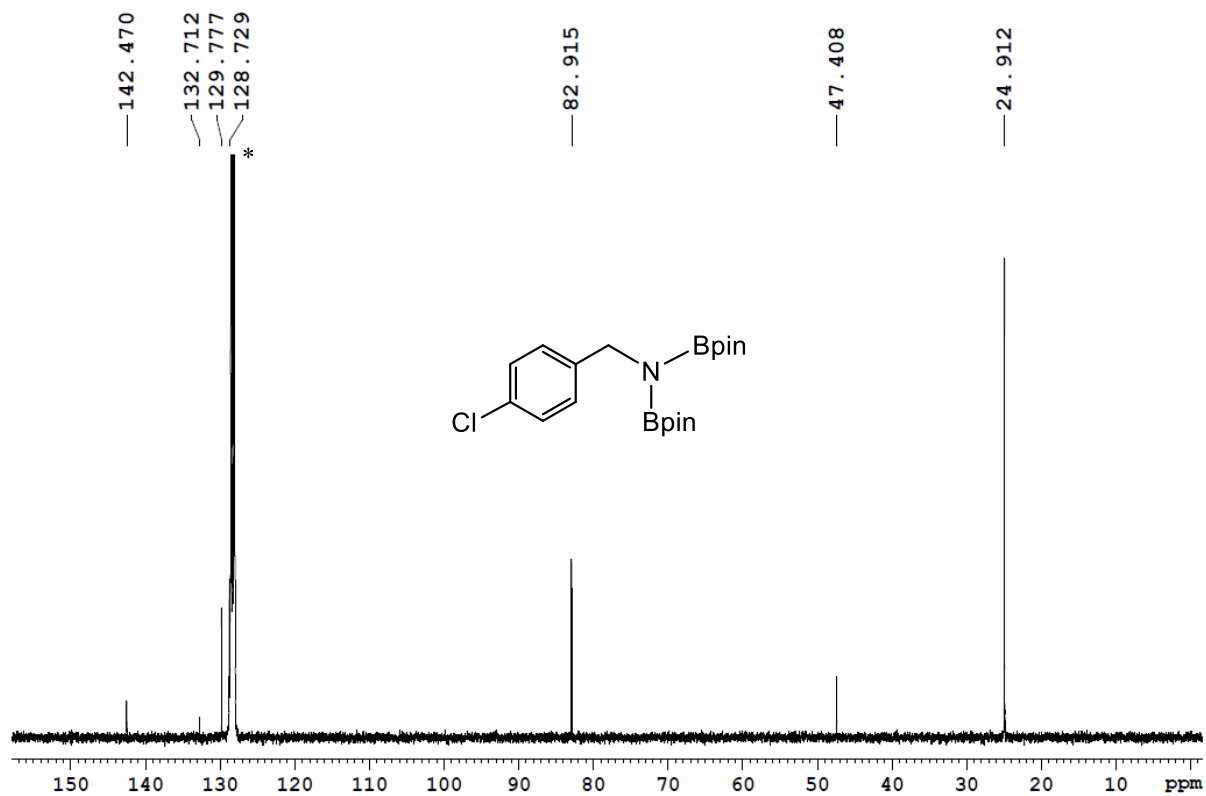


Figure C9. <sup>13</sup>C{<sup>1</sup>H} spectrum of 4-chloro benzonitrile dihydroboration product. \* is benzene-*d*<sup>6</sup>.

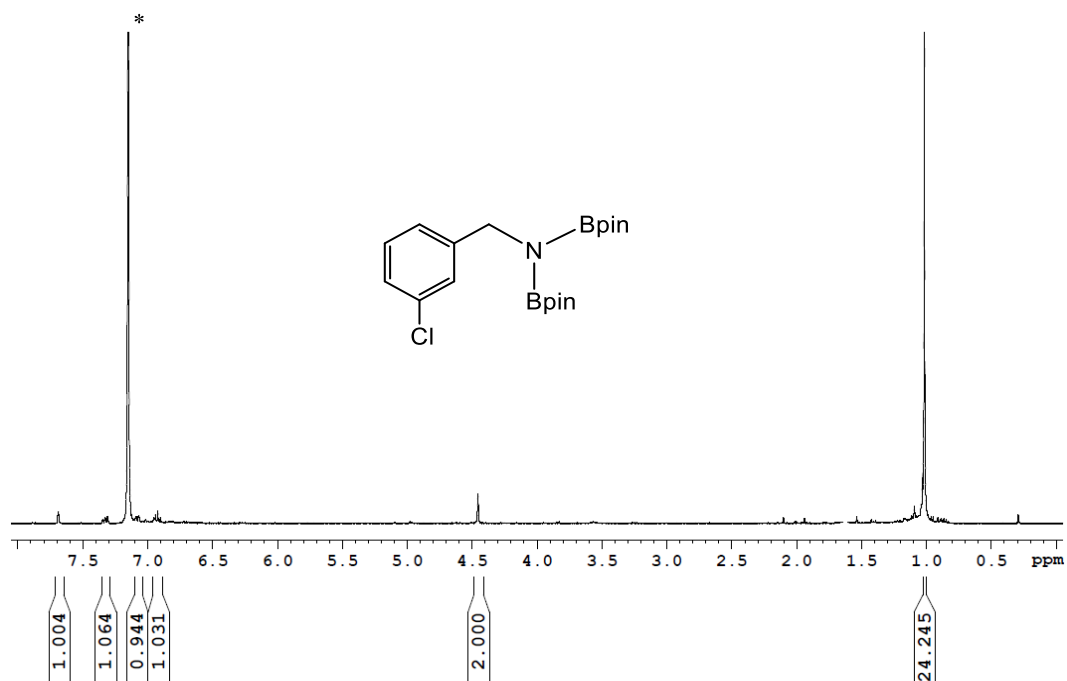


Figure C10.  $^1\text{H}$  spectrum of 3-chloro benzonitrile dihydroboration product. \* is benzene- $d^6$ .

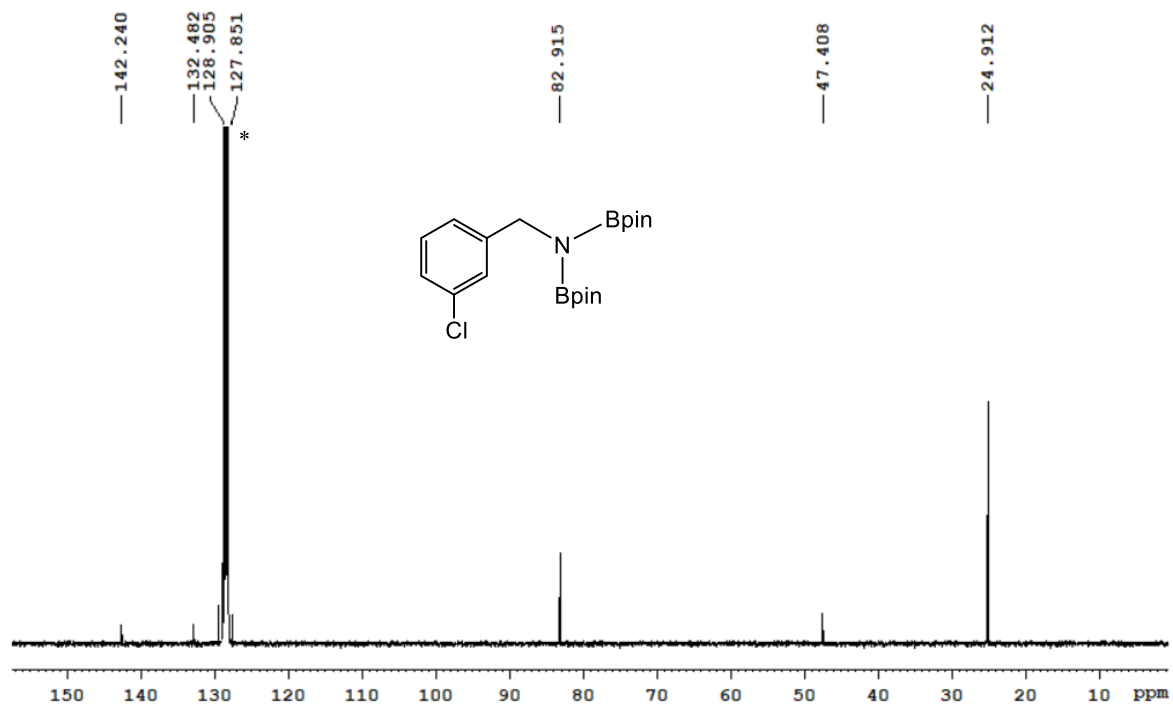


Figure C11.  $^{13}\text{C}\{^1\text{H}\}$  spectrum of 3-chloro benzonitrile dihydroboration product. \* is benzene- $d^6$ .

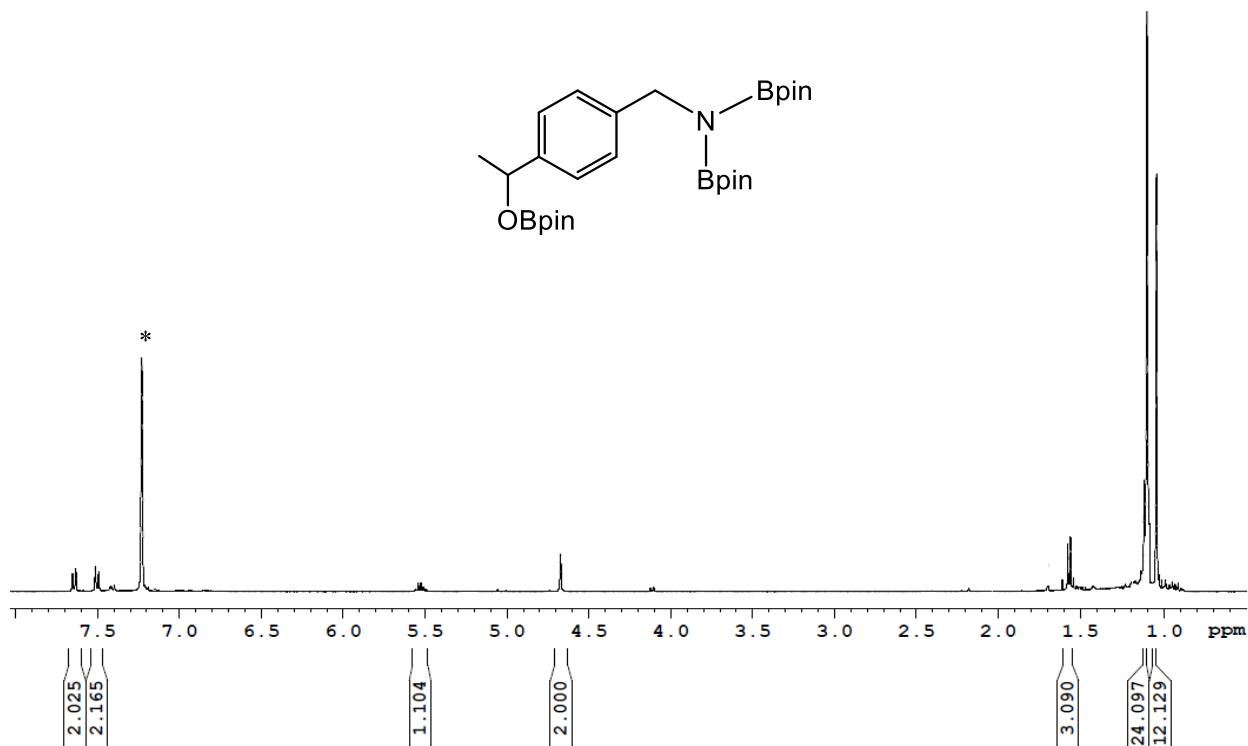


Figure C12. <sup>1</sup>H spectrum of 4-acetyl benzonitrile trihydroboration product. \* is benzene-*d*<sup>6</sup>.

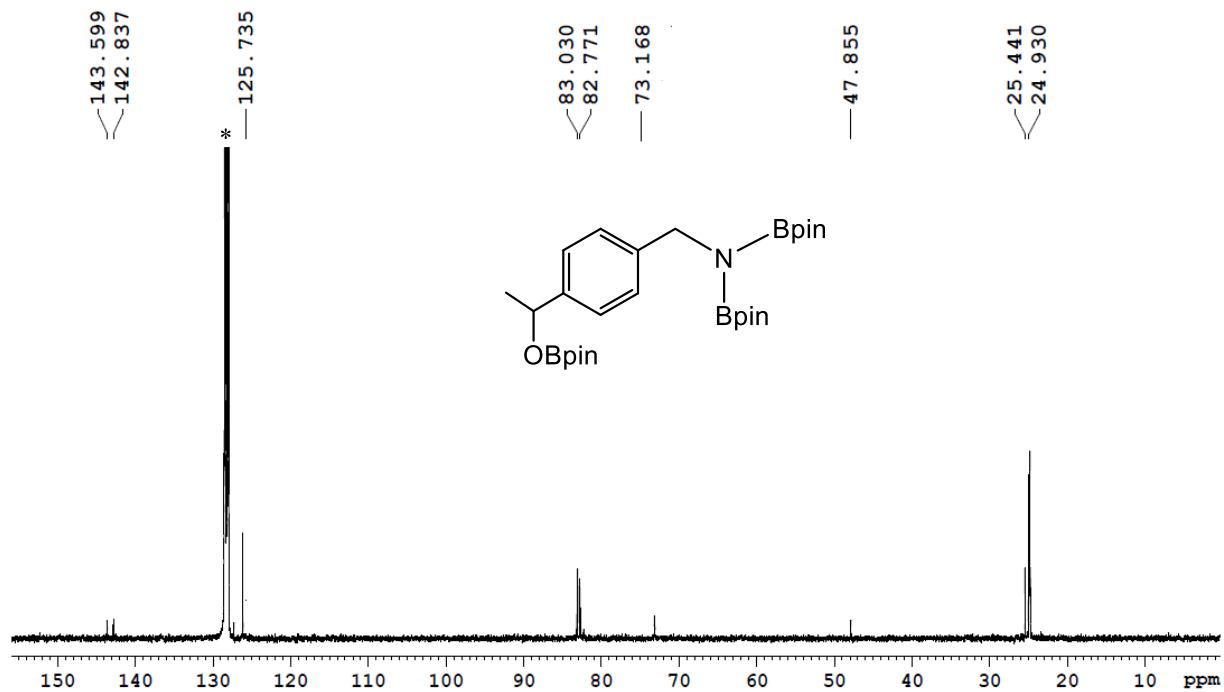


Figure C13. <sup>13</sup>C{<sup>1</sup>H} spectrum of 4-acetyl benzonitrile trihydroboration product. \* is benzene-*d*<sup>6</sup>.

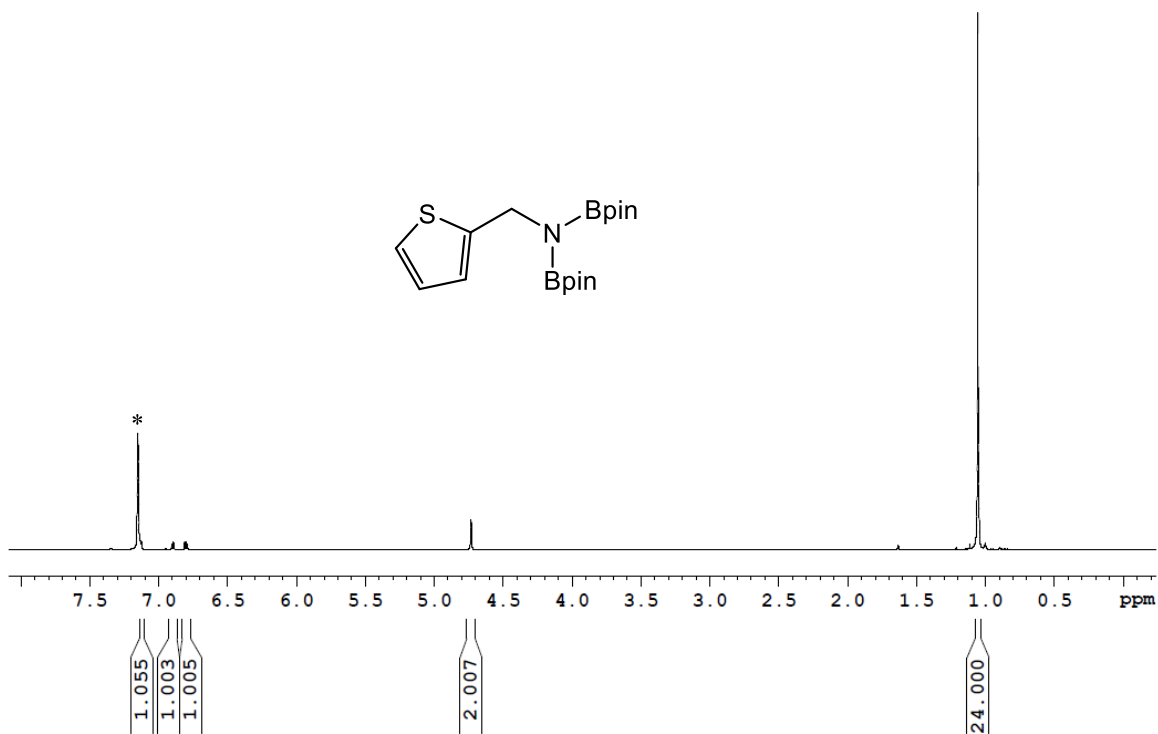


Figure C14. <sup>1</sup>H spectrum of 2-cyanyl-thiophene dihydroboration product. \* is benzene-*d*<sup>6</sup>.

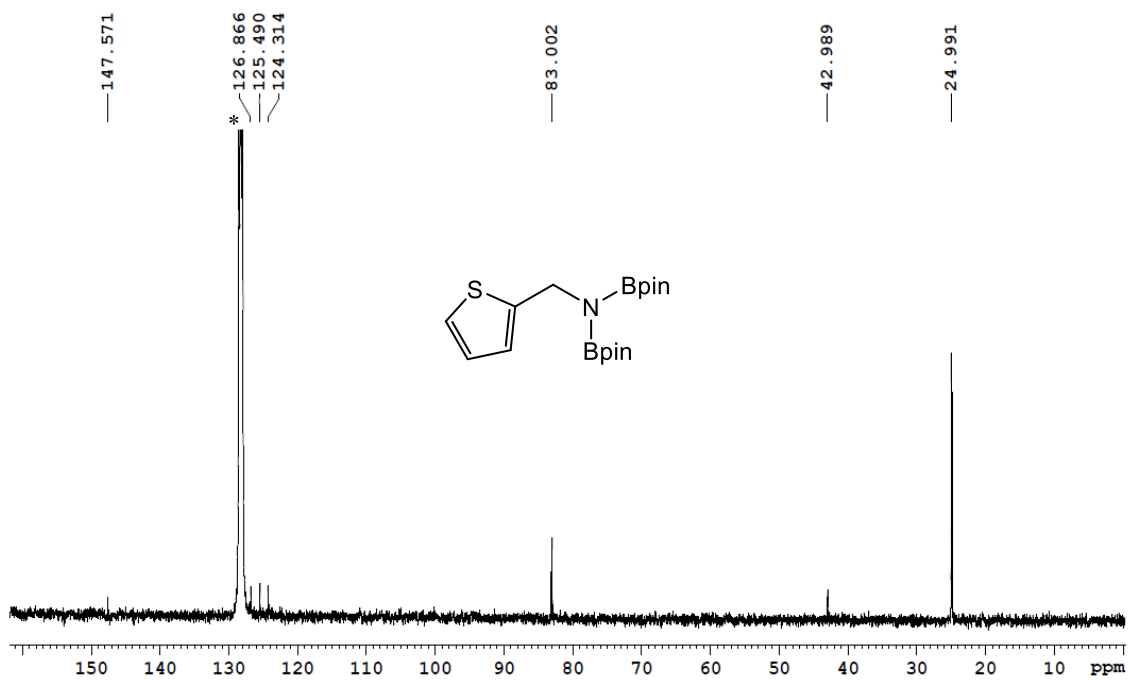


Figure C15. <sup>13</sup>C{<sup>1</sup>H} spectrum of 2-cyanyl-thiophene benzonitrile dihydroboration product. \* is benzene-*d*<sup>6</sup>.

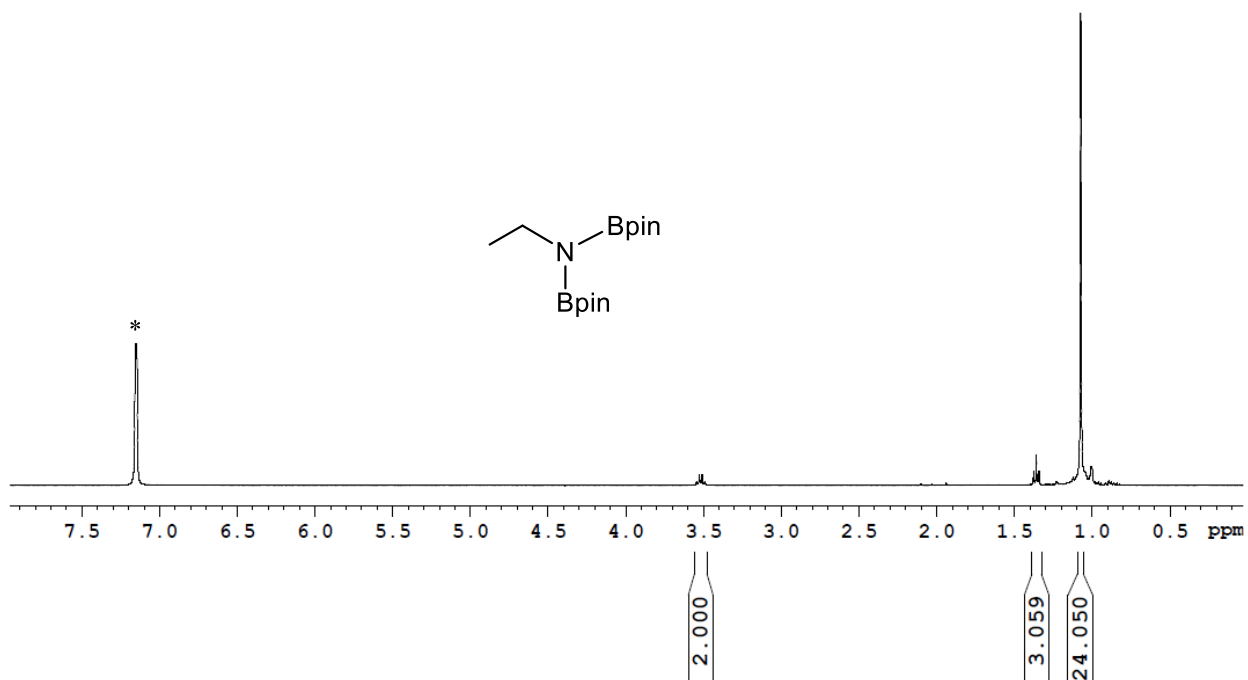


Figure C16.  $^1\text{H}$  spectrum of acetonitrile dihydroboration product. \* is benzene- $d^6$ .

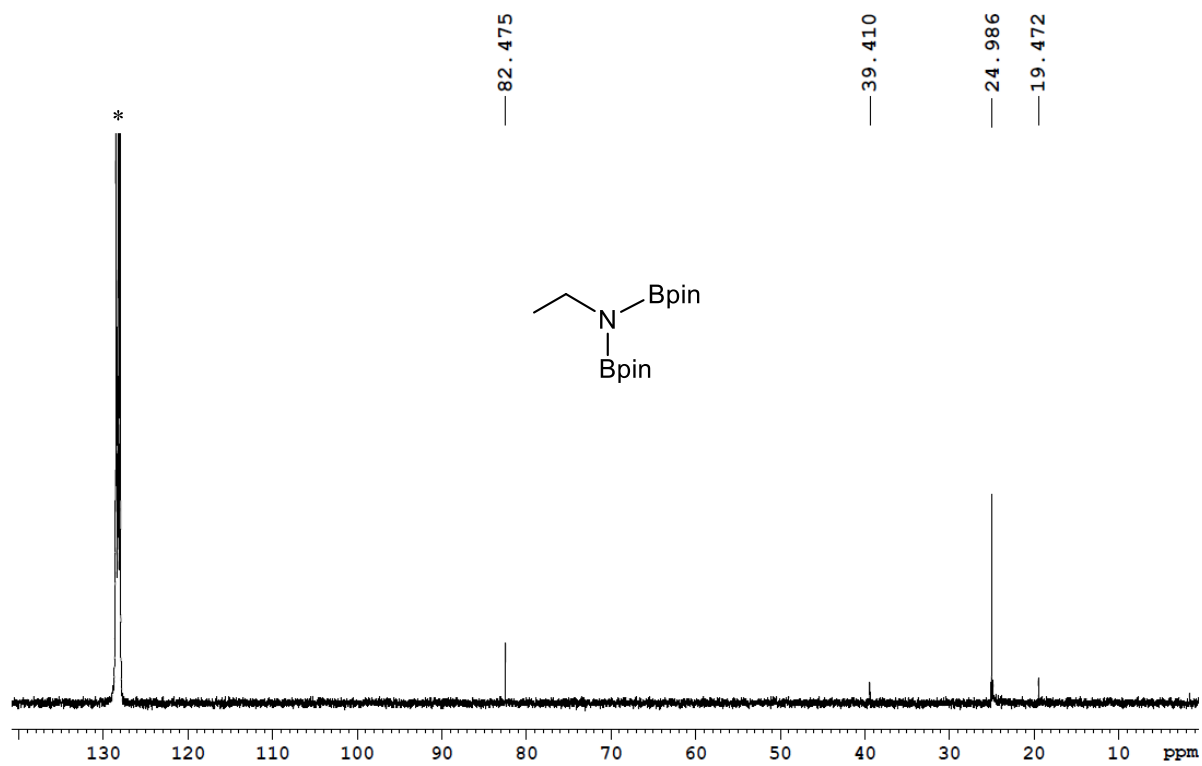


Figure C17.  $^{13}\text{C}\{^1\text{H}\}$  spectrum of acetonitrile dihydroboration product. \* is benzene- $d^6$ .

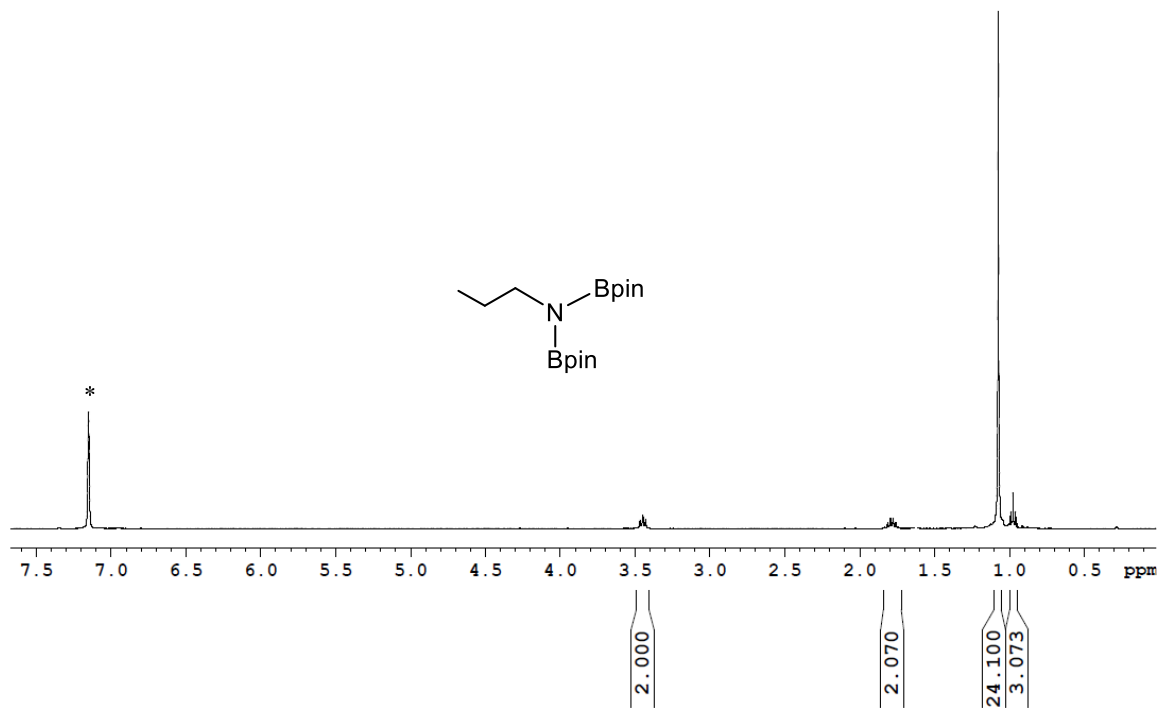


Figure C18.  $^1\text{H}$  spectrum of propionitrile dihydroboration product. \* is benzene- $d^6$ .

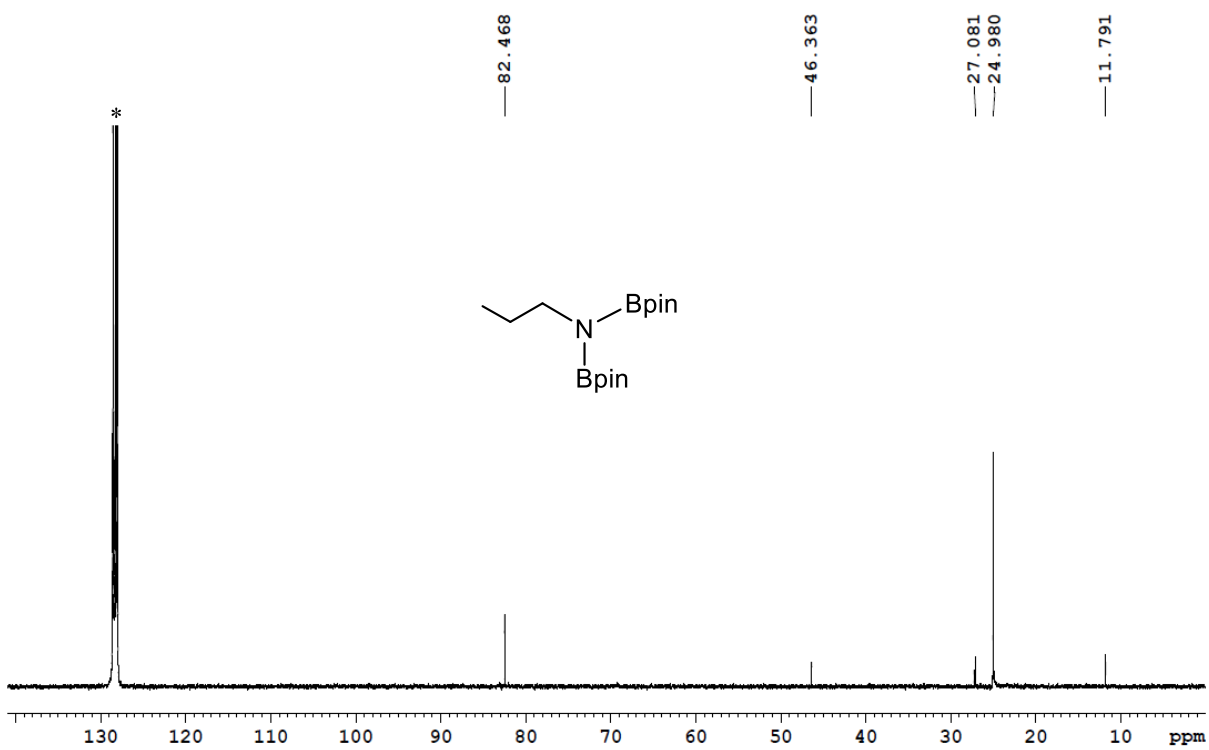


Figure C19.  $^{13}\text{C}\{^1\text{H}\}$  spectrum of propionitrile dihydroboration product. \* is benzene- $d^6$ .

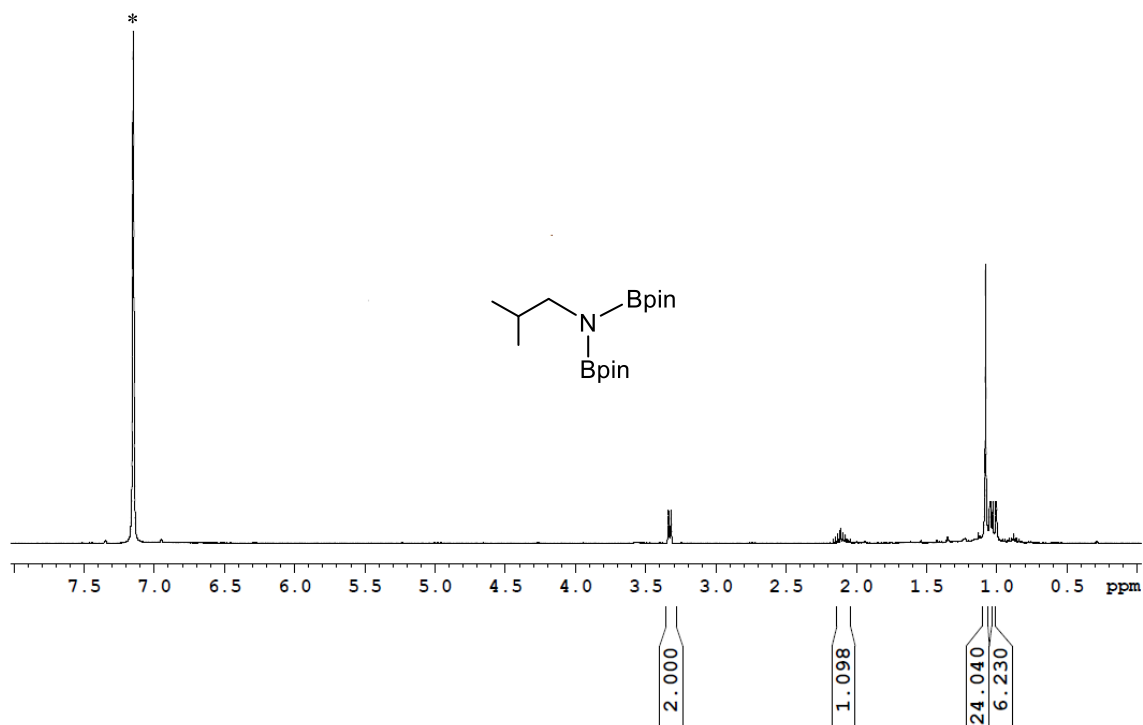


Figure C20.  $^1\text{H}$  spectrum of isobutylnitrile dihydroboration product. \* is benzene- $d^6$ .

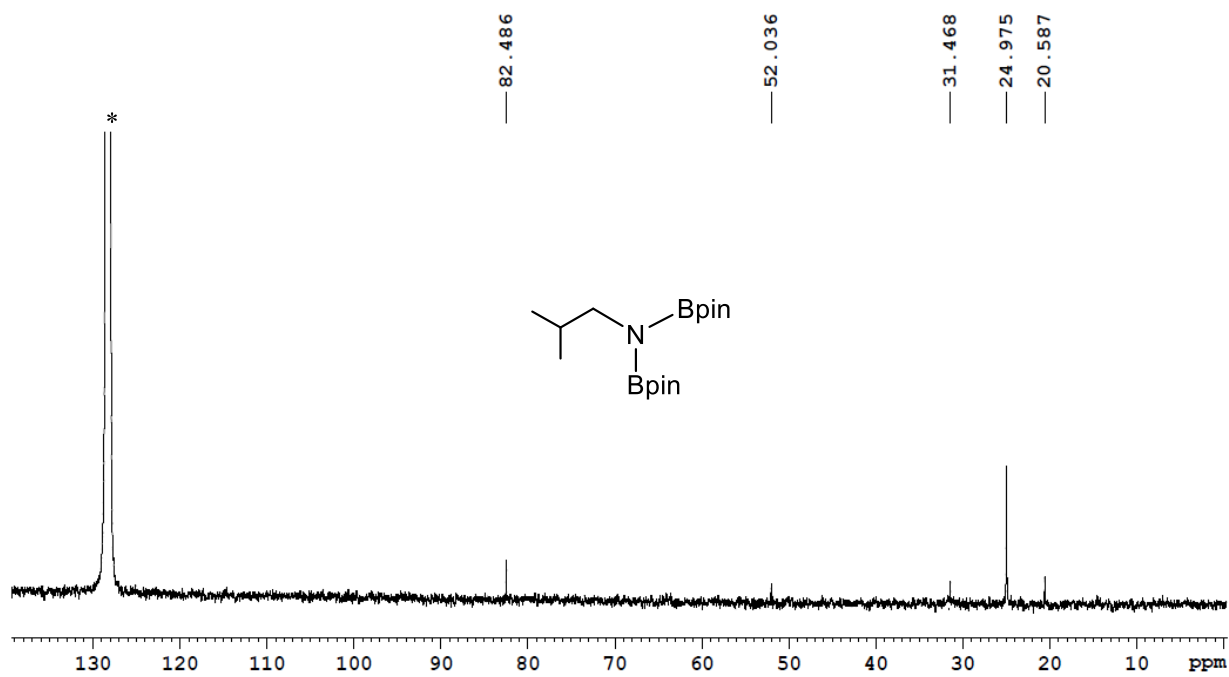
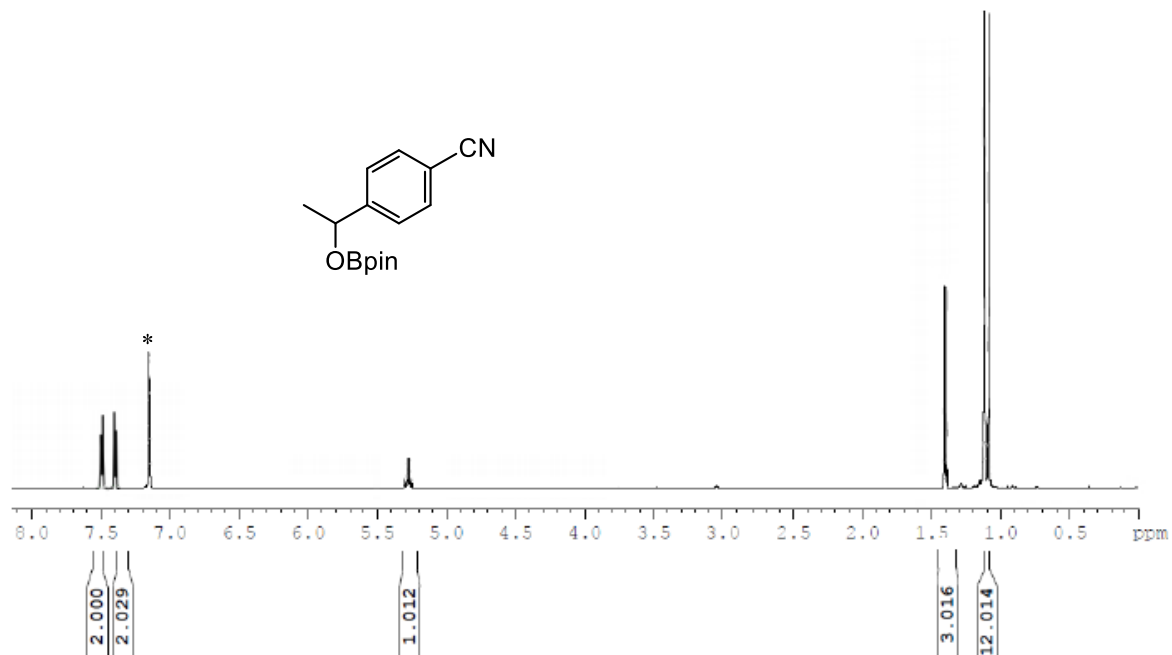
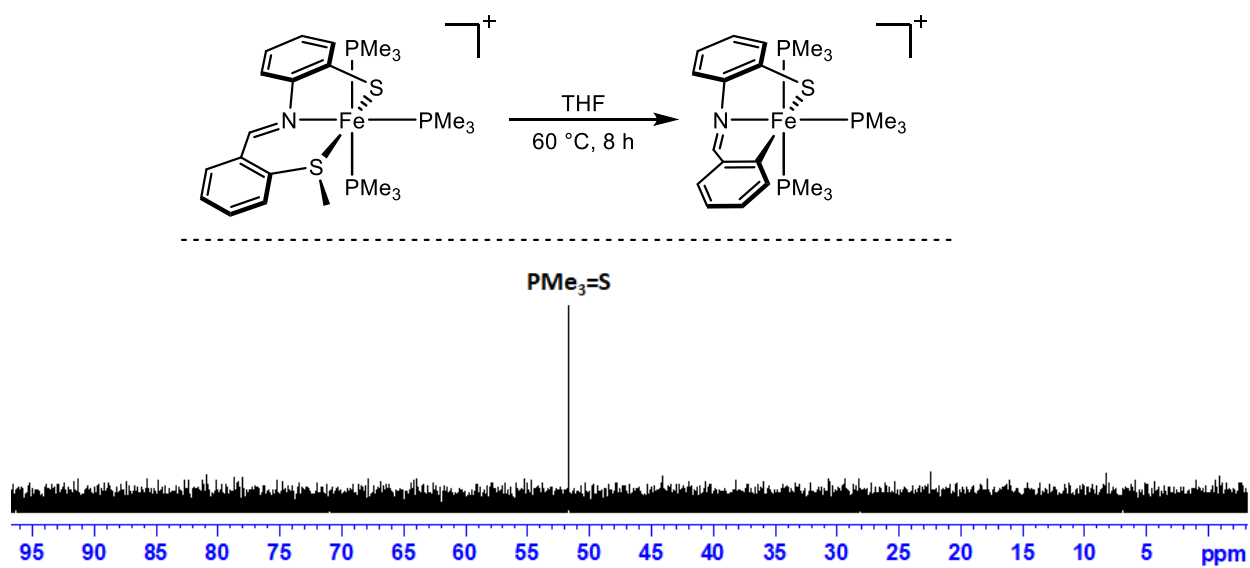


Figure C21.  $^{13}\text{C}\{^1\text{H}\}$  spectrum of isobutylnitrile dihydroboration product. \* is benzene- $d^6$ .



**Figure C22.**  $^1\text{H}$  spectrum of 4-acetyl benzonitrile hydroboration product. \* is benzene- $d^6$ .



**Figure SC23.**  $^{31}\text{P}\{^1\text{H}\}$  NMR spectrum of crude reaction mixture during formation of  $[\text{Fe}(\text{CNS})(\text{PMe}_3)_3](\text{OTf})$  (**4.2 $\text{Fe}$** ) showing  $\text{S}=\text{PMe}_3$  co-product.

**Table C1. Crystal data and structure refinement for Mn( $\kappa^3$ -S<sup>Me</sup>NS)(CO)<sub>3</sub> (4.1<sub>Mn</sub>).**

Identification code	tb271_fin
Empirical formula	C <sub>17</sub> H <sub>12</sub> MnNO <sub>3</sub> S <sub>2</sub>
Formula weight	397.34
Temperature/K	200(2)
Crystal system	monoclinic
Space group	P2 <sub>1</sub> /n
a/Å	9.0462(6)
b/Å	18.5124(13)
c/Å	9.7604(7)
$\alpha$ /°	90
$\beta$ /°	93.8678(19)
$\gamma$ /°	90
Volume/Å <sup>3</sup>	1630.8(2)
Z	4
$\rho_{\text{calc}}$ /cm <sup>3</sup>	1.618
$\mu$ /mm <sup>-1</sup>	1.080
F(000)	808.0
Crystal size/mm <sup>3</sup>	0.390 × 0.180 × 0.100
Radiation	MoK $\alpha$ ( $\lambda$ = 0.71073)
2 $\Theta$ range for data collection/°	4.4 to 56.604
Index ranges	-12 ≤ h ≤ 11, -24 ≤ k ≤ 24, -13 ≤ l ≤ 12
Reflections collected	19706
Independent reflections	4034 [R <sub>int</sub> = 0.0407, R <sub>sigma</sub> = 0.0347]
Data/restraints/parameters	4034/0/218
Goodness-of-fit on F <sup>2</sup>	1.025
Final R indexes [I ≥ 2 $\sigma$ (I)]	R <sub>1</sub> = 0.0326, wR <sub>2</sub> = 0.0732
Final R indexes [all data]	R <sub>1</sub> = 0.0525, wR <sub>2</sub> = 0.0835
Largest diff. peak/hole / e Å <sup>-3</sup>	0.42/-0.30

**Table C2. Bond Lengths for Mn( $\kappa^3$ -S<sup>Me</sup>NS)(CO)<sub>3</sub> (4.1<sub>Mn</sub>).**

Atom	Atom	Length/Å	Atom	Atom	Length/Å
C1	C2	1.395(3)	C11	C12	1.386(3)
C1	C6	1.402(3)	C12	C13	1.382(3)
C1	S1	1.754(2)	C13	S2	1.784(2)
C2	C3	1.386(3)	C14	S2	1.794(2)
C3	C4	1.379(3)	C15	O1	1.146(3)
C4	C5	1.386(3)	C15	Mn1	1.797(2)
C5	C6	1.390(3)	C16	O2	1.149(3)
C6	N1	1.440(2)	C16	Mn1	1.805(2)
C7	N1	1.285(3)	C17	O3	1.143(3)
C7	C8	1.461(3)	C17	Mn1	1.802(2)
C8	C9	1.390(3)	N1	Mn1	2.0587(16)
C8	C13	1.409(3)	S1	Mn1	2.3898(6)
C9	C10	1.383(3)	S2	Mn1	2.3592(6)
C10	C11	1.376(3)			

Appendix D – Chapter 5

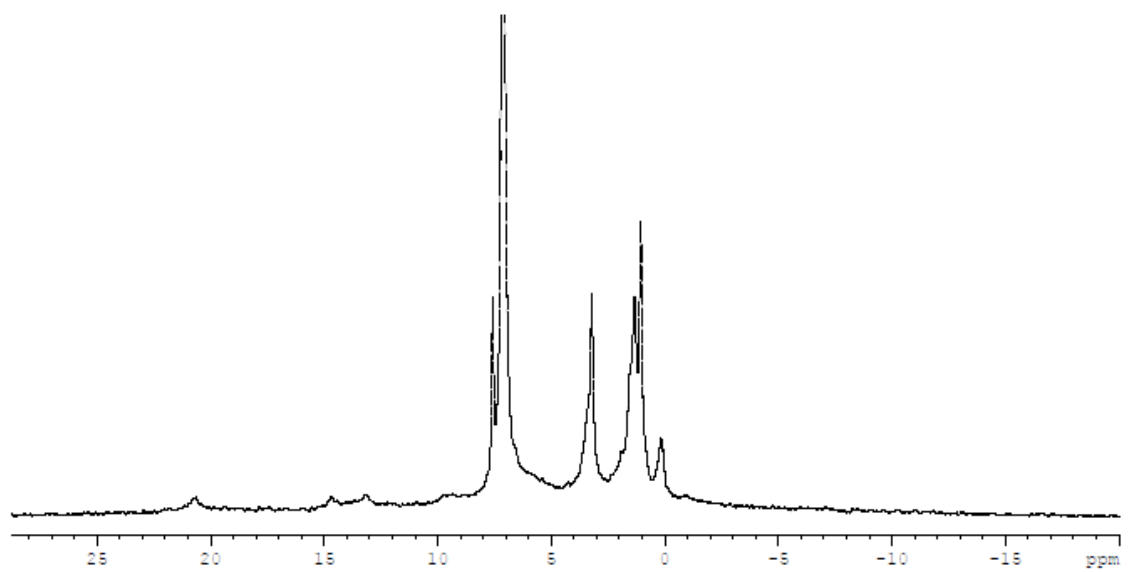


Figure D1.  $^1\text{H}$  NMR spectrum of  $5.1\text{Fe}^-$  in  $\text{C}_6\text{D}_6$ .

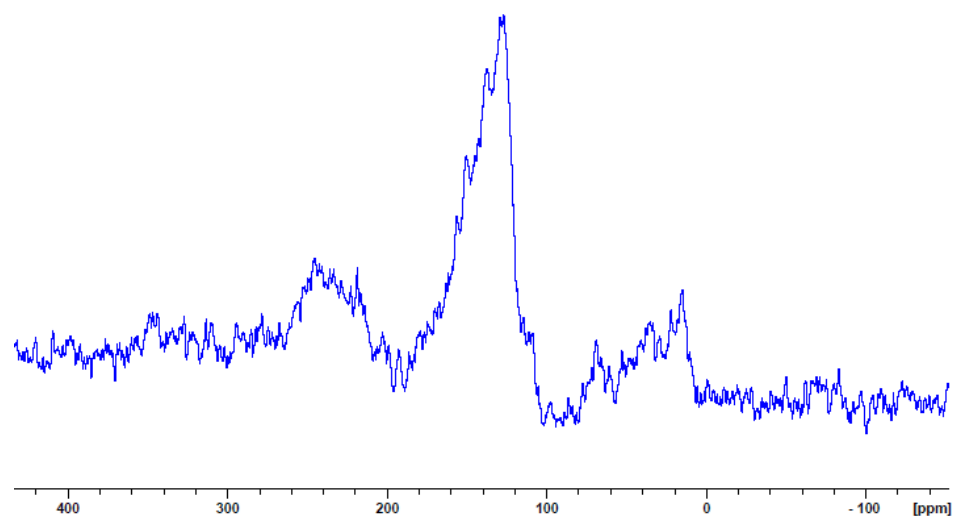
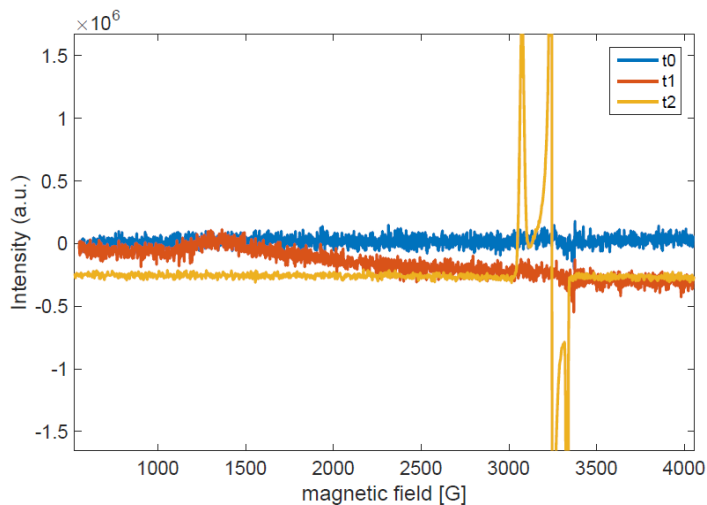
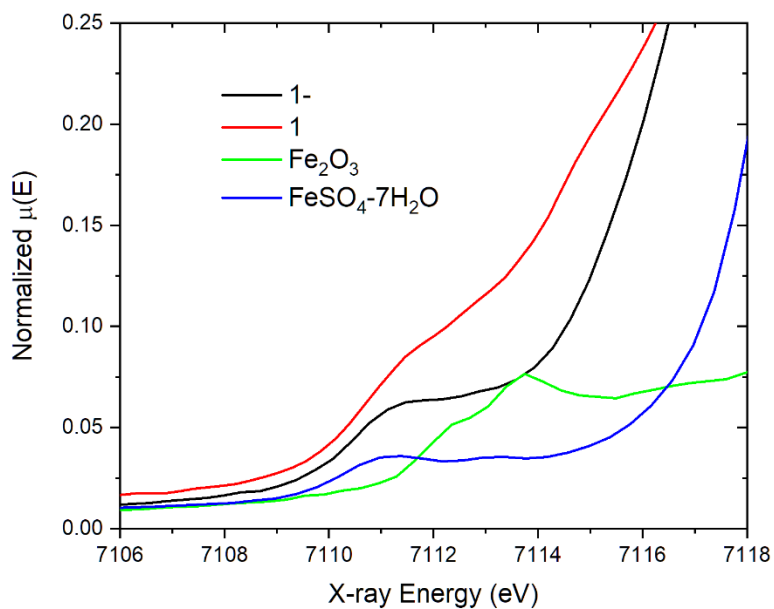


Figure D2.  $^{13}\text{C}\{^1\text{H}\}$  solid-state NMR spectrum of  $5.1\text{Fe}$  (dimer).



**Figure D3.** 100 K EPR spectra of  $5.1\text{Fe}$  ( $t_0$ ; blue line);  $5.1\text{Fe}^-$  recorded after bulk reduction at  $-900\text{ mV}$  ( $t_1$ ; orange line); and  $5.1\text{Fe}^+$  recorded after bulk oxidation at  $+300\text{ mV}$  ( $t_2$ ; yellow line).



**Figure D4.**  $5.1\text{Fe}^-$  (black line),  $5.1\text{Fe}$  (red line),  $\alpha\text{-Fe}_2\text{O}_3$ , and  $\text{FeSO}_4\cdot 7\text{H}_2\text{O}$  XANES showing approximately the region of the pre-edge peak fits.

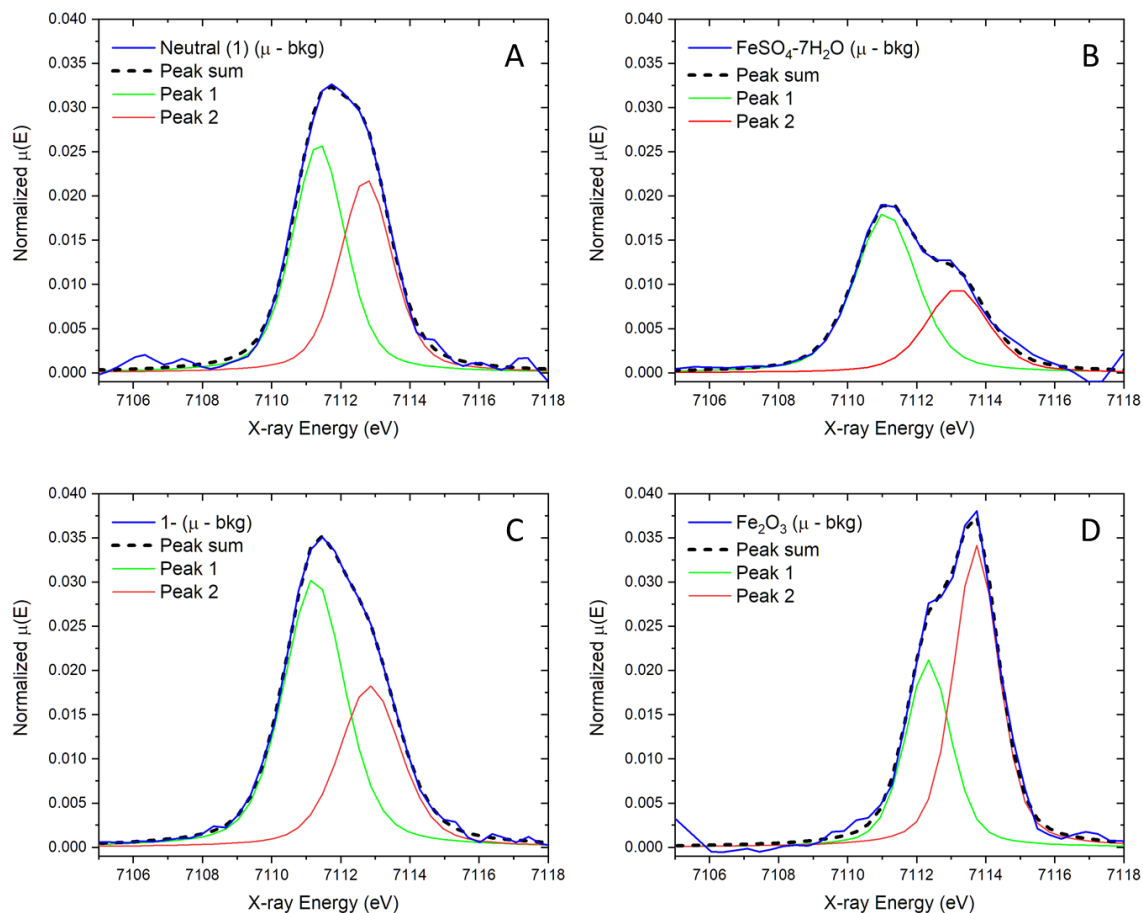


**Figure D5.** XANES pre-edge fits with two pseudo-Voigt peaks.

**Table D1.** Pre-edge fit results.

Sample	Centroid (eV)	Peak Energy (eV)	Peak Height (normalized)	Peak Width (eV fwhm)
Neutral ( $5.1\text{Fe}$ )	$7111.83 \pm 0.06$	$7111.23 \pm 0.02$	$0.0304 \pm 0.002$	$2.10 \pm 0.07$
		$7112.84 \pm 0.04$	$0.0183 \pm 0.002$	
Anionic ( $5.1\text{Fe}^-$ )	$7111.98 \pm 0.07$	$7111.36 \pm 0.04$	$0.0259 \pm 0.001$	$1.81 \pm 0.08$
		$7112.72 \pm 0.07$	$0.0219 \pm 0.002$	
$\alpha\text{-Fe}_2\text{O}_3$	$7113.19 \pm 0.07$	$7113.72 \pm 0.04$	$0.0342 \pm 0.005$	$1.54 \pm 0.09$
		$7115.73 \pm 0.15$	$0.0265 \pm 0.001$	
$\text{FeSO}_4\cdot 7\text{H}_2\text{O}$	$7111.77 \pm 0.07$	$7111.06 \pm 0.05$	$0.0182 \pm 0.001$	$2.11 \pm 0.14$
		$7113.13 \pm 0.11$	$0.0095 \pm 0.001$	

**Table D2.** Comparison of potential energies (kcal/mol) and spin density values for each fragment of  $5.1\text{Fe}$  across potential spin states.

Spin State	Potential Energy	Spin Density		
		Fe	$\kappa^3\text{-SNS}$	$\kappa^2\text{-SN}$
Closed shell singlet	0			
Open shell singlet	12	1.64	-0.86	-0.78
Triplet	-11.4	2.54	0.16	-0.7
Quintet	-4.3	2.4	0.8	0.8

**Table D3.** Comparison of potential energies (kcal/mol) and spin density values for each fragment of  $5.1\text{Fe}^{\cdot-}$  across potential spin states.

Spin State	Potential Energy	Spin Density		
		Fe	$\kappa^3\text{-SNS}$	$\kappa^2\text{-SN}$
Doublet	0	1.03	-0.09	0.05
Quartet	-8.9	2.71	0.13	0.16
Sextet	-2.7	3.95	0.47	0.58

**Table D4.** Comparison of potential energies (kcal/mol) and spin density values for each fragment of  $5.1\text{Fe}^+$  across potential spin states.

Spin State	Potential Energy	Spin Density		
		Fe	$\kappa^3\text{-SNS}$	$\kappa^2\text{-SN}$
Doublet	0	2.54	-0.74	-0.79
Quartet	14.8	2.69	-0.62	0.93
Sextet	27.4	2.92	1.11	0.97

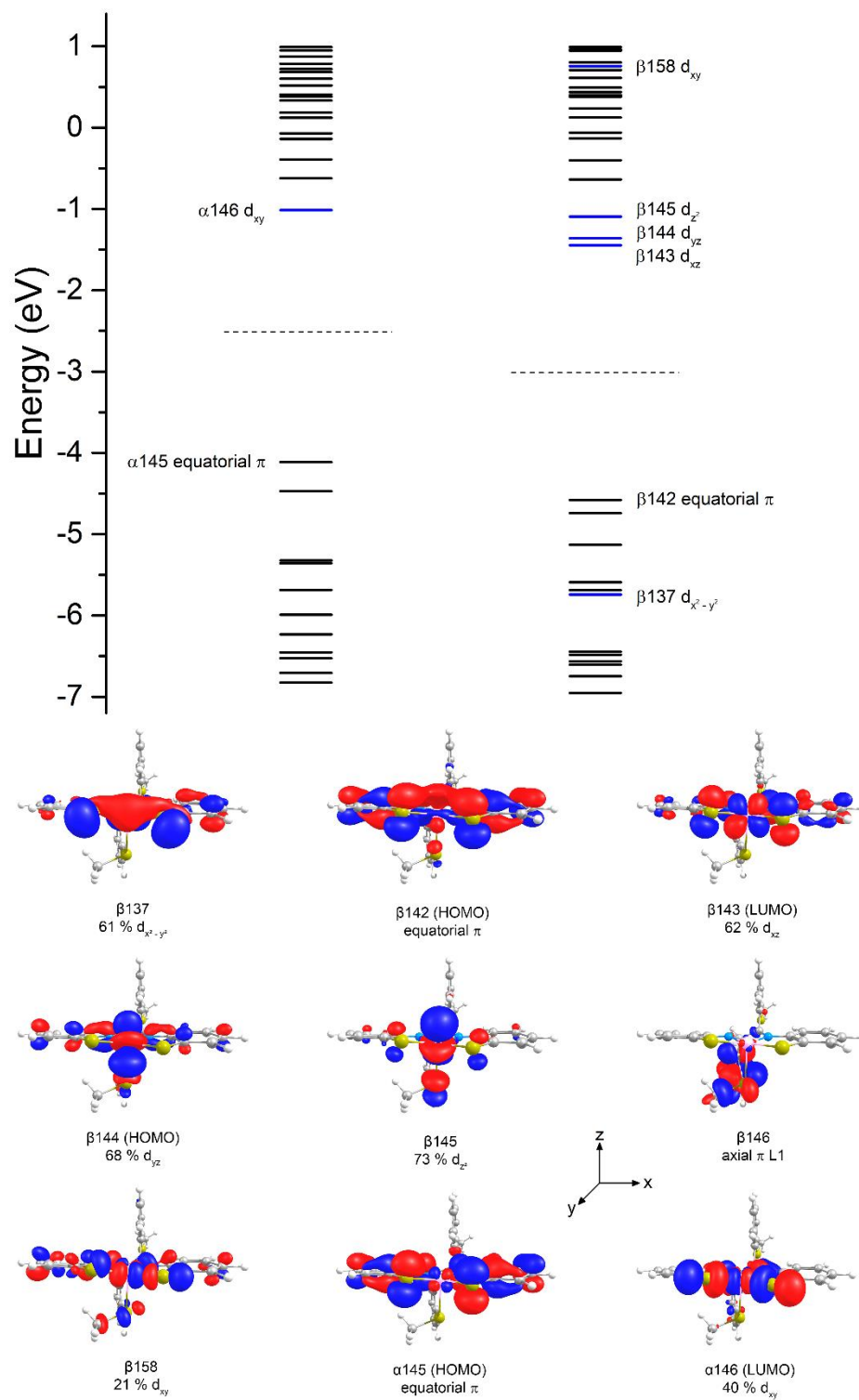


Figure D6. Calculated FMO energy level diagram for **5.1Fe<sup>-</sup>** and selected orbital depictions.

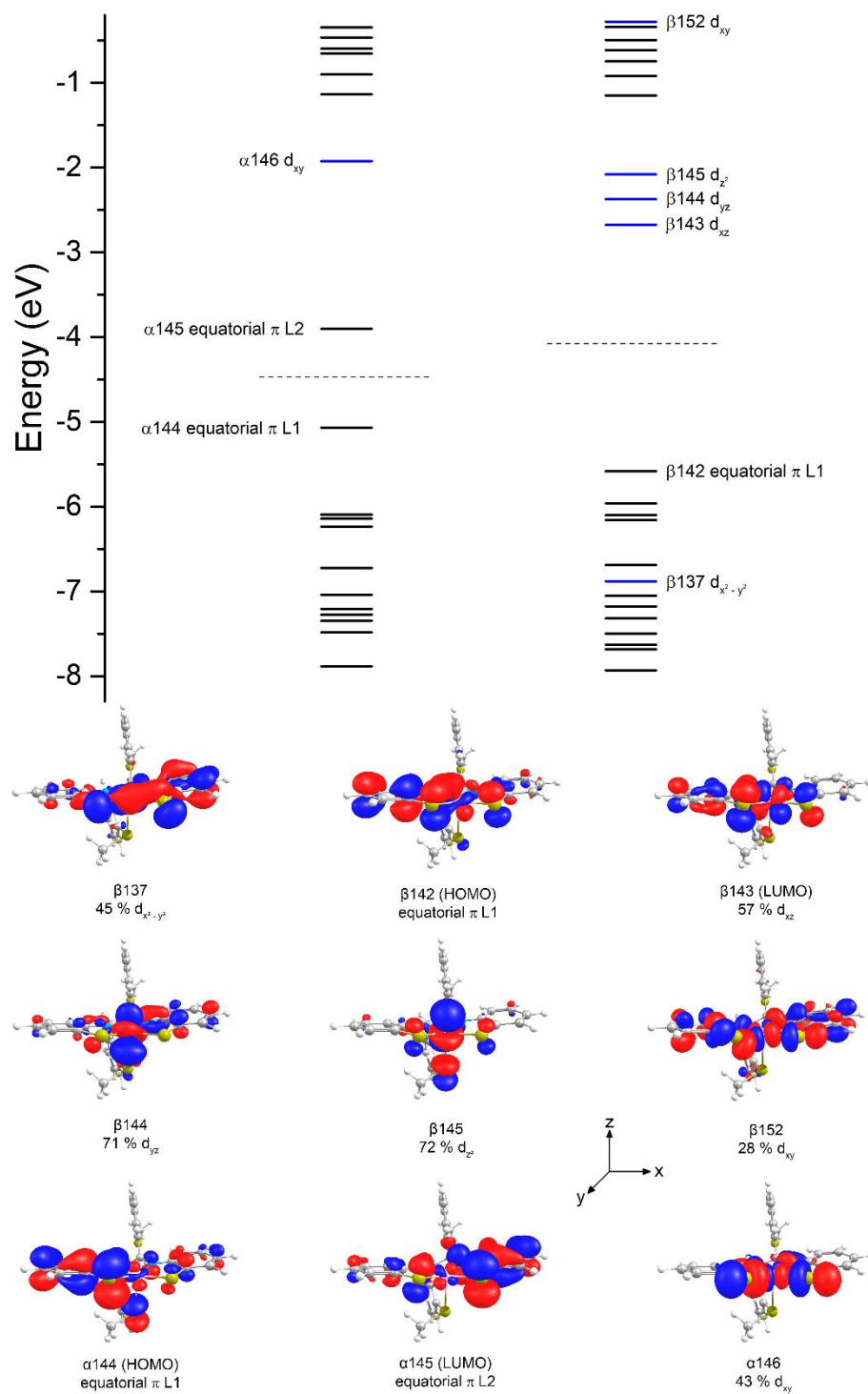
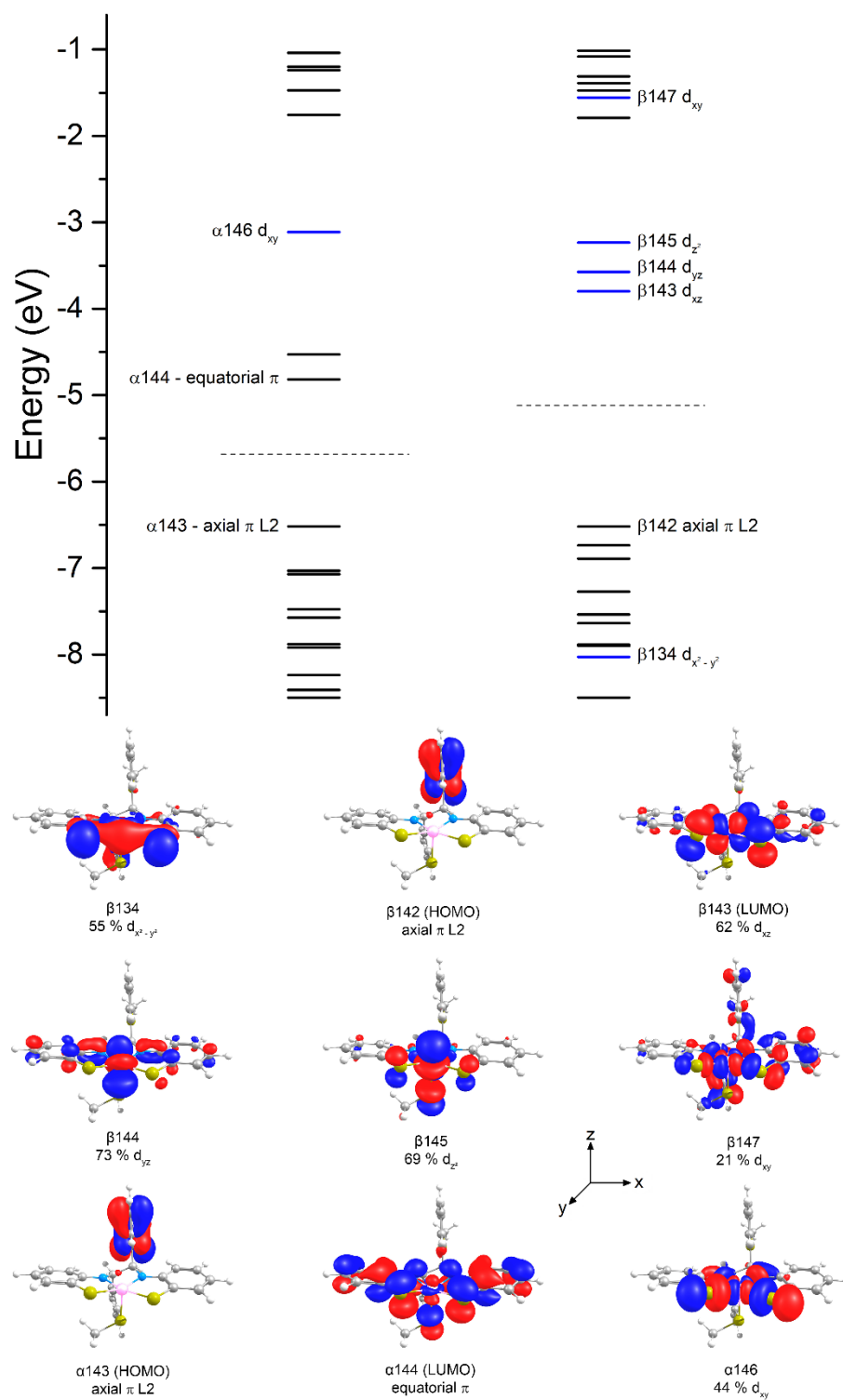


Figure D7. Calculated FMO energy level diagram for **5.1<sub>Fe</sub>** and selected orbital depictions.



**Figure D8.** Calculated FMO energy level diagram for  $5.1\text{Fe}^+$  and selected orbital depictions.

**Table D5.** Occupancies of the d orbitals for  $5.1\text{Fe}^-$ ,  $5.1\text{Fe}$  and  $5.1\text{Fe}^+$ .

Anion	Neutral	Cation
-------	---------	--------

$\alpha$ manifold	Occupied (%)	Unoccupied (%)	Occupied (%)	Unoccupied (%)	Occupied (%)	Unoccupied (%)
$d_x^2 - y^2$	80.26	19.74	81.99	18.01	83.68	16.32
$d_{xz}$	80.83	19.17	79.00	21.00	76.63	23.37
$d_{yz}$	85.84	14.16	84.93	15.07	85.02	14.98
$d_z^2$	85.34	14.66	84.21	15.79	83.15	16.85
$d_{xy}$	51.88	48.12	48.10	51.90	48.92	51.08

$\beta$ manifold	Occupied (%)	Unoccupied (%)	Occupied (%)	Unoccupied (%)	Occupied (%)	Unoccupied (%)
$d_x^2 - y^2$	57.88	42.12	63.07	36.93	60.95	39.05
$d_{xz}$	16.23	83.77	13.92	86.08	19.37	80.63
$d_{yz}$	26.74	73.26	29.40	70.60	31.91	68.09
$d_z^2$	15.60	84.40	19.70	80.30	16.21	83.79
$d_{xy}$	28.69	71.31	25.23	74.77	23.29	76.71

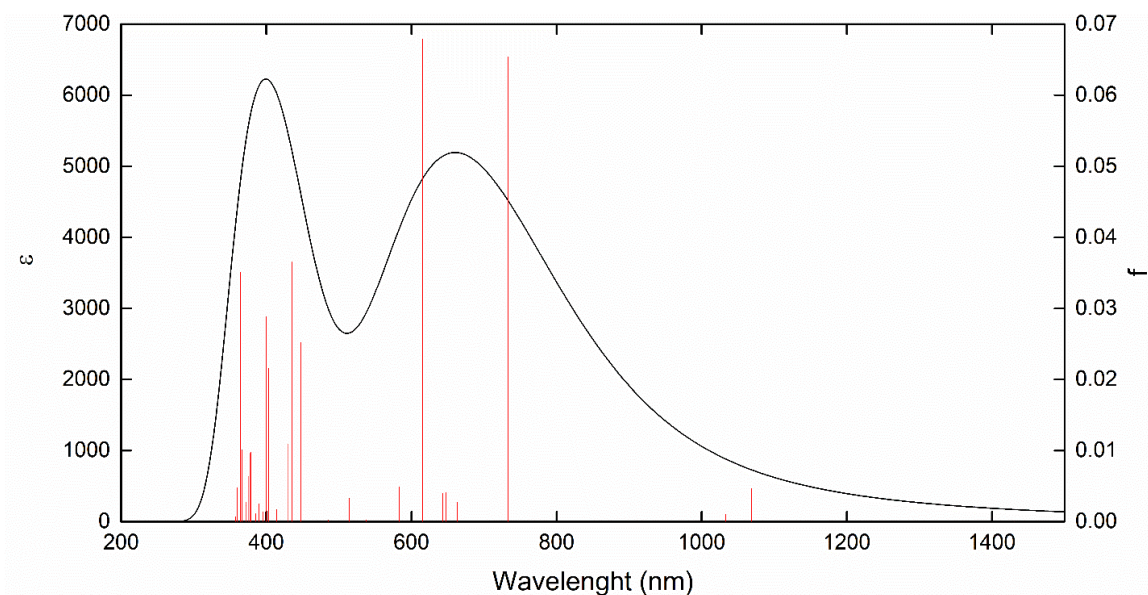


**Figure D9.** Calculated TDDFT spectrum for  $5.1\text{Fe}^+$  (half-field of peak at half-height is  $2500\text{ cm}^{-1}$ ). Spectrum was calculated for first 30 excited states.

**Table D6.** Observed transitions in TDDFT and their composition for  $5.1\text{Fe}^+$ .

wavelength (nm)	oscillator strength*	transition	%	type of transition
1068.7	0.0047	$\beta 137 \rightarrow \beta 143$	63.72	d-d
		$\beta 139 \rightarrow \beta 143$	18.82	LMCT
733.31	0.0654	$\beta 141 \rightarrow \beta 144$	84.35	LMCT
647.39	0.0041	$\alpha 145 \rightarrow \alpha 146$	72.23	LMCT
		$\beta 141 \rightarrow \beta 143$	16.19	LMCT
643.12	0.004	$\beta 141 \rightarrow \beta 145$	85.66	LMCT
615.59	0.0679	$\beta 142 \rightarrow \beta 143$	81.78	LMCT
583.25	0.0049	$\beta 142 \rightarrow \beta 145$	44.15	LMCT
		$\beta 141 \rightarrow \beta 144$	42.20	LMCT
		$\beta 141 \rightarrow \beta 143$	10.15	LMCT
447.85	0.0252	$\beta 140 \rightarrow \beta 143$	96.34	LMCT
435.36	0.0365	$\beta 140 \rightarrow \beta 144$	90.11	LMCT
430.37	0.0109	$\alpha 145 \rightarrow \alpha 147$	87.99	ligand
403.08	0.0216	$\alpha 145 \rightarrow \alpha 148$	56.82	ligand
		$\beta 139 \rightarrow \beta 143$	15.70	LMCT
		$\beta 140 \rightarrow \beta 145$	10.80	LMCT
400.18	0.0288	$\beta 140 \rightarrow \beta 145$	77.10	LMCT
		$\alpha 145 \rightarrow \alpha 148$	17.03	ligand

378.58	0.0098	$\beta 139 \rightarrow \beta 144$ $\alpha 145 \rightarrow \alpha 152$ $\beta 137 \rightarrow \beta 144$	38.59 11.21 10.68	LMCT ligand d-d
366.87	0.0101	$\alpha 145 \rightarrow \alpha 149$	95.82	ligand
364.04	0.0351	$\beta 142 \rightarrow \beta 146$ $\beta 140 \rightarrow \beta 146$ $\beta 143 \rightarrow \beta 146$	27.28 25.62 21.29	LMCT LMCT LMCT
359.81	0.0048	$\beta 139 \rightarrow \beta 145$ $\alpha 144 \rightarrow \alpha 148$ $\beta 141 \rightarrow \beta 146$	43.73 21.47 11.33	LMCT ligand ligand

\* Transitions with oscillator strength higher than 0.004 are shown.

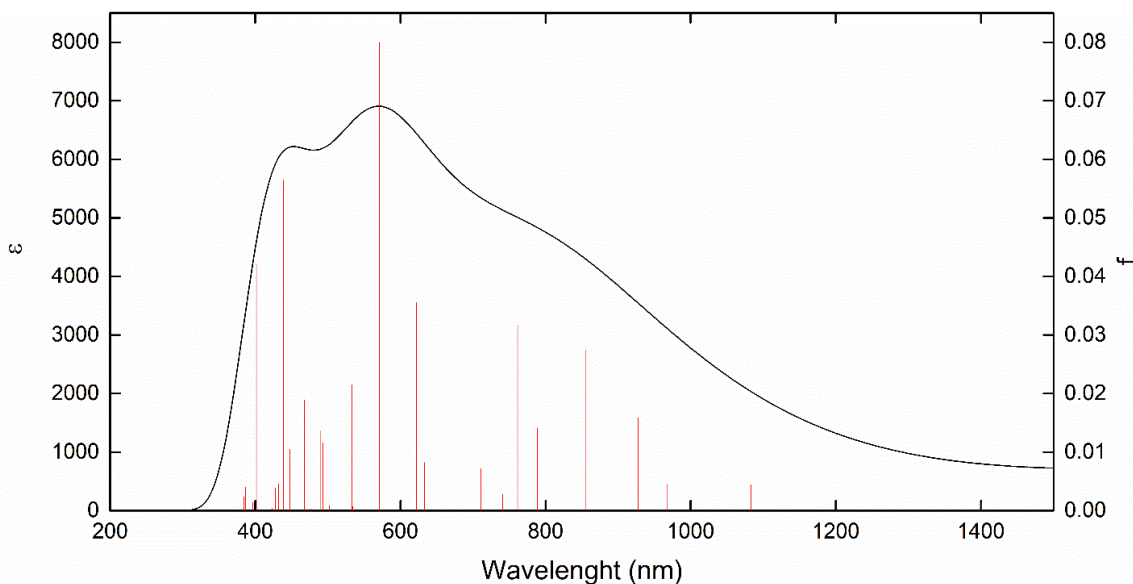


**Figure D10.** Calculated TDDFT spectrum for **1** (half-field of peak at half-height is  $2500 \text{ cm}^{-1}$ ). Spectrum was calculated for first 30 excited states.

**Table D7.** Observed transitions in TDDFT and their composition for **5.1Fe**.

wavelength (nm)	oscillator strength*	transition	%	type of transition
1082.87	0.0044	$\beta 137 \rightarrow \beta 143$ $\beta 138 \rightarrow \beta 143$	29.80 25.83	d-d LMCT
927.61	0.0158	$\alpha 141 \rightarrow \alpha 145$	81.89	ligand
855.76	0.0274	$\alpha 143 \rightarrow \alpha 145$ $\alpha 142 \rightarrow \alpha 145$ $\beta 142 \rightarrow \beta 144$ $\beta 142 \rightarrow \beta 143$	34.86 23.68 12.88 12.42	ligand ligand LMCT LMCT
788.6	0.0140	$\beta 142 \rightarrow \beta 144$ $\alpha 143 \rightarrow \alpha 145$	29.62 23.91	LMCT ligand

Appendices – Appendix C

		$\beta 141 \rightarrow \beta 144$	16.44	LMCT
761.47	0.0317	$\beta 142 \rightarrow \beta 143$	35.36	LMCT
		$\beta 142 \rightarrow \beta 145$	14.22	LMCT
		$\alpha 143 \rightarrow \alpha 145$	12.55	ligand
		$\beta 137 \rightarrow \beta 145$	10.26	d-d
711.10	0.0071	$\beta 142 \rightarrow \beta 145$	50.46	LMCT
		$\beta 141 \rightarrow \beta 145$	18.59	LMCT
633.32	0.0082	$\alpha 144 \rightarrow \alpha 146$	71.39	LMCT
		$\alpha 140 \rightarrow \alpha 145$	21.83	ligand
621.64	0.0356	$\alpha 140 \rightarrow \alpha 145$	49.95	ligand
		$\alpha 144 \rightarrow \alpha 146$	26.66	LMCT
		$\beta 141 \rightarrow \beta 143$	15.59	LMCT
571.09	0.0799	$\beta 141 \rightarrow \beta 143$	54.52	LMCT
		$\alpha 140 \rightarrow \alpha 145$	18.62	ligand
		$\beta 142 \rightarrow \beta 143$	17.56	LMCT
532.8	0.0215	$\beta 141 \rightarrow \beta 144$	51.36	LMCT
		$\beta 142 \rightarrow \beta 144$	17.89	LMCT
493.04	0.0116	$\beta 140 \rightarrow \beta 143$	33.11	LMCT
		$\beta 139 \rightarrow \beta 143$	26.13	LMCT
		$\alpha 135 \rightarrow \alpha 145$	12.43	ligand
		$\alpha 137 \rightarrow \alpha 145$	11.36	ligand
489.37	0.0136	$\alpha 139 \rightarrow \alpha 145$	30.98	ligand
		$\beta 140 \rightarrow \beta 143$	16.56	LMCT
		$\beta 141 \rightarrow \beta 145$	13.21	LMCT
		$\beta 139 \rightarrow \beta 143$	12.90	LMCT
		$\alpha 137 \rightarrow \alpha 145$	11.85	ligand
467.49	0.0189	$\beta 141 \rightarrow \beta 145$	43.72	LMCT
		$\beta 141 \rightarrow \beta 145$	18.16	LMCT
		$\alpha 137 \rightarrow \alpha 145$	14.85	ligand
447.81	0.0104	$\alpha 137 \rightarrow \alpha 145$	54.09	ligand
		$\alpha 135 \rightarrow \alpha 145$	17.95	ligand
		$\alpha 136 \rightarrow \alpha 145$	12.96	ligand
		$\alpha 138 \rightarrow \alpha 145$	11.81	ligand
438.53	0.0564	$\beta 140 \rightarrow \beta 144$	56.71	LMCT
		$\beta 139 \rightarrow \beta 144$	42.00	LMCT
401.62	0.0421	$\beta 140 \rightarrow \beta 145$	49.11	LMCT
		$\beta 139 \rightarrow \beta 145$	39.31	LMCT

\* Transitions with oscillator strength higher than 0.004 are shown.

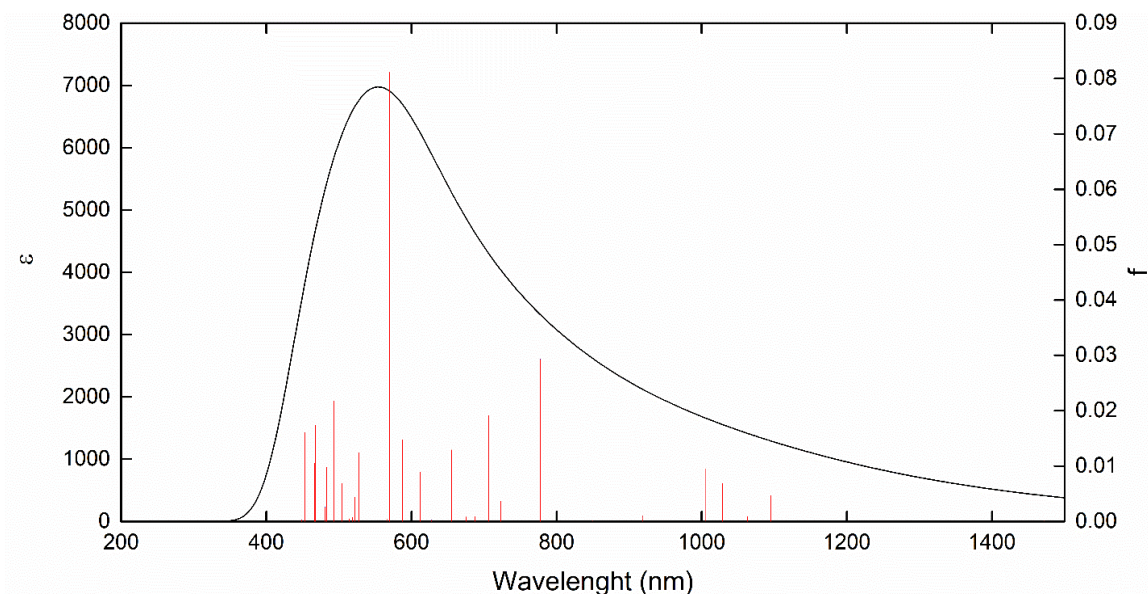


**Figure D11.** Calculated TDDFT spectrum for  $5.1\text{Fe}^+$  (half-field of peak at half-height is  $2500\text{ cm}^{-1}$ ). Spectrum was calculated for first 30 excited states.

**Table D8.** Observed transitions in TDDFT and their composition for  $5.1\text{Fe}^+$ .

wavelength (nm)	oscillator strength*	transition	%	type of transition
1095.52	0.0046	$\beta 134 \rightarrow \beta 143$	47.01	d-d
		$\beta 135 \rightarrow \beta 143$	11.87	LMCT
		$\alpha 142 \rightarrow \alpha 144$	10.30	ligand
1028.88	0.0068	$\alpha 142 \rightarrow \alpha 144$	48.22	ligand
		$\alpha 142 \rightarrow \alpha 145$	17.24	ligand
		$\alpha 143 \rightarrow \alpha 144$	16.60	ligand
1005.82	0.0095	$\alpha 141 \rightarrow \alpha 144$	66.83	ligand
		$\alpha 141 \rightarrow \alpha 145$	20.50	ligand
777.54	0.0293	$\beta 140 \rightarrow \beta 144$	70.13	LMCT
		$\beta 141 \rightarrow \beta 143$	16.03	LMCT
705.99	0.0191	$\beta 141 \rightarrow \beta 143$	53.24	LMCT
		$\beta 140 \rightarrow \beta 144$	21.16	LMCT
		$\beta 140 \rightarrow \beta 145$	10.68	LMCT
655.56	0.0129	$\beta 141 \rightarrow \beta 144$	53.19	LMCT
		$\alpha 140 \rightarrow \alpha 144$	20.53	ligand
587.32	0.0147	$\alpha 139 \rightarrow \alpha 144$	73.31	ligand
		$\alpha 140 \rightarrow \alpha 144$	13.44	ligand
570.10	0.0811	$\alpha 140 \rightarrow \alpha 145$	56.69	ligand
		$\alpha 139 \rightarrow \alpha 145$	16.25	ligand
527.47	0.0124	$\alpha 138 \rightarrow \alpha 144$	60.71	ligand
		$\alpha 139 \rightarrow \alpha 145$	13.04	ligand
		$\alpha 136 \rightarrow \alpha 144$	10.24	ligand

Appendices – Appendix C

		$\beta 141 \rightarrow \beta 145$	10.24	LMCT
493.55	0.0217	$\alpha 137 \rightarrow \alpha 144$ $\alpha 133 \rightarrow \alpha 144$	41.59 35.42	ligand ligand
467.58	0.0174	$\beta 139 \rightarrow \beta 143$ $\alpha 142 \rightarrow \alpha 146$	53.59 21.93	LMCT LMCT
466.30	0.0105	$\beta 139 \rightarrow \beta 143$ $\alpha 141 \rightarrow \alpha 146$ $\alpha 142 \rightarrow \alpha 146$	37.25 28.85 11.32	LMCT LMCT LMCT
453.18	0.0160	$\alpha 138 \rightarrow \alpha 145$ $\alpha 135 \rightarrow \alpha 144$	72.36 14.66	ligand ligand

\* Transitions with oscillator strength higher than 0.004 are shown.

**Table D10.** Occupancies of disordered molecules in THF.

Molecule	Occupancy ratio
O(1),C(29)..C(32)	not disordered (1:0)
O(2),C(33)..C(36)	0.556(15):0.444(15)
O(3),C(37)..C(40)	0.60(2):0.40(2)
O(4),C(41)..C(44)	0.50(2):0.50(2)
O(5),C(45)..C(48)	0.69(3):0.31(3)
O(6),C(49)..C(52)	0.515(14):0.485(14)

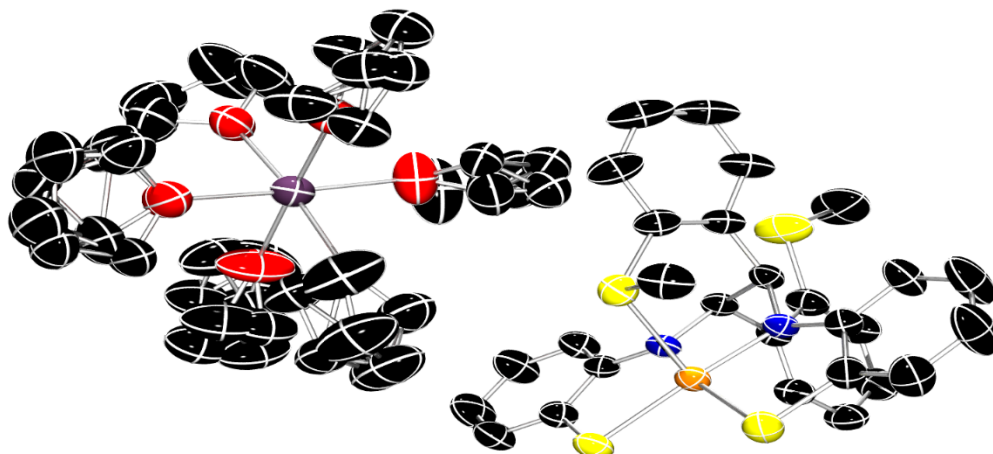


**Figure D12.** Molecular Structure of  $[\text{Na}(\text{THF})_6][\text{Fe}(\text{N}_2\text{S}_3)]$  (**5.1Fe**).

**Table D11.** Crystal data and structure refinement for  $[\text{Na}(\text{THF})_6][\text{Fe}(\text{N}_2\text{S}_3)]$  (**5.1Fe**).

Identification code	Fe[N2S2]anion
Empirical formula	$\text{C}_{52}\text{H}_{72}\text{FeN}_2\text{NaO}_6\text{S}_4$
Formula weight	1028.19
Temperature/K	200(2)
Crystal system	Monoclinic
Space group	$\text{P2}_1/\text{n}$
$a/\text{\AA}$	12.4381(6)
$b/\text{\AA}$	16.6547(7)
$c/\text{\AA}$	26.5220(13)
$\alpha/^\circ$	90
$\beta/^\circ$	102.078(2)
$\gamma/^\circ$	90
Volume/ $\text{\AA}^3$	5372.5(4)
Z	4
$\rho_{\text{calc}}/\text{g/cm}^3$	1.271
$\mu/\text{mm}^{-1}$	0.492
F(000)	2188.0
Crystal size/ $\text{mm}^3$	$0.420 \times 0.300 \times 0.090$
Radiation	$\text{MoK}\alpha$ ( $\lambda = 0.71073$ )
$2\theta$ range for data collection/ $^\circ$	3.14 to 50.5
Index ranges	$-14 \leq h \leq 14, -19 \leq k \leq 19,$ $-31 \leq l \leq 29$
Reflections collected	50812

Independent reflections	9694 [ $R_{\text{int}} = 0.0694$ , $R_{\text{sigma}} = 0.0670$ ]
Data/restraints/parameters	9694/719/748
Goodness-of-fit on $F^2$	1.027
Final R indexes [ $I \geq 2\sigma(I)$ ]	$R_1 = 0.0566$ , $wR_2 = 0.1399$
Final R indexes [all data]	$R_1 = 0.1142$ , $wR_2 = 0.1715$
Largest diff. peak/hole / $e \text{ \AA}^{-3}$	0.74/-0.57

**Table D12.** Bond lengths for  $[\text{Na}(\text{THF})_6][\text{Fe}(\text{N}_2\text{S}_3)]$  (**5.1Fe**).

Atom	Atom	Length/Å	Atom	Atom	Length/Å
C1	C2	1.372(5)	C33'	C34'	1.519(15)
C1	C6	1.423(5)	C33'	C36'	2.04(2)
C1	S1	1.767(4)	C34'	C35'	1.463(14)
C2	C3	1.379(6)	C35'	C36'	1.509(14)
C3	C4	1.383(6)	O3	C37	1.394(6)
C4	C5	1.382(6)	O3	C40'	1.417(11)
C5	C6	1.390(5)	O3	C40	1.477(9)
C6	N1	1.367(4)	O3	Na1	2.403(4)
C7	N1	1.461(4)	C37	C38	1.452(7)
C7	C8	1.522(5)	C38	C39	1.443(11)
C7	C21	1.538(5)	C38	C39'	1.530(13)
C8	C13	1.403(5)	C39	C40	1.443(11)
C8	C9	1.408(5)	C39'	C40'	1.472(13)
C9	C10	1.388(6)	O4	C44	1.390(7)
C10	C11	1.370(7)	O4	C41	1.452(10)
C11	C12	1.376(6)	O4	C41'	1.454(11)
C12	C13	1.393(6)	O4	Na1	2.417(4)
C13	S2	1.794(4)	C41	C42	1.469(12)
C14	S2	1.804(4)	C42	C43	1.491(12)
C15	C16	1.383(5)	C43	C44	1.521(11)
C15	C20	1.420(5)	C44	C43'	1.445(12)
C15	S3	1.760(4)	C41'	C42'	1.484(13)
C16	C17	1.389(6)	C42'	C43'	1.473(13)
C17	C18	1.391(6)	O5	C45	1.418(6)
C18	C19	1.381(5)	O5	C48	1.424(9)
C19	C20	1.401(5)	O5	C48'	1.465(12)
C20	N2	1.368(4)	O5	Na1	2.425(4)
C21	N2	1.463(4)	C45	C46'	1.493(14)
C21	C22	1.517(5)	C45	C46	1.513(9)
C22	C23	1.390(5)	C46	C47	1.435(10)

*Appendices – Appendix C*

C22	C27	1.405(5)	C47	C48	1.397(10)
C23	C24	1.383(5)	C46'	C47'	1.457(14)
C24	C25	1.371(6)	C47'	C48'	1.444(13)
C25	C26	1.381(6)	O6	C49	1.417(12)
C26	C27	1.378(6)	O6	C49'	1.422(11)
C27	S4	1.780(4)	O6	C52	1.423(11)
C28	S4	1.785(5)	O6	C52'	1.442(12)
C29	O1	1.383(6)	O6	Na1	2.393(4)
C29	C30	1.472(8)	C49	C50	1.517(14)
C30	C31	1.480(8)	C50	C51	1.479(12)
C31	C32	1.492(8)	C51	C52	1.505(13)
C32	O1	1.415(6)	C49'	C50'	1.521(13)
O2	C36	1.410(9)	C50'	C51'	1.498(11)
O2	C36'	1.432(12)	C51'	C52'	1.505(13)
O2	C33	1.439(10)	Fe1	N1	1.859(3)
O2	C33'	1.440(12)	Fe1	N2	1.876(3)
O2	Na1	2.407(4)	Fe1	S3	2.2262(11)
C33	C34	1.572(12)	Fe1	S1	2.2267(11)
C34	C35	1.503(12)	Fe1	S2	2.5601(12)
C35	C36	1.459(11)	Na1	O1	2.381(4)

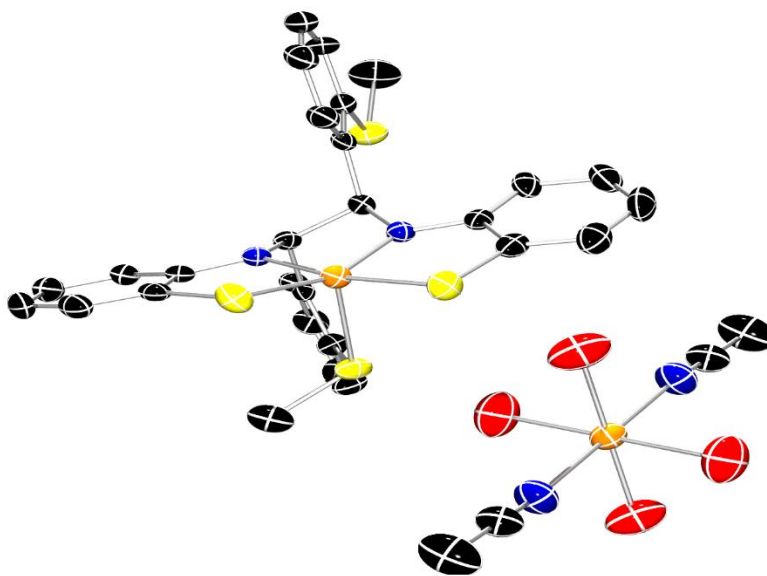


**Figure D13.** Molecular Structure of  $[\text{Fe}(\text{N}_2\text{S}_3)][\text{Fe}(\text{OH})_2(\text{NCMe})_4]$  (**5.1<sub>Fe</sub>**) (monomer).

**Table D13.** Crystal data and structure refinement for  $[\text{Fe}(\text{N}_2\text{S}_3)][\text{Fe}(\text{OH})_2(\text{NCMe})_4]$  (**5.1<sub>Fe</sub>**) (monomer).

Identification code	Fe[N <sub>2</sub> S <sub>2</sub> ]
Empirical formula	C <sub>64</sub> H <sub>66</sub> N <sub>8</sub> O <sub>4</sub> S <sub>8</sub> Fe <sub>3</sub>
Formula weight	1435.27
Temperature/K	200.05
Crystal system	Triclinic
Space group	P-1
a/Å	7.682(3)
b/Å	11.492(4)
c/Å	20.435(8)
α/°	92.702(5)
β/°	100.625(5)
γ/°	108.191(5)
Volume/Å <sup>3</sup>	1673.9(11)
Z	1
ρ <sub>calc</sub> /cm <sup>3</sup>	1.424
μ/mm <sup>-1</sup>	0.943
F(000)	744.0
Crystal size/mm <sup>3</sup>	0.32 × 0.17 × 0.15
Radiation	MoKα (λ = 0.71073)
2θ range for data collection/°	3.754 to 56.856
Index ranges	-10 ≤ h ≤ 10, -15 ≤ k ≤ 15, -27 ≤ l ≤ 27
Reflections collected	17240
Independent reflections	17240 [R <sub>int</sub> = ?, R <sub>sigma</sub> = 0.0841]
	324

Appendices – Appendix C

Data/restraints/parameters	17240/4/408
Goodness-of-fit on F <sup>2</sup>	0.979
Final R indexes [I>2σ (I)]	R <sub>1</sub> = 0.0533, wR <sub>2</sub> = 0.1037
Final R indexes [all data]	R <sub>1</sub> = 0.0884, wR <sub>2</sub> = 0.1165
Largest diff. peak/hole / e Å <sup>-3</sup>	0.69/-0.42

**Table D14.** Bond Lengths for [Fe(N<sub>2</sub>S<sub>3</sub>)]Fe(OH)<sub>2</sub>(NCMe)<sub>4</sub> (**5.1<sub>Fe</sub>**) (monomer).

Atom	Atom	Length/Å	Atom	Atom	Length/Å
Fe1	S1	2.2289(16)	C13	C14	1.376(7)
Fe1	N8	1.866(4)	C14	C15	1.392(6)
Fe1	S18	2.2319(15)	C15	S16	1.772(5)
Fe1	N25	1.864(4)	S16	C17	1.788(5)
Fe1	S33	2.5266(16)	S18	C19	1.773(5)
Fe2	N35	2.188(4)	C19	C20	1.354(6)
Fe2	N35 <sup>1</sup>	2.188(4)	C19	C24	1.416(6)
Fe2	O38 <sup>1</sup>	2.189(5)	C20	C21	1.379(7)
Fe2	O38	2.189(5)	C21	C22	1.382(7)
Fe2	O39 <sup>1</sup>	2.206(4)	C22	C23	1.373(6)
Fe2	O39	2.206(4)	C23	C24	1.405(6)
S1	C2	1.766(5)	C24	N25	1.361(5)
C2	C3	1.387(6)	N25	C26	1.460(5)
C2	C7	1.396(6)	C26	C27	1.532(6)
C3	C4	1.404(7)	C27	C28	1.378(6)
C4	C5	1.369(7)	C27	C32	1.395(6)
C5	C6	1.384(6)	C28	C29	1.381(6)
C6	C7	1.404(6)	C29	C30	1.348(7)
C7	N8	1.378(5)	C30	C31	1.364(7)
N8	C9	1.461(5)	C31	C32	1.398(6)
C9	C10	1.509(6)	C32	S33	1.785(5)
C9	C26	1.551(6)	S33	C34	1.814(5)
C10	C11	1.393(6)	N35	C36	1.115(6)
C10	C15	1.406(6)	C36	C37	1.450(7)
C11	C12	1.387(6)	C41	C42	1.453(8)
C12	C13	1.374(7)	C41	N40	1.107(7)

## Appendix E – Copyright Permission

 **ACS Publications**  
Most Trusted. Most Cited. Most Read.

**Mechanistic Study of Metal–Ligand Cooperativity in Mn(II)-Catalyzed Hydroborations: Hemilabile SNS Ligand Enables Metal Hydride-Free Reaction Pathway**

**Author:** Matthew R. Elsby, Mina Son, Changjin Oh, et al  
**Publication:** ACS Catalysis  
**Publisher:** American Chemical Society  
**Date:** Aug 1, 2021

*Copyright © 2021, American Chemical Society*

### PERMISSION/LICENSE IS GRANTED FOR YOUR ORDER AT NO CHARGE


This type of permission/license, instead of the standard Terms and Conditions, is sent to you because no fee is being charged for your order. Please note the following:

- Permission is granted for your request in both print and electronic formats, and translations.
- If figures and/or tables were requested, they may be adapted or used in part.
- Please print this page for your records and send a copy of it to your publisher/graduate school.
- Appropriate credit for the requested material should be given as follows: "Reprinted (adapted) with permission from {COMPLETE REFERENCE CITATION}. Copyright {YEAR} American Chemical Society." Insert appropriate information in place of the capitalized words.
- One-time permission is granted only for the use specified in your RightsLink request. No additional uses are granted (such as derivative works or other editions). For any uses, please submit a new request.

If credit is given to another source for the material you requested from RightsLink, permission must be obtained from that source.

BACK

CLOSE WINDOW

 **ACS Publications**  
Most Trusted. Most Cited. Most Read.

**Iron-SNS and -CNS Complexes: Selective Caryl–S Bond Cleavage and Amine-Borane Dehydrogenation Catalysis**

**Author:** Matthew R. Elsby, Karine Ghostine, Uttam K. Das, et al  
**Publication:** Organometallics  
**Publisher:** American Chemical Society  
**Date:** Oct 1, 2019

*Copyright © 2019, American Chemical Society*

### PERMISSION/LICENSE IS GRANTED FOR YOUR ORDER AT NO CHARGE

This type of permission/license, instead of the standard Terms and Conditions, is sent to you because no fee is being charged for your order. Please note the following:

- Permission is granted for your request in both print and electronic formats, and translations.
- If figures and/or tables were requested, they may be adapted or used in part.
- Please print this page for your records and send a copy of it to your publisher/graduate school.
- Appropriate credit for the requested material should be given as follows: "Reprinted (adapted) with permission from {COMPLETE REFERENCE CITATION}. Copyright {YEAR} American Chemical Society." Insert appropriate information in place of the capitalized words.
- One-time permission is granted only for the use specified in your RightsLink request. No additional uses are granted (such as derivative works or other editions). For any uses, please submit a new request.

If credit is given to another source for the material you requested from RightsLink, permission must be obtained from that source.

BACK

CLOSE WINDOW

## VITA AUCTORIS

NAME: Matthew Ryan Elsby

PLACE OF BIRTH: Windsor, ON

YEAR OF BIRTH: 1993

EDUCATION: Holy Names High School, Windsor, ON, 2011

University of Windsor, B.Sc., Windsor, ON, 2015

University of Windsor, M.Sc., Windsor, ON, 2017

University of Ottawa, Ph.D., Ottawa, ON, 2021